Prifysgol Cymru
Y Drindod Dewi Sant
University of Wales
Trinity Saint David

Multi-Angle Beam Generation and Steering via Meander-Line-Coil EMATs

by

Sam Hurrell

Supervised by: Professor Peter Charlton, Dr Stephen Mosey

This research was undertaken under the auspices of TWI Technology Centre Wales

Submitted in partial fulfilment for the award of the degree of Doctor of Philosophy

University of Wales Trinity Saint David

2025

Abstract

This thesis investigates Meander-Line Coil (MLC) Electromagnetic Acoustic Transducers (EMATs) for the purposes of Non-Destructive Testing (NDT), focusing on their theoretical foundations, simulated modelling, and experimental validations. Whilst the detection of defects was not investigated, this work thoroughly examines the EMAT's capability as a conventional transducer to steer the angle of its oblique ultrasonic waves. This culminates in the innovative generation of multi-angle bulk waves simultaneously from a single EMAT. The practical applications of a multi-angle EMAT include the ability to perform sectoral scans, currently only possible by Phased Array (PA) Ultrasonic Testing (PAUT). This is beneficial as EMATs are not restricted to using a coupling liquid for their operation, allowing them to be used on high-temperature materials or in hazardous areas where a coupling medium is unacceptable.

The thesis begins with an overview of modern NDT methods (particularly Ultrasonic Testing (UT)) and explores the principles of electromagnetism relevant to EMATs. An in-depth analysis of EMATs covers their transduction methods, design configurations, and historical development, along with their associated electronic circuitry.

A significant portion of this thesis involves constructing and validating a 2D Finite Element Method (FEM) model of the MLC EMAT using 'COMSOL Multiphysics' and understanding its properties through parametric studies. The following experimental validation focuses on the MLC EMAT's performance on non-ferromagnetic workpieces in comparison to the simulations to assess their accuracy. Further investigations examine the transmitted bulk waves via parametric studies on both the EMAT's magnetic and coil configurations. This research concludes with an exploration of generating multi-angle bulk waves by modifying the transmission signals through EMAT coils. These waves are analysed using the Fast Fourier Transform (FFT) to extract an individual angle's A-scan from the overall complex signal received, demonstrating the feasibility of this novel approach.

This study shows that EMATs can accurately steer the direction of their bulk waves as a function of frequency, supported by reliable simulated modelling and experimental evidence. The primary outcome of the research is the proof of concept for simultaneous transmission and reception of multi-angle waves via EMAT technology. This has the potential to enhance the EMAT's defect detection by an increased coverage, the triangulation of these defects from different angled waves, and a greater range of flaw orientation.

Acknowledgements

I would start by expressing my gratitude to my UWTSD supervisor Professor Peter Charlton, for his support and guidance over the duration of this study. His scientific attitude and devotion to research was incredibly influential in the way I conducted my own. I am grateful also to my co-supervisor Doctor Stephen Mosey for his technical support and advice on electrical theory and writing.

To my colleagues at TWI Technology Centre Wales (past and present), the NDT research environment has been a fantastic location to conduct this study. My thanks goes particularly to Doctor Owen Rees-Lloyd, as his previous study in EMATs built the foundation for my research. His day-to-day support guided me both academically and professionally. I would also like to thank Doctor Richard Lewis for his industrial supervision. His procurement of both laboratory equipment ensured that this PhD could have taken place. I extend my thanks to the funding from both Knowledge Economy Skills Scholarship (KESS 2) and TWI Ltd.

Lastly, I would like to thank my Jenny, whose love and patience towards me cannot be overestimated.

Contents

Glossary

AC	Alternating Current
AE	Acoustic Emission
CFL	Courant-Friedrichs-Lewy
CSA	Cross Sectional Area
DC	Direct Current
ECT	Eddy Current Testing
EMAT	Electro-Magnetic Acoustic Transducer
EMF	Electro-Motive Force
FEM	Finite Element Method
FFT	Fast Fourier Transform
MFL	Magnetic Flux Leakage
MLC	Meander-Line-Coil
NDT	Non-Destructive Testing
PA	Phased Array
PC	Pitch-Catch
PE	Pulse-Echo
PI	Penetrant Inspection
PLA	Poly-Lactic Acid
PPM	Periodic Permanent Magnet
PRF	Pulse Repetition Frequency
RLC	Resistor-Inductor-Capacitor
RSU	Roller Sperry Unit
RToA	Relative Time of Arrival
R_x	Reception EMAT
SDP	Standard Depth of Penetration
SF	Scale Factor
SH	Shear-Horizontal
SHM	Structural Health Monitoring
SNR	Signal-to-Noise Ratio
SV	Shear-Vertical
ToA	Time of Arrival
ToF	Time of Flight
T_x	Transmission EMAT
UT	Ultrasonic Testing

Nomenclature

v_c	Compression Wave Velocity (m/s)
v_s	Shear Wave Velocity (m/s)
f	Frequency (Hz)
λ	Wavelength (m)
θ	Angle (°)
E	Electric field strength (V/m)
ρ_v	Volume charge density (C/m³)
ε_0	Permittivity of free space (F/m)
B	Magnetic flux density (T)
t	Time (s)
μ_0	Permeability of free space (H/m)
I	Current (A)
r	Radius (m)
J_e	Electric current density (A/m²)
H	Magnetic field strength (A/m)
F_L	Lorentz Force Density (N/m²)
u	Displacement (m)
d	Coil spacing (m)
Z	Electrical Impedance (Ω)
R	Resistance (Ω)
X_L	Inductive Reactance (Ω)
X_C	Capacitive Reactance (Ω)
V	Voltage (V)
f_{res}	Resonant Frequency (Hz)
L	Inductance (H)
C	Capacitance (F)
δ	Standard Depth of Penetration (m)
σ_e	Electrical conductivity (S)
h_{max}	Maximum Mesh size (m)
N	Number of mesh elements per wavelength (1/m)
Δ	Change in
τ	Time delay (s)
σ	Standard deviation (s)
x	x-position (m)

Chapter 1 - Introduction

1.1. Motivation

During the 19th century, as a result of the industrial revolution, the railway network boomed as goods could be transported faster, cheaper, in greater quantities, and across larger distances [1]. This took a toll on the iron rails (meant as a superior replacement to the wood-steel composite rails) until it was accepted that they were too brittle and too weak due to their required replacement every three months. The first steel rails were made in England in 1857, and a steel railroad was trialled in 1862, proving their advantage of increased strength and flexibility over iron [2]. By the 1900s, the flat bottomed T-rail (seen in Figure 1.1) had become the most popular rail profile and continues to be so. Whilst the steel rails today remain strong, they are not immune to damage and like the previous iron rails, they require regular inspection to prevent service failure.

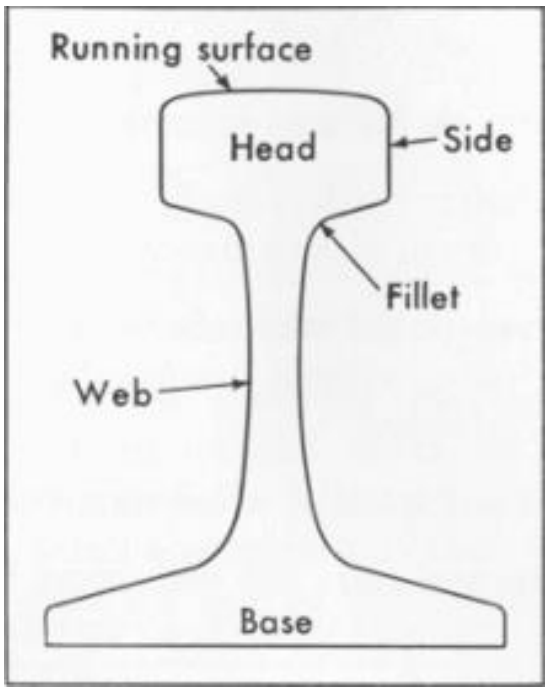

Figure 1.1: Flat Bottomed T-Rail [3]

Rail track may possess different types of defects due to being subjected to different sources of external damage. Such damage includes sudden compressive loads from the weight of moving trains, thermal fatigue from changing yearly climate causing expansion, and corrosion (such as rust) from

environmental exposure. Crack defects can initiate at the track's surface boundary and propagate through the material due to various sources of fatigue stress. These defects grow until reaching a critical crack length, at which the remaining uncracked material is incapable of supporting the load and thus rapidly fractures. Such defects have led to train derailment and loss of life [4], so it is as important as ever to locate these growing defects before they can reach a critical length. Figure 1.2 shows an example of rail track with various internal defects that can occur.

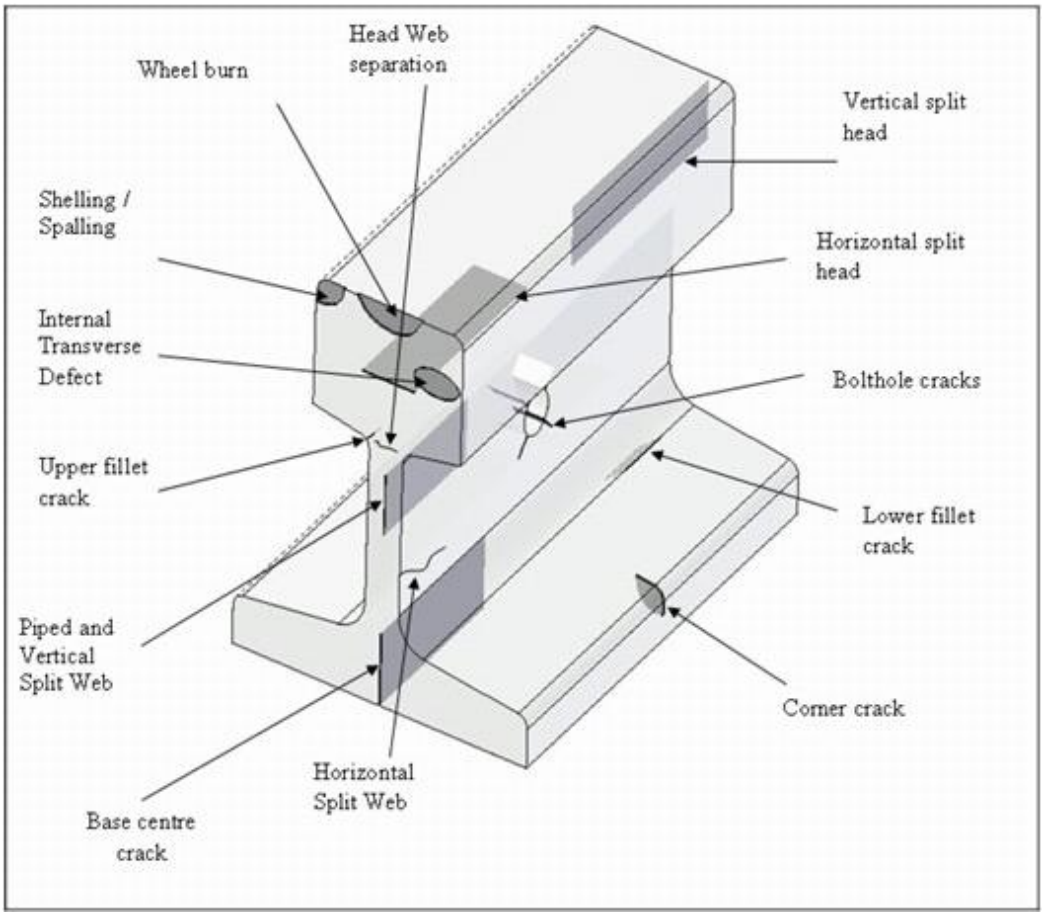

Figure 1.2: Internal Rail Defects [5]

The ability to evaluate the state of a component is a crucial aspect of industry, as it allows for the detection and measurement of internal features within material components. Within the context of rail track inspection, this is a necessity as reliable safety assurances are paramount for the wellbeing of the general public. Non-Destructive Testing (NDT) methods are used to monitor the physical state of materials without permanently damaging the material, and different methods have been employed throughout the history of rail track inspection [6, 7, 8, 9].

Rail inspections were originally performed visually by inspectors walking along the installed track with a Sands mirror [10]. Though accepted as the most efficient method of inspection at the time, this method was incapable of detecting internal defects. One such defect is an internal transverse fissure at the head of the rail, which caused the derailment in Manchester, New York in 1911 that killed 29 people and injured 62 more [11]. This incident brought the transverse defect into infamy and encouraged other railroads to investigate their rails for the presence of these internal defects. The result of these investigations showed that the transverse fissure was prevalent and galvanised the development of an inspection method that could locate and size internal defects in the rails. In 1923, Dr. Elmer Sperry started development on a detector car that could use magnetic induction to scan for rail defects whilst in motion, and the first working detector car was built in 1927. In 1949, the modification of the detector car to include Ultrasonic Testing (UT) was offered, and by 1960 the process of UT had developed to the point of automation so as to work in tandem with the induction method [3].

Sperry Rail's transition from magnetic induction to ultrasonic testing led to the invention of the ultrasonic wheel probe, also known as a Roller Search Unit (RSU) [12], seen in Figure 1.3. The RSU consists of an assembly of nine ultrasonic probes within a couplant filled wheel that allows for rolling contact across a rail's top surface. Fixed in position relative to the rail's top surface, the RSU's probe assembly consists of probes at different angles to transmit angled ultrasonic beams into the steel rail (as seen later in Figure 2.13). The angles within the steel are at 0° (normal to the rail's surface as seen in Figure 1.3), and both 37° and 70°, each in a forward and backward facing direction. Three 70° probes in each direction are used to scan the entirety of the rail head for longitudinal defects, and the 0° and 37° probes scan the rail web for cracks propagating from the bolt holes. The assembly's coverage moves laterally across the rail as the wheel's outer surface (also called the tyre) rotates onto the rail and conforms over the rail head. For efficient ultrasonic transmission, liquid couplant is required between the polyurethane tyre and the rail's surface. Whilst in motion, the probes generate ultrasonic waves which travel through the tyre, into the steel, and reflect off of any internal defects that are

present (such as those seen in Figure 1.2). The reflected waves return to the RSU and are received by the probes. A defect propagating in the same orientation as an ultrasonic wave pathway would likely go undetected, however multiple waves at different angles allow for a higher probability of detection.

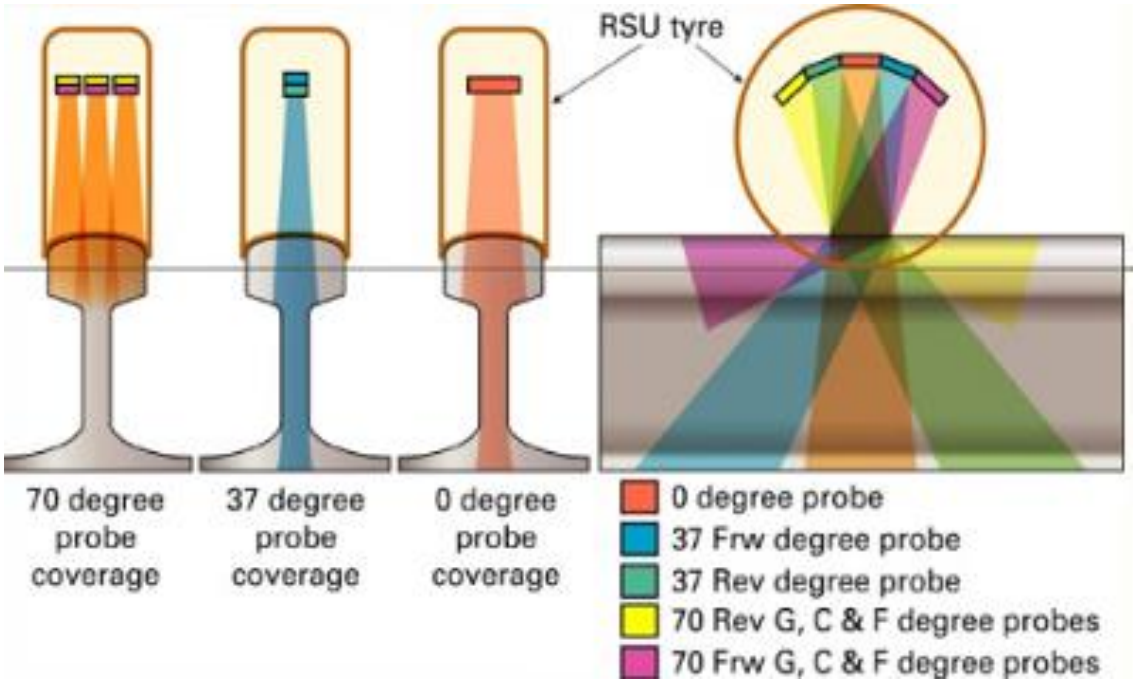

Figure 1.3: Sperry RSU Design [13]

The RSU can be used in both a forward and backward direction and can be mounted onto Sperry trains or manual Sperry sticks [14]. Whilst capable of running up to speeds of 65km/h, the trains are driven at speeds of 45km/h to ensure safe and accurate detection of defects making them capable of scanning 150-210km of rail track in a single night. Sperry sticks are pedestrian versions of the RSU that are manually pushed along the rail to confirm the presence of the defects detected by the train. Comparing the results from the Sperry train to the Sperry stick showed a 90-95% success rate in the identification of defects, and the Sperry stick's increased accuracy via its low speed enables it the capability of sizing internal defects [15]. Further development is ongoing to improve the success rate of the RSU on the Sperry trains in order to minimise the deployment time for the Sperry stick and staff.

Traditional UT has limitations however, most notably its reliance on a liquid couplant to facilitate the transmission of the ultrasonic waves between the probe and material. An NDT method that overcomes this necessity is the Electromagnetic Acoustic Transducer (EMAT) [16], which utilises eddy current

fields induced in an electrically conductive material, within a bias magnetic field to produce Lorentz forces. These forces, acting near the surface of the material, generate ultrasonic waves that travel into the bulk material or across the material's surface. Different configurations of the magnet and coils are used to transmit different ultrasonic wave modes. Once such configuration is the Meander-Line-Coil (MLC) EMAT, which is capable of transmitting angled ultrasonic waves into the material or across the material's surface. Studies have shown that this EMAT configuration is capable of changing the ultrasonic beam's angle of propagation by changing its physical design or frequency of the induced eddy currents (as defined in Figure 2.14) [17, 18, 19].

1.2. Aims and Objectives

The aim of this work was to evaluate the possibility of replicating the Sperry RSU's coherent multi-angle ultrasonic methodology with EMAT technology, specifically investigating the feasibility of transmitting ultrasonic waves at its angles of 0°, 37°, and 70°. Additionally, the capacity of steering the ultrasonic bulk waves by changing its angle via frequency. This would overcome the necessity to manually exchange the UT probes for ones of different angles.

Building on previous work with surface wave MLC EMATs [20], the novelty of this work incorporated: the steering of angled shear waves transmitted from an MLC EMAT; a study on the physical design of the EMAT; and the transmission of shear waves at multiple angles simultaneously. Objectives of this study included:

- Design of a Finite Element Method (FEM) model of an MLC EMAT generating ultrasonic waves within a metallic sample. Due to the complexities of simulating the magnetostriction mechanism, these samples would be made of aluminium (for reasons stated in Chapter 3).
- Analysis of the effects of steering on the MLC EMAT's bulk wave directivity and magnitude.
- Investigation into the performance of the MLC EMAT when transmitted with a signal of multiple individual signals simultaneously.

1.3. Organisation of the Thesis

This thesis is structured into eight chapters. Listed below are the purposes of each chapter followed by a brief summary of what each contains.

Chapter 1 serves as an introduction, providing the historical context that motivated this work. The general aims and objectives of the study are also stated, as well as the structure of the thesis and the novel contributions to knowledge that were a direct result from this work.

Chapter 2 is devoted to the background theory of the relevant knowledge. The chapter begins with an assessment of modern day NDT methods, especially a detailed summary of UT. The topic of electromagnetism is then explored to describe the interaction between the electric and magnetic fields, providing a foundation to the EMAT's method of wave transmission and detection. A large proportion of this chapter is dedicated to the subject of EMATs themselves, detailing their transduction methods, design configurations, and electronic circuitry. This chapter closes with a scientific literature review of the research that has gone into EMATs and concludes with an overview of the major conclusions drawn from this chapter.

Chapter 3 explains the use of FEM via 'COMSOL Multiphysics'. This chapter details the model's 2D structural geometry and physics interfaces that enabled the models to simulate the operation of the EMAT. Included also are parametric studies on the EMAT's constituent magnet and coils, illustrating the effect that each has on the EMAT's overall performance. The chapter closes with a description of the simulated EMAT model used for the majority of the thesis.

Chapter 4 provides the results from both the simulated and experimental testing. The chapter begins with a description of the experimental test setup and its differences from the FEM model. The samples chosen for both testing methods possessed geometries that would enable the EMAT's beam directivity to be graphed across a range of steering angles. Selected simulations were then experimentally tested within the laboratory to validate their accuracy, and those of the simulated results as a whole.

Chapter 5 continues the work of Chapter 4, but with a focus on how the EMAT's beam directivity is affected by changes to the EMAT's magnetic configuration. These changes include: the number of magnets used; the width of the magnet(s); and their orientation. This work was conducted primarily through FEM modelling, however one of the alternate magnetic configurations was selected for experimental validation.

Chapter 6 explores the effect that the coils played on the EMAT's beam directivity. Numerous parametric studies were conducted including: the shear wave steering angles; the number of coils within the array; and the coil spacing. These were carried out in order to push the steering limits set by the previous two chapters.

Chapter 7 examines the EMAT's capability to generate multi-angle shear waves. These used the same simulation setup as the work in Chapters 4 and 5, however the transmission signals through the coils was altered to produce separate angled waves simultaneously. This chapter explores the permutation of angles that could be steered, determined via Fast Fourier Transform (FFT), and how their results could be filtered and used for real-world applications.

Chapter 8 ends the thesis with a discussion of the major conclusions drawn, followed by a summary of the work presented, and the suggested directions for future work to follow.

1.4. Contributions of the Thesis

Within the duration of this work, many unique and novel discoveries were made in the area of MLC EMATs for shear wave generation. The contributions of this work include:

- A study on the relationship between the theoretical steering angle of the shear wave and: its actual reception angle; its magnitude; and its coverage. This was achieved through the use of experimentally validated simulated models.

- A proposed method of simulating an EMAT's reception signal using displacement data extracted from the simulations. This negated the necessity for more complex modelling methods and provided a simple solution to process results for a higher degree of accuracy.
- Parametric studies on the effects that the EMAT's magnetic field had on the shear waves across steering angles. These include:
    - The width of the magnet
    - The number of magnets within a single EMAT
    - The directions of magnetisation
    - The configurations within pitch-catch setups
- Parametric studies on the effects that the EMAT's coil configuration had on the shear waves across steering angles. These include:
    - The number of coils within an array
    - The coil spacing
- Evaluation and development of a multi-angle steering MLC EMAT utilising complex transmission signalling. This work utilises the previous chapters to create a custom beam directivity with numerous maxima that could prove capable of defect location.

1.5. Publications

Journal Papers:

1. S. Hurrell, P. Charlton, S. Mosey, O. Rees-Lloyd, R. Lewis. Study on the steering capability of a meander-line coil EMAT. *Insight*, 65 (2), February 2023, pp 95-102. Awarded the John Grimwade medal at the 61st annual BINDT conference September 2024.

Conference Papers:

1. S. Hurrell, P. Charlton, S. Mosey, O. Rees-Lloyd, R. Lewis. Study on the Beam Directivity of a Steerable Meander-Line Coil EMAT. Presented at BINDT Telford September 2022.

2. S. Hurrell, P. Charlton, S. Mosey, O. Rees-Lloyd, R. Lewis. Multi-Angle Steering of a Meander-Line Coil EMAT. Presented at BINDT Edinburgh September 2025. Awarded the William Gardner award.

Chapter 2 - Theory

2.1. Introduction

This chapter presents the background theory and basic principles of EMATs, whilst simultaneously reviewing the historical literature on their operation and development within real world applications. The chapter begins with a look into various NDT techniques, before a more thorough investigation into the technique of ultrasonic testing. Maxwell's electromagnetic equations are later discussed followed by an assessment of magnetic materials, as these topics directly relate to the transmission and reception of EMATs. EMATs themselves are reviewed in great detail, specifically their transduction methods, configurations, and applications, highlighting their primary advantages and limitations.

2.2. Methods of Non Destructive Testing (NDT)

NDT encompasses a wide variety of inspection methods, capable of measuring defects at and beneath the surface of materials without creating long term damaging effects. Different NDT techniques exist in order to detect and examine different types of defects within a variety of materials. A limitation to many of these methods are the types of material that can be tested. A thorough cleaning of the test part or removal of painted coatings may be required to access the area under inspection. Conversely, the area may need to be coated in a coupling substance to adhere sensors to the component's surface and facilitate their inspection. In most cases however, these NDT methods are both expensive and cumbersome to employ when inspecting large areas of material.

2.2.1. Penetrant Inspection (PI)

PI can be divided into a colouring method and a fluorescence method, but the working principle is the same. The material to be examined must be cleaned of contaminants, and a liquid penetrant is applied to seep into any surface-breaking defects. The excess penetrant is then removed, and a powder-based

developer applied to make the penetrant-filled defect visible. The colouring method displays the penetrant-filled defects under visible light, whilst the fluorescence method displays them under the irradiation of ultraviolet light [21].

2.2.2. Magnetic Flux Leakage (MFL)

MFL uses magnetic phenomena to detect surface and near-surface defects within ferromagnetic materials. The working principle is that when a ferromagnetic material is magnetized, defects cause local distortion of the magnetic flux resulting in magnetic flux leakages from these defects. Magnetic sensors can detect this flux leakage, and be analysed to interpret the locations and depth of the defect [22].

2.2.3. Acoustic Emission (AE)

AEs are the radiation of elastic waves travelling through a material. These are emitted when the material experiences a sudden change to its structure (such as cracking, impacting, or plastic deformation). The waves from these defects propagate through the material as elastically deforming waves, which are detected by piezoelectric transducers. Unlike NDT methods, AE is a Structural Health Monitoring (SHM) method, whereby the equipment can be left on the testing material to continuously monitor for lengthy periods of time. Multiple sensors are used to triangulate the source of the wave via Time of Arrival (ToA) [23].

2.2.4. Eddy Current Testing (ECT)

ECT deploys an electrical coil fed by an Alternating Current (AC) to induce alternating electrical currents into an electrically conductive material. These included currents are known as eddy currents, and the direction of their magnetic field is such that it opposes the direction of the changing magnetic field inducing them (according to Lenz's law). ECT uses its coil to simultaneously induce and measure the eddy currents within the sample via their electrical impedance. Any variations to the coil's electrical resistance and inductive reactance may suggest defects within the material's structure. This

method is limited to electrically conductive materials (primarily metallic materials, graphite, and carbon fibre composites) [24]. Understanding their electromagnetic principles was crucial to the topic of EMATs and are discussed in greater detail later in Section 2.5.4.

2.3. Ultrasonic Testing (UT)

UT remains one of the most popular methods of NDT [25]. The working principle behind this method involves high-frequency sound energy in the form of ultrasonic waves transmitted from the surface of a material by a transducer. These waves travel through the material and reflect off of any changes in acoustic impedance that they encounter. These changes can be caused by cracks, density changes, or the back surface of the opposite side of the material. The times that the reflected waves arrive at a receiver are recorded and graphed on a computer as an A-scan (amplitude against time).

Defect signals indicate the size, depth, and type of damage within the material. UT can be applied to fields such as flaw detection, dimensional measuring, and material characterization. It is common for this NDT method to use a Pulse-Echo (PE) configuration, where a single transducer is used as emitter and receiver, but it may also be performed via a Pitch-Catch (PC) setup, where two transducers act as either emitter or receiver. An example of UT used to detect a defect in a PE setup is seen in Figure 2.1.

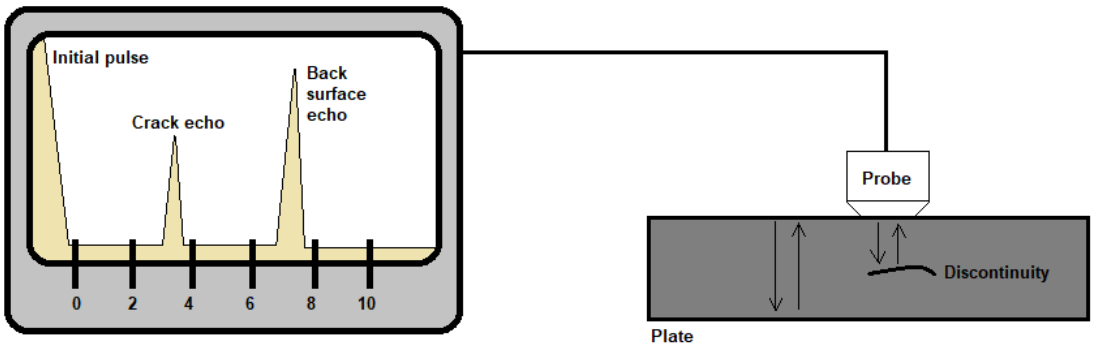

Figure 2.1: Ultrasonic Testing Operation Example [26]

2.3.1. Advantages and Disadvantages of UT

As with all NDT methods, UT holds many strengths and weaknesses compared to other methods. A list of the key advantages and disadvantages is shown in Table 2.1.

Table 2.1. UT Advantages and Disadvantages

Advantages	Disadvantages
Sensitive to surface/subsurface defects	Surface must be accessible
Used on a wide range of materials	Skill and training required
Best penetration depth for flaw detection	Couplant required
Only single-sided access needed	Complex dimensions are difficult to inspect (rough, irregular shape, small, thin, non-homogenous materials)
Highly accurate for determining flaw size and shape	Linear defects parallel to sound beam may go undetected
Minimal part preparation required	Reference standards required
Instantaneous results	
Detailed images produced	

The ultrasonic wave velocity is determined by the elastic modulus of the material it travels through. The frequency of the ultrasonic wave is set to determine its wavelength within the material, shown in Equation 2.1. For a defect to stand a reasonable chance of detection, the frequency chosen must allow the wavelength to be no more than double the size of the defect. This means that discontinuities smaller than this distance possess a lower chance of being detected. The sensitivity therefore increases with frequency, however if the frequency is too high then sound would tend to scatter from the coarse grain structure and any small material imperfections. In these cases, lower frequencies are required for these evaluations [25].

$$v = f \times \lambda \qquad \text{Equation 2.1}$$

where v = wave velocity of a material (m/s); f = frequency of the wave (Hz); λ = wavelength (m).

In order to measure with ultrasonic waves at an angle, a wedge is introduced between the piezoelectric probe and the material's surface, shown

in Figure 2.2. The shape of the wedge enables the wave to be refracted into the material at a single fixed angle, allowing for flaws to be detected from side on. Depending on the size of the material, the waves could reflect off of the backwall to improve the detectability of flaws close to the surface.

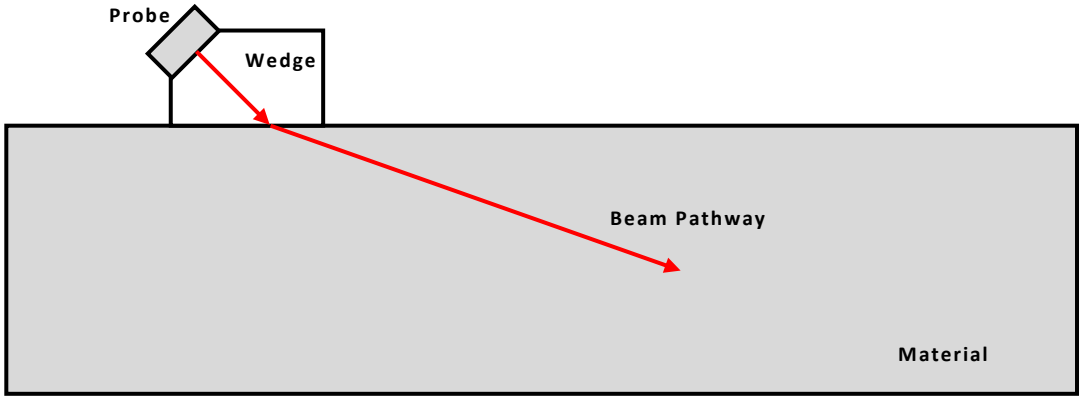

Figure 2.2: Angled UT Probe Diagram

2.3.2. Ultrasonic Wave Modes

There are a myriad of NDT applications via UT and EMATs, due to the various ultrasonic wave modes that they can transmit. It is important to understand these wave modes, how they propagate, and how they are used within NDT.

Within an infinite solid medium, mechanical waves propagate as a 'bulk wave'. These are comprised of two wave modes: compression (or longitudinal) and shear (or transverse). Figure 2.3 shows an illustration of the wave propagation for both wave modes.

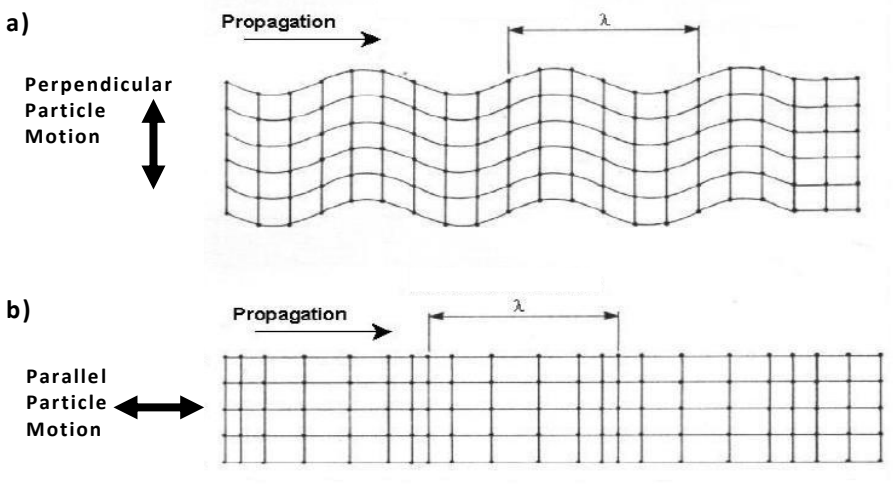

Figure 2.3: Bulk Wave Components, adapted from [27]. a) Shear Wave showing particle motion perpendicular to wave propagation. b) Compression Wave showing particle motion parallel to wave propagation.

The particle motion for compression waves is orientated parallel to its propagation direction. The particles push-and-pull adjacent particles through elastic interconnection. The particle motion for shear waves is perpendicular to the propagation direction. This wave mode can only propagate via particles that are joined together in rigid materials. This means that while compression waves can travel through solids, liquids, and gases due to the elasticity in these states of matter, shear waves are constrained to solids only. The wave velocity of both wave modes is described in Equation 2.2 and Equation 2.3.

$$v_c = \sqrt{\frac{E(1-\mu)}{\rho(1+\mu)(1-2\mu)}} \qquad \text{Equation 2.2}$$

$$v_s = \sqrt{\frac{E(1-\mu)}{2\rho(1+\mu)}} = \sqrt{\frac{G}{\rho}} \qquad \text{Equation 2.3}$$

where v_C = compression wave velocity (m/s); E = Young's modulus (N/m²); μ = Poisson's ratio; ρ = material density (kg/m³); v_S = shear wave velocity (m/s); G = shear modulus (N/m²).

The value of the shear wave velocity compared to the compression wave velocity is approximately 50% within the same medium. This means that the wavelength of the shear waves is also approximately 50% that of the compression waves (according to Equation 2.1). This makes shear waves more sensitive to defects than compression waves.

Within a finite solid medium, boundary conditions are set through the introduction of the material's surface. The two bulk wave modes interact with the material's surface to form a Rayleigh wave, shown in Figure 2.4. For Rayleigh waves, the particle motion is elliptical in an anticlockwise direction as the wave travels from left-to-right. Due to the surface boundary condition, Rayleigh waves are most concentrated within a depth of one wavelength and can only propagate in two dimensions (unlike the three dimensions for bulk waves). This subjects the Rayleigh waves to less attenuation than bulk waves as distance increases in the same medium. Thus, Rayleigh waves are typically used for flaw detection at the surface of materials over a larger distance [25].

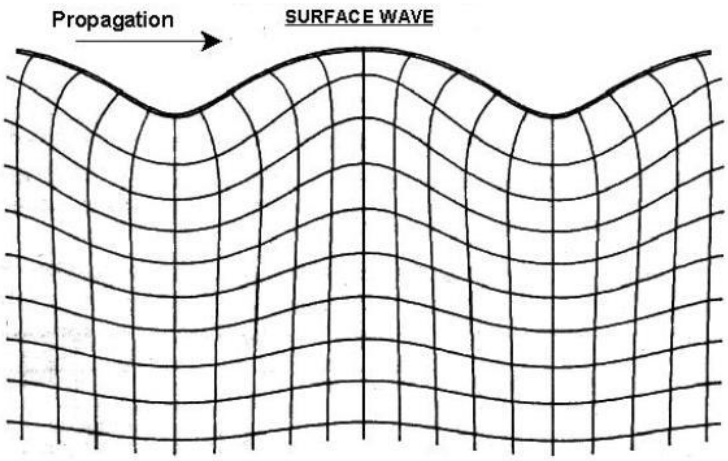

Figure 2.4: Rayleigh Wave [27]

When a second surface is introduced within a few wavelengths of the first, the medium becomes a thin structure that fully constrains the wave within it. The motion of both bulk waves impose on one another to form one of two new wave modes: Symmetrical and Asymmetrical. These new wave modes are known as Lamb waves, shown in Figure 2.5. Similar to Rayleigh waves, the particle motion is elliptical in an anticlockwise direction near the material's surfaces. Due to the decreased volume that they are enclosed by Lamb waves are capable of propagating over a far greater distance than Rayleigh waves, but only within thin structures. Rayleigh and Lamb waves are known as 'guided waves' due to their propagation within the materials parallel to its surface. This makes them well suited to examining plates and pipes over long distances [25].

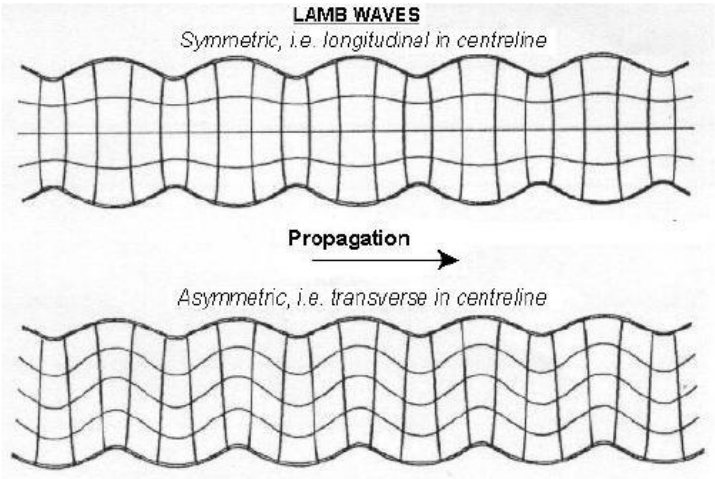

Figure 2.5: Symmetric and Asymmetric Lamb Waves [27]

2.3.3. Material Propagation

The further these ultrasonic waves travel from their original source the weaker they become. This is called 'attenuation' and is due to the combined effects of absorption and scattering. Absorption occurs when the wave energy is lost as thermal energy from the vibrating the molecules of the material. Scattering is the randomly directed reflection of wave energy from materials with a coarse-grain structure. Less energy is scattered from a longer wavelength, therefore low frequency compression waves are better suited to inspect these types of materials. Attenuation is defined as the decay rate of the wave as it propagates through the material, shown in Equation 2.4.

$$A = A_0 e^{-\alpha x} \qquad \text{Equation 2.4}$$

where A = amplitude of wave after travelling distance x (%); A_0 = initial amplitude (%); α = attenuation coefficient (1/m); x = distance travelled by wave (m).

The energy lost from attenuation is relatively small compared to energy lost through reflection from boundaries of different materials. As previously mentioned, ultrasonic wave velocity is determined by the type of material being tested. This is due to the acoustic impedance of the material, shown in Equation 2.5. The boundary where two different materials meet (e.g. the material's surface in contact with air) causes a fraction of wave energy to be reflected due to the differences in acoustic impedances or 'impedance mismatch'. The greater the impedance mismatch, the greater the percentage of energy that will be reflected at the boundary or 'reflection coefficient', shown in Equation 2.6. The remaining energy that is not reflected travels through the boundary into the second material and is calculated by the 'transmission coefficient', shown in Equation 2.7.

$$Z = \rho \times v \qquad \text{Equation 2.5}$$

$$R = \left(\frac{Z_2 - Z_1}{Z_2 + Z_1}\right)^2 \qquad \text{Equation 2.6}$$

$$T = 1 - R \qquad \text{Equation 2.7}$$

where Z = acoustic impedance (kg/m²s); R = reflection coefficient; T = transmission coefficient.

This explains why piezoelectric transduction necessitates the use of a coupling medium, reducing the energy lost from the transfer of wave energy from the transducer to the material's surface. The difference in acoustic impedances particularly impacts these waves when travelling through their boundary at an angle. Due to the different acoustic velocities between materials, a wave passing through the material's boundary at an incident angle is refracted at another angle. The angle of refraction is calculated using Snell's Law, shown in Equation 2.8.

$$\frac{\sin\theta_1}{v_1} = \frac{\sin\theta_2}{v_2} \qquad \text{Equation 2.8}$$

where θ_1 = angle of incidence (°); v_1 = wave velocity of material-1 (m/s); θ_2 = angle of refraction (°); v_2 = wave velocity of material-2 (m/s).

Snell's law shows that the greater the ratio of acoustic impedance, the greater the angle of refraction for a given incident angle. This law applies to both compression and shear waves and is calculated from their respective velocities.

At low angles of incidence for compression waves, some energy can cause particle motion in the transverse direction. This generates shear waves into the material, in addition to the refracted compression waves. This is called 'mode conversion' and can complicate the reading of ultrasonic waves due the differing acoustic velocities. Snell's law applies to these mode conversions, and both the compression wave's velocity and incident angle can be used to calculate the angle of refraction for both compression and shear waves. Equation 2.8 explains why shear waves are refracted less than compression waves due to their reduced velocity, and Figure 2.6 illustrates this working principle.

As the angle of incidence increases for compression waves, a greater proportion of wave energy is mode converted to the shear waves. An angle of incidence that refracts a compression wave at an angle of 90° into the material is known as the 'first critical angle'. Beyond this angle, all refracted wave energy is mode converted to the shear waves. For angled UT inspection, shear waves beyond the first critical angle are commonly used to avoid introducing

compression waves into the material, simplifying the A-scan of the returning waves.

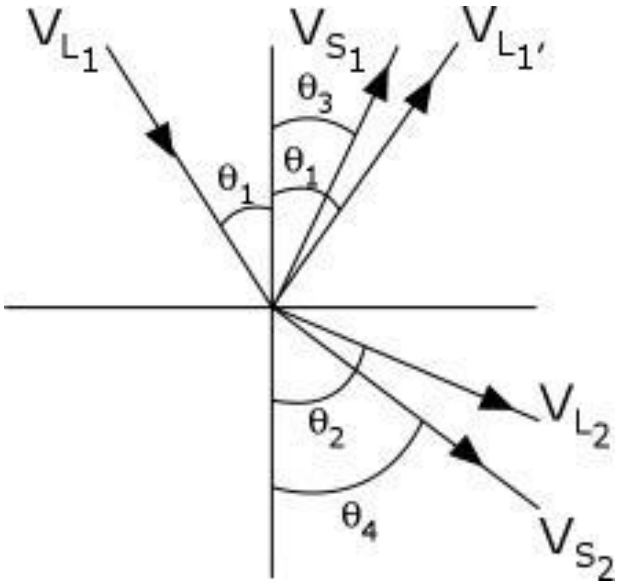

Figure 2.6: Snell's Law and Mode Conversion [28]

As the angle of incidence increases further, the refracted shear wave would begin to lose energy to the surface wave. An angle of incidence that refracts a shear wave at an angle of 90° into the material is known as the 'second critical angle'. Beyond this angle, all wave energy is mode converted to surface waves.

2.4. Electromagnetics

2.4.1. Maxwell's Equations

Electromagnetic phenomena and forces are characterised and governed by electromagnetic field equations known as 'Maxwell's equations'. They describe how both magnetic and electric fields coexist and are generated. These equations are shown in Equation 2.9-Equation 2.11 & Equation 2.13.

2.4.1.1. Gauss' Laws

Gauss' Law describes the relationship between an electrically charged particle and its static electric field. A particle that holds an electric charge generates an electric field, which becomes weaker the further from the particle you observe. Written in the differential form, this is represented by Equation 2.9.

While electric fields originate from electric monopoles, Gauss' law for magnetism states that magnetic monopoles do not exist. This is due to a magnet's north and south pole forming a dipole, in which a magnetic field can be thought as wrapping around. Written in the differential form, this is represented by Equation 2.10.

$$\nabla . E = \frac{\rho_V}{\varepsilon_0} \qquad \text{Equation 2.9}$$

$$\nabla . B = 0 \qquad \text{Equation 2.10}$$

where $\nabla . E$ = divergence of the electric field (V/m²); ρ_V = volume charge density (C/m³); ε_0 = permittivity of free space (F/m); $\nabla . B$ = divergence of the magnetic flux density (T/m).

2.4.1.2. Faraday's Law

Faraday's law of induction describes how a spatially varying magnetic field interacts with a time varying electric field and vice versa. The law states that a current will be induced in a conductor when exposed to a changing magnetic field. The induced current's magnetic field will oppose the initial changing magnetic field that created it (according to Lenz's law of electromagnetic induction). From Faraday's experiment of moving a magnet towards and away from a coil connected to a galvanometer, he concluded that whenever there is relative motion between a conductor and a magnetic field, the magnetic flux linkage (defined as the product of the coil's inductance and the current flowing through it) within the coil changes. This change in flux linkage induces an Electro-Motive Force (EMF) across the coil. From this conclusion, two laws were formulated:

Faraday's 1st law: any change in the magnetic field of a coil will induce an EMF. If the coil's circuit is closed, the induced current will circulate. The magnetic field may be changed by: moving a magnet to/from the coil; moving the coil into or out of the magnetic field; changing the area of a coil in the magnetic field; or rotating the coil relative to the magnet.

Faraday's 2nd law: the magnitude of an EMF equals the rate of change of flux linkages in a coil. The induced EMF in the coil may be increased by: increasing the number of turns; increasing the magnetic field strength; or

increasing the speed of relative motion between the coil and the magnet. These two laws combined in the differential form are represented by Equation 2.11.

$$\nabla \times E = -\frac{\Delta B}{\Delta t} \qquad \text{Equation 2.11}$$

where $\nabla \times E$ = curl of the electric field (V/m²); $\Delta B/\Delta t$ = rate of change of magnetic flux density (T/s).

Modern day applications of Faraday's laws include electrical generators, induction cookers, and electromagnetic flow meters. The most well-known application is the power transformer as it allows the generated magnetic flux from a primary coil's current to induce a current within the secondary coil while the two coils share the same core. The transformer is crucial in electrical power grids, as the two coils possessing a different number of turns allow for high initial voltages to be lowered and later raised.

2.4.1.3. Ampere's Law

The flow of electrons through a long straight wire generates a circular magnetic field perpendicular to it in free space. The strength of the field is proportional to the magnitude of the electric current density through the wire, shown in Equation 2.12.

$$B = \frac{\mu_0 I}{2\pi r} \qquad \text{Equation 2.12}$$

where μ_0 = permeability of free space (H/m); I = current (A); r = radius of circular magnetic field around a wire (m).

When current flows through two parallel wires, the magnetic fields generated by both wires will interact and cause a force on each wire. The direction of force on each wire is dependent on the direction of current flowing through the parallel wires: like flow will attract the two wires; and opposite flow will repel them. In addition to current flowing through a conductor, there is the added movement of electrons contained within the atoms, known as 'displacement current density'. This can happen when these atoms become polarised by an externally applied electric field, known as 'dielectric polarisation', however this value is usually negligible. These two different types

of electric current in motion both induce magnetic fields and so may be written together in the differential form, represented by Equation 2.13.

$$\nabla \times B = \mu_0 \left(J_e + \varepsilon_0 \frac{\Delta E}{\Delta t} \right) \qquad \text{Equation 2.13}$$

where $\nabla \times B$ = curl of the magnetic field (T/m); J_e = electric current density (A/m²); $\Delta E/\Delta t$ = rate of change of electric field (V/ms).

Equation 2.9-Equation 2.11 & Equation 2.13 show the generalised maxwell's equations. In matter, Equation 2.14-Equation 2.17 apply.

$$\nabla . E = 4\pi\rho_V \qquad \text{Equation 2.14}$$

$$\nabla . B = 0 \qquad \text{Equation 2.15}$$

$$\nabla \times E = -\frac{1}{c}\frac{\Delta B}{\Delta t} \qquad \text{Equation 2.16}$$

$$\nabla \times B = \frac{1}{c}\left(4\pi J_e + \frac{\Delta E}{\Delta t} \right) \qquad \text{Equation 2.17}$$

where c = speed of light (m/s).

2.4.2. Magnets

If a magnet broke in half, it would not separate into a north and a south pole but instead would become two smaller magnets each with their own north and south poles. Following this line of reason, a magnet could be broken down to its individual atoms which would each still possess a magnetic field. The atom's electrons orbiting its nucleus create this magnetic field (according to Ampere's Law) and its field strength and orientation is known as the 'magnetic moment'. The overall magnetic field and net magnetic moment from the pairing of electrons can result in a wide array of magnetic behaviours in materials, adhering to Equation 2.18.

$$B = \mu H = \mu_0 \mu_R H = \mu_0 (H + M) \qquad \text{Equation 2.18}$$

where B = magnetic flux density (T); H = magnetic field strength (A/m); μ = absolute permeability of the material (H/m); μ_R = relative permeability of the material; M = magnetisation of the material.

The three most common magnetic behaviours within all materials are: Diamagnetism; Paramagnetism; and Ferromagnetism. In diamagnetic materials, all the electrons in the atoms are paired thus there is no net magnetic moment.

When applied with an external magnetic field, the material is repelled due to the external field inducing an opposite magnetic field within it. A trait of these materials is that their magnetic permeability is less than that of the permeability of a vacuum. Such materials include water, carbon, and superconductors.

In paramagnetic materials, there are unpaired electrons, so all atoms have incomplete atomic orbitals. The magnetic moment from these unpaired electrons aligns with an external magnetic field, resulting in attraction between the material and the external magnet. Only a small proportion of moments align with the external field, and they cannot retain their magnetisation due to thermal motion. A trait of these materials is that their magnetic permeability is slightly greater than that of the permeability of a vacuum. Such materials include aluminium, titanium, and copper.

In ferromagnetic materials, the spin of the unpaired electrons lines up naturally without the need for an external magnetic field. These magnetic dipoles group together and form magnetic domains that each contain their own individual magnetic field, therefore ferromagnetic materials can be considered as being made up of many small magnets. In an unmagnetized state, the material is formed up of multiple domains in random orientations, weakening or cancelling out a resultant magnetism. An external magnetic field aligns these domains and once removed hard magnetic materials retain their magnetism whilst soft magnetic materials do not. A common example of domain realignment is turning a paper clip into a temporary magnet by rubbing it with a magnet many times. A trait of these materials is that their magnetic permeability is much greater than that of the permeability of a vacuum. Such materials include iron, cobalt, and nickel.

For both diamagnetic and paramagnetic materials, the relative permeability of the material remains constant. For ferromagnetic materials however, the relationship between magnetic flux density and field strength is non-linear. Figure 2.7 shows an example of this non-linear relationship in the form of a hysteresis loop.

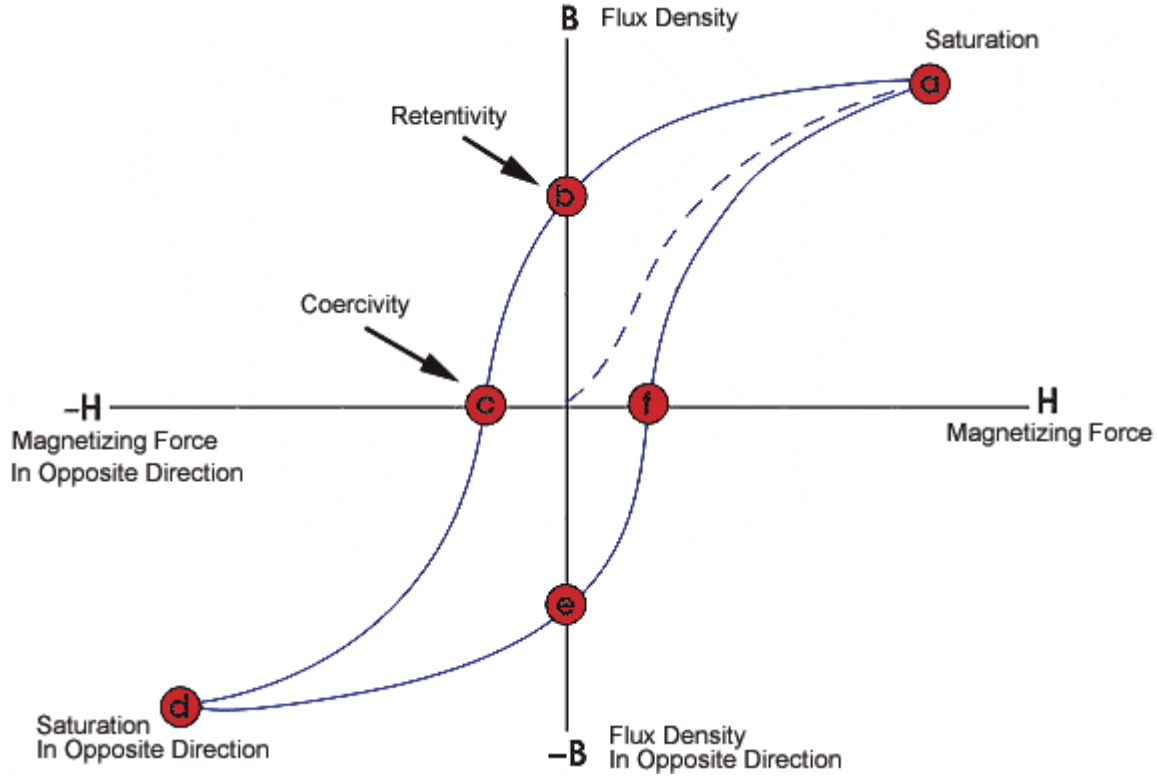

Figure 2.7: B-H curve for a ferromagnetic material, adapted from [29]

The material begins in an unmagnetized state, until the external magnetising field is applied and causes the material's magnetic domains to align with its direction. As this field strength increases, most of the domains begin to irreversibly grow into alignment. The gradient of this section (represented by the linear section of the dashed line in Figure 2.7) allows for the absolute permeability of the material to be measured. The magnetic flux density continues to increase and begins to plateau as almost all of the domains rotate and align with the direction of the magnetic field. Further increase in the applied field strength causes little increase in the flux density. At this point, the material has reached magnetic saturation (represented by point 'a' in Figure 2.7).

From the point of magnetic saturation, reduction of the external magnetising field strength back to zero would not cause the material to become demagnetised. The material instead retains a residual value of magnetic flux density (also called remanence) due to the majority of the magnetic domains maintaining alignment and not returning to their original orientation. This is the material's retentivity (represented by point 'b' in Figure 2.7). It must be noted that any difference between the remanence and retentivity may be due to the material not previously being magnetised to the saturation level. As the

external magnetic field is further reduced (increasing in the opposite direction) the material's remanence reduces to zero. This is due to the reversed magnetic field reorientating enough domains to cancel out the net magnetic flux within. The value of external magnetic force required to remove the material's residual magnetic flux is known as its coercive force (represented by point 'c' in Figure 2.7). As the external magnetic field is reduced further, the material will become magnetically saturated in the opposite direction (represented by point 'd' in Figure 2.7). The values of both magnetic saturation points would be equal in magnitude but opposite in direction, as would the retentivity and coercivity points (represented by points 'e' and 'f' respectively in Figure 2.7) if the external magnetic field were increased back to a positive maximum.

As ferromagnetic materials become magnetised, shape change occurs in either its length or volume due to the magnetic domains aligning with surrounding magnetic fields, shown in Figure 2.8. The source of the magnetic field determines the type of magnetostriction that occurs.

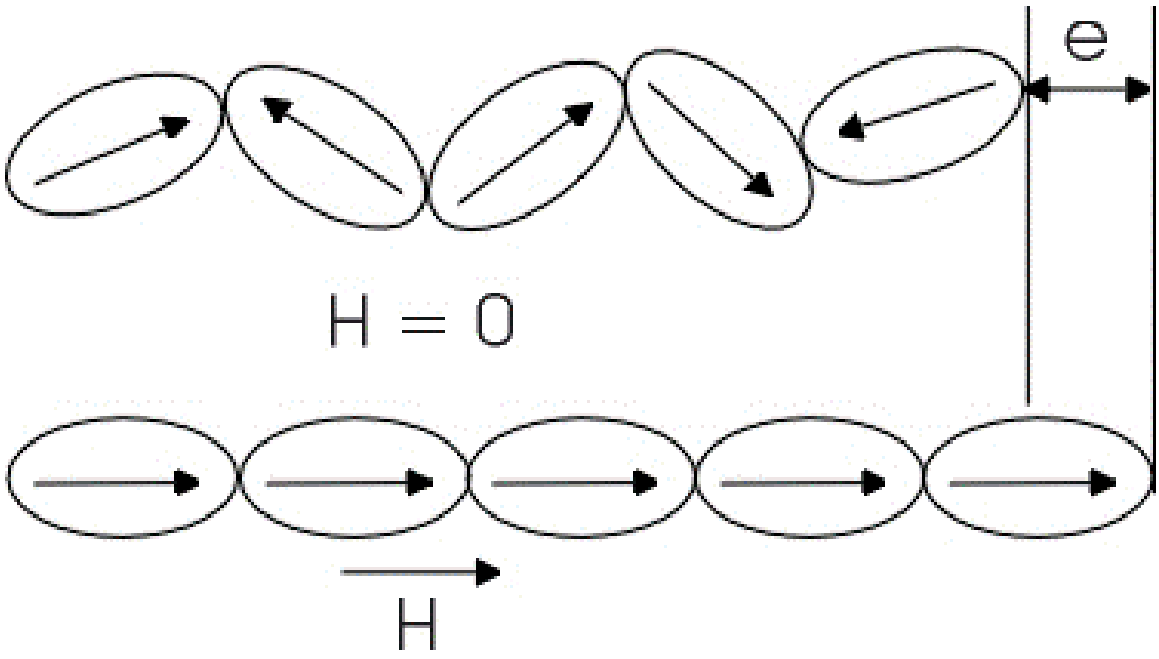

Figure 2.8: Magnetostriction principle [30]

'Spontaneous magnetostriction' occurs when the material transitions from a paramagnetic to a ferromagnetic material by being cooled through its 'Curie temperature'. When heated above its Curie temperature, the material loses its ferromagnetic properties due to the massive amount of thermal energy randomly aligning the magnetic dipoles. As the material is cooled through this

temperature point, the dipoles align into domains with their own magnetic field This results in spontaneous magnetostriction of the domain, where the dipoles generate their own magnetic field that aligns them. This type of magnetostriction causes a change in volume for isotropic materials but not shape. 'Field-induced magnetostriction' is when an external magnetic field is applied to a ferromagnetic material below the Curie temperature. The magnetic domains in the material align with the external field which causes shape change via shear strains.

2.5. EMATs

EMATs are a non-contact method of NDT, that uses a bias magnetic field and a coil of wire to transmit ultrasonic waves into electrically conductive materials. Their transduction method makes them capable of transmitting and receiving a variety of wave modes (listed in Section 2.3.2) without the necessity of a coupling medium. This enables them to be used in high-speed inspection, high-temperature inspection, and applications that preclude the use of liquid couplant.

2.5.1. Transduction Methods

EMATs consist of a permanent magnet and a coil driven by an AC, that generate static and dynamic magnetic fields respectively. Together they are capable of generating ultrasonic waves into ferromagnetic and electrically conductive materials by a combination of the transduction methods displayed in Equation 2.19: Lorentz forces, magnetisation forces, and magnetostriction forces.

$$F = F_L + F_M + F_{mag} \qquad \text{Equation 2.19}$$

where F = total force acting upon tested material (N); F_L = Lorentz force (N); F_M = magnetisation force (N); F_{mag} = magnetostrictive force (N).

The primary transduction that the EMAT uses is dependent on the material type being inspected.

2.5.1.1. Lorentz Force

When an electric charge travels within a magnetic field there is a resultant force. An electrically conductive material is composed of a lattice of positive ions surrounded by a sea of negative electrons. When an electric field is produced from the coil's AC, a force is exerted on the material's electrons known as a 'Coulomb force'. This force accelerates the electrons to an average velocity, which then becomes subjected to Lorentz force due to their motion while in the presence of a bias magnetic flux density. The combination of the electric and magnetic forces acting upon the electrons is shown in Equation 2.20.

$$F_e = -(n_e e v_e \times B_s) - n_e e E \qquad \text{Equation 2.20}$$

where n_e = electron density (C/m³); e = electron charge (C); v_e = average electron velocity (m/s); E = electric field strength (V/m).

The speeding electrons collide with the material's ion lattice and transfer their momentum to the ions causing movement [31]. The force from the electrons colliding with the ions is shown in Equation 2.21.

$$F_i = N_i Z_i (E + v_i \times B_s) + n_e e E \qquad \text{Equation 2.21}$$

where N_i = ion density (C/m³); Z_i = ion charge (C); v_i = average ion velocity (m/s).

The total force of the electrons colliding with the ions is approximately equal to the Lorentz force acting on the electrons for two reasons: the Coulomb force acting on both the ions and electrons are equal and opposite due to the lack of overall electric charge ($n_e e = N_i Z_i$) thus cancelling each other out; and the velocity of the ions is so small ($v_i \approx 0$) that the Lorentz force acting upon them is negligible. Equation 2.20 and Equation 2.21 can therefore be combined and reduced to Equation 2.22 which equates to the Lorentz force acting upon the electrons.

$$F_L = -n_e e v_e \times B_s = J_e \times B_s \qquad \text{Equation 2.22}$$

When the AC-driven coil is placed adjacent to an electrically conductive material, the coil's changing magnetic field induces alternating eddy currents in the material with their own magnetic fields. The eddy current's electrons

interact with the EMAT's bias magnetic field to produce Lorentz forces in the material which (due to the alternating eddy current densities) also alternates. This alternating force generates ultrasonic waves in the material, whose frequency is determined by the frequency of the AC. This Lorentz effect also works in reverse, whereby the movement of charged particles within a magnetic field produces an electric field, shown in Equation 2.23. The EMAT's wave reception works by this reciprocal Lorentz effect, as these dynamic electric fields result in dynamic magnetic fields which induces dynamic electric fields within the EMAT's coil. This enables ultrasonic waves to be received by EMATs.

$$E = \frac{du}{dt} \times B_0 \qquad \text{Equation 2.23}$$

where du/dt = rate of change of particle displacement (m/s).

2.5.1.2. Magnetisation Force

The magnetisation forces are those that act upon ferromagnetic materials only due to a spatially varying magnetic field distribution [32]. This is determined by the magnetic energy density of a magnetised sample within a magnetic field, shown in Equation 2.24. The magnitude of the magnetisation force is relatively small compared to the Lorentz force and is typically ignored in simulated modelling [33]. If the bias magnetic field is tangential to the surface of a ferromagnetic material, the magnetisation force is of similar magnitude to the Lorentz force, but opposite in its direction, thus they cancel out [34]. If the material being tested were solely electrically conductive, there would be no magnetising force, and the total force would be generated by the Lorentz force.

$$F_M = -\nabla . U_M = \nabla H . u_0 M \qquad \text{Equation 2.24}$$

where U_M = magnetic energy density.

2.5.1.3. Magnetostrictive Force

As previously mentioned, field-induced magnetostriction is a transduction principle applicable only to ferromagnetic materials, important to the generation of elastic waves. The static stress from the bias magnetostrictive force superimposes on the dynamic stresses from the Lorentz forces. These

total into a dynamic force that causes dynamic stresses in the material, which propagate as mechanical elastic waves through the material.

The degree of strain that the ferromagnetic material undergoes in the presence of a bias magnetic field is dependent upon the material. The materials are therefore distinguished by their magnetostrictive curves, shown in Figure 2.9(a). This shows the magnitude of the material's magnetostrictive strain as a result of the applied bias magnetic field. As with the Lorentz force transduction method, magnetostrictive forces work in reverse. This is known as the 'Villari effect' [35], and describes the change in a ferromagnetic material's magnetisation due to the application of stress.

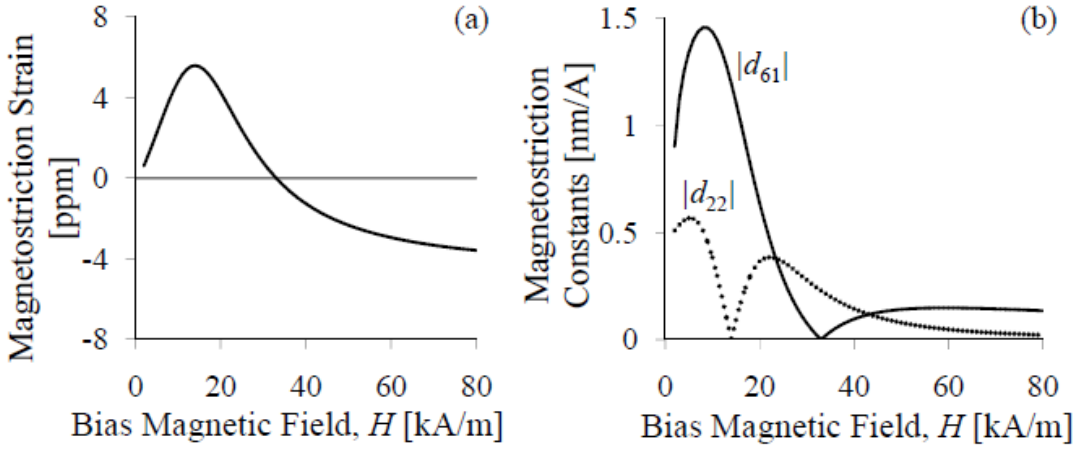

Figure 2.9: Static magnetostriction curve and abstolue values of magnetostriction constants [36]

Without a large current through the coils, the bias magnetic field from the magnet is assumed to be greater than the dynamic magnetic field from the coils. The magnetostrictive strain can therefore be approximated locally as a linear relationship between the magnetic field and stress, as shown in Equation 2.25. This is the most commonly used method of modelling the EMAT's magnetostrictive strain. The matrix of piezomagnetic strain coefficients for a magnetic field directed vertically (in the y-axis) is shown in Equation 2.26.

$$\varepsilon_I = \mathrm{d}_{Ij}^{MS} H_j + s_{IJ}^{H} \sigma_{IJ} \qquad \text{Equation 2.25}$$

$$d_{Ij} = \begin{pmatrix} 0 & -\frac{d_{22}}{2} & 0 \\ 0 & d_{22} & 0 \\ 0 & -\frac{d_{22}}{2} & 0 \\ 0 & 0 & d_{61} \\ 0 & 0 & 0 \\ d_{61} & 0 & 0 \end{pmatrix} \qquad \text{Equation 2.26}$$

where I,J = 1-6 and j = x,y,z; ε_I = magnetostrictive strain; H_j = magnetic field; σ_{IJ} = stress; d_{Ij} = piezomagnetic strain coefficients.

d_{22} within Equation 2.26 describes the behaviour of the material when the bias magnetic field is parallel to the dynamic magnetic field. This is the first derivative of the static magnetostriction curve with respect to the magnetic field and is represented by Equation 2.27. d_{61} describes the behaviour of the material when the bias and dynamic magnetic fields are perpendicular to one another. This value is directly proportional to the total magnetostrictive strain, and Equation 2.28 shows this value as defined by Ogi and Hirao [37].

$$d_{22} = \frac{d\varepsilon}{dH_y} \qquad \text{Equation 2.27}$$

$$d_{61} = \frac{3\varepsilon}{H_y} \qquad \text{Equation 2.28}$$

The absolute values of these two coefficients in relation to the bias magnetic field is shown in Figure 2.9(b). The maximum magnitude of the magnetostrictive force produced by the EMAT occurs at the maximum values of these two coefficients. It is important therefore to consider the value of the bias magnetic field with respect to the material's magnetostricitve properties.

2.5.2. EMAT Configurations

The configuration of the EMAT's magnetic field and coils allows the transducer to excite different wave modes into the material. As previously mentioned, the AC-driven coil induces eddy currents within electrically conductive materials. When the induced eddy currents interact with the magnet's bias magnetic field, Lorentz forces are produced within the material which generates ultrasonic waves. The most common EMAT configurations are divided into two categories: normal-beam and angle-beam.

2.5.2.1. Normal-Beam EMATs

Normal-beam EMATs transmit bulk waves into the material, propagating perpendicular to the surface they enters. Figure 2.10 shows one of the simplest and most common configurations of the normal-beam EMATs: the spiral-coil EMAT (also known as a pancake-coil EMAT).

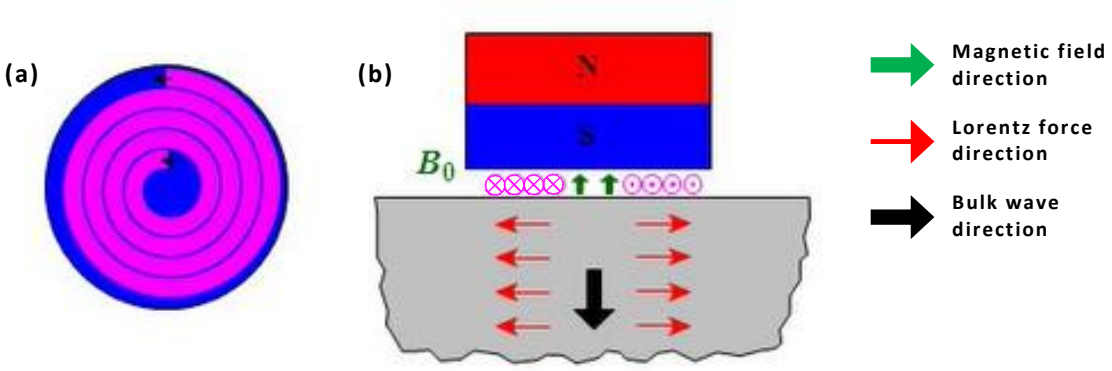

Figure 2.10: Spiral-Coil EMAT, adapted from [38]

Figure 2.10(a) shows the spiral-coil EMAT from a worm's-eye view, with the circular coil of wire beneath the cylindrical magnet. Figure 2.10(b) shows the spiral-coil EMAT from a landscape view, with the coil between the magnet and the material's surface. The direction of the AC driving the coil is denoted by the black arrows in Figure 2.10(a) with their corresponding directions denoted in Figure 2.10(b) (where the pink dotted circles indicate AC out of the page and pink crossed circles indicate AC into the page). The eddy currents are induced in the opposite direction to the coil's AC and interact with the vertical magnetic field (denoted by the green arrows in Figure 2.10(b)). Fleming's left-hand rule for electric motors can be used to work out the direction of the Lorentz forces (denoted by the red arrows in Figure 2.10(b)). With the left hand's index finger, middle finger, and thumb at orthogonal axes, orientating the index and middle fingers in alignment with the magnetic field and induced eddy current respectively results in the thumb aligning with the Lorentz force. These Lorentz forces generate radially polarised shear waves that propagate normal to the surface of the material (denoted by the black arrow in Figure 2.10(b)).

Figure 2.11 shows a second normal-beam EMAT: the rectangular-coil EMAT (also known as a racetrack-coil EMAT or elongated spiral-coil EMAT).

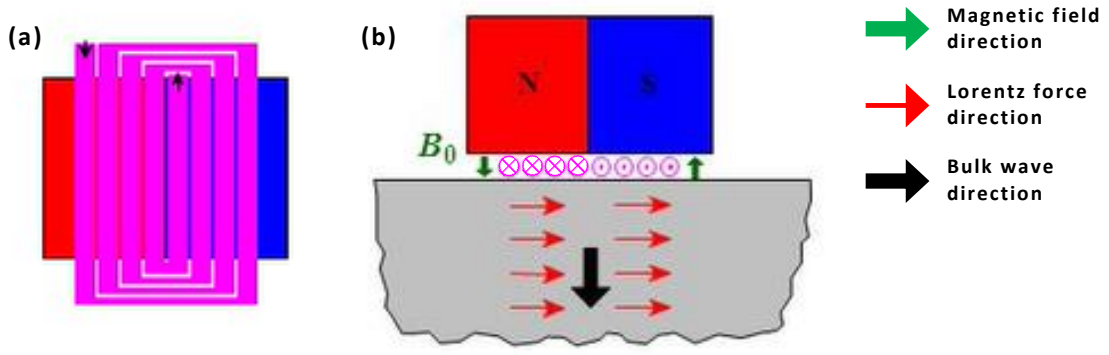

Figure 2.11: Rectangular-Coil EMAT, adapted from [38]

Figure 2.11(a) shows that the direction of AC through the rectangular-coils is the same as that of the spiral-coils in Figure 2.10(a), however this EMAT's coil runs are straight rather than circular. Figure 2.11(b) shows that the direction of the vertical bias magnetic field is not constant, but rather it inverts. This results in the Lorentz forces aligning in the same direction, thus generating linearly polarised shear waves that propagate normal to the material's surface. Figure 2.12 shows the final normal-beam EMAT: the butterfly-coil EMAT (also known as a symmetrical-coil EMAT, double-spiral-coil EMAT, or longitudinal wave EMAT).

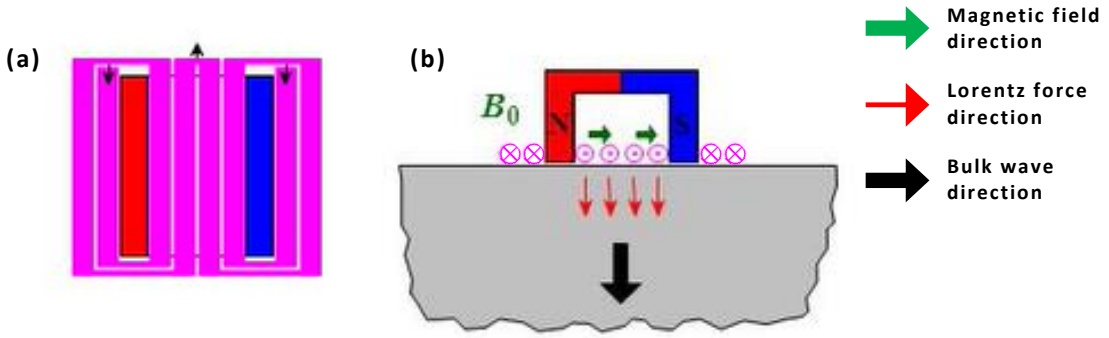

Figure 2.12: Butterfly-Coil EMAT, adapted from [38]

Figure 2.12(b) shows that the magnet for this EMAT is shaped similar to a horseshoe magnet to provide a constant horizontal magnetic field, parallel to the surface of the material. The single coil wraps around each of the magnet's poles, essentially forming two spiral-coils in opposing directions. This creates a uniform direction of AC within the horizontal magnetic field, as show in Figure 2.12(a). The magnetic field and eddy current density (both parallel to the material's surface) produce vertical Lorentz forces, that generate compression waves that propagate normal to the material's surface. The ability to generate compression waves allows this EMAT to inspect coarser grain structure

materials better than the previous two shear wave EMATs. Due to its bias magnetic field directed tangentially to the surface, this EMAT configuration is not suitable to inspection of ferromagnetic materials (as explained in Section 2.5.1.2).

2.5.2.2. Angle-Beam EMATs

Angle-beam EMATs transmit bulk waves into the material, that propagate at an angle to the surface they enter. A major advantage EMAT technology has over other forms of UT is their unique capacity to excite Shear Horizontal (SH) waves. Unlike conventional Shear Vertical (SV) waves whose particle motion is perpendicular to the surface plane (in-plane), the particle motion of SH-waves is parallel to the surface (out-of-plane). This is a guided wave mode typically used for the NDT of surfaces or plates [39], and is not easily excited by traditional UT sensors. Figure 2.13 shows the EMAT configuration that is widely used for exciting SH-waves: the Periodic-Permanent-Magnet (PPM) EMAT.

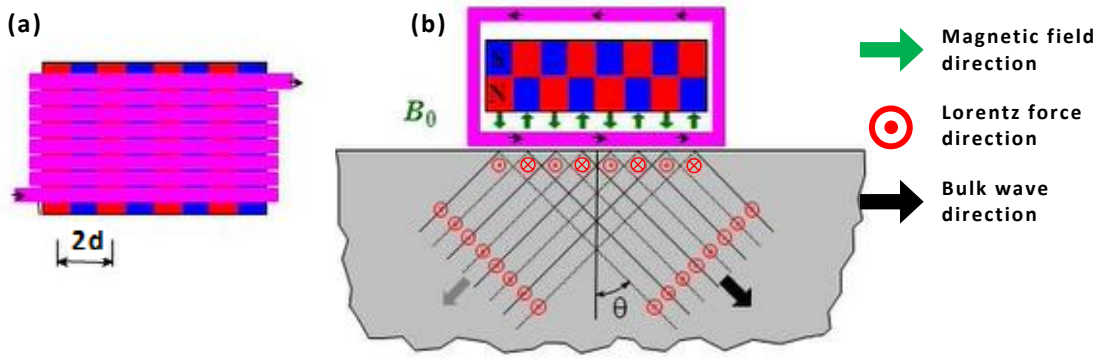

Figure 2.13: PPM EMAT, adapted from [38]

Figure 2.13(a) shows the PPM EMAT's array of permanent magnets that provide alternating magnetic fields normal to the material's surface. Looped around this magnetic array is the coil, with straight runs carrying the AC in a uniform direction, as shown in Figure 2.13(b). This combination produces alternating Lorentz forces parallel to the material's surface, which generates the SH-waves into the material. The wavelength of the SH-waves is determined by the spacing of the magnetic array's alternate spacing (denoted in Figure 2.13(a) as $2d$). The magnet's spacing also determines the angle of propagation for the SH-waves through the bulk material in both directions (denoted in Figure 2.13(b) as θ), and their relationship is shown in Equation 2.29.

$$\sin\theta = \frac{\lambda}{2d} = \frac{v_s}{(2d \times f)} \qquad \text{Equation 2.29}$$

where θ = propagation angle of shear waves (°); d = spacing between two adjacent magnets (mm).

Figure 2.14 shows the final example of an angle-beam EMAT. This is one of the most common angle-beam EMATs and the topic of this thesis: the Meander-Line-Coil (MLC) EMAT.

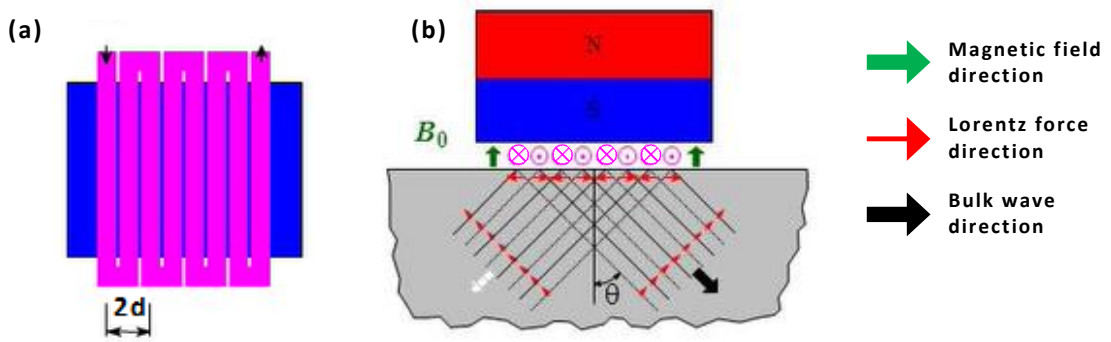

Figure 2.14: MLC EMAT, adapted from [38]

Figure 2.14(a) shows the serpentine design of the coil, with straight runs underneath the magnet. Figure 2.14(b) shows that the magnet produces a normal magnetic field, which interacts with the alternating eddy currents from the MLC's alternating directions to produce periodic alternating Lorentz forces parallel to the material's surface. This operation is similar to the PPM EMAT, as both the SV-wave's wavelength and angle of transmission are dependent on the coil spacing (denoted in Figure 2.14(a) as *2d*)) and the frequency of the AC. This EMAT configuration is also capable of transmitting compression waves, and their angle is also calculated using Equation 2.29 by substituting the material's shear wave velocity with compression wave velocity. At low frequencies, the MLC EMAT is able to transmit Rayleigh waves across the material's surface, with a wavelength equal to double the spacing of the MLC's runs. This EMAT is also capable of transmitting guided Lamb waves on thinly plated samples.

2.5.3. EMAT Advantages and Disadvantages

Compared to conventional UT methods, EMATs have a number of advantages and limitations. A list of the EMAT's advantages and disadvantages is shown in Table 2.2 and are explained in greater detail in this section.

Table 2.2: EMAT Advantages and Disadvantages

Advantages	Disadvantages
Non-contact wave transduction [40]	
Wave mode variety [36]	Low transduction efficiency [42]
Does not require a coupling medium	Material dependent
Unaffected by rough/coated surfaces	Physical size limitations
Variance in surface lift-off [41]	

Due to the EMAT's ability to transmit and receive ultrasonic waves via its electromagnetic transduction methods, they do not require to be in direct contact with the material. This allows EMATs to operate on surfaces that may not only be difficult to reach but also impossible or undesirable to do so (e.g. materials that are heated to extreme temperatures or within irradiated locations [43]). The ability to scan without contact also eliminates the need for any liquid couplant between the transducer and material, simplifying its deployment. This means that no surface preparation is be required before scanning, as EMATs are less sensitive to surface conditions (e.g. dirt, oxides, oils, or paint). EMATs also negate the necessity to clean the material of couplant or debris post-scanning.

As previously mentioned, the EMAT configuration determines the wave mode that is transmitted and includes both bulk waves and guided waves (Rayleigh, Lamb, and SH-wave). The bulk waves can be transmitted normal to the surface or at an angle without requiring a wedge or any intermediary boundaries. SH-wave generation cannot be easily done with traditional NDT methods and has been proven to be superior to bulk waves in certain applications [44].

EMATs do however have limitations, the primary disadvantage being their low transduction efficiency. This efficiency decays exponentially as the lift-off distance between the EMAT's face-plate and the material's surface increases. Reasonable lift-off for EMAT operation is generally limited to 0-3mm. Huang et al [42] have documented an EMAT PC setup to work with both transducers at a lift-off of 2mm, and that increases in lift-off affected the

transmitter more than the receiver. This transduction efficiency and subsequent Signal-to-Noise Ratio (SNR) is hindered further by its frequency and application.

EMATs are limited to operating on electrically conductive and ferromagnetic materials due to the EMAT's transduction method typically consisting of Lorentz and magnetostrictive forces. This excludes other materials that UT is capable of inspecting (e.g. plastics, ceramics, and composites). Specialised training is required operate the EMAT, particularly if it is in a PE setup (rather than a PC setup). Angle-beam EMATs at low angles transmit multiple wave modes with a single pulse (as with UT). This can complicate the reception A-scan with multiple overlapping signals, complicating result interpretation. The EMAT's design can also make difficult to handle, as they are typically larger compared to other NDT transducers. Additionally, their strong magnetic fields can make their handling near ferromagnetic materials troublesome and potentially hazardous [45].

2.5.4. Electrical Circuits

The EMAT's poor transduction efficiency puts a greater emphasis on its electronic components and circuitry to maximise its efficiency [40]. The EMAT's coils must be driven by high-power pulsers to increase the eddy currents densities that they induce. For maximum efficiency, the EMAT's Resistance-Inductance-Capacitance (RLC) circuit must be analysed.

2.5.4.1. RLC Circuits

EMAT circuits can be considered to be composed of three primary components: resistors; inductors; and capacitors, as shown in Figure 2.15. The values of these three components are dependent on the EMAT's AC frequency and the material that it is operating on. When AC flows through each of these components: resistors dissipate energy; inductors store in energy in a magnetic field; and capacitors store energy in an electric field. These storages of energy convert back into electrical current once the polarity of the AC reverses. While voltage and current are in phase across the resistor (as with a Direct Current

(DC) circuit), the voltage across the inductor and capacitor causes the voltage to become out of phase with the current.

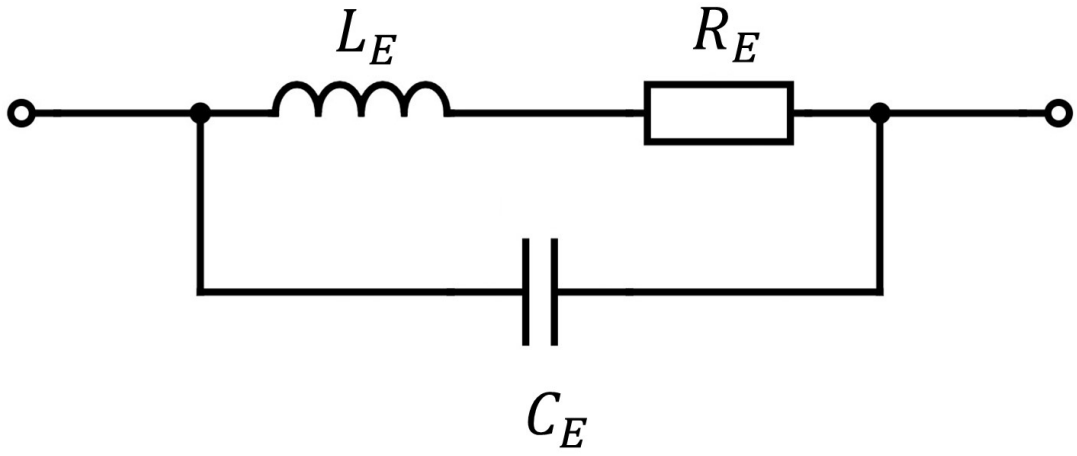

Figure 2.15: EMAT Circuit Diagram [20]

Ohm's law can be applied to the inductor and capacitor within this AC circuit, however these give a different type of resistance called 'reactance'. Reactance is the opposition to a change of current or voltage due to inductance or capacitance. In a purely inductive circuit (no capacitive reactance), the voltage leads current by a phase of 90°. Conversely, the voltage lags behind current by a phase of 90° in a purely capacitive circuit. The combined effects of resistance and reactance opposing the AC is called 'impedance' and is a vector quantity expressed in terms of amplitude and phase. The RLC circuit's impedance is determined by the values of its constituent components (according to Equation 2.30) and affects its voltage output (according to Equation 2.31).

$$Z = \sqrt{R^2 + (X_L - X_C)^2} \qquad \text{Equation 2.30}$$

$$Z = \frac{V}{I} \qquad \text{Equation 2.31}$$

where Z = Impedance (Ω); R = Resistance (Ω); X_L = inductive reactance (Ω); X_C = capacitive reactance (Ω); V = Voltage (V).

To maximise its power output (increasing its transduction efficiency) the EMAT's RLC circuit must have its inductive and capacitive reactances matched to equate the circuit's impedance to its resistance. The precise RLC circuit design varies depending on the EMAT's coil configuration and application, however both reactances are dependent on the frequency of the AC, as shown in Equation 2.32 and Equation 2.33. The frequency at which the inductive and

capacitive reactances equate is known as the 'resonant frequency', and can be calculated by combining Equation 2.32 and Equation 2.33 into Equation 2.34.

$$X_L = 2\pi f L \qquad \text{Equation 2.32}$$

$$X_C = \frac{1}{2\pi f C} \qquad \text{Equation 2.33}$$

$$f_{res} = \frac{1}{2\pi\sqrt{LC}} \qquad \text{Equation 2.34}$$

where f_{res} = resonant frequency (Hz); L = inductance (H); C = capacitance (F).

Given that the frequency of the transmitted waves are dependent on the frequency of the AC, the RLC circuit must be designed to have its resonant frequency equal to the desired frequency of the wave. As discussed later in Section 4.2, the inductance of the EMAT circuit at a given frequency was measured using an impedance analyser. This enabled capacitors to be applied in parallel to the EMAT, improving its transduction efficiency.

2.5.4.2. Skin Depth

The Lorentz force transduction is reliant on the distribution and magnitude of the induced eddy currents. Eddy currents however are not evenly distributed throughout the material but are concentrated at the surface of the material. Their density decreases exponentially as distance from the surface increases. This phenomenon is known as the 'skin effect' and is measured using the Standard Depth of Penetration (SDP), shown in Equation 2.35. The SDP is defined as the depth at which the eddy current intensity is 1/e (approximately 37%) that of the surface intensity. The SDP is proportional to the power of the density decrease: at a depth of 3SDP, the eddy current density decreases to $1/e^3$ its surface value (approximately 5%). The only variable an operator can control to change the SDP is the frequency of the AC, as the remaining variables in Equation 2.35 are material properties.

$$\delta = \frac{1}{\sqrt{\pi f \mu \sigma_e}} \qquad \text{Equation 2.35}$$

where δ = SDP (mm); σ_e = electrical conductivity of the material (S).

2.6. EMATs in Literature

EMATs have been to topic of research over many years, due to their advantage of non-contact transmission and reception of ultrasonic waves. Much work has gone into optimising their design and studying their effects within given applications.

Given the MLC EMAT's bidirectional wave transmission (as shown in Figure 2.14(b)) the task of achieving unidirectional wave transmission has been undertaken. Wang et al [46] used two MLCs within a single array, offset by half a coil spacing and driven by two separate high-power signals out of phase by 90°. This was capable of transmitting both shear and Rayleigh waves in a single direction at approximately twice the amplitude, agreeing well with corresponding modelling results. This study also compared the performance of line-focused coils compared to unfocused and found that the unidirectional focused coil had a better performance than unfocused. Li et al [47] applied the same methodology to detect slot defects at the base of a rail track (at a height of 176mm). The defect response for the unidirectional EMAT was likewise found to be approximately twice that of the bidirectional EMAT and made approximately 7-10% stronger by line-focusing. Rather than organising two separate MLCs in a single array, Shi et al [48] used two regular MLC arrays to increase the SNR in a PE setup. It was found that the greatest SNR was achieved by positioning the receiver MLC above the transmitter MLC and horizontally offset by half a coil spacing.

The use of unidirectional EMATs is not limited to the MLC configuration. Kubrusly, Kang, and Dixon [49] investigated the design of PPM EMATs that would generate SH-waves in a single direction. As with the MLC EMAT, the arrangement of magnets was stacked at an offset distance equal to half the magnet spacing. Coupled with a second linear-coil driven by a high-power pulser out of phase by 90°, SH-waves were transmitted unidirectionally across the surface of an aluminium plate. A similar study by Sun et al [50] also looked at a unidirectional PPM EMAT, however its design used arcing magnets to focus the SH-waves to a single point. This study differed by angling it's bias magnetic

field relative to a single coil, which increased the SH-waves in one direction while suppressing it in the other.

Further development on point-focusing PPM EMATs was documented by Sun et al [51], whereby parametric studies looked at increasing its SNR as a receiver EMAT. The work concluded that the two biggest influences on signal intensity were the lift-off of the coils and the number of magnets in the array. Studies that have looked into the optimisation of EMATs by parametric study of their components have been conducted for other configurations. Sun et al [52] investigated optimising a point-focusing spiral-coil EMAT, whose 2D axisymmetric model was akin to that of an MLC EMAT. Five parameters were selected to investigate the EMAT's, and it was found that the lift-off had the greatest effect on signal intensity.

The correlation of SNR with lift-off is a recurring conclusion [40, 51, 52], with studies such as that by Ding et al [55] agreeing that the EMAT's lift-off should be kept below 3mm for sufficient SNR. There are situations however where this limit must be overcome. Petcher, Potter, and Dixon [56] investigated transmitting Rayleigh waves across a steel rail while at high speeds, with variations in the rail's surface that could damage the EMAT. It was found that the lift-off of the magnet alone could be increased to over 10mm from the surface, with the coil (protected by a titanium wear plate) skimming across the rail's surface. The EMAT's transduction efficiency is affected more by the coil's lift-off than the magnet's, leading to optimisation of the coil array. Wu et al [57] performed parametric studies on a spiral-coil EMAT's design, and was capable to increase the transduction efficiency by 22.5% on aluminium by exchanging the coil's circular Cross-Sectional Area (CSA) for a square. Further improvements could be made by: decreasing the CSA; decreasing the driving frequency; decreasing the coil spacing; and by increasing the current within the coils.

Beyond the two primary components of the magnet and coil, further improvements have been made to the EMAT's physical design. Lan et al [58] also investigated the optimisation of an EMAT via parametric studies, however an Fe-based 1K107 nanocrystalline ribbon was also applied to the upper surface

of the MLC to increase the eddy current density it induced into a metal plate. The optimised design increased the surface wave amplitude by a Scale Factor (SF) of ~4.51, and the application of 0.6mm of 1K107 ribbon increased it further by ~1.35. Iron-based film has been used as a means of increasing an EMAT's transduction efficiency in other studies. Dhayalan et al [59] investigated the application of a soft iron-based alloy beneath the magnet to increase the magnetic flux density. The use of this magnetic flux concentrator increased the amplitude ratio of a Rayleigh wave EMAT PC setup by a SF of ~2.15 over 100mm.

A large proportion of studies on EMATs in a PC setup have involved the Rayleigh wave mode, however their shear wave transduction has also been greatly explored. Xiang and Edwards [60] used racetrack coils with a normal magnetic field to reflect oblique shear waves off of the backwall of a 60mm thick aluminium sample, to be registered by a receiver EMAT. It was discovered via a parametric study of the operating frequency that the shear waves generated had the greatest magnitude at an angle of 30-40°. This helped to inform the separation distance between the two EMATs for the given material. Jie et al [17] also varied the frequency of an EMAT for the purposes of exploring the effect that this had on the shear wave directivity and amplitude. Its frequency was changed over a number of coil spacings to detect fatigue cracking in a wind turbine's main shaft. Using the larger coil spacing of 1.6mm, a maximum amplitude was achieved at an angle of approximately 45°, however this could be deflected up to 60°. The error in sizing and locating the defect could be reduced by changing the angle and position of the transmitted beam for the same line-focused coil.

Within the context of rail track inspection, Dixon, Edwards, and Jian [61] employed an EMAT system to identify crack defects within the surfaces of rail track head. Two EMATs in a PC setup were set apart on either end of a rail track with a corner transverse crack between them. An FFT of the received Rayleigh wave signal showed that a higher proportion of the lower frequencies propagated underneath the cracks. Small variations in the Rayleigh wave's velocity were also recorded from around the rail head, indicating asymmetry and thus changes in both microstructure and stress. Further research with this EMAT setup found a correlation between drops in amplitude over regions of

the rail's head with longitudinal cracks [62]. Li et al [63] used a spiral-coil EMAT to inspect subsurface cracking of rail track. An increase in frequency decreased the beam divergence in the EMAT's normal shear waves and was experimentally proven to reach a limit at over 3MHz. This narrowing of beam divergence increased the SNR of the crack's signal.

Yi et al [64] proposed the use an array of EMATs to inspect rail track: one spiral-coil EMAT to detect longitudinal cracks in the rail web or base; one 37° MLC EMAT to detect transverse cracks around the rail's bolt hole and its base; two 60° MLC EMATs oriented either parallel or perpendicular to the direction of rail track to detect transverse cracks and longitudinal cracks respectively within the rail head; and one unidirectional 90° MLC EMAT to detect transverse cracks at the rail head's surface. While the overall system could only be simulated, experimental testing with the spiral-coil EMAT was performed to locate the depths of the rail's bolt hole and base. These echoes were detected after signal averaging and could be measured after cross-correlation algorithm signal processing.

2.7. Summary

This chapter has explored the operating principle of EMATs, specifically the means by which they transmit and receive ultrasonic waves, and how their design influences the wave modes transmitted. Their place within both NDT and research has also been discussed, specifying their advantages and limitations, and their advances within academic literature.

Chapter 3 - Finite Element Method (FEM)

The purpose of this chapter is to detail the simulated FEM models that were used throughout the study, specifically regarding: their structural and physics-based design; the data that was exported; and the conclusions that were drawn from them.

3.1. Introduction

FEM is a mathematical modelling tool that builds complex and dynamic systems on a computer, in order to calculate approximate solutions for a given application [65, 66]. These solutions are calculated by the governing equations dictated by the given time or space dependent problems. In the case of EMATs, these governing equations relate to electromagnetism and solid mechanics. The models are composed of elemental shapes (usually triangular or rectangular for 2D models) with node points at each of these element vertices. The accuracy of the model is improved by increasing the total number of elements in the areas of interest, albeit at the cost of a larger computational load and thus longer runtime. Via FEM modelling, time and money can be saved as entire structures can be recreated, easily modified, and calculated for the specific outputs, negating the necessity for full experimental testing and user deployment.

In this context of this work: the system would be of an EMAT transmitting ultrasonic waves within an aluminium sample, thus the applications would include electromagnetic induction and ultrasonic wave propagation. The 2D simulations would allow both the electromagnetic features (magnetic field lines and eddy current densities) and ultrasonic waves to be visualised within the aluminium, and values of displacement to be extracted from the surfaces of the samples. Aluminium was chosen as the sample's material given that:

1. As a non-ferromagnetic material, the only transduction method would be Lorentz forces, simplifying the ultrasonic wave generation. Previous studies have detailed the complexities that arise from

modelling the EMAT's magnetostriction transduction, due to their combination of hysteresis effects and changing magnetostriction curves with applied or residual stresses in the material [33, 67].

2. Aluminium and other non-ferromagnetic materials are commonly used in industry and routinely in need of evaluation via NDT.
3. Many scientific papers on the topic of EMATs test on aluminium, allowing their conclusions to be used as comparisons to this work.

'COMSOL Multiphysics' is an FEM analysis software widely accepted by academic establishments for constructing accurate scientific models and has been shown to operate accurately in a myriad of scientific papers [68, 69, 70]. COMSOL is also capable of coupling the EMAT's governing equations together and solving them automatically. Since the EMAT's operation hinges on the interaction between its bias magnetic field and induced eddy current densities, it was important to analyse these two components separately before assembling them into a single EMAT model. The physical dimensions for these components were measured from a real-world experimental MLC EMAT.

3.2. Governing Equations

The two physics interfaces for the EMAT model include electromagnetics and ultrasonic wave propagation. Each of these interfaces are governed by a different set of equations, thus the two COMSOL package required were: the AC/DC module; and the Structural Mechanics module [71].

The AC/DC module is capable of solving the electromagnetic governing equations, derived from Maxwell's equations (Equation 2.9-Equation 2.11 & Equation 2.13). These governing equations describe the behaviour of the electromagnetic fields based upon the model's chosen physics interface. A quasi-static approximation is applied to Ampere's law (Equation 2.13) to neglect the lagging of induced fields, reducing it to Equation 3.1. The Helmholtz decomposition theorem can be applied to certain differentiable vector fields to re-express them to the sum of irrotational and solenoidal vector fields. This allows for both the magnetic and electric fields to be rewritten in terms of a

scalar potential and a vector potential, defined in Equation 3.2 and Equation 3.3 respectively.

$$\nabla \times B = \mu_0 J_e \qquad \text{Equation 3.1}$$

$$\mathrm{B} = \nabla \times A \qquad \text{Equation 3.2}$$

$$E = -\nabla V - \frac{dA}{dt} \qquad \text{Equation 3.3}$$

where A = magnetic vector potential; V = scalar potential.

Using Equation 3.1-Equation 3.3 with Equation 2.18, the simulated model defines Ampere's law as Equation 3.4, and Equation 3.5 represents the divergence of this law.

$$J_e = \sigma \frac{dA}{dt} + \nabla \times \left(\frac{\nabla \times A}{\mu_0} - M\right) - \sigma v \times (\nabla \times A) + \sigma \nabla v \qquad \text{Equation 3.4}$$

$$\nabla . \left(-\sigma \frac{dA}{dt} + \sigma v \times (\nabla \times A) - \sigma \nabla v + J_e\right) = 0 \qquad \text{Equation 3.5}$$

Equation 3.4 and Equation 3.5 act as simultaneous equations to solve for A and J_e, from which all other electromagnetic values are derived. For time-dependent magnetic simulations, COMSOL's default value for the scalar potential is equal to zero, allowing A and J_e to be solved via FEM.

The structural mechanics module is capable of solving the ultrasonic wave propagation. This governing equation is represented by Equation 3.6, and is directly solved by FEM. Via FEM, all other quantities in this module can be derived.

$$\rho \frac{d^2 u}{dt^2} = F_V - \nabla . \sigma \qquad \text{Equation 3.6}$$

where F_V = Force per unit volume (N/m³).

3.3. Magnet Model

The MLC EMAT used a neodymium magnet (NdFeB) graded at N42, and its corresponding physical and magnetic properties is stated in Table 3.1. The magnet was coated with three layers of: nickel; copper; and nickel, for a smooth surface finish and to improve resistance to corrosion. The magnetic

face was positioned tangentially to the tested material's surface (as seen in Figure 2.14(b)) to provide the EMAT its vertical bias magnetic field.

Table 3.1: N42 NdFeB Magnet Properties [72]

Property	Value
Magnetic Dimensions (W x H x D)	20mm x 20mm x 40mm
Remanence	1.31T
Coercive Force	> 915kA/m
Max. Operating Temperature	80°C

The aluminium sample was designed to be semicircular (for reasons explained in Section 3.5). This sample was 100mm in radius, with the magnet positioned at the centre of the surface, as shown in Figure 3.1. The lift-off between the bottom of the magnet and the sample's surface was varied in order to perform parametric studies of the effects that lift-off had on the aluminium. The entire model was surrounded by a boundary of air, with 20mm layers at the end in which artificial infinite element domains were constructed. These infinite element domains were necessary, as they provided a magnetic insulation boundary at an acceptable distance away from the magnet, so as to not interfere with the results.

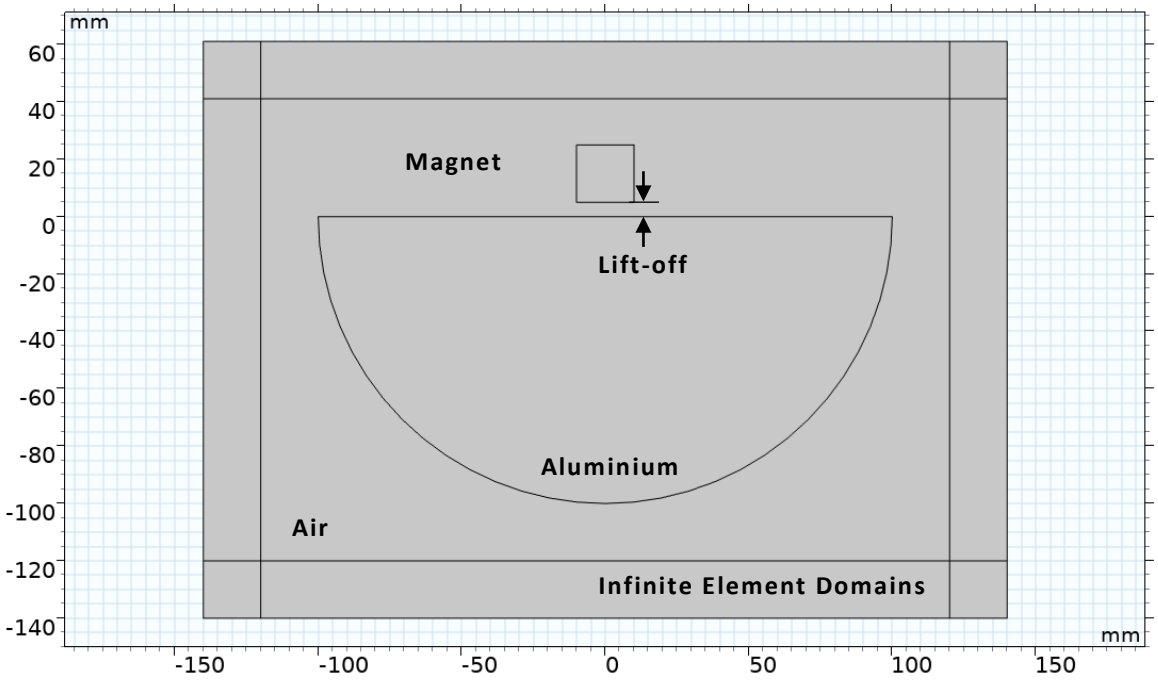

Figure 3.1: COMSOL 2D Model of N42 Magnet over Aluminium

From COMSOL's material library: 'N42 (Sintered NdFeB)' was used for the magnet; standard aluminium (σ_e = 37.74MS/m) was used for the sample; and air was used for its respective parts within the model. From the AC/DC module, the 'Magnetic Fields (mf)' physics interface was used to define the magnet's magnetisation model as 'remanent flux density', and the direction of magnetisation for the MLC EMAT was positive in the vertical. A free triangular mesh was used for the finite domains of the model, with a maximum element size of 0.1mm for both the magnet and the aluminium. The relevant distribution and mapped meshes were used for the infinite domains. Since the bias magnetic field was the only variable simulated, the model required only a stationary study step to compute its effects within the aluminium.

A parametric study was performed to observe how the magnet's lift-off affected the magnetic flux density at the aluminium's surface. Figure 3.2 shows COMSOL's 2D plot of the magnetic field within the sample, and Figure 3.3 shows both the components and magnitude of magnetic flux density across the aluminium's surface for a lift-off of 0mm.

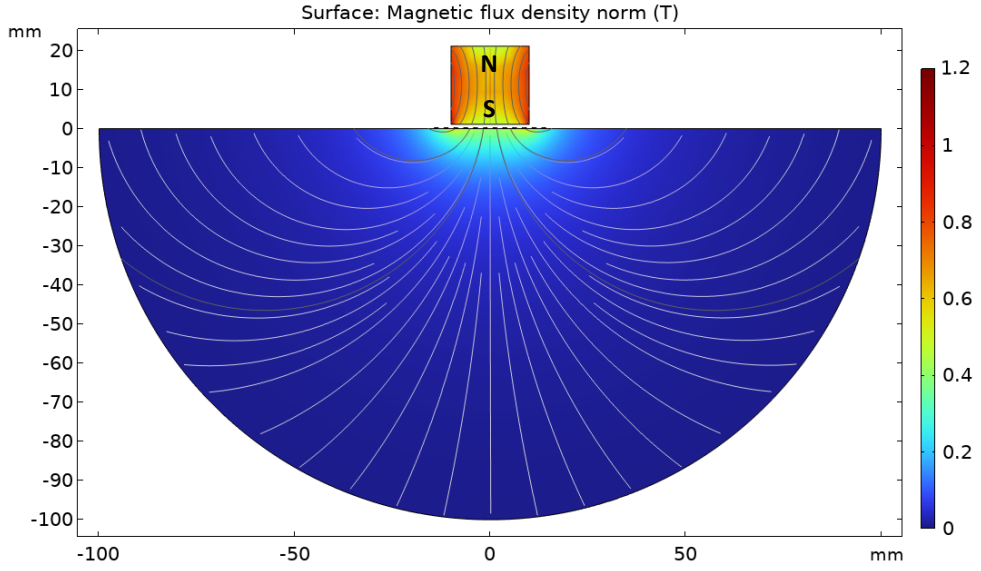

Figure 3.2: Colour-plot of Magnet-1

Figure 3.3 shows that the magnetic flux density concentrates at the edges of the magnet. The orientation of the magnetic field was calculated from the two components of magnetic flux density using Equation 3.7, where: 0° points vertically down; ±180° points vertically up; -90° points horizontally to the left; and +90° points horizontally to the right.

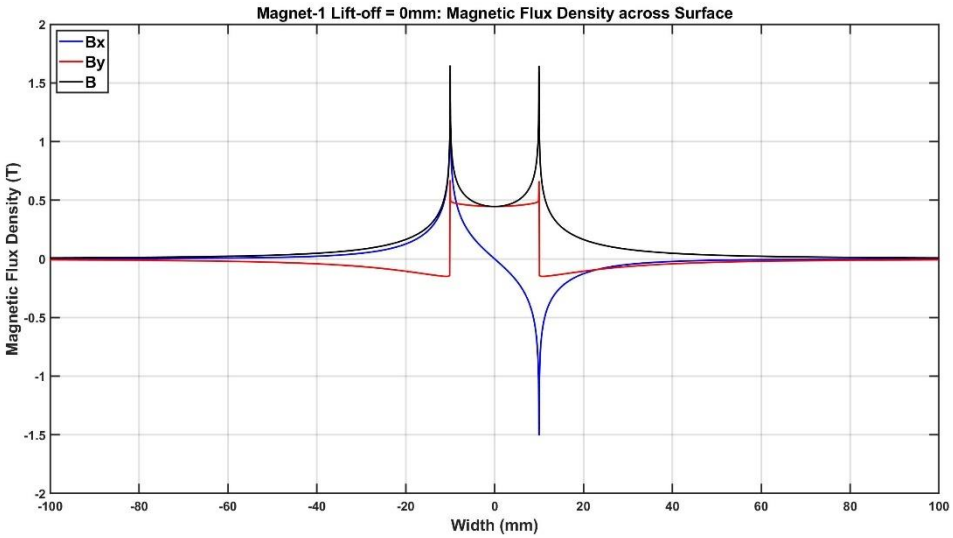

Figure 3.3: Graph of Magnetic Flux Density across the Aluminium Sample's Surface at 0mm lift-off

$$\theta_B = \begin{cases} 90 + sin^{-1}\left(\frac{B_y}{\sqrt{{B_x}^2 + {B_y}^2}}\right), B_x \geq 0 \\ -\left[90 + sin^{-1}\left(\frac{B_y}{\sqrt{{B_x}^2 + {B_y}^2}}\right)\right], B_x < 0 \end{cases} \quad \text{Equation 3.7}$$

where θ_B = angular orientation of magnetic flux density (°); B_x = x-component of magnetic flux density (T); B_y = y-component of magnetic flux (T).

Figure 3.4 shows the orientation of the magnetic field across the surface of the aluminium, based upon the results shown in Figure 3.3. From the corners of the magnet at ±10mm, the vertical component of magnetic flux density inverts from positive (upwards) directly beneath the magnet to negative (downwards) outside of the magnet. Since the induced eddy current densities from the coil retain their alternating direction, this inversion of the magnetic flux density also inverts the alternating orientation of the Lorentz forces that were beyond the corners of the magnet.

Figure 3.5 and Figure 3.6 show that the maximum value of magnetic flux density at the surface of the sample decreases as lift-off increases, due to the lines of magnetic flux spreading over a larger area. The data also shows that the position of maximum magnetic flux density on the sample's surface shifts from beneath the edge of the magnet to beneath the centre as lift-off increased.

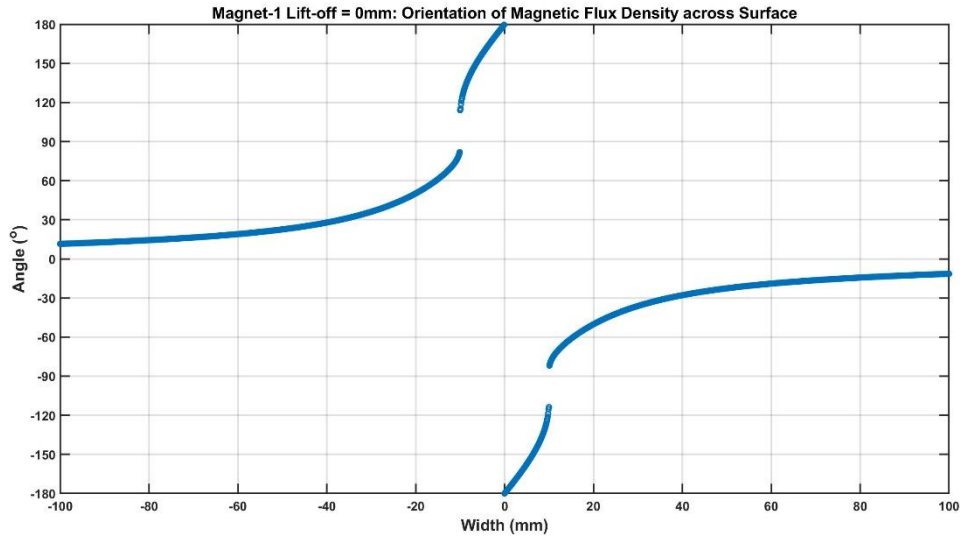

Figure 3.4: Graph of Magnetic Field Orientation across the Aluminium Sample's Surface at 0mm lift-off

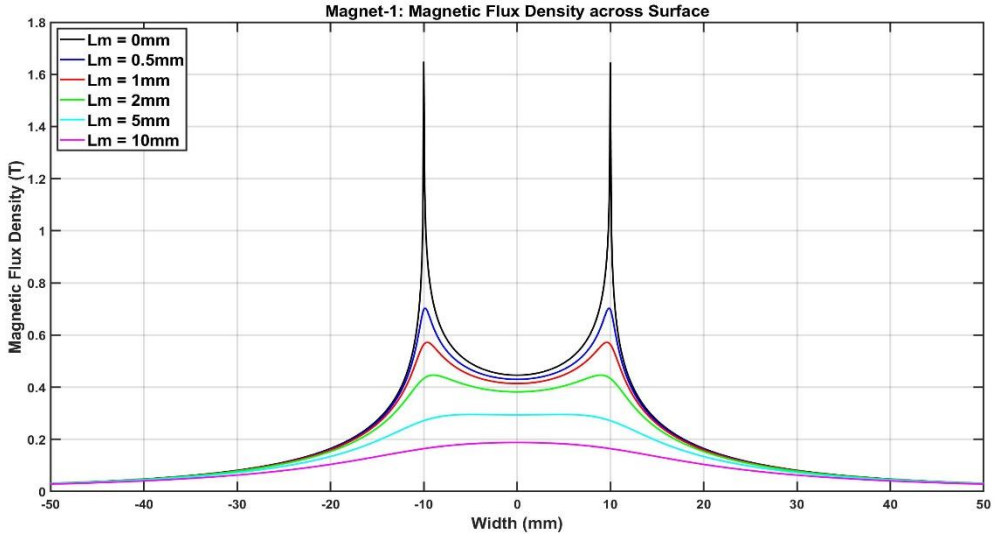

Figure 3.5: Graph of Magnetic Flux Magnitude across Aluminium Sample's Surface for increasing lift-off

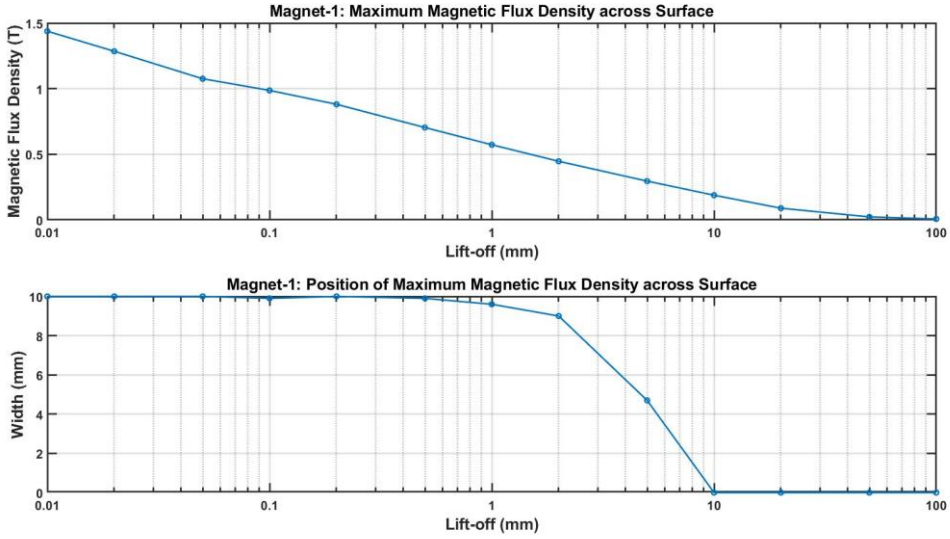

Figure 3.6: Graphs of Maximum Magnetic Flux Density at Surface of Aluminium Sample for increasing Lift-off

Due to their low transduction efficiency, much work has gone into optimising the performance of EMATs by altering their structural design [49, 50, 70]. Jia, Ouyang, and Zhang [74] improved the performance of a spiral-coil EMAT by exchanging its cylindrical magnet for an annular magnet around a smaller cylindrical magnet. Using the same spiral-coil, this new magnetic configuration increased the EMAT's SNR from 4.08dB to 13.96dB.

A second parametric study was therefore performed on different magnetic configurations. This was done to investigate the effect that this had on the magnetic flux density at the surface of the aluminium, and whether an alternative magnetic configuration could be used to optimise the MLC EMAT's transduction efficiency (explored in Chapter 5). Alternate configurations included changing the width of the magnet and/or stacking multiple magnets together in alternating polarity (akin to a PPM EMAT). The limits imposed to the number of magnetic configurations simulated included:

1. The magnets must remain N42-NdFeB block magnets with vertically directed magnetic fields.
2. The magnets must fit into the experimental MLC EMAT's casing (40mm x 40mm x 20mm) giving a total width of 40mm and a total height of 20mm.
3. The magnets must be able to be bought from commercial suppliers.

These requirements limited the magnets used to three different widths: 20mm; 40mm; and 10mm. The magnetic configurations simulated are listed in Table 3.2, and Figure 3.7-Figure 3.13 show the magnetic fields of the alternate configurations. Table 3.2 also includes the number of peaks in magnetic flux density across the surface at 1mm lift-off, and how many of those peaks fell within the width of the coil array (stated later in Section 3.4 to be equal to 28.5mm). These number of peaks tends to be equal to the number of magnets used plus one. This was due to the large concentrations of magnetic flux density at the corners of each magnetic configuration. It is desirable to have these peak values within the width of the coil array to increase the EMAT's transduction efficiency (according to Equation 2.22).

Table 3.2: Vertical Magnetic Configuration Design

Magnet Number	Magnetic Configuration	Number of Peaks across Surface at 1mm Lift-off	Number of Peaks within Coil Array at 1mm Lift-off
1	20mm	2	2
2	40mm	2	0
3	20mm-20mm	3	1
4	10mm-20mm-10mm	2	2
5	10mm	2	2
6	10mm-10mm	1	1
7	10mm-10mm-10mm	4	2
8	10mm-10mm-10mm-10mm	5	3

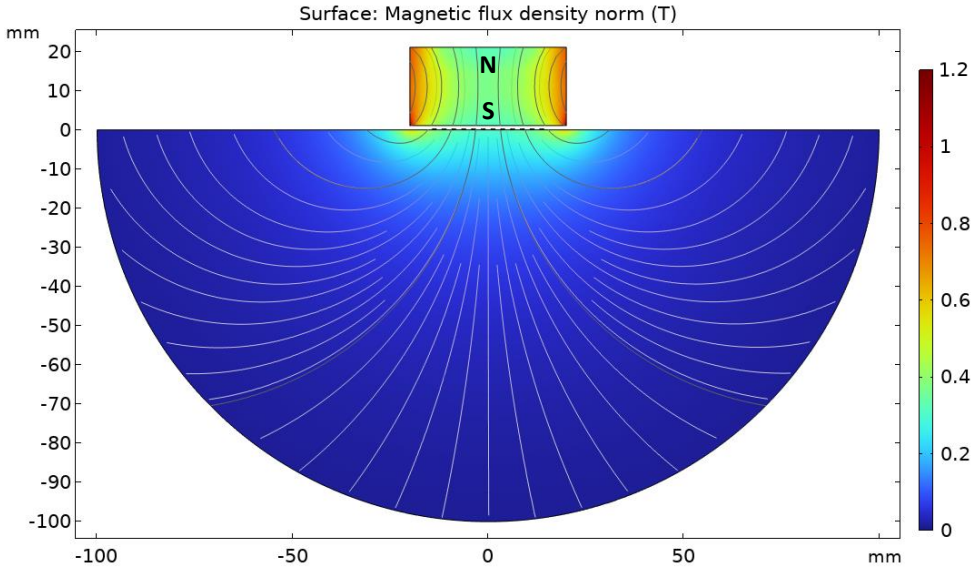

Figure 3.7: Colour-plot of Magnet-2

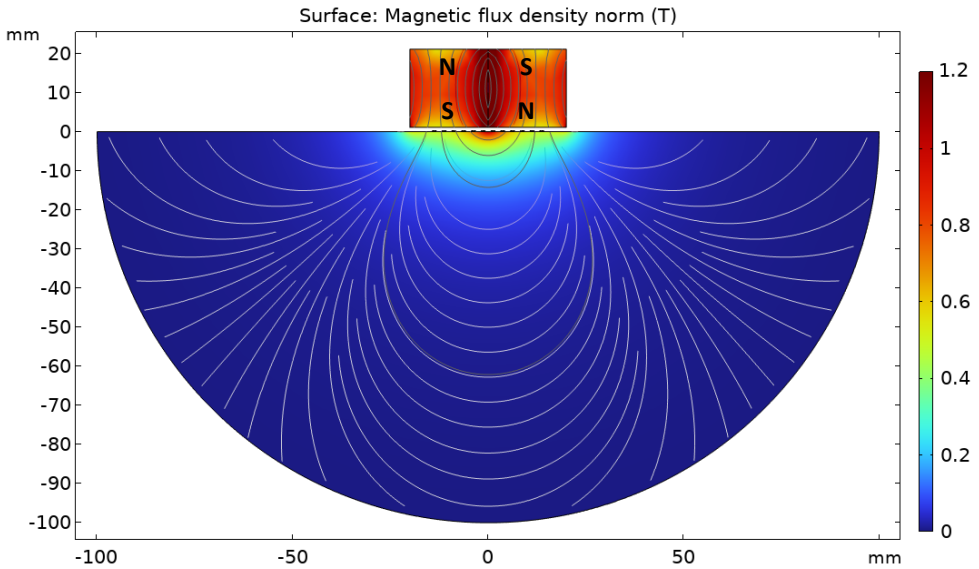

Figure 3.8: Colour-plot of Magnet-3

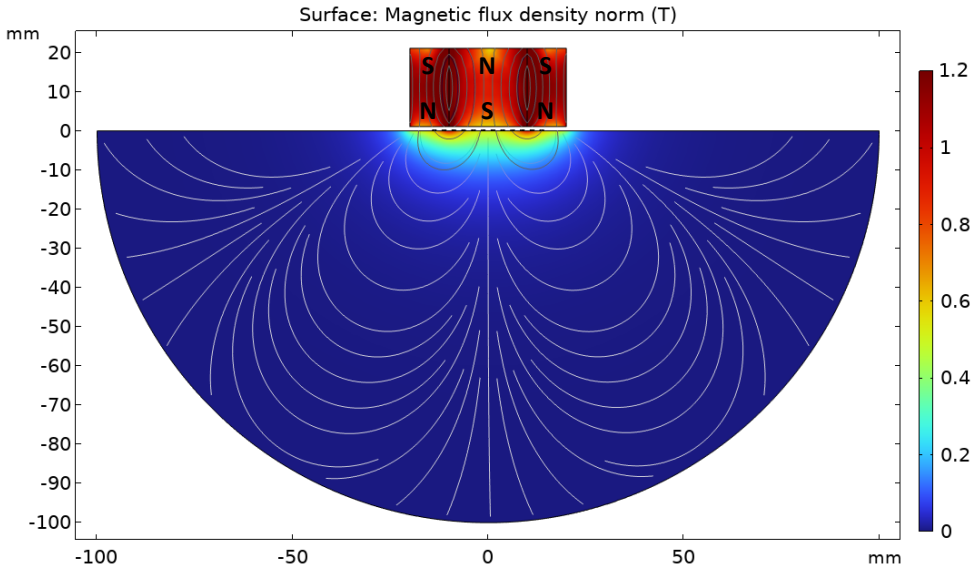

Figure 3.9: Colour-plot of Magnet-4

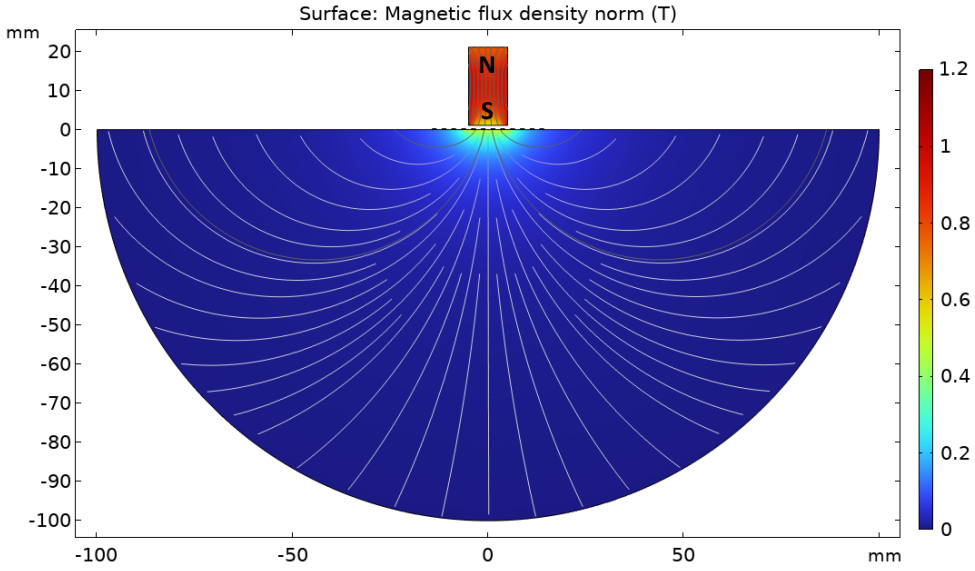

Figure 3.10: Colour-plot of Magnet-5

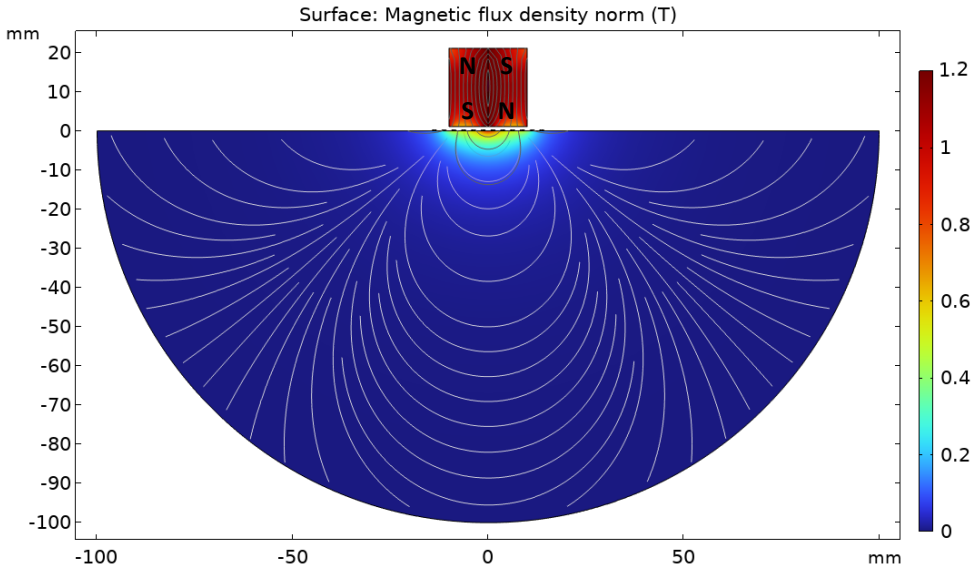

Figure 3.11: Colour-plot of Magnet-6

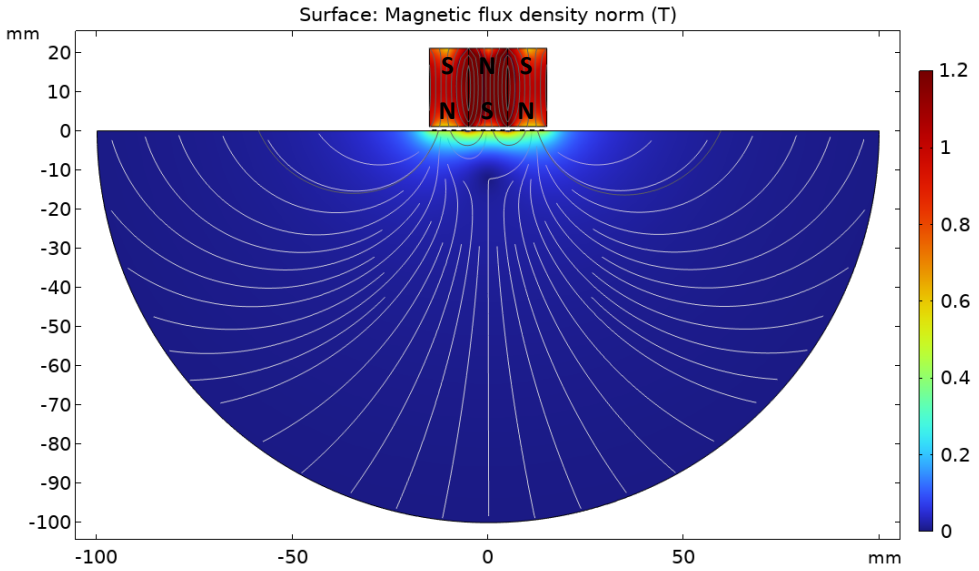

Figure 3.12: Colour-plot of Magnet-7

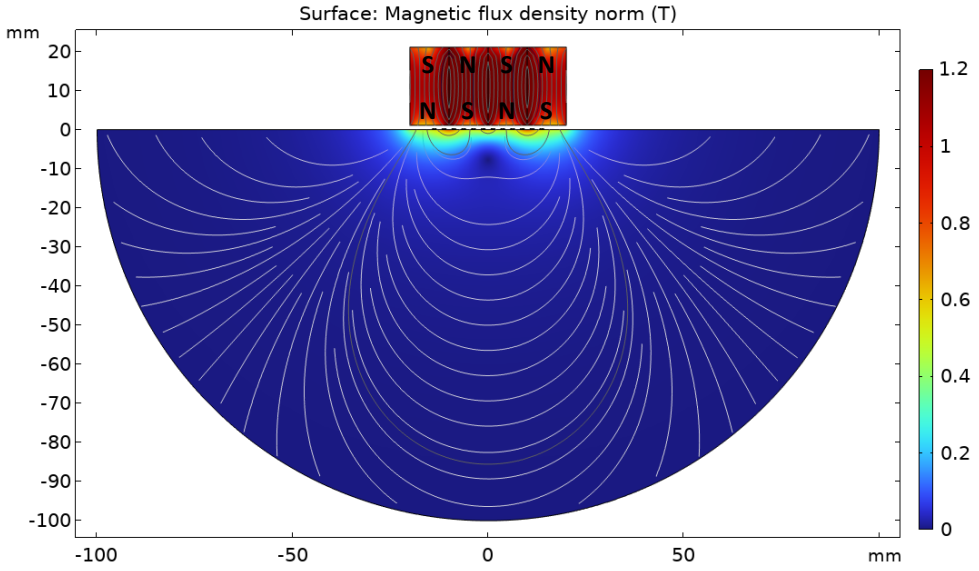

Figure 3.13: Colour-plot of Magnet-8

Figure 3.14 and Figure 3.15 show the magnitudes and positions respectively of maximum magnetic flux density across the aluminium's surface for these magnetic configurations. Figure 3.14 shows that the magnetic configurations with the largest magnetic flux density were those with two or more magnets in its configuration, with Magnet-3 as the greatest. These values of magnetic flux density originate from beneath the positions where the vertical polarity of the magnetic field inverts (at the corners of the magnets). Magnets 1, 2, & 5 by comparison possess lower magnetic flux densities from beneath the corners of their single magnets, however they decay more steadily as lift-off increases.

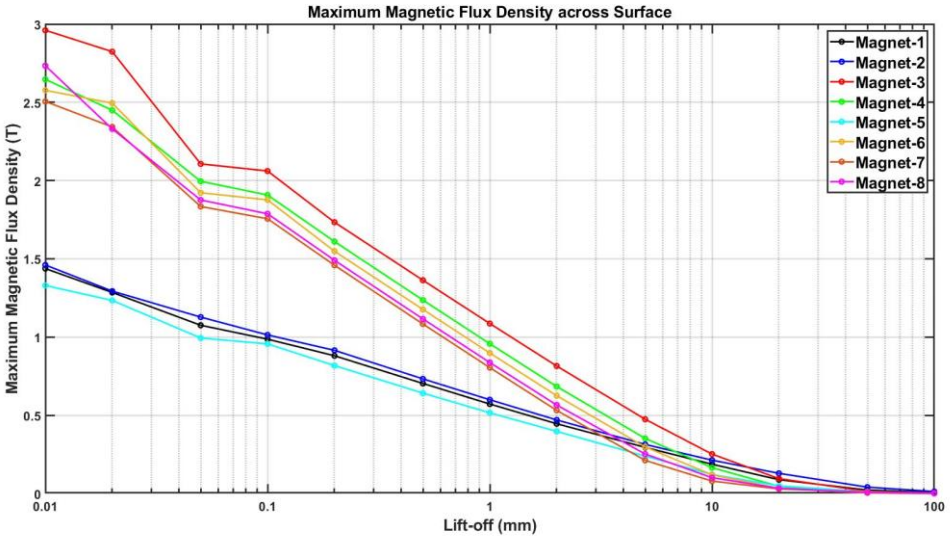

Figure 3.14: Graph of Maximum Magnetic Flux Density at Surface of Aluminium Sample for Magnetic Configurations

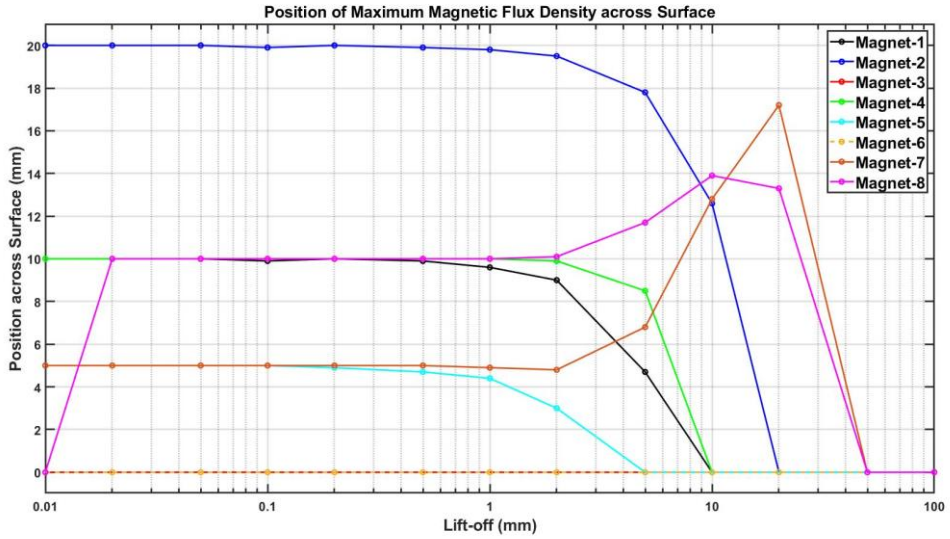

Figure 3.15: Graph of Position of Maximum Magnetic Flux Density at Surface of Aluminium Sample for Magnetic Configurations

Figure 3.15 shows that as lift-off increases, the position of maximum magnetic flux tends to move from the corners of magnets to the centre of the overall magnetic configuration. This is due to the y-component of magnetic flux density at the centre of the configuration becoming proportionally greater than the x-component at a given point, as shown in Figure 3.5. This trend is certainly true for Magnets 1, 2, 4, & 5, while Magnets 3 & 6 keep a constant position at 0mm due to having two magnets of equal width concentrating the magnetic flux density at the centre of the surface. For Magnets 7 & 8 however, the position of maximum flux density moves away from the inner magnet's corners where the polarity reverses and closer to the edges of the overall magnetic configuration.

3.4. Coils Model

The experimental MLC consisted of six turns of a printed copper coil track within a 25/25/0 plastic coverlay, shown in Figure 3.16. Each turn consisted of two coil runs, the spacing interval between each run was 2.5mm, and each run was made up of three strands to spread the induced eddy current density across the surface more evenly. Figure 3.16 is annotated with the coil numbers for each run, as well as to highlight the overall width and depth of the coil array. Figure 3.17 shows the simulated dimensions of the coil's CSA for a single turn.

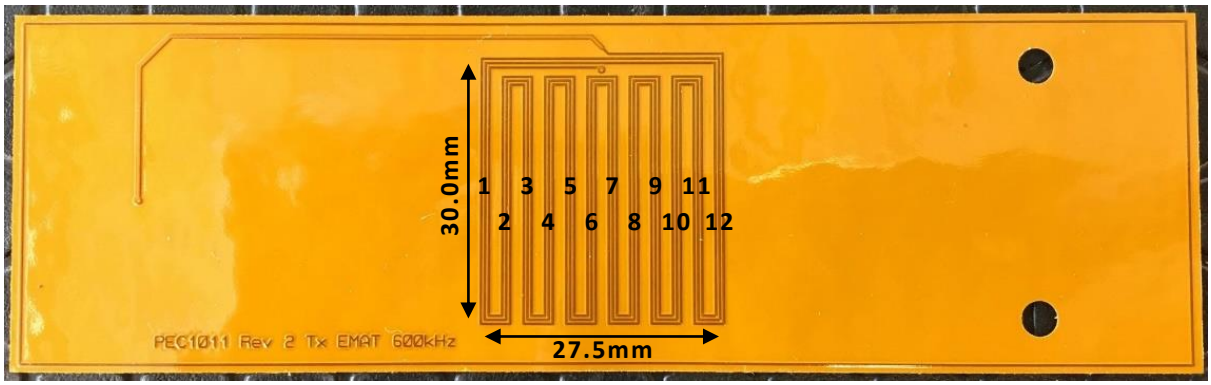

Figure 3.16: Experimental MLC design

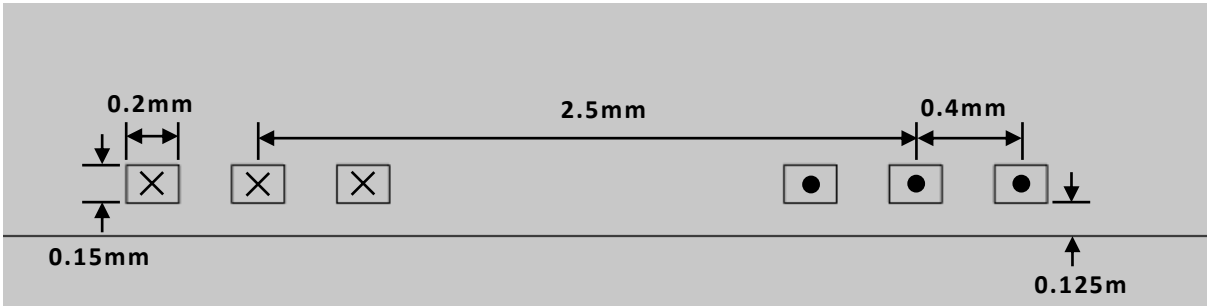

Figure 3.17: Simulated Design of MLC at 0mm Lift-off

The design of the coil model mostly followed that of the magnetic model, however there were a few key differences. The thickness of the plastic coverlay added an additional 0.125mm to any lift-off applied, so for an MLC lift-off of 0mm (shown in Figure 3.17) the actual lift-off is 0.125mm. The centre of this coil array (between coils 6 & 7) was positioned at the centre of the aluminium's surface. Standard copper from COMSOL's material library (σ_e = 59.98MS/m) was used for the coils, however the plastic coverlay was omitted as it had no effect on the electromagnetic properties. The coil domain within the 'Magnetic Fields (mf)' physics interface defined the coil's meandering direction of current flow, with a maximum current amplitude of 6A. This value was chosen to emulate the maximum current of the experimental EMAT's transmission signal.

Due to the direction of AC, z-components of eddy current density were extracted from the aluminium.

The same parametric study on the effects of lift-off were performed on the MLC, to recording the induced eddy current density at the aluminium's surface. A second parametric study on the frequency of the AC through the coils was also conducted, as this was how the shear waves would be steered (according to Equation 2.29). This model therefore required a frequency study step, replacing the stationary study step used for the magnet's model.

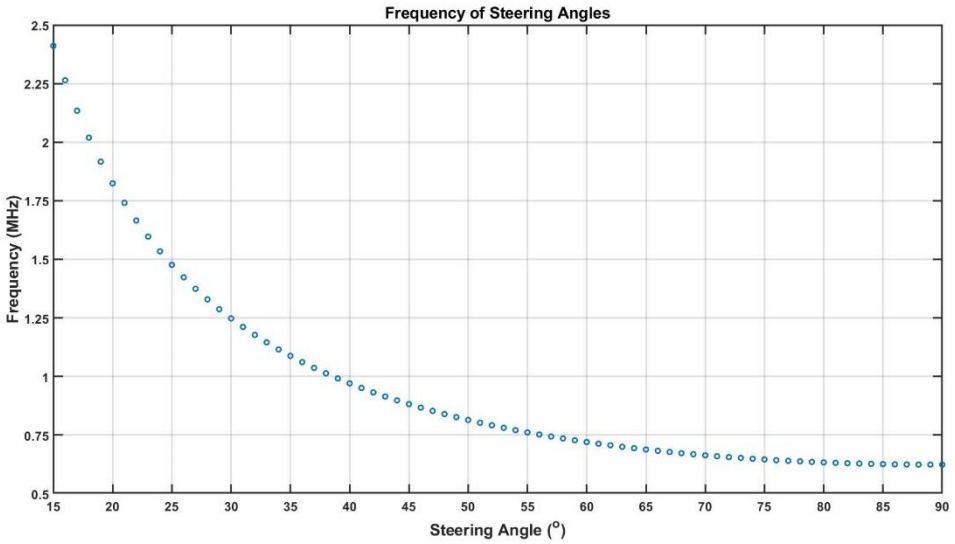

Figure 3.18: Frequency across Steering Angles

Figure 3.18 shows the values of frequency calculated for steering angles of 15-90°. The frequency range of 0.6240-2.4110MHz has an SDP range of 0.1037-0.0528mm respectively within the aluminium's surface, according to Equation 2.35. Values of eddy current density required extraction at 0.01mm increments to allow for at least five nodes per skin depth for all steering angles, necessitating a maximum mesh size of 0.01mm. As it was impractical to achieve this mesh across the entire aluminium sample, an area of high-mesh density was constructed directly beneath the MLC where the eddy currents would be induced. This area extended horizontally from -30mm to 30mm to cover the complete width of the MLC, and vertically from the surface to 0.50mm below to cover approximately five skin depths for the steering angle range. The remaining aluminium used a standard mesh due to a lack of any relevant data.

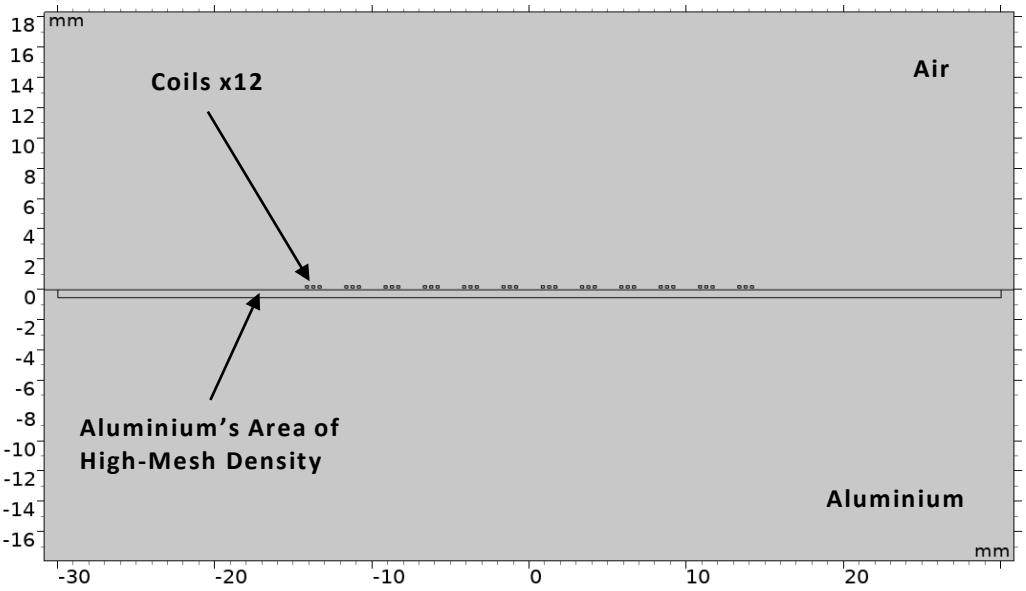

Figure 3.19: COMSOL 2D Model of MLC over Aluminium

Figure 3.19 shows the design of the coil model, annotated to show the area of high-mesh density. Figure 3.20 shows the maximum value of eddy current density across the surface of the aluminium as lift-off increased, for the 15° and 90° steering angles. There is a noticeable exponential decay in eddy current density as lift-off increases, both at and beneath the surface of the aluminium.

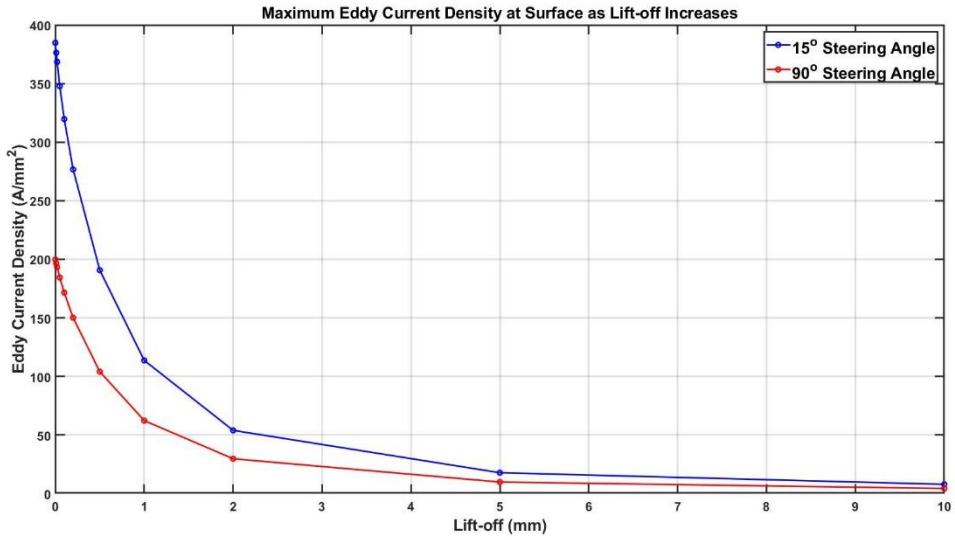

Figure 3.20: Maximum Eddy Current Density across Lift-off

Figure 3.21 and Figure 3.22 show the distribution of the eddy current density at the surface of the aluminium as lift-off increases, for the 15° and 90° steering angles respectively.

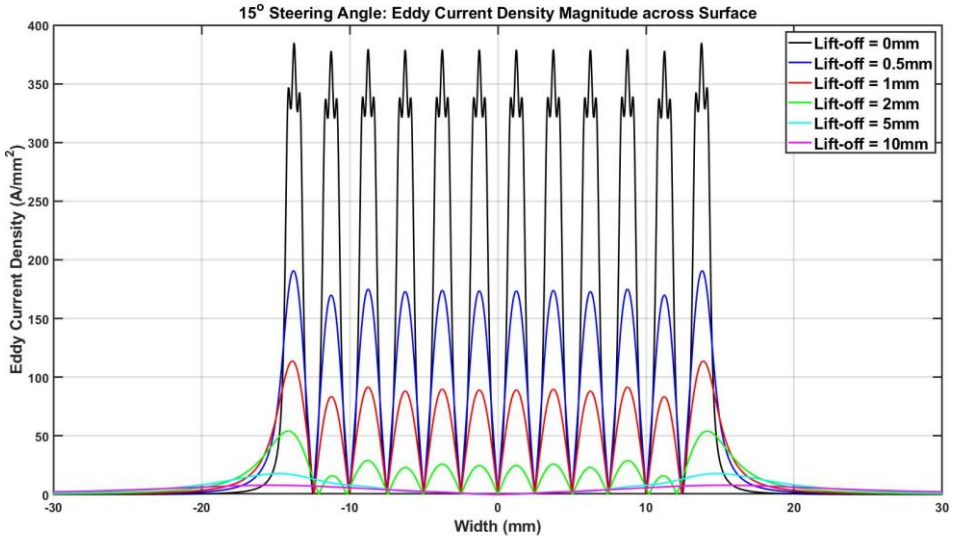

Figure 3.21: Eddy Current Density Profiles for 15° Steering Angle

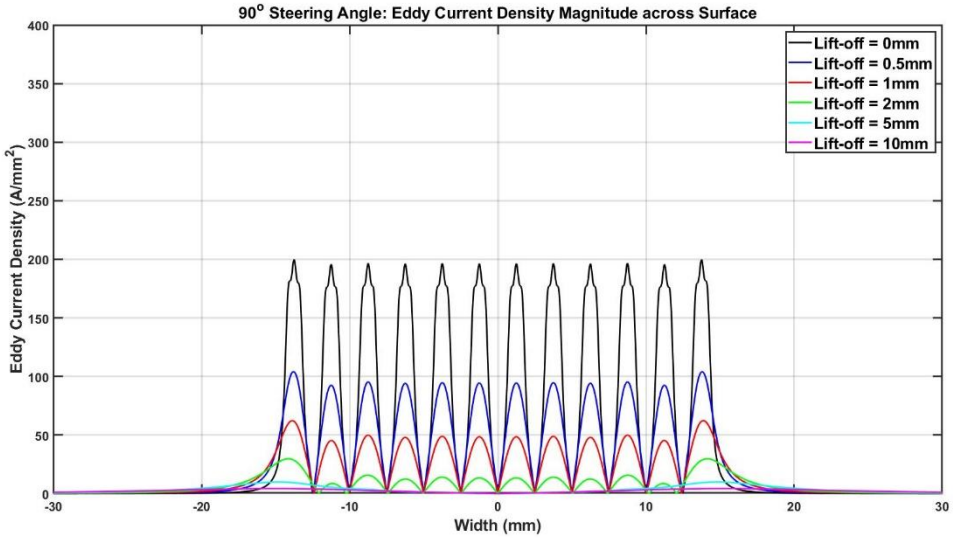

Figure 3.22: Eddy Current Density Profiles for 90° Steering Angle

Between these two extreme steering angles, the maximum value of eddy current density at the surface decreases from 385A/mm² to 200A/mm² at 0mm lift-off. Despite this drop, the decay in eddy current density as lift-off increases remains proportional across steering angles, as seen in Figure 3.23.

It is also noticeable from the 15° steering angle that the eddy current profile at 0mm MLC lift-off is well-defined enough to plot the induction from each coil strand. This is due to the reduced SDP concentrating the eddy currents at the surface. As the steering angle increases, the SDP also increases causing the eddy currents to become more dispersed at the surface, thus causing the eddy current profile to lose its definition. Figure 3.24 shows the values of eddy current density for steering angles of 15° and 90° as depth increases.

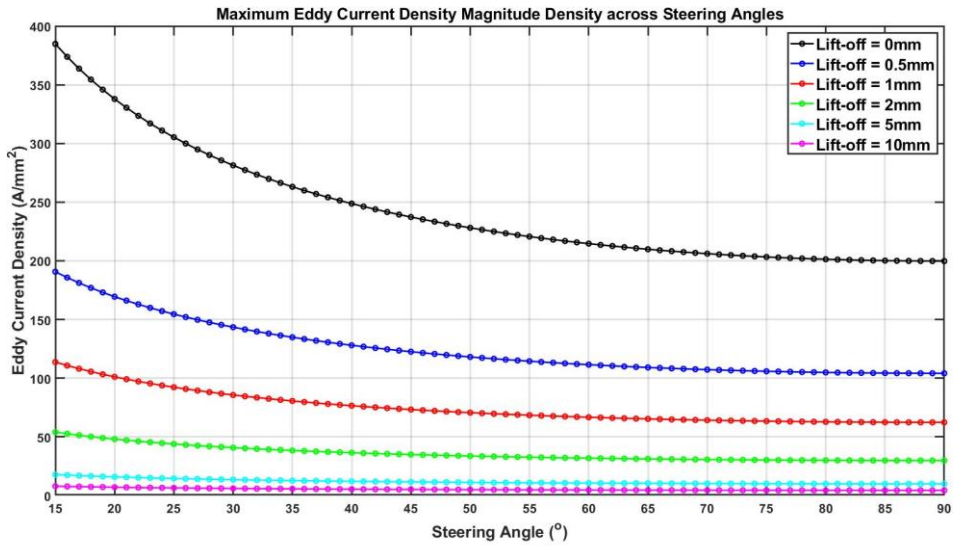

Figure 3.23: Maximum Eddy Current Density across Steering Angles

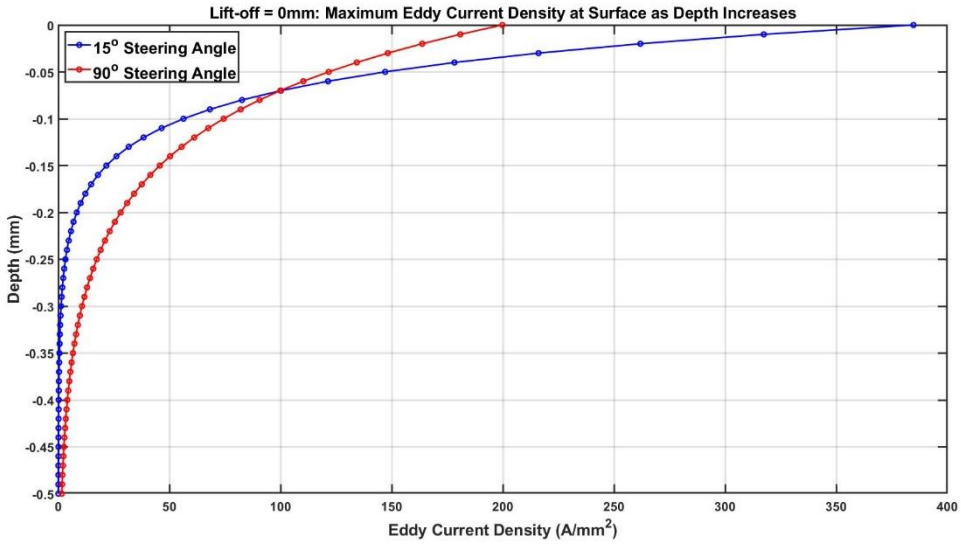

Figure 3.24: Maximum Eddy Current Density across Depth

Figure 3.24 shows that the induced eddy current density for the 15° steering angle decays at a faster rate with depth than the 90° steering angle, due to its comparatively greater eddy current density at the surface and reduced SDP. For steering angles of 15° and 90° (with SDPs of 0.0528mm and 0.1037mm respectively) the values of eddy current density at 3SDP would be equal to their surface values (of 385A/mm² to 200A/mm² respectively) scaled by a factor of $1/e^3$. These values were measured at 17.8A/mm² and 9.7 A/mm² respectively, demonstrating the effect of skin depth. These exponential decreases were the same for the variety of lift-offs.

What is noteworthy from Figure 3.21 and Figure 3.22 was that for all eddy current profiles, the position of maximum eddy current density is located beneath coils 1 and 12. This is due to their positions at the ends of the coil

array, meaning that they had only one neighbouring coil (rather than two) in an alternating direction to reduce its induced eddy currents. Moving inward from the ends of the array, the value of eddy current density oscillated until it reached a centre. A third parametric study was conducted on the number of coils within the array, to observe whether this pattern of behaviour remained consistent. The number of coils reduced from twelve to two in increments of two. Figure 3.25 shows the peak values of eddy current density induced from each of the coils within all six arrays, at an MLC lift-off of 0mm (as explained in Figure 3.17).

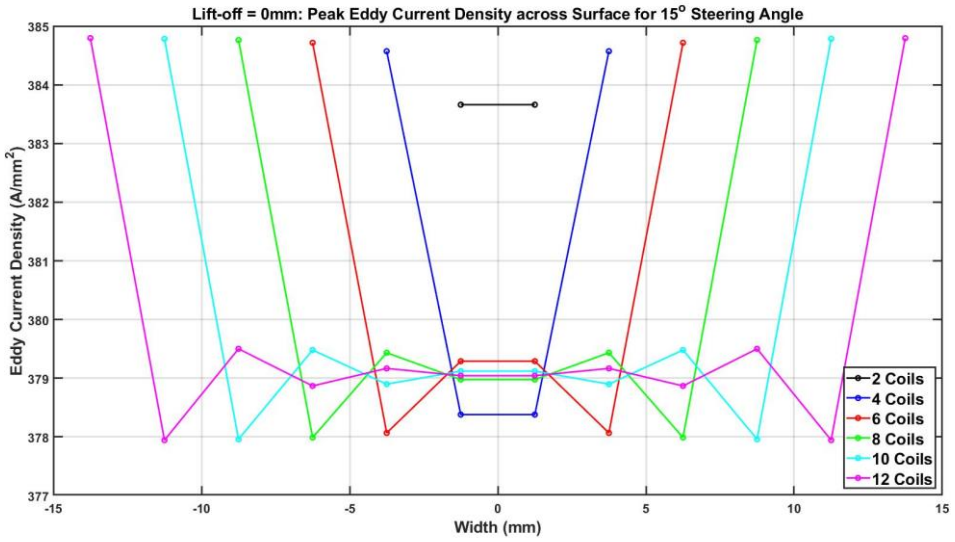

Figure 3.25: Maximum Eddy Current Density Peaks across Number of Coils at 0mm lift-off

This pattern remains consistent for all steering angles and for lift-offs up to 2mm. Beyond 2mm lift-off, the eddy current profiles become so distributed that only two peaks are measured. By this point however, the maximum eddy current density values decay so much that they would be impractical to use.

3.5. EMAT Model

To build a model of the complete EMAT, both magnet and coil models were combined into a single 2D model. The primary difference with this model was the inclusion of the multiphysics coupling between the 'Magnetic Fields' and the 'Solid Mechanics' physics interfaces. This permitted the simulation of the ultrasonic waves generated from the Lorentz forces, calculated by the induced eddy current and the bias magnetic field within the aluminium (according to

Equation 2.22). The stationary study step was used to calculate the magnet's static magnetic field, however the coil's frequency study step was replaced with two time-dependent steps: the first to simulate the produced Lorentz forces via the multiphysics coupling; and the second to simulate the ultrasonic wave propagation via the solid mechanics physics interface only.

The reason for two separate time-dependent study steps was due to the multiphysics coupling within the first step. This required the area of high-mesh density from the coil model, which created a greater computational load. This area of high-mesh density was not required within the second step due to the simulation of the wave propagation only. Figure 3.26 shows the difference in meshing between these two time-dependent study steps.

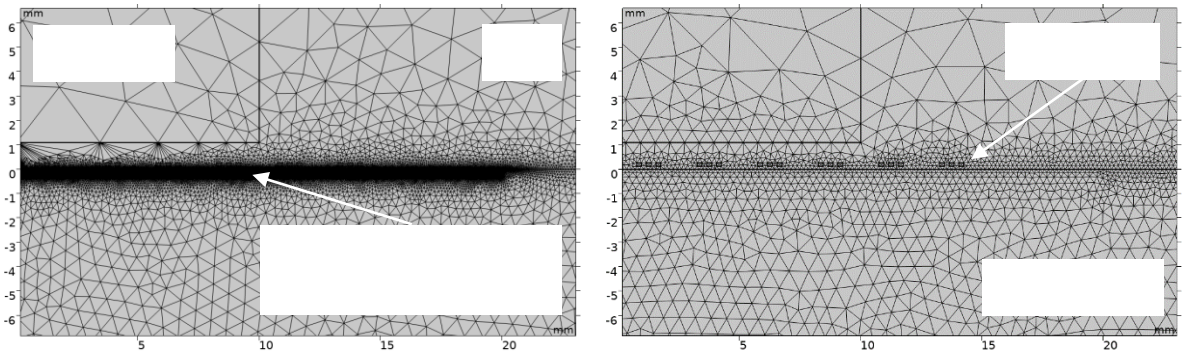

Figure 3.26: COMSOL model's mesh beneath the EMAT for: first time-dependent study step (left); and second time-dependent study step (right)

To further reduce the computational load, changes were made to the mesh density of the model. Mesh convergence tests were conducted on different sections of the model. Firstly, maximum mesh size within the bulk material (within which the bulk waves propagated) was set at a value of six elements per wavelength. This number of elements per wavelength changed the desired results by less than 0.8% (as shown in Figure 3.27) and has been accepted in previous literature [75]. This maximum mesh size value changed for a given steering angle, in accordance with Equation 3.8. Using this mesh density, further mesh convergence tests were performed on the high-mesh density area's mesh density and depth (seen in Figure 3.28 and Figure 3.29 respectively). From these results the high-mesh area was given a depth of three SDP, and a maximum mesh size of five elements per skin depth.

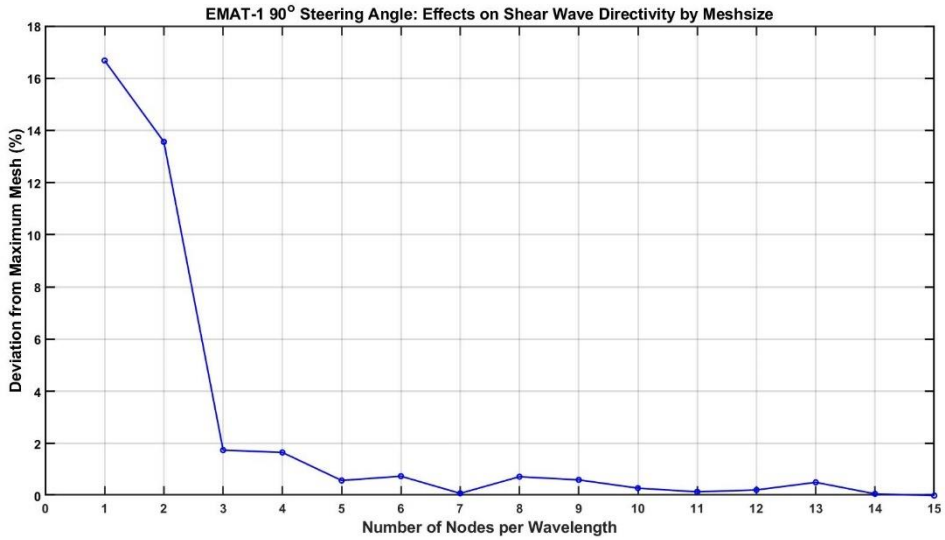

Figure 3.27: Bulk Material Mesh Convergence Graph

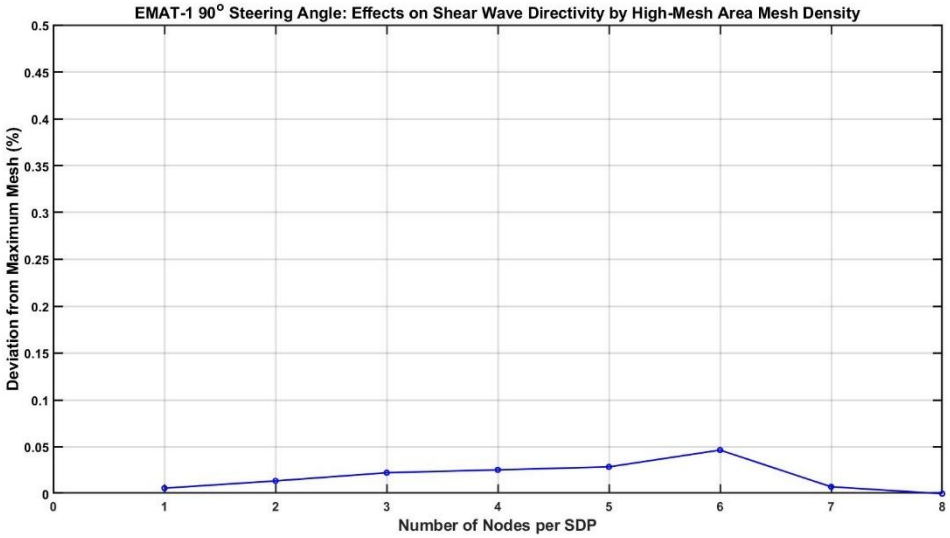

Figure 3.28: High-Mesh Area Mesh Convergence Graph

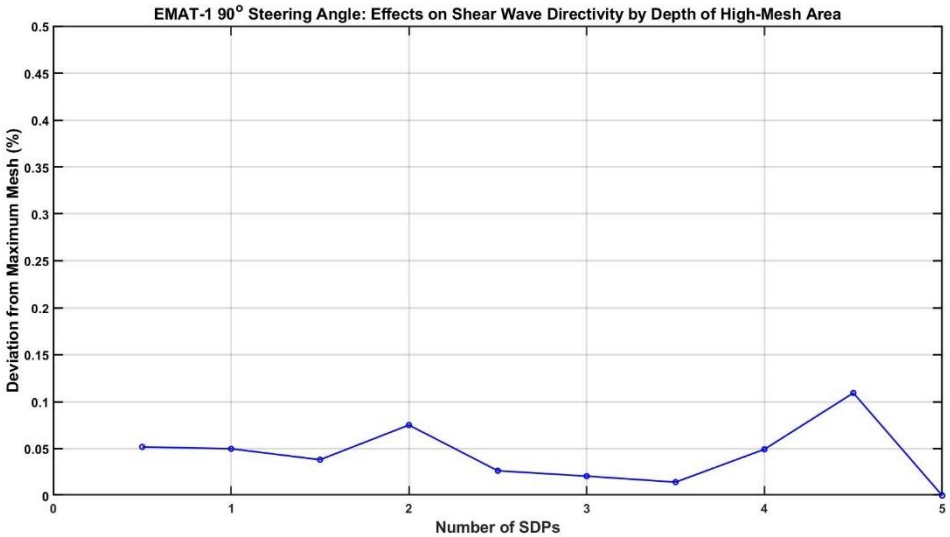

Figure 3.29: High-Mesh Area Depth Mesh Convergence Graph

$$h_{max} = \frac{\lambda_{min}}{N} = \frac{2d \times sin\,\theta}{N}$$ Equation 3.8

where h_{max} = maximum mesh size (m); λ_{min} = minimum wavelength (m); N = number of mesh elements per wavelength (1/m).

The width of this high-mesh area was also decreased from 60mm to 40mm, as Figure 3.21 and Figure 3.22 shows that the induced eddy current density reduces to less than 1% the maximum value at 20mm from the centre. These values provided a compromise between the number of simulations that could be run, the time taken to run them, and their overall accuracy.

When solving time-dependent (transient) models it is important to consider the length of the timestep, as it resolves the wave equation across time just as the mesh resolves it across space. Since longer timesteps do not make optimal use of the mesh and shorter timesteps do not increase the simulations runtime without any significant improvement to the results, the relationship between these two values was made proportional to the Courant-Friedrichs-Lewy (CFL) number [76], shown in Equation 3.9. The model used COMSOL Multiphysics' default implicit 2nd-order generalised alpha method to solve transient acoustic problems, and the 2nd-order Lagrange elements in space. This meant that to reduce the temporal discretization errors a CFL < 0.2 should be used [77], however a CFL < 0.1 was used within these models for greater stability.

$$CFL = \frac{v_s \times \Delta t}{h_{max}} \qquad \text{Equation 3.9}$$

where CFL = Courant-Friedrichs-Lewy number; Δt = timestep (s).

A gaussian window was used to modulate the transmission signal within the coils, shown in Equation 3.10. The reason that a modulated gaussian pulse was preferable over a purely sinusoidal pulse is explained by Hong, Sun and Kim [78], but in summary: its time and frequency localisation are better due to the pulse energy being concentrated near the centre. While the method of experimental signal transmission (discussed later in Section 4.2) was as a voltage pulse, a current pulse was chosen for this thesis due to its direct proportionality to the induced Lorentz forces (as shown in Equation 2.22).

$$I(t) = I_{max} \times e^{-\frac{(t-\tau)^2}{2\sigma^2}} cos\big(2\pi f(t-\tau)\big) \qquad \text{Equation 3.10}$$

where $I(t)$ = current of signal at time 't (µs)' (A); I_{max} = maximum current amplitude = 6A; τ = time delay (s); σ = standard deviation (s).

The current pulse was designed to emit multiple peaks with the maximum at the centre (occurring at $t = \tau$), that could be used for ToA calculations. The amplitude of the respective peaks was equal across the range of angles, as the standard deviation was inversely proportional to the frequency ($\sigma = 1.2/f$).

To further reduce its computational load, the timeframe of the first time-dependent step was limited to the period in which the transmission signal's peaks were greater than 1% of the maximum amplitude. A range of at least 3σ from the centre of a normal distribution is typically used, however for this range it was increased to 3.125σ (equal to $3.75/f$) to allow the pulse to complete 7.5 cycles. The time delay was rounded up to the nearest timestep (expressed in Equation 3.11) which resulted in the timeframe of the first time-dependent study step ranging from 0µs to 2τ for each steering angle. Figure 3.30 shows the transmission signals for steering angles of 15° and 90° for a coil spacing of 2.5mm, and Table 3.3 shows the simulation variables across that range of steering angles.

$$\tau = roundup\left[\frac{3.75}{f \times \Delta t}\right] \times \Delta t \qquad \text{Equation 3.11}$$

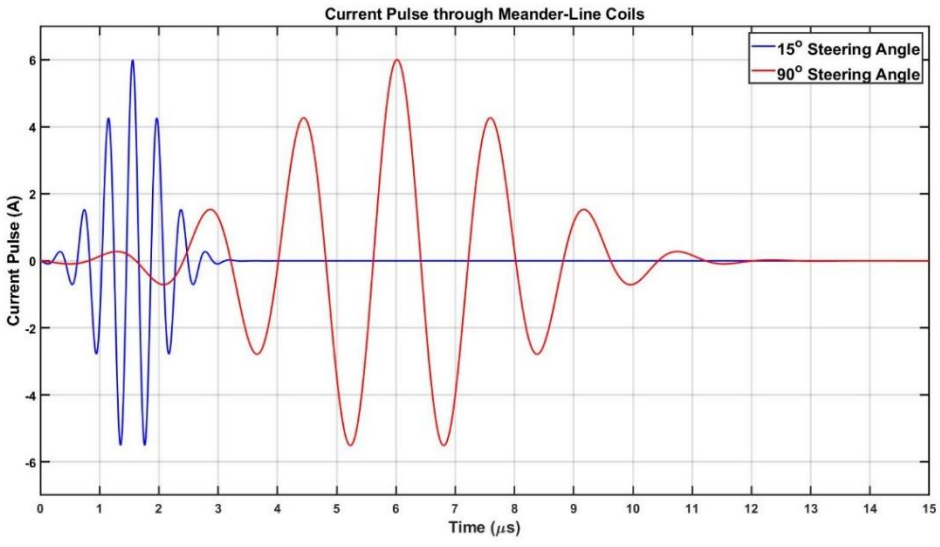

Figure 3.30: Graph of current pulse profile through coils for 15° and 90° steering angles

Table 3.3: EMAT model variables for a given steering angle

a (°)	f (MHz)	σ (µs)	hmax (mm)	Δt (ns)	τ (µs)	CFL
15	2.4110	0.4977	0.2157	6.60	1.5576	0.0955
20	1.8245	0.6577	0.2850	9.00	2.0610	0.0985
25	1.4765	0.8127	0.3522	11.25	2.5425	0.0997
30	1.2480	0.9615	0.4167	13.20	3.0096	0.0988
35	1.0879	1.1030	0.4780	15.00	3.4500	0.0979
40	0.9708	1.2361	0.5357	16.50	3.8775	0.0961
45	0.8825	1.3598	0.5893	18.75	4.2563	0.0993
50	0.8146	1.4732	0.6384	20.00	4.6200	0.0977
55	0.7618	1.5753	0.6826	20.00	4.9400	0.0914
60	0.7205	1.6654	0.7217	22.50	5.2200	0.0973
65	0.6885	1.7429	0.7553	24.00	5.4480	0.0991
70	0.6640	1.8071	0.7831	25.00	5.6500	0.0996
75	0.6460	1.8575	0.8049	25.00	5.8250	0.0969
80	0.6336	1.8939	0.8207	25.00	5.9250	0.0950
85	0.6264	1.9158	0.8302	26.40	5.9928	0.0992
90	0.6240	1.9231	0.8333	26.40	6.0192	0.0988

The timeframe of the second time-dependent study step for each steering angle ranged from 2τ to the end of the simulation at 99µs, as this included the return of the shear waves to the MLC. The value of the timestep was calculated using Equation 3.9 and rounded down to the nearest value, such that dividing 99µs by it would produce an integer number of timesteps for the duration of the model.

The design of the magnet and coils (discussed in Sections 3.3-3.4) was unchanged for the EMAT model, however their lift-off distances were set at fixed values. The MLC's lift-off was set at 0mm, meaning that the copper coils had an actual lift-off of 0.125mm due to their design (as explained in Figure 3.17). The magnet's lift-off however was set at 1.1mm. This was based off of the experimental EMAT's design, consisting of: the 0.4mm-thick MLC; three layers of 0.2mm-thick plastic shims; and one layer of 0.1mm-thick copper tape.

The inclusion of the copper and plastic layers in this order diminished any induced eddy currents (and thus Lorentz forces) within the nickel surface of the magnet. These forces generated ultrasonic waves in the magnet's surface that were received up by the EMAT when used in a PE configuration. Figure 3.31 shows the effect that these plastic shims and copper tape had on the received signals from the experimental MLC EMAT in a PE setup. Not only is the signal far noisier, but it could not be filtered out and resulted in a reduced SNR for the received shear wave.

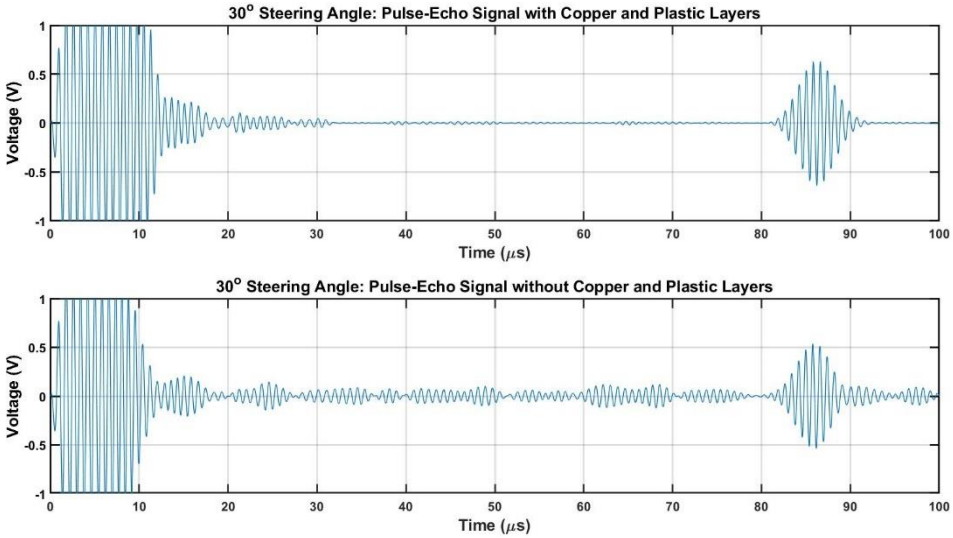

Figure 3.31: MLC EMAT PE Signal

The shape of the aluminium sample was semicircular (100mm in radius) to measure the beam directivity of the bulk waves. The x & y components of displacement were extracted from the sample's curved surface across time, to plot the beam directivity of each bulk wave and locate their positions of maximum displacement. Components of displacement were preferable over its magnitude, as they could be used to differentiate between the two types of bulk waves striking the surface based on particle movement (as discussed in Section 4.3.1). The components of displacement were extracted from -90° to 90° across the curved surface (as shown in Figure 3.32) at 0.1° intervals, and from -100mm to 100mm across the flat surface at 0.25mm intervals.

Within the context of rail track inspection, the EMAT would transmit and receive waves in its direction of travel along the track, similar to Yi et al [64] and Edwards et al [79]. The 2D model of the rail track would be rectangular when viewed from side-on, rather than the flat-bottomed rail profile shown in

Figure 1.1. The second shape of the aluminium sample used in this thesis therefore was rectangular (340mm wide by 100mm high). Its shape was used to develop an understanding of the MLC EMAT's steered shear waves across a flat backwall surface before being applied to more complex shapes.

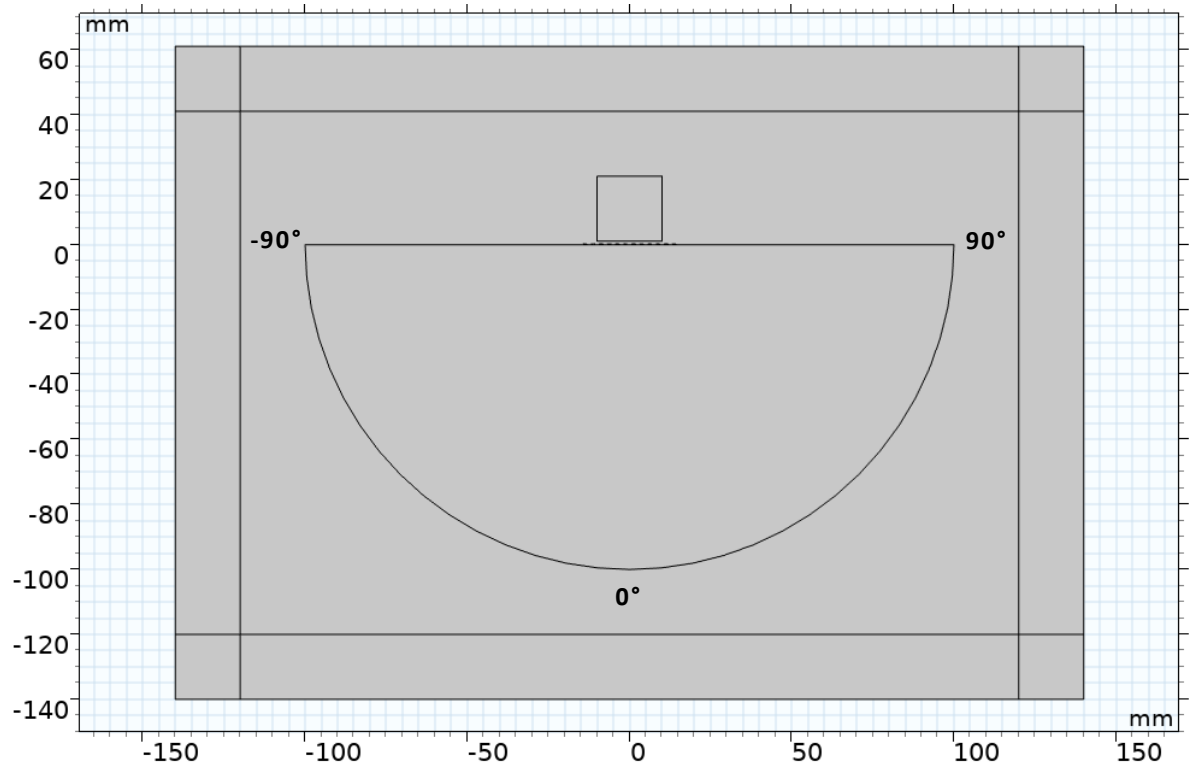

Figure 3.32: EMAT Semicircular Model

As with the semicircular sample, x & y components of displacement were extracted from the surfaces across time, however this was to measure the shear wave steerability across the backwall. Due to its bidirectional transmission, the transmission EMAT (T_x) was positioned 50mm from the edge of the sample's surface. This meant that the shear waves that reflected off of the sample's sidewall onto the backwall could be isolated in time from the shear waves that propagated directly to the backwall. The x & y components of displacement were also extracted at 0.25mm intervals from 0mm to 275mm across the backwall (as shown in Figure 3.33), as this range (over a height of 100mm) would permit a maximum transmission angle of 70° from T_x to be measured.

For both aluminium samples, electromagnetic values were also extracted from the area of high-mesh density directly beneath the EMAT. These values included the x & y components of magnetic flux density and the z-component of eddy current density (as they were in the magnet and coil models). These values were extracted from the first time-dependent study step (during which

the area of high-mesh density existed) and could be used to show the EMAT's electromagnetic behaviour during transmission.

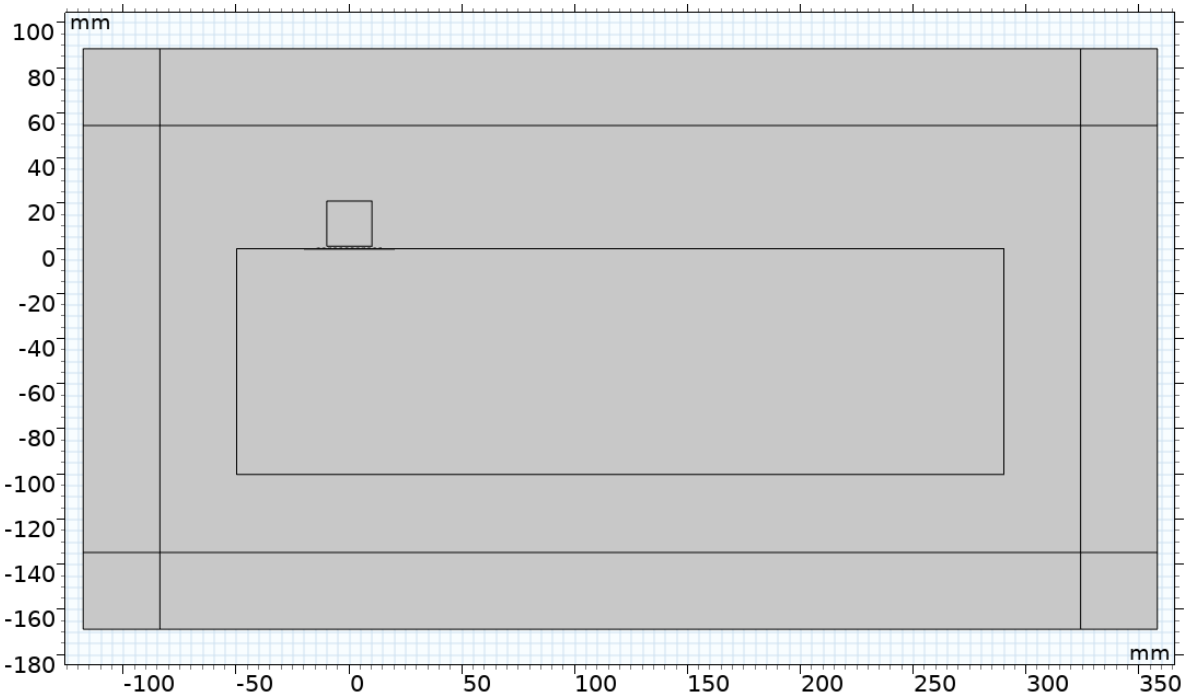

Figure 3.33: EMAT Rectangular Model

The results and data analysis of these simulated models is discussed in Section 4.3.1, however Figure 3.34 shows an example colour-plot of this EMAT model. Figure 3.34 has been annotated to highlight the various wave modes transmitted bidirectionally.

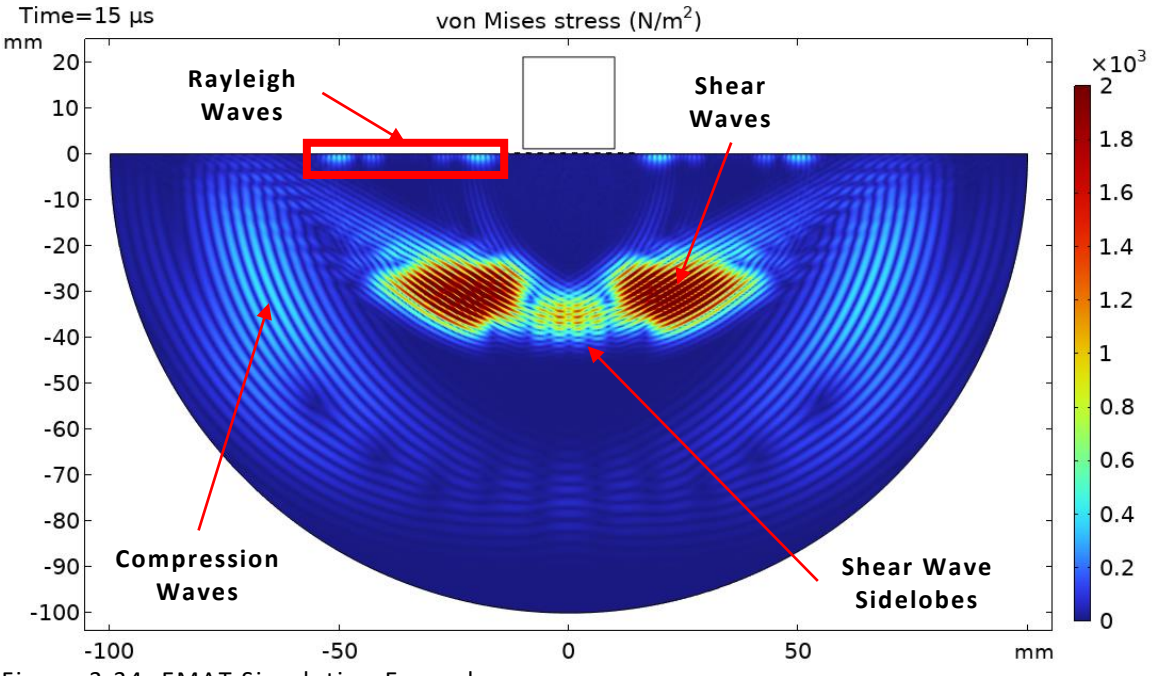

Figure 3.34: EMAT Simulation Example

The compression waves reached the curved surface first due to their greater wave velocity and were reflected or mode converted back to the EMAT.

The two angled shear waves were greater in magnitude than any other wave mode and were next to reach the curved surface. Between these two shear waves were sidelobes angled close to 0°. The Rayleigh waves are seen propagating from the EMAT, across the flat surface, to the curved surface via the corners of the sample at ±90°.

3.6. Summary

A description of the various FEM models was provided within this chapter. These models were of the magnet and MLC individually, culminating in the design of the EMAT model itself. The effects that lift-off has on the electromagnetic properties within the aluminium sample was explored, and the parametric studies performed on the magnetic configurations and number of coils are continued in Chapters 5 and 6 respectively. The trade-offs made in the areas and densities of the EMAT model's mesh has been discussed, however the correlation between the results of these models and the experimental testing was what was ultimately important and is the focus of the next chapter.

Chapter 4 - MLC EMAT Beam Directivity and Steerability

The previous chapter details the simulation models crucial for this thesis, as they enabled a myriad of tests to be run remotely at minimal cost. This chapter explains the results from the numerous simulations performed, and from the experimental testing performed to validate these models.

4.1. Introduction

With the EMAT simulation models constructed, they required validation by experimental setups. Once the experimental results had reliably corroborated the simulated results, further simulations were then performed to investigate the EMAT via parametric studies, without the necessity of experimental verification. The aluminium samples described in Section 3.5 were manufactured according to their simulated counterpart's design, at a depth of 70mm. Using an "Olympus OmniScan MX2" and 4MHz 0° shear and compression probes, the shear and compression wave velocities of the homogeneous aluminium were measured at 3.12mm/µs and 6.40mm/µs respectively. These velocities were entered into the EMAT model's design for greater accuracy.

4.2. Experimental Setup

Since the simulated EMAT's design was based on the experimental MLC EMAT, and the aluminium samples were manufactured to match those in the model's, the primary differences between the simulated and experimental tests was the transmission and reception of the ultrasonic waves. For a PC configuration, T_x was compressed into a fixed position on the aluminium sample's surface and connected to the high-voltage RF burst output of a "RITEC SNAP system". The SNAP system was used due to its high 5kW power burst, its 0.5-5MHz frequency range, and its credibility from a number of EMAT studies [44, 45, 70].

The SNAP system's two gated amplifiers were used to produce separate carrier and modulation frequencies that were multiplied together to produce a single Hanning window pulse. The simulation's gaussian pulse was designed to replicate the SNAP system's Hanning window pulse. The carrier signal consisted of a six-cycled sinusoidal pulse (the frequency of which was calculated from the given steering angle via Equation 2.29) at a 90° phase shift, and the modulation signal consisted of a single-cycled cosinusoidal pulse (the frequency of which was kept as one-sixth of the carrier signal's frequency) with a DC offset. Figure 4.1 shows both the carrier and modulation signals to generate the Hanning window for a steering angle of 30°, as well as the simulated gaussian pulse. Due to the SNAP system's maximum Pulse Repetition Frequency (PRF) firing rate limitation, the firing rate for all steering angles was kept at 250Hz.

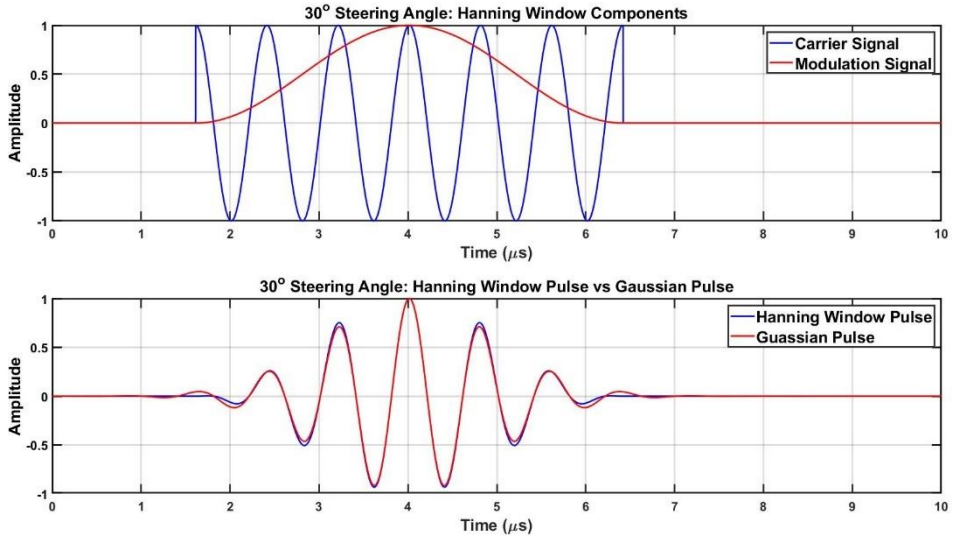

Figure 4.1: EMAT transmission signals

Capacitors were used in parallel with both EMATs to match their electrical impedance and improve their transduction efficiency. Their capacitance was measured by connecting T_x to a "Solartron SI 1260 impedance/gain-phase analyser" whilst on the aluminium sample, and a peak voltage of 3V at the required frequency was passed through the coils. Values of parallel inductance and resistance were recorded and used to calculate an average inductance and resistance at the given frequency. Equation 4.1 (derived from Equation 2.34) was used to calculate the capacitance required in parallel with the EMATs while on the aluminium sample for a given frequency.

$$C = \frac{1}{L(2\pi f_{res})^2} \qquad \text{Equation 4.1}$$

Standard ceramic capacitors were used for the reception EMAT (R_x) as the induced voltage from the received waves was not sufficient to breach their 50V limit, however T_x required leaded high-voltage ceramic RF power capacitors. Table 4.1 shows the experimental variables across a range of steering angles, including the values of capacitance measured by the impedance analyser for T_x.

Table 4.1: EMAT experimental variables for a given steering angle

Angle (°)	Modulation Frequency (MHz)	Time Delay (µs)	Measure Inductance (µH)	Resistance (Ω)	Calculated Capacitance (nF)	Measured Capacitance (nF)
15	0.4018	2.8568	1.7325	9.0314	2.5153	2.5073
20	0.3041	3.2568	1.7614	7.7033	4.3202	4.3160
25	0.2461	3.6443	1.7960	6.9712	6.4692	6.4795
30	0.2080	4.0163	1.8286	6.4963	8.8938	8.8995
35	0.1813	4.3701	1.8589	6.1562	11.5134	11.6048
40	0.1618	4.7028	1.8838	5.8911	14.2684	14.3086
45	0.1471	5.0121	1.9075	5.6946	17.0524	17.0496
50	0.1358	5.2954	1.9288	5.5419	19.7921	19.8148
55	0.1270	5.5507	1.9487	5.4242	22.4004	22.4428
60	0.1201	5.7761	1.9618	5.3283	24.8706	24.8632
90	0.1040	6.4202	2.0113	5.1007	32.3440	32.3594

Due to their low transduction efficiency, R_x was connected to a “Sonemat Standalone Amplifier SAA1000” [80] for a signal gain of +30dB. For a further enhancement to the received signal, the amplifier’s output was connected to the SNAP system’s internal superheterodyne receiver channels. It is recommended by the SNAP system’s user guide [81] that the high-pass filter “*should be set to as high a frequency as possible but below the lowest frequency of operation during a measurement*”, and that the low-pass filter “*should be set above the highest frequency of operation during a measurement*”. Following these recommendations with the SNAP system’s standard settings, the SNAP’s

amplifier had high-pass and low-pass filters of 0.05MHz and 20MHz respectively. An output gain of +40dB from the SNAP system was also applied for all the experimental testing, unless stated otherwise. The SNAP's superheterodyne receiver had its detector tracking enabled to the first harmonic frequency of the pulse's carrier frequency. Additionally, the output of the SNAP system's RF burst monitor was recorded as according to [81] "*the RF Burst Monitor signal provides an accurate representation of the high-power signal at -60dB*", and this data would be compared to the results of the simulated models.

While T_x remained in a fixed position, R_x was repositioned across the surfaces of the samples at regular intervals. An oscilloscope was used to display the filtered signal from the SNAP system and record an average of sixteen signals from the ultrasonic waves received by R_x. These signals were exported as A-scans from each position across the surface. Figure 4.2 shows this experimental setup for a PC EMAT configuration on the semicircular aluminium sample.

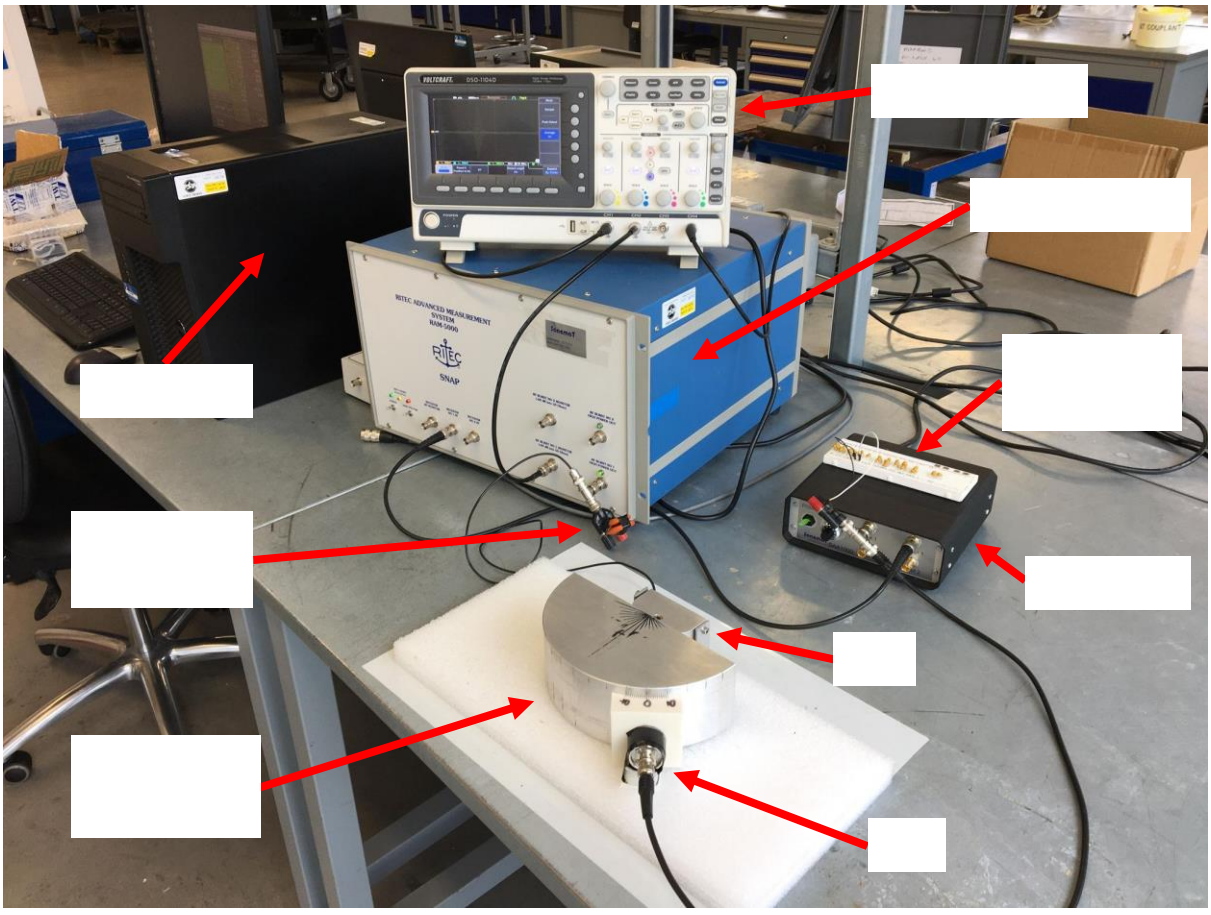

Figure 4.2: Experimental EMAT Setup

4.3. Beam Directivity

Using the EMAT model with a semicircular aluminium sample, parametric studies were performed on the steering angle of the transmitted shear waves. The results of these simulations were compared to experimental setups of the same model to validate their accuracy.

4.3.1. Simulated Results

Figure 4.3-Figure 4.18 show the colour-plots for steering angles of 15-90° at 5° intervals. These colour-plots were taken at a timestep of 'τ + 19.8µs', as the shear waves would not yet have reached the curved surface of the sample, and thus the effects of the change in steering angle were more apparent. The Rayleigh waves would also not yet have reached the curved surface at this time, however the compression waves would have reflected and (if applicable) mode-converted off of it and overlay on top of the shear waves.

From Figure 4.3-Figure 4.18, the intensity of the shear waves appears to reach a maximum at a steering angle of 30°. It is at this steering angle that the first critical angle is reached. Rearranging Snell's Law (Equation 2.8) to compare the steering angles of the shear and compression waves (based upon their respective velocities in the aluminium) shows that the first critical angle (as described in Section 2.3.3) is at a shear wave steering angle of 29.18° (~30° steering angle). It is at this steering angle that the compression wave energy is being converted to the shear waves. Figure 4.3-Figure 4.6 are annotated with arrows to highlight the compression wave's main lobe and how both its magnitude and reception angle changes from steering angles of 15-30°.

The reception angle of the shear waves increases with their steering angle until approximately 50° (Figure 4.10) when a steering limit is reached. Beyond this steering angle, their reception angle does not increase at the same rate as with the previous steering angles. At this steering limit, the Rayleigh waves also begin to supplant the shear waves as the dominant wave mode. This is due to the EMAT transmitting shear waves at the second critical angle.

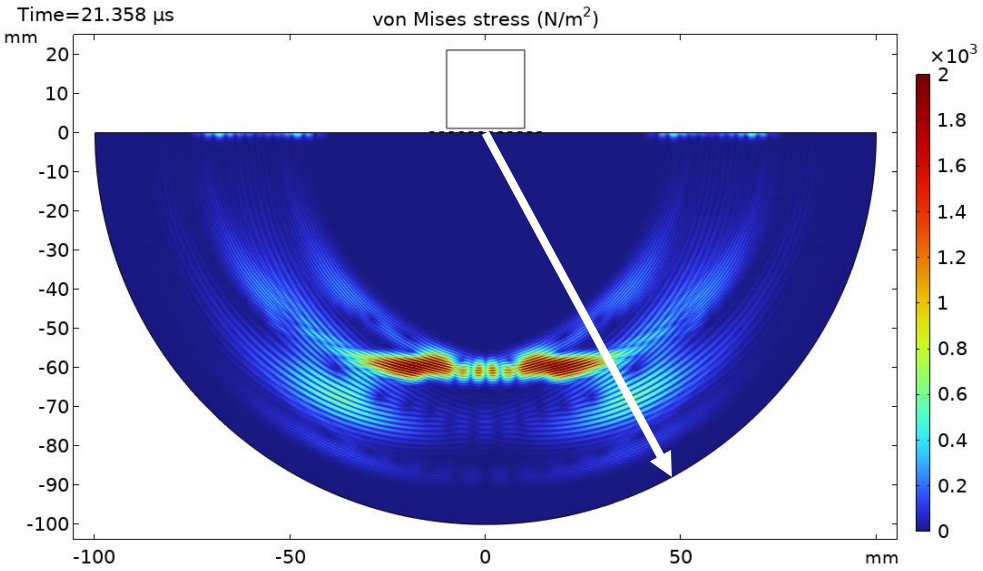

Figure 4.3: 15° Steering Angle EMAT on Semicircular Sample, annotated to indicate direction of Compression Wave

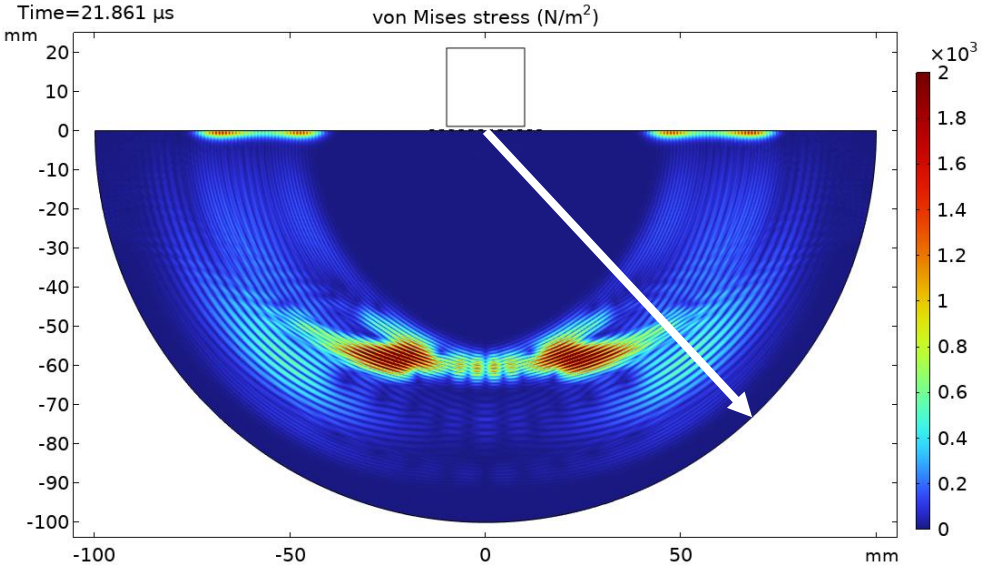

Figure 4.4: 20° Steering Angle EMAT on Semicircular Sample, annotated to indicate direction of Compression Wave

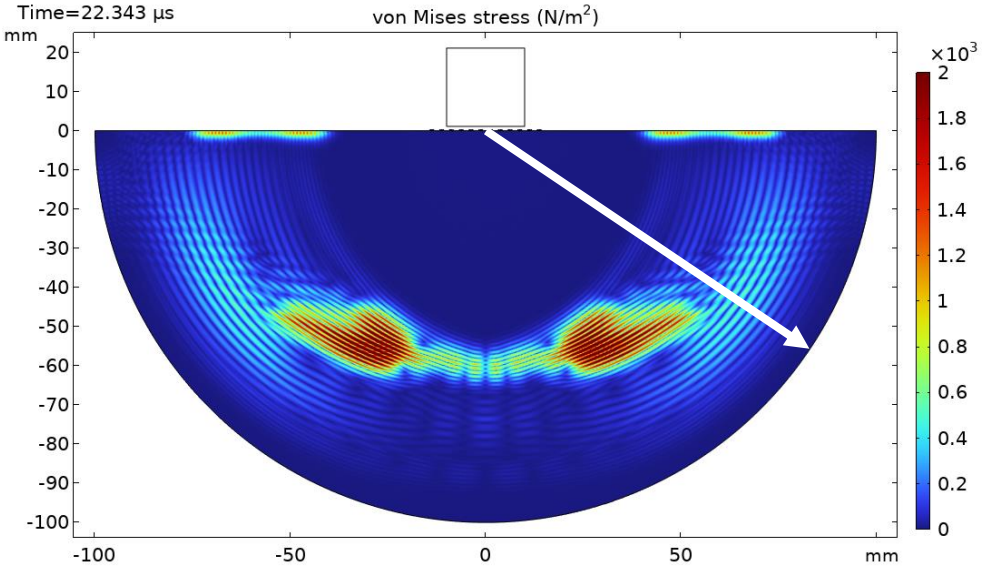

Figure 4.5: 25° Steering Angle EMAT on Semicircular Sample, annotated to indicate direction of Compression Wave

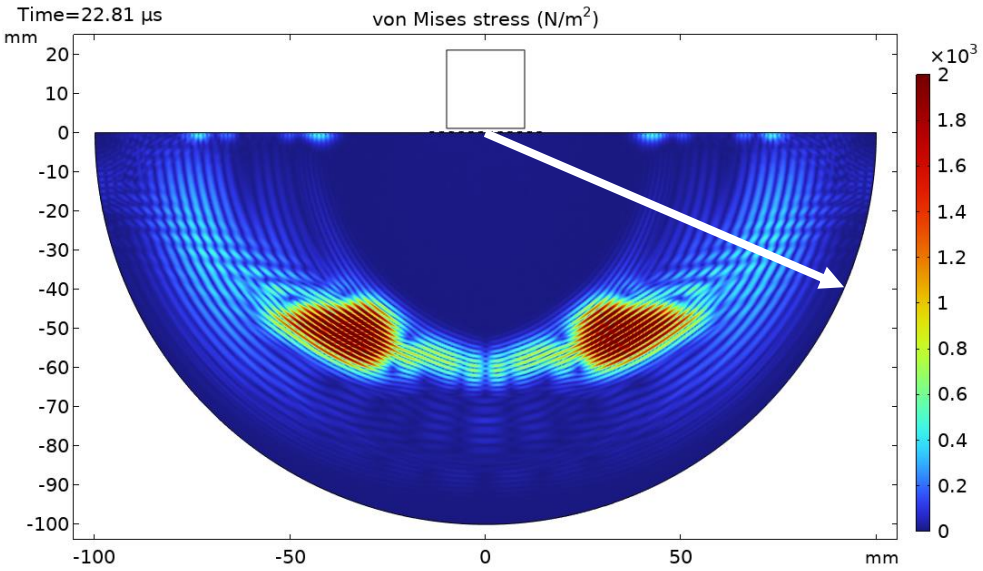

Figure 4.6: 30° Steering Angle EMAT on Semicircular Sample, annotated to indicate direction of Compression Wave

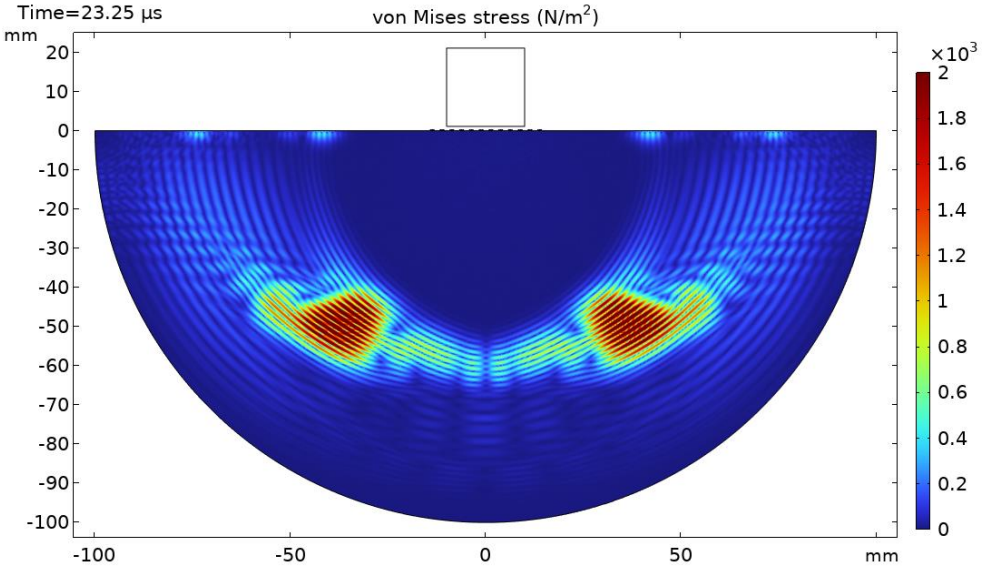

Figure 4.7: 35° Steering Angle EMAT on Semicircular Sample

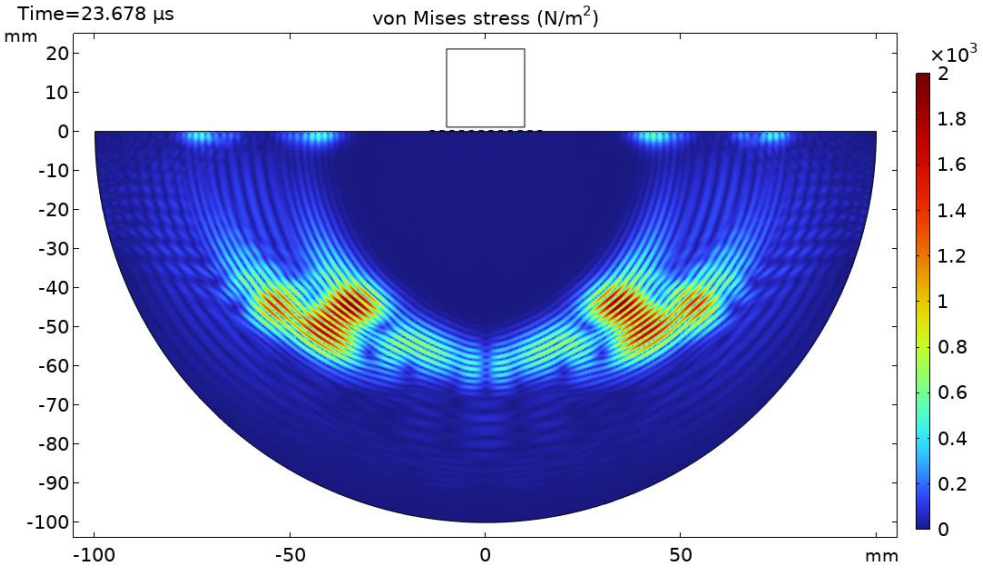

Figure 4.8: 40° Steering Angle EMAT on Semicircular Sample

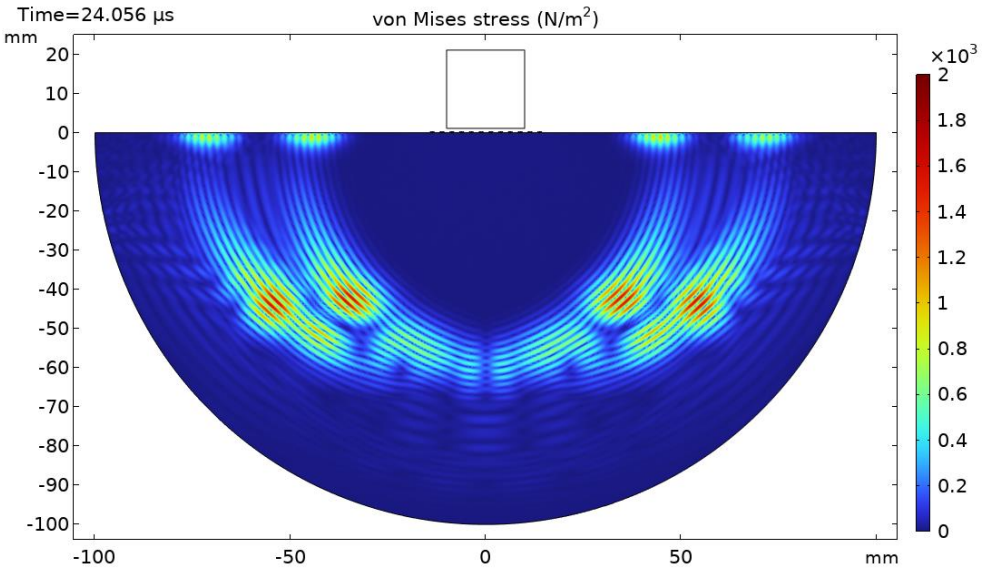

Figure 4.9: 45° Steering Angle EMAT on Semicircular Sample

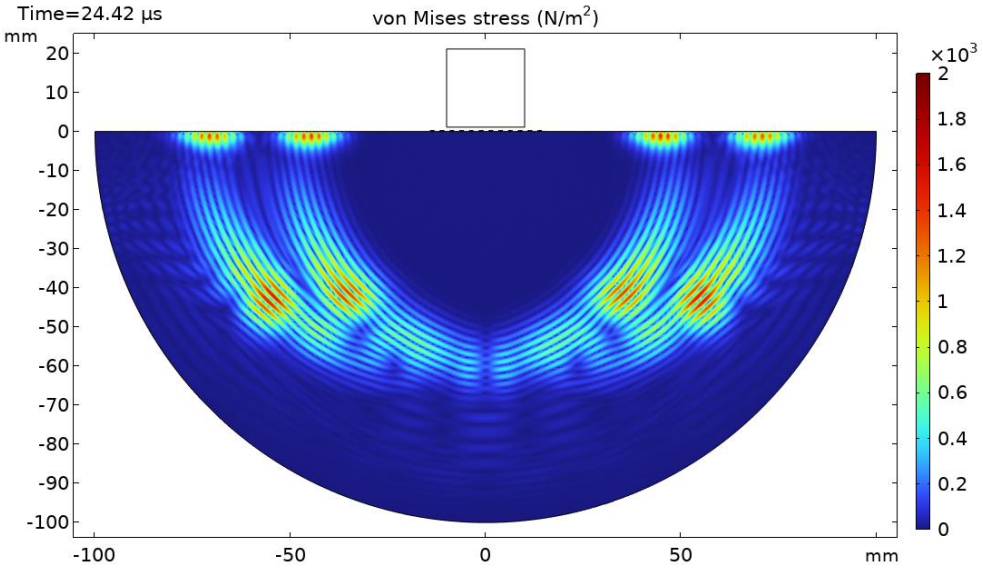

Figure 4.10: 50° Steering Angle EMAT on Semicircular Sample

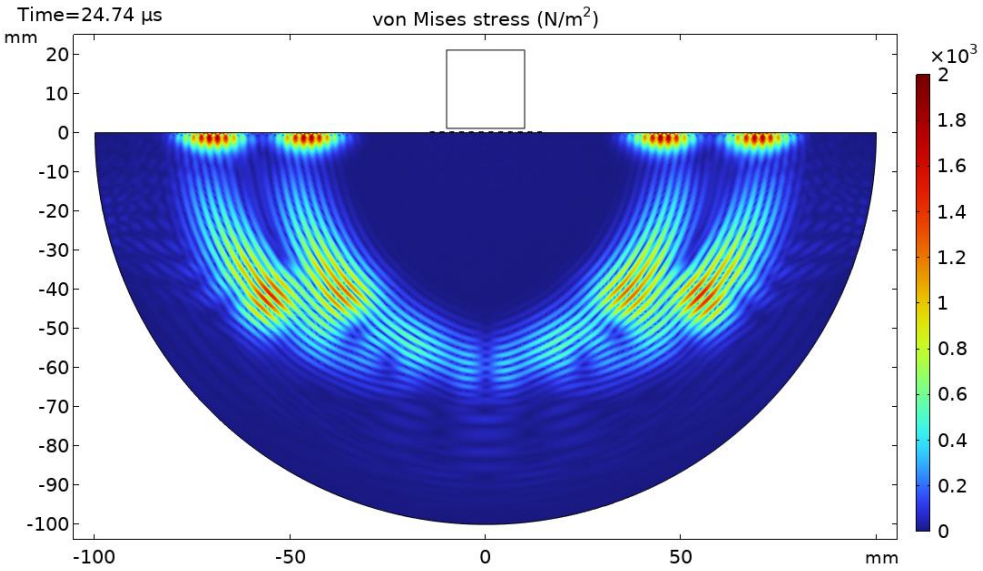

Figure 4.11: 55° Steering Angle EMAT on Semicircular Sample

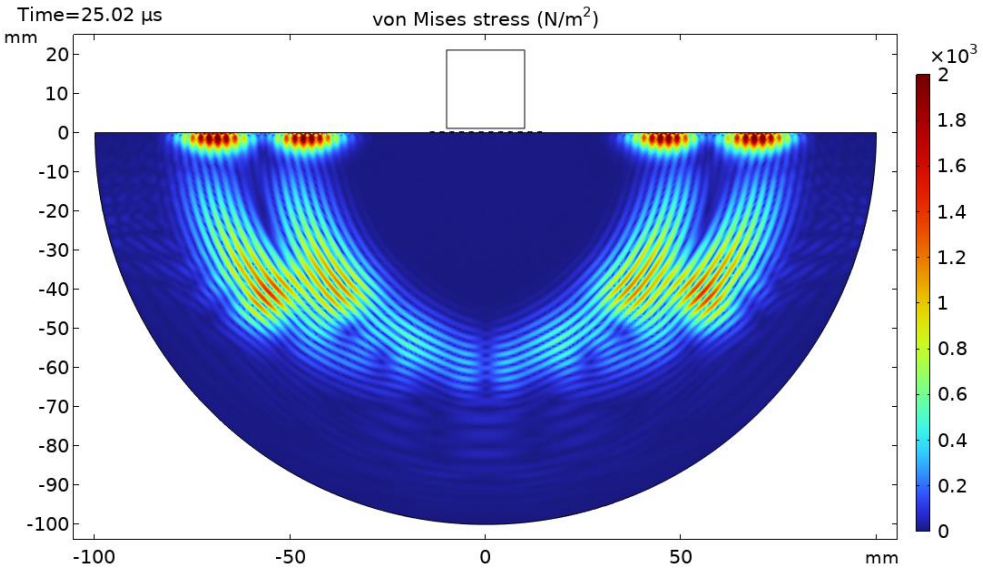

Figure 4.12: 60° Steering Angle EMAT on Semicircular Sample

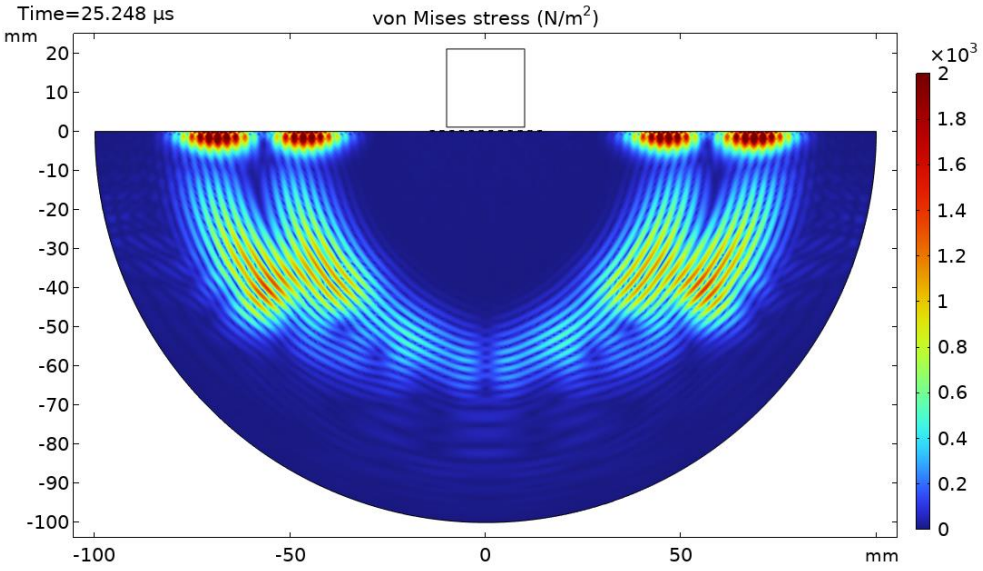

Figure 4.13: 65° Steering Angle EMAT on Semicircular Sample

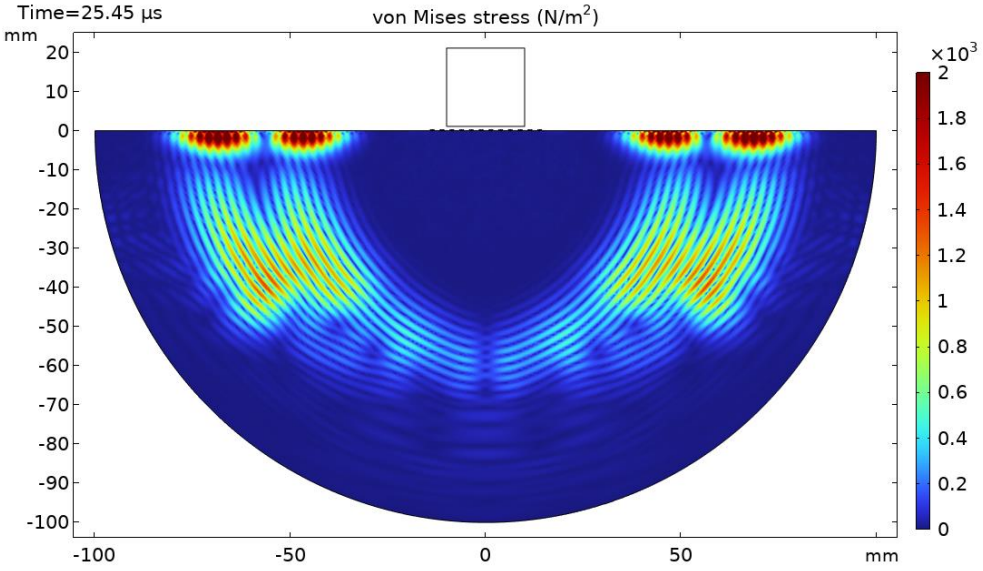

Figure 4.14: 70° Steering Angle EMAT on Semicircular Sample

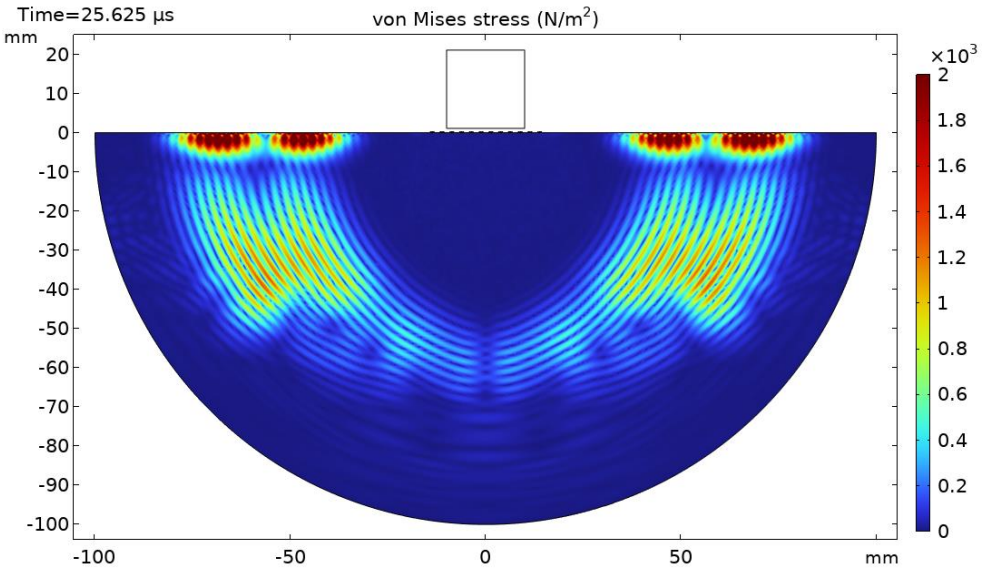

Figure 4.15: 75° Steering Angle EMAT on Semicircular Sample

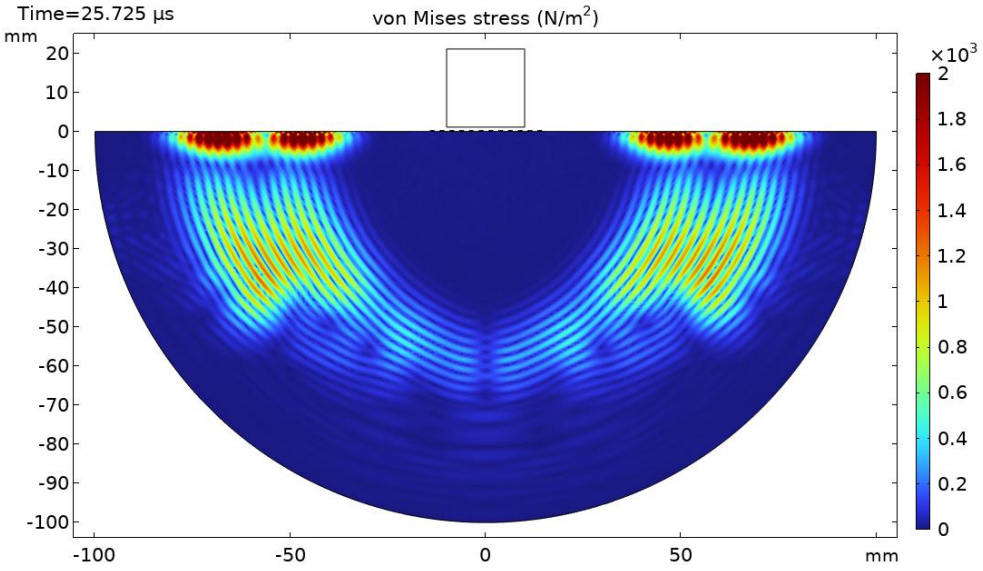

Figure 4.16: 80° Steering Angle EMAT on Semicircular Sample

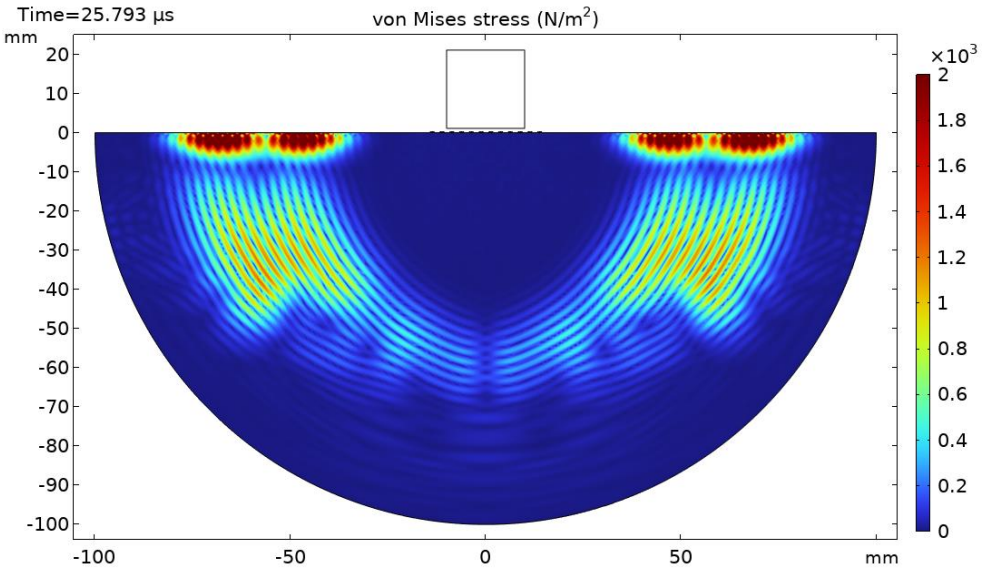

Figure 4.17: 85° Steering Angle EMAT on Semicircular Sample

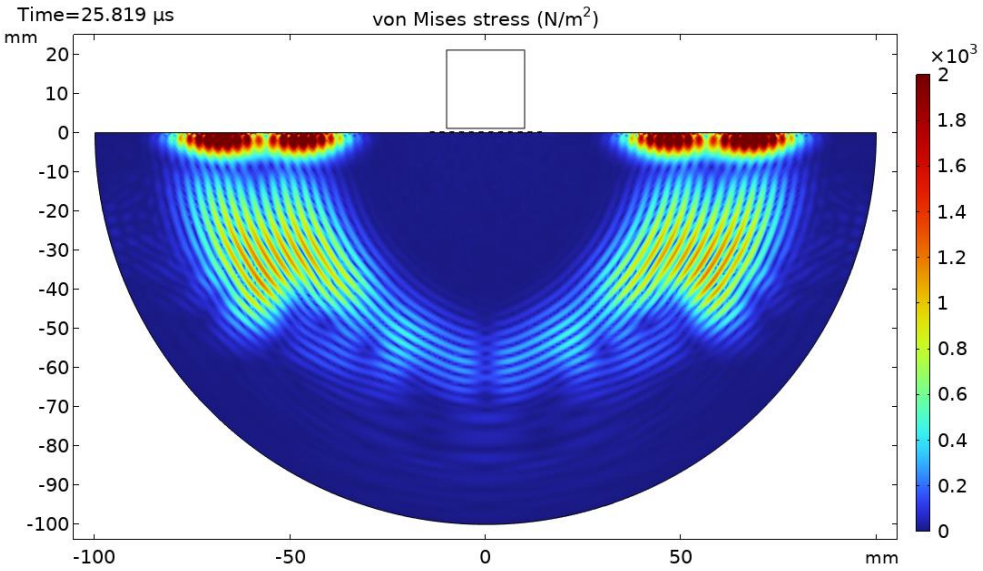

Figure 4.18: 90° Steering Angle EMAT on Semicircular Sample

What is most noticeable from these figures (particularly from the 45° steering angle onwards) was that the transmitted shear waves appear to be transmitted as two split-waves in each direction. It is clearly seen from the flat surface of Figure 4.3-Figure 4.18 that this extended to the Rayleigh waves also. Figure 4.19-Figure 4.22 show graphs of displacement magnitude against time from different reception angles across the curved surface for steering angles of 15°, 30°, 45°, and 90°. From these graphs, the individual split-waves for all three wave modes are annotated where appropriate.

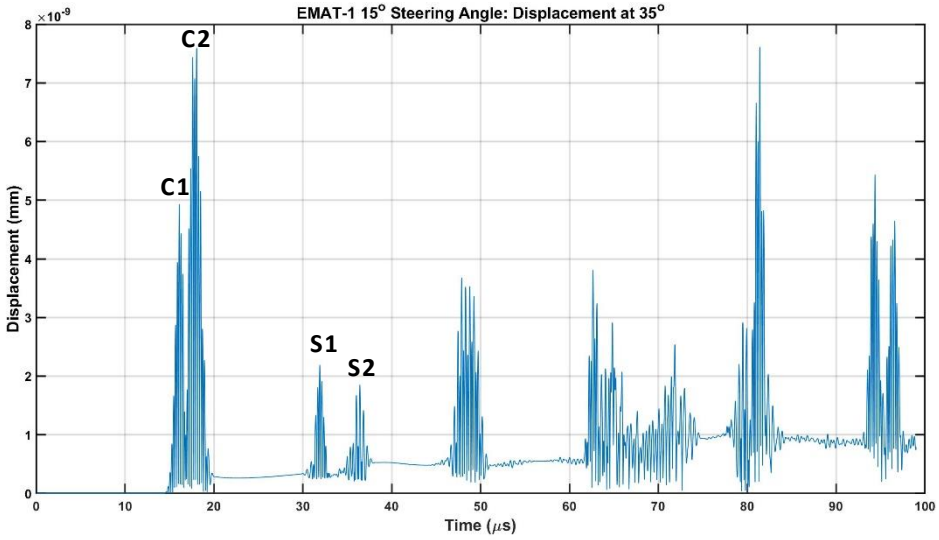

Figure 4.19: Graph of Displacement Magnitude across Time at 35° for 15° steering angle

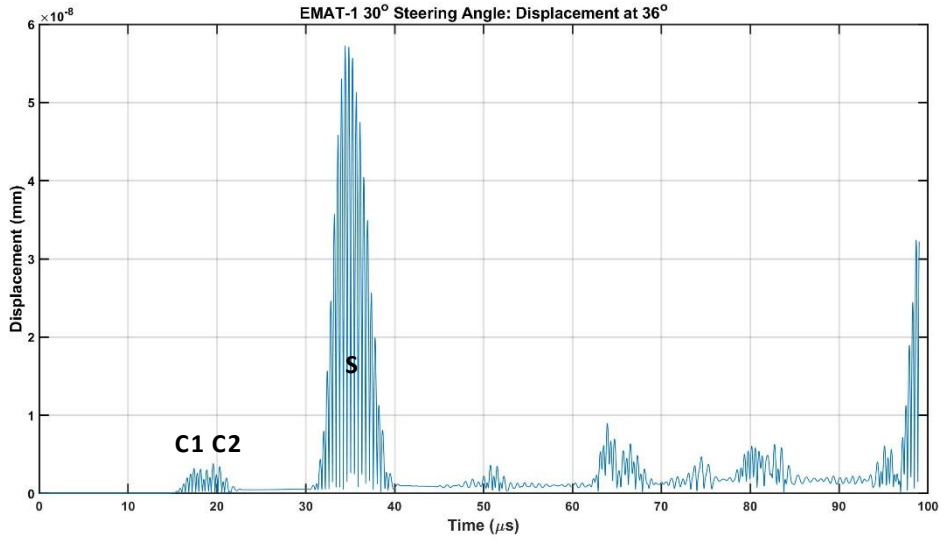

Figure 4.20: Graph of Displacement Magnitude across Time at 36° for 30° steering angle

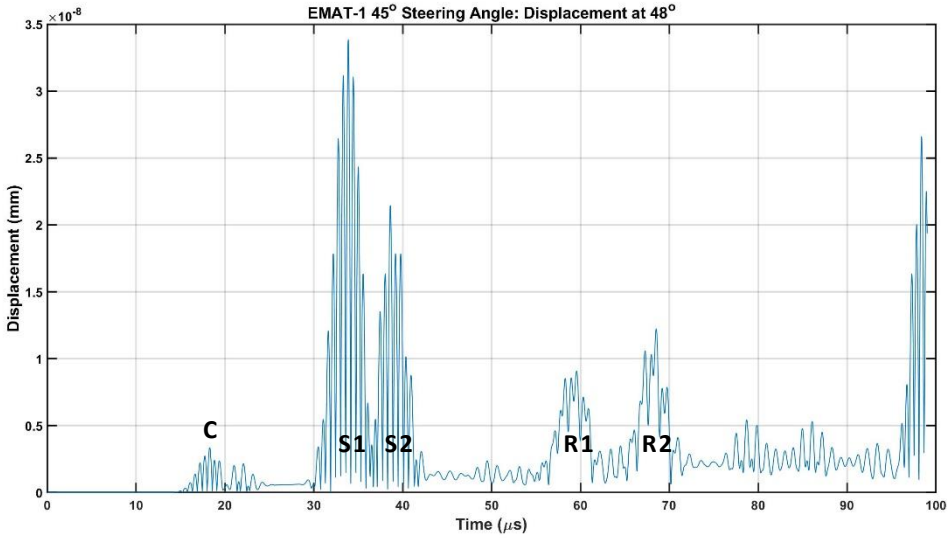

Figure 4.21: Graph of Displacement Magnitude across Time at 48° for 45° steering angle

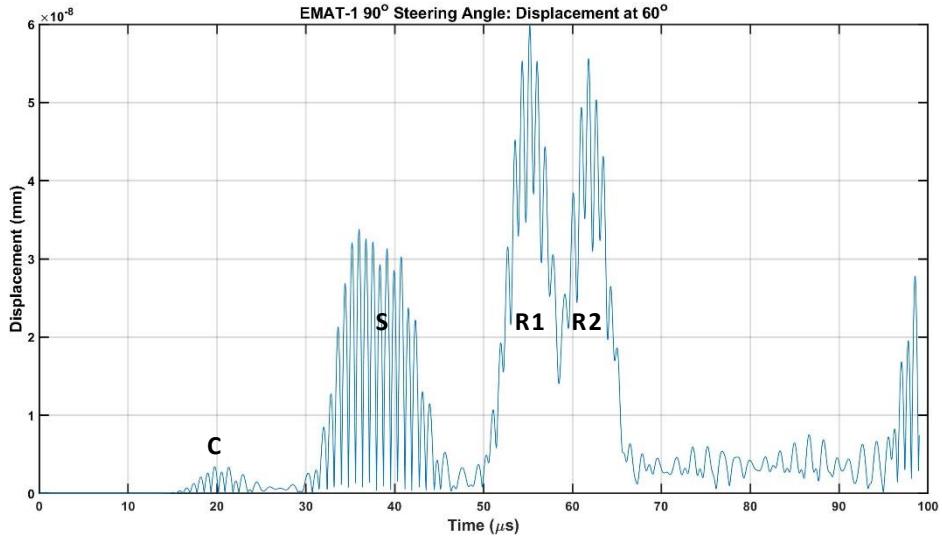

Figure 4.22: Graph of Displacement Magnitude across Time at 60° for 90° steering angle

Figure 4.19 shows that the compression waves similarly exhibited this split-wave behaviour at lower steering angles, but Figure 4.21 shows that they merge into a single wave as the steering angle increases. This behaviour is also seen with the shear waves as they begin to merge from Figure 4.21-Figure 4.22, however it is not seen with the Rayleigh waves as the frequency does not continue to decrease beyond this steering angle. It is also shown from both Figure 4.3-Figure 4.9 and Figure 4.19-Figure 4.21 that as the steering angle increases from 15-45°, the split-waves begin to merge into a single wave before separating. This is due to the two split-waves superimposing on each other, producing a shear wave displacement at approximately 30°.

The particle motion of the shear and compression waves are perpendicular to and parallel to their direction of propagation respectively (as previously stated in Section 2.3.2). Since the EMAT was positioned at the centre of the semicircular sample's flat surface, the bulk waves should propagate at an angle normal to any point across the sample's curved surface. Equation 4.2-Equation 4.3 were therefore used with the components of displacement at a given point from across the sample's curved surface to determine the wave mode striking the curved surface based on its direction of displacement.

$$u_s = u_x \cos\theta_r + u_y \sin\theta_r \qquad \text{Equation 4.2}$$

$$u_c = u_x \sin\theta_r - u_y \cos\theta_r \qquad \text{Equation 4.3}$$

where u_s = displacement tangential to the curved surface (m); u_c = displacement normal to the curved surface (m); u_x = x-component of displacement (m); u_y = y-component of displacement (m); θ_r = angle normal to the curved surface (°).

Positive values of u_s and u_c are orientated anti-clockwise and outwards from the sample's surface respectively. For each reception angle, the tangential and normal displacements were calculated at each timestep and filtered through a bandpass filter, with cutoff frequency limits of ±1/3 of the transmission signal's frequency (e.g. for a 30° steering angle the frequency was 1.248MHz, thus bandpass limits of 0.832-1.664MHz). Figure 4.23-Figure 4.26 show the results of this process using the data shown in Figure 4.19-Figure 4.22.

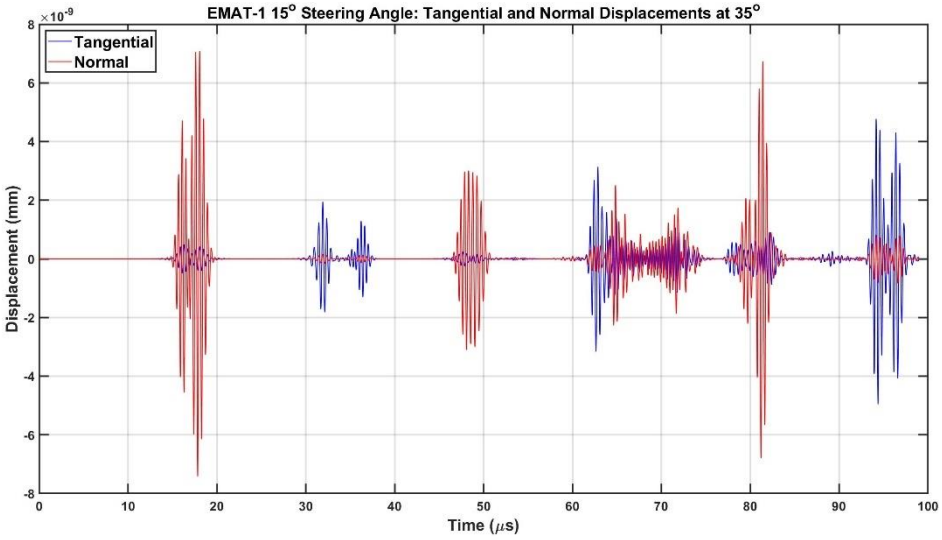

Figure 4.23: Graph of Directional Displacement across Time at 35° for 15° Steering angle

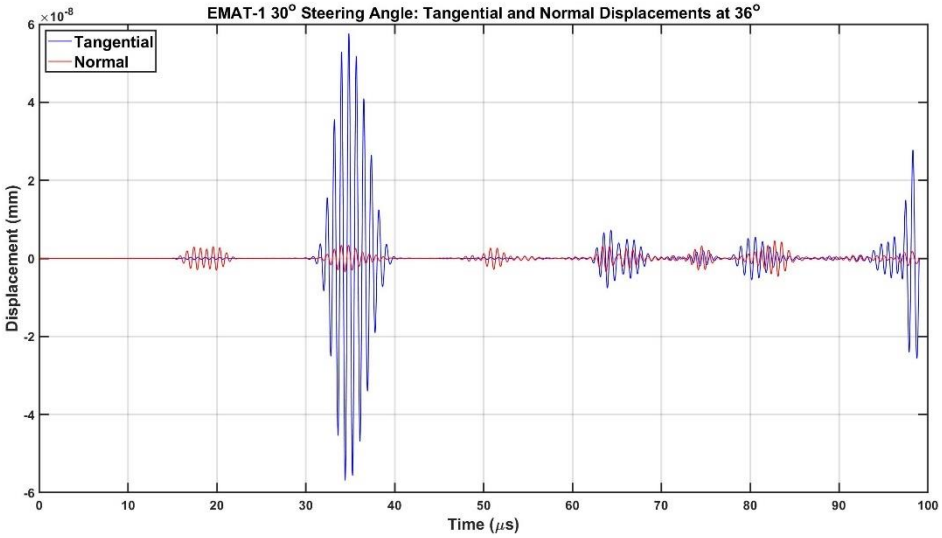

Figure 4.24: Graph of Directional Displacement across Time at 36° for 30° Steering angle

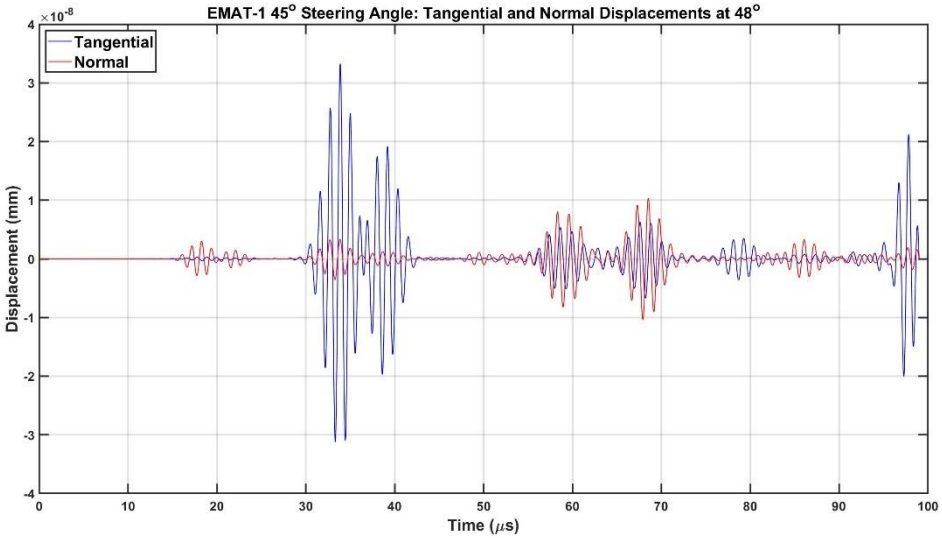

Figure 4.25: Graph of Directional Displacement across Time at 48° for 45° Steering angle

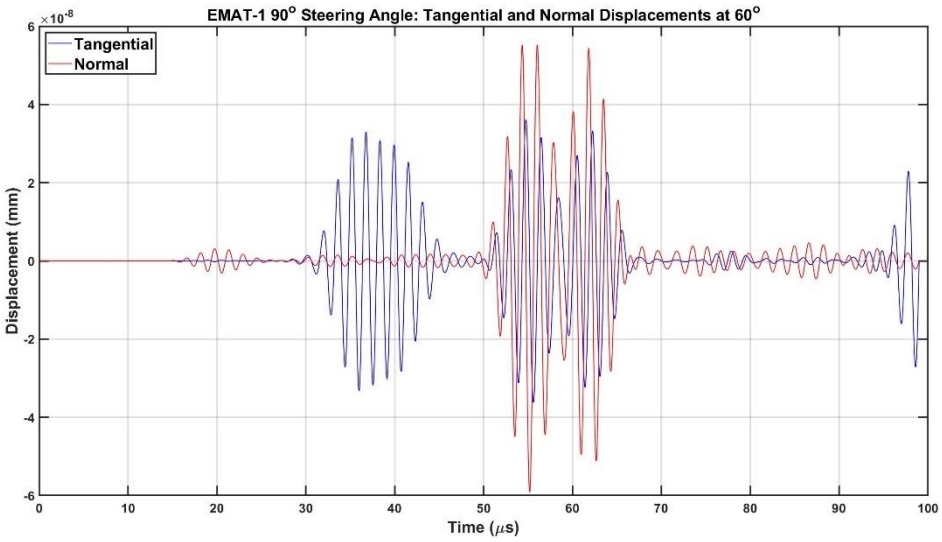

Figure 4.26: Graph of Directional Displacement across Time at 60° for 90° Steering angle

The use of Equation 4.2 and Equation 4.3 on the components of displacement is clearly able to differentiate between wave modes at a given reception angle. The peak values of tangential displacement are far larger than those of normal displacement for the shear waves (in accordance with their particle motion) and vice versa for the compression waves. The Rayleigh waves however possess both tangential and normal displacements due to their elliptical particle motion (as discussed in Section 2.3.2).

The semicircular sample enabled a plot of the directivity patterns for both the shear and compression waves to be drawn for each steering angle. At each reception angle from across the curved surface, the maximum values of each differentiated bulk wave was recorded and graphed into a directivity plot. At reception angles beyond 75°, the shear waves arrived at similar times to the Rayleigh waves, and it became impossible to differentiate between them and extract the maximum shear wave value. The reception angle limits for the shear wave directivity plots were therefore capped at ±75°. Figure 4.27-Figure 4.42 show these bulk wave directivity plots for the simulations shown in Figure 4.3-Figure 4.18. When comparing these directivity plots using directional displacement to ones derived from the displacement magnitudes, the minimum correlation coefficient across steering angles was calculated at 0.9993. This means that Equation 4.2 and Equation 4.3 enabled bulk wave characterisation in the A-scans without any corruption of results.

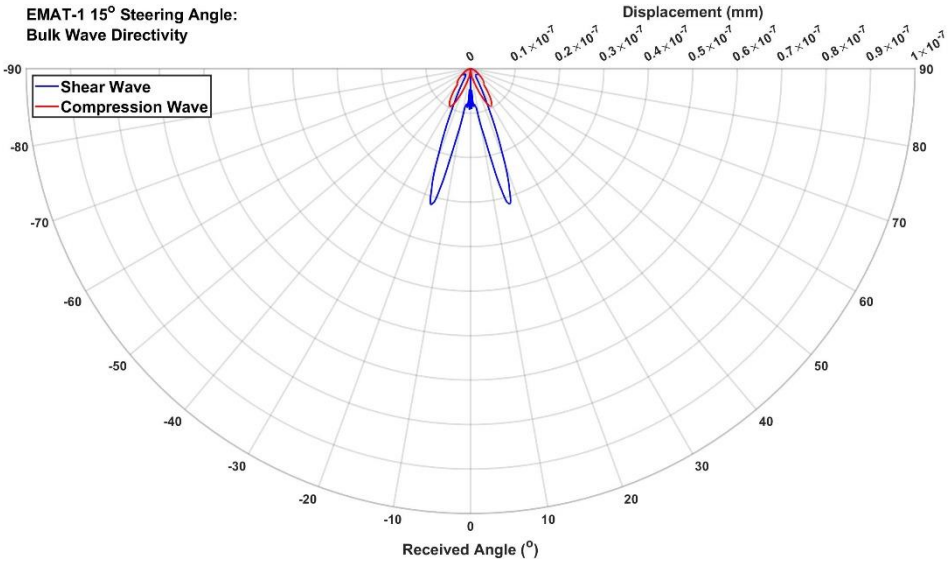

Figure 4.27: Bulk Wave Directivity Plot for 15° Steering Angle

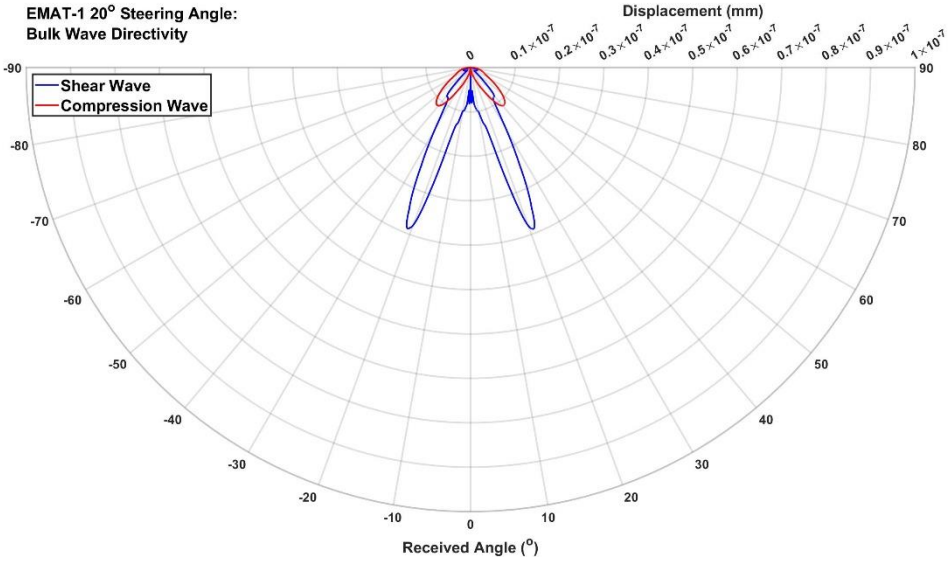

Figure 4.28: Bulk Wave Directivity Plot for 20° Steering Angle

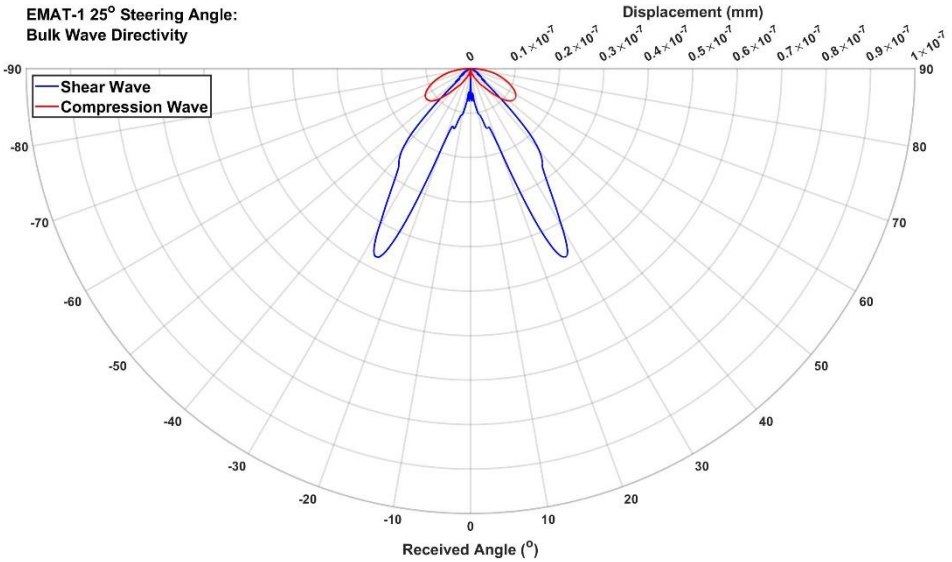

Figure 4.29: Bulk Wave Directivity Plot for 25° Steering Angle

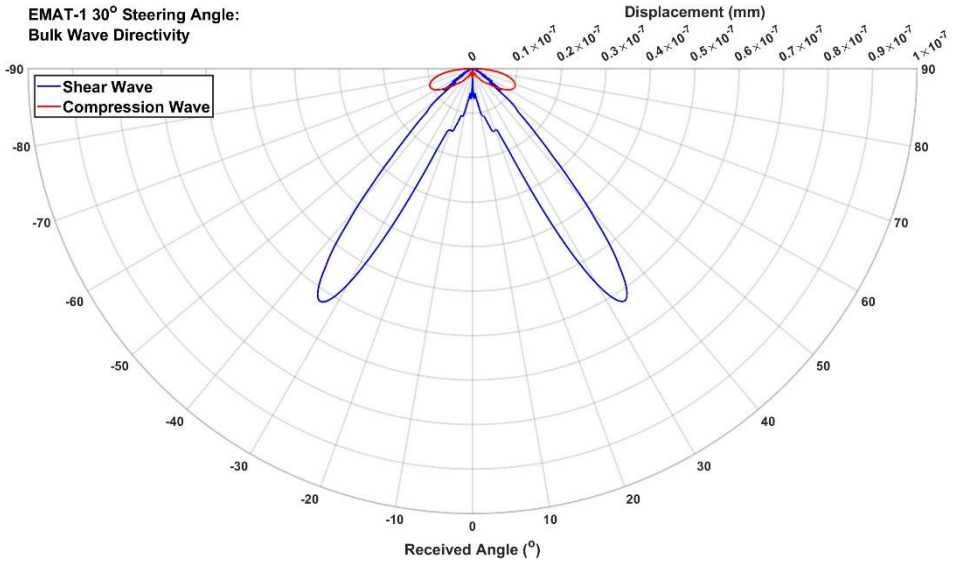

Figure 4.30: Bulk Wave Directivity Plot for 30° Steering Angle

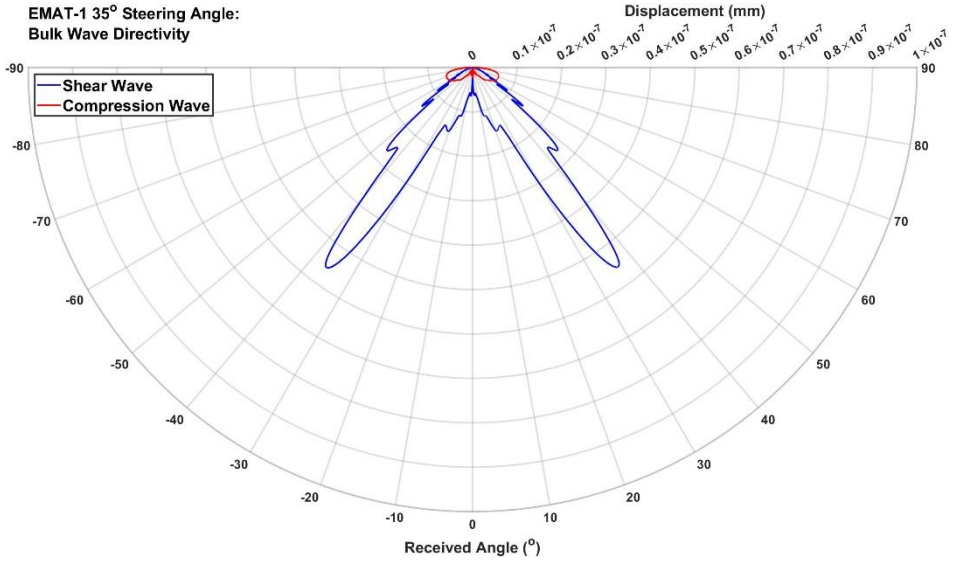

Figure 4.31: Bulk Wave Directivity Plot for 35° Steering Angle

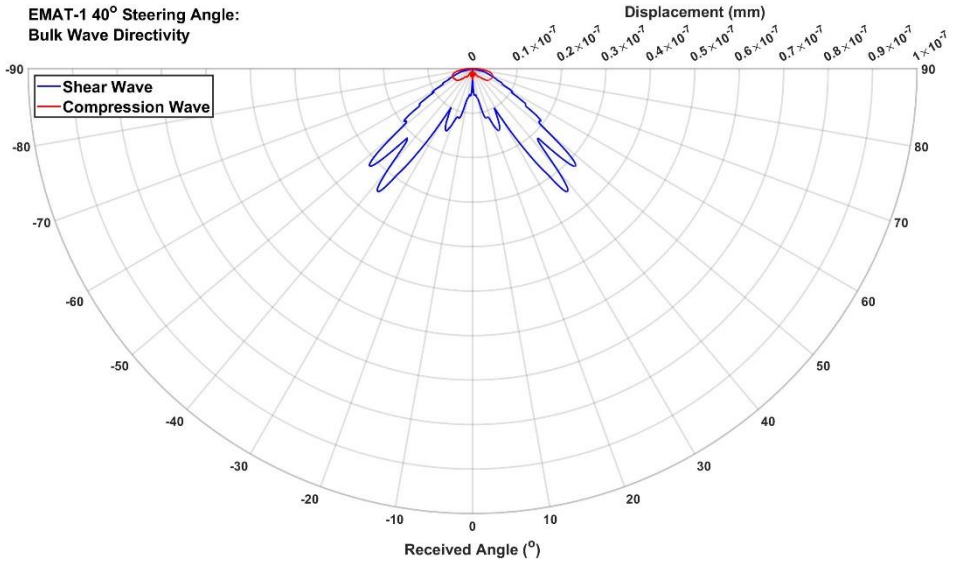

Figure 4.32: Bulk Wave Directivity Plot for 40° Steering Angle

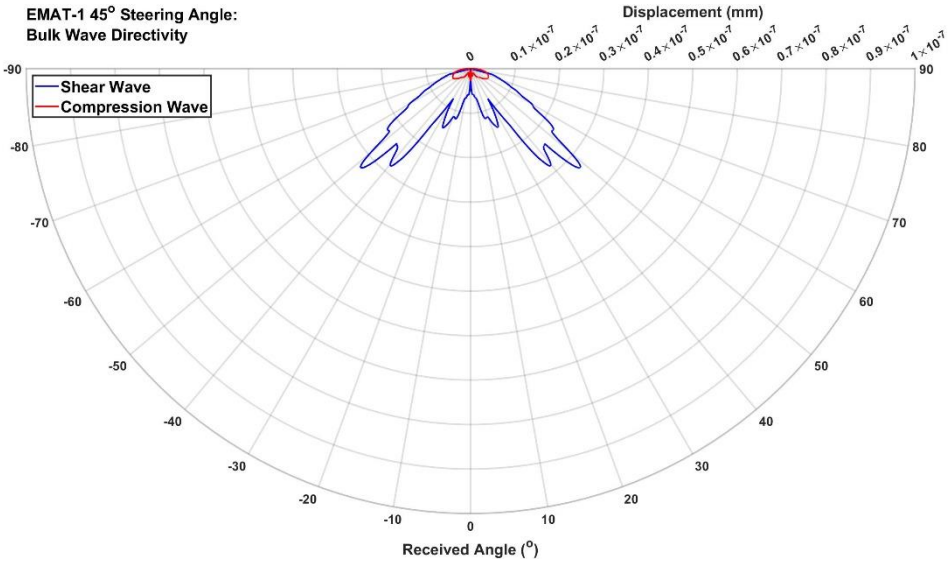

Figure 4.33: Bulk Wave Directivity Plot for 45° Steering Angle

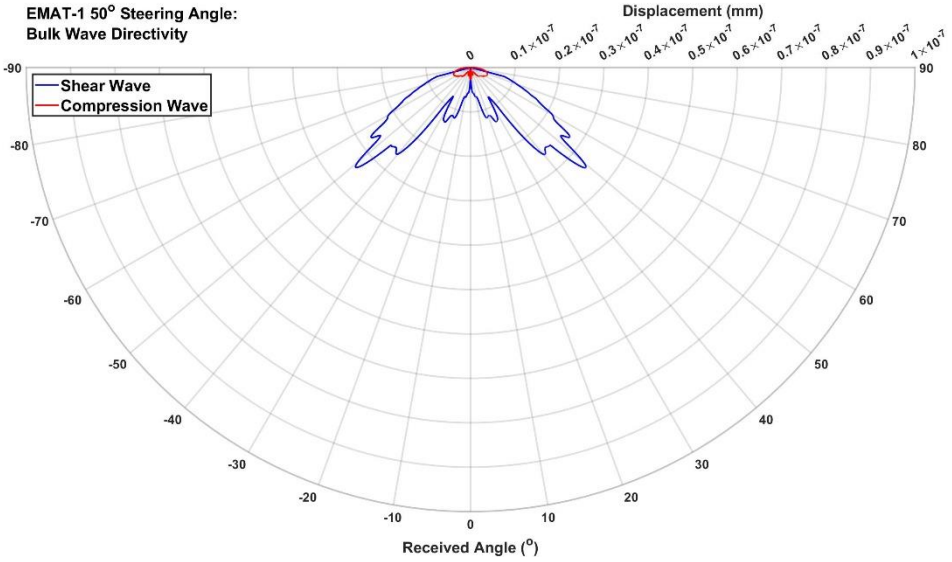

Figure 4.34: Bulk Wave Directivity Plot for 50° Steering Angle

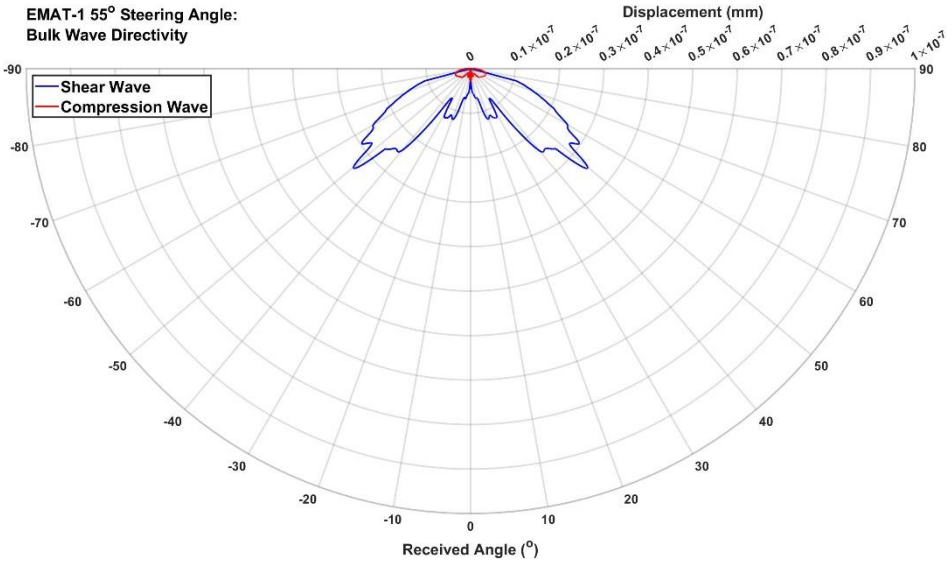

Figure 4.35: Bulk Wave Directivity Plot for 55° Steering Angle

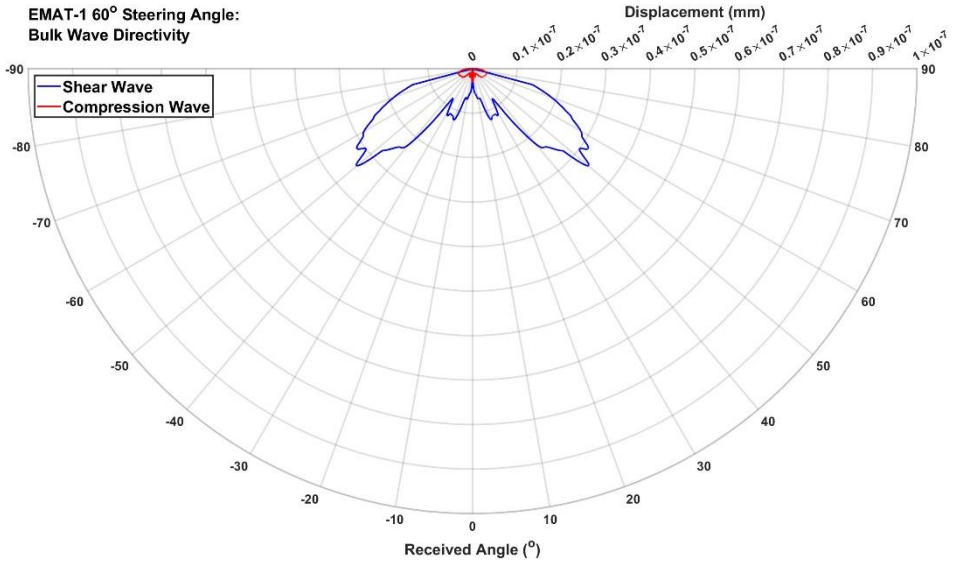

Figure 4.36: Bulk Wave Directivity Plot for 60° Steering Angle

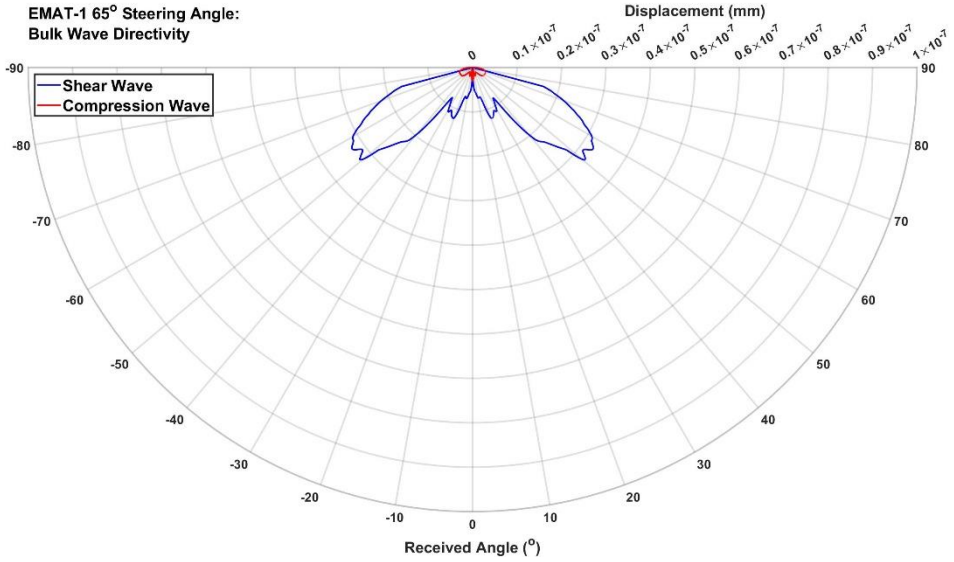

Figure 4.37: Bulk Wave Directivity Plot for 65° Steering Angle

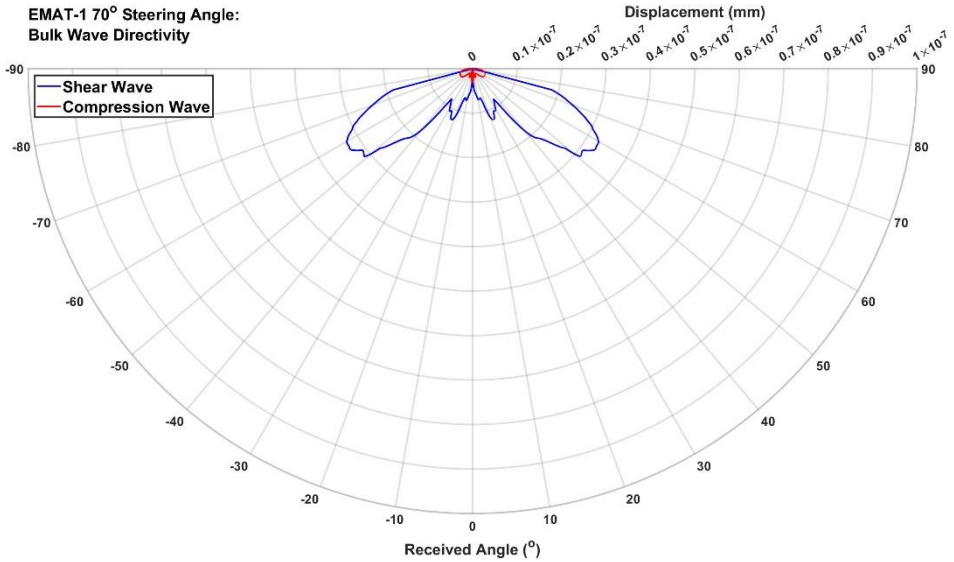

Figure 4.38: Bulk Wave Directivity Plot for 70° Steering Angle

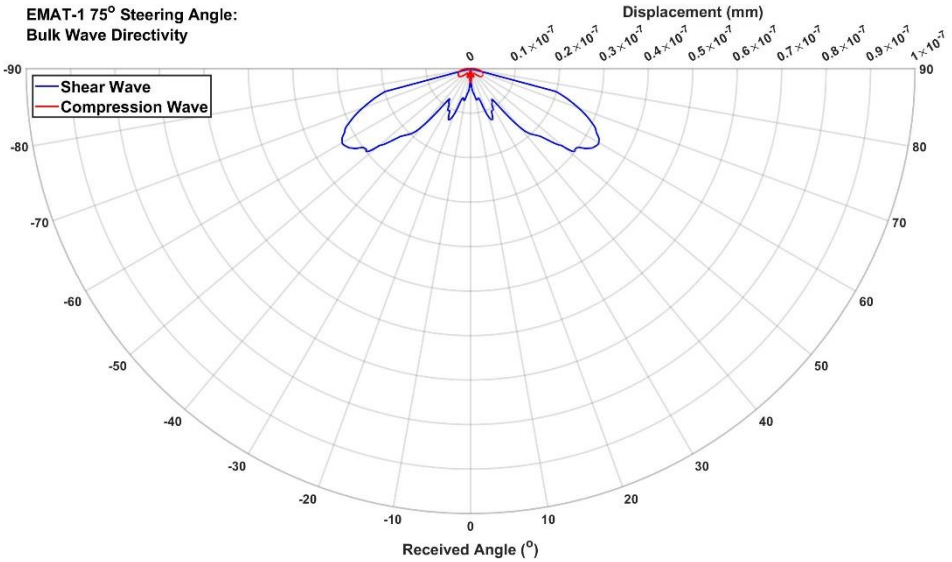

Figure 4.39: Bulk Wave Directivity Plot for 75° Steering Angle

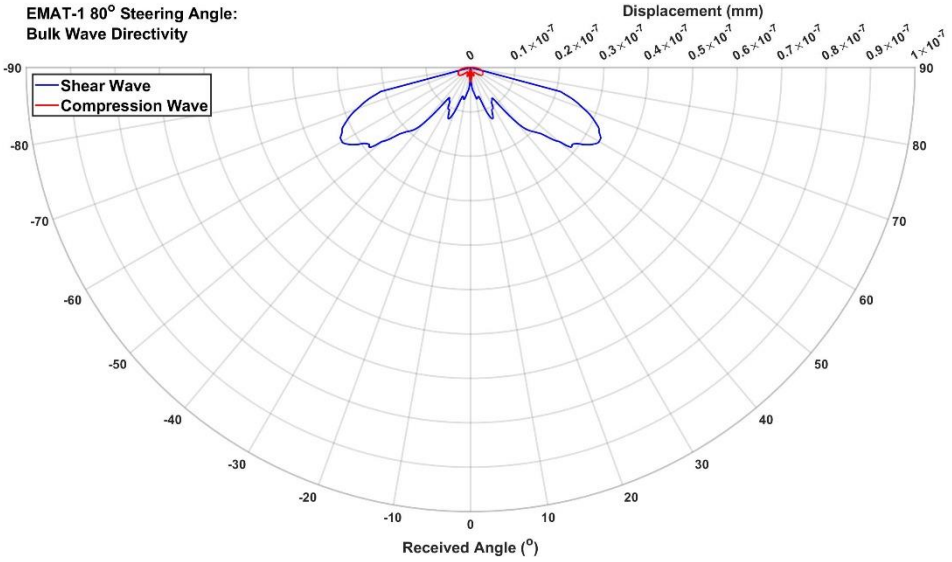

Figure 4.40: Bulk Wave Directivity Plot for 80° Steering Angle

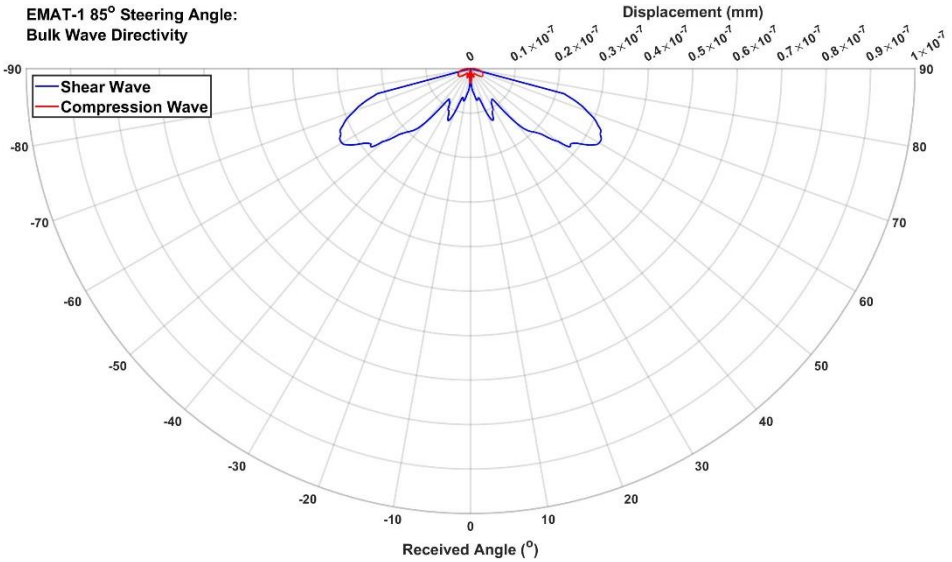

Figure 4.41: Bulk Wave Directivity Plot for 85° Steering Angle

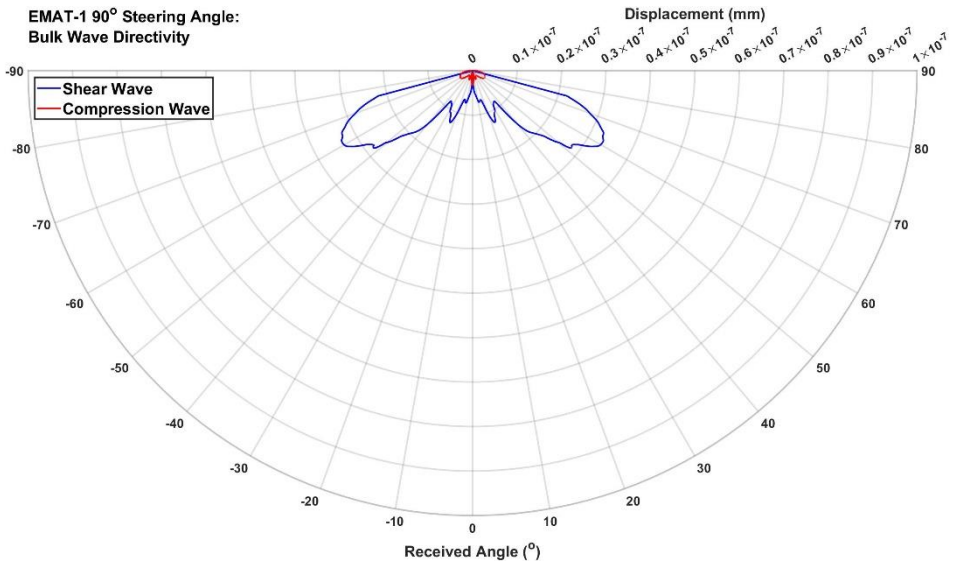

Figure 4.42: Bulk Wave Directivity Plot for 90° Steering Angle

Figure 4.43 shows the maximum directional displacements for each of the three wave modes as the steering angle increased from 15-90° at 1° intervals. While the bulk wave displacements were extracted from the directivity plots, the Rayleigh wave displacements were taken from the reception angles at ±90°. Due to the values of maximum displacement being comparatively larger for the Rayleigh waves than the bulk waves, these were graphed using the right axis with an increased scale factor of 5.

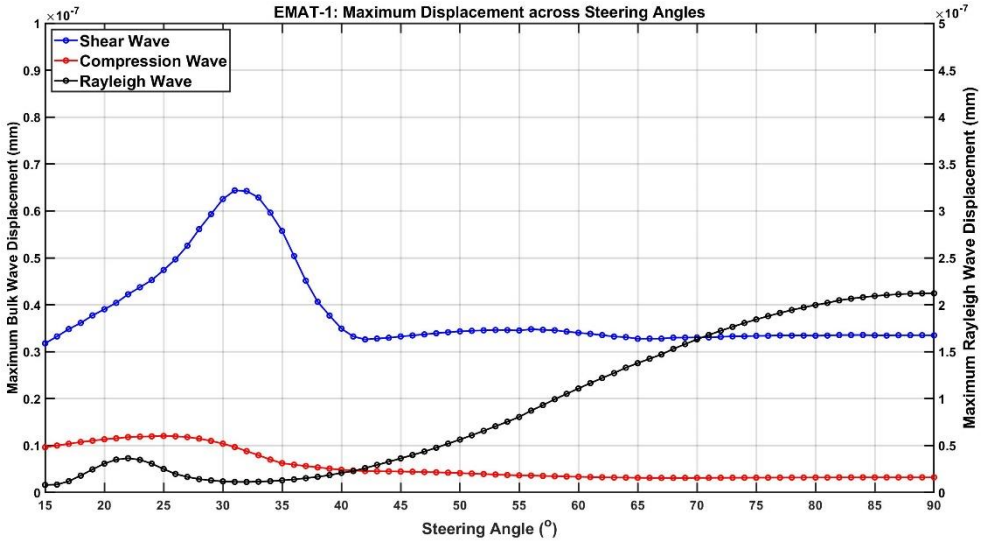

Figure 4.43: Graph of Maximum Displacement across Steering Angles

From the 15° steering angle, the maximum shear wave displacement gradually increases to its peak value at the 31° steering angle. From here, the maximum shear wave displacement gradually decreases to a trough value at the 42° steering angle, and from there plateaus for the remaining steering angles. A similar pattern of behaviour is seen with the maximum compression

wave displacements, however its peak value occurs at a lower steering angle of 25°. It is likely that the compression wave displacement also gradually increases from steering angles lower than 15°.

From Figure 4.3-Figure 4.18 & Figure 4.43, the maximum Rayleigh wave displacement gradually increases from a trough value at the 32° steering angle (as the maximum shear wave displacement begins to decrease from its peak). As the steering angle increases, the maximum displacement of the Rayleigh waves increases until it overtakes that of the shear waves at a 45° steering angle. After reaching a maximum rate of increase at the 56° steering angle, it begins to plateau until it reaches its peak at the 90° steering angle. There is also a smaller peak at the 22° steering angle. This is due to the frequency at this steering angle being the third harmonic of the frequency at the 90° steering angle, and has been documented as affecting both lamb and SH-waves [82, 83].

Figure 4.44 shows the reception angles at which the maximum shear waves displacement occurs across the range of steering angles. Included within these results are error bars indicating the shear wave beamwidth (defined as the range of reception angles with displacements above a cutoff of -6dB the maximum) for that particular steering angle. Graphed on the right axis is the Relative Time of Arrival (RToA), defined in Equation 4.4. By graphing the maximum shear wave displacement in both time and space, the effect that the steering angle has on the shear waves was further explored.

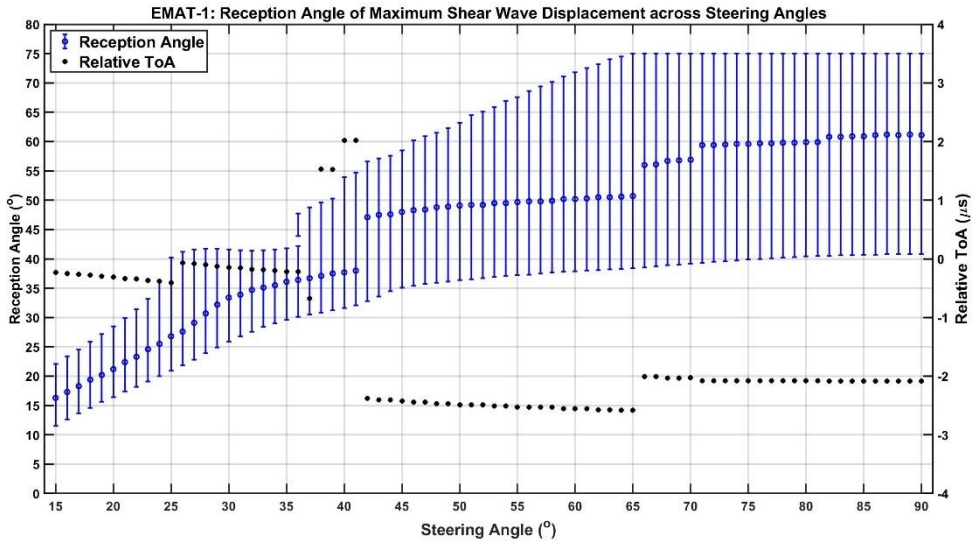

Figure 4.44: Graph of Shear Wave Reception Angles across Steering Angles

$$RToA = ToA - \tau - \frac{r}{v_S} \quad \text{Equation 4.4}$$

RToA values equal to zero suggests that the shear wave originated from the centre of the flat surface, while positive or negative values suggest that the origin positions were further or closer than the centre. Previous work on this subject (included in Appendix A) investigated the relationship between the reception angle of maximum shear wave displacement and its RToA [84]. While that body of work had differences in the simulation's setup (most notably different lift-offs for both the magnet and coil and a maximum mesh size of five elements per wavelength) the numerical method remains the same.

It was immediately noticeable that reception angle does not increase linearly across the steering angle range. There are sudden increases in the reception angle which correlate with sudden changes in pattern for the RToA. The sudden changes in the RToA was used to separate the steering angle range into six sections: A (15-25°), B (26-36°), C (37-41°), D (42-65°), E (66-70°), and F (71-90°).

Section A sees the increase of steering angle from 15° to 25° linearly increase the reception angle from 16.3° to 26.8° and linearly decrease the RToA from -0.233µs to -0.405µs. The linear change in both of these values was due to the maximum peak in the reception angle's A-scan (from which these results were both derived) originating from the same wavefront in the same split-wave. The shear wave increases in both displacement and reception angle as the steering angle increases, however the RToA decreases as the reception angle gets closer to the wavefront's origin position (the origin positions of the EMAT's split-waves are discussed in greater detail below). The lower range (defined as the distance from the beamwidth's lower limit to the reception angle) gradually increases in magnitude from 4.8-5.9°, however there is a far greater increase in the upper range (particularly at the 22° steering angle) from 5.8-13.4°. This is due to the increase in steering angle causing a sidelobe angled at approximately 40° to emerge, which extends the beamwidth's upper limit. This is seen in the 25° steering angle beam directivity plot (Figure 4.29).

This emerging sidelobe causes a sudden increase in the RToA and the transition into Section B. Within this section, the maximum displacement

increases to its 31° steering angle peak before diminishing. While the RToA across this section linearly decreases from -0.068µs to -0.221µs, its sudden increase from section A is due to the maximum displacement occurring from another wavefront. This secondary wavefront lags behind Section A's wavefront by half a cycle (defined as $0.5/f$) which for a 25° steering angle is equal to 0.3375µs, corresponding with the sudden change in RToA between the 25-26° steering angles. Section B's change in reception angle loses its linear correlation with the change in steering angle as it increases to its maximum increase rate at the 28° steering angle before decreasing to its minimum increase rate between the 33-34° steering angles. The beamwidth's lower range continues to gradually increase from 5.8-6.3°, however the upper range decreases such that the upper limit remains between 41.2-42.2°. It is at the end of section B that another sidelobe begins to emerge at a reception angle of approximately 46°. The displacement of this sidelobe is above the -6dB cutoff, thus it creates a secondary beamwidth range from 43.9-47.7°. This secondary beamwidth merges into the primary range as the steering angle increases into Section C.

The reception angles within Section C continue the trend from Section B, from the 32° steering angle onwards. Section C's first steering angle of 37° re-correlates its RToA with Section A's trend, while the four remaining steering angles group into two pairs (38-39° and 40-41°) based on their far greater RToAs. Like the transition from Sections A to B, the reason for these increases in RToA is due to the peak displacement occurring from wavefronts that strike the curved surface later than those of lower steering angles. The amount of time that the wavefronts lag behind is 2.5 cycles and 0.5 cycles for 37-38° and 39-40° respectively, as shown in Figure 4.45. It is also observed from these A-scans that the signals begin to separate from a single superimposed wave into the two split-waves.

The transition from Section C to Section D sees both a sudden increase in reception angle and a large decrease in RToA. The change in reception angle is due to the higher-angled sidelobe supplanting the main lobe, as shown in Figure 4.32 and Figure 4.33. The decrease in RToA is due to the new main lobe's maximum displacement occurring from the first split-wave to arrive rather than

the second, which remains consistent across Section D. As the steering angle increases from 42-65°, there is a reception angle increase of less than 4°, suggesting that the EMAT has reached a steering limit. It was decided that the MLC reached a steering angle limit at 40° [84], however as those models used different lift-off distances for both the magnet and coil compared to those in these model's, a new steering angle limit of 48° was determined, as the rate of increase in reception angle compared to steering angle began to plateau.

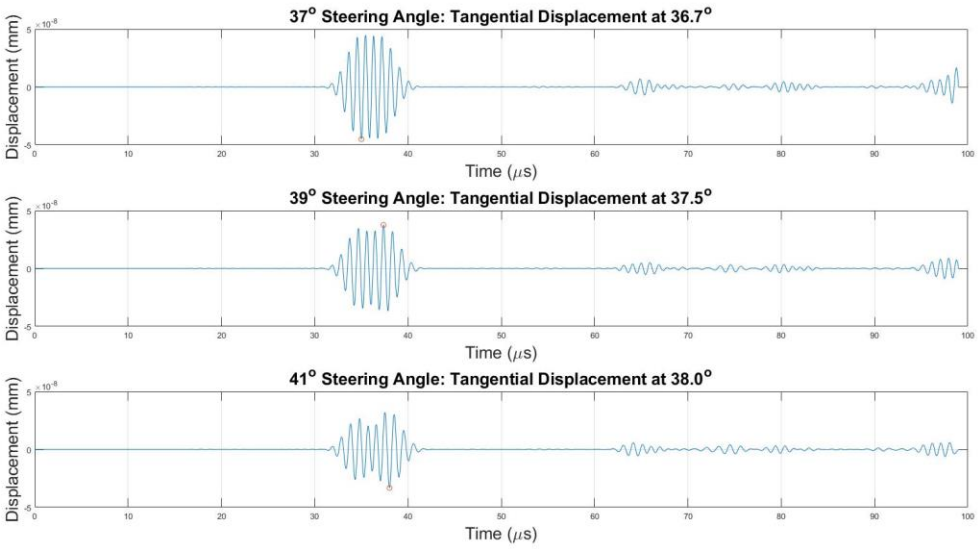

Figure 4.45: A-scans from Maximum Reception Angle from Section C Steering Angles, highlighted in red is the maximum shear wave displacement

Both Sections E and F change in the same manner as their predecessors as steering angle increases. Sudden increases in reception angle are due to a higher-angled sidelobe becoming the main lobe. The RToA changes accordingly with the reception angle, and the lower RToA values are due to the values of displacement originating from the first of the split-waves to strike the sample's curved surface.

For an EMAT positioned at the centre of the flat surface of the semicircular sample, it would make sense for the RToA to be equal to 0μs across all steering angles, however Figure 4.44 shows this not to be the case. The RToAs for Sections A and B remain close to this value due to their single shear wave, however those of Sections C-F diverge significantly from this value depending on which of the split-waves has the larger displacement. Due to the sample's constant radius and shear wave velocity, the only explanation for the

two split-waves with different RToAs is two different origin positions of the shear waves.

For a single steering angle, the Time of Flight (ToF) (equal to 'ToA – τ') for both split-wave peaks was multiplied by the shear wave velocity to calculate two distances between the two origin positions and a given reception angle. These distances from various reception angles were used to triangulate the origin position of each split-wave. The reception angles used were ones whose A-scans clearly show the two split-waves (e.g. Figure 4.23, Figure 4.25 & Figure 4.45). Assumptions made for this method included: the direct correlation between the transmission signal's time delay and the time travelled by the split-waves; and that the origin positions were at the surface due to the shallow depth of the eddy current densities. Figure 4.46 shows this triangulation process for the 90° steering angle, with blue and red arcs through the origin positions to the left and right of the centre respectively. These arcs calculated an average origin position of ±11.6042mm from the centre of the flat surface.

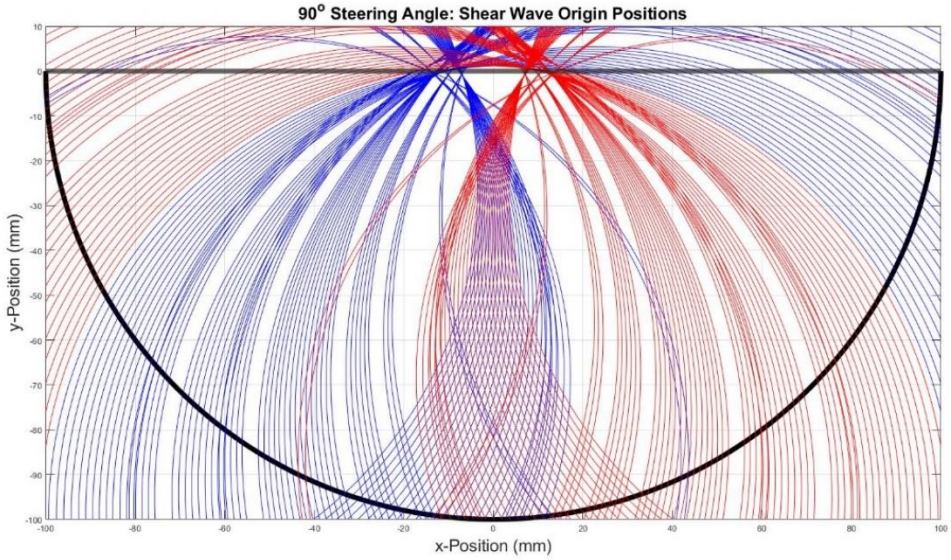

Figure 4.46: Plot of Shear Wave Origin Positions for a 90° Steering Angle

The origin positions for the split-waves are explained using the electromagnetic data extracted from the area of high-mesh density beneath the EMAT. From the x & y components of magnetic flux density and the z-component of eddy current density, x & y components of Lorentz Force density were calculated at regular points beneath the EMAT using Equation 4.5 and Equation 4.6.

$$F_{L,x} = -B_y \times J_{e,z} \quad \text{Equation 4.5}$$

$$F_{L,y} = B_x \times J_{e,z} \quad \text{Equation 4.6}$$

where $F_{L,x}$ = x-component of Lorentz force density (N/m²); $F_{L,y}$ = y-component of Lorentz force density (N/m²); $J_{e,z}$ = z-component of induced eddy current density (A/m²).

From these components, not only was the magnitude of the Lorentz force density known, but also its angular orientation via Equation 3.7. Due to the changing eddy current density induced from the MLC's changing transmission signal, the point in time from which these values were taken was when the induced eddy current density was at its absolute maximum. Figure 4.47 shows this as a plot from the sample's flat surface for the 15° steering angle, marked to show the phase lag from the time delay at the surface. The phase lag at the flat surface for steering angles of 15-90° ranges from 45.8-51.3°, approximate to one radian. As the depth increases from beneath this coil, the phase lag decreases at a rate of approximately one radian per skin depth. This is shown in Figure 4.48 and is consistent with previously established skin effect formulae [85].

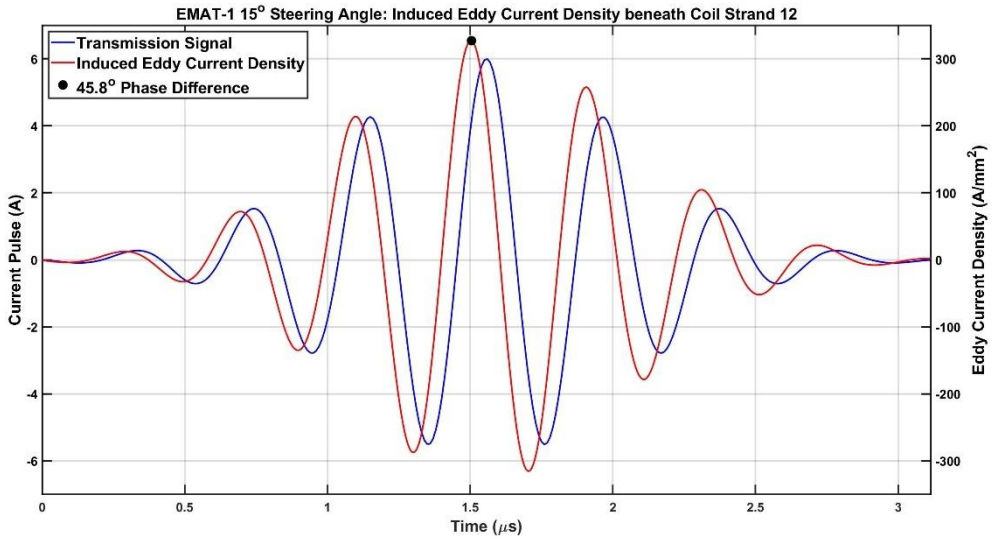

Figure 4.47: Plot of induced Eddy Current Density across Time

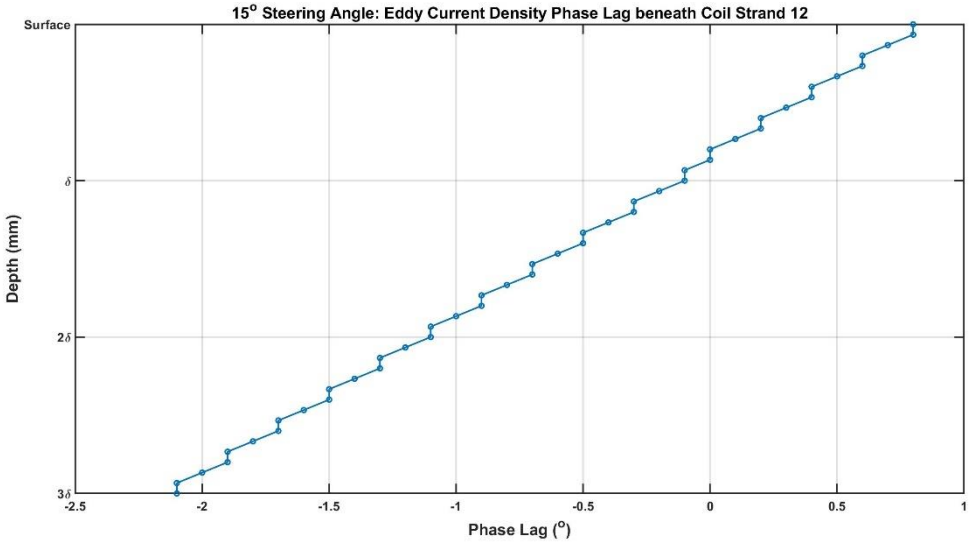

Figure 4.48: Plot of Induced Eddy Current Density Phase Lag across Depth

Figure 4.49 and Figure 4.50 show the components and orientation of the Lorentz force density respectively, at the point in time highlighted in Figure 4.47. Figure 4.49 also includes the components of the bias magnetic field to illustrate the effects that they had on the components of Lorentz force density.

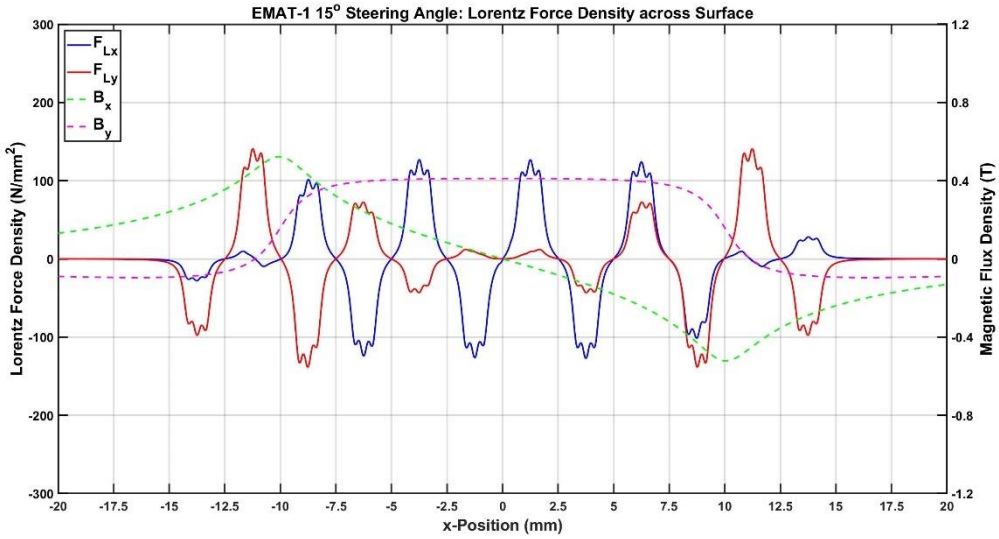

Figure 4.49: Plots of Lorentz Force Density Components across Surface

It is clear from Figure 4.49 that the maximum values of Lorentz force density come from beneath coils 3 and 10 in the array, positioned at ±8.75mm. The reason for this is due to the magnetic flux density for this magnetic configuration (shown in Figure 3.3). Coils 3 and 10 were beneath the concentrations of magnetic flux density at the edges of the magnet.

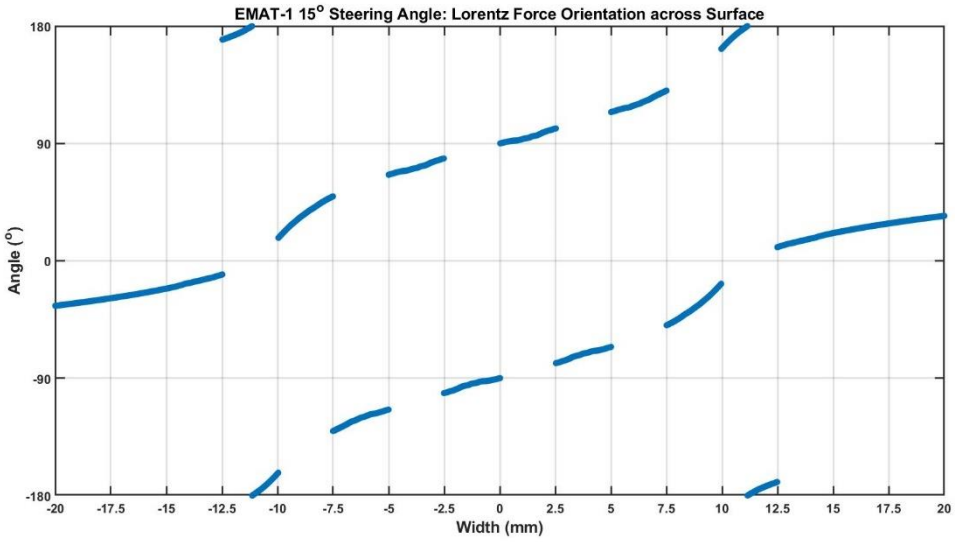

Figure 4.50: Plot of Lorentz Force Density Orientation across Surface

The maximum Lorentz force densities due to the concentrations of magnetic flux density were initially thought to be responsible for the split-waves. Figure 4.50 however shows that the orientation of the Lorentz forces become vertical beneath coils 2 and 11, positioned at ±11.14mm. These x-positions are closer in value to those of the average origin positions for the split-waves (shown in Figure 4.46). It was concluded that the orientation of the Lorentz force density determined the origin positions of the split shear waves, rather than its magnitude.

4.3.2. Experimental Results

Based on the simulated results, steering angles of 65-85° were omitted from experimental testing due to the limited variance of their results, leaving steering angles of 15-60° at 5° intervals & 90°. Additionally due to T_x's shear wave origin positions, an R_x with an MLC was not deemed suitable as its reception positions would likely be in the same positions and the EMAT would not be able to conform to the sample's curved surface. R_x instead consisted of a 'Sonemat shear wave EMAT (HWS2225-GC)' [86] to measure the transmitted shear waves. As the faceplate of this EMAT was also unable to conform to the sample's curved surface, custom probe housings were designed and 3D-printed out of Poly-Lactic Acid (PLA) plastic. This probe housing was designed to: hold R_x within a 32mm diameter central hole; have a concave surface to conform to the semicircular sample's curved surface; and have markings from -10° to 10°

at 1° intervals. Figure 4.51 shows the CAD drawing of the probe housing for the EMAT shear probe.

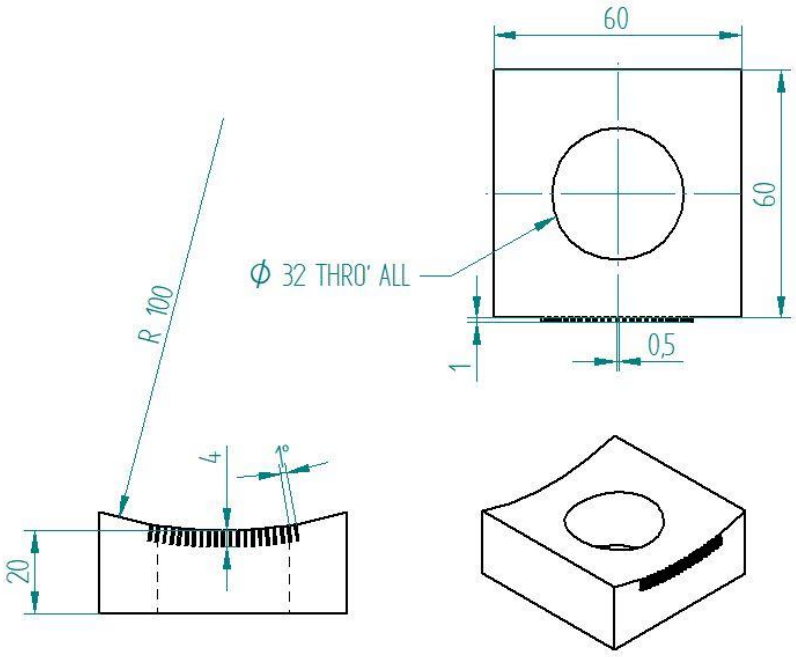

Figure 4.51: CAD Drawing of EMAT Shear Probe Housing

This probe housing ensured that the centre of R_x's faceplate was tangential to the curved surface, at the same height as the centre of T_x. R_x was positioned across this surface from -90° to 90° at 1° intervals and recorded an average signal from each position. Figure 4.52 shows the two experimental EMATs on the semicircular aluminium sample.

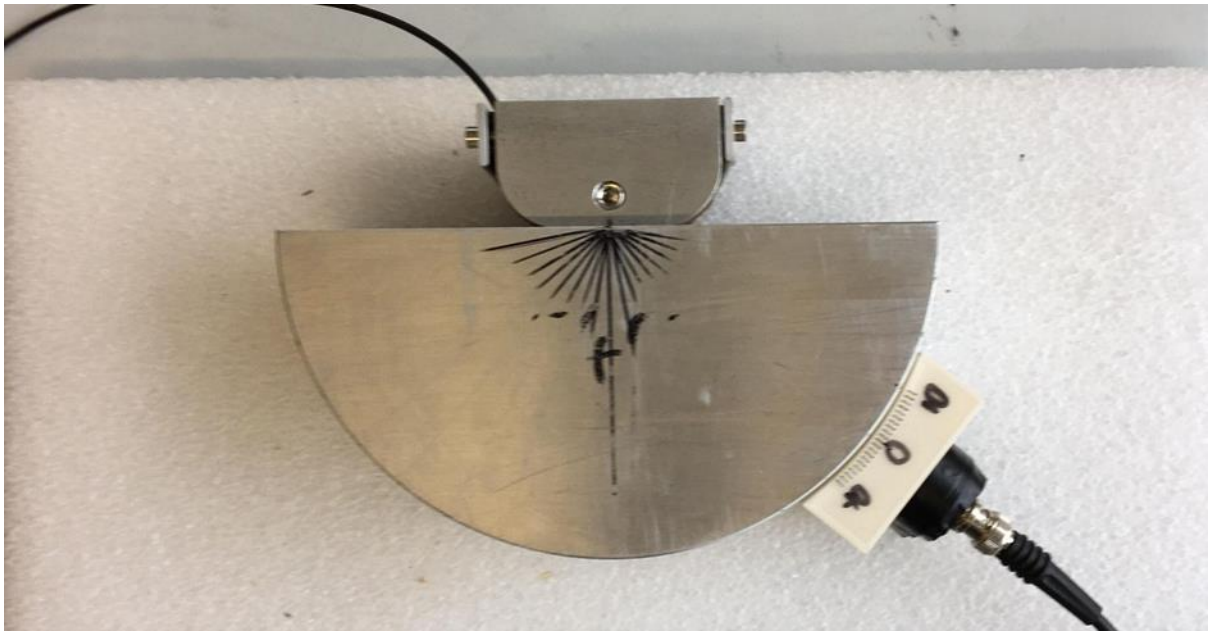

Figure 4.52: EMAT Beam Directivity Experimental Setup

Like the simulated data, the recorded signals were filtered through a bandpass filter with cutoff frequency limits of ±1/3 of the carrier signal

frequency. Because of this, the high-pass filter in the SNAP's amplifier was increased to 1MHz for steering angles of 15° and 20°, as this not only decreased the ringing of the received signal, but any data filtered out by the bandpass filter would have already been filtered out by the high-pass filter. Additionally, the SAA1000 amplifier's gain was reduced from +30dB to +20dB for steering angles 20-50°, as the recorded signal was beyond the SNAP's internal amplifier maximum voltage output of 4V. The shear wave's maximum amplitude from each reception angle was recorded to create a beam directivity of the filtered experimental signal data. The experimental shear wave data was normalised and compared to the normalised simulated shear wave displacement data for each steering angle. Figure 4.53-Figure 4.63 show both of these normalised shear wave directivity plots for each steering angle.

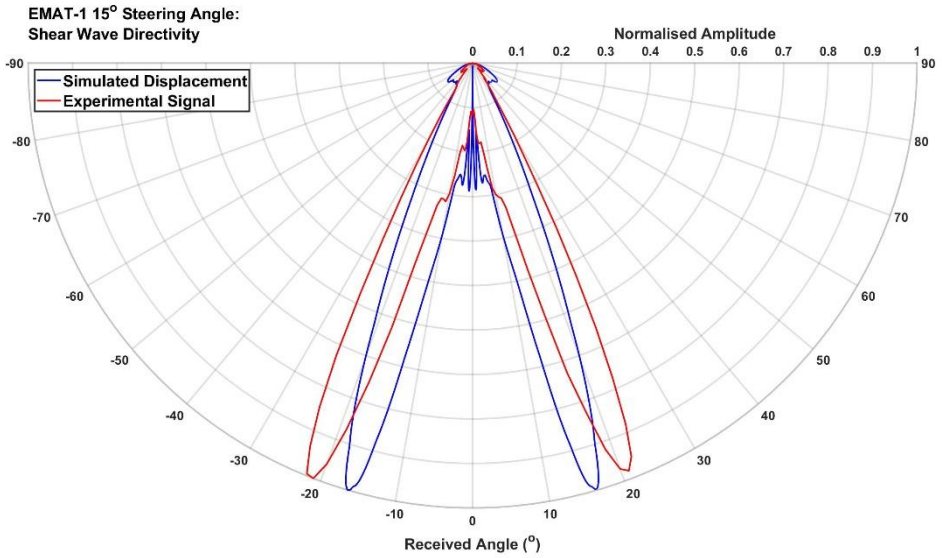

Figure 4.53: Shear Wave Directivity Plots for 15° Steering Angle

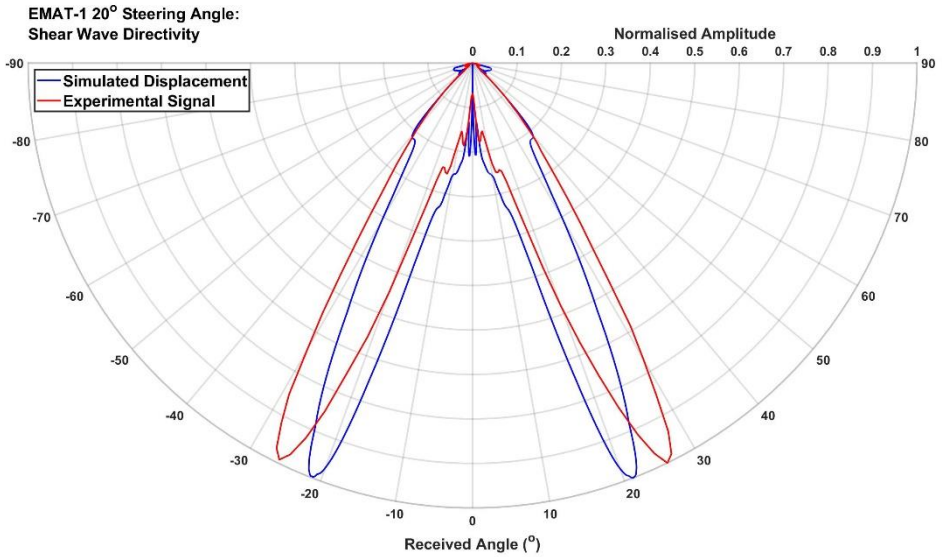

Figure 4.54: Shear Wave Directivity Plots for 20° Steering Angle

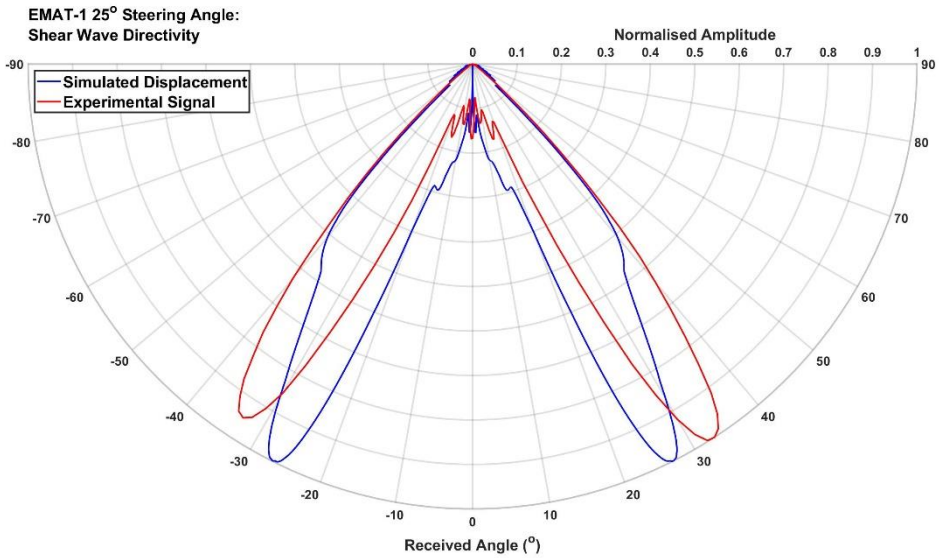

Figure 4.55: Shear Wave Directivity Plots for 25° Steering Angle

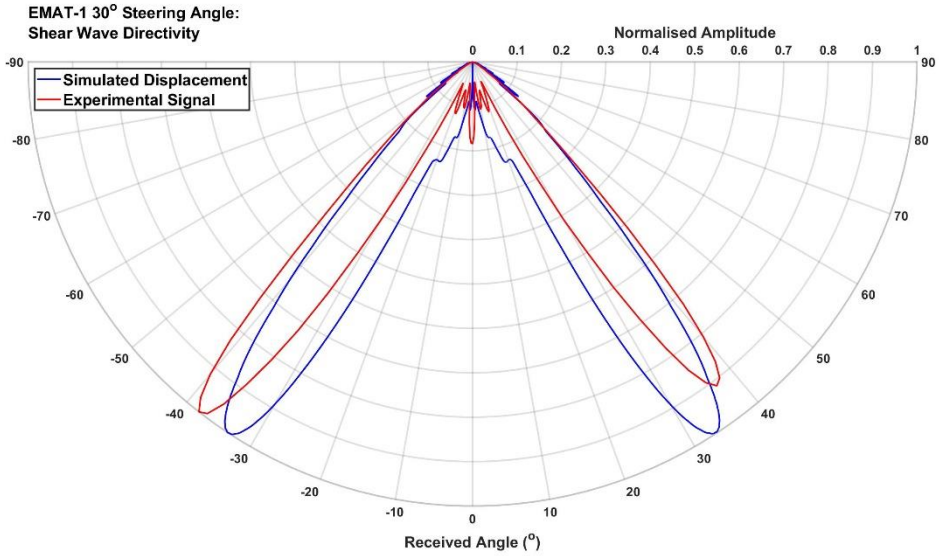

Figure 4.56: Shear Wave Directivity Plots for 30° Steering Angle

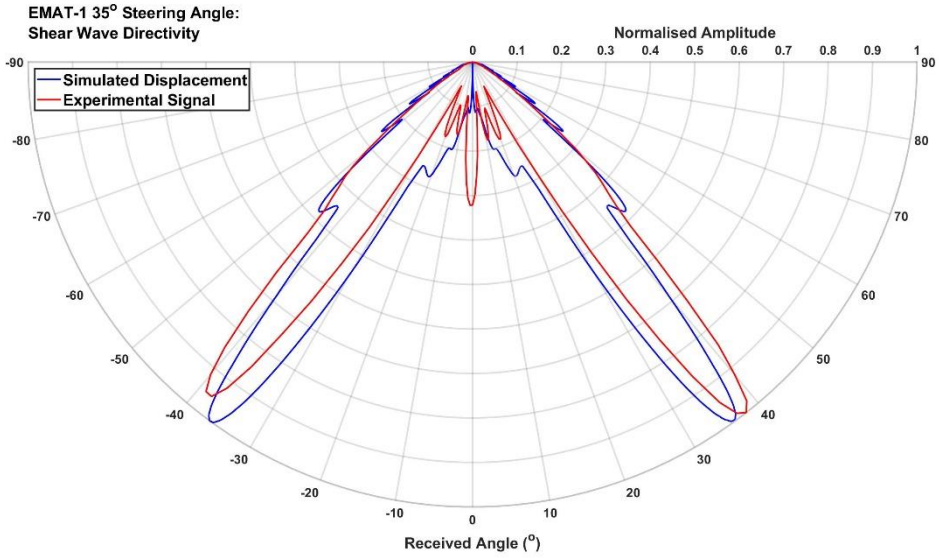

Figure 4.57: Shear Wave Directivity Plots for 35° Steering Angle

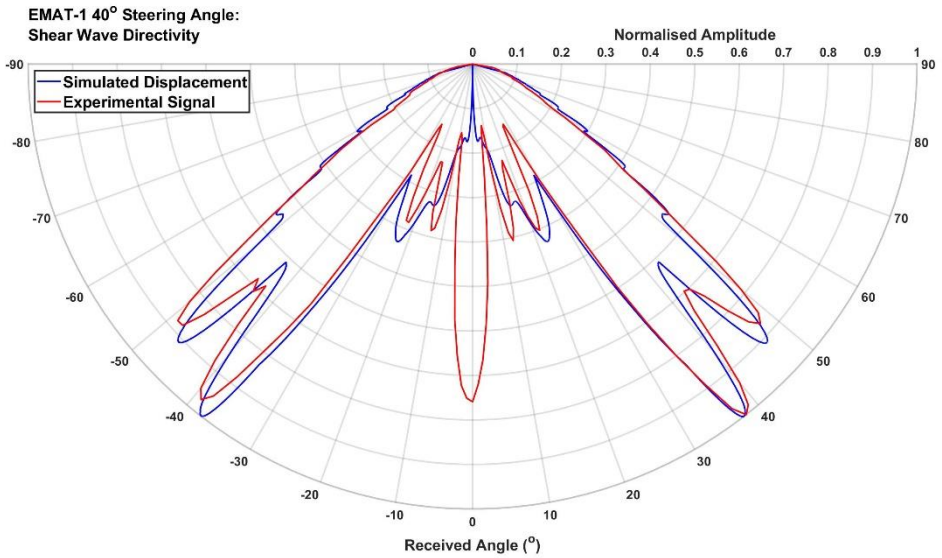

Figure 4.58: Shear Wave Directivity Plots for 40° Steering Angle

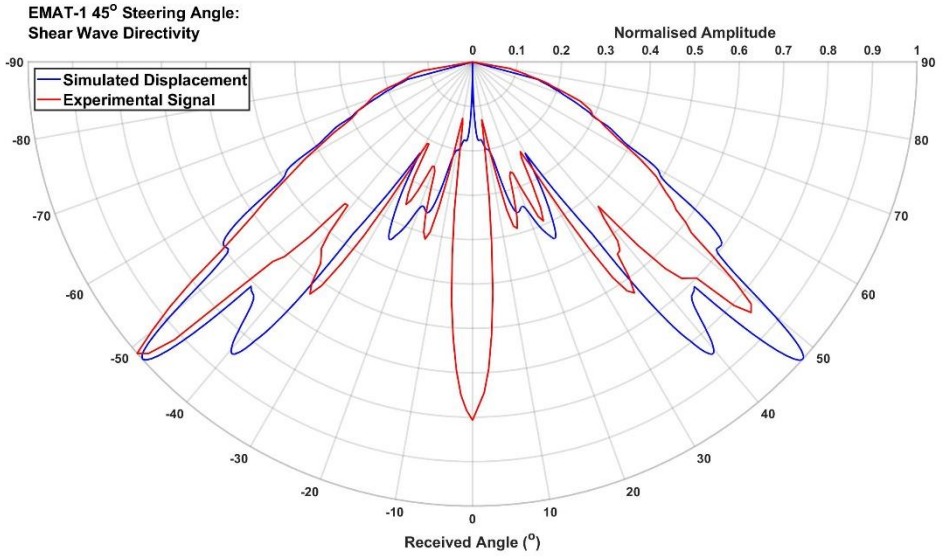

Figure 4.59: Shear Wave Directivity Plots for 45° Steering Angle

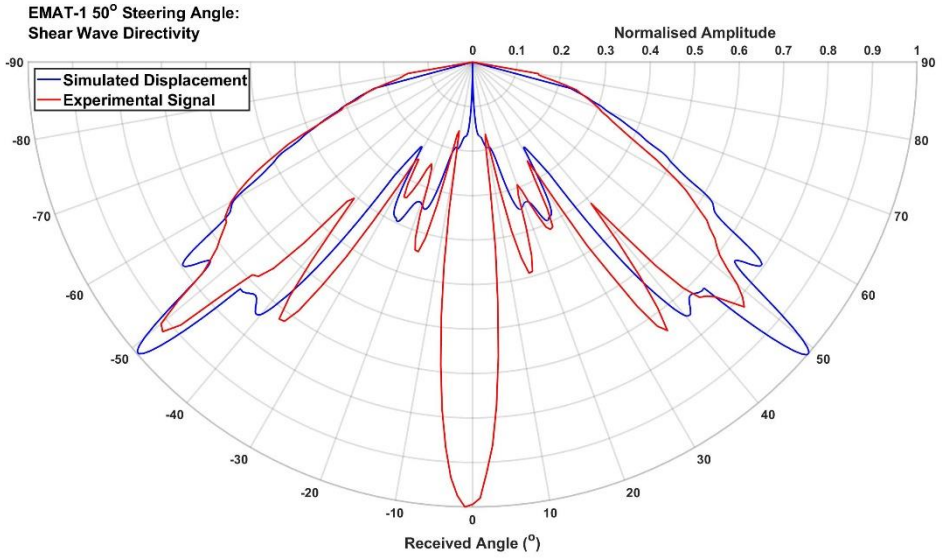

Figure 4.60: Shear Wave Directivity Plots for 50° Steering Angle

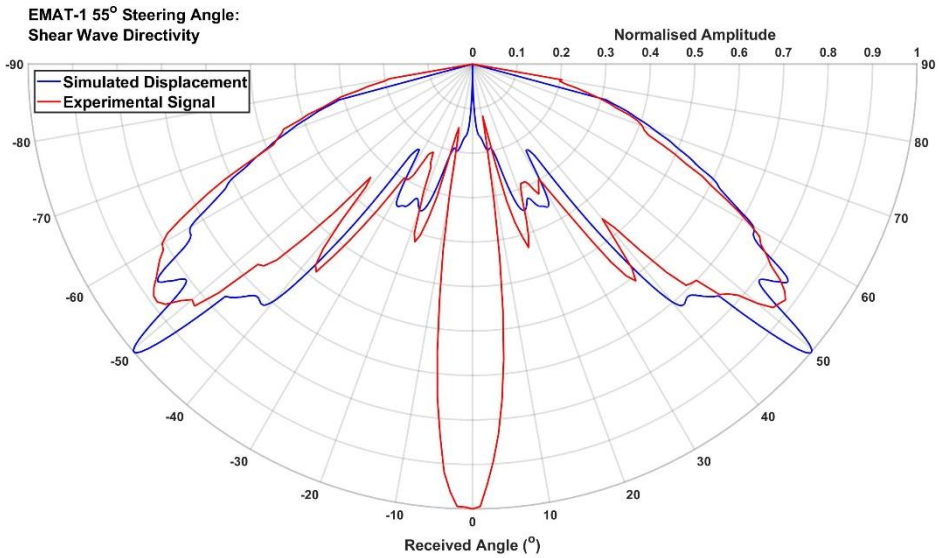

Figure 4.61: Shear Wave Directivity Plots for 55° Steering Angle

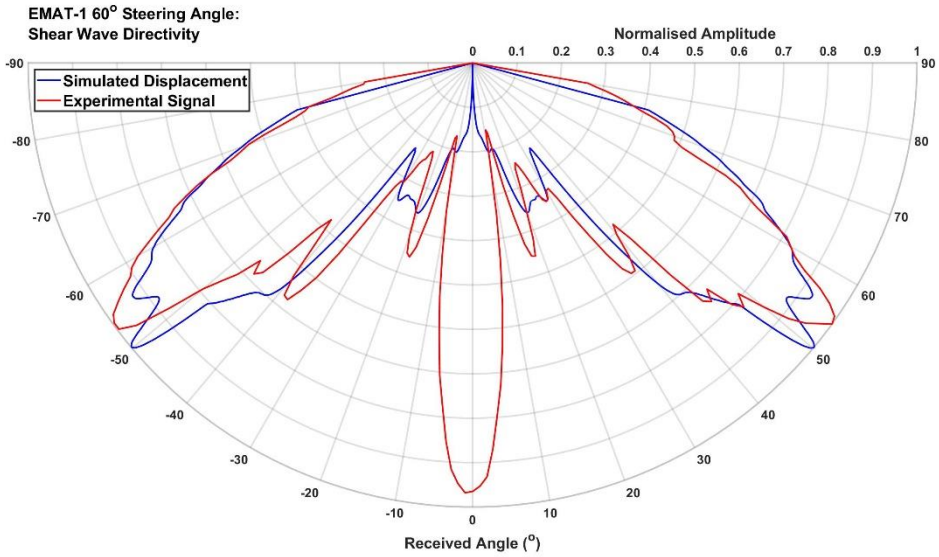

Figure 4.62: Shear Wave Directivity Plots for 60° Steering Angle

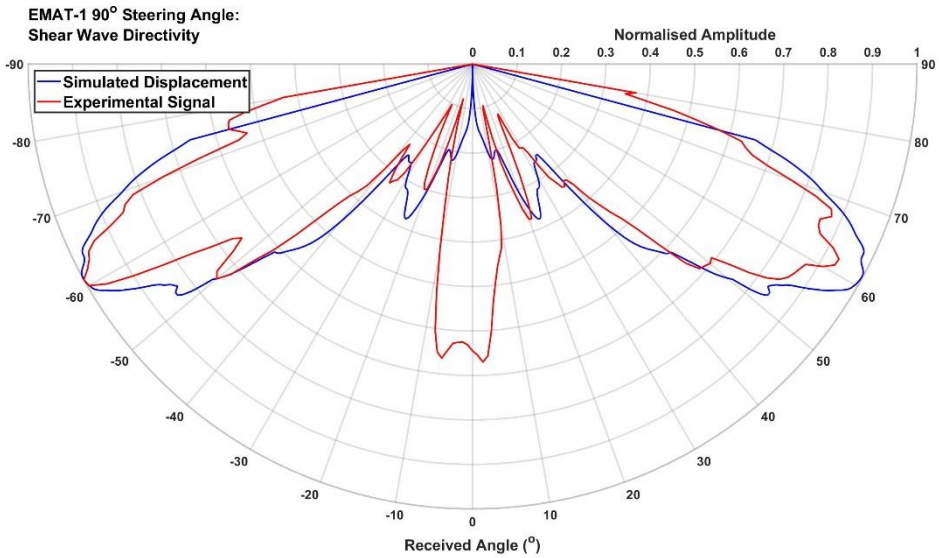

Figure 4.63: Shear Wave Directivity Plots for 90° Steering Angle

It is clearly seen from Figure 4.53-Figure 4.63 that the simulated and experimental results correlate well with one another, in both the main lobe and the side lobes. R_x was capable of detecting the transmitted Rayleigh waves near the edges of the flat surface (however their signal was far weaker further down the curved surface compared to the simulated signal), explaining why the experimental beam directivity plots were capped at ±80°. What is most notable (particularly from Figure 4.56-Figure 4.63) is the growth of a lobe at 0°, which not only deviates dramatically from the simulated results, but is also not in continuity with the MLC EMAT's nature as an angled beam EMAT.

This phenomenon was explained by replacing the shear wave R_x with an "Olympus V156-RM": a single element shear wave transducer with a propagation direction normal to the surface [87]. The reason that this UT probe was used to receive the shear waves was due to its shear wave polarisation direction being in a single alignment, as opposed to the shear wave R_x which was polarised radially due to its spiral-coil. The UT probe was therefore able to determine the direction of particle motion by its own orientation relative to the sample's curved surface. Figure 4.64 shows the shear wave directivity measured by the UT probe orientated both in-plane (polarisation in the x & y axis) and out-of-plane (polarisation in the z axis), at 5° intervals across the sample's curved surface for the 45° steering angle.

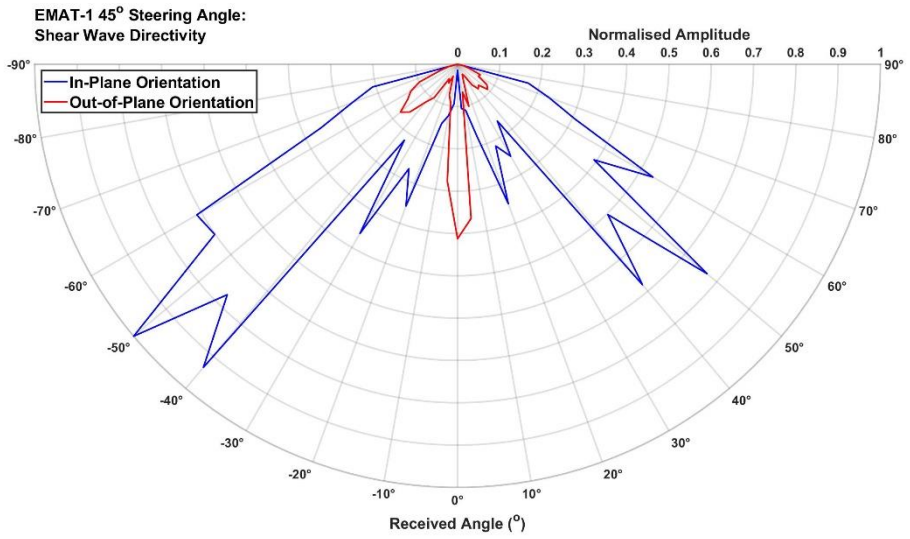

Figure 4.64: Shear Wave Directivity Plots for 45° Steering Angle via Shear Wave UT Probe

Figure 4.64 shows that the angled shear waves oscillate in-plane (as with the simulated results) while the 0° lobe oscillate out-of-plane. This explains not

only why the 2D models could not simulate the 0° lobe, but also how the radially polarised shear wave R_x was able to detect it. As previously explained, the shear waves from the MLC EMAT are generated from the interaction of the bias magnetic field and eddy current densities induced by the meandering coils. It is theorised that the 0° lobe was generated from the sections of coil that connect these meandering coils. These would have induced eddy current densities in the x-axis, producing Lorentz forces in the z-axis, creating out-of-plane shear waves.

Figure 4.65 shows the maximum shear wave signal voltage for each steering angle's beam directivity. This is compared to the model's maximum shear wave displacement. Due to the reduced SAA1000 gain of +20dB for steering angles of 20-50°, R_x recorded A-scans from positions of low signal for these angles at +30dB, which were then used to increase the maximum signal by a SF. This is how the maximum experimental signals for steering angles 25° and 30° are greater than the SNAP's maximum 4V output limit.

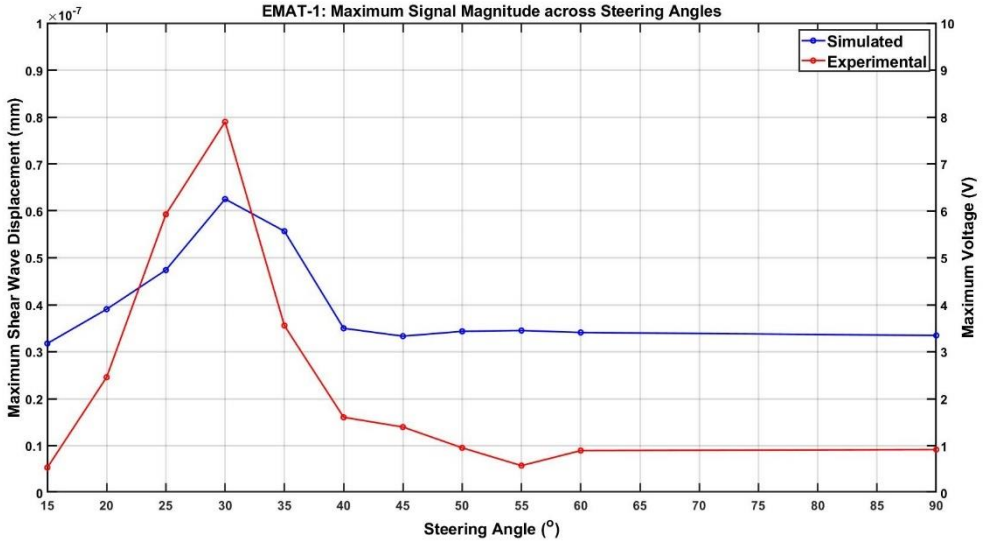

Figure 4.65: Shear Wave Magnitude Comparison

It is very noticeable that there is a disparity between these two sets of values (explaining why Figure 4.53-Figure 4.63 were graphed as normalised plots). One reason for this disparity is that the comparison is made between two different values: the perfectly tangential simulated displacement from a single point in 2D space representing the ultrasonic shear wave; and the voltage signal induced into R_x by the shear wave.

The design of R_x is also not optimised for the curved surface, with: a magnetic field normal to the curved surface, straight coils perpendicular to the tangential displacement of the shear waves (in the z-axis) are best suited to receive them. R_x's flat circular coil on a curved surface however resulted in the coils closest to the curved surface being directionally parallel to the shear wave particle motion. Despite this, the correlation coefficient between the simulated and experimental results (shown in Figure 4.65) was calculated at 0.9119.

Figure 4.66 shows the reception angles of the maximum shear wave signal and (like Figure 4.44) has included error bars to indicate the shear wave -6dB beamwidth. Due to the nature of the experimental testing's 0° lobe, it was removed from Figure 4.66. Between the two datasets, the correlation coefficient for the maximum signal's reception angles was calculated at 0.9915, the beamwidth's upper and lower limits were calculated at 0.9826 and 0.9933 respectively. While the experimental results tend to be higher in reception angle, the correlation coefficients between these two datasets validated the simulations as accurate models of the experimental setup.

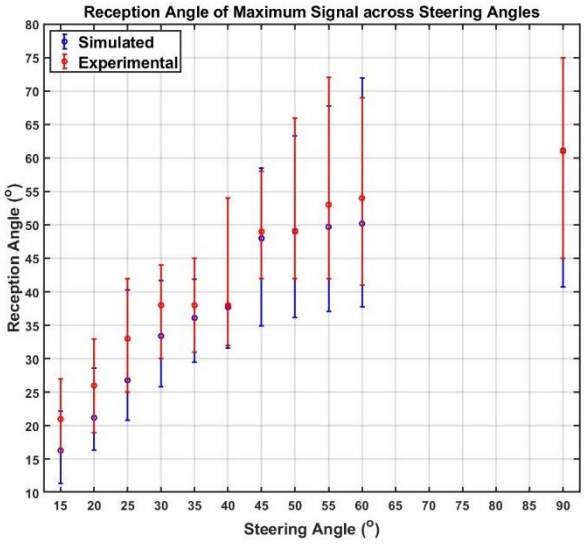

Figure 4.66: Shear Wave Reception Angle Experimental Validation

4.4. Beam Steerability

The model studying the MLC EMAT's beam steerability followed the same design as the model studying the EMAT's beam directivity, with one difference: the transmitted shear waves were measured across the backwall of a

rectangular aluminium sample. Components of displacement extracted from across the backwall were used to locate the magnitude and position of the shear wave's main lobe as the steering angle changed. Previous work on this topic is documented in [88] (included in Appendix A), however further novel work had been undertaken since then and is detailed in the following section.

4.4.1. Beam-spread Profiling

In addition to measuring the magnitude and position of the shear wave across the backwall, the internal reflections and mode conversions within the sample were also analysed. This was done to determine the hierarchy of magnitudes for different propagation pathways. The end-time of these simulations was therefore set to 198µs. Simulations were performed for steering angles of 20-60° at 5° intervals & 90°, and Figure 4.67-Figure 4.76 show the colour-plots of these models. The 15° steering angle was omitted due to the immense density of the mesh overwhelming the computational capacity.

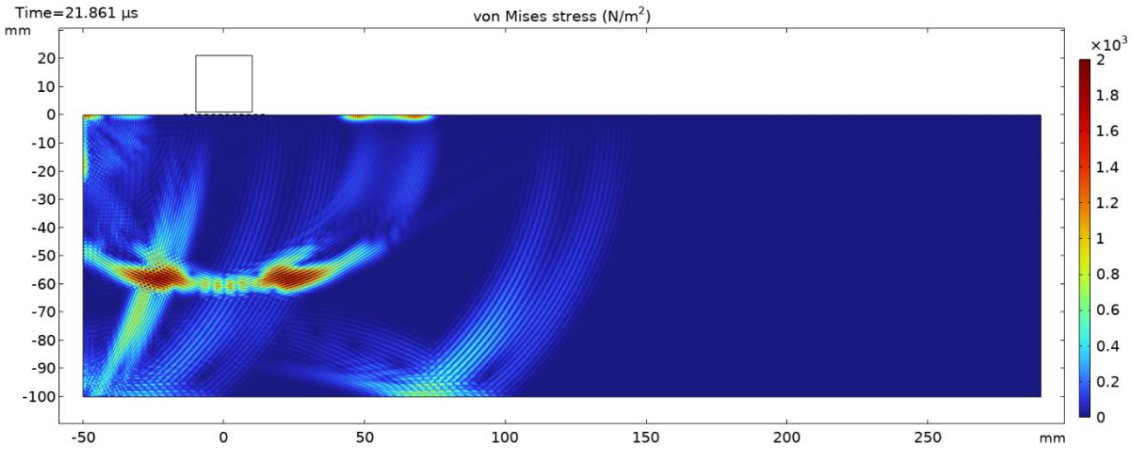

Figure 4.67: 20° Steering Angle EMAT on Rectangular Sample

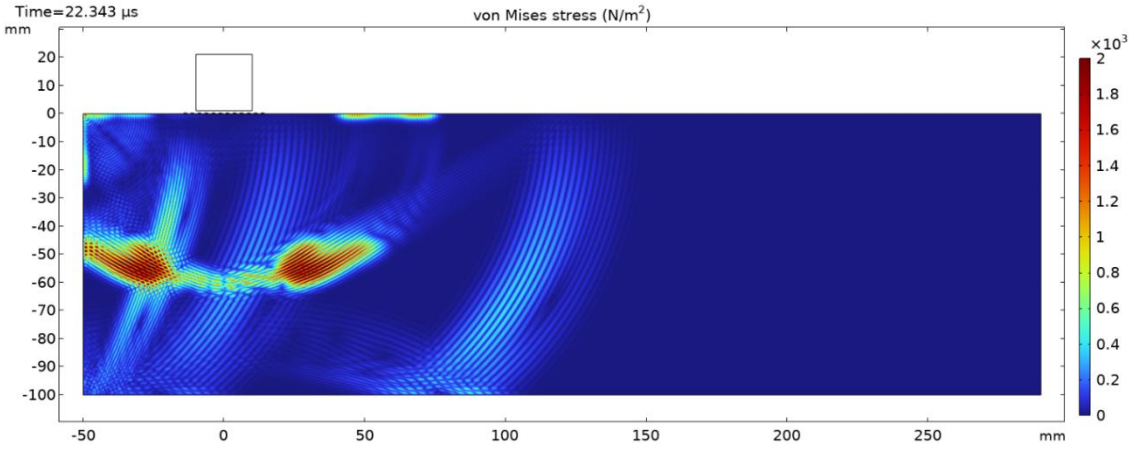

Figure 4.68: 25° Steering Angle EMAT on Rectangular Sample

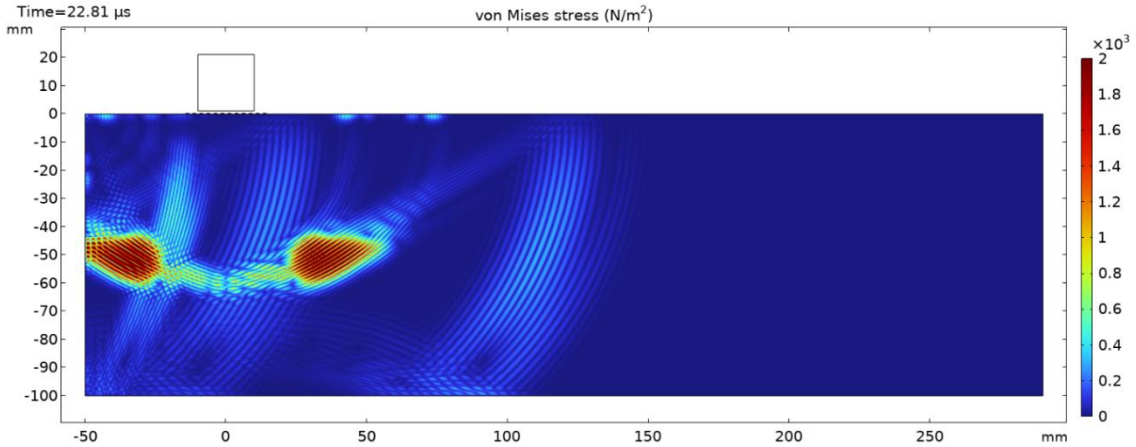

Figure 4.69: 30° Steering Angle EMAT on Rectangular Sample

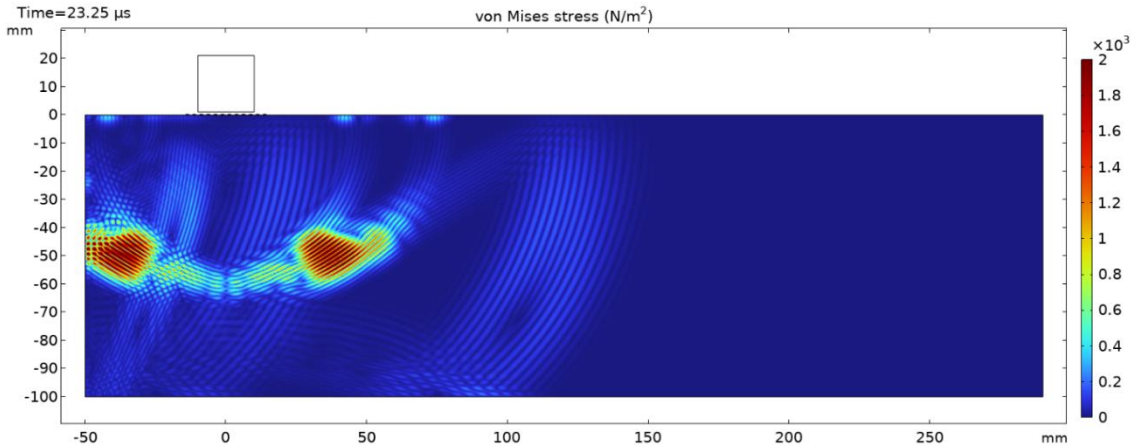

Figure 4.70: 35° Steering Angle EMAT on Rectangular Sample

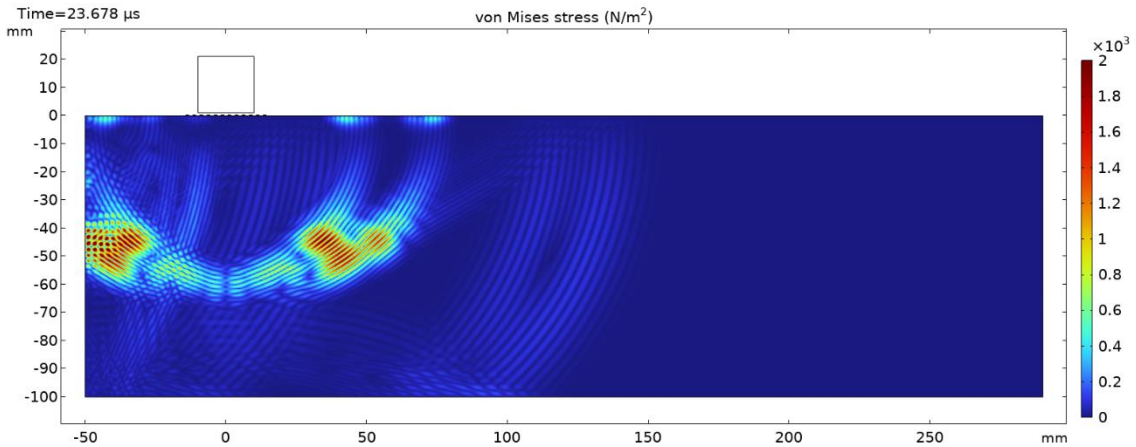

Figure 4.71: 40° Steering Angle EMAT on Rectangular Sample

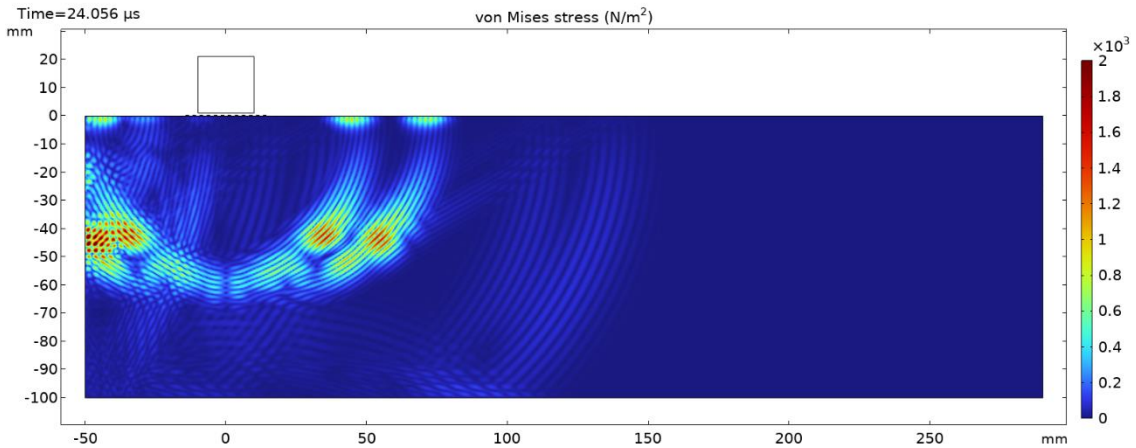

Figure 4.72: 45° Steering Angle EMAT on Rectangular Sample

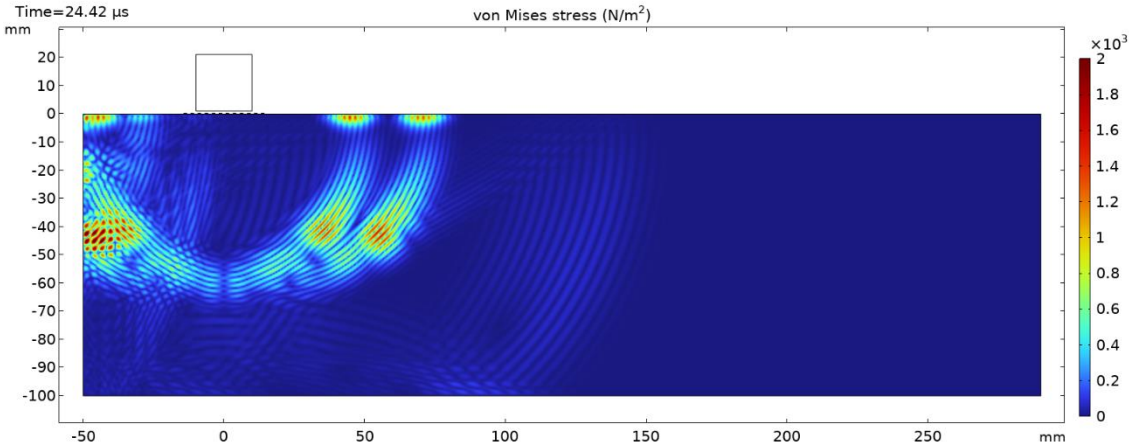

Figure 4.73: 50° Steering Angle EMAT on Rectangular Sample

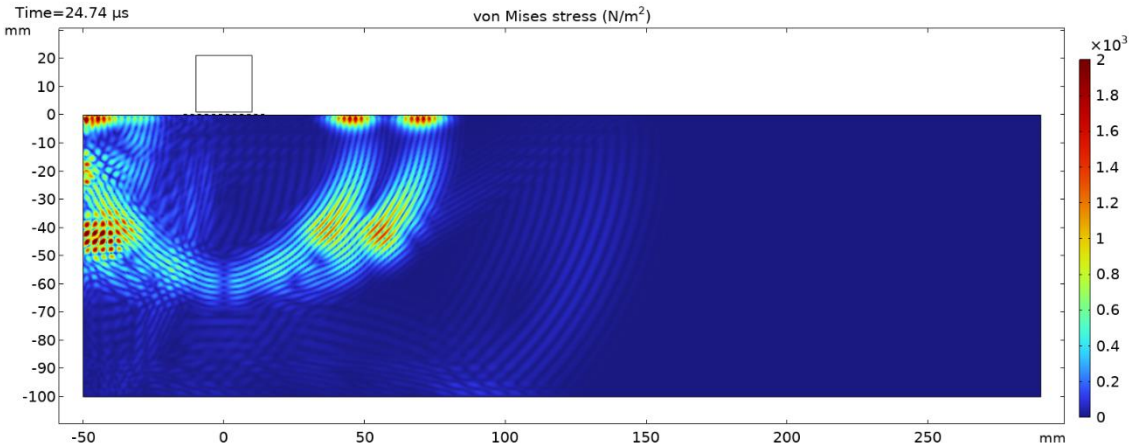

Figure 4.74: 55° Steering Angle EMAT on Rectangular Sample

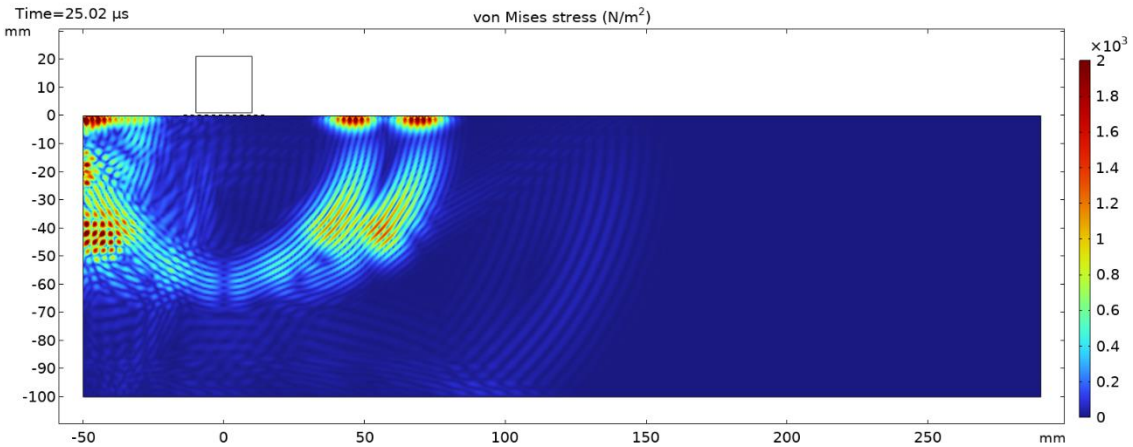

Figure 4.75: 60° Steering Angle EMAT on Rectangular Sample

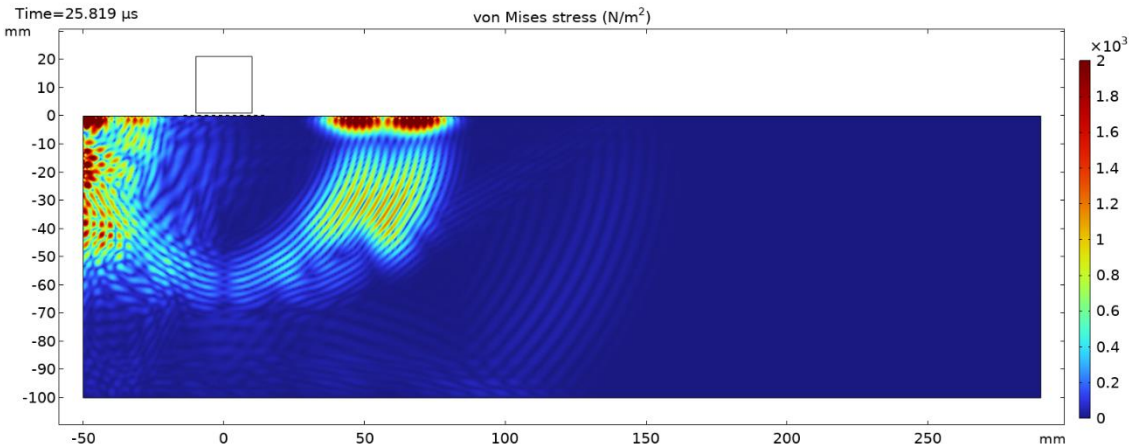

Figure 4.76: 90° Steering Angle EMAT on Rectangular Sample

Since the shape of the aluminium sample is the only difference between these simulations and those of the beam directivity study, the transmitted shear waves behave in the same manner. As the steering angle increases: the shear waves reach a maximum magnitude near a 30° steering angle; the shear waves reach a steering limit near 50°; the magnitude of the Rayleigh waves increases; the compression waves reached their first critical angle and diminished; and the shear waves were transmitted as split-waves from the corners of the EMAT.

Where the semicircular sample enables Equation 4.2 and Equation 4.3 to differentiate between the different wave modes based on their directional displacement, this method could not be used on the flat backwall as the its angle relative to T_x is not constant across it. Due to the different wave velocities and T_x's offset however, the different wave modes could be identified in the A-scans via basic ToA calculations. Figure 4.77 illustrates the rectangular sample with three pathways from T_x to the backwall for different wave modes.

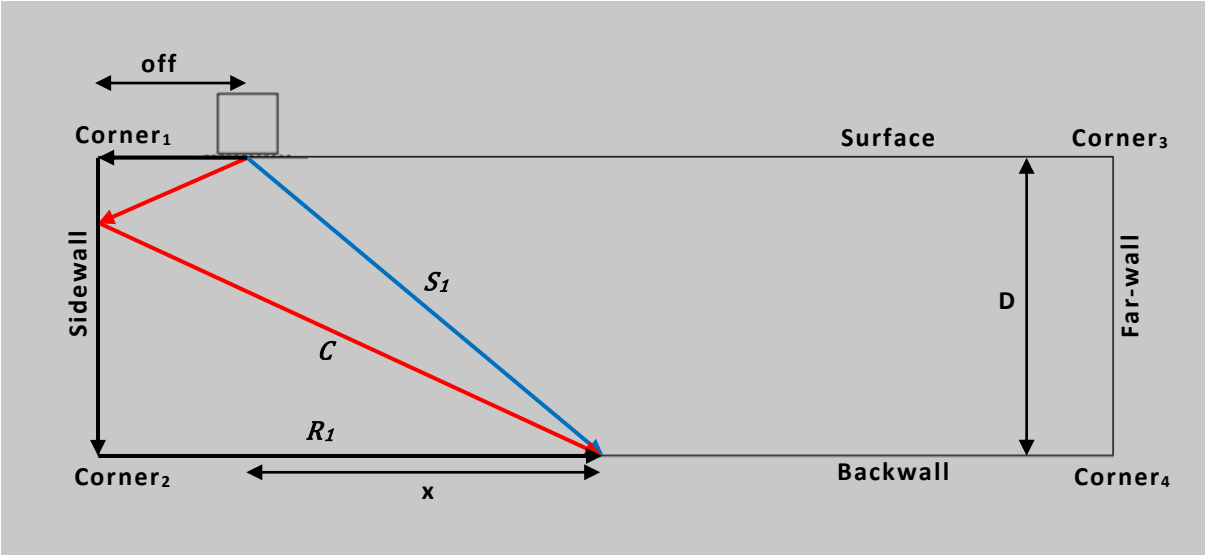

Figure 4.77: Ultrasonic pathways from T_x to a backwall x-position

Annotated on Figure 4.77 are the names of the four surfaces and corners that the various waves interact with. These assisted in defining the various propagation pathways and calculating their ToA as a function of distance. The pathways shown in Figure 4.77 are labelled as such:

- $S_1 = T \xrightarrow{S} R$
- $C_2 = T \xrightarrow{C} Side \xrightarrow{C} R$
- $R_1 = T \xrightarrow{R} Cor_1 \xrightarrow{R} Cor_2 \xrightarrow{R} R$

Equation 4.7-Equation 4.9 define the timeframes within which each of the propagation pathways above (also annotated on Figure 4.77) were expected on the A-scan at a given x-position across the backwall. These include a gating halfwidth of six cycles to allow for error in the ToA of each wave mode's maximum peak. The velocity of the Rayleigh wave could not be inputted into model, however it was calculated by experimental testing (as explained later in this section) to be 2.88mm/µs.

$$S_1 = \tau + \frac{\sqrt{x^2 + D^2}}{v_s} \pm \frac{6}{f} \qquad \text{Equation 4.7}$$

$$C_2 = \tau + \frac{\sqrt{\left(x + (2 \times off)\right)^2 + D^2}}{v_c} \pm \frac{6}{f} \qquad \text{Equation 4.8}$$

$$R_1 = \tau + \frac{x + (2 \times off) + D}{v_r} \pm \frac{6}{f} \qquad \text{Equation 4.9}$$

where S_1 = direct shear wave ToA; x = x-position on backwall (mm); D = depth of rectangular sample (equal to 100mm); C_2 = reflected compression wave ToA; off = offset distance from T_x to the sidewall (equal to 50mm); R_1 = direct Rayleigh wave ToA.

The experimental testing was performed in much the same manner as with the beam directivity tests: steering angles of 20-60° at 5° intervals & 90° were tested; the SNAP amplifier's high-pass filter was set at 1MHz for the 20° steering angle and 0.05MHz for the remaining steering angles; an oscilloscope recorded an average A-scan of signal sixteen signals at each x-position; the recorded A-scan was filtered through a bandpass filter with cutoff frequency limits of ±1/3 of the carrier signal frequency. The differences between the two experimental test setups were: R_x used an MLC EMAT of the same design as T_x due to the sample's flat surface; R_x was positioned from 0-275mm at 1mm intervals across the backwall. Figure 4.78 shows the two experimental MLC EMATs on the rectangular aluminium sample.

Figure 4.78: EMAT Beam Steerability Experimental Setup

The displacement magnitude (in lieu of the directional displacement) is compared to the experimental results, due to its excellent correlation coefficient of 0.9993 to the values of directional displacement. The experimental data was also graphed as absolute values to better compare to the simulated displacement magnitudes at each x-position and better observe the conformity between the two datasets. In addition to the A-scans across the rectangular sample's backwall, R_x also recorded A-scans across the surface of the rectangular sample from 100-275mm at 5mm intervals. This was done not only to measure the internal mode conversions reflecting off of the surface, but also to observe how the generated Rayleigh waves are affected by the change in steering angle.

The plots of displacement magnitude are graphed in line with the experimental A-scans, and the peaks in these two datasets had a propagation pathway attributed to it (by use of ToA gating). An issue with the ToA gating is not only that different waves can strike a surface at the same time, but that different gates can overlap and cause one wave mode to be read as another. As this issue pertained to both the experimental and simulated datasets however (and the purpose of the experimental testing is to validate the quality of the simulations), this was not regarded as a significant issue. Additionally, the simulation's ability to visualise the waves propagating through the material allowed a propagation pathway to be assigned to the peaks in these signals.

Figure 4.79-Figure 4.82 show the results of the two datasets for a 30° steering angle from different x-positions across the backwall. The simulated results also show the ToA gating (defined in Equation 4.7-Equation 4.9) to illustrate the process of pathway identification. A cutoff voltage was applied to the experimental signals (-20dB of the maximum voltage peak across the backwall), and a propagation pathway was attributed to any signal above it. These propagation pathways were determined by the simulated peaks that occur within a close point in time and are also annotated on these figures.

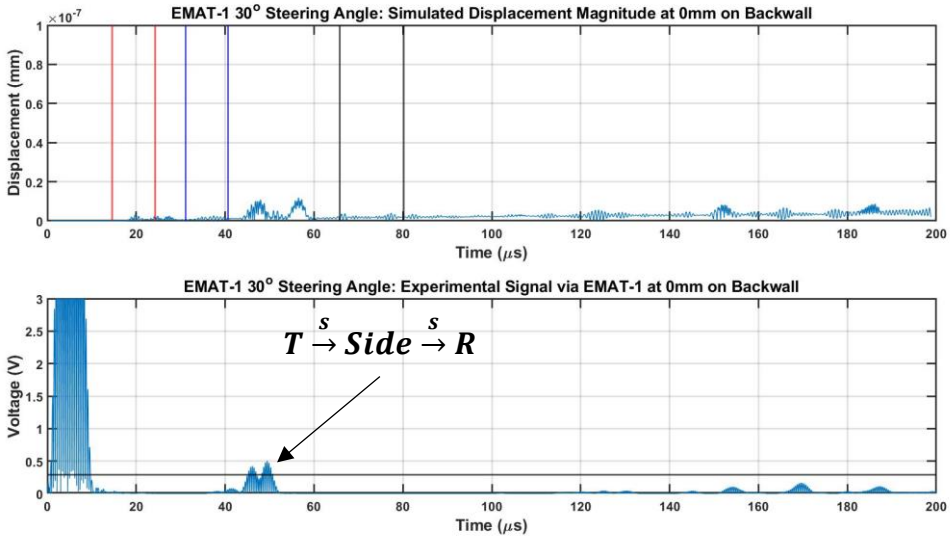

Figure 4.79: Simulated vs Experimental data for 30° Steering Angle at 0mm across the backwall, annotated with the experimental signal peak's propagation pathway

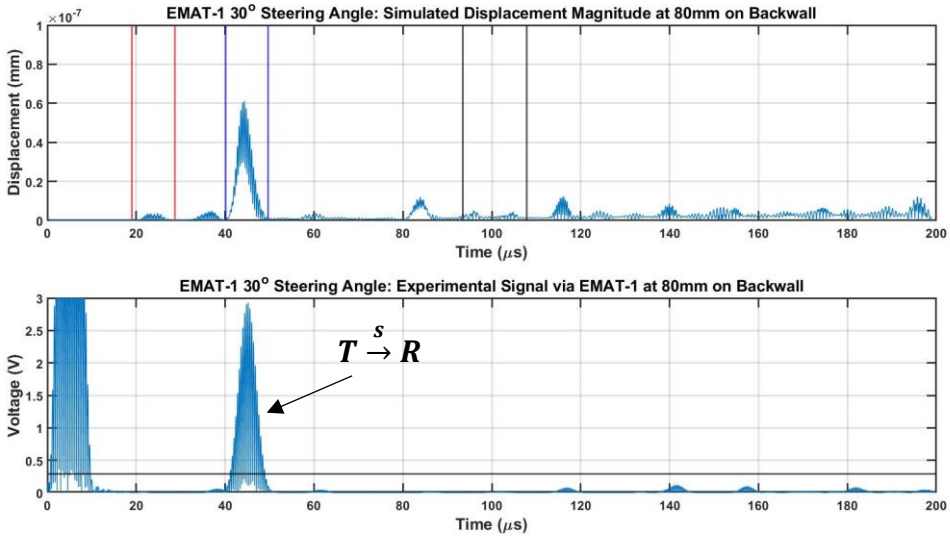

Figure 4.80: Simulated vs Experimental data for 30° Steering Angle at 80mm across the backwall, annotated with the experimental signal peak's propagation pathway

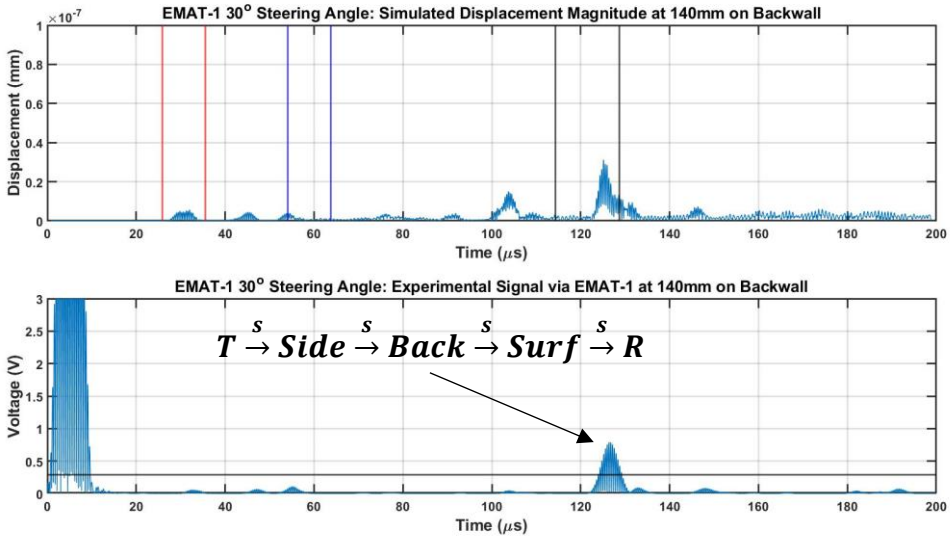

Figure 4.81: Simulated vs Experimental data for 30° Steering Angle at 140mm across the backwall, annotated with the experimental signal peak's propagation pathway

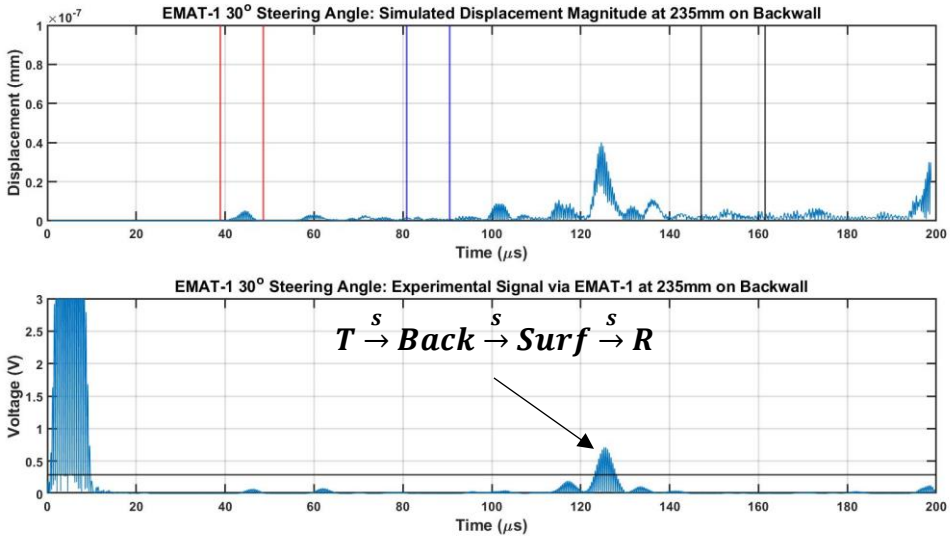

Figure 4.82: Simulated vs Experimental data for 30° Steering Angle at 235mm across the backwall, annotated with the experimental signal peak's propagation pathway

There appears to be a strong correlation between the experimental and simulated datasets shown in Figure 4.79-Figure 4.82, as the peak experimental signals received by R_x occur at similar times to those of the peak displacements. It is also noteworthy that the experimental signals have less noise than the simulated displacement due to the multiple filters that the data passes through.

The first received signal above the -20dB cutoff was from the x-position directly beneath T_x and was identified as the shear wave that reflected off of the sidewall. The simulated results show a second peak 10µs after the ToA of this experimental signal peak. This was identified as a Rayleigh wave that was

generated by the shear wave directly striking Cor2. Hutchins, Nadeau, and Cielo [89] have documented the effects of bulk waves mode-converting to surface waves when interacting with a rectangular slot (akin to a corner-trap), and this type of mode-conversion was also predicted in the FEM modelling of Bond and Saffari [90]. Despite its magnitude in the simulated results, R_x was incapable of detecting these mode-converted Rayleigh waves across the backwall. Additionally, R_x could not detect the Rayleigh waves transmitted across the surface from T_x for the 20° and 25° steering angles (shown in Figure 4.67 and Figure 4.68 respectively). It is unclear if this is due to simulation error or the design of R_x being unsuitable to detecting third harmonic Rayleigh waves. The other experimental signal peaks were identified as shear waves, and their propagation pathways as: directly from T_x to R_x; reflecting off of the sidewall, backwall, surface, and to R_x; and reflecting off of the backwall, surface, and to R_x.

Due to the lack of a simulated model for the 15° steering angle, its experimental signals were identified by both ToA gating and comparison to the pathways of the other steering angles. For all steering angles, the propagation pathways that produced an experimental signal peak above their voltage cutoff are recorded in Appendix B. The maximum voltage peak from across the backwall (and thus the voltage cutoff) changed across steering angles. Figure 4.83 shows the maximum voltage peak for a given propagation pathway as the steering angle increased.

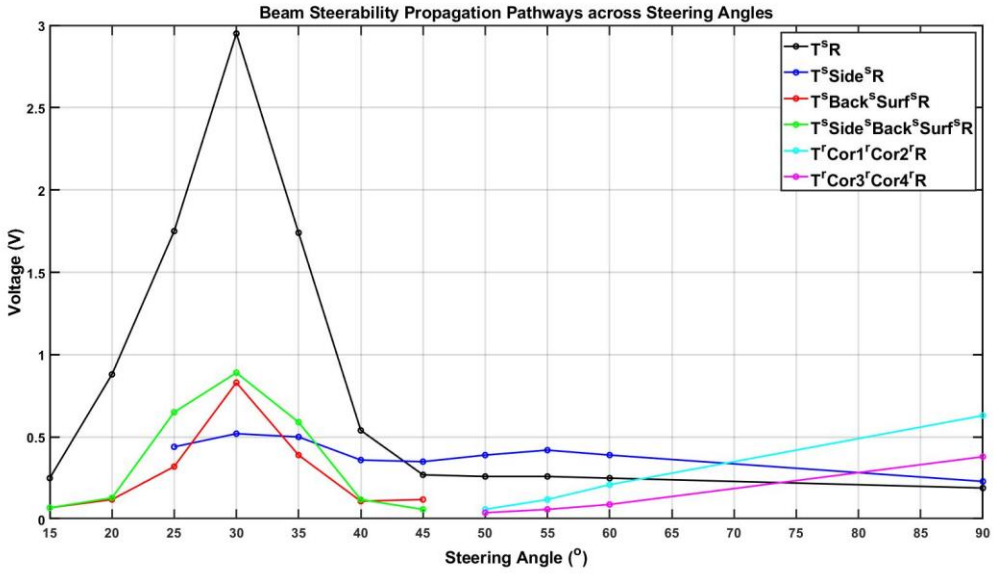

Figure 4.83: Beam Steerability Propagation Pathways to the Backwall

From steering angles of 15-40°, the propagation pathway that produced the maximum voltage is the direct shear waves, however this is supplanted by the shear waves that reflected off of the sidewall for the remaining steering angles. The Rayleigh wave that travelled across the sidewall began to be detected at a 50° steering angle, and it increased in magnitude until it produced the greatest signal voltage at the 90° steering angle. The ToA gating for the 20° and 25° steering angles was complicated by the mode-converting compression waves. The differing wave velocities across unknown surface positions meant that automatic gating was not wholly reliable, however the experimental voltage peaks could still be identified via the simulations.

At each x-position across the backwall, the maximum signal from the direct shear wave was ToA-gated for both datasets. This was used to create simulated and experimental shear wave profiles across the backwall and measure their beam-spread. The beam-spread is defined as the difference in backwall x-positions whose maximum signal voltages were -6dB that of the maximum voltage across the backwall. Figure 4.84 shows the shear wave backwall profiles for the 30° steering angle and is annotated to show their beam-spreads. This process was repeated for all steering angles and their profiles correlate very well with one another (as shown later in Table 4.2).

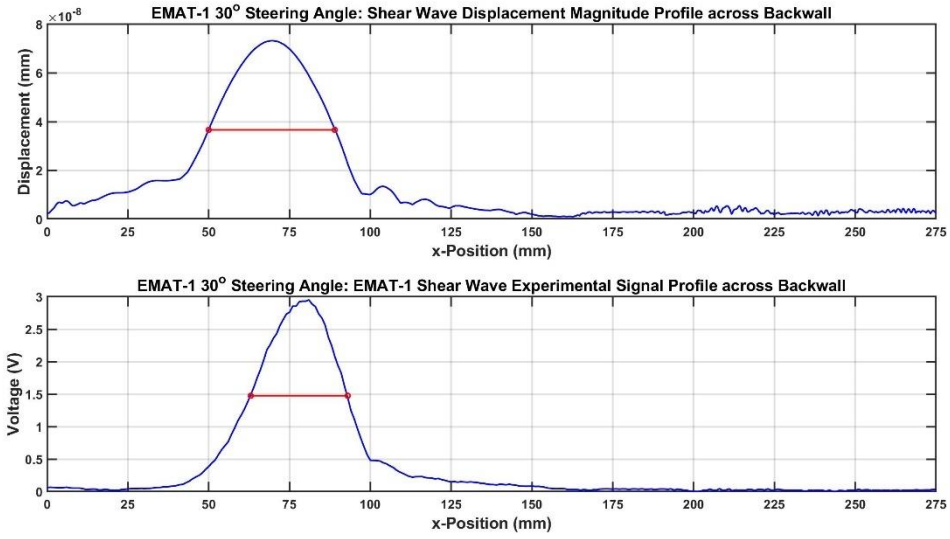

Figure 4.84: Shear Wave Profiles for 30° Steering Angle

The magnitudes of each dataset's profile peak was graphed against the steering angle and is shown in Figure 4.85. The x-positions at which both profile's peaks occurred were expressed as reception angles across a 100mm

depth. From Figure 4.84, these x-positions of 70mm and 81mm equal reception angles of 35.0° and 39.0° respectively. This process was also applied to the upper and lower limits of the profile's beam-spread. Figure 4.86 shows these reception angles graphed against their respective steering angles, with the beam-spreads graphed as error bars.

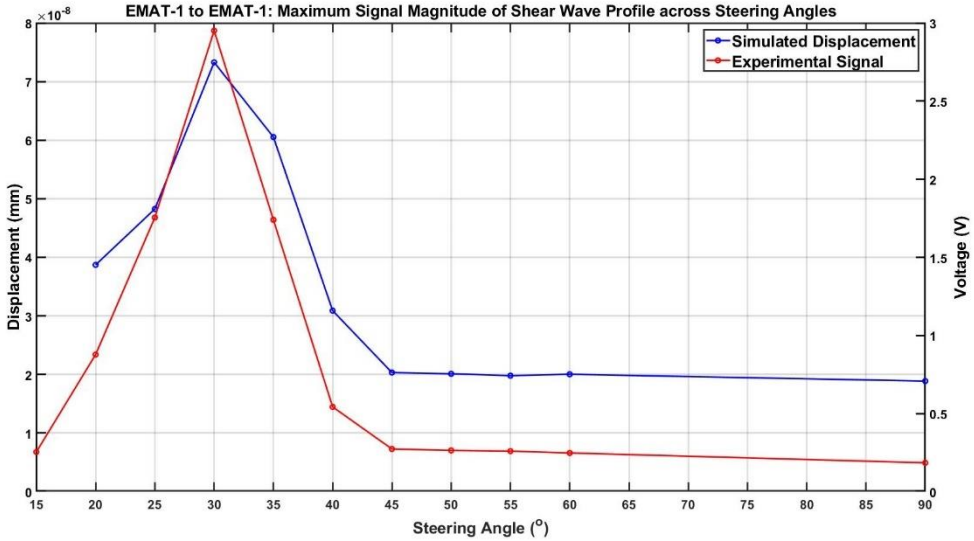

Figure 4.85: Plot of the Shear Wave Backwall Profile's Maximum Amplitude across Steering Angles

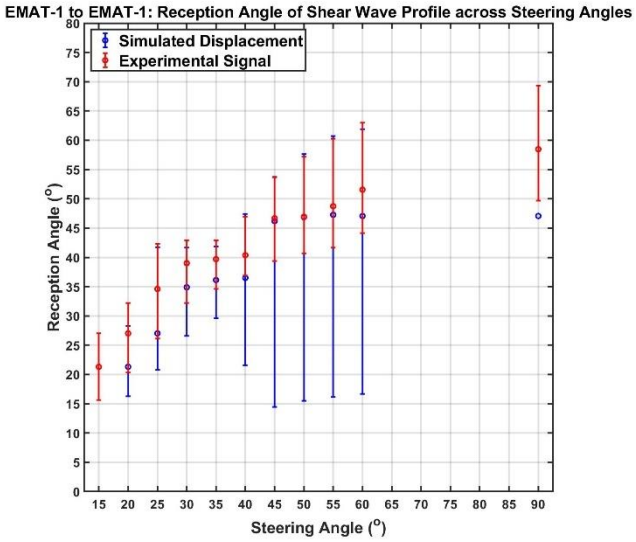

Figure 4.86: Shear Wave Reception Angle across Steering Angles

There is a good correlation coefficient of 0.9790 between the magnitudes of the backwall profile peaks for both datasets (excluding the 15°). This is also the case for the profile peak's reception angles with a correlation coefficient of 0.9327, however the correlation coefficient for the beam-spread limits are 0.9957 and -0.2323 for the upper and lower limits respectively. The reason for the lower limit's low correlation coefficient is due to the magnitude

at a given x-position across the backwall profile compared to its peak. These respective magnitudes are greater for the simulated displacement than for the experimental results. This extends to Figure 4.85, and explains why the simulated displacement dataset is greater compared to its maximum at 30° than the experimental voltage.

There is no measurable beam-spread for the 90° steering angle's simulated dataset, as the profile for the direct shear wave did not drop to a point below -6dB of the peak value such that a reliable beam-spread could be called. Figure 4.87 shows the 90° steering angle's shear wave profiles for both datasets, which had a correlation coefficient of -0.2059. To counter this, backwall profiles of the shear wave reflecting off of the sidewall onto the backwall were graphed, as shown in Figure 4.88. While this did increase the correlation coefficient between the two datasets to 0.6546, it still could not be used to measure a -6dB beam-spread.

Like the beam directivity results, the reception angle for the experimental results tend to be higher than those of the simulated results, particularly at lower steering angles. While this could be attributed to the different types of filtering or the different variables measured (displacement magnitude vs induced voltage), their accuracy was sufficient to confirm the simulated model's accuracy.

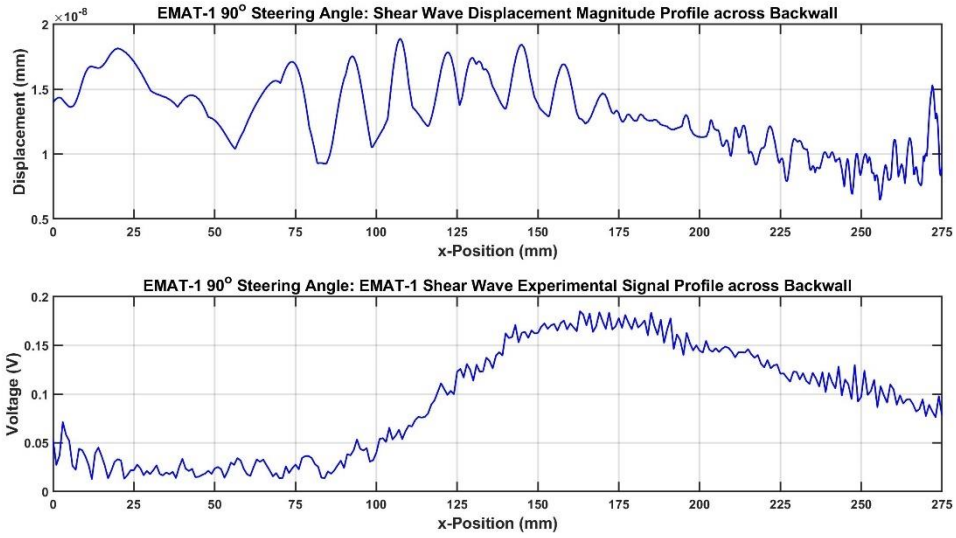

Figure 4.87: Shear Wave Profiles for 90° Steering Angle

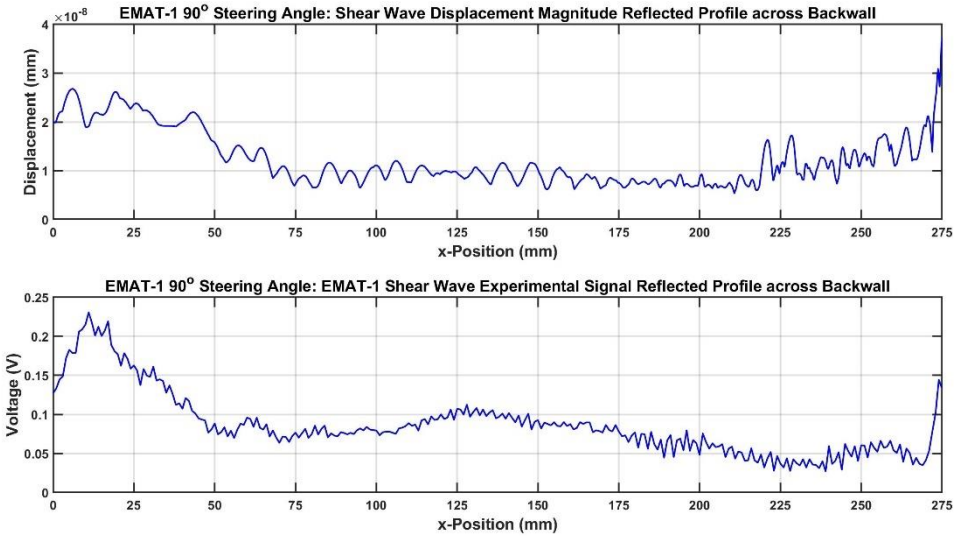

Figure 4.88: Reflected Shear Wave Profiles for 90° Steering Angle

The Rayleigh wave velocity was calculated with the 90° steering angle. The ToA of its peak voltage was recorded at each x-position across the backwall. Figure 4.89 shows these x-positions graphed against the ToAs, and it is noticeable that the number of outliers increased as the x-position reaches the end of the backwall. This was due to the imposition from the Rayleigh waves travelling across the surface and far-wall. Without the outliers, the gradient of the remaining data calculated a Rayleigh wave velocity of 2.88mm/µs.

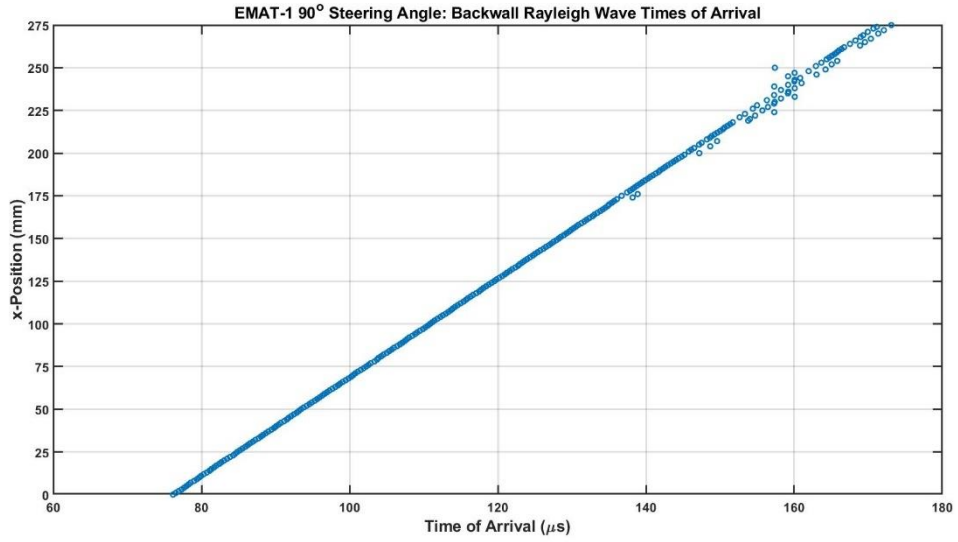

Figure 4.89: Plot of Rayleigh wave ToA across the backwall for 90° Steering Angle

4.4.2. Simulated Reception EMAT

As previously discussed in Section 4.3.1, T_x transmitted each of the three wave modes in the form of two split-waves originating from approximately ±10mm from its centre. While that phenomenon was explored for the MLC EMAT's

transmission, it was not considered for the reception of the waves due to the use of a spiral-coil EMAT as the receiver.

Figure 4.90 shows three A-scans from the surface x-position of 100mm from T_x at a 90° steering angle: the simulated x-component of displacement; the experimental voltage from R_x; and the received signal from the shear wave UT probe. The Rayleigh wave recorded by R_x shows a single peak at 40µs, however both the simulated x-displacement and shear probe's signal show this wave as two peaks. These two peaks recorded by the UT probe prove that not only does T_x transmit the Rayleigh waves (and by extension the bulk waves) as split-waves from near the corners of the EMAT, but that R_x was also receiving from its corners. The two Rayleigh split-waves from the corners of T_x were recorded as a single peak in the experimental A-scan due to them superimposing when they each reached the two corners of R_x.

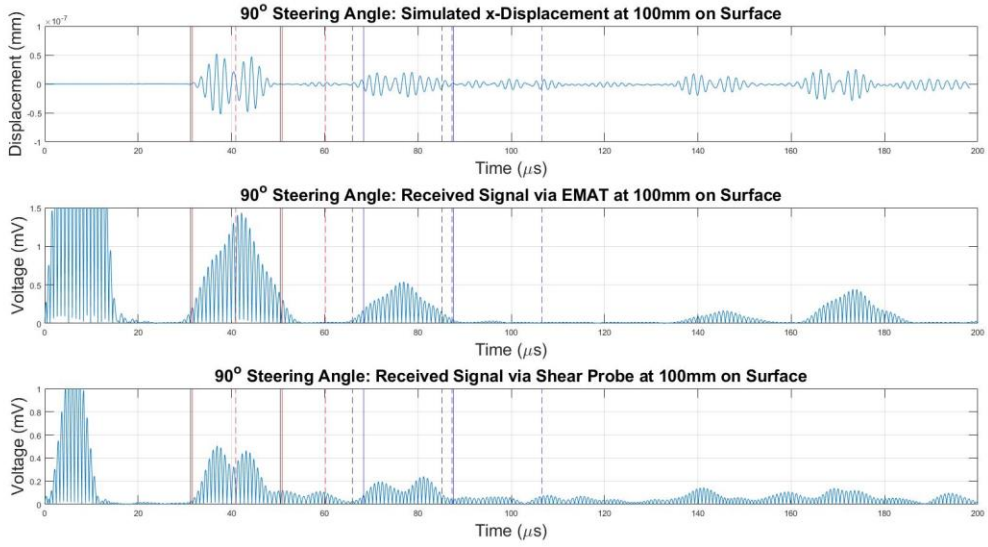

Figure 4.90: Experimental vs Simulated data for 90° Steering Angle at 100mm across the surface

In an attempt to decrease the difference between the simulated and experimental results, an alternative solution was devised to measure the three wave modes on the rectangular sample. As previously stated in Section 2.5.1.1, when charged particles move within a magnetic field, they generate an electric field. An approximation for the current induced into the MLC (and by extension the received signal from R_x) was calculated by estimating the rate of change of particle motion at each point beneath the MLC array and making it a product of the magnetic flux density at that point.

The angle of magnetic flux density at a given position was found via Equation 3.7 and the electromagnetic data extracted from the area of high-mesh density. The particle velocity was estimated as the rate of change of displacement, at an angle 90° greater than that of the magnetic flux density. Equation 4.2 was used with the angle of magnetic flux density to calculate the component of displacement in this direction. The particle motion was therefore calculated as the difference in this directional displacement between timesteps, divided by the timestep. An approximation for the electric current induced into the MLC from a given point on the surface beneath it could be calculated from the components of both displacement and magnetic flux density at each timestep, as shown in Equation 4.10.

$$I_{(t)} \propto \frac{\Delta u_{x(t)} \cos\theta_r + \Delta u_{y(t)} \sin\theta_r}{\Delta t} \times B_0 \qquad \text{Equation 4.10}$$

The positions from which the components of magnetic flux density were taken were from the high-mesh area directly beneath the EMAT: from -20mm to 20mm at 0.01mm intervals, as with the beam directivity models. The x & y components of displacement from the rectangular sample's backwall and surface were extracted at 0.1mm intervals and so required resampling at 0.01mm intervals. At each x-position for the backwall and surface, the dynamic electric field was estimated via Equation 4.10 at ±20mm at 0.01mm intervals. Due to the values of induced eddy current density being highest directly beneath the coils (as shown in Figure 3.21 and Figure 3.22) these dynamic electric field values were then multiplied by the values of eddy current density induced at the surface. This acted both as a SF to enhance the values of electric field directly beneath the coils, and to invert the direction of the induced eddy current for each alternate coils due to the out-of-plane direction of the MLC. These values were then summed together and divided by the number of positions (equal to 4001) at each timestep to produce the simulated signal's amplitude across time. The resultant signal was passed through the same bandpass filter as those used for the experimental signals. This method of signal simulation effectively created a simulated R_x for the models.

Thring [91] used a similar method for detecting Rayleigh waves, as the motion of the particles from an ultrasonic wave was dependent on the type of

wave being propagated. This method used calculated elliptical particle motion that was integrated across the skin depth for more accurate values. This approach was not adopted for this body of work, since the simulated reception signal was required to receive both bulk and Rayleigh waves. COMSOL multiphysics models have been used to calculate the induced voltage for a reception EMAT. Qu et al [18] used one such model in a similar study: using two MLC EMATs in a PC setup to compare the performance between different steering angles. The simulated voltage agreed very well with the measured experimental voltage from the R_x for steering angles of 30° and 45°. Similar models capable of calculating induced voltage by means of a moving mesh interface were proposed for this study, however this increased the computational runtime of the models too much to justify their inclusion. The simulated signals are more representative of the experimental signals, as they recorded the split shear waves as a single peak, as shown in Figure 4.91 when compared to Figure 4.90).

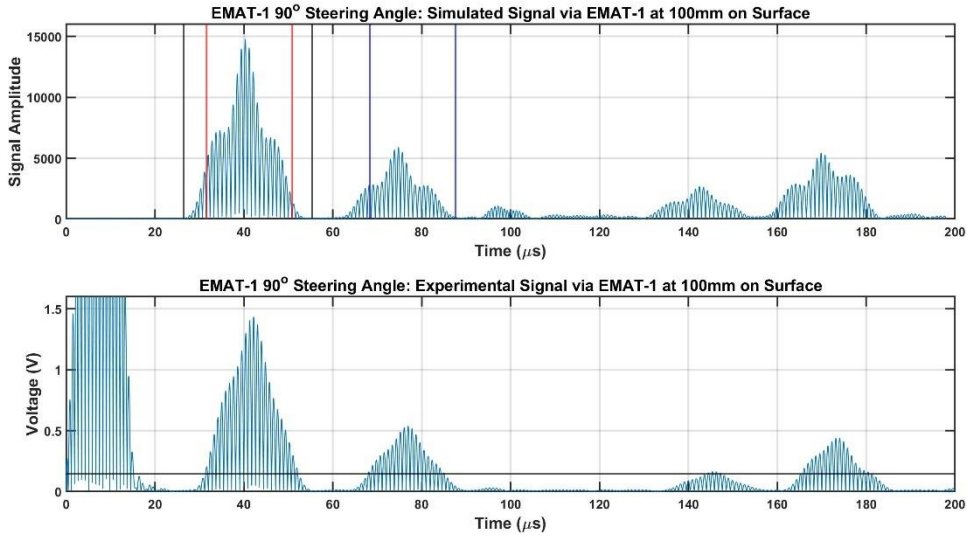

Figure 4.91: Experimental vs Simulated data for 90° Steering Angle at 100mm across the surface

The simulated received signals were analysed in comparison to the experimental results for each steering angle as before. Figure 4.92-Figure 4.95 show this comparison at the same backwall x-positions as Figure 4.79-Figure 4.82. This method of signal simulation proved more accurate than the simulated displacement magnitudes, as the simulated R_x did not register either the Rayleigh wave mode-converted by the shear wave striking Cor_2, or the Rayleigh wave generated by its 3rd harmonic.

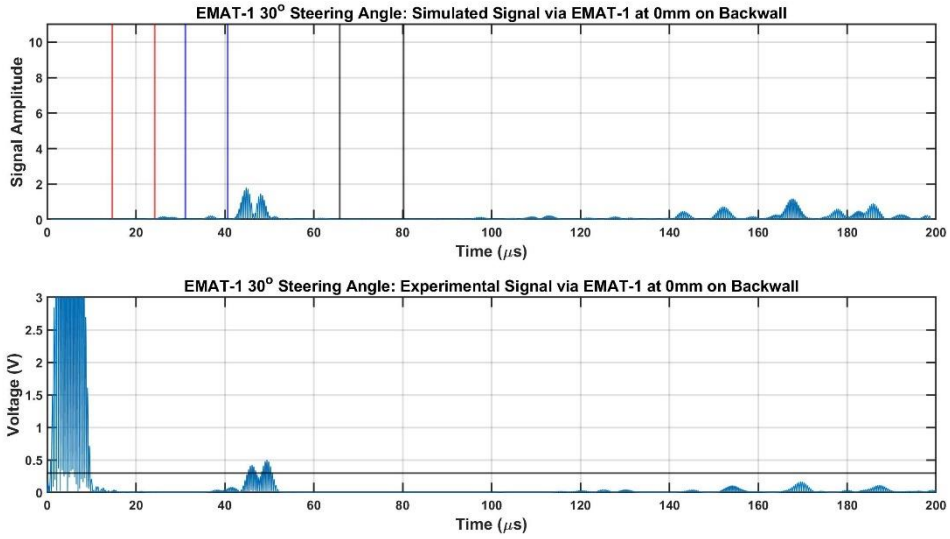

Figure 4.92: Simulated Signal vs Experimental Signal for 30° Steering Angle at 0mm across the backwall

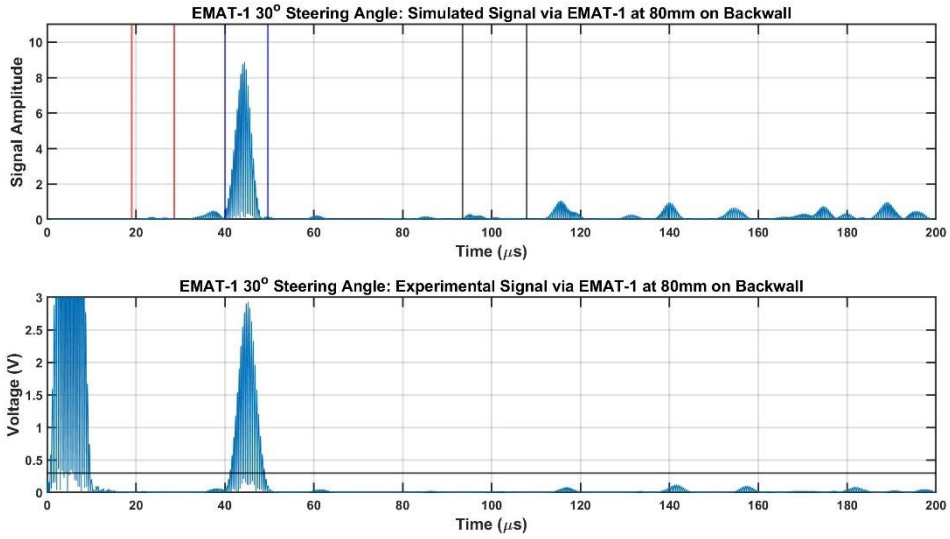

Figure 4.93: Simulated Signal vs Experimental Signal for 30° Steering Angle at 80mm across the backwall

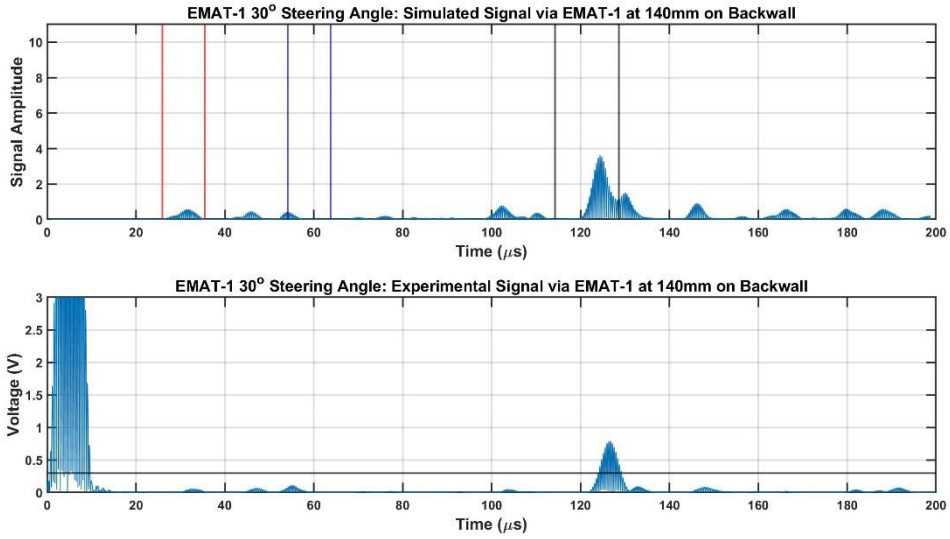

Figure 4.94: Simulated Signal vs Experimental Signal for 30° Steering Angle at 140mm across the backwall

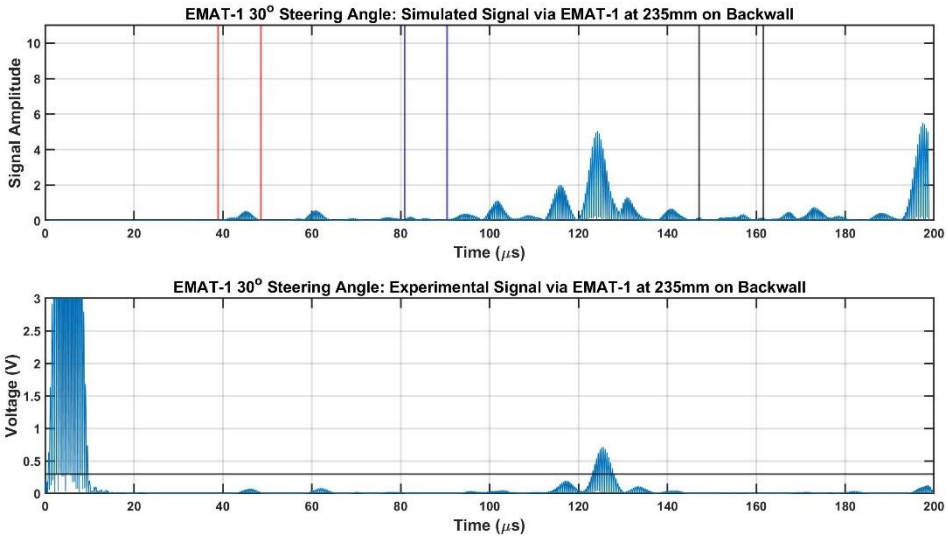

Figure 4.95: Simulated Signal vs Experimental Signal for 30° Steering Angle at 235mm across the backwall

Figure 4.96 shows the simulated signal's shear wave backwall profile compared to the experimental profile for a 30° steering angle. Additionally, Figure 4.97 shows how the use of this simulated signal enables a beam-spread to be drawn for the direct shear wave profile at the 90° steering angle. Figure 4.98 shows the reception angles of the shear wave's profile peaks and beam-spread limits across steering angles using this method. There is an increase in the correlation coefficient from 0.9327 to 0.9932 when comparing the simulated signal (rather than comparing the displacement magnitude) to the experimental signal. Additionally, the correlation of beam-spread limits were significantly improved from 0.9957 & -0.2323 to 0.9989 & 0.9966 for the upper and lower limits respectively.

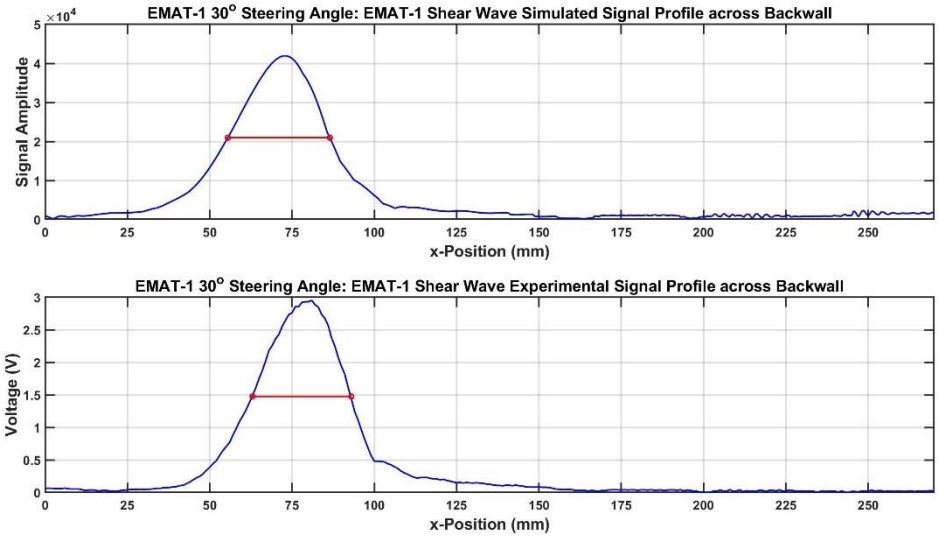

Figure 4.96: Shear Wave Profiles for 30° Steering Angle

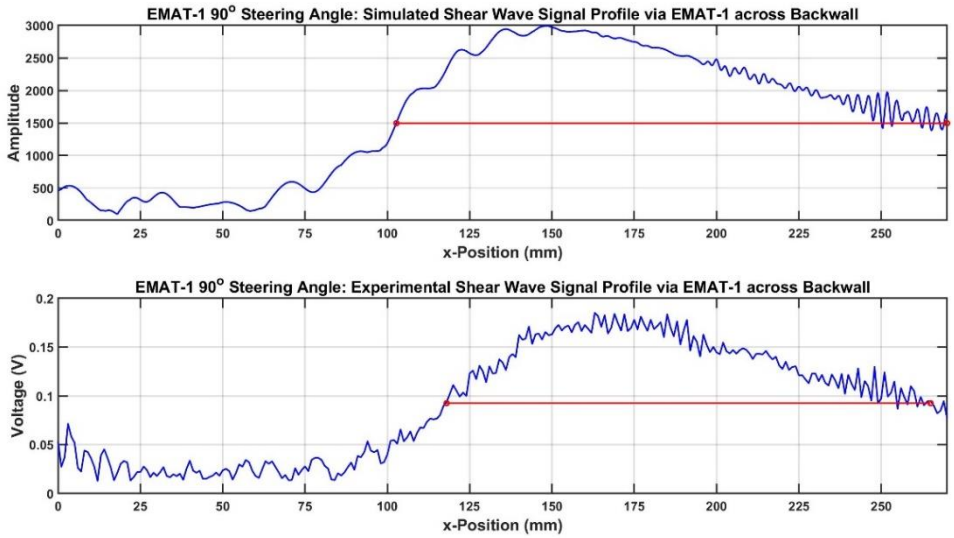

Figure 4.97: Shear Wave Profiles for 90° Steering Angle

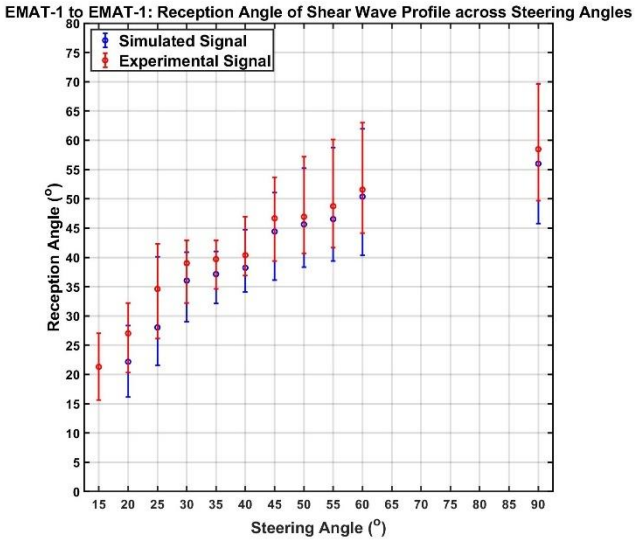

Figure 4.98: Plot of the Shear Wave Backwall Profile's Reception Angle across Steering Angles

Comparing the maximum amplitude of the simulated signals to those of the experimental for the shear wave backwall profile ones produced a correlation coefficient of 0.9380. This is a decrease from a coefficient of 0.9790 for the comparison of displacement magnitude to the experimental signal. This is due to the simulated signal's trend deviating significantly from the experimental signal at the 20° steering angle, as seen in Figure 4.99.

It is unclear what caused the increased amplitude at the 20° steering angle. It was initially theorised to be due the method of calculating the signal induced into the coils becoming inefficient at higher frequencies. The induced electric field at a given point was estimated by multiplying the rate of change of particle displacement by the magnetic flux density (shown in Equation 4.10).

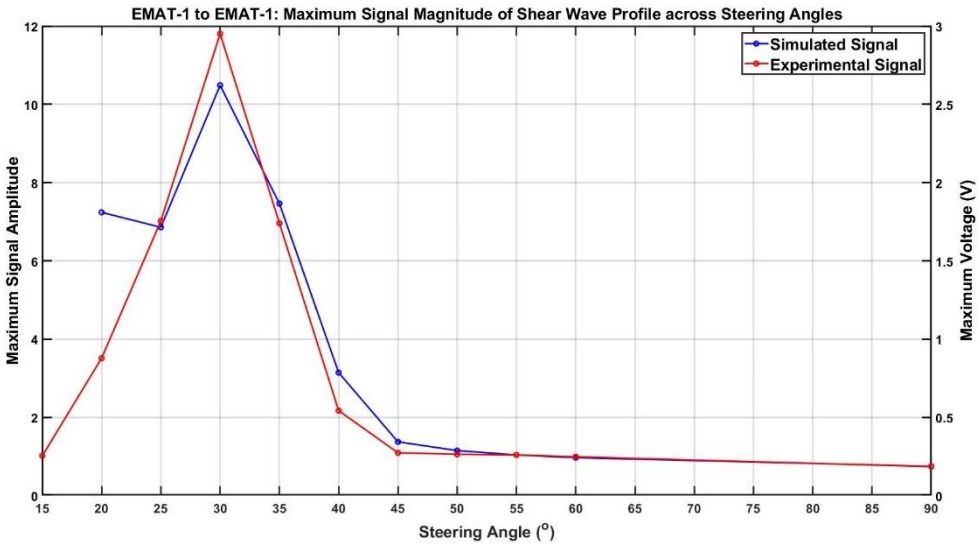

Figure 4.99: Plot of the Shear Wave Backwall Profile's Skewed Maximum Amplitude across Steering Angles

Figure 4.100 shows the results from Figure 4.43 adapted to show the maximum particle velocity for all three wave modes across steering angles. This was calculated by dividing the change in directional displacement between timesteps by the timestep, in the same manner as Equation 4.10. Figure 4.100 shows that that the particle velocity skewed to become larger in magnitude at lower steering angles, and thus higher frequencies. This was confirmed by extracting the components of velocity from the sample's curved surface for the beam directivity simulation. The correlation coefficient between the results of Figure 4.100 and Figure 4.43 was calculated as 0.7648.

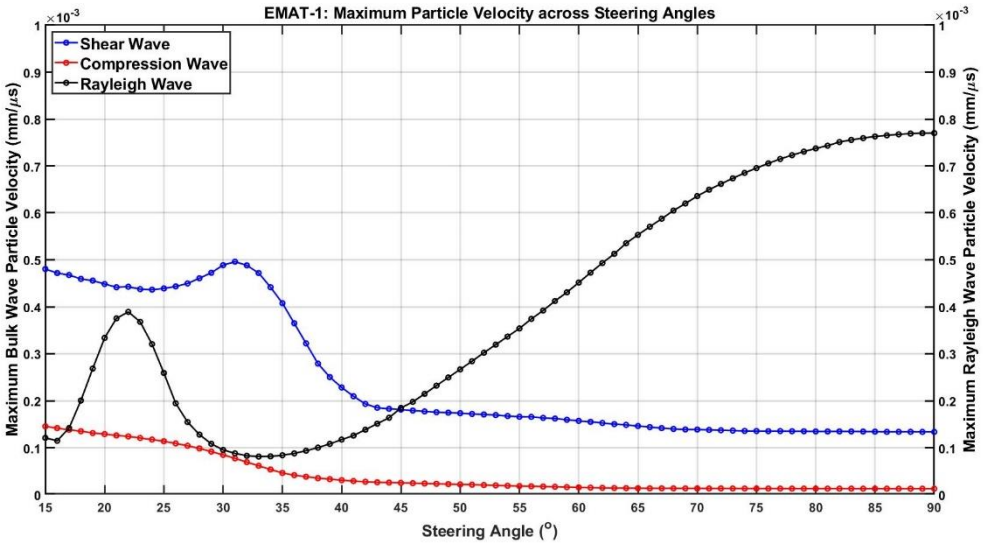

Figure 4.100: Graph of Maximum Particle Velocity across Steering Angles

Due to the experimental results showing a greater conformance to the values of particle displacement rather than velocity, further refinement to the

process of simulating the A-scan signals was required. This was done by dividing the calculated results of velocity from Figure 4.100 by the frequency of its steering angle. Figure 4.101 shows that this corrected the skew present in Figure 4.100 and improved the correlation coefficient from 0.7648 to 0.9935.

The process of dividing the amplitude of the simulated signal by the frequency of the steering angle was used on the results from Figure 4.99, and are shown in Figure 4.102. This decreased the increased amplitude at the 20° steering angle and increased the correlation coefficient from 0.9380 to 0.9641.

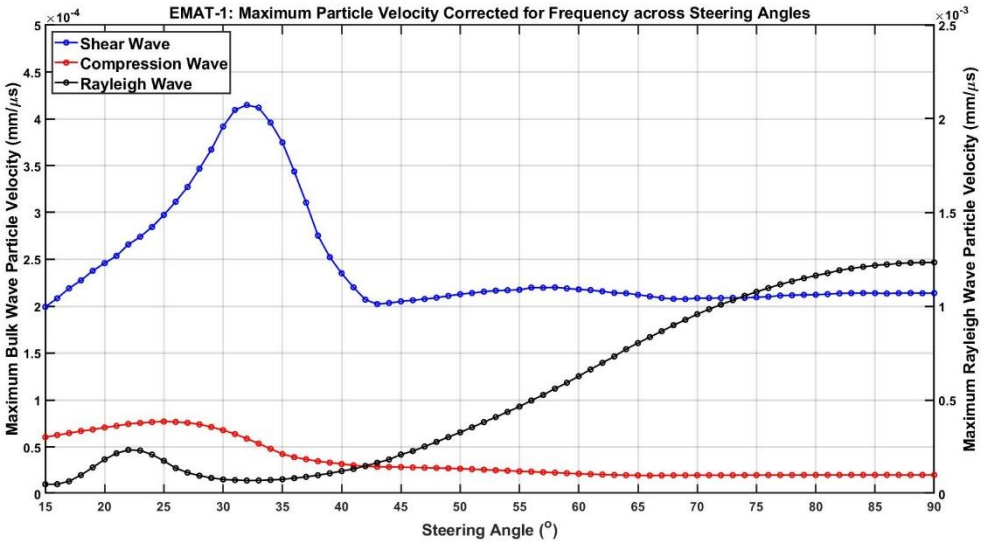

Figure 4.101: Graph of Maximum Particle Velocity corrected for Frequency across Steering Angles

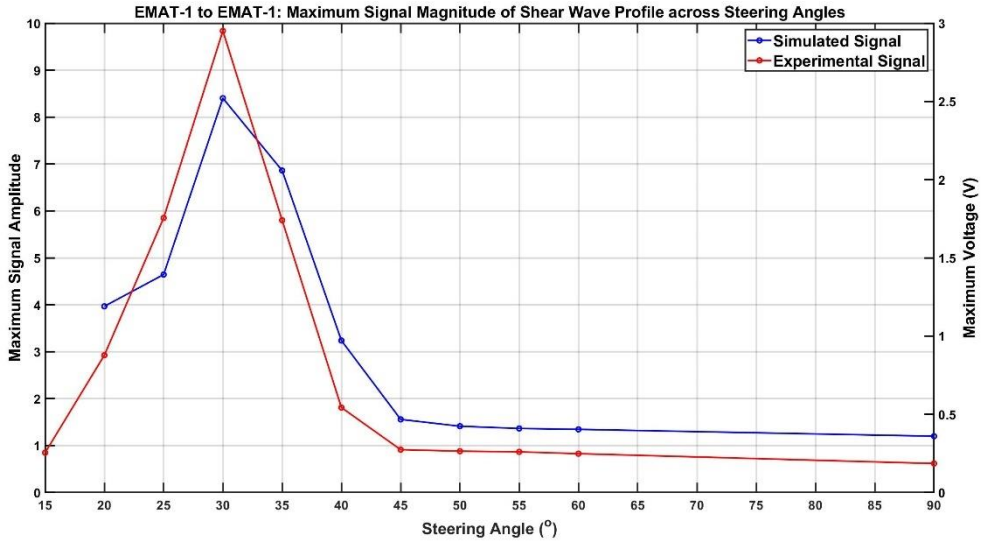

Figure 4.102: Plot of the Shear Wave Backwall Profile's Maximum Amplitude across Steering Angles

Table 4.2 contains the complete list of correlation coefficients between both the displacement magnitudes and the simulated signals to the

experimental signals for the shear wave backwall profile across steering angles. Included in this table are the correlation coefficients for the backwall profile from the shear wave reflected off of the sidewall onto the backwall. For each steering angle, there tends to be a noticeable increase in correlation coefficient for both the direct and reflected shear wave backwall profiles when using the simulated signal over the displacement magnitude. This is not the case for the reflected shear wave profiles for steering angles of 20-40°, however since these steering angles did not produce a shear wave with a reception angle above 45° (as shown in Figure 4.98) this was not regarded as an issue.

Table 4.2: Experimental Validation Correlations

Steering Angle (°)	Direct Shear Wave Correlation		Reflected Shear Wave Correlation	
	Displacement Magnitude	Simulated Signal	Displacement Magnitude	Simulated Signal
20	0.7875	0.8163	0.7814	0.7758
25	0.8825	0.9177	0.6807	0.6473
30	0.8794	0.9240	0.6334	0.6530
35	0.8559	0.9040	0.7370	0.6585
40	0.7869	0.8724	0.8334	0.7498
45	0.7339	0.8940	0.8656	0.8944
50	0.7060	0.9495	0.8753	0.9553
55	0.6508	0.9550	0.8747	0.9717
60	0.5426	0.9399	0.8798	0.9766
90	-0.2059	0.9353	0.6546	0.8908

4.5. Summary

The focus of this chapter was the relationship between the desired steering angle driving the MLC EMAT, and the actual reception angle of the shear waves. This was studied through the use of simulated models of an MLC EMAT over aluminium samples that were validated through the use of experimental testing.

The EMAT's beam directivities for its shear and compression waves were calculated from the curved surface of a semicircular sample, and its shear wave steerability was measured from the backwall of a rectangular sample. For both samples, the magnitude of the shear waves reached a maximum value at a steering angle near 30°. A steering limit of 45° was ultimately called for this EMAT, for near this steering angle: the shear wave directivity falls from its peak value; the Rayleigh waves begin to supplant the shear waves as the greater wave mode; and the reception angle barely increases with the steering angle. The maximum reception angle that the shear wave attained was at 61.1°, however this was at the cost of a reduced displacement and larger beamwidth.

This chapter also described the method of simulating a reception EMAT's signal from the wave modes striking a flat surface. This method uses the same simulated values of displacement and is capable of producing A-scans that closer resemble those of the experimental testing. This method has been shown to further increase the accuracy of the results extracted from the models.

Chapter 5 - Modified Magnetic Configurations

The previous chapter was dedicated to the complete simulated and experimental analysis of the standard experimental MLC EMAT. This chapter seeks to explore modifications to the magnetic configuration that could improve the operation of the MLC EMAT. Alternative magnetic configurations at the same lift-off were explored to change the bias magnetic field by varying the dimensions, directions, and number of magnets involved.

5.1. Introduction

As previously discussed in Section 3.3, studies have looked into improving EMAT performance by changes to their physical design. Pei et al [73] used a new magnetic configuration for a Rayleigh wave PC setup via MLC EMATs, to which the new magnetic configuration increased the generation and detection efficiencies by SFs of 2.19 & 2.44 respectively. This was due to the replacement of a single permanent magnet with two, creating a central concentration of magnetic flux density and increasing the EMAT's transduction efficiency. While that study explored the effects of the magnet's geometry on the SNR of the EMAT, it was only in relation to the Rayleigh waves rather than the bulk waves.

5.2. Vertical Magnetic Configurations

To explore the effects of different magnetic configuration on the transmission of bulk waves, the beam directivity models were repeated using the alternate magnetic configurations from Section 3.3. Sections 5.2.1-5.2.7 are each dedicated to one of these different magnetic configurations and how they affected the intensity and direction of the transmitted wave modes across a range of steering angles. The results from these simulations are compared to those of the EMAT from Section 4.3.1, henceforth known as EMAT-1. The time required to simulate each steering angle from 15-90° at 1° intervals was deemed too great, and so simulations were initially conducted at 5° intervals.

It was observed from these initial results that the maximum displacement was derived from a steering angle between 25-40° across these magnetic configurations. Further simulations were then undertaken for steering angles of 26-39° at 1° intervals.

5.2.1. EMAT-2: 1x 40mm Wide Magnet

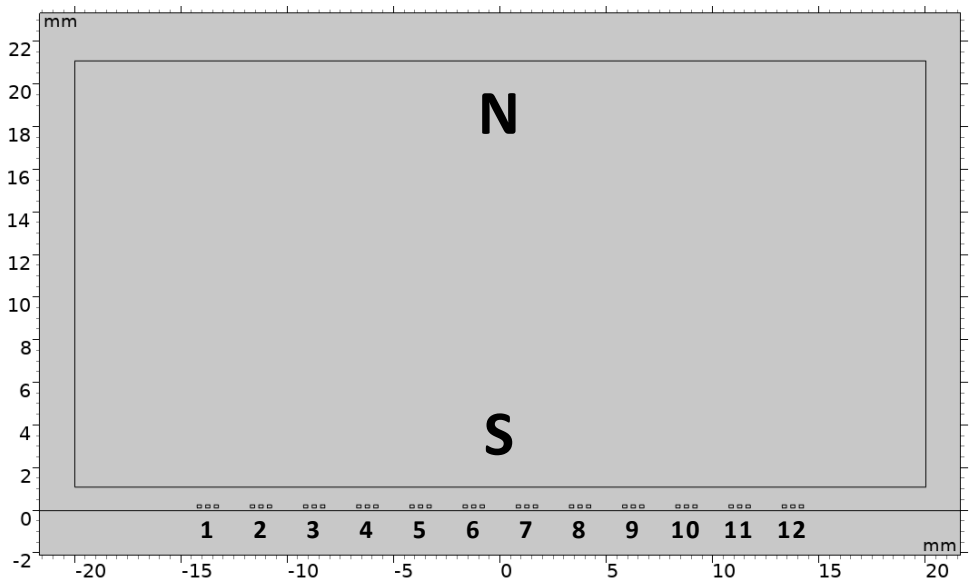

Figure 5.1: EMAT-2 Design

Increasing the magnet's width from 20mm to 40mm has little impact on the value of maximum magnetic flux density (as shown in Figure 3.14) however it does re-position the concentrations of magnetic flux density (located at the corners of the magnet) to outside of the coil array, as shown in Figure 5.1. This decreases the magnetic flux density that interacts with the eddy current densities induced beneath coils, resulting in weaker Lorentz force densities. Additionally, due to the corners of the magnet being outside of the coil array, the vertical direction of magnet flux density does not invert within the eddy current's area of effect. Not only does this mean that the x-components of Lorentz force density remained larger than the y-components across the coil array, but the alternating directions of the horizontal Lorentz force density remain consistent with those of an ideal MLC EMAT. This is seen for EMAT-2 in Figure 5.2 when compared to EMAT-1 in Figure 4.49. These decreases in magnetic flux density decrease the displacements of each wave mode for a given steering angle (compared to EMAT-1) as shown in Figure 5.3. The changes in the -6dB beamwidth across steering angles are also shown in Figure 5.4.

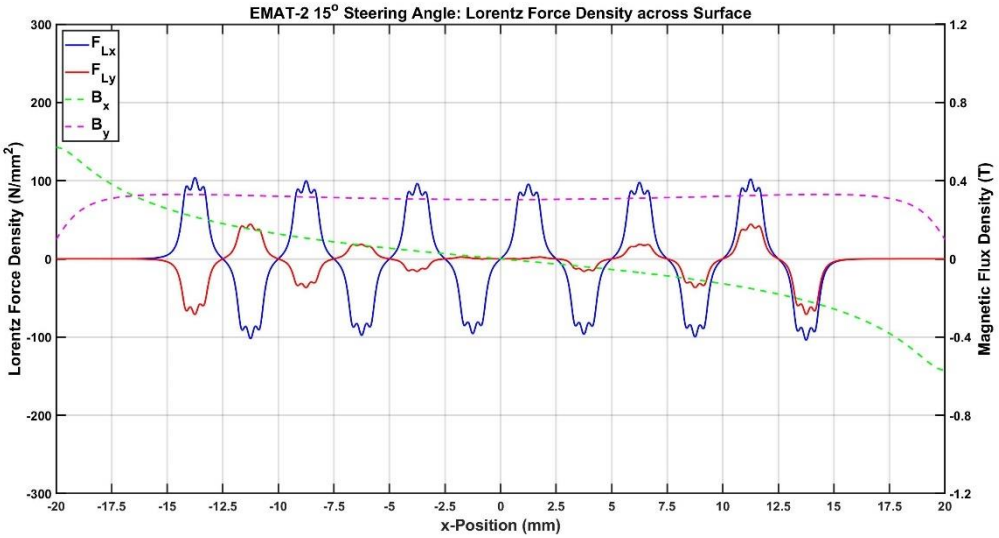

Figure 5.2: Plots of Lorentz Force Density Components across Surface for EMAT-2

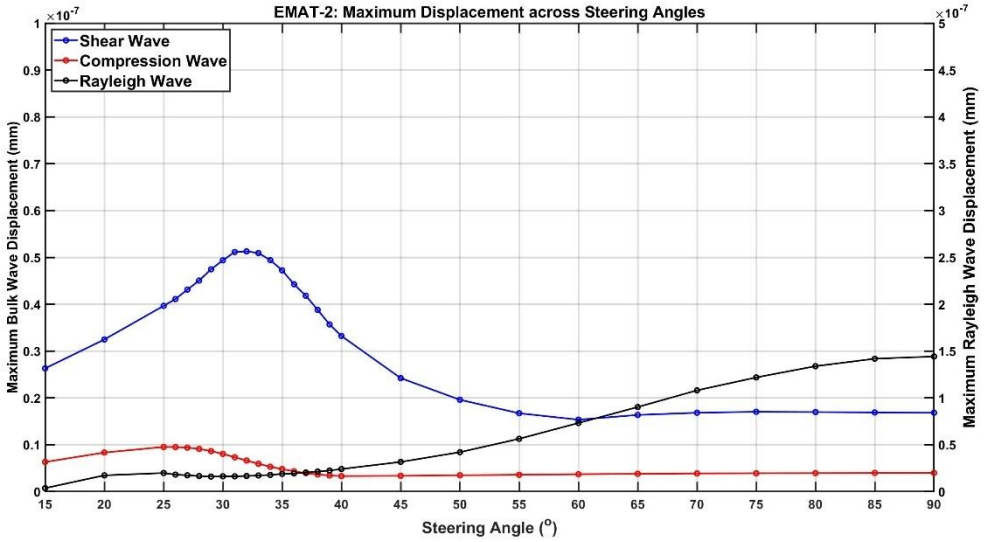

Figure 5.3: Graph of Maximum Displacement across Steering Angles for EMAT-2

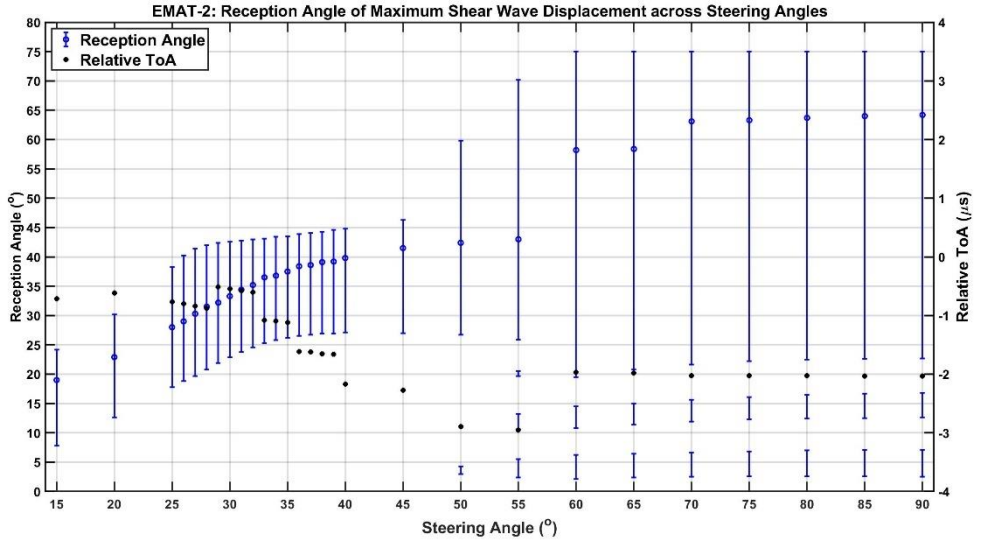

Figure 5.4: Graph of Shear Wave Reception Angles across EMAT-2 Steering Angles

For steering angles from 15-35°, the pattern of behaviour for EMAT-2's shear waves are comparable to those of EMAT-1, albeit with larger beamwidths and reduced magnitudes. As the steering angle increases to 45°, EMAT-2's beamwidth is narrower than EMAT-1's due to the reduction of sidelobes within each of the split-waves. Figure 5.5 shows the directivity plot for EMAT-2's 40° steering angle, and the reduced sidelobes are clearly seen when compared to EMAT-1's in Figure 4.32.

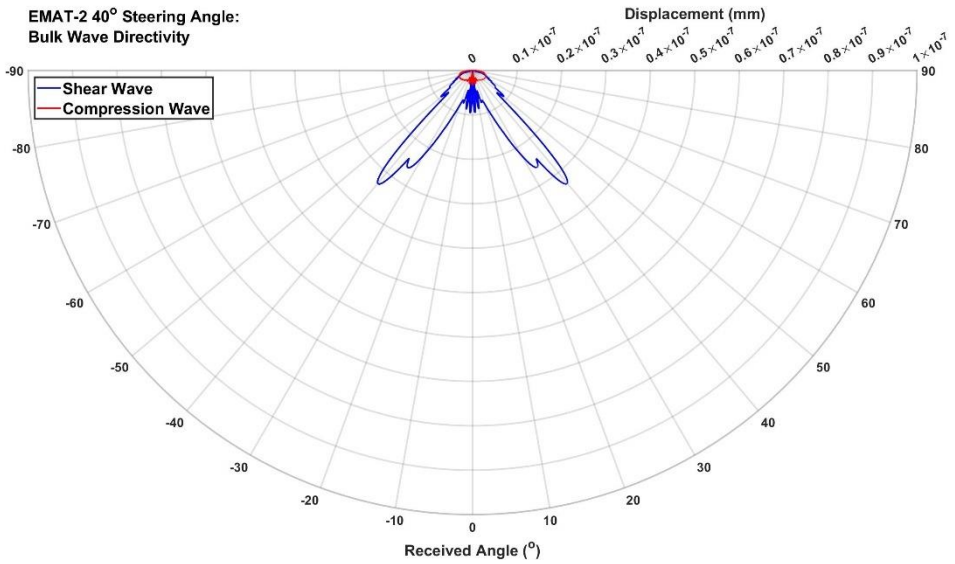

Figure 5.5: Bulk Wave Directivity Plot for EMAT-2 40° Steering Angle

The colour-plots for EMAT-2 show that the EMAT continues to transmit shear waves as two split-waves. The reductions in sidelobes however create a single stress concentration within each of the split-waves. This is shown in Figure 5.6 when compared to Figure 4.9 for a 45° steering angle. Beyond this steering angle, these single stress concentrations become as weak in magnitude as the wavefront's sidelobes, causing the large beamwidths in Figure 5.4.

The origin positions for the split-waves from steering angles of 15-37° were calculated at approximately 2mm further from the centre than for EMAT-1. For the 42-90° steering angles, the RToA values approximate those of EMAT-1 suggesting the same origin position. The reception angle at 90° shows the A-scan for the Rayleigh wave arriving at the corner of the semicircular sample's flat surface. Comparing the 90° A-scans for EMATs 1 & 2 in Figure 5.7 shows that the ToA from each of the two peaks changes little by the increase in magnet width.

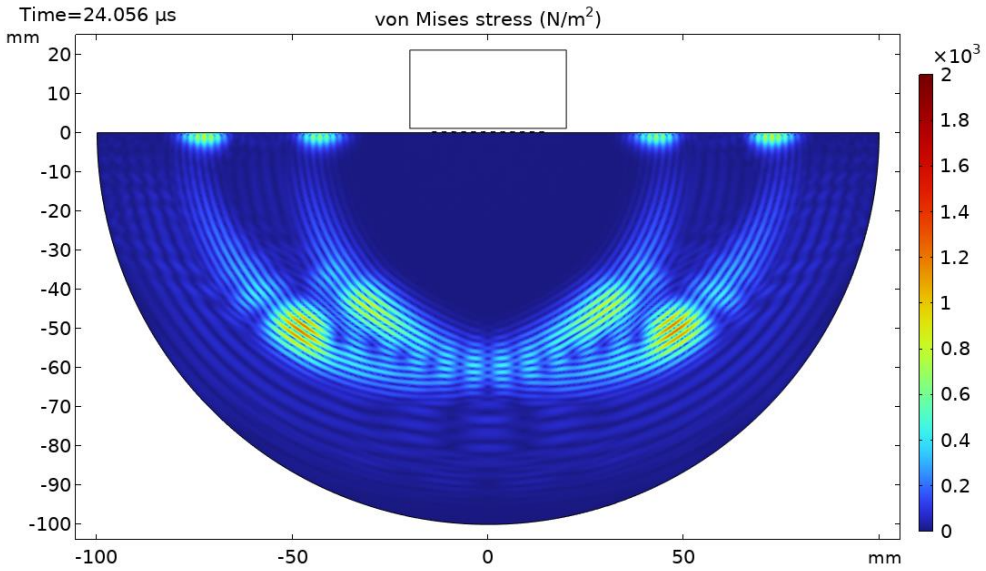

Figure 5.6: Colour-plot of EMAT-2 45° Steering Angle

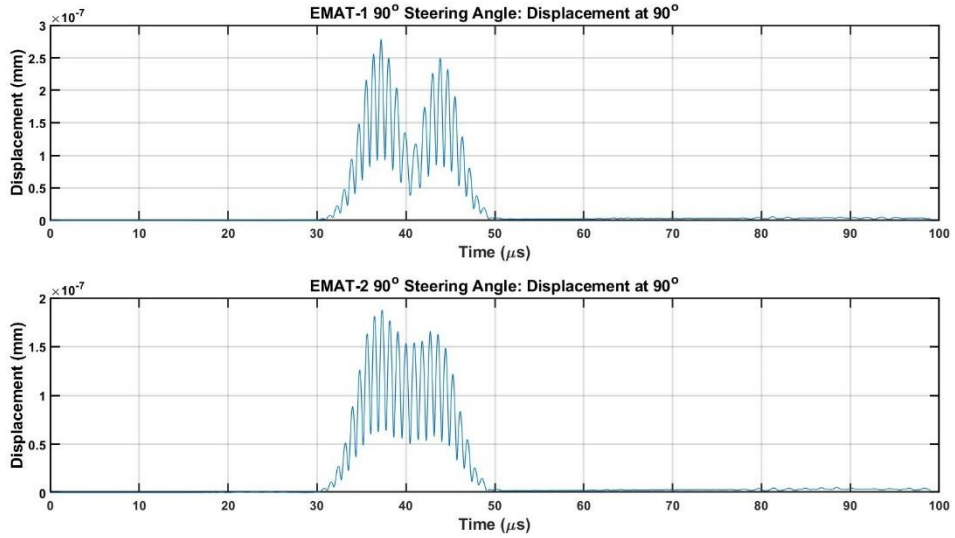

Figure 5.7: A-scans at 90° for EMATs 1 & 2 90° Steering Angle

Figure 5.7 shows that the maximum Rayleigh wave displacement reduces by approximately a third between EMATs 1 & 2. It is also noticeable that the maximum values of displacement between the two peaks does not significantly decrease for EMAT-2. Both of these are due to the lack of concentrations in magnetic flux density within the coil array.

5.2.2. EMAT-3: 2x 20mm Wide Magnets

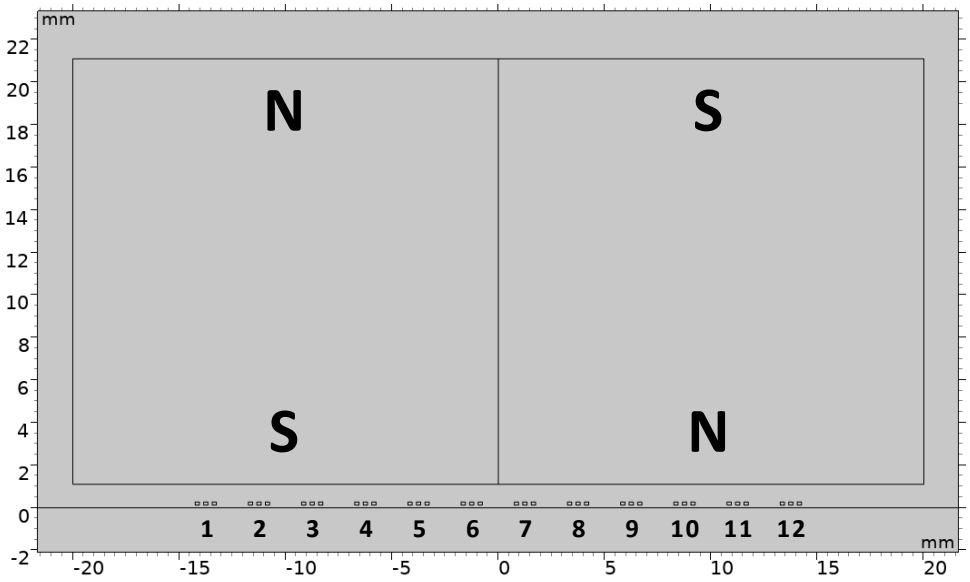

Figure 5.8: EMAT-3 Design

The two 20mm-wide magnets with alternating poles create a large concentration of magnetic flux density at the centre of the EMAT, as shown in Figure 5.8. This not only increases the maximum value of the Lorentz force density but also causes the orientation of Lorentz force density to become more vertical at the centre of the EMAT, as seen in Figure 5.9.

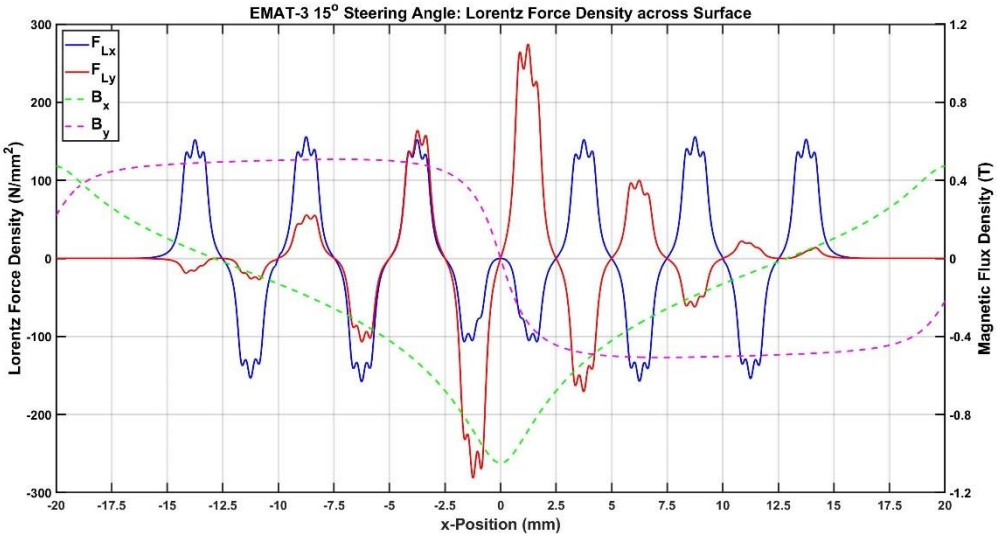

Figure 5.9: Plots of Lorentz Force Density Components across Surface for EMAT-3

This increase in magnetic flux density increases the displacement for each wave mode at given steering angle compared to EMAT-1, as shown in Figure 5.10. A noticeable change from both EMATs 1 & 2 is that the shear wave displacement does not swiftly decrease after reaching its maximum at a 33° steering angle. As the steering angle continues to 90°, the ratio between the

maximum and minimum displacements is much lower than those of EMATs 1 & 2. This is explained by the beamwidths and RToAs across steering angles for EMAT-3, shown in Figure 5.11.

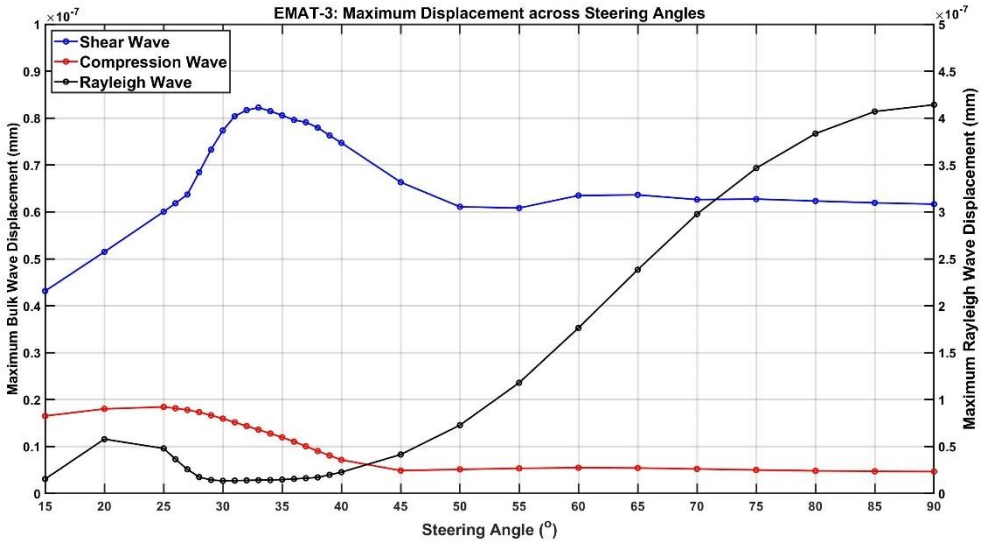

Figure 5.10: Graph of Maximum Displacement across Steering Angles for EMAT-3

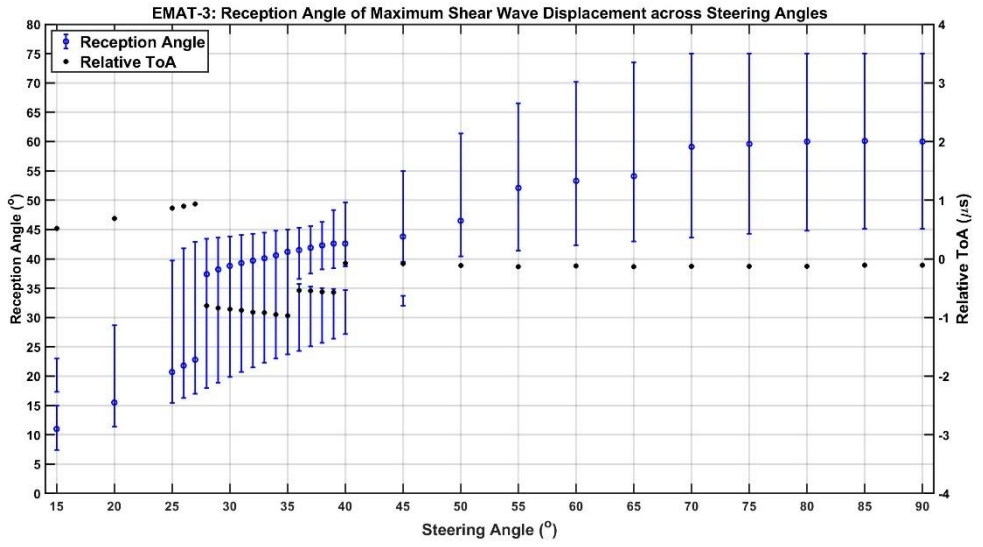

Figure 5.11: Graph of Shear Wave Reception Angles across EMAT-3 Steering Angles

At a 15° steering angle, two distinct shear wave lobes in each direction are visible from the beam directivity plot, shown in Figure 5.12. These two lobes merge as the steering angle increases, and at 28° the main lobe is supplanted by the higher-angled secondary lobe. This supplantation causes both the sudden increase in reception angle, and the RToA to change from positive to negative suggesting that its origin position moves from one side of the EMAT to the other. Another observation from the lower steering angle's shear waves is the presence of three split-waves compared to the two from EMATs 1 & 2.

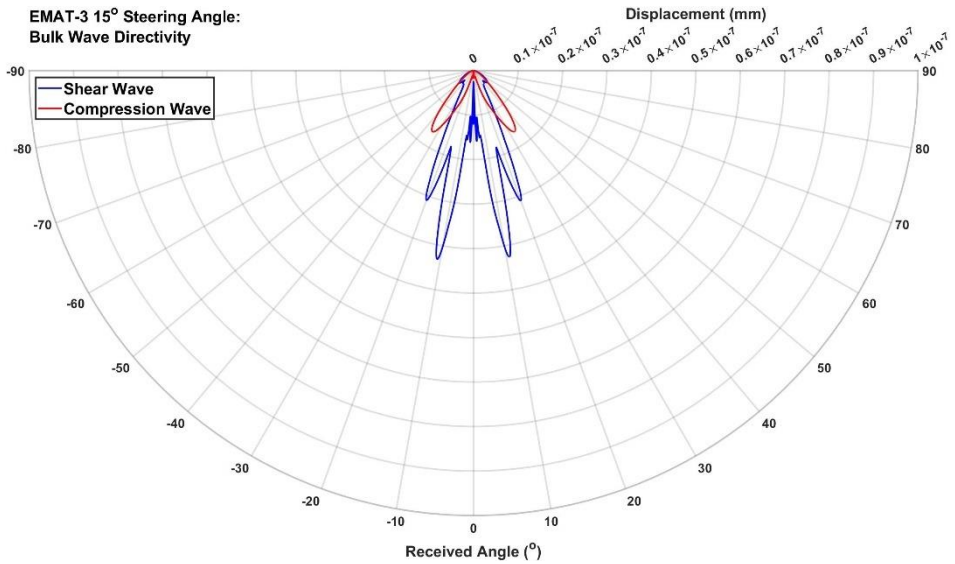

Figure 5.12: Bulk Wave Directivity Plot for EMAT-3 15° Steering Angle

As the steering angle increases from 40-90°, the displacement did not significantly change, and the RToA retains its trend at ~0µs. These are explained by the colour-plot of EMAT-3's 60° steering angle, shown in Figure 5.13.

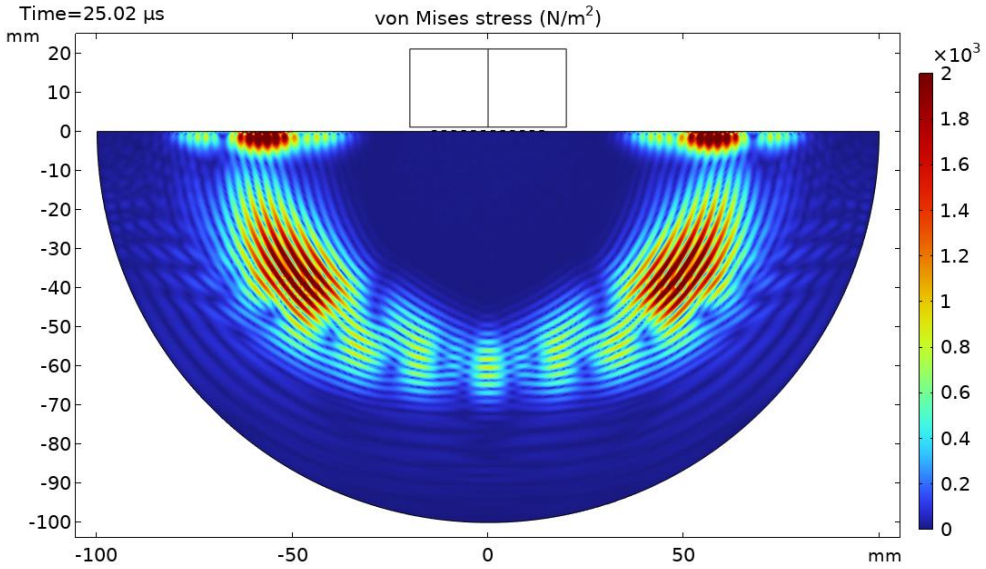

Figure 5.13: Colour-plot of EMAT-3 60° Steering Angle

The two magnets within EMAT-3 cover coils 1-6 & 7-12 respectively, as shown in Figure 5.8. Due to their inverted directions of vertical magnetisation, EMAT-3 can be considered as being made up of two adjacent sub-EMATs, each with a single 20mm-wide magnet and six coils. This consideration explains both the presence of the two distinct shear wave lobes in each direction for the lower steering angles, and their corresponding RToAs.

Unlike the higher steering angles of EMATs 1 & 2, the split-waves appear to merge into a single wave originating from the centre of the EMAT, explaining

the RToA ~0µs. For EMATs 1 & 2, each of the origin positions for the split-waves was located near the corners of their EMAT. EMAT-3's two adjacent sub-EMATs would make four EMAT corners but given the close proximity of the two sub-EMATs at the centre, the two split-waves superimpose and are measured as one. This explains the presence of a third split-wave for the lower steering angles. As the steering angle increases, all the split-waves superimpose into a single shear wave due to their proximity and increased wavelength. This increases the shear wave displacement and prevents the gradual decrease at higher steering angles, seen for EMATs 1 & 2.

The Rayleigh waves also implemented this behaviour, as three distinct peaks at the surface are seen in Figure 5.13. As the steering angle increases to 90°, these three peaks superimpose into a single peak with a magnitude double that of EMAT-1's (shown later in Figure 5.30). It is also noticeable from Figure 5.13 that a sidelobe is generated from the centre of the EMAT, normal to the sample's flat surface. This is due to the two innermost coils (coils 6 and 7) generating Lorentz forces in the same horizontal direction, thus polarising shear waves that propagate normal to the material's surface. This behaviour is the same as that of the rectangular-coil EMAT, shown in Figure 2.11.

5.2.3. EMAT-4: 1x 20mm Wide and 2x 10mm Wide Magnets

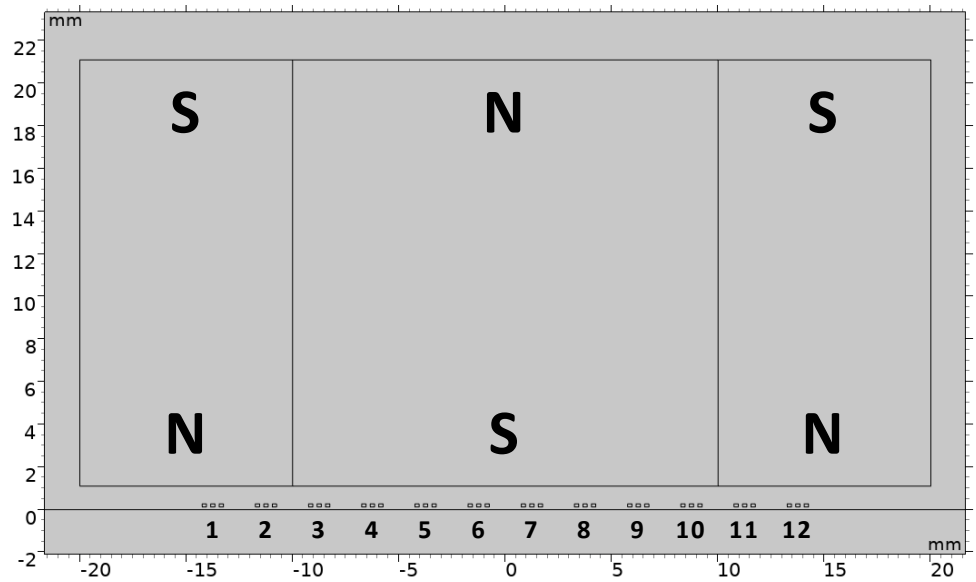

Figure 5.14: EMAT-4 Design

This magnetic configuration is similar to that of EMAT-1, with a 20mm-wide magnet at the centre of the magnetic configuration, as seen in Figure 5.14. The

changes made by the addition of 10mm-wide magnets on either side can be seen in the Lorentz force density distribution shown in Figure 5.15, compared to Figure 4.49 for EMAT-1.

The presence of these adjacent magnets causes an evenly distributed magnetic flux density for the two coils on each side of the coil array and increases the vertical component of magnetic flux density at the ends of the coil array. It also causes both coils 2 & 3 and 10 & 11 to generate Lorentz forces in the same horizontal direction, as with coils 6 & 7 for EMAT-3. These changes cause a significant impact on the magnitude and beamwidth of the shear waves, shown in Figure 5.16 and Figure 5.17 respectively.

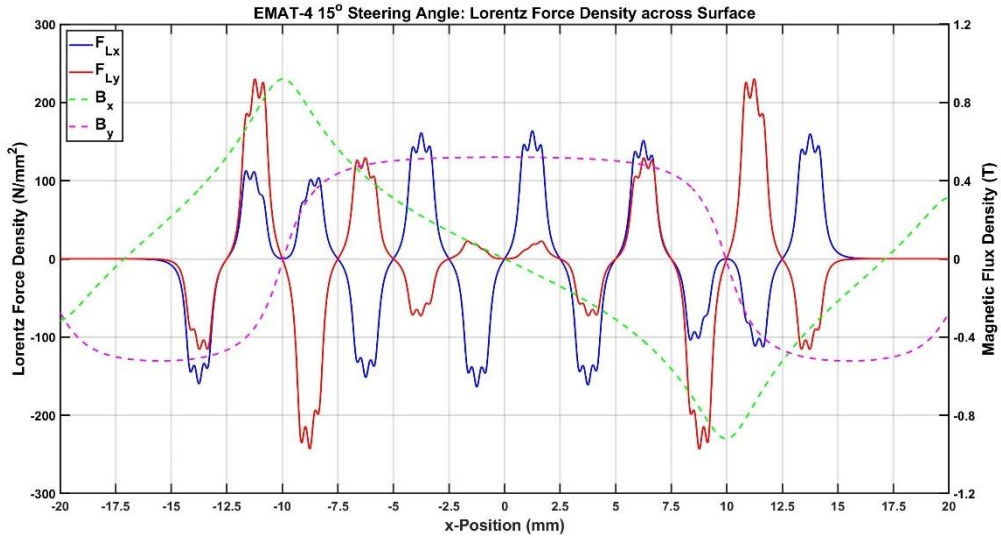

Figure 5.15: Plots of Lorentz Force Density Components across Surface for EMAT-4 15° Steering Angle

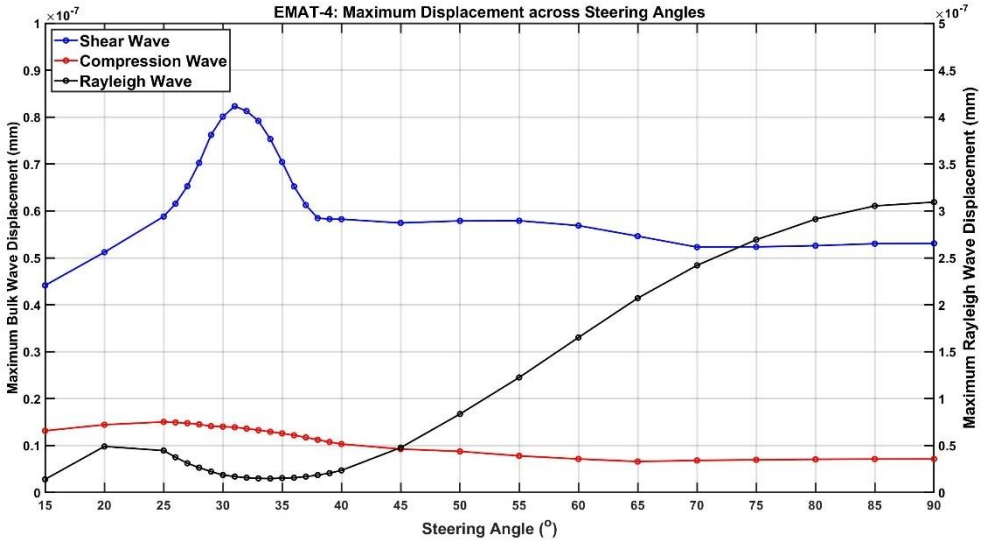

Figure 5.16: Graph of Maximum Displacement across Steering Angles for EMAT-4

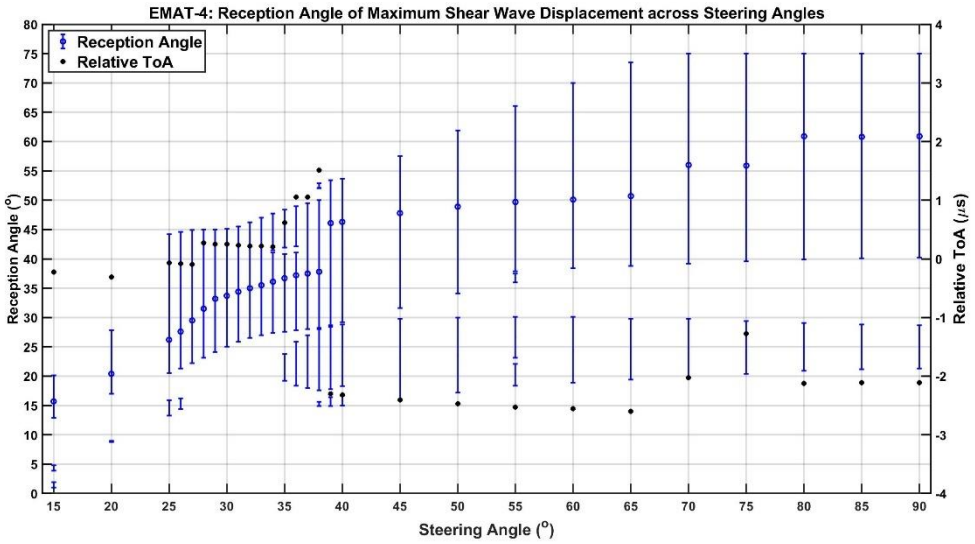

Figure 5.17: Graph of Shear Wave Reception Angles across EMAT-4 Steering Angles

The displacement of EMAT-4's shear waves are closer in magnitude to those of EMAT-3 for a given steering angle, due to the greater value of magnetic flux density from the adjacent magnets. While EMAT-4's reception angle and RToA behave in a similar manner to those of EMAT-1, the addition of 10mm-wide magnets causes the sidelobes across each wavefront to become greater in magnitude than EMAT-1's. This causes an increase in the beamwidth for the majority of steering angles.

EMAT-3 explores how the ends of adjacent sub-EMATs produce separate split-waves that superimpose and are measured as one. Since coils 1 & 2 and 11 & 12 are each beneath 10mm-wide magnets, EMAT-4 can be considered as being made up of three sub-EMATs: an eight-coil sub-EMAT with a two-coil sub-EMAT on either side. This explains the increased magnitude of the split-waves and particularly their lower-angled sidelobes. This is seen in Figure 5.18 when compared to Figure 4.12.

The performance of two-coil EMATs is explored later in Section 6.3, however the conclusion drawn is that they reach a lower steering limit at a lower steering angle. The sidelobes at reception angles of 15-30° for EMAT-4 increase in magnitude as they are transmitted from these sub-EMATs. Despite the sidelobes increasing magnitude, their direction within the beam directivity remains the same as those for EMAT-1 for a given steering angle. This is exemplified by Figure 5.19 when compared to Figure 4.31.

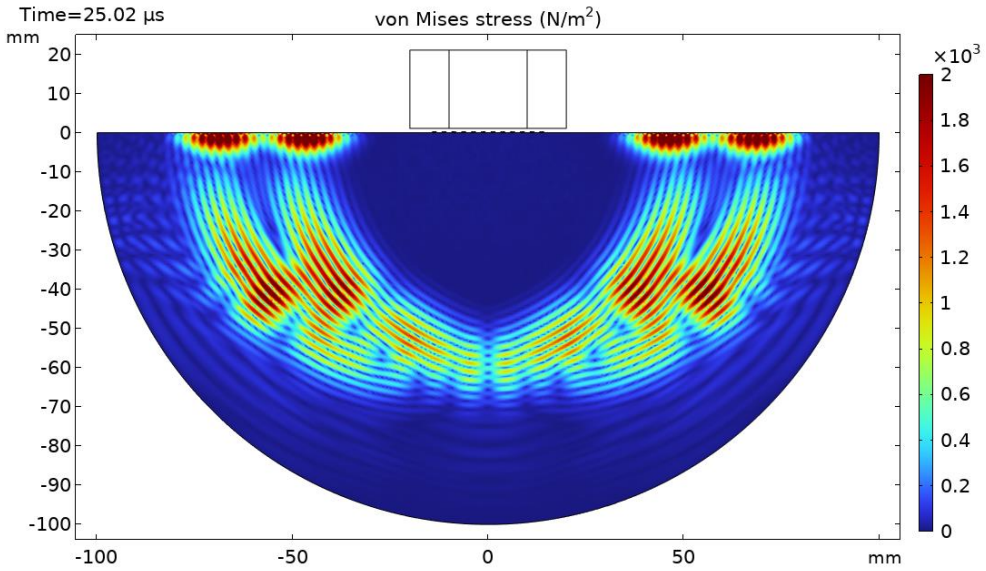

Figure 5.18: Colour-plot of EMAT-4 60° Steering Angle

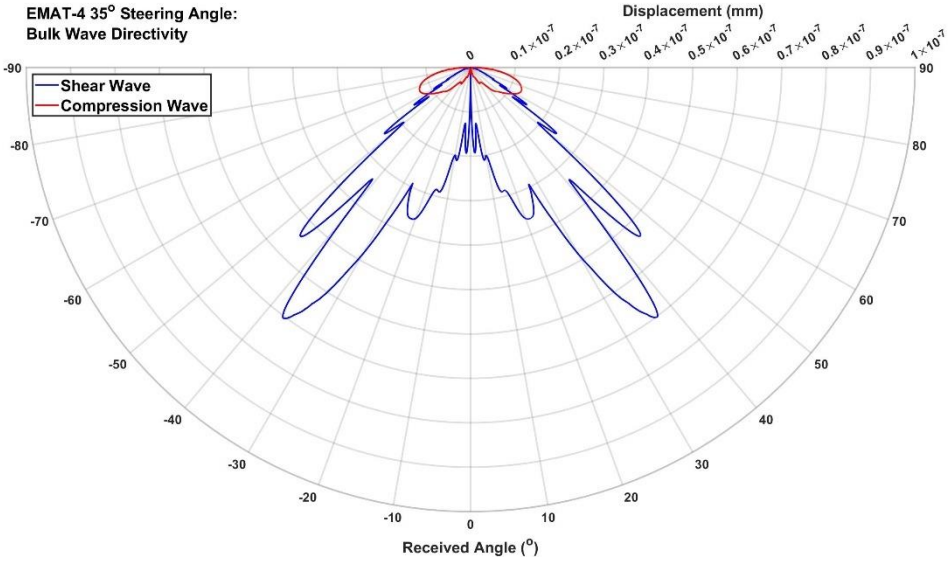

Figure 5.19: Bulk Wave Directivity Plot for EMAT-4 35° Steering Angle

5.2.4. EMAT-5: 1x 10mm Wide Magnet

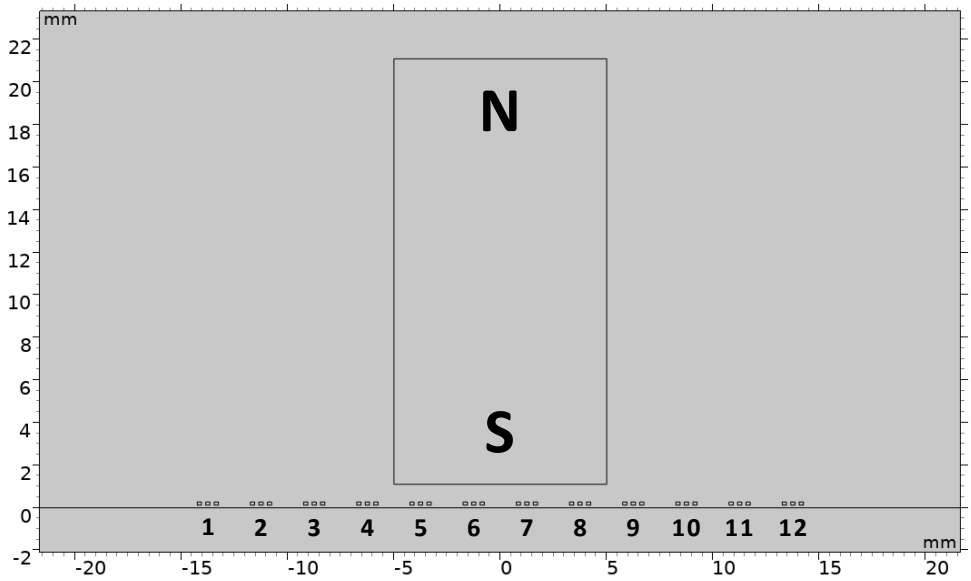

Figure 5.20: EMAT-5 Design

As was the case with EMAT-2, the change in the magnet's width does not significantly change the maximum magnetic flux density at the surface, however it does reposition the concentrations of magnetic flux density. Like EMAT-1, the corners of the magnet are still within the coil array (encompassing coils 5-8 as seen in Figure 5.20) however the magnetic flux density retains its vertical direction up to coils 4 & 9. This essentially creates a central six-coil sub-EMAT between two three-coil sub-EMATs that each possess a weaker inverted magnetic field. This results in coils 3-4 and coils 9-10 inducing Lorentz force densities in the same horizontal directions, weaker in magnitude to those at the centre of the surface, as seen in Figure 5.21.

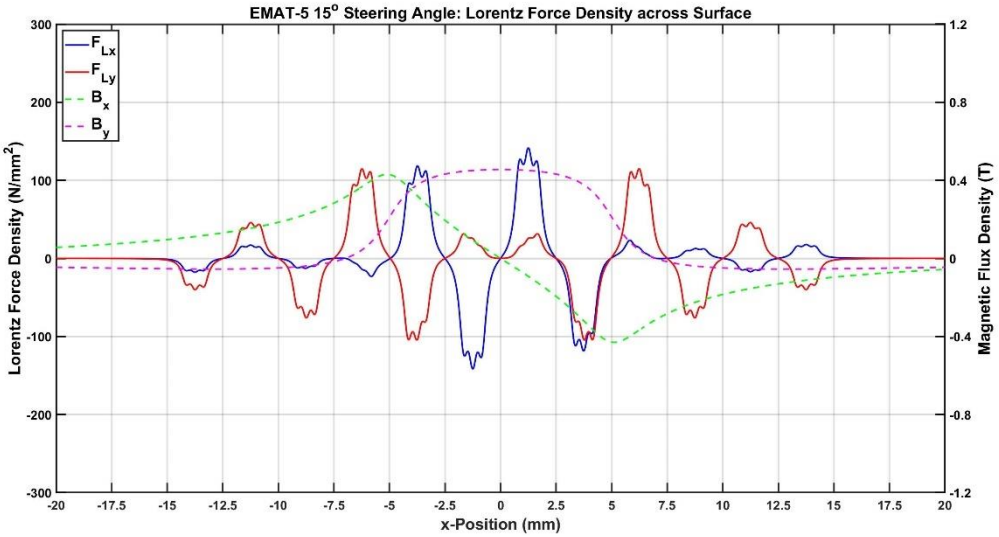

Figure 5.21: Plots of Lorentz Force Density Components across Surface for EMAT-5 15° Steering Angle

The single magnet reduces the displacements of the three wave modes compared to EMATs 1 & 3. The shear wave displacements are similar in magnitude to those of EMAT-2 for steering angles of 15-50°, however from 50-90° they increase. The reason for the increase in shear wave displacement from the 50° steering angle onwards is due to EMAT-5's split-waves. EMAT-5's design is essentially the same as EMAT-4: a central sub-EMAT enclosed by two smaller sub-EMATs. This means that the three sub-EMATs create two superimposed split-waves that originates from between coils 3-4 and coils 9-10. This explains the similarity in beamwidths across steering angles between these two EMAT configurations, as seen in Figure 5.23.

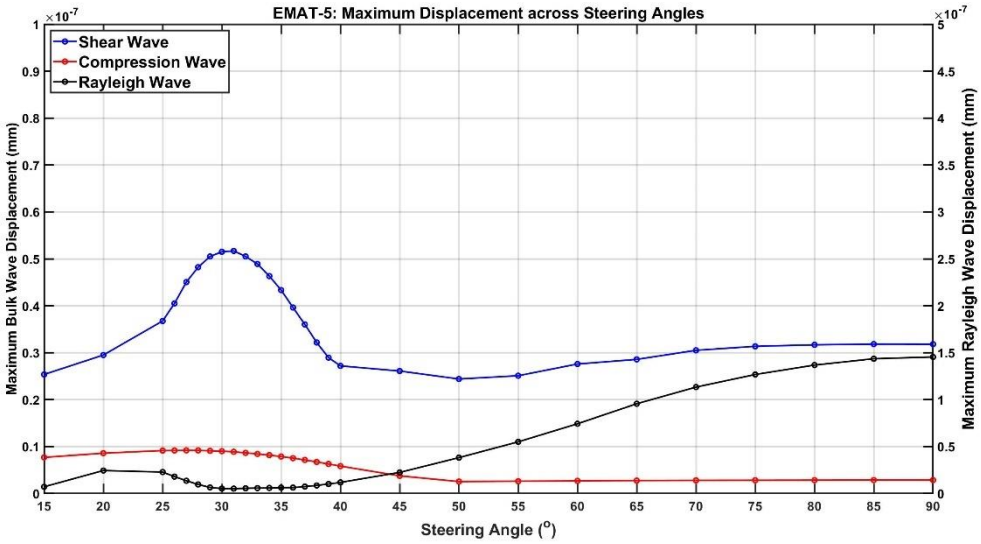

Figure 5.22: Graph of Maximum Displacement across Steering Angles for EMAT-5

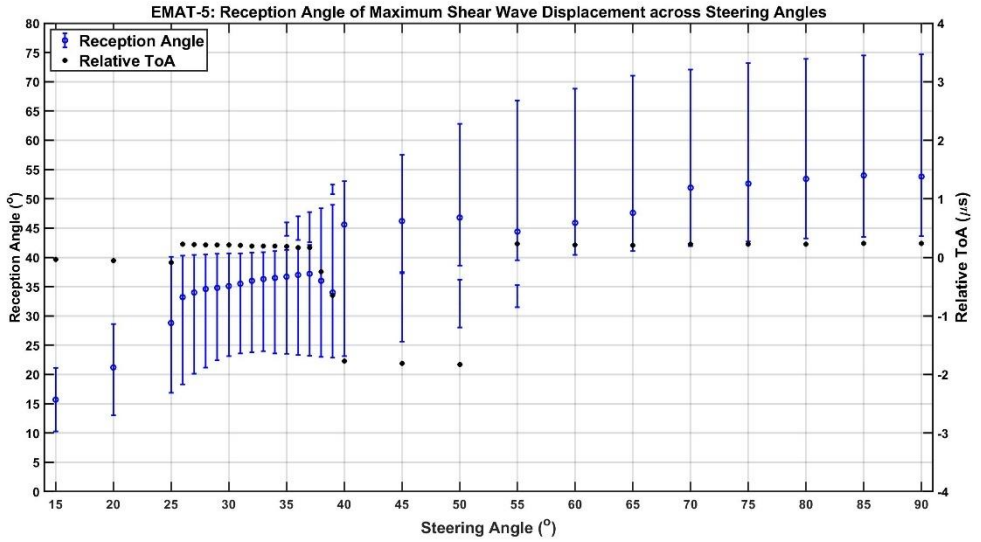

Figure 5.23: Graph of Shear Wave Reception Angles across EMAT-5 Steering Angles

A noticeable difference in beamwidths between these two EMATs is the absence of sidelobes between reception angles of 15-30°. This is due to the low values of magnetic flux and Lorentz force densities for the three-coil sub-EMATs that generate them. The two split-waves are transmitted from between the three sub-EMATs and superimpose into a single wave only at the region of maximum displacement. Two additional split-waves were detected from the A-scans across the curved surface for the 15° steering angle. Figure 5.24 shows two such A-scans and have been annotated to highlight all four split-waves. These additional split-waves originated from the ends of the coil array, due to their lower magnitude and position in time.

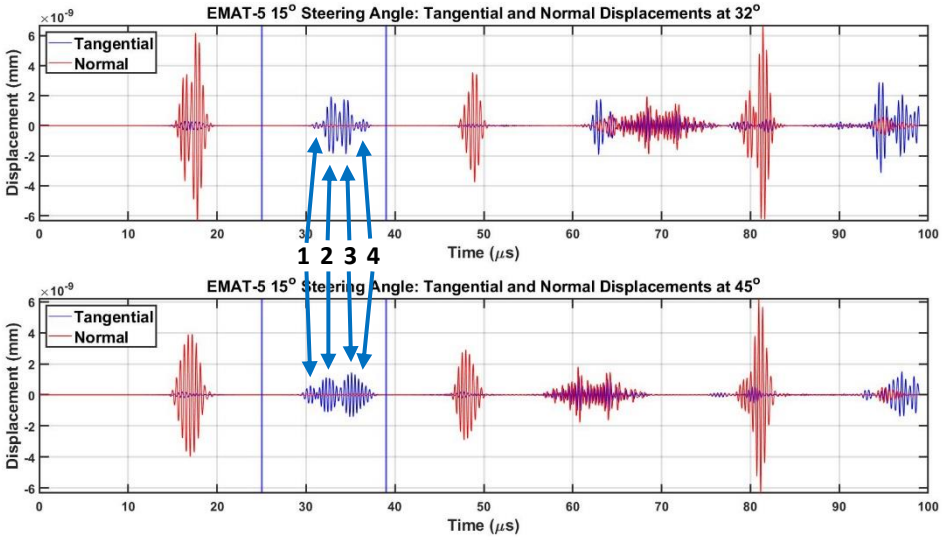

Figure 5.24: Graph of Directional Displacement across Time at 32° & 45° for EMAT-5 15° Steering angle, annotated to highlight the four split-wave peaks

5.2.5. EMAT-6: 2x 10mm Wide Magnets

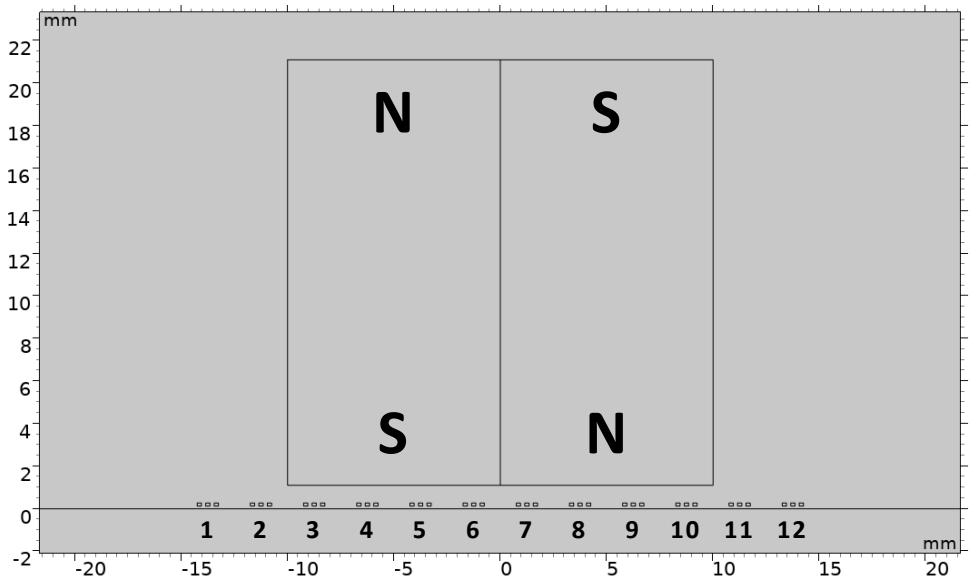

Figure 5.25: EMAT-6 Design

The magnetic configuration of two 10mm-wide magnets in alternating directions does not physically encompass the entire coil array, as shown in Figure 5.25. Despite this, the bias magnetic field from each magnet enables their respective half of the coil array to be within a single vertical direction. Coupled with a concentration of magnetic flux density at the centre of the EMAT, this magnetic configuration's design is akin to that of EMAT-3. The main difference between EMATs 6 & 3 is the weakening vertical magnetic flux density toward the ends of the coil array, reducing the x-component of Lorentz force density, as shown in Figure 5.26.

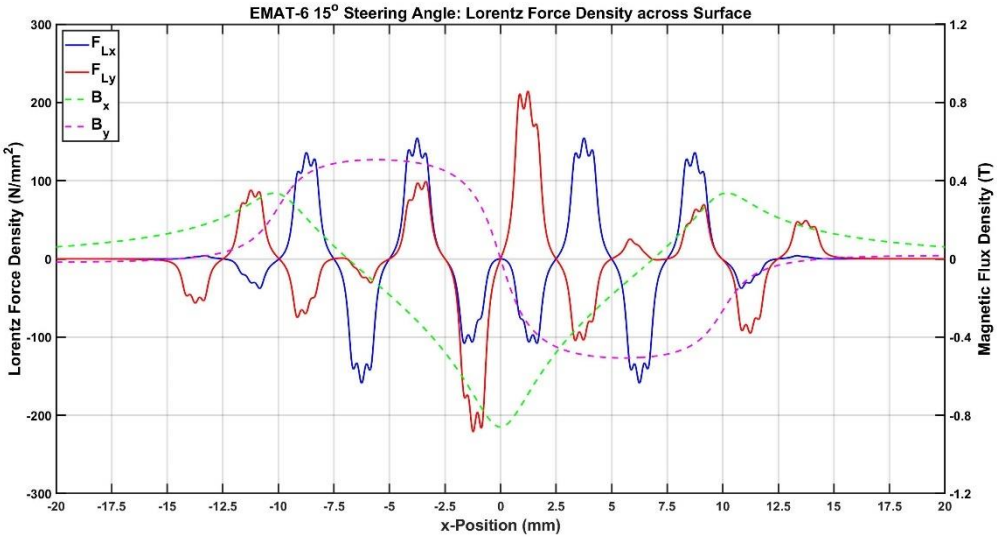

Figure 5.26: Plots of Lorentz Force Density Components across Surface for EMAT-6 15° Steering Angle

Figure 5.27 and Figure 5.28 show the results of this magnetic configuration across steering angles. As expected, these results resemble those of EMAT-3 due to their similar designs. Despite being lower in magnitude due to the lower magnetic flux density, the shear wave displacements across steering angles behave in a similar manner to those of EMAT-3. The two sub-EMATs transmit two distinct shear wave lobes in each direction at lower steering angles, explaining the sudden increase in reception angle between the 20-25° steering angles. These split-waves combine into a single shear wave originating from the centre at higher steering angles.

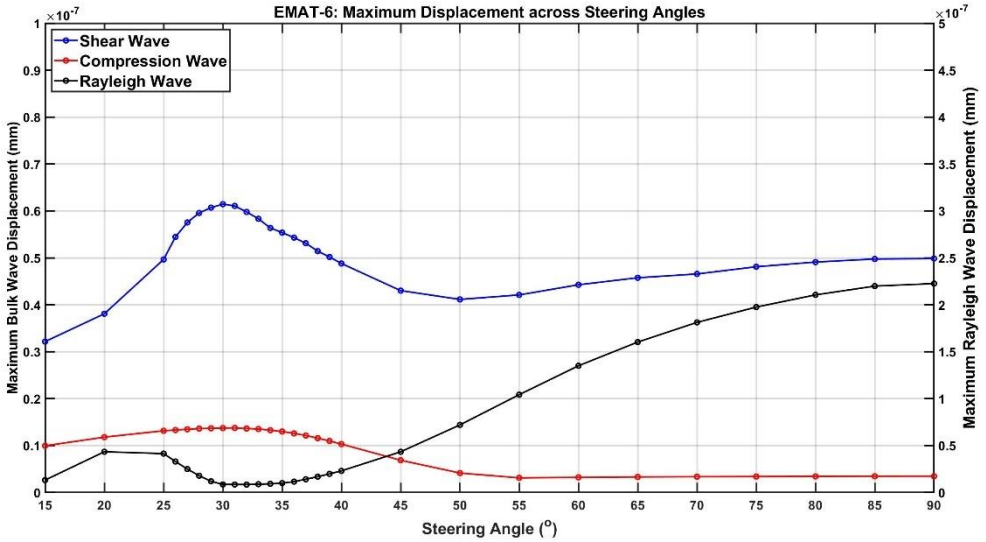

Figure 5.27: Graph of Maximum Displacement across Steering Angles for EMAT-6

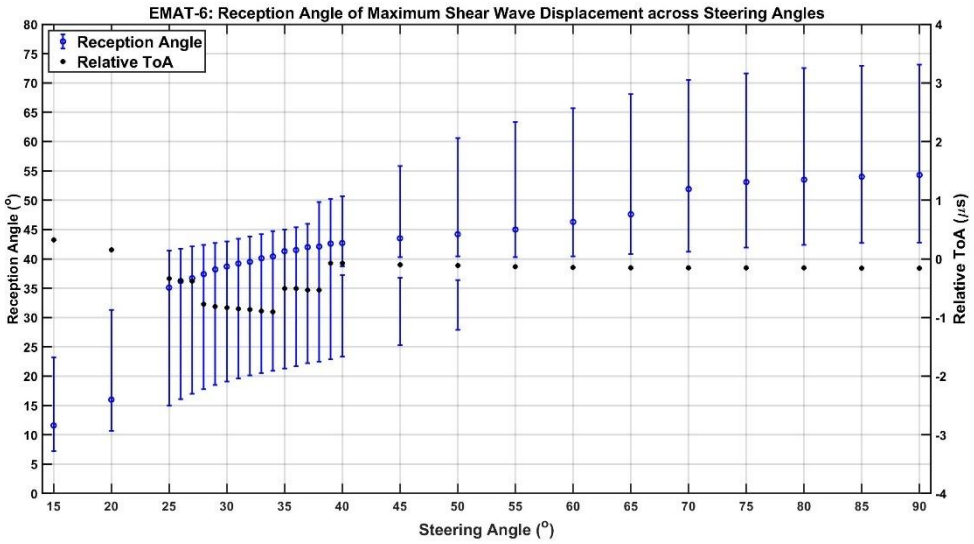

Figure 5.28: Graph of Shear Wave Reception Angles across EMAT-6 Steering Angles

One noticeable difference between EMATs 6 & 3 is the presence of two additional split-waves at the higher steering angles. Figure 5.29 shows the colour-plot for EMAT-6's 60° steering angle which highlights these split-waves when compared to Figure 5.13 for EMAT-3. The transmitted Rayleigh waves also highlight these additional split-waves. From Figure 5.29 and Figure 5.13, a single large Rayleigh wave is seen between two smaller Rayleigh waves. At the 90° steering angle however, EMAT-6 retains these three Rayleigh waves while for EMAT-3 they all superimpose into a single peak. Figure 5.30 shows the A-scan for these Rayleigh waves arriving at the corner of the sample for EMATs 3 & 6.

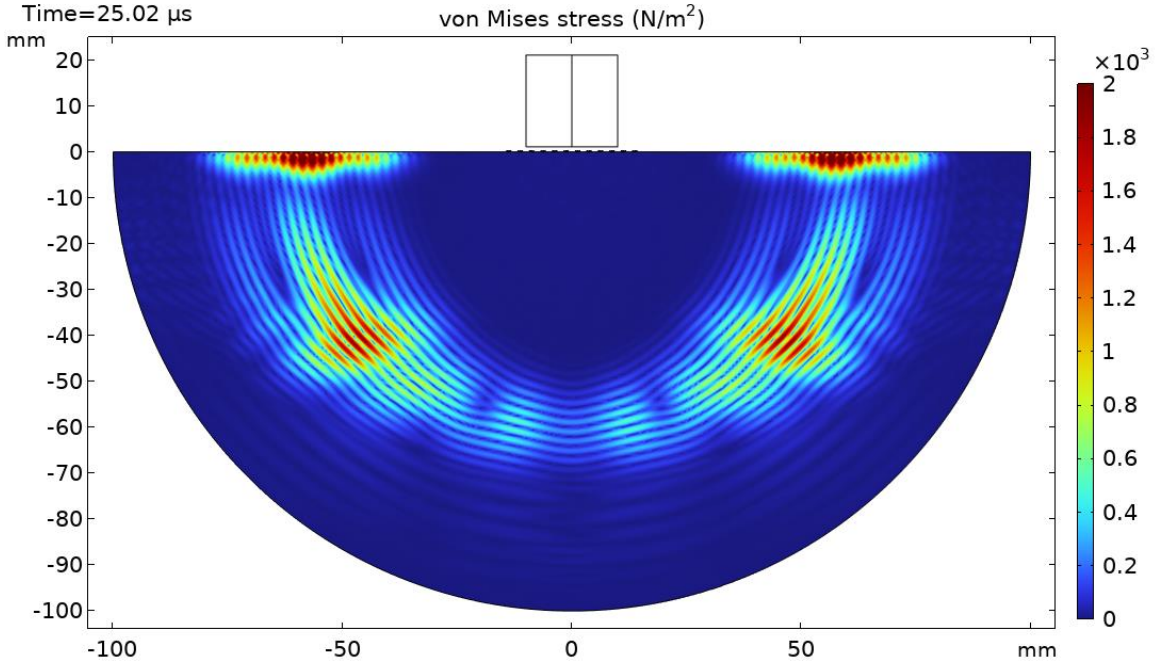

Figure 5.29: Colour-plot of EMAT-6 60° Steering Angle

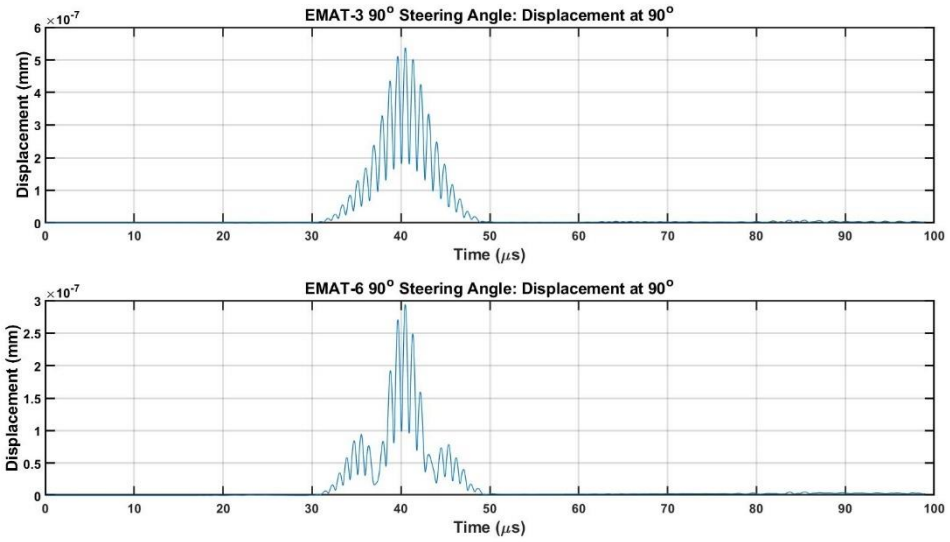

Figure 5.30: A-scans at 90° for EMAT-3 & EMAT-6 90° Steering Angle

5.2.6. EMAT-7: 3x 10mm Wide Magnets

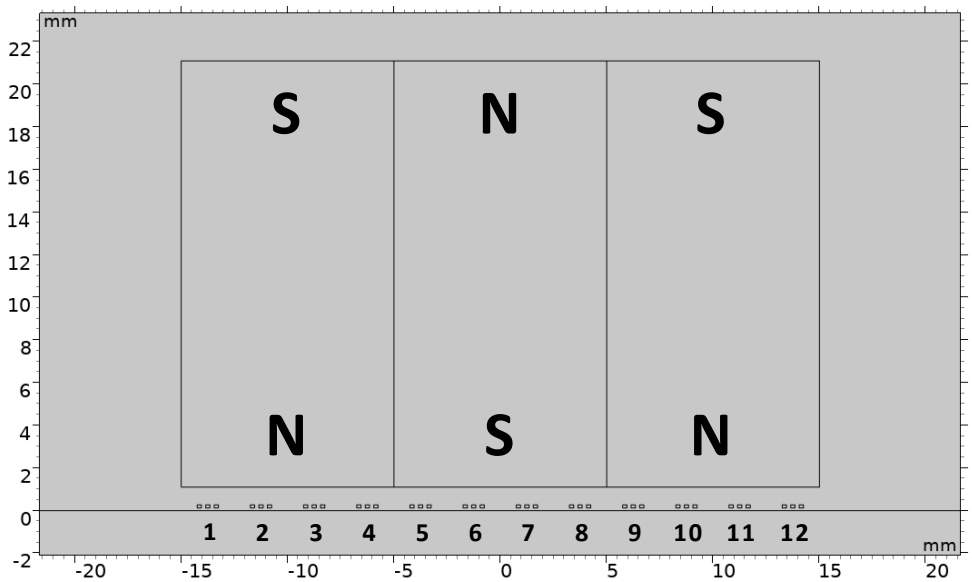

Figure 5.31: EMAT-7 Design

EMAT-7's magnetic configuration is similar in design to both EMATs 4 & 5: a central magnet between two inverted magnetic fields, as seen in Figure 5.31. These create three four-coil sub-EMATs, as shown in Figure 5.32. It is expected therefore that both the shear wave displacement and beamwidth is similar in pattern to those of EMAT-5, as that was also considered as being composed of three sub-EMATs. Figure 5.33 however shows the presence of twin peaks of maximum shear wave displacement, which is a significant deviation from all of the previous magnetic configurations. These twin peaks are caused by the interference of the distinct shear wave lobes from each of the sub-EMATs.

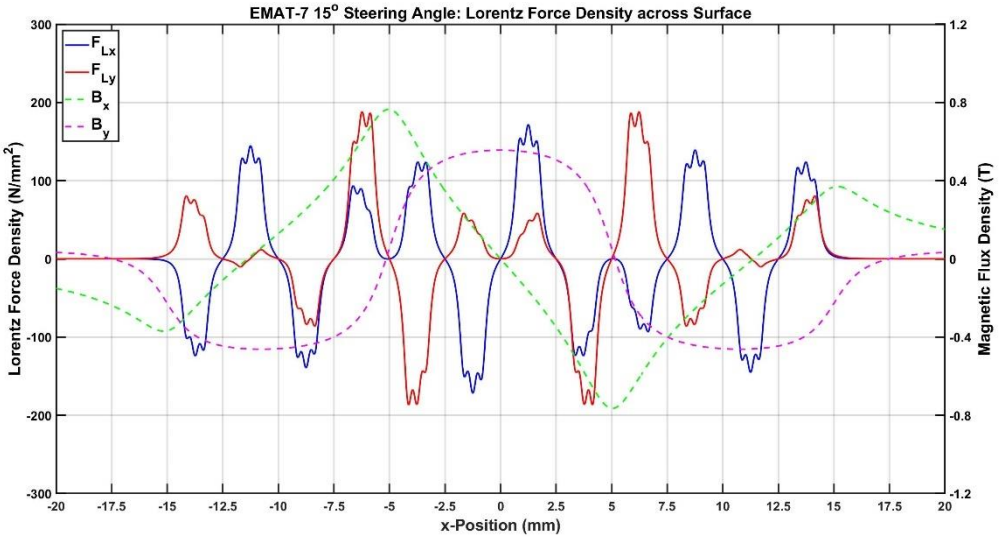

Figure 5.32: Plots of Lorentz Force Density Components across Surface for EMAT-7 15° Steering Angle

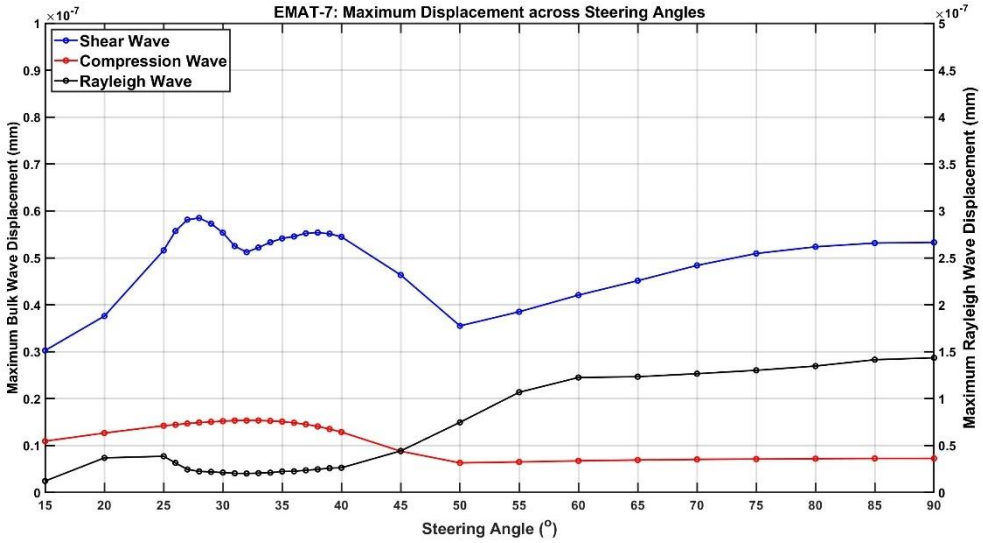

Figure 5.33: Graph of Maximum Displacement across Steering Angles for EMAT-7

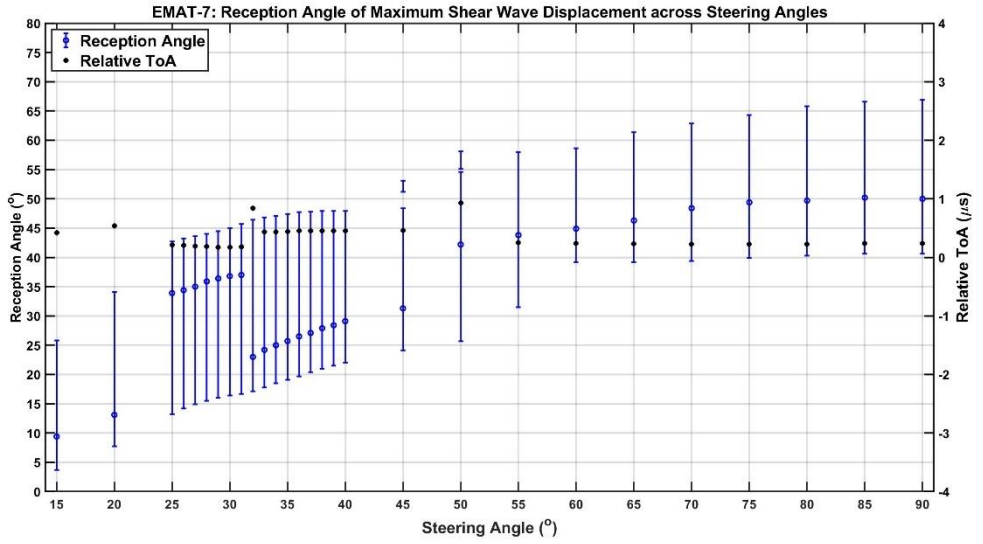

Figure 5.34: Graph of Shear Wave Reception Angles across EMAT-7 Steering Angles

Graphs of the shear wave reception angles for EMATs 1, 2 & 4 show that as the steering angles increases, the reception angle linearly increases until approximately 29-33° when the gradient of this linear trend reduces. Figure 5.34 however shows that the reception angle increases linearly with steering angle from 15-45°, with the exception of the 25-31° steering angles when this trend is offset to higher reception angles. It is within this offset range that the first of the shear wave's maximum displacement peaks occur. Sudden increases in reception angle have occurred with previous magnetic configurations when the steering angles increased to: 42° for EMAT-1; 28° for EMAT-3; 39° for EMAT-4; and 25° for EMAT-6. The difference between these sudden increases and those of EMAT-7 is that the reception angle does not then decrease afterwards. This sudden increase and decrease is also shown for EMAT-5 in Figure 5.23 from steering angles of 40-50°, however this is not accompanied by any significant change in displacement.

The reason for this temporarily increased reception angle range is the emergence of higher-angled sidelobes that increase to a maximum displacement and then reduce in magnitude to become supplanted by the originally dominant lobes. The originally dominant lobes then reach their maximum displacement at the 38° steering angle, creating the second maximum shear wave displacement peak. The originally dominant shear wave lobes are transmitted from the central sub-EMAT, while the higher-angled sidelobes are transmitted from the sub-EMAT closest to the reception angle. This is not reflected in the RToA however, as the reception angle's A-scan could not distinguish between the split-waves that had superimposed at the reception angle of maximum displacement.

These three sub-EMATs generate four split-waves, and increasing the steering angle further causes the two innermost split-waves to merge into one at the reception angle of maximum displacement only. This is seen in Figure 5.35, in addition to the Rayleigh waves that are shown to emulate these four split-waves. At the 90° steering angle, the A-scan from the corner of the sample graphs only the Rayleigh wave peaks originating from the two innermost split-waves. Due to their close proximity and weak magnitude, the Rayleigh waves from the outermost split-waves are imposed onto the innermost split-waves

and are seen leading and trailing these two peaks. Figure 5.36 shows this A-scan compared to that of EMAT-5, due to both of these configurations possessing the same number of sub-EMATs. No Rayleigh waves are seen leading or trailing the two peaks for EMAT-5. This is due not only to the weak Lorentz forces at the ends of the coil array, but also due to the two innermost split-waves originating closer to the ends of the coils than those of EMAT-7.

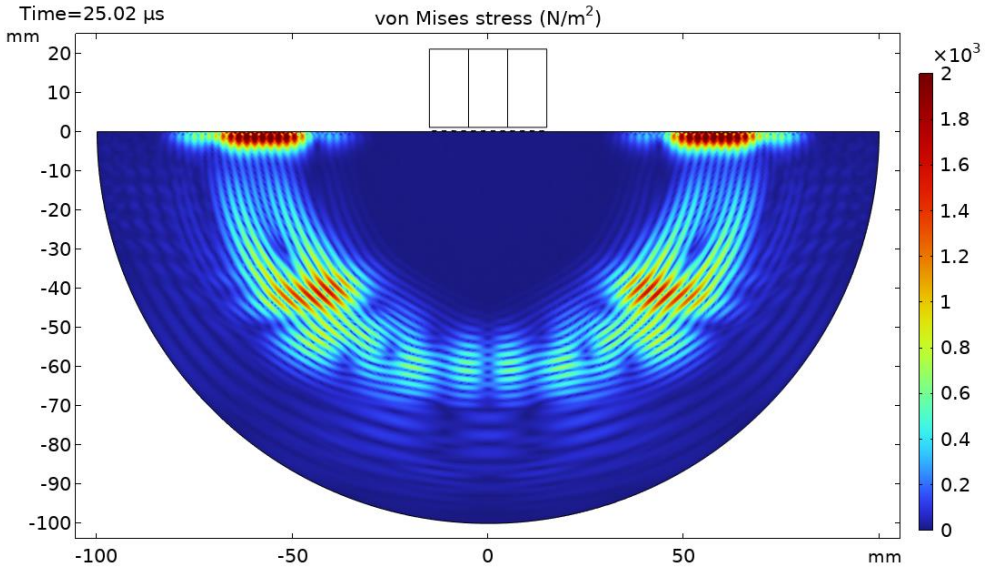

Figure 5.35: Colour-plot of EMAT-7 60° Steering Angle

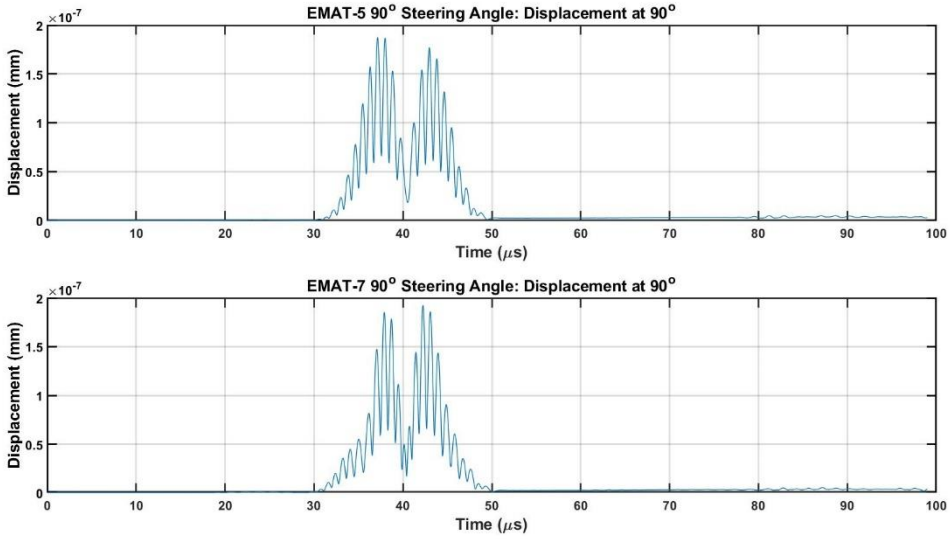

Figure 5.36: A-scans at 90° for EMAT-5 and EMAT-7 90° Steering Angle

5.2.7. EMAT-8: 4x 10mm Wide Magnets

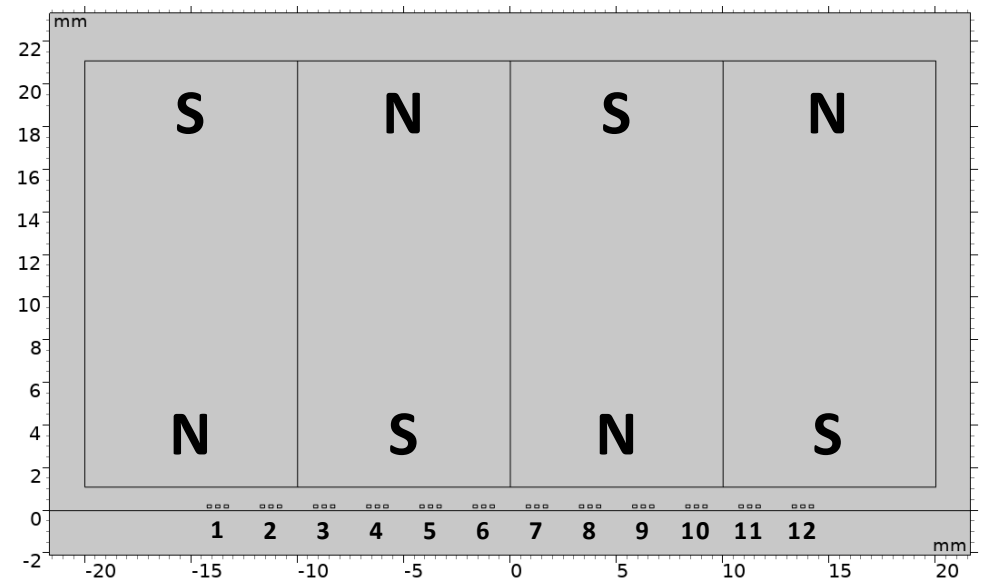

Figure 5.37: EMAT-8 Design

This final EMAT configuration (composed of four 10mm-wide magnets as seen in Figure 5.37) was expected to combine the conclusions of EMAT-6 and EMAT-4, due to the two central and exterior magnets respectively. This creates two four-coil sub-EMATs within two two-coil sub-EMATs (as seen in Figure 5.38) and the effect that this has on the shear wave displacement is shown in Figure 5.39.

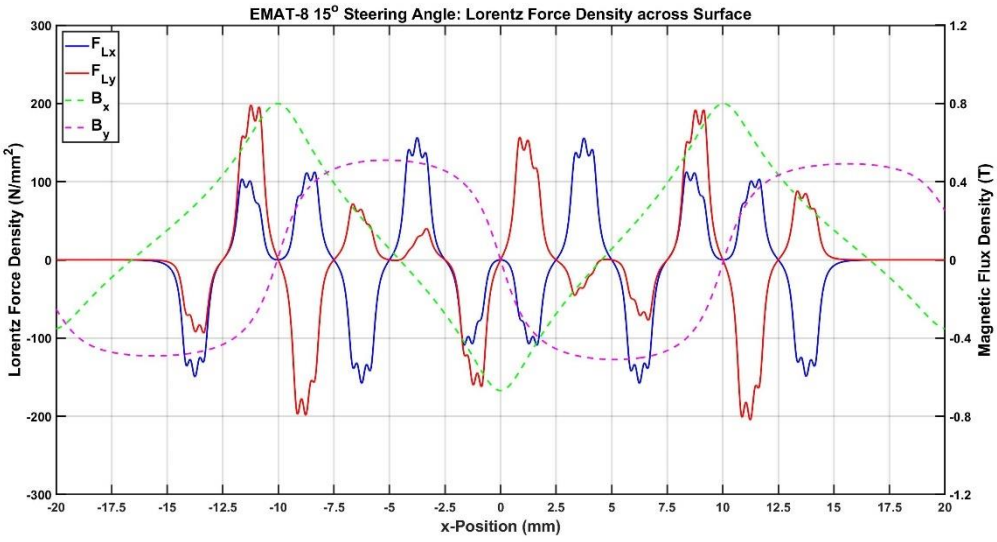

Figure 5.38: Plots of Lorentz Force Density Components across Surface for EMAT-8 15° Steering Angle

EMAT-8 displays the same pattern of twin shear wave displacement peaks as EMAT-7. EMAT-8's sub-EMATs are not at the same positions as those for EMAT-7, however they still generate higher-angled sidelobes which are responsible for the first shear wave displacement peak. The RToAs for this first peak (shown in Figure 5.40) suggest that this shear wave lobe originated from

one of the two sub-EMATs furthest from the reception angle. The numerous sub-EMATs (each with strong magnetic flux densities) transmit multiple shear wave lobes that increase the beamwidth at lower steering angles beyond those of the other EMAT configurations.

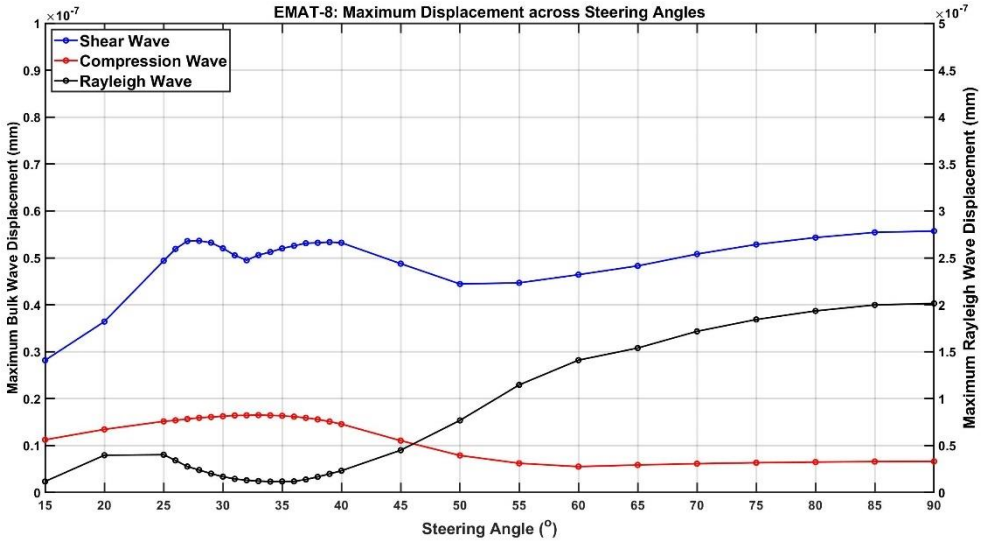

Figure 5.39: Graph of Maximum Displacement across Steering Angles for EMAT-8

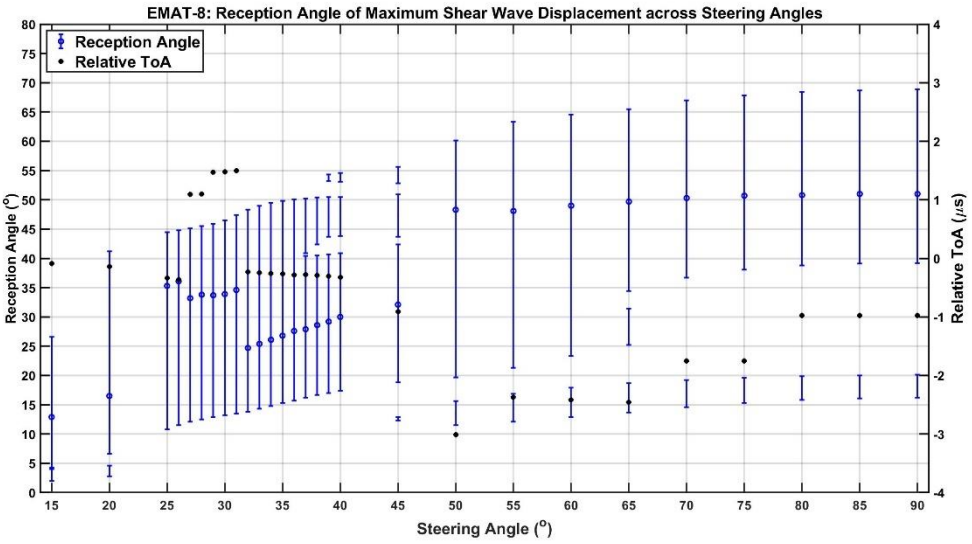

Figure 5.40: Graph of Shear Wave Reception Angles across EMAT-8 Steering Angles

EMAT-7's 90° steering angle caused the two innermost split-waves to merge at the reception angle of maximum displacement, which increased its shear wave displacement compared to other magnetic configurations at the same steering angle. The same steering angle for EMAT-8 increases the maximum shear wave displacement further, such that it is the maximum shear wave displacement across the range of steering angles. This is a significant deviation from the typical 30-35° steering angle range seen with the previous EMATs. This maximum value is not only due to the increased shear wave

displacement at the 90° steering angle, but also due to the decreased displacements of the twin shear wave peaks. These changes are a consequence of the interaction between the numerous split-waves.

These split-waves caused both constructive and destructive interference between themselves. Figure 5.41 shows the colour-plot for a 60° steering angle which could be compared to Figure 5.18 and Figure 5.29 for EMATs 4 & 6 respectively to highlight the effect of these interferences. Figure 5.41 shows an absence between the exterior split-waves, greater than that of EMAT-4 despite the fact that a single wavefront would have been generated from its centre akin to EMAT-6.

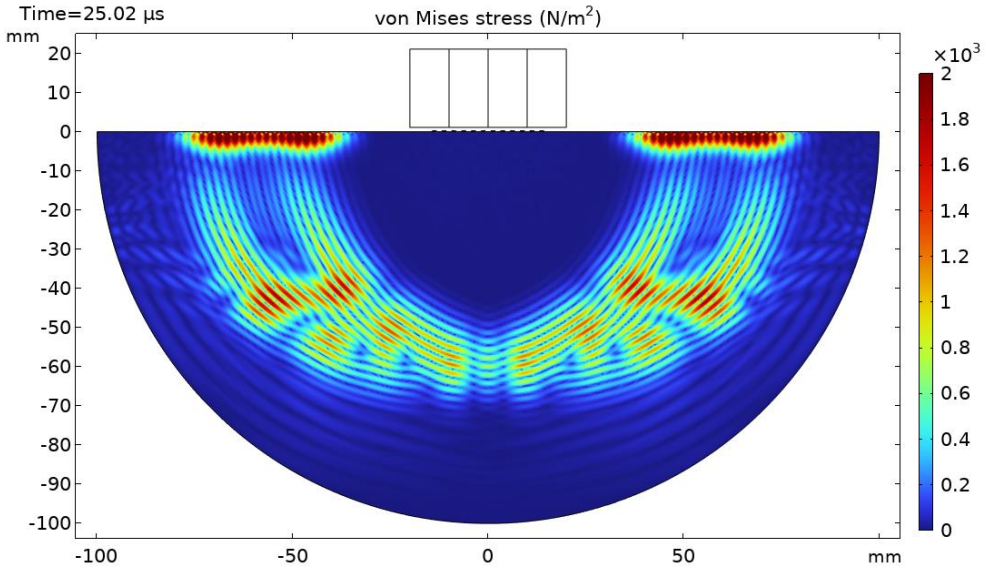

Figure 5.41: Colour-plot of EMAT-8 60° Steering Angle

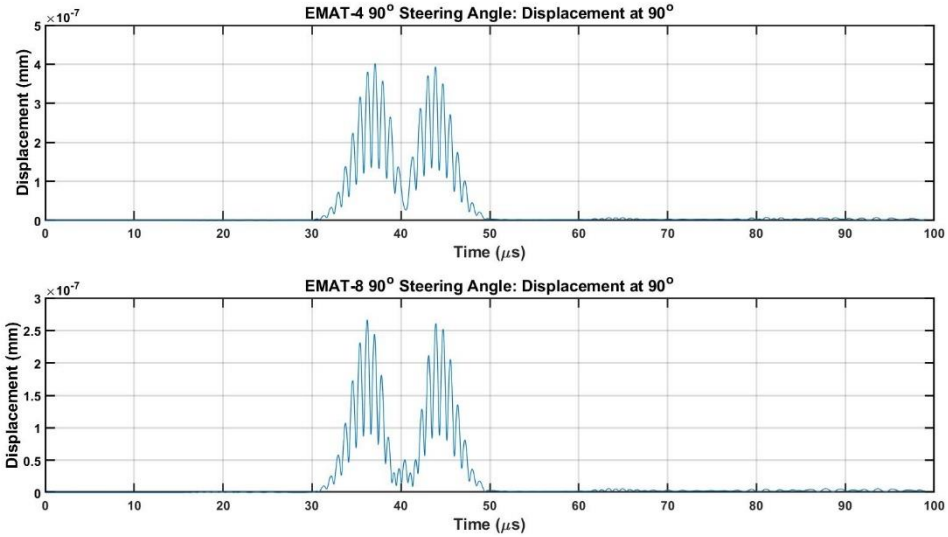

Figure 5.42: A-scans at 90° for EMAT-4 and EMAT-8 90° Steering Angle

Despite the destructive interference of the central split-waves, the A-scan of the Rayleigh wave shows an additional smaller peak between the two

expected peaks. These expected peaks originate from between coils 2-3 and 10-11 (as was the case for EMAT-4) however the smaller peak for EMAT-8 originates from the destructively interfered central split-wave. This is shown in Figure 5.42, which compares the Rayleigh wave A-scans for EMATs 4 & 8 at a 90° steering angle.

5.3. Horizontal Magnetic Configurations

Section 5.2 shows that differing magnetic configurations result in changes to: the magnitude of the three wave modes; the magnitude of the sidelobes compared to the main lobes; and the separating/merging/increased number of split-waves. One of the more important observations however was that the maximum reception angle attainable was via EMAT-2 at 64.2°, however the shear wave directivity was of low displacement and a beamwidth encompassing almost the entirety of the curved surface. In an attempt to extend the reception angle of the MLC EMAT, additional magnetic configurations are explored with horizontal directions of magnetic flux density.

Qu et al [18] compared the performance of an MLC EMAT when its direction of magnetisation was changed from vertical to horizontal. This was performed via a PC setup on a rectangular sample (akin to the test setup in Section 4.4) across a steering angle range of 30-60°. Qu et al [18] concluded that the normalised amplitude of the shear waves had lower variance when the magnetisation direction was horizontal, and that the horizontal magnetisation enabled scanning at a greater angle. While the ratios between these amplitudes of normalisation show that the maximum magnitude from the vertically directed EMAT was greater for both the simulated and experimental results, it encouraged exploration within this work for a greater reception angle. EMAT-1's magnet was rotated 90° to create a horizontal magnetic field, and the effect that this had on the lines of magnetic flux density is shown in Figure 5.43.

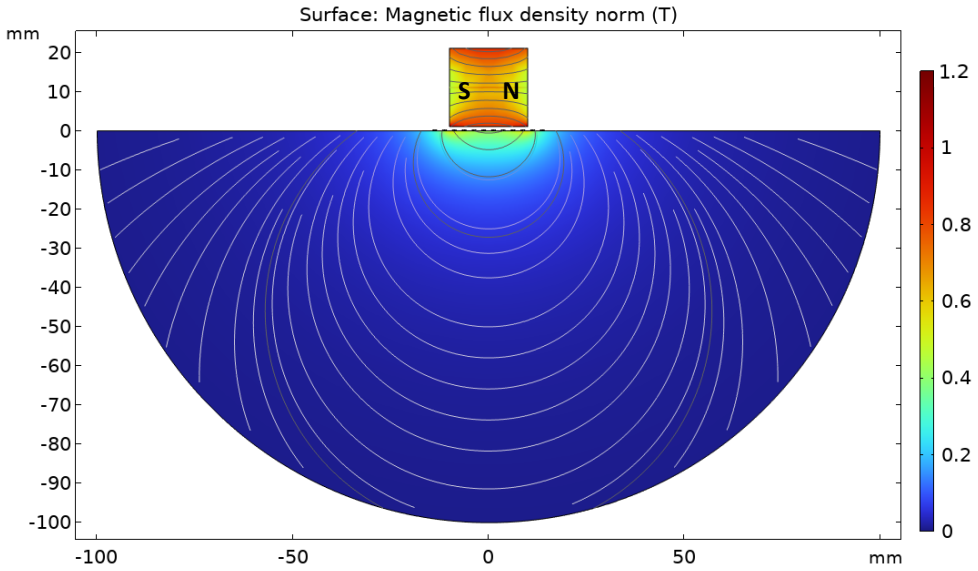

Figure 5.43: Colour-plot of Magnet-9

The same beam directivity simulations as before were repeated, and Figure 5.44 and Figure 5.45 show the maximum displacement of the three wave modes and the shear wave reception angles respectively across steering angles. The shear wave displacement shown in Figure 5.44 corroborates the conclusion by Qu et al [18], in that there is little variance in the magnitude across steering angles. These results are also consistent with those in Section 5.2, with a maximum shear wave displacement peak generally within a steering angle range of 30-35°. The results shown in Figure 5.45 however are very similar to those of EMAT-3, shown in Figure 5.11. These similarities include: two distinct lobes at a 15° steering angle; a sudden increase in reception angle at lower steering angles; a shear wave lobe normal to the surface; and a single shear wave at higher steering angles.

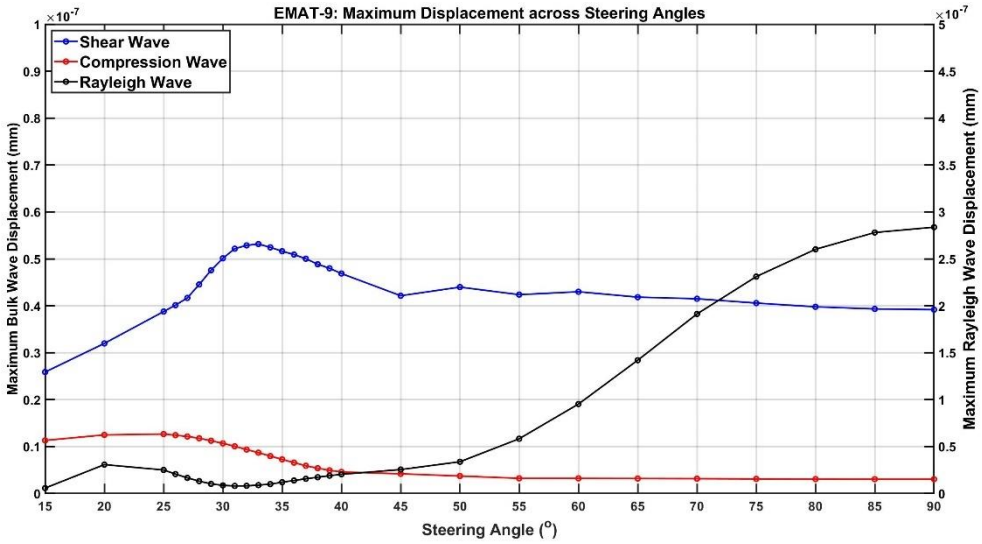

Figure 5.44: Graph of Maximum Displacement across Steering Angles for EMAT-9

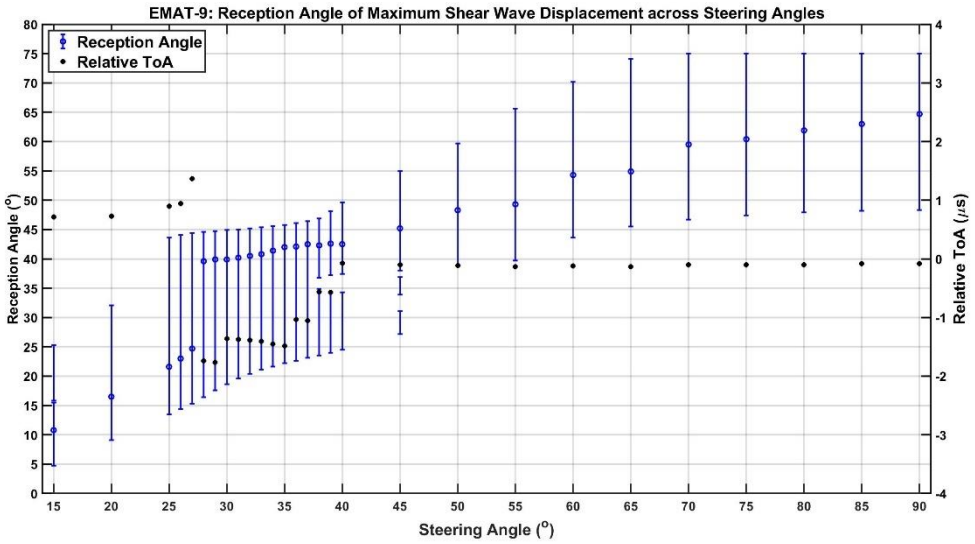

Figure 5.45: Graph of Shear Wave Reception Angles across EMAT-9 Steering Angles

The similarity between EMATs 9 & 3 is revealed by the orientations of Lorentz force density for both EMATs, shown in Figure 5.46. While EMAT-9's magnet produced a constant horizontal direction of magnetic flux density across the surface, the vertical direction inverts at the centre, just as it does for EMAT-3. This means that EMAT-9 can also be considered as being composed of two six-coil sub-EMATs.

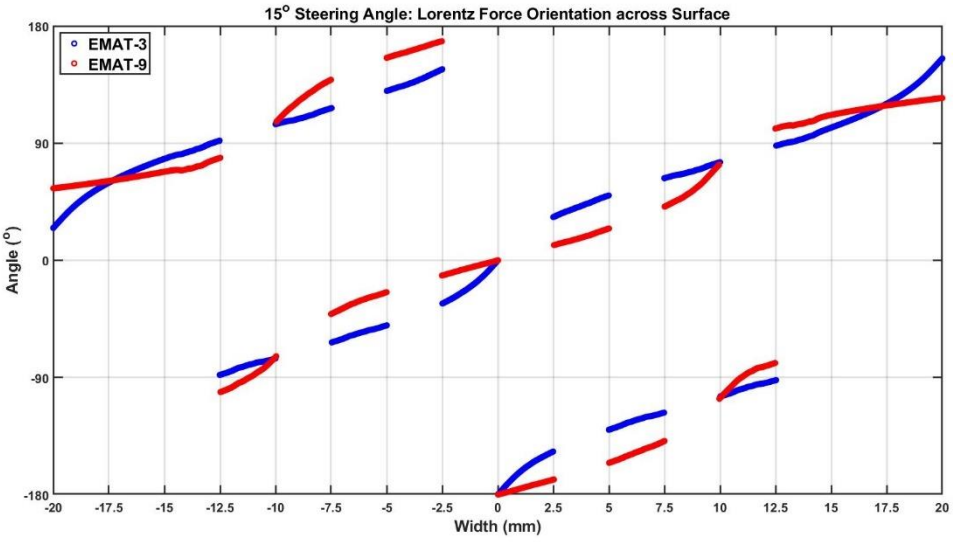

Figure 5.46: Plot of Lorentz Force Density Directions across Surface

Despite the orientations of Lorentz force density being almost equal for EMATs 9 & 3, the magnitudes of their components are different across the surface. This is due to the differing positions and number of magnetic flux concentrations from the magnets. The components of Lorentz force density for EMAT-9 is shown in Figure 5.47. Comparing them to EMAT-1 (Figure 4.49) shows that the 90° rotation of the square magnet causes EMAT-9's x-component of

Lorentz force density to be equal in magnitude and direction to the y-component of Lorentz force density for EMAT-1. Comparing them to EMAT-3 (Figure 5.9) highlights the effect that differing positions of magnetic flux density concentration has on these forces, but how it ultimately has minimal effect on either the reception angle or beamwidth of the shear waves.

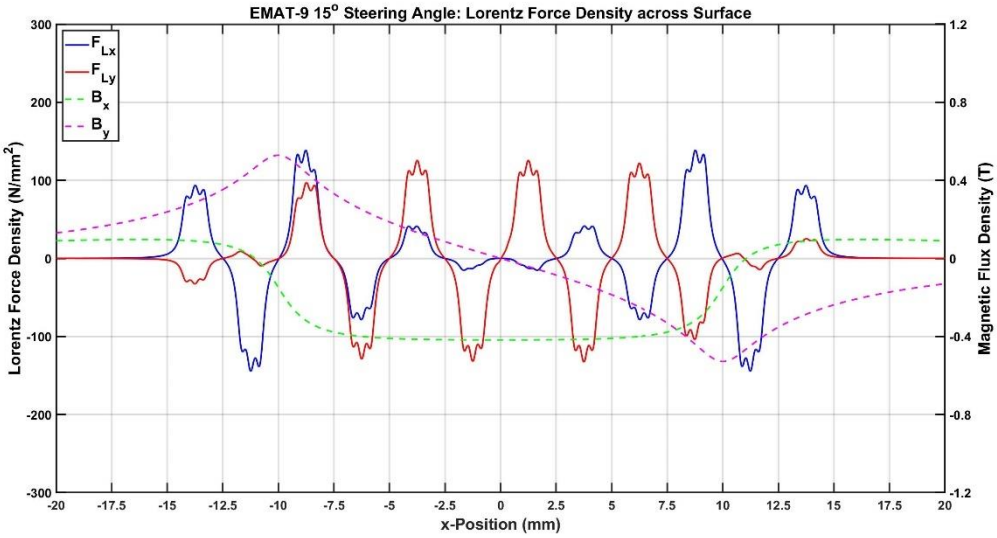

Figure 5.47: Plots of Lorentz Force Density Components across Surface for EMAT-9

Using the same magnets and restrictions as stated in Section 3.3, a second list of magnetic configurations is drawn in Table 5.1. The same parametric studies were then performed on these additional horizontal magnetic configurations, and the magnetic fields at 1mm lift-off is shown in Figure 5.48-Figure 5.52.

Table 5.1: Horizontal Magnetic Configuration Design

Configuration Number	Configuration	Number of Peaks across Surface at 1mm Lift-off	Number of Peaks within Coil Array at 1mm Lift-off
9	20mm	2	2
10	20mm-20mm	2	0
11	10mm	2	2
12	10mm-10mm (v)	2	2
13	10mm-10mm (h)	2	0
14	10mm-10mm-10mm-10mm	2	0

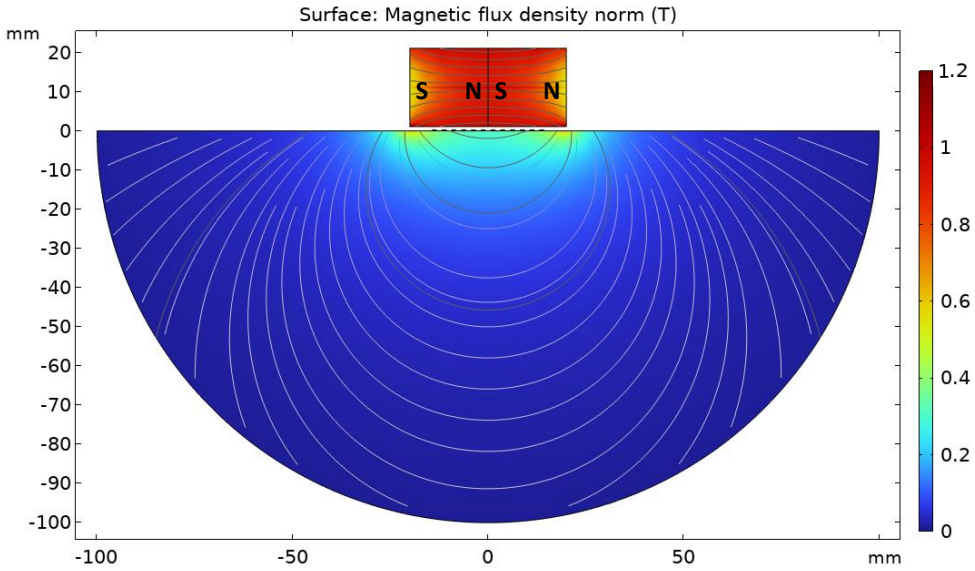

Figure 5.48: Colour-plot of Magnet-10

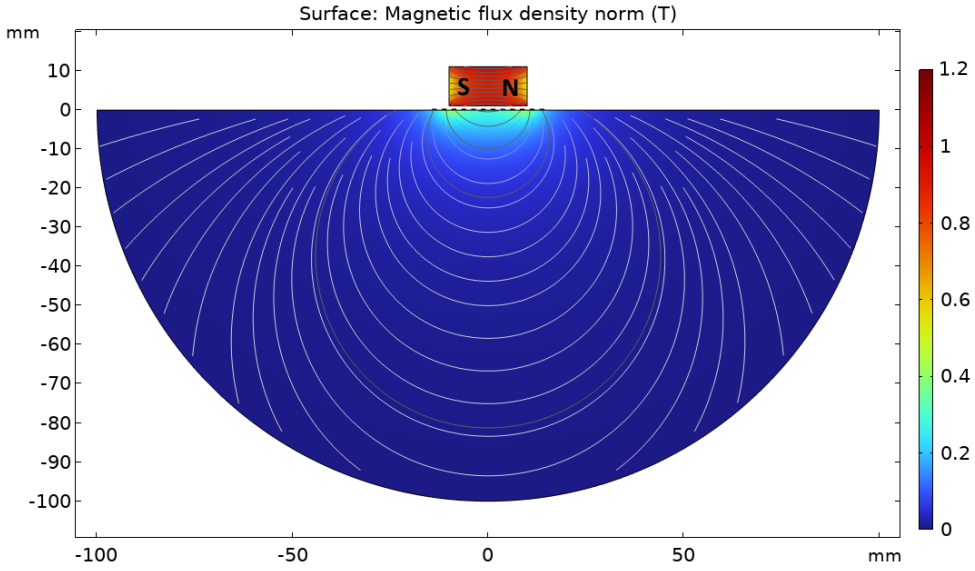

Figure 5.49: Colour-plot of Magnet-11

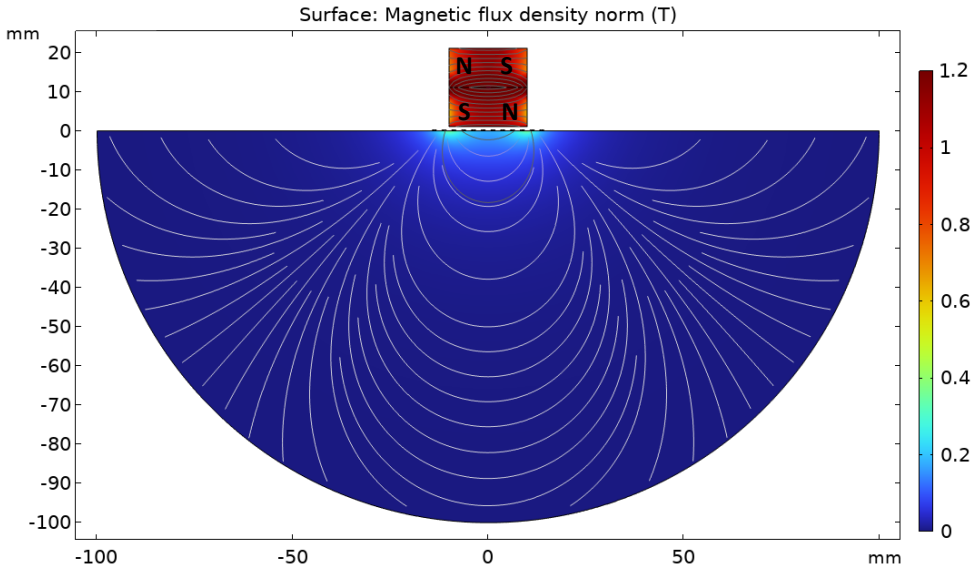

Figure 5.50: Colour-plot of Magnet-12

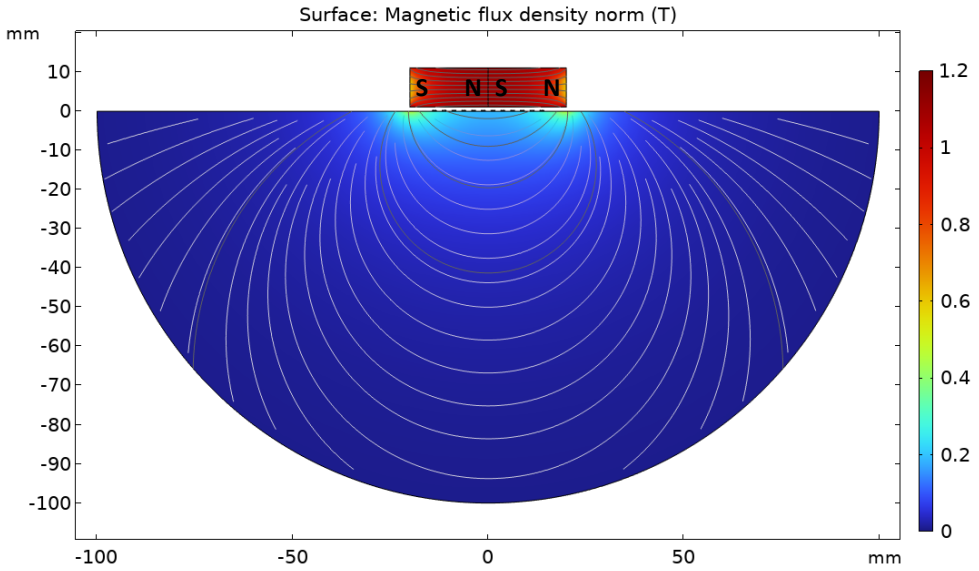

Figure 5.51: Colour-plot of Magnet-13

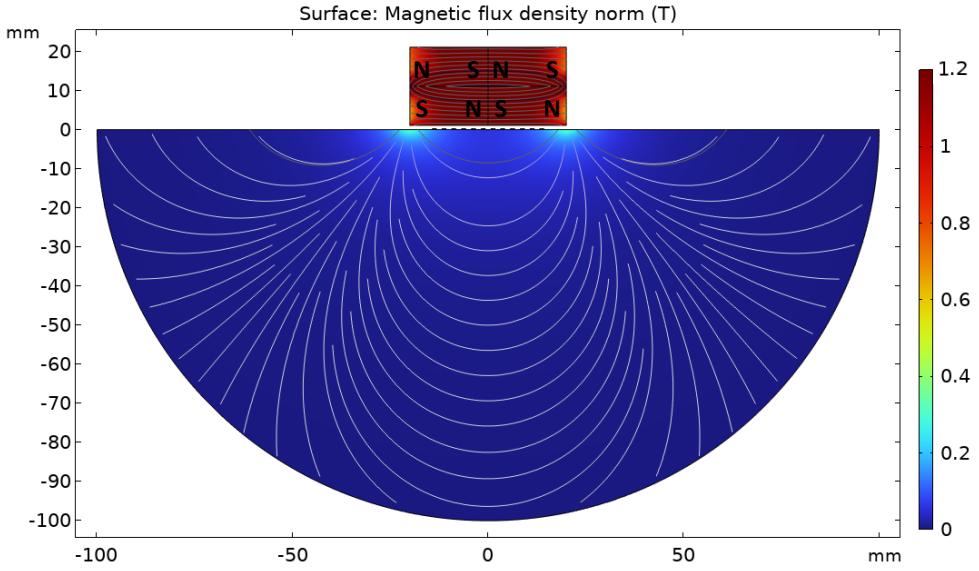

Figure 5.52: Colour-plot of Magnet-14

Both the magnitudes and positions of maximum magnetic flux density as lift-off increases for magnets 9-14 is shown in Figure 5.53 and Figure 5.54 respectively. Figure 5.53 shows very little change in the maximum value of magnetic flux density across the magnetic configurations for a given lift-off. The decrease of the magnet's height from 20mm to 10mm (for EMATs 9 & 10 to EMATs 11 & 13 respectively) has the effect of weakening the magnetic flux density. Kang et al [92] had documented a decrease in surface wave amplitude from an MLC EMAT due to a decrease in magnet height. The magnetic flux density was decreased further however by the introduction of a second magnet above the first one. The hierarchy of these magnetic configurations also shows that the number of magnets included does not significantly alter the maximum value of magnetic flux density at the surface.

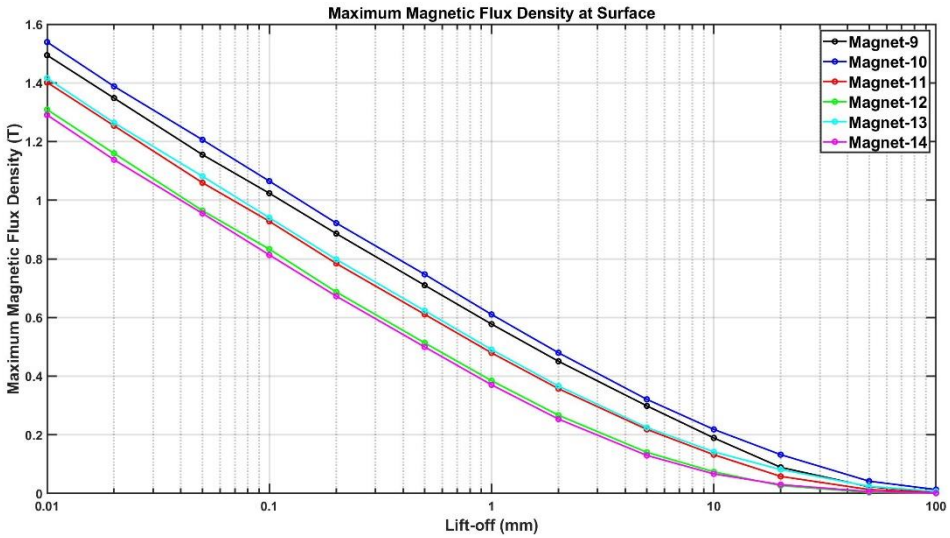

Figure 5.53: Graph of Maximum Magnetic Flux Density at Surface for Horizontal Magnetic Configurations

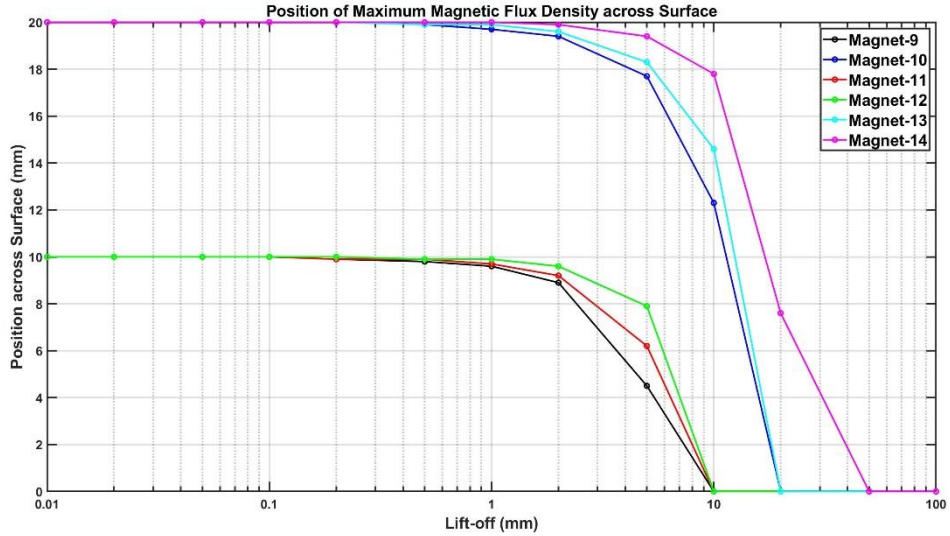

Figure 5.54: Graph of Maximum Magnetic Flux Density Position at Surface for Horizontal Magnetic Configurations

Figure 5.54 shows that magnets 9-14 can be separated into two groups: 20mm-wide and 40mm-wide configurations. Within a single group, there is a limited degree of change in the position of the maximum magnetic flux density as lift-off increases. The same beam directivity simulations were performed on EMATs 10-14, and Figure 5.55 and Figure 5.56 show the displacements and reception angles across steering angles for EMAT-10. While the shear wave displacement for EMAT-10 is remarkably lower than that of the previous EMATs, the reception angle and beamwidth bear a striking resemblance to that of EMAT-3 shown in Figure 5.11. The reception angle was measured at 67.6° for a 90° steering angle, however the RToA was not approximate to 0µs. This means that the origin position of the shear waves is not near the centre of the EMAT.

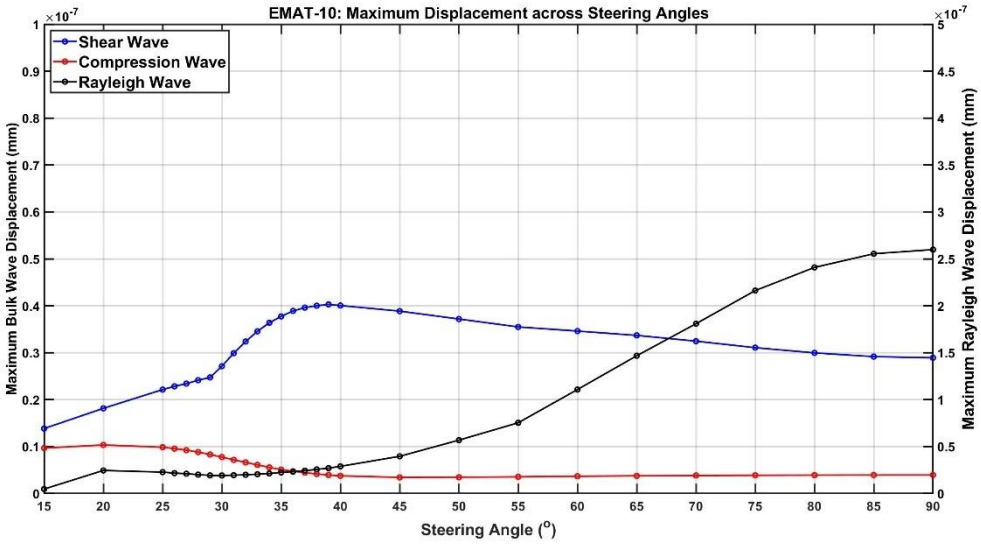

Figure 5.55: Graph of Maximum Displacement across Steering Angles for EMAT-10

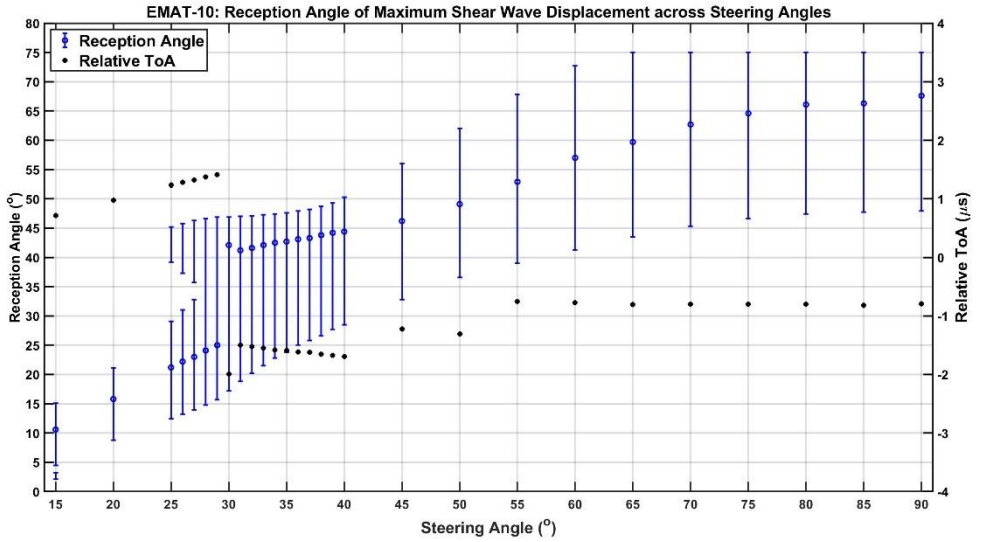

Figure 5.56: Graph of Shear Wave Reception Angles across EMAT-10 Steering Angles

Like EMAT-9, the vertical direction of magnetic flux density inverts and therefore can be considered to be composed of two sub-EMATs. Unlike EMAT-9 however, the concentrations of magnetic flux density lie outside the coil array. This causes the x-components of Lorentz force density to maximise at the ends of the coil array (as seen in Figure 5.57) and become equal in magnitude and direction to the y-component of Lorentz force density for EMAT-2 (as seen in Figure 5.9).

It is from underneath these maximised x-components of Lorentz force density that each of the two split-waves originate. Analysis of EMAT-10's colour-plots and beam directivity plots show that the two distinct lobes are present at lower steering angles. At higher steering angles, the split-waves merge into a single wave only at the region of maximum displacement, akin to

EMAT-6. It is due to the large difference in the origin positions for the split-wave that the RToA was not equal to 0µs.

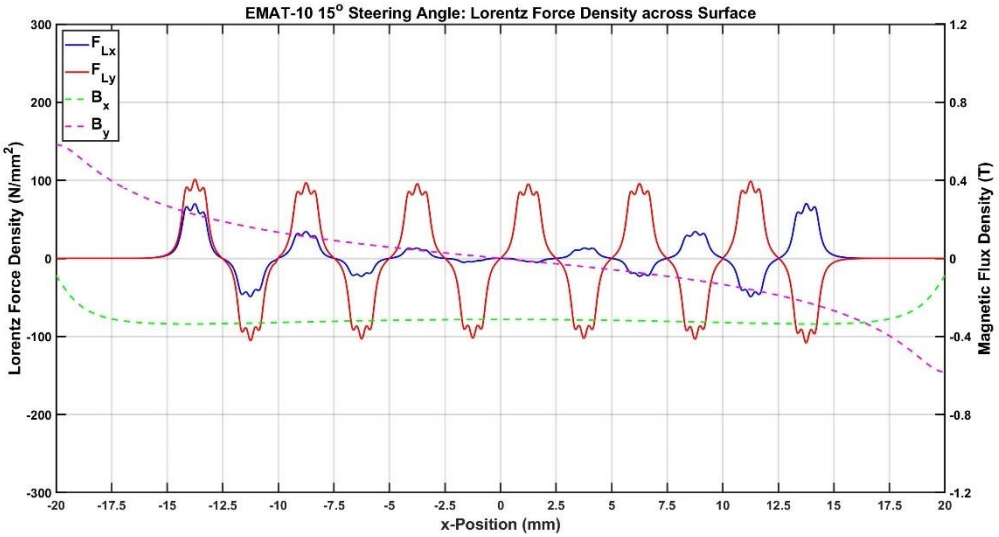

Figure 5.57: Plots of Lorentz Force Density Components across Surface for EMAT-10

Despite EMATs 9 & 10 being thought of as two six-coil EMATs due to their distributions of x-component of Lorentz force densities, they transmit a different number of split-waves. Initially, the number of split-waves for both EMATs was counted as two, however a further inspection of their A-scans at the 90° reception angle for their 30° steering angles reveal this not to be the case. The number of split-waves at this steering angle was registered as four and two for EMATs 9 & 10 respectively, as seen in Figure 5.58.

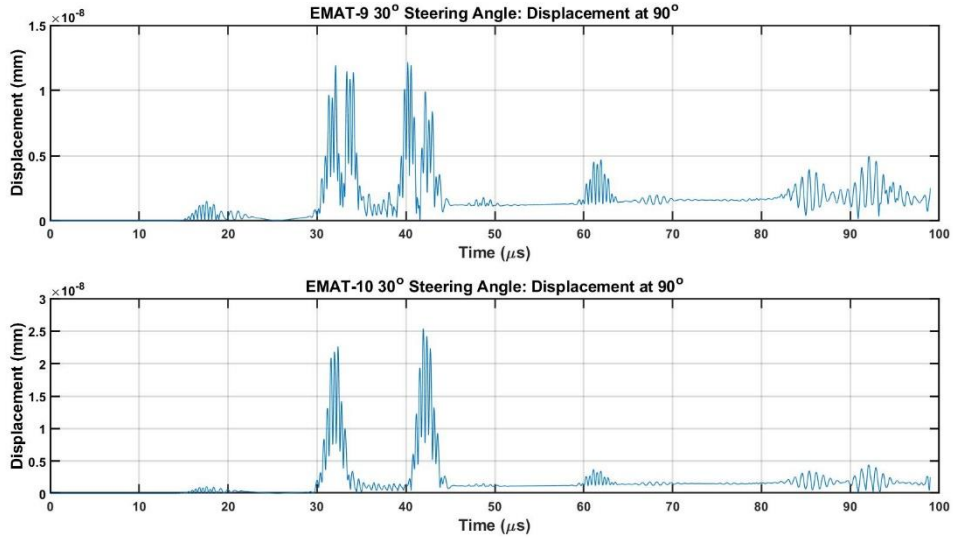

Figure 5.58: A-scans at 90° for EMAT-9 and EMAT-10 30° Steering Angle

EMATs 11 & 12 transmitted the same number of split-waves as EMAT-9, and the same is true for EMATs 13 & 14 for EMAT-10. The only difference between these configurations is the width of the magnetic configuration, and

thus the concentrations of magnetic flux density. The ToA for EMAT-10's two split-waves is approximate to the ToAs of EMAT-9's two outermost split-waves. This is due to their origin positions located at the ends of the coil array. EMAT-9's two innermost split-waves are due to the concentrations of magnetic flux density. EMAT-9's coil array is separated by these magnetic flux concentrations into the following sub-coil arrays: coils 1-2, coils 3-10, coils 11-12. It is from the ends of coils 3-10 that EMAT-9's two innermost split-waves had been transmitted.

Reviewing previous vertical magnetic configurations at a 30° steering angle revealed more split-waves than initially recorded. These additional split-waves were found at a higher frequency, as decreasing the frequency merged split-waves. Across the magnetic configurations, the ToA of the first and last split-wave was constant (aside for simulation errors) due to their origin positions at the ends of the coil array. Additional split-waves were due to the number of sub-coil arrays, as well as their position. The number of split-waves generated therefore was equal to the number of sub-coil ends within the coil array. The only exception to this were sub-coil arrays of only two coils, as these merged into one wave.

Due to the similarity of their magnetic fields, the results from EMATs 11 & 12 show the same pattern of behaviour as those from EMAT-9, and the same is true for EMATs 13 & 14 regarding EMAT-10. For this reason, the results from EMATs 11-14 are not discussed in this section and are recorded in Appendix C. A summary of results from these magnetic configurations and their relevant data is shown in Table 5.2.

Table 5.2: Magnetic Configurations Summary

EMAT	Magnet Layups (mm)	Shear Wave of Maximum Displacement			Maximum Reception Angle (°)	Maximum Displacement (mm x10^{-8})	
		Steering Angle (°)	Reception Angle (°)	Beamwidth Reception Angle (°)		Shear Wave	Rayleigh Wave
1	20	31	33.9	14.7	61.1	6.44	21.22
2	40	32	35.2	18.4	64.2	5.13	14.42
3	20-20	33	40.1	22.2	60.0	8.22	41.42
4	10-20-10	31	34.4	19.6	60.9	8.23	30.94
5	10	31	35.5	17.1	53.8	5.17	14.55
6	10-10	30	38.7	23.9	54.3	6.14	22.26
7	10-10-10	28	35.9	28.5	50.0	5.85	14.35
8	10-10-10-10	90	51.0	33.6	51.0	5.57	20.14
9	20	33	40.8	24.3	64.7	5.32	28.38
10	20-20	39	44.2	21.6	67.6	4.03	25.99
11	10	33	40.9	24.5	61.9	4.08	20.85
12	10-10 (v)	31	40.4	25.7	61.4	2.87	12.78
13	10-10 (h)	39	44.2	21.4	67.6	2.57	16.56
14	10-10-10-10	44	46.7	25.0	64.8	1.10	6.85

5.4. Beam Steerability with Alternate Magnetic Configuration

As with EMAT-1, experimental testing was performed using one of the alternate magnetic configurations from Sections 5.2-5.3, to ensure the accuracy of the simulated reception signal method (described in Section 4.4.2) for alternate EMAT configurations. The experimental validation was done using the beam steerability setup described in Sections 4.2 and 4.4 for the same steering angles. The configuration chosen for testing was EMAT-3 due to its large

maximum shear and Rayleigh wave displacements and its use in other academic literature [73]. Pei et al [73] compared the use of modified EMATs in a PC setup and concluded that replacing the single magnet EMATs with ones of two alternating magnets (akin to EMAT-3's design) improved the peak-to-peak voltage amplitude of the received Rayleigh wave signal by a factor of ~5.3.

EMATs 1 & 3 as transmitter and/or receiver was used not only to analyse the shear wave backwall profile in the same manner as Section 4.4, but also how the different magnetic configuration affected its amplitude and beam-spread. Comparisons were made between the simulated displacement magnitudes, the experimental signals, and the simulated signals. Figure 5.59-Figure 5.62 show the shear wave backwall profiles for these three datasets, for a given PC configuration at a 30° steering angle.

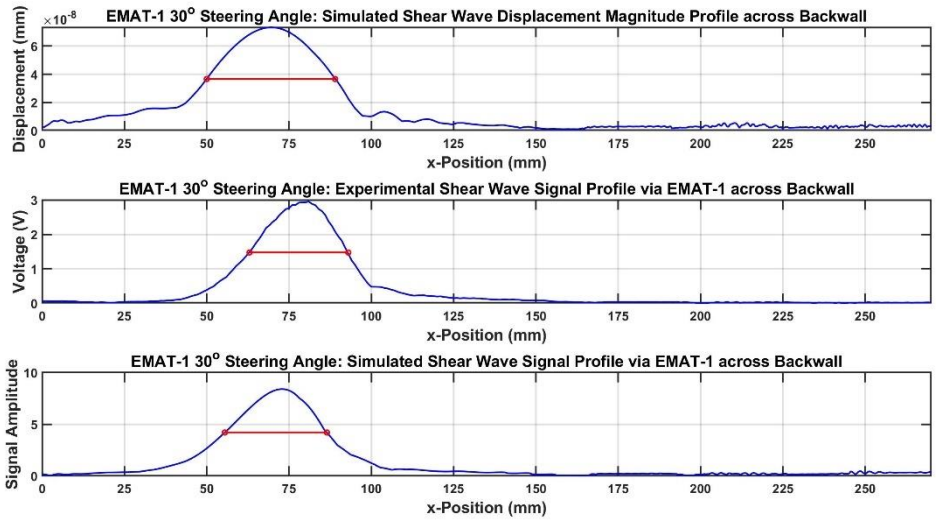

Figure 5.59: Shear Wave Profiles for EMAT-1 30° Steering Angle to EMAT-1

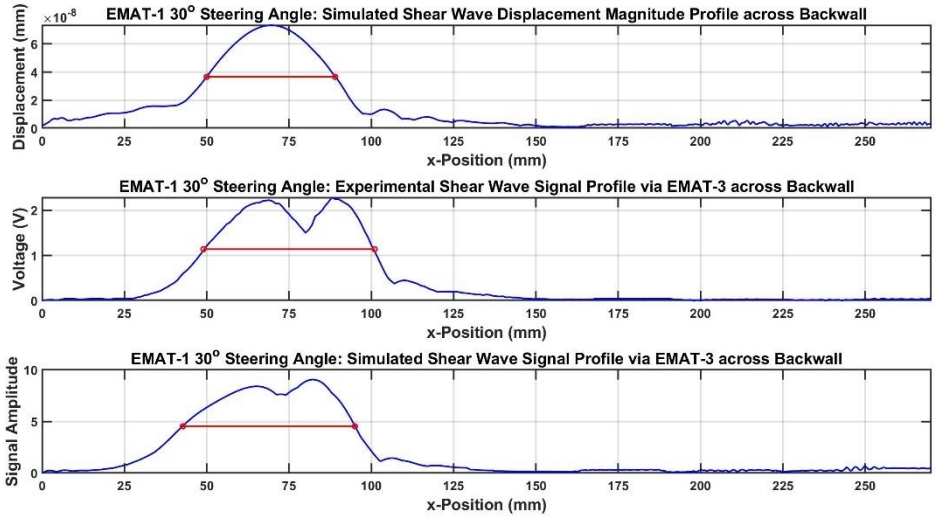

Figure 5.60: Shear Wave Profiles for EMAT-1 30° Steering Angle to EMAT-3

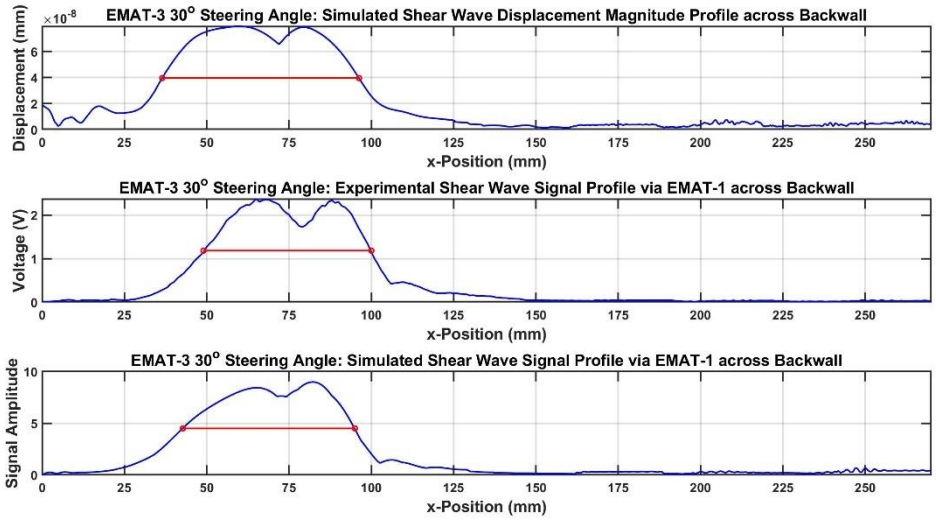

Figure 5.61: Shear Wave Profiles for EMAT-3 30° Steering Angle to EMAT-1

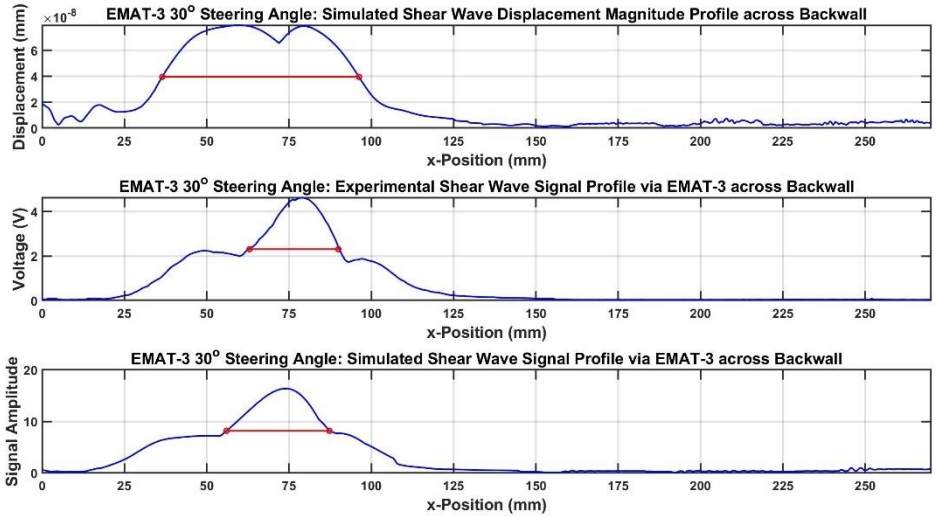

Figure 5.62: Shear Wave Profiles for EMAT-3 30° Steering Angle to EMAT-3

There is obviously no change in simulated displacement between different R_xs, however its backwall profile is closer in shape to those recorded by the experimental EMAT-1 R_x's for a given T_x. When using different EMAT configurations in a PC setup, there are two distinct peaks in both the experimental and simulated signal profiles. A summary of each dataset's profile peak data for all PC setups is shown in Table 5.3, where the values and positions of the two peaks (if present) are recorded.

From Section 4.3.1, the shear wave beam directivity for EMAT-1's 30° steering angle was measured as a single lobe angled at 33.4°, thus the profile's peak was expected at an x-position of 66mm. For EMAT-3, the distinct shear wave lobes were angled at 26.3° and 38.8°, suggesting profile peaks at x-positions of 49mm and 80mm respectively. The simulated displacement results

in Table 5.3 support this for both T_x configurations. The differences between these estimated and measured x-positions for both T_x's was attributed to the lobes striking the flat backwall at an angle rather than normal to a curved surface.

Table 5.3: Shear Wave Backwall Profile Data for EMAT PC Setups at 30° and 90° Steering Angles

EMAT PC Setup		**1-1**	**1-3**	**3-1**	**3-3**
Simulated Displacement	**Maximum Magnitude (mm)**	7.3291×10^{-8}		7.9237×10^{-8}	
	x-Position of Peak 1 (mm)	69.75		59.00	
	x-Position of Peak 2 (mm)	-		79.75	
Experimental Signal	**Maximum Amplitude (V)**	3.35	3.00	3.00	5.20
	x-Position of Peak 1 (mm)	81	88	65	79
	x-Position of Peak 2 (mm)	-	69	88	-
Simulated Signal	**Maximum Amplitude**	8.40	9.06	8.99	16.37
	x-Position of Peak 1 (mm)	72.75	82.25	82.25	73.75
	x-Position of Peak 2 (mm)	-	65.50	65.50	-
Maximum Rayleigh Wave Simulated Displacement at 160mm on Surface (mm)		8.4731×10^{-8}		1.6412×10^{-7}	
Maximum Rayleigh Wave Experimental Signal Amplitude at 160mm on Surface (V)		1.52	2.05	2.02	3.27
Maximum Rayleigh Wave Simulated Signal Amplitude at 160mm on Surface		5.91	7.15	7.36	14.25

For EMATs 1-1, the difference in profile peak's x-positions between the simulated displacement and the experimental datasets (69.75mm and 81mm respectively) is approximately 10mm: the same distance from the centre of the EMAT to the magnetic flux concentration at the corner of the single magnet. A shear wave UT probe was used across the backwall to confirm this, measuring the profile peak at an x-position of 70mm. This means that EMAT-1's profile peak x-position offset is due to the design of R_x.

There is little difference between the experimental results for EMATs 1-3 and EMATs 3-1, with peaks measured at 65/69mm and 88mm. Additionally the simulated signal profiles for these two setups had a correlation coefficient

of 0.9999. This suggests that the backwall profile is the same for a PC setup of two different EMAT configurations, regardless of which was transmitter or receiver. The distance between the two experimental peaks is approximately 20mm, the same width as the magnets used in both EMAT configurations. As previously mentioned in Section 5.2.2, EMAT-3 can be considered as being composed of two sub-EMATs, positioned 20mm apart. This explains why the single lobe transmitted from EMAT-1 was recorded as two peaks, as it was recorded by each sub-EMAT as R_x moved across the backwall. This also explains the two profile peaks for EMATs 3-1 as each sub-EMAT produced a single lobe that was read by EMAT-1 (with an approximate 10mm offset).

For EMATs 3-3, the largest of the simulated displacement's two peaks was at 59mm. This is likely due to the main lobe at 38.8° having a greater distance to cover and thus was more attenuated than its shallower lobe. There is little difference in profile peak x-positions between the simulated displacement and the experimental signal datasets (79.75mm and 79mm respectively), while the experimental data only recorded a single peak at 79mm. Despite recording a single peak, the experimental profile shows two smaller peaks on either side of the main peak below the -6dB threshold, located at 49mm and 97mm. These two additional peaks are due to mismatches between T_x's two shear wave lobes and R_x's two sub-EMATs. The voltage at which the main peak was recorded is greater than EMATs 1-1's single peak by a SF of ~1.55. This is explained by the two sub-EMATs from R_x matching the two shear wave beams transmitted by the two sub-EMATs from T_x.

For all PC setups, the x-positions at which R_x measured the experimental or simulated peaks suggests that the two transmitted shear wave lobes are detected by the concentrations of magnetic flux density on the left-hand side of R_x. This explains the 10mm offset for EMATs 1-1 and the 20mm distance between peaks for EMATs 1-3 & 3-1. Figure 5.64 shows illustrations of these T_x-R_x mismatches to better explain their impact on the shear wave backwall profile peaks.

The magnitude of the Rayleigh waves at the 90° steering angle from the sample's surface was also measured to see if similar conclusions could be

drawn for these PC EMAT setups as to those from Pei et al [73]. In keeping with this, R_x was positioned 160mm away from T_x on the surface of the rectangular sample. The peak amplitude for each dataset is also included in Table 5.3. Replacing EMAT-1 with EMAT-3 for R_x increased the peak amplitude of the Rayleigh waves by a SF of ~1.35. By replacing EMAT-1 with EMAT-3 for T_x, the peak amplitude recorded by EMAT-1 increased by a SF of ~1.33. Finally, by replacing EMAT-1 with EMAT-3 as both T_x and R_x, the SNR of the EMAT PC system increased by an overall SF of ~2.15.

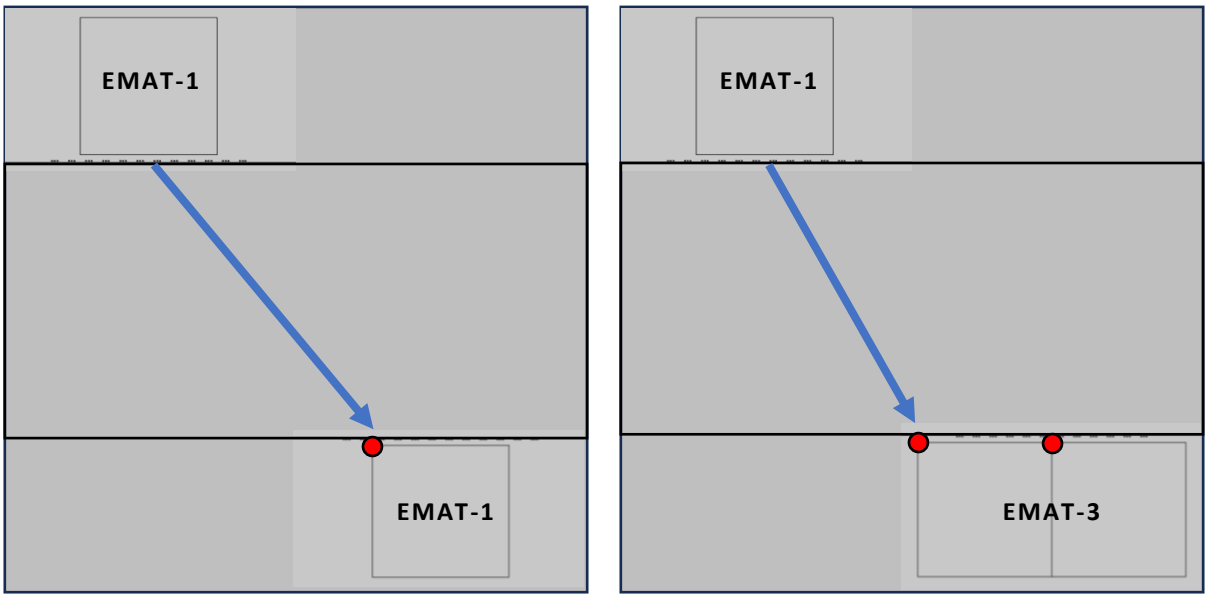

Figure 5.63: EMAT PC Mismatch for EMAT-1 30° Steering Angle Beam Steerability. The blue arrows indicate shear wave lobes and the red dots indicate concentrations of magnetic flux density

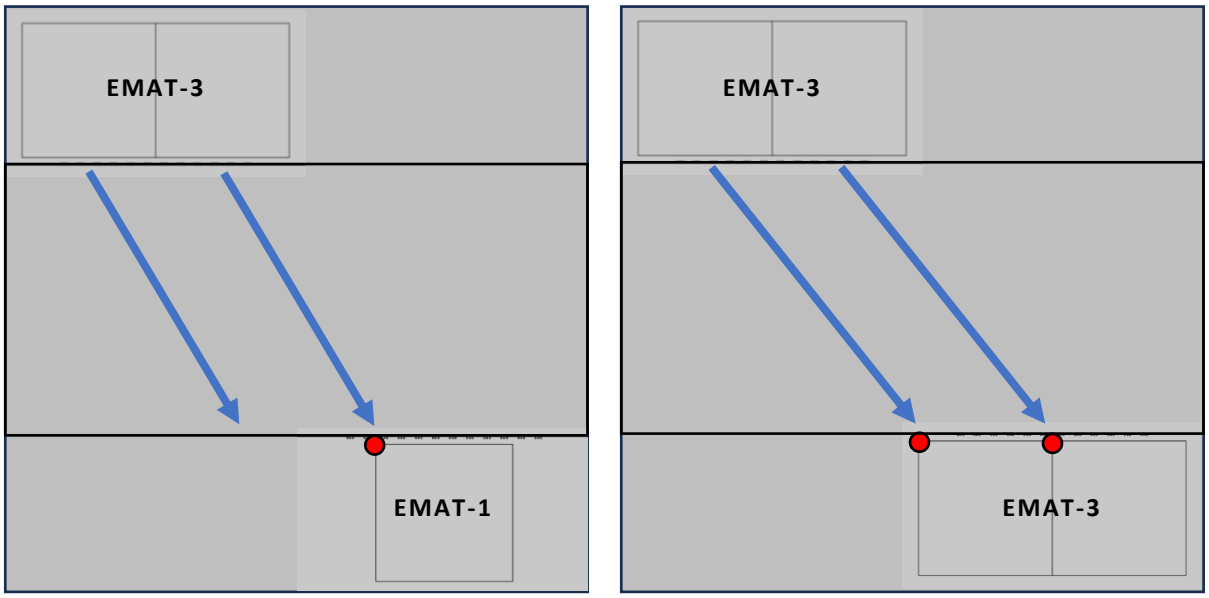

Figure 5.64: EMAT PC Mismatch for EMAT-3 30° Steering Angle Beam Steerability. The blue arrows indicate shear wave lobes and the red dots indicate concentrations of magnetic flux density

The differences between these SF enhancements and those listed in Pei et al [73] were attributed to the many differences in the experimental setups. These differences include: the dimensions; the materials; the lift-offs for both the magnet and MLC; the current signals driving the EMAT; and the data analysis methodology. While the exact values differ between these two studies, the overall point stands that an EMAT PC setup can be enhanced by alternative magnetic configurations with a greater concentrations of magnetic flux density.

The SF values for the 30° steering angle's experimental signals show a decrease from EMATs 1-1 when using different EMATs within the same PC setup. This was not the case for the simulated signals which show a small increase. Exchanging EMAT-1 for EMAT-3 as both T_x and R_x for the simulated signals caused a far greater SF increase of ~1.95 compared to the experimental signal's SF of ~1.55. The difference in these SF increases was attributed to the previously discussed issues present in the simulated signal's calculated amplitude. The amplitude enhancements of the simulated Rayleigh wave signals however correlate well with those of the experimental signals. The SF increases from EMATs 1-1 for EMATs 1-3, 3-1, & 3-3 were calculated at 1.21, 1.25, & 2.41 respectively.

While the SFs for the simulated signals vary, they do however follow similar trends to those of the experimental testing. The simulated signal method demonstrates that it is capable of calculating whether an alternate magnetic configuration can increase the SF of the PC setup. From the simulated model of EMAT-1 at a 30° steering angle, backwall profiles were constructed using the simulated signal method with the alternative magnetic configurations listed in Sections 5.2 and 5.3.

Figure 5.65 shows the amplitudes from these profile peaks and found that EMAT-4 would increase the SF of the system by an even greater value. The same was true for the reception of Rayleigh waves at the 90° steering angle, also in Figure 5.65. Additionally, Figure 5.66 shows the reception angles and beam-spread of these profile peaks. These are compared to the experimental beam-spread to observe their accuracy. The increased amplitude from EMAT-4 is due to its similar design to that of EMAT-1, with the 10mm-wide magnets on

either side of the 20mm-wide central magnet increasing the concentrations of magnetic flux density at the corners. This explains why there is also little variation in the reception angle and beam-spread.

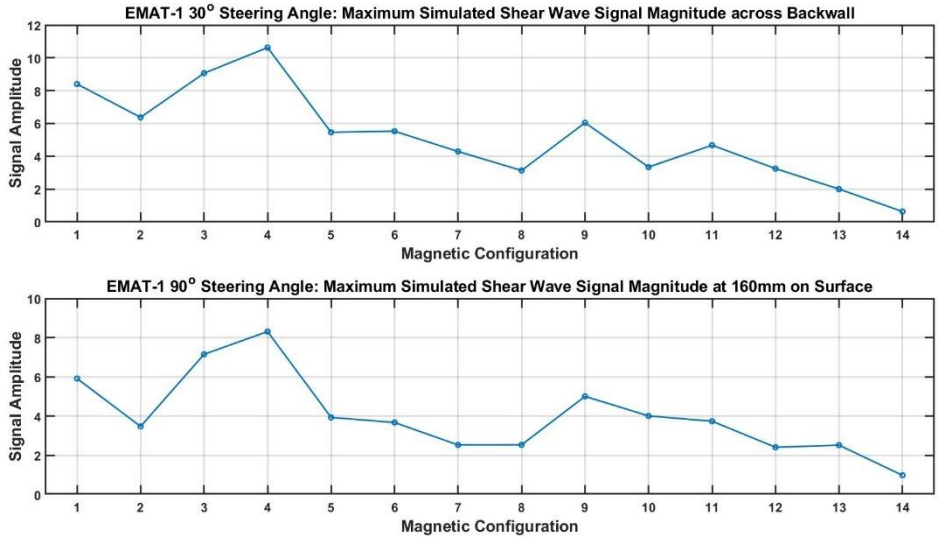

Figure 5.65: Simulated Signal Amplitudes from EMAT-1 30° and 90° Steering Angles

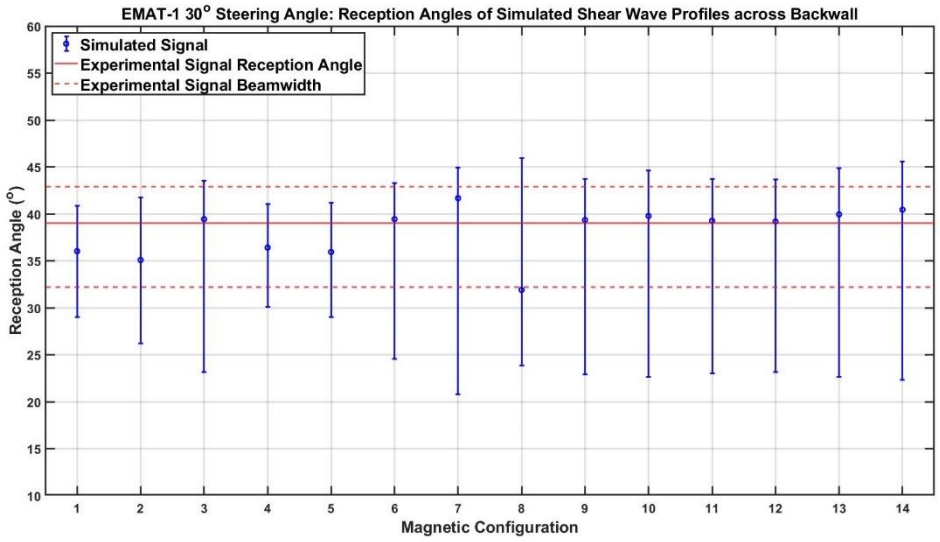

Figure 5.66: Simulated Signal Reception Angles from EMAT-1 30° Steering Angle

Further simulations were performed with different magnetic configurations for T_x at a 30° steering angle. The backwall profiles were constructed using the simulated signal method, and the maximum amplitudes are shown in Figure 5.67 as a matrix colour-plot. The PC setups which produced the greatest signal amplitudes are: EMATs 3 & 4 to EMATs 1, 3, 4, 6 & 9; and EMATs 7 & 8 to EMATs 7 & 8, with EMATs 3-3 being the maximum. The symmetry in Figure 5.67 lends credence to the earlier suggestion that the same backwall profile is produced when the two different EMATs are exchanged in a PC setup. There are discrepancies in the matrix colour-plot's symmetry

(particularly with EMAT-6), however this is likely due to errors in the simulated signal's amplitude calculation. The same process was also performed on EMAT PC setups at a 90° steering angle for Rayleigh waves across the surface, shown in Figure 5.68. Like with the backwall profile, the greatest amplitudes arose from: EMATs 3 & 4 to EMATs 1, 3, 4, 9 & 10; and EMATs 9 & 10 to EMATs 3, 4, 9 & 10, with EMATs 3-3 being the maximum.

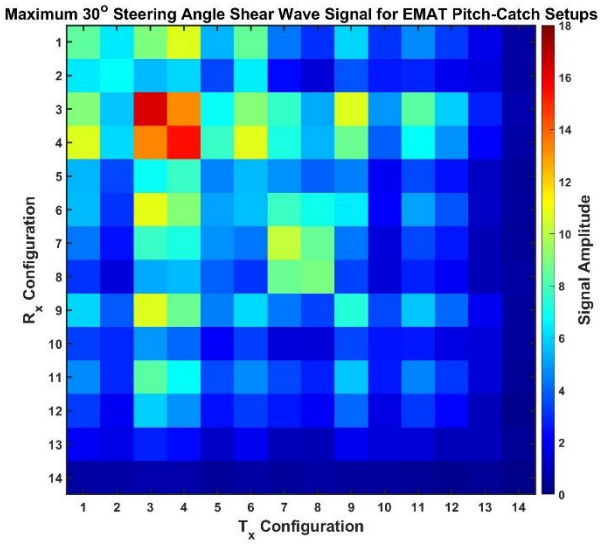

Figure 5.67: Simulated Signal Amplitudes for all EMAT PC Setups at 30° Steering Angle

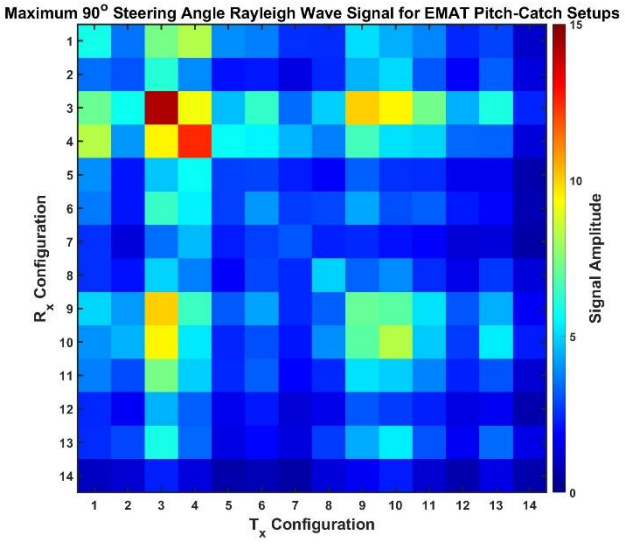

Figure 5.68: Simulated Signal Amplitudes for all EMAT PC Setups at 90° Steering Angle

For all PC setups at a 30° steering angle, the correlation coefficient increase when comparing the simulated signal's profile peaks to those of the experimental signal's, rather than the simulated displacements. Table 5.4-Table 5.6 show these correlation coefficients for the shear wave backwall profiles across steering angles for a given PC setup. In keeping with Table 4.2, these correlations include both the direct and reflected shear wave profiles.

Table 5.4: Experimental Validation Correlations for EMATs 1-3

Steering Angle (°)	Direct Shear Wave Correlation		Reflected Shear Wave Correlation	
	Displacement Magnitude	Simulated Signal	Displacement Magnitude	Simulated Signal
20	0.9550	0.8343	0.7914	0.8263
25	0.9419	0.9306	0.4197	0.5223
30	0.8996	0.9463	0.5938	0.6808
35	0.8254	0.8891	0.8076	0.6518
40	0.7873	0.8399	0.8584	0.6639
45	0.6874	0.8558	0.8808	0.8680
50	0.6074	0.8992	0.8873	0.9767
55	0.6276	0.9495	0.8769	0.9631
60	0.5494	0.9541	0.8662	0.9600
90	-0.2283	0.9326	0.5430	0.8043

Table 5.5: Experimental Validation Correlations for EMATs 3-1

Steering Angle (°)	Direct Shear Wave Correlation		Reflected Shear Wave Correlation	
	Displacement Magnitude	Simulated Signal	Displacement Magnitude	Simulated Signal
20	0.8817	0.8528	0.7753	0.8149
25	0.9057	0.9319	0.4548	0.4799
30	0.9168	0.9586	0.6613	0.6321
35	0.8874	0.9182	0.6692	0.5730
40	0.8829	0.9022	0.6688	0.6090
45	0.8181	0.9316	0.7924	0.8629
50	0.8186	0.9618	0.8871	0.9751
55	0.8161	0.9789	0.9352	0.9844
60	0.6640	0.9650	0.9122	0.9729
90	-0.2625	0.9671	0.5508	0.7745

Table 5.6: Experimental Validation Correlations for EMATs 3-3

Steering Angle (°)	Direct Shear Wave Correlation		Reflected Shear Wave Correlation	
	Displacement Magnitude	Simulated Signal	Displacement Magnitude	Simulated Signal
20	0.9248	0.8500	0.8773	0.8595
25	0.9204	0.9400	0.5724	0.5498
30	0.9209	0.9555	0.6436	0.6794
35	0.8995	0.9219	0.5637	0.6213
40	0.8833	0.8788	0.7133	0.7648
45	0.8587	0.8867	0.8355	0.8873
50	0.8546	0.9414	0.9175	0.9723
55	0.7931	0.9671	0.9341	0.9804
60	0.6540	0.9676	0.9083	0.9708
90	-0.2985	0.9746	0.5503	0.8034

Table 5.4-Table 5.6 exhibit a similar trend to those in Table 4.2: a general improvement in correlation coefficient when using the simulated signal results over the simulated displacement results. There are more instances of where using the simulated signal decreases the correlation coefficient however, most notably at the lower steering angles of 20-25° for the direct shear wave profiles. This is explained by Figure 5.69, which shows all three shear wave backwall profiles from EMATs 1-3 for the 20° steering angle.

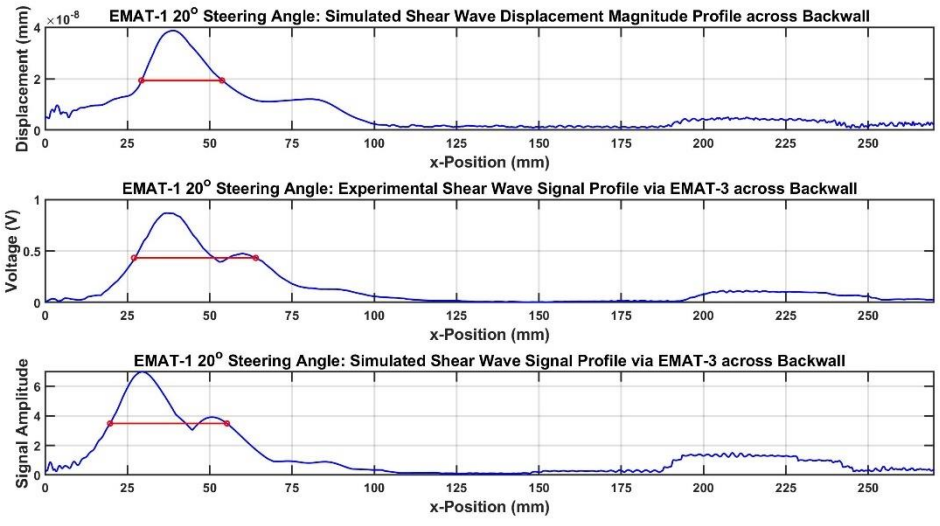

Figure 5.69: Shear Wave Profiles for EMAT-1 20° Steering Angle to EMAT-3

It is noticeable that the simulated signal's profile closer resembles the experimental signal's profile in shape rather than the simulated displacement's, yet it has a lower correlation coefficient calculated for it. This is due to the large difference in x-positions between the maximum peaks of the three datasets. By shifting these three profile plots to align their maximum peaks at the same x-position, the correlation coefficient for the simulated signal and displacement compared to the experimental signal data increases from 0.9529 to 0.9838 respectively. This explains why many of the correlation coefficients decrease when changing the profile dataset.

Figure 5.70-Figure 5.75 show the reception angles and beam-spreads for both the simulated displacement and simulated signals compared to the experimental signals across steering angles, for a given PC configuration. Following the conclusions drawn by comparing Figure 4.86 to Figure 4.98, the shear wave profile's beam-spread tends to become narrower for the simulated signal than for the displacement. This is not the case for the 20° steering angle however, as the beam-spread widens to closer resemble the beam-spread length of the experimental testing. Additionally the simulated signal enables the beam-spread to be drawn for the 90° steering angle.

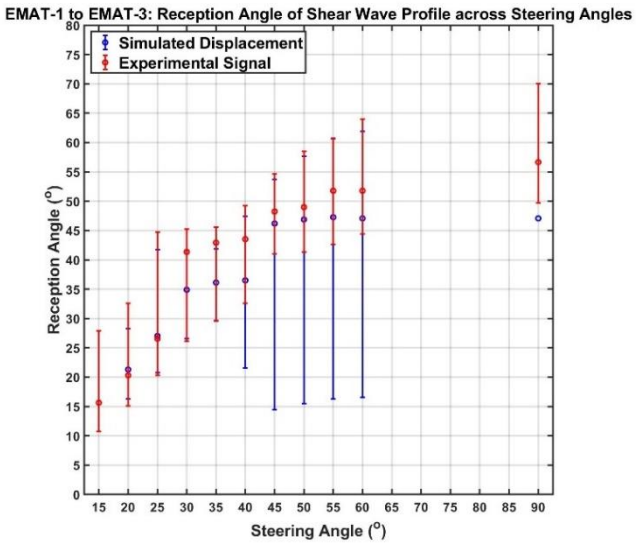

Figure 5.70: Shear Wave Displacement Magnitude Profile's Reception Angle across Steering Angles for EMATs 1-3

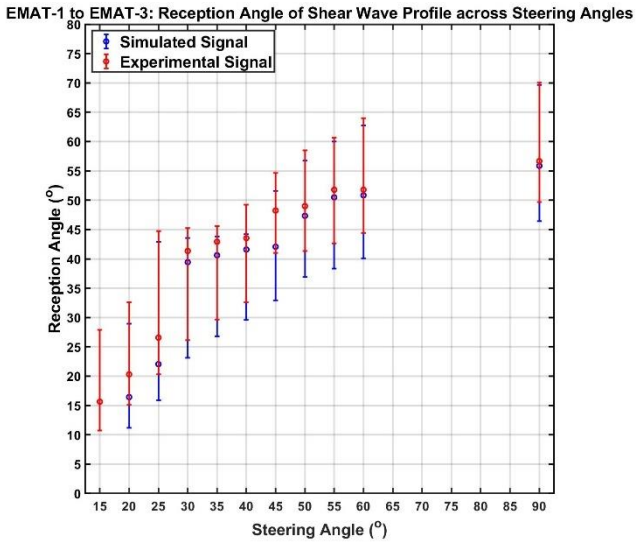

Figure 5.71: Shear Wave Simulated Signal Profile's Reception Angle across Steering Angles for EMATs 1-3

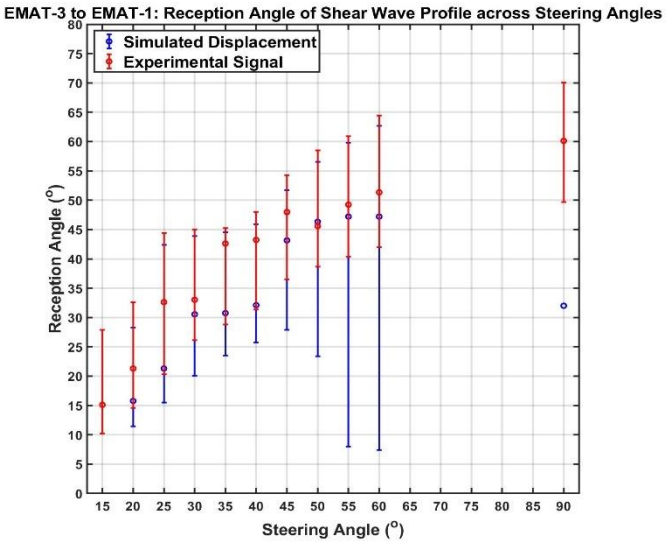

Figure 5.72: Shear Wave Displacement Magnitude Profile's Reception Angle across Steering Angles for EMATs 3-1

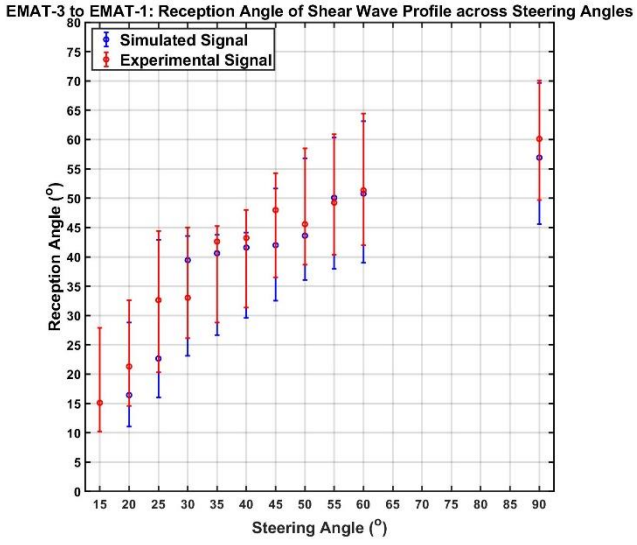

Figure 5.73: Shear Wave Simulated Signal Profile's Reception Angle across Steering Angles for EMATs 3-1

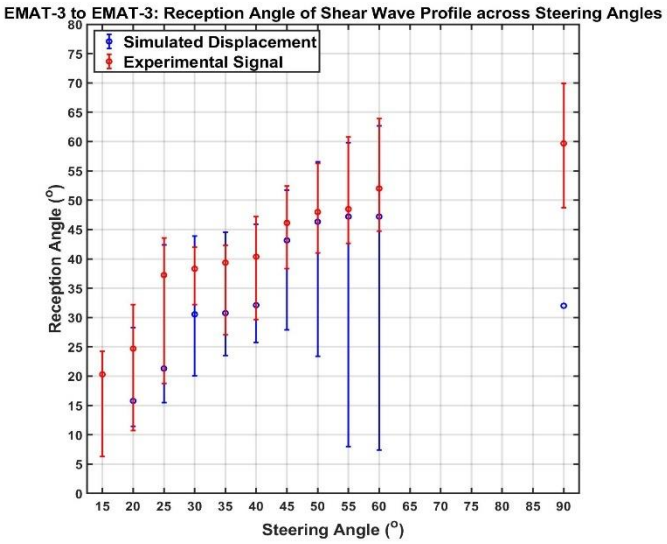

Figure 5.74: Shear Wave Displacement Magnitude Profile's Reception Angle across Steering Angles for EMATs 3-3

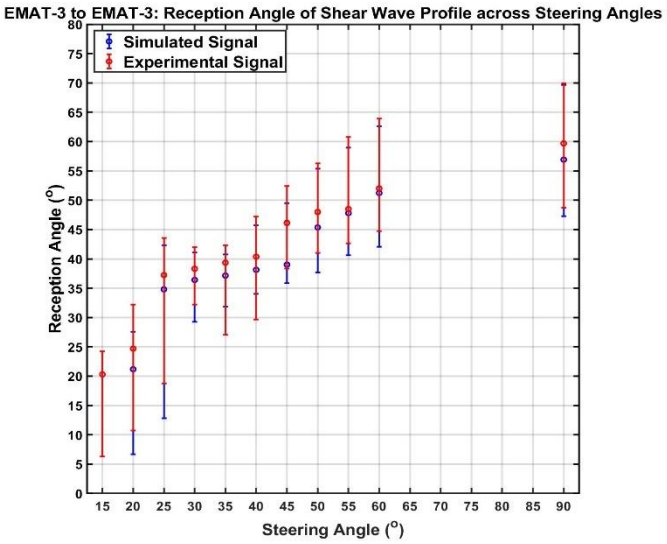

Figure 5.75: Shear Wave Simulated Signal Profile's Reception Angle across Steering Angles for EMATs 3-3

Figure 5.76-Figure 5.79 shows the normalised maximum amplitudes for the three datasets, for all four PC setups respectively. Following the skew correction stated in Section 4.4.2, the simulated signals were divided by their steering frequencies to counter the effects of the skew in magnitude at lower steering angles. These results show that the simulated signal's amplitude across steering angles is far closer in magnitude to those of the experimental signal's across the PC setups. The exception to this is at the 20° steering angle due to its higher frequency, even when corrected for this.

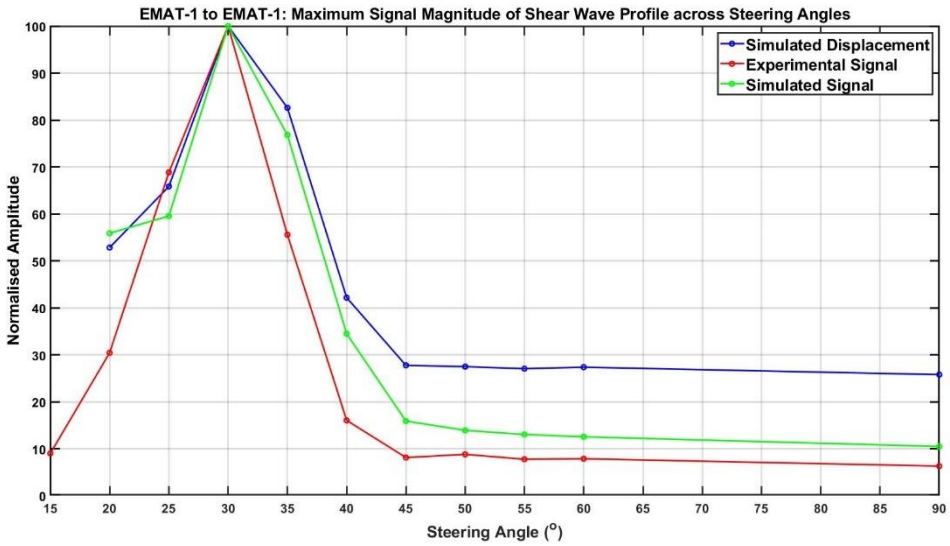

Figure 5.76: Plot of the Shear Wave Backwall Profile's Maximum Amplitudes across Steering Angles for EMATs 1-1

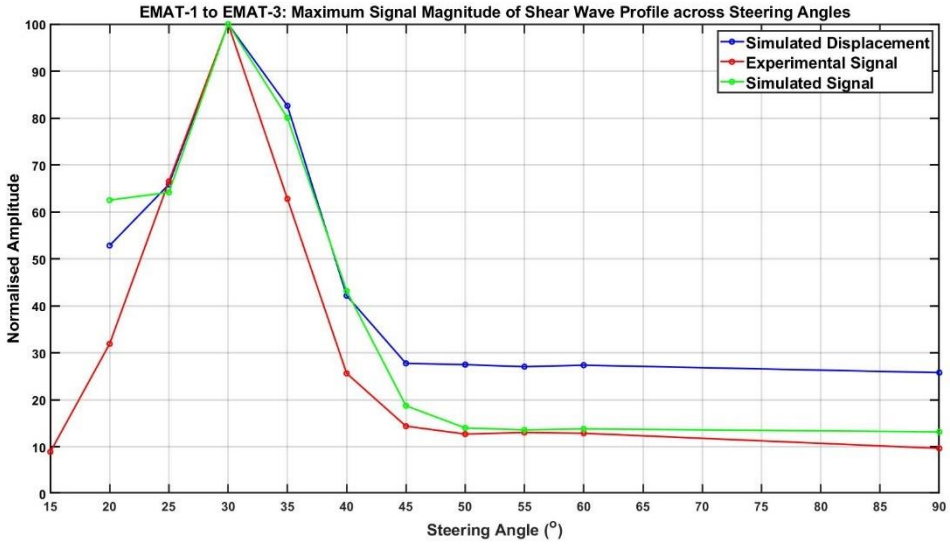

Figure 5.77: Plot of the Shear Wave Backwall Profile's Maximum Amplitudes across Steering Angles for EMATs 1-3

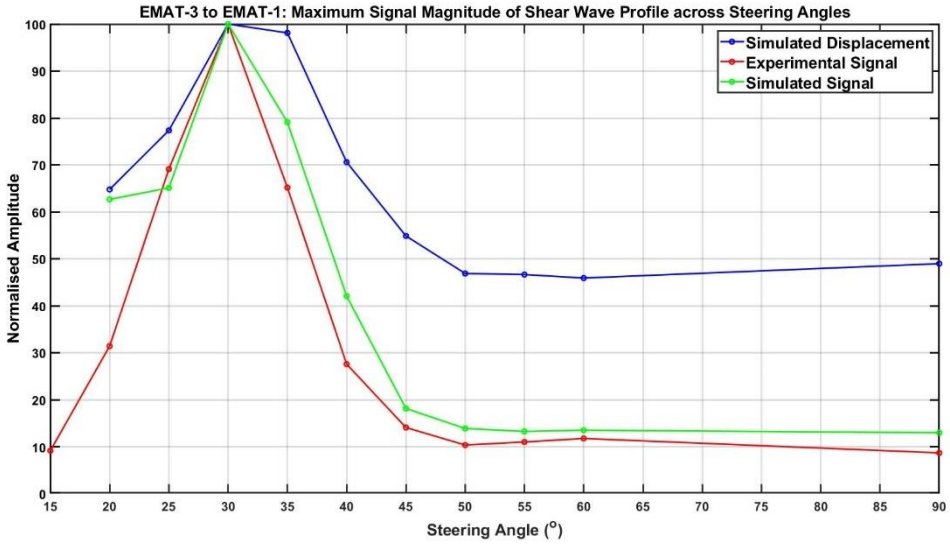

Figure 5.78: Plot of the Shear Wave Backwall Profile's Maximum Amplitudes across Steering Angles for EMATs 3-1

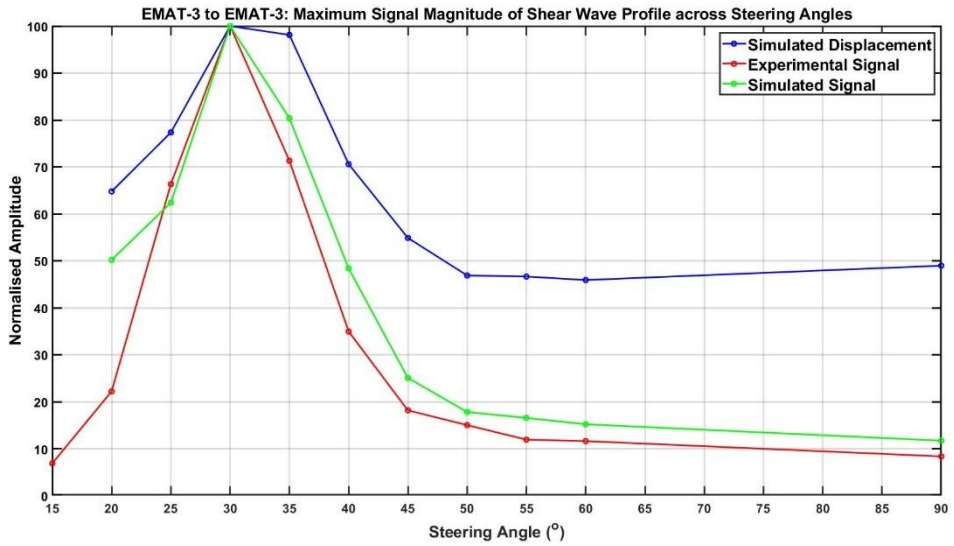

Figure 5.79: Plot of the Shear Wave Backwall Profile's Maximum Amplitudes across Steering Angles for EMATs 3-3

Table 5.7 summarises the correlation coefficients for the normalised amplitudes, reception angles, and beam-spread limits across the range of steering angles, for the two simulated datasets when compared to the experimental one.

Table 5.7: Overall Beam Steerability Correlation Results with differing EMAT PC Configurations

EMAT PC Setup		**1-1**	**1-3**	**3-1**	**3-3**
Maximum Amplitude	**Simulated Displacement**	0.9625	0.9788	0.9380	0.9517
	Simulated Signal	0.9481	0.9450	0.9506	0.9605
Reception Angle (°)	**Simulated Displacement**	0.9327	0.9652	0.7227	0.7147
	Simulated Signal	0.9932	0.9930	0.9375	0.9841
Beam-spread Lower Limit (°)	**Simulated Displacement**	-0.2323	-0.3980	0.0012	-0.0034
	Simulated Signal	0.9966	0.9911	0.9967	0.9625
Beam-spread Upper Limit (°)	**Simulated Displacement**	0.9957	0.9970	0.9961	0.9845
	Simulated Signal	0.9989	0.9955	0.9947	0.9967

5.5. Summary

This chapter compared the performances of the MLC EMAT based on different magnetic configurations. These various designs were assessed based upon their beam directivities, derived from the same simulated models as detailed in Chapter 4.

The magnetic configurations that generated the greatest shear wave magnitude tended to be those with concentrations of magnetic flux density within their coil array. This was achieved by changing the width of the magnet, or the number of magnets within the EMAT. The larger the magnetic flux density within the coil array, the greater the transduction efficiency for both transmission and reception of the ultrasonic waves.

Introducing concentrations of magnetic flux into the coil array's area of induced eddy current densities however inverted the directions of the magnetic flux density. This effectively turned the MLC EMAT into multiple sub-EMATs, each generating their own split-waves that superimposed onto neighbouring ones. While this could increase the magnitude of the shear waves, it also increased the number of sidelobes transmitted and thus beamwidth.

The capabilities of calculating the simulated signal within a reception EMAT was also tested with the alternate magnetic configurations. This method continued to provide an alternative method of measuring simulated data and even proved capable of assessing the optimal pairing of MLC EMATs within a PC setup.

Chapter 6 - Modified Coil Configurations

The previous chapter detailed the exploration of optimising the MLC EMAT through alternative magnetic configurations. This chapter seeks to explore modifications that could be made to the design of the EMAT's MLC. This would uncover whether the EMAT could be driven at a higher steering angle than the results from the previous two chapters.

6.1. Introduction

One of the prevailing conclusions from Chapter 5 was that the shear waves transmitted from the MLC EMAT tend to reach a steering limit of approximately 40°, and a maximum reception angle of approximately 60°. While the exact value fell within a range of 50-65° across the different magnetic configurations, the EMAT was incapable of transmitting beyond this angle. For the standard EMAT-1 configuration, the A-scans at these reception angles revealed that the shear waves from which the maximum displacement was derived came from the split-wave originating from the closer concentration of magnetic flux density (beneath corner of the EMAT). The other magnetic configurations show the same behaviour with the exception of magnetic configurations 3 & 7 due to their higher magnetic flux concentrations positioned beneath the centre of the EMAT.

To better explore the EMAT's steering limit and whether it could be surpassed, the model for studying the EMAT's beam directivity was adapted to investigate the effect that the coils have on the split nature of the shear waves. The primary difference with this model was the removal of the 'Magnetic Fields' physics interface, and thus its Multiphysics coupling to the 'Solid Mechanics' physics interface. This was done to replace the irregular magnetic flux density with a uniform one. A 'Body Load' domain was added to the 'Solid Mechanics' physics interface, constrained to the area of high-mesh density beneath the coils. The load type within this area was the force per unit volume (Lorentz force density) with an x-component equal to the induced eddy current density

multiplied by 1T (Equation 2.22), and a y-component equal to 0N/mm³. This (essentially created a uniform magnetic flux density equal to 1T in the vertical direction).

The three chosen parametric studies on the coil array were: the steering angle; the number of coils in the array; and the coil spacing. Within Chapters 4 and 5, the modelled Rayleigh waves overlapped with the shear waves at the semicircular aluminium sample's reception angles of 75-90°. The sample's radius in this model was therefore increased to 125mm, enabling measurement up to a reception angle of 80°. Initial simulations for the 5.0mm coil spacing at this radius value however showed that the Rayleigh waves still overlapped with the shear waves across most of the curved surface of the sample. Since the beam directivity plots were measured from the sample's curved surface every 0.1°, the solution to this problem was to make the radius of the sample proportional to the coil spacing (by a SF of 50). This not only allowed beam directivities up to reception angles of 80° for all coil spacing values, but it also relieved the burden of the even higher-mesh density from the 1.2mm coil spacing's increased frequency (in accordance with Equation 3.8). To reduce the computational runtime further, the simulation's end time was made proportional to the coil spacing (by a SF of 24μs/mm) to end immediately after the shear waves struck the sample's curved surface.

6.2. Steering Angle

The same steering angles of 15-60° at 5° intervals and 90° were used due to the little difference from steering angles of 65-85°. Figure 6.1-Figure 6.11 show the beam directivities for the twelve-coil arrays, spaced at 2.5mm, across the stated steering angles. The beam directivity plots for these simulations were constructed in the same manner as those in Section 4.3.1. Due to the semicircular sample's differing radii between coil spacings, the magnitude of displacement was replaced with amplitude, normalised to the largest displacement for a given coil spacing. Magnitudes therefore could not be compared across different coil spacings.

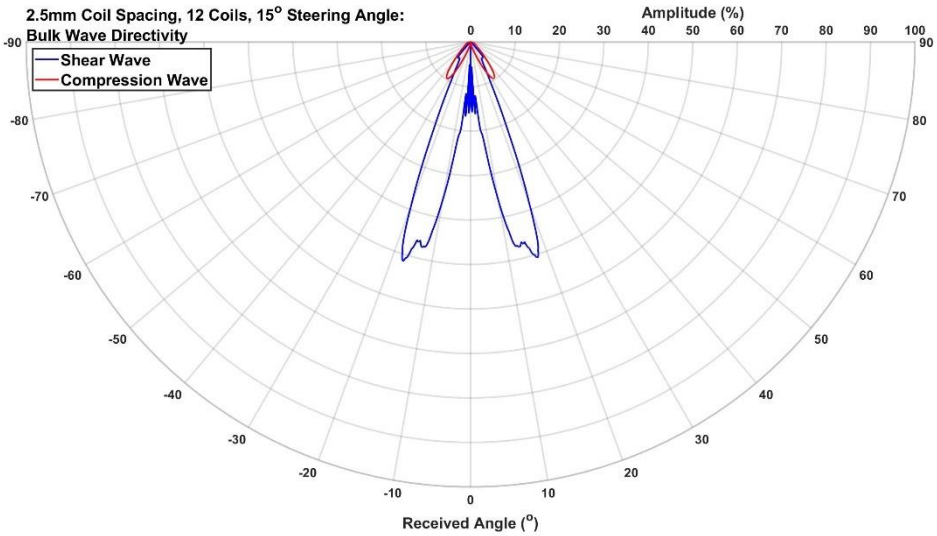

Figure 6.1: Bulk Wave Directivity Plot for 15° Steering Angle with 2.5mm Coil Spacing and 12 Coils

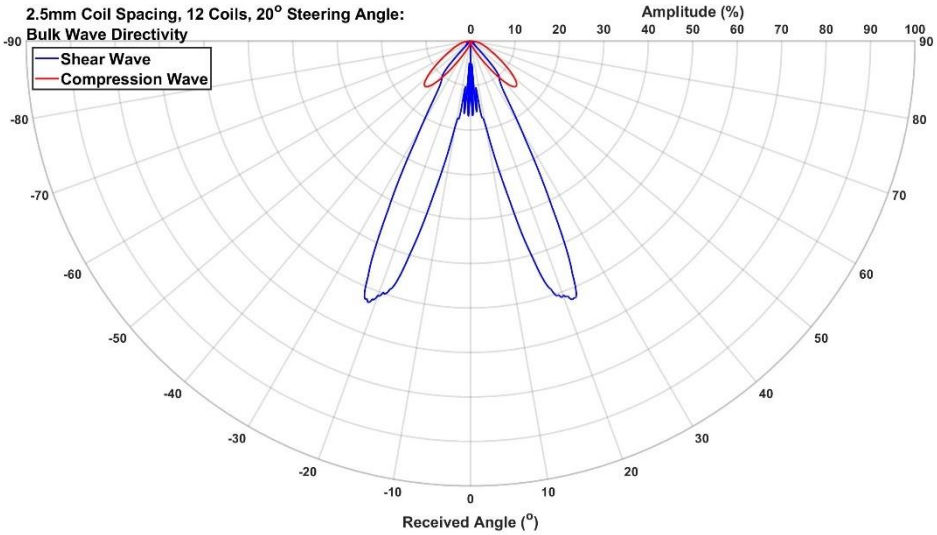

Figure 6.2: Bulk Wave Directivity Plot for 20° Steering Angle with 2.5mm Coil Spacing and 12 Coils

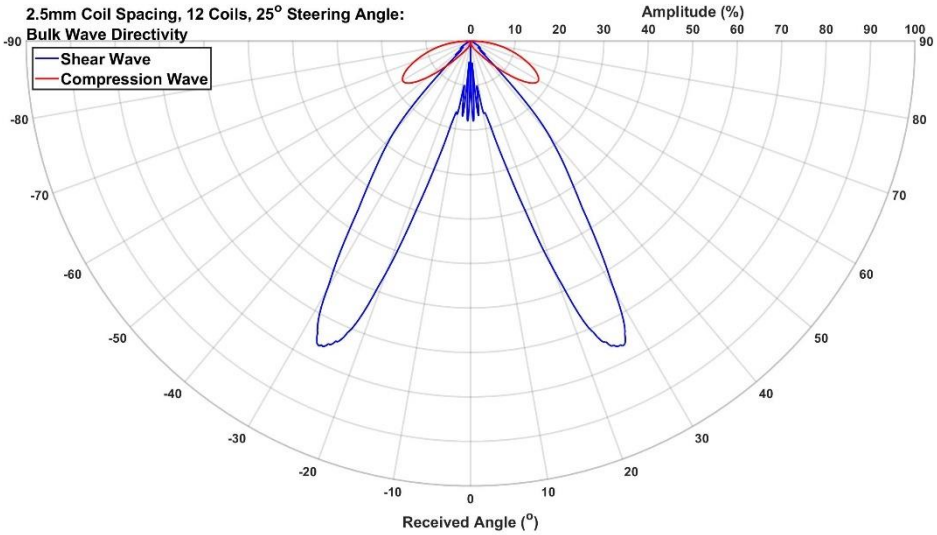

Figure 6.3: Bulk Wave Directivity Plot for 25° Steering Angle with 2.5mm Coil Spacing and 12 Coils

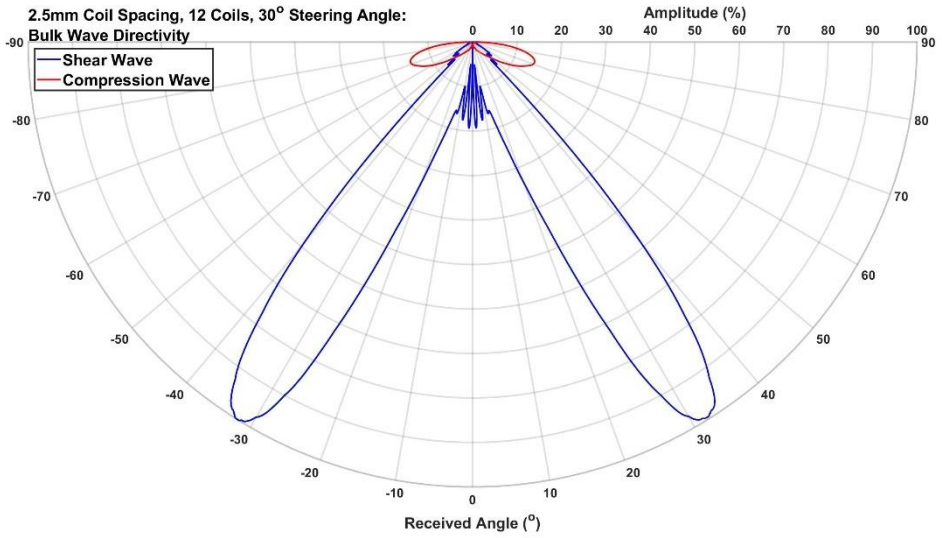

Figure 6.4: Bulk Wave Directivity Plot for 30° Steering Angle with 2.5mm Coil Spacing and 12 Coils

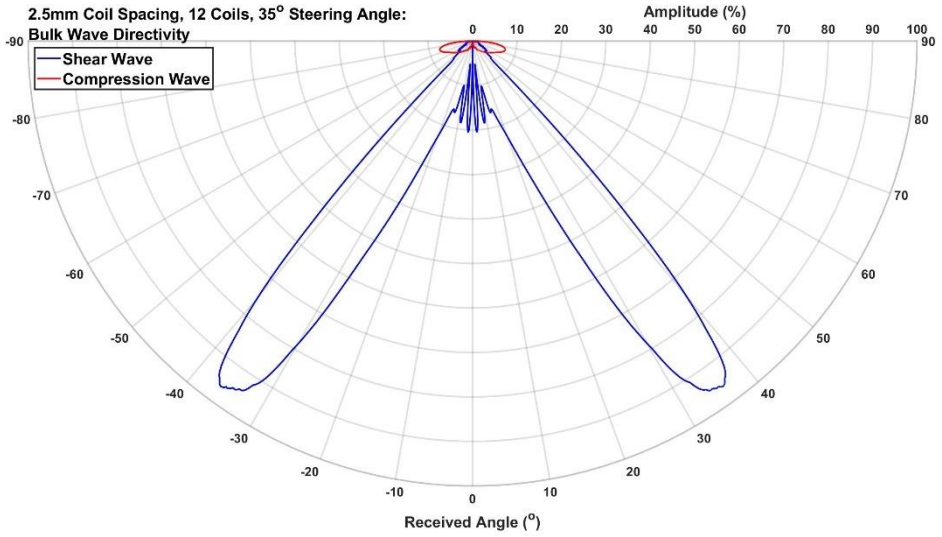

Figure 6.5: Bulk Wave Directivity Plot for 35° Steering Angle with 2.5mm Coil Spacing and 12 Coils

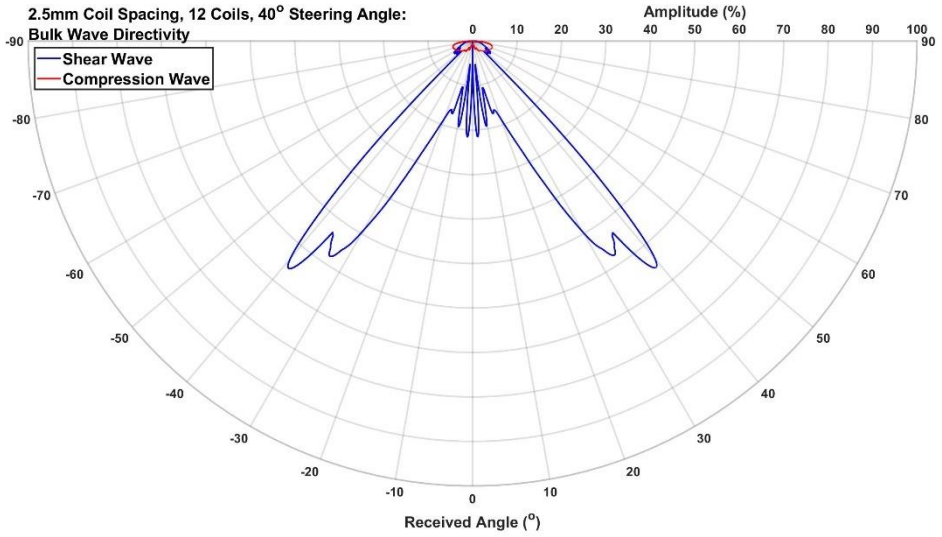

Figure 6.6: Bulk Wave Directivity Plot for 40° Steering Angle with 2.5mm Coil Spacing and 12 Coils

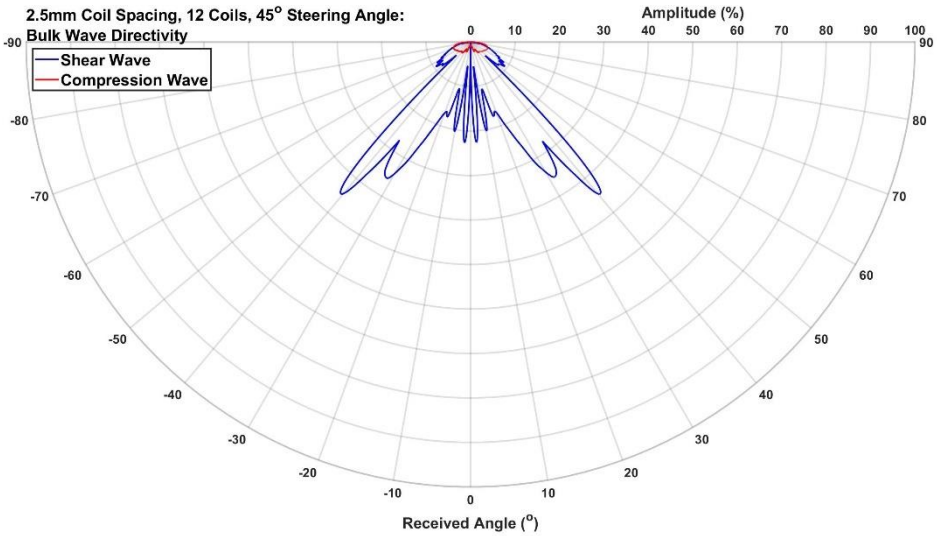

Figure 6.7: Bulk Wave Directivity Plot for 45° Steering Angle with 2.5mm Coil Spacing and 12 Coils

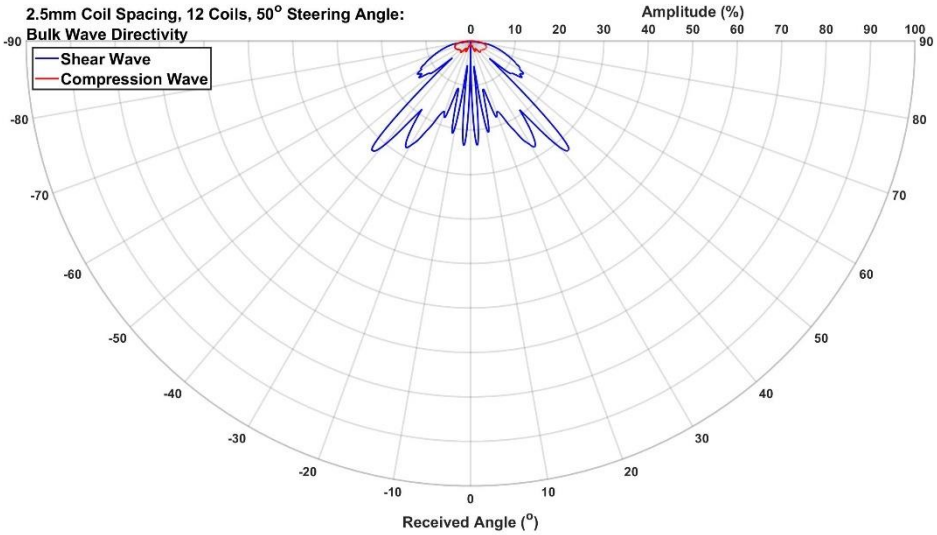

Figure 6.8: Bulk Wave Directivity Plot for 50° Steering Angle with 2.5mm Coil Spacing and 12 Coils

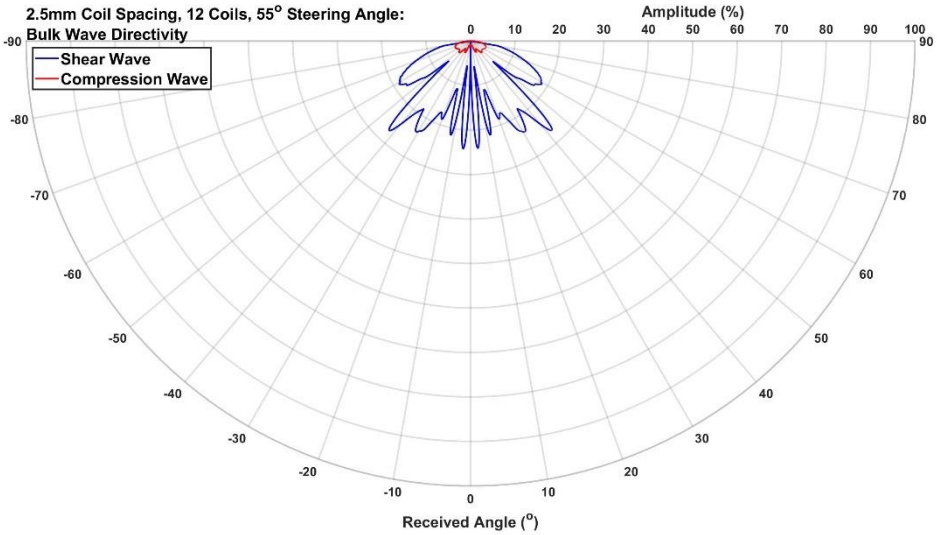

Figure 6.9: Bulk Wave Directivity Plot for 55° Steering Angle with 2.5mm Coil Spacing and 12 Coils

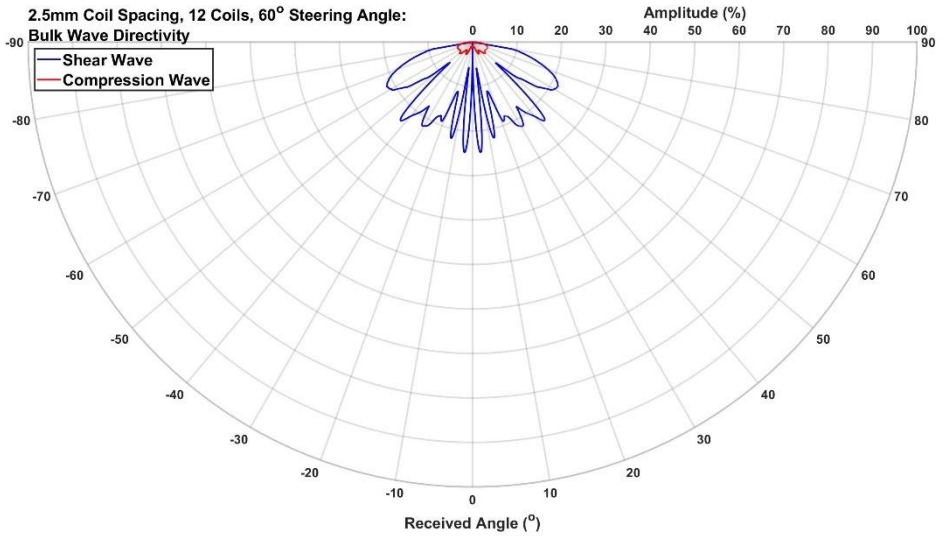

Figure 6.10: Bulk Wave Directivity Plot for 60° Steering Angle with 2.5mm Coil Spacing and 12 Coils

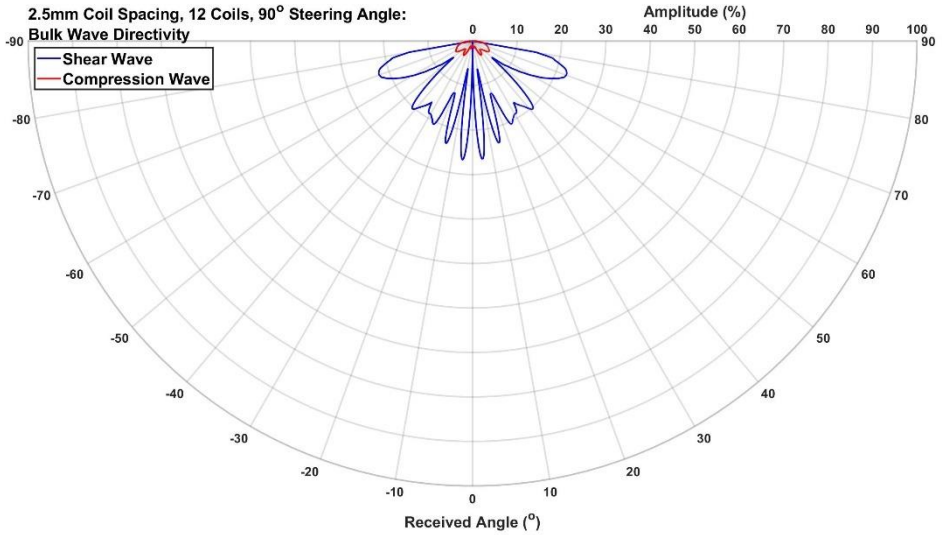

Figure 6.11: Bulk Wave Directivity Plot for 90° Steering Angle with 2.5mm Coil Spacing and 12 Coils

Compared to the beam directivities in Section 4.3's Figure 4.27-Figure 4.42, there were apparent similarities and differences. The main beam follows a similar pattern of behaviour to EMAT-2 in Section 5.2.1: the magnitude increases to a maximum value near 30°; the reception angle reaches a limit near 40°, and the magnitude decreases to a minimum value near the 60° steering angle where it plateaus. Figure 6.12 shows the maximum amplitudes of the three wave modes for this model across steering angles.

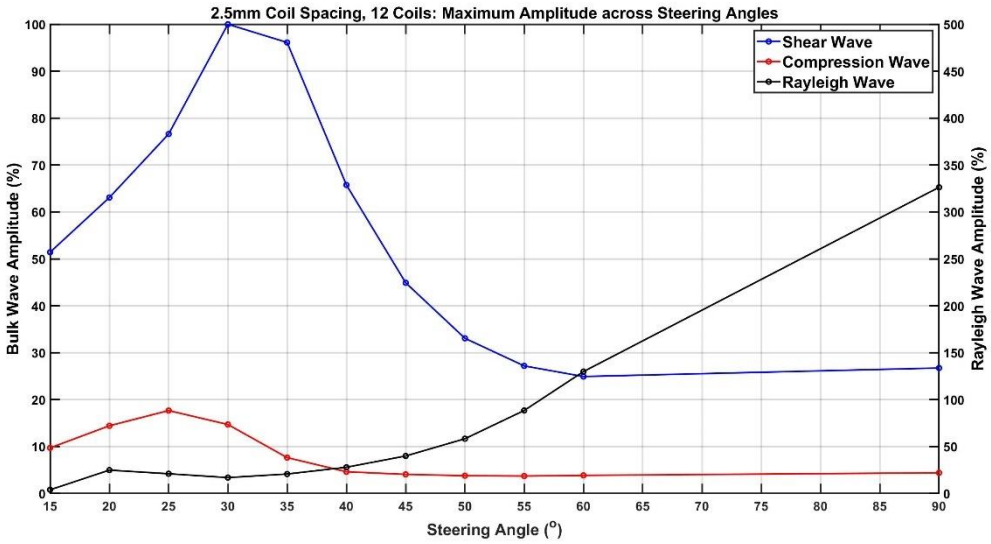

Figure 6.12: Graph of Maximum Amplitude across Steering Angles with 2.5mm Coil Spacing and 12 Coils

The imposition of an ideal vertical magnetic field appears to increase the number of sidelobes generated, as well as their magnitude compared to the main lobe. Most of these sidelobes are angled between 0° and the main lobe, however an additional sidelobe at 60° begins to emerge as the steering angle reaches 45°. At the 90° steering angle, not only does this sidelobe become more dominant than the previous main lobe, but it reaches a 70° reception angle, breaking the maximum reception angle limit concluded in Chapter 5. As this sidelobe increases however, the other sidelobes also increase in magnitude and create a wide -6dB beamwidth. Figure 6.13 shows how the beamwidth changes with steering angle, as well as the RToA.

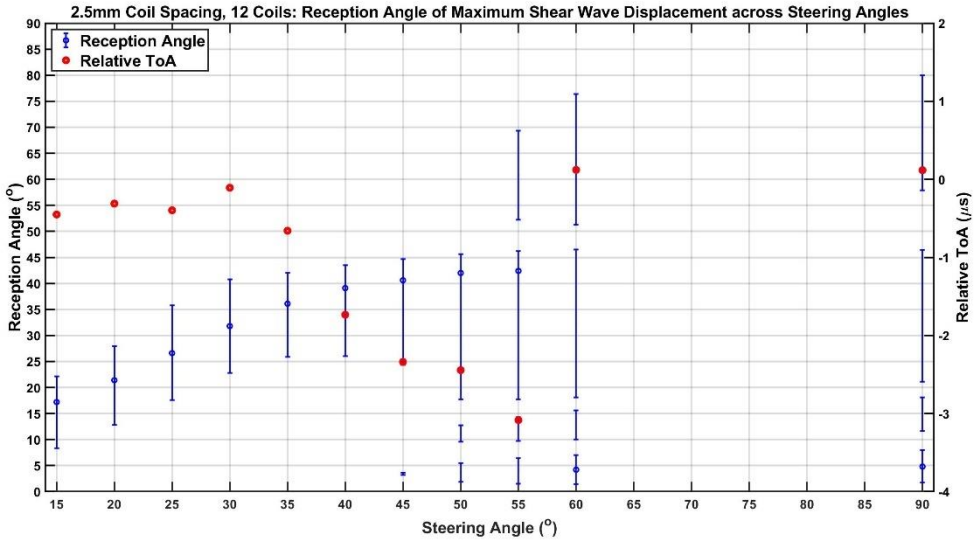

Figure 6.13: Graph of Shear Wave Reception Angles across Steering Angles with 2.5mm Spacing and 12 Coils

6.3. Number of Coils

The number of coils in the array ranged from two to twelve in steps of two, and the effect that this had on the transmitted shear waves is most clearly seen in Figure 6.14-Figure 6.19, for a steering angle of 60°. With only two coils, the main shear wave beam is angled at approximately 35°, with only low-amplitude sidelobes angled at 70°. The number of sidelobes across the directivity range increases proportionally to the number of coils in the array plus the two 70° lobes. These increasing numbers of sidelobes begin to merge as the number of coils reaches six, and by ten they become difficult to differentiate.

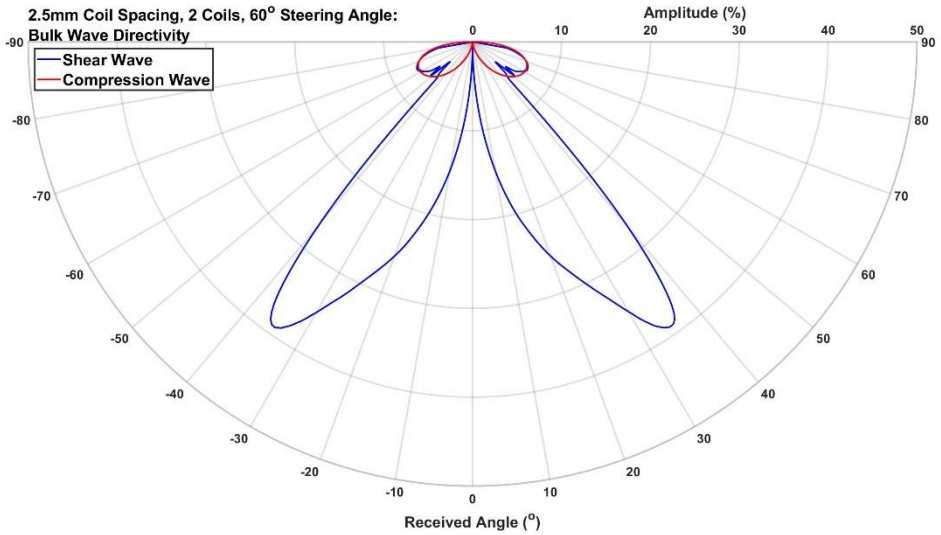

Figure 6.14: Bulk Wave Directivity Plot for 60° Steering Angle with 2.5mm Spacing and 2 Coils

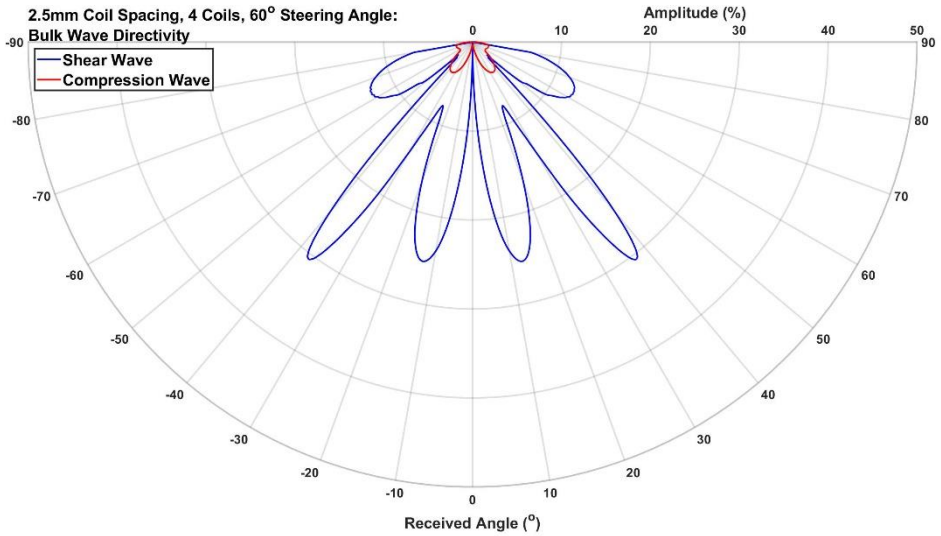

Figure 6.15: Bulk Wave Directivity Plot for 60° Steering Angle with 2.5mm Spacing and 4 Coils

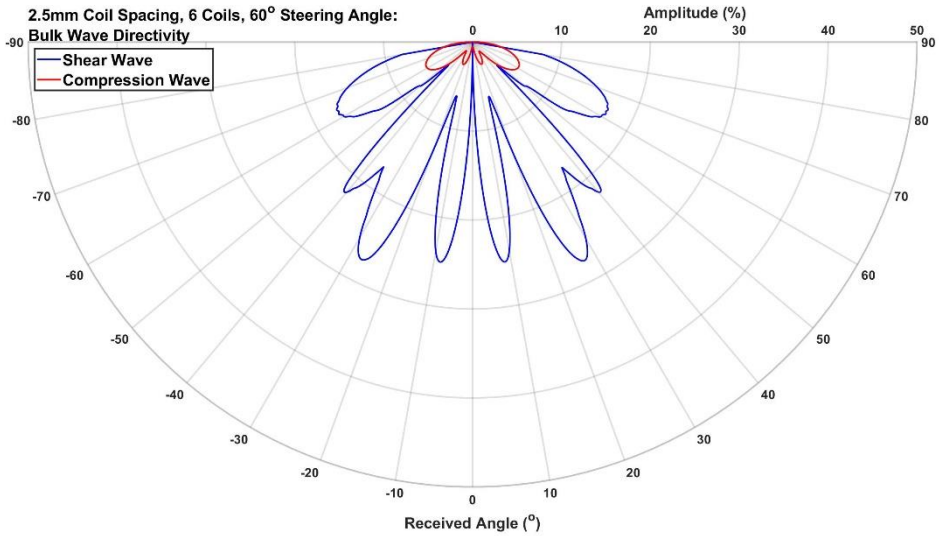

Figure 6.16: Bulk Wave Directivity Plot for 60° Steering Angle with 2.5mm Spacing and 6 Coils

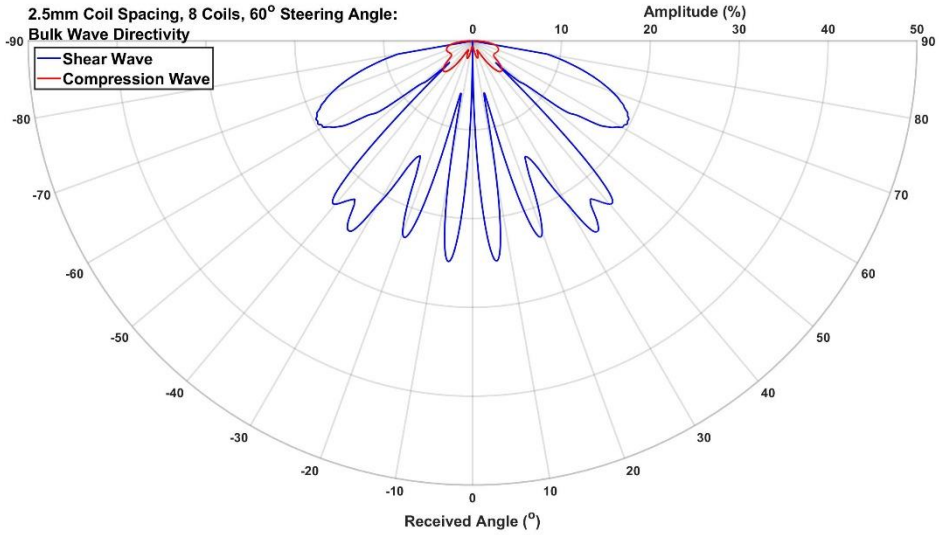

Figure 6.17: Bulk Wave Directivity Plot for 60° Steering Angle with 2.5mm Spacing and 8 Coils

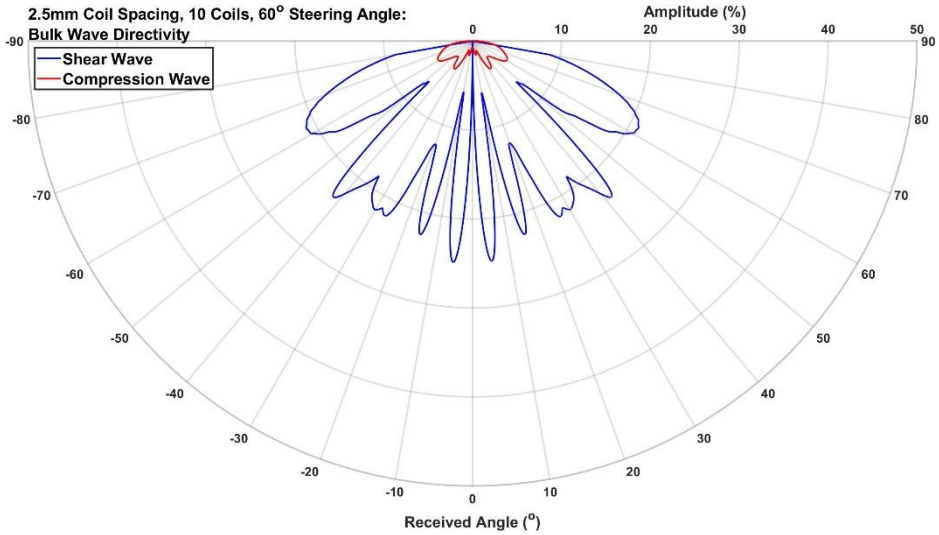

Figure 6.18: Bulk Wave Directivity Plot for 60° Steering Angle with 2.5mm Spacing and 10 Coils

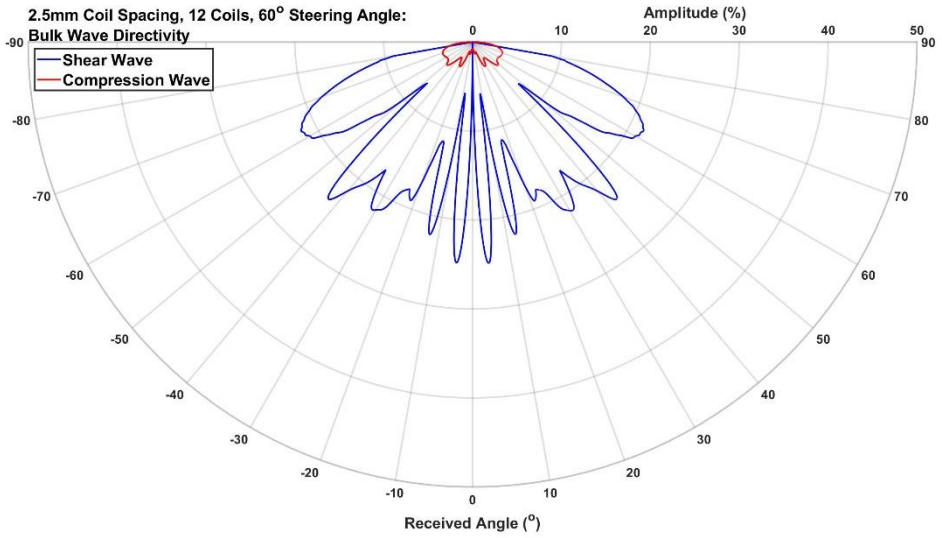

Figure 6.19: Bulk Wave Directivity Plot for 60° Steering Angle with 2.5mm Spacing and 12 Coils

Reviewing Figure 6.1-Figure 6.11, the main lobe is seen to have been made up of two sidelobes that merge together. It is also noticeable that the sidelobes shift in their angular orientation to accommodate their increasing number between the two main lobes. The only sidelobes that do not follow this trend are the 70° sidelobes. The same steering angles as before were simulated across the number of coils. Figure 6.20 shows how the amplitude of the maximum shear wave changes across steering angles for each number of coils. It is immediately noticeable that as the number of coils increases: the maximum shear wave amplitude increases; and the steering angle that generates this amplitude tends to decrease. Figure 6.21-Figure 6.25 show the reception angles for the shear waves as the number of coils increases from two to ten.

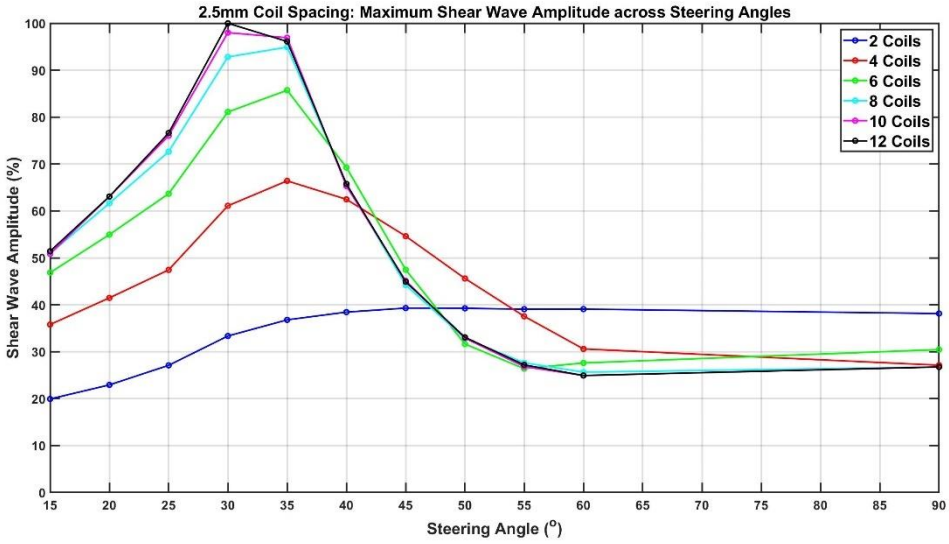

Figure 6.20: Graph of Maximum Shear Wave Amplitude across Steering Angles and Number of Coils for 2.5mm Coil Spacing

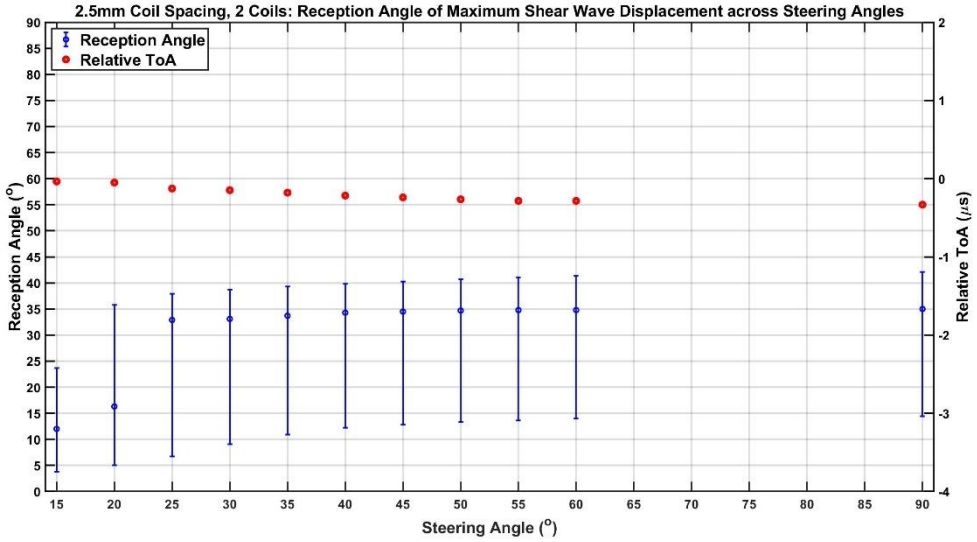

Figure 6.21: Graph of Shear Wave Reception Angles across Steering Angles with 2.5mm Spacing and 2 Coils

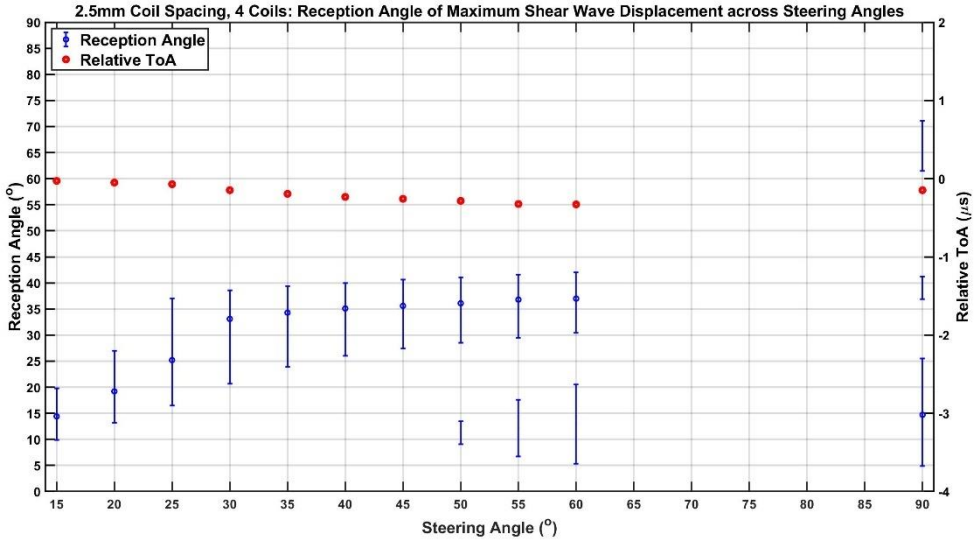

Figure 6.22: Graph of Shear Wave Reception Angles across Steering Angles with 2.5mm Spacing and 4 Coils

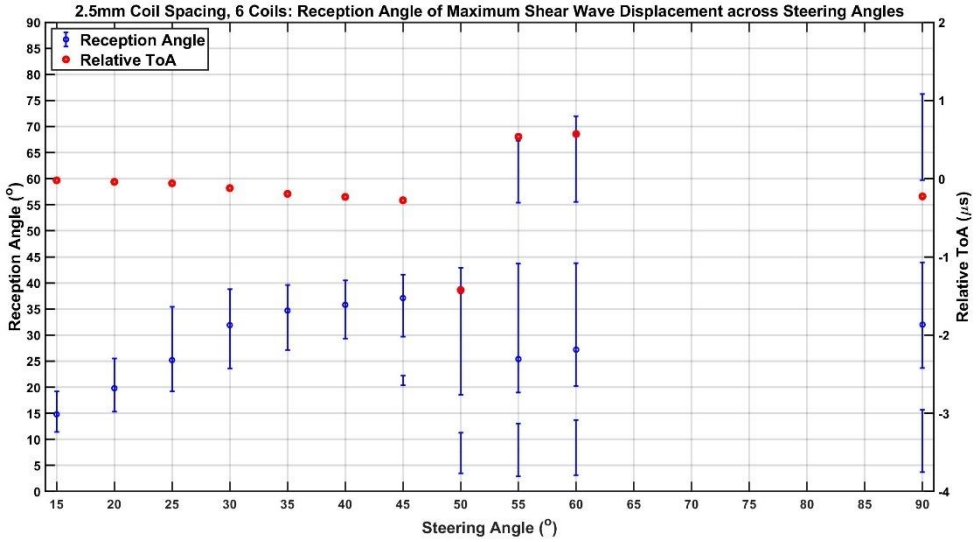

Figure 6.23: Graph of Shear Wave Reception Angles across Steering Angles with 2.5mm Spacing and 6 Coils

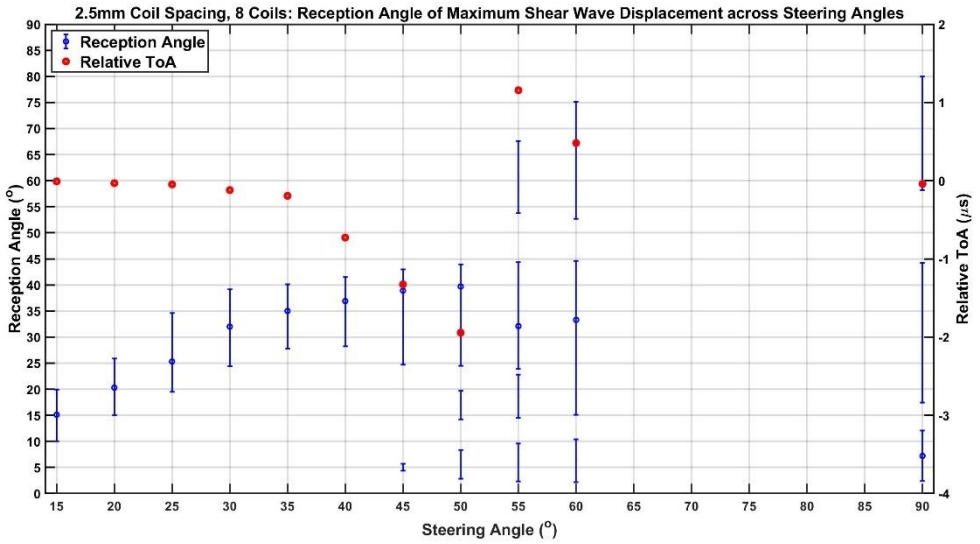

Figure 6.24: Graph of Shear Wave Reception Angles across Steering Angles with 2.5mm Spacing and 8 Coils

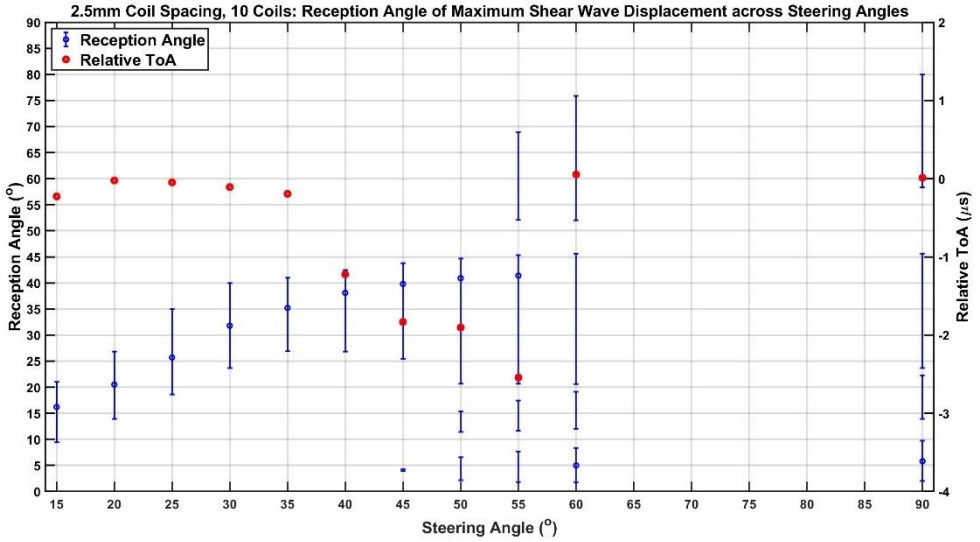

Figure 6.25: Graph of Shear Wave Reception Angles across Steering Angles with 2.5mm Spacing and 10 Coils

For two coils, the steering limit is reached at 25° as beyond this point neither the reception angle nor the limits of the wide beamwidth vary significantly by increasing the steering angle. By increasing the number of coils to four, the steering limit is delayed to 30°. There is also a far narrower beamwidth for the main lobe across the steering angles, with the emergence of sidelobes from 50° onwards, and the higher-angled sidelobe at 90°. When the number of coils increases to six, the steering limit is again limited to 35° and the main lobe's beamwidth is even tighter up to 45°. During these steering angles (and those from the previous number of coils) the RToA maintained a linear relationship from 0-0.33μs (excluding the 90° steering angle with four coils), suggesting the origin position of the shear waves is located beneath the

centre of the coil array. From 50-60°, the RToA deviates from this trend by approximately ±1µs, suggesting that the shear wave had become two split-waves. This is due to the distance between the ends of the coil array increasing.

Once the number of coils increases to eight, the split-waves become more noticeable. Sudden changes in RToA remain related to sudden changes in reception angle due to the sidelobes becoming dominant. The relationship between the steering and reception angles is approximately equal from steering angles of 15-35°, but from 35-50° there is a new linear trend with an overall 5° increase in reception angle. This relationship is beginning to emulate that of EMAT-2 (shown in Figure 5.4) due to the lack of any magnetic flux concentrations or inversions of magnetic direction. At the 90° steering angle, the sidelobes closest to 0° (with RToAs ~ 0µs) have become the dominant lobes and this stays true for the remaining number of coils.

As the number of coils increases to ten and then twelve: the steering limit reaches a maximum at 40° (where no sidelobes are present); the split-waves closest to the curved surface produce the largest shear wave amplitude (that continue to increase slightly in reception angle) from steering angles 40-55°; and the sidelobes closest to 0° become the dominant lobes from steering angles 60-90°. The effects of increasing the number of coils are summarised by Figure 6.26.

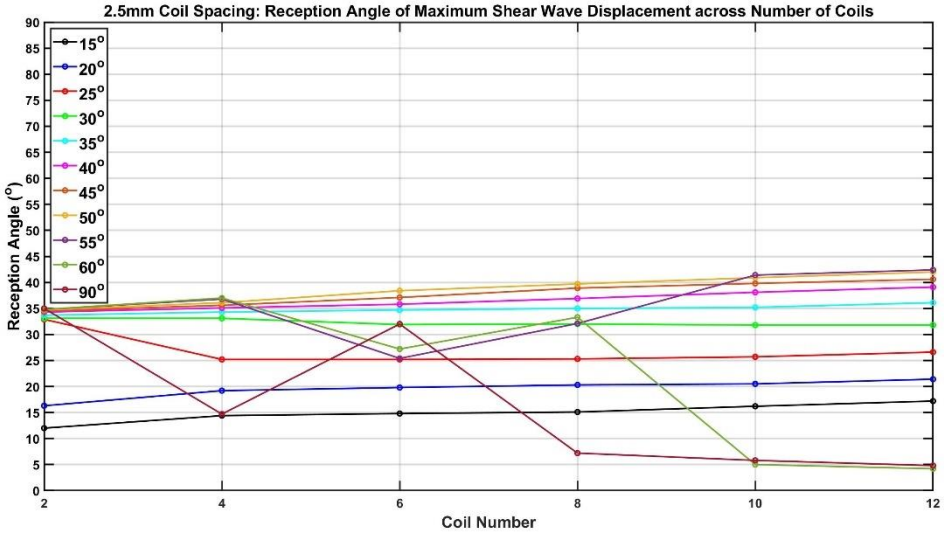

Figure 6.26: Graph of Shear Wave Reception Angle across Number of Coils for 2.5mm Coil Spacing

6.4. Coil Spacing

The third parametric study performed with this model was the coil spacing: altered to either 1.2mm (the minimum spacing possible due to the coil's CSA) or 5.0mm, shown in Figure 6.27 and Figure 6.28 respectively. To accommodate the different coil spacings, the frequency of the pulse for a given steering angle differed from the values in Table 3.3 to transmit the shear waves to their respective steering angles, in accordance with Equation 2.29.

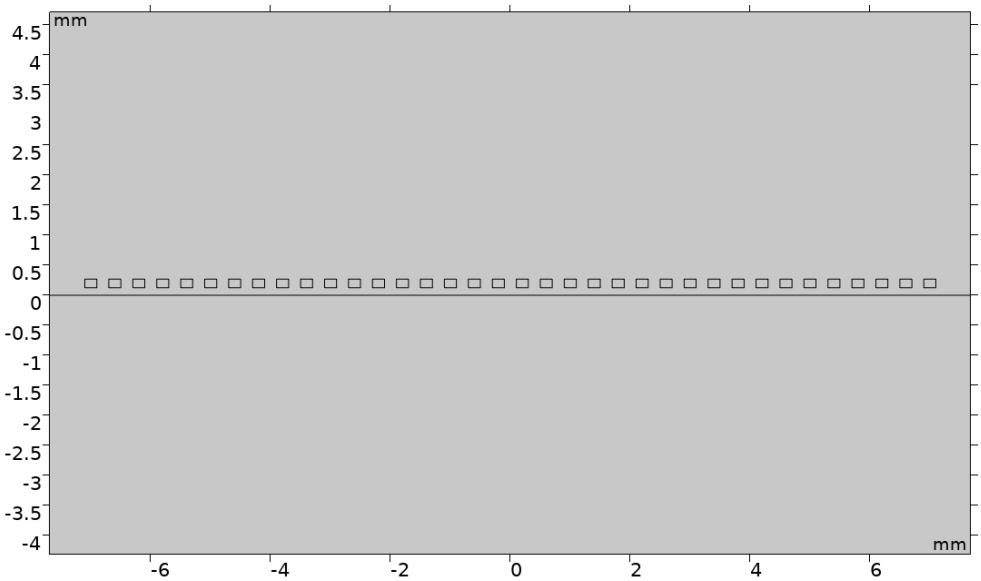

Figure 6.27: 1.2mm Coil Spacing

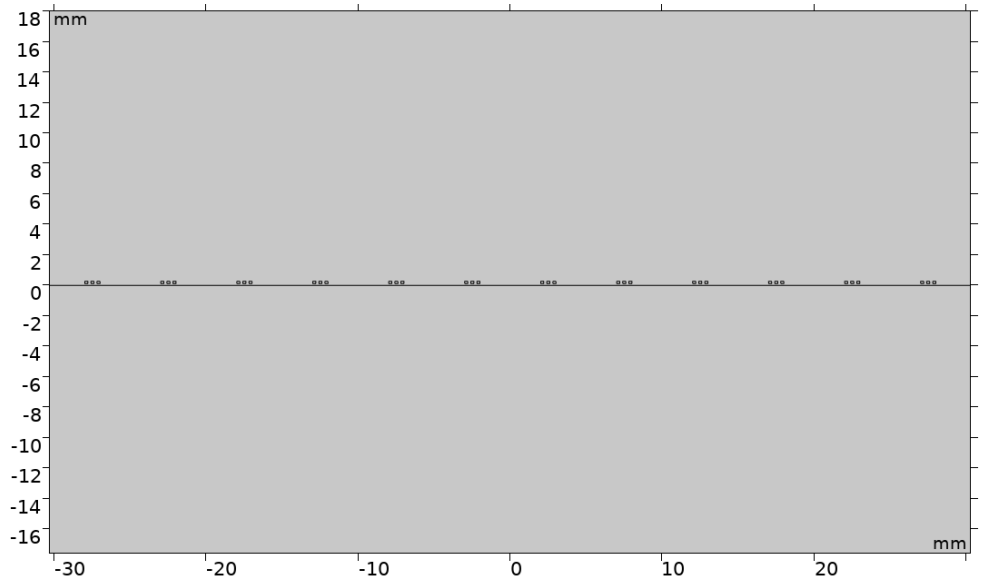

Figure 6.28: 5.0mm Coil Spacing

As previously explained, the shear wave magnitude is displayed as amplitude (rather than displacement) due to the sample's changing radii. Therefore, how the amplitude changes across coil spacings is not considered, but rather how it changes within a given coil spacing. This is best exemplified

by Figure 6.29-Figure 6.31, which shows how increasing the coil spacing affects the shear wave beam directivity for a 90° steering angle with twelve coils. The beam directivity could be compared across steering angles, due to the values of displacement being extracted from 0.1° intervals across the curved surface.

As the coil spacing increases, the direction of the sidelobes remains constant (aside from simulation errors). Most notably, the magnitude of the 70° sidelobe increases relative to the other sidelobes as the coil spacing increases. Further simulations of twelve coils at a 90° steering angle were conducted for an ever expanding coil spacing, to increase the amplitude of the 70° sidelobe. Figure 6.32 show the amplitudes of the beam directivity's sidelobes compared to the sidelobe nearest to 0° for these coil spacings.

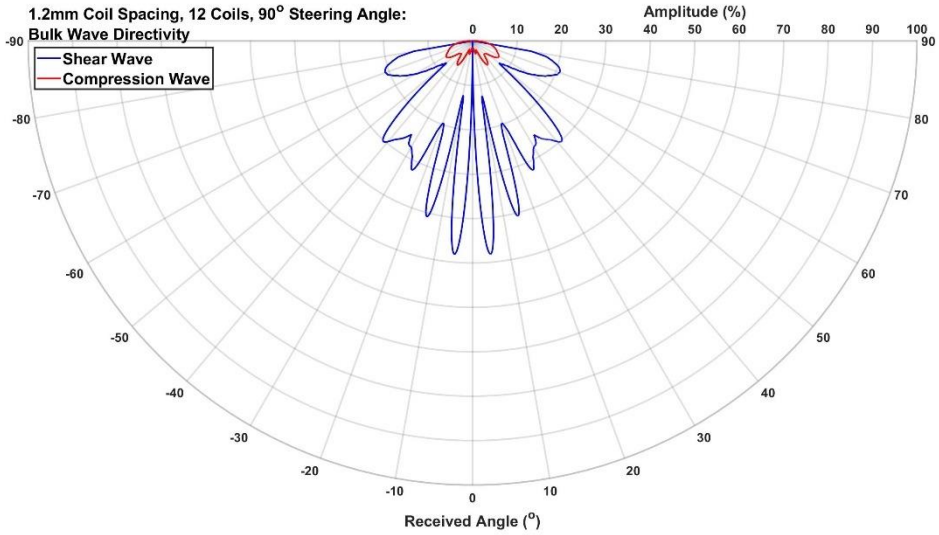

Figure 6.29: Bulk Wave Directivity Plot for 90° Steering Angle with 1.2mm Spacing and 12 Coils

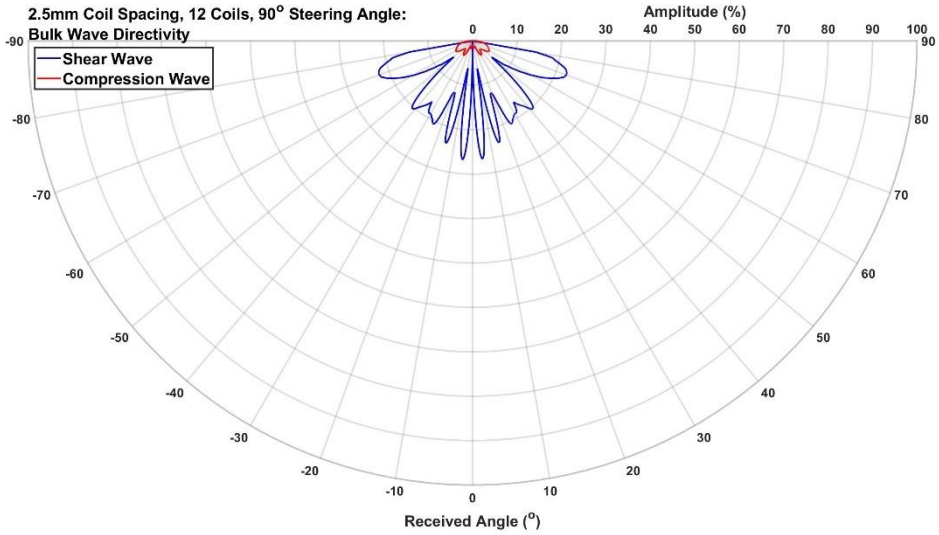

Figure 6.30: Bulk Wave Directivity Plot for 90° Steering Angle with 2.5mm Spacing and 12 Coils

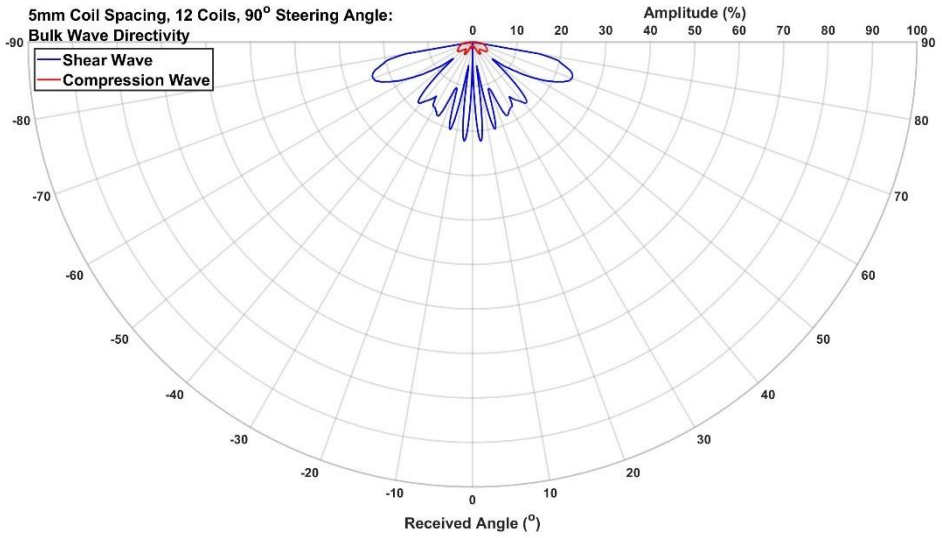

Figure 6.31: Bulk Wave Directivity Plot for 90° Steering Angle with 5.0mm Spacing and 12 Coils

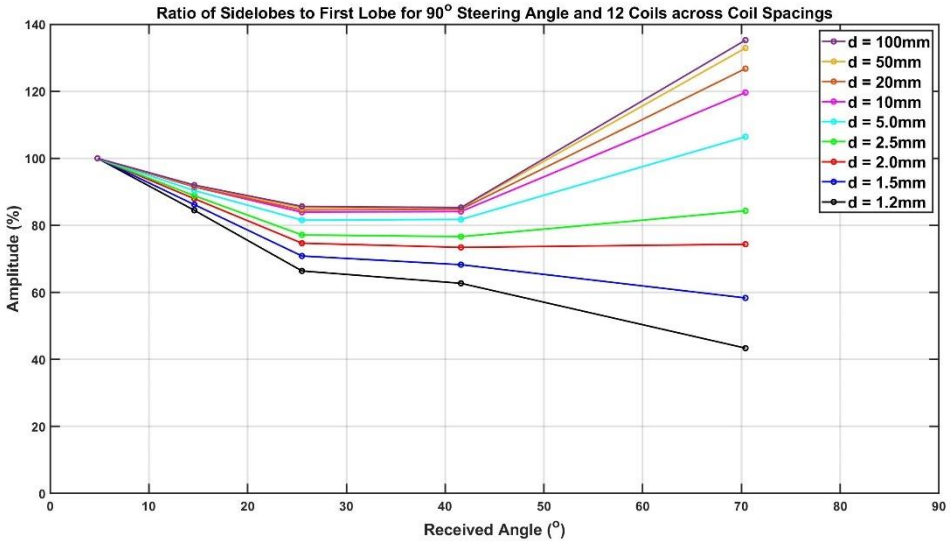

Figure 6.32: Graph of Shear Wave Sidelobe Amplitudes across Coil Spacings

Figure 6.32 shows that the 70° sidelobe could be increased in amplitude to 135% that of the sidelobe nearest to 0°. It is obviously not practical however to use an MLC EMAT with a 100mm coil spacing, thus the coil strands were reduced in size to produce a coil array with a far smaller CSA. To achieve the beam directivity of the 100mm coil spacing for a coil spaced at 2.5mm, the coil strand's height and width were reduced by a SF of 40 (100/2.5). While this reduction in coil CSA did not increase the 70° sidelobe amplitude to 135%, it did increase it to 113%.

Figure 6.33 and Figure 6.34 show how the maximum shear wave amplitude across steering angles for a given number of coils was affected by the changing coil spacing. As with the 2.5mm spacing, the maximum shear wave

amplitude increases, and the steering angle that generates this amplitude decreases as the number of coils increases. What was different however was that as the coil spacing increases: the range of the maximum amplitudes between two to twelve coils tends to increase; and the steering angle that generates the greatest shear wave across steering angles for a given number of coils tends to decrease.

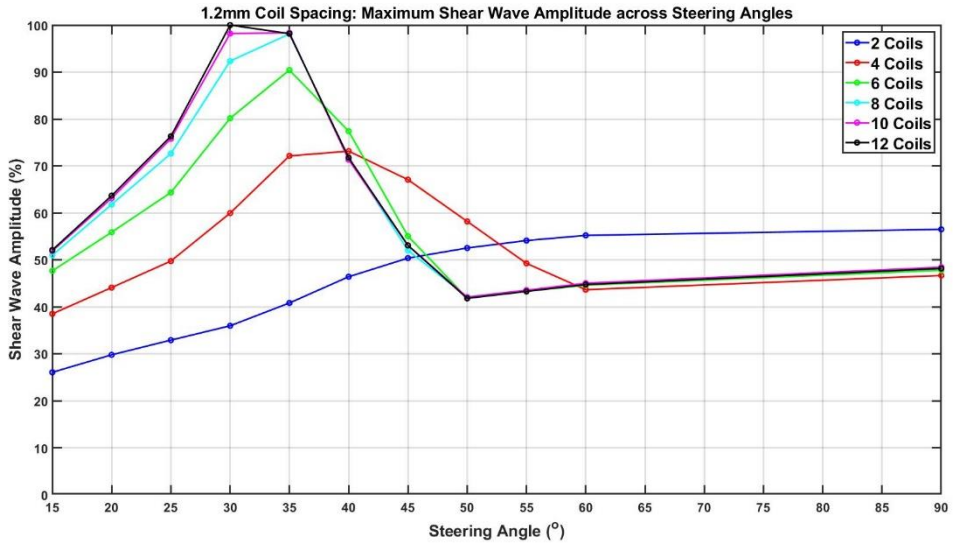

Figure 6.33: Graph of Maximum Shear Wave Amplitude across Steering Angles and Number of Coils for 1.2mm Coil Spacing

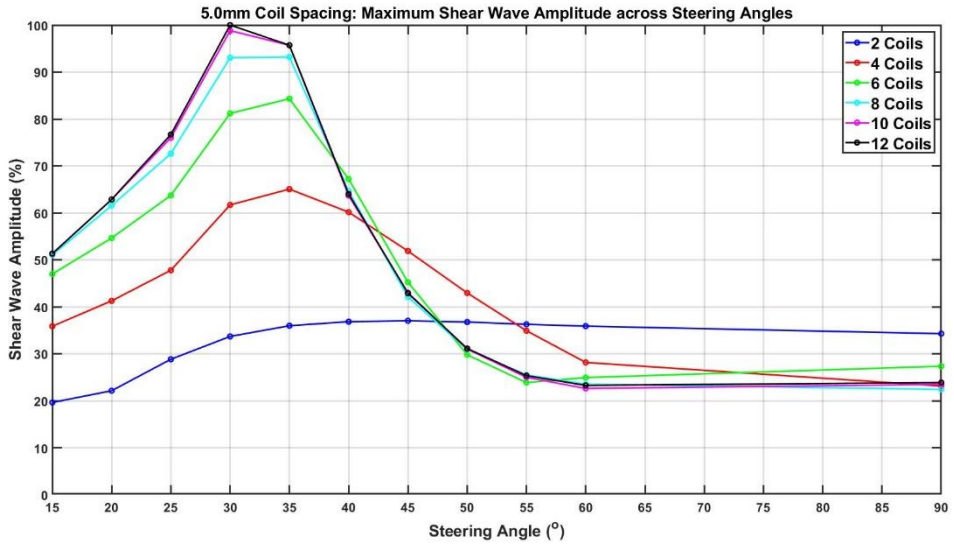

Figure 6.34: Graph of Maximum Shear Wave Amplitude across Steering Angles and Number of Coils for 5.0mm Coil Spacing

Figure 6.35-Figure 6.46 show the shear wave reception angle and beamwidth for coil spacings of 1.2mm and 5.0mm, as the number of coils increases from two to twelve. Following the 2.5mm spacing with two coils, the maximum angle that can be reached is 35°, however the steering angle that reaches this limit is lowered by an increase in coil spacing.

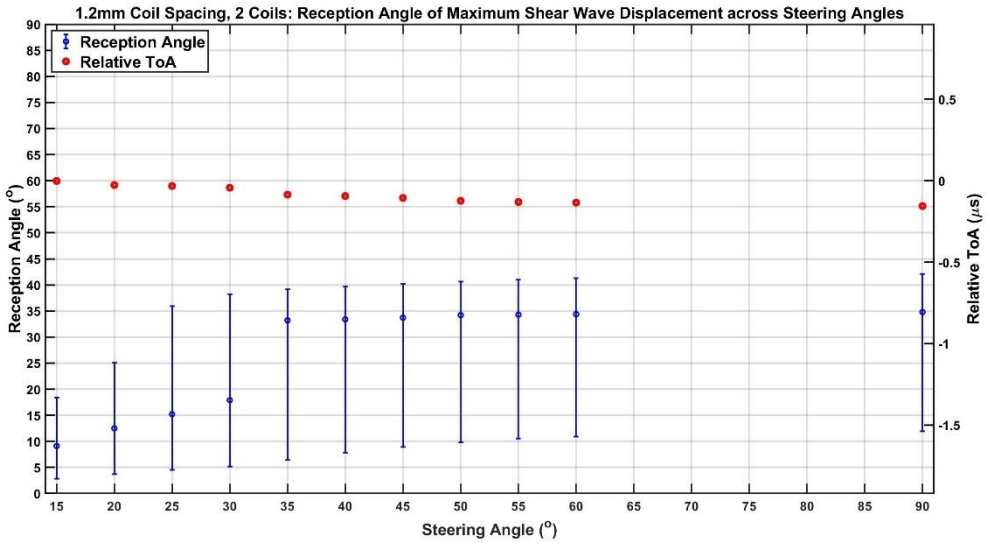

Figure 6.35: Graph of Shear Wave Reception Angles across Steering Angles with 1.2mm Spacing and 2 Coils

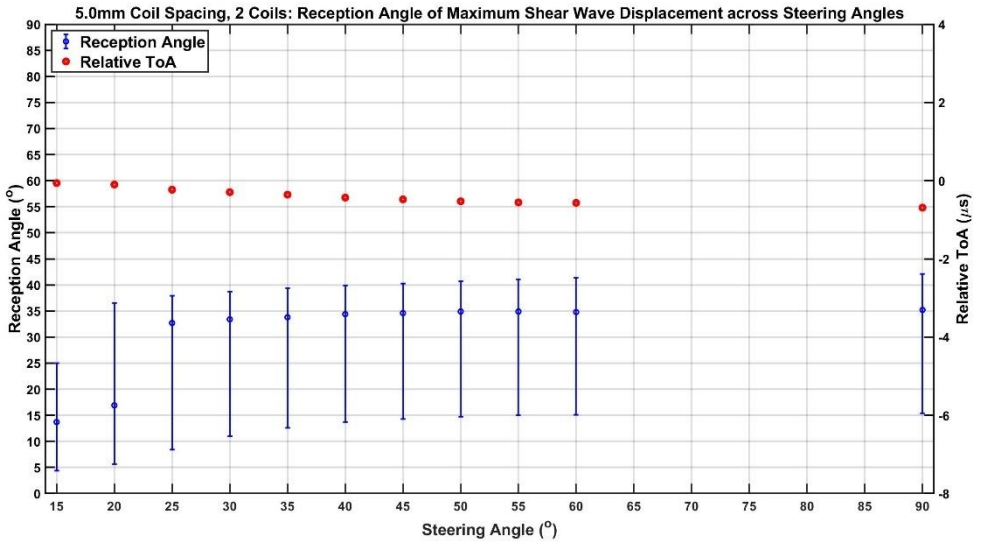

Figure 6.36: Graph of Shear Wave Reception Angles across Steering Angles with 5.0mm Spacing and 2 Coils

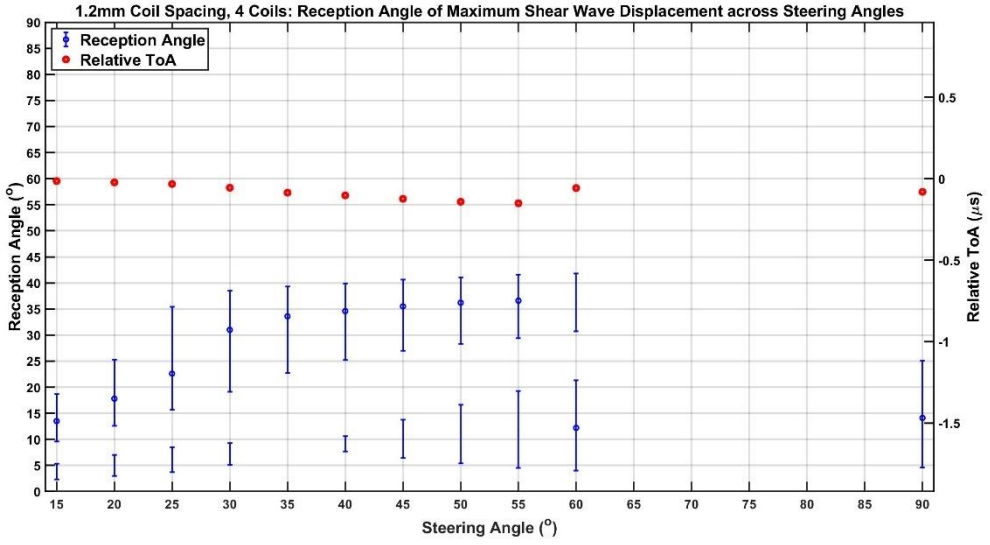

Figure 6.37: Graph of Shear Wave Reception Angles across Steering Angles with 1.2mm Spacing and 4 Coils

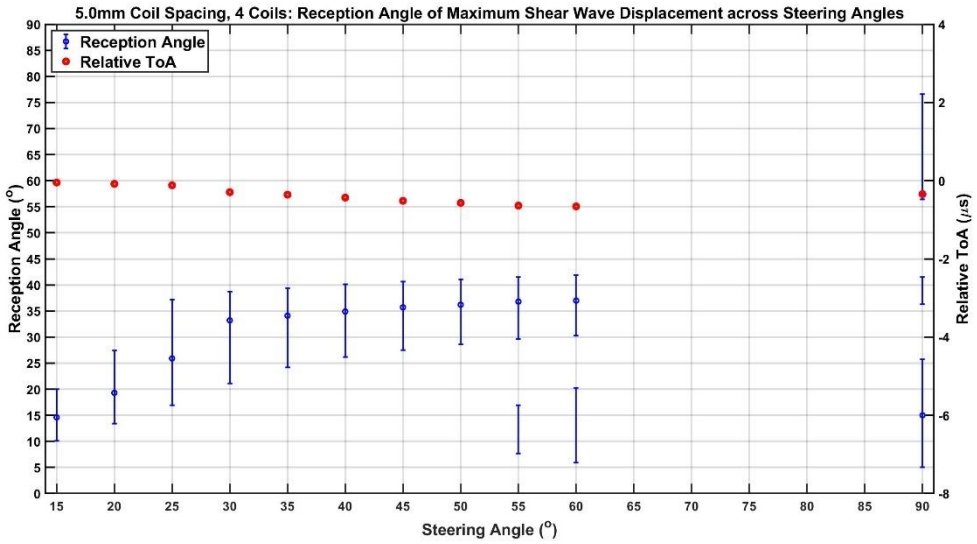

Figure 6.38: Graph of Shear Wave Reception Angles across Steering Angles with 5.0mm Spacing and 4 Coils

With four coils, a similar tightening of the main lobe's beamwidth is seen, however there is a difference in the behaviour of the sidelobe. This sidelobe exceeds the -6dB limit at: a 20° steering angle for the 1.2mm spacing; 50° for the 2.5mm spacing; and 55° for the 5.0mm spacing. This provides further evidence to the conclusion that decreasing the coil spacing increases the magnitude of the sidelobes. Additionally, the sidelobe becomes the dominant lobe earlier at the 60° steering angle for lower coil spacings. The 70° sidelobe however does not breach the -6dB limit for the 1.2mm coil spacing and does not do so for the remaining number of coils.

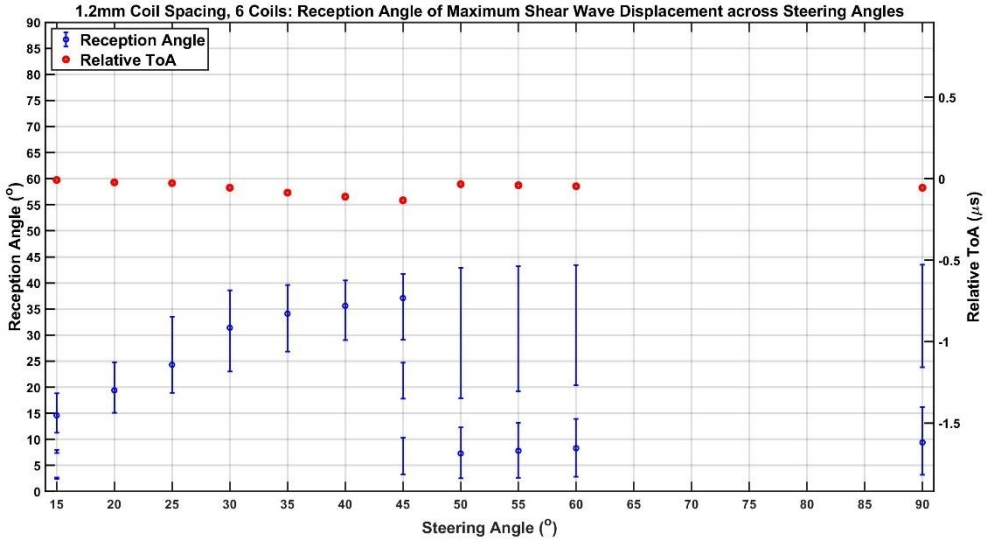

Figure 6.39: Graph of Shear Wave Reception Angles across Steering Angles with 1.2mm Spacing and 6 Coils

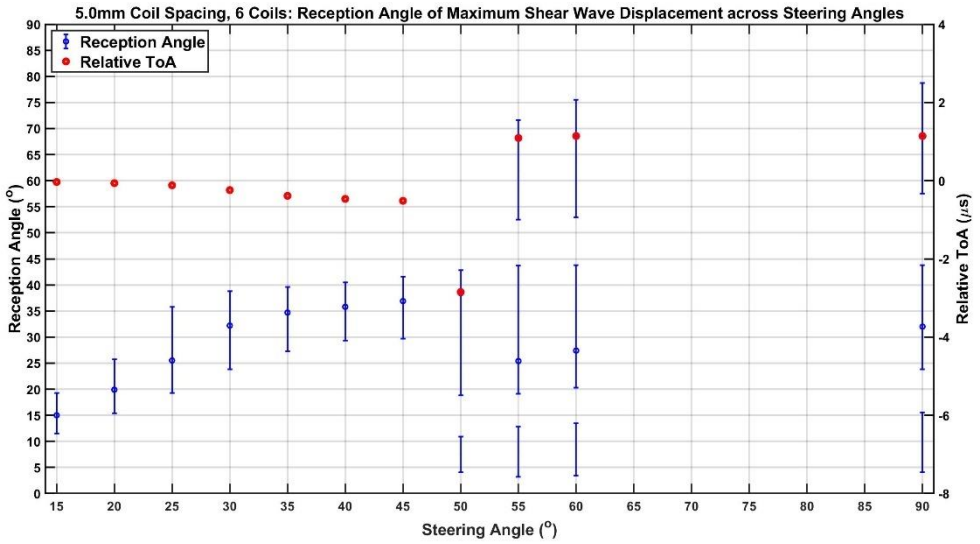

Figure 6.40: Graph of Shear Wave Reception Angles across Steering Angles with 5.0mm Spacing and 6 Coils

At six coils, the RToAs from the 5.0mm coil spacing models deviate in the same manner as those from the 2.5mm coil spacing, due to split-waves emerging from the increased MLC width. Slight deviations from the linear RToA trend can be seen for all coil spacings with four coils onwards (including Figure 6.22) when the sidelobe directed nearest to 0° supplants the main beam. This suggests that the main beam and the sidelobe nearest 0° share the same origin position, with their slight deviations being due to the small change in distance to their reception angles. The values of RToA between coil spacings change greatly between coil spacings due to the changing radii of the sample, however it is their behavioural pattern that yields significant results.

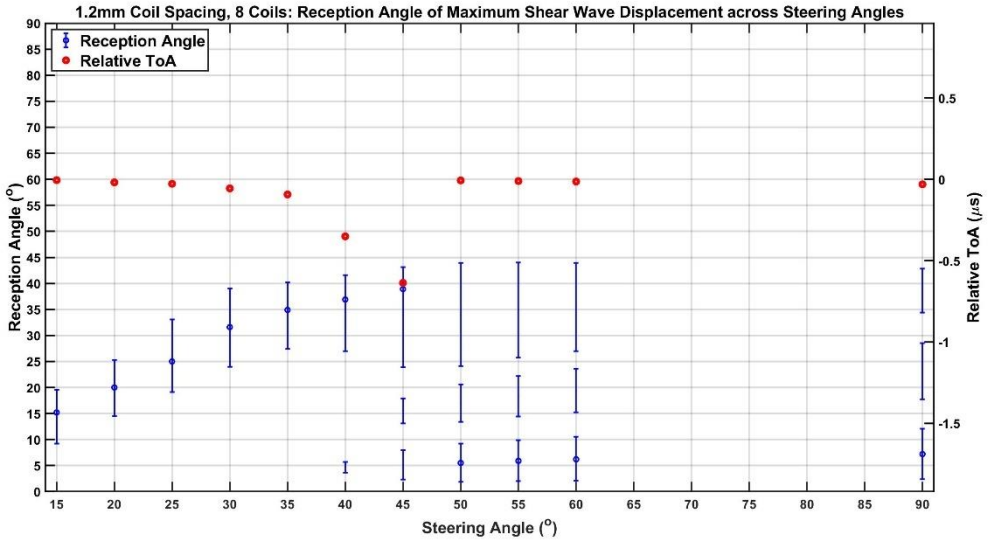

Figure 6.41: Graph of Shear Wave Reception Angles across Steering Angles with 1.2mm Spacing and 8 Coils

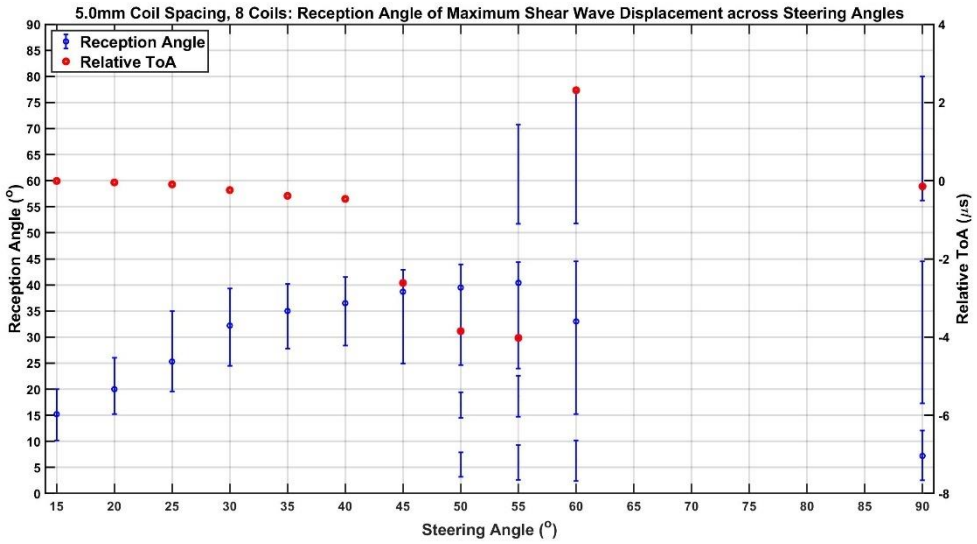

Figure 6.42: Graph of Shear Wave Reception Angles across Steering Angles with 5.0mm Spacing and 8 Coils

It is with eight coils that the 1.2mm spaced models truly broke their linear trend for RToA across steering angles. This deviation occurs for the 1.2mm coil spacing at the 40° steering angle (as with the 2.5mm coil spacing) but not the 5.0mm. At the 45° steering angle, all three coil spacings show that the maximum shear wave comes from the split-wave closest to the curved surface. From 50° onwards, the reception angle and RToA are dependent on which sidelobe becomes the dominant lobe. The RToA for a 5.0mm coil spacing is approximate to: 0µs for reception angles between 5-10°; 1-2µs for reception angles between 30-35°; and -2--4µs for reception angles between 37-42°. Once the 90° steering angle is reached, the sidelobe closest to 0° becomes the dominant lobe for all coil spacings, and this remains true for the remaining number of coils for the 1.2mm and 2.5mm coil spacings (as shown in Figure 6.32).

The pattern of behaviour with ten coils is akin to that of twelve coils for the range of coil spacings. The linear trend of RToAs that is present at the lower steering angles for the lower number of coils is interrupted by a reduced RToA at the lowest steering angles. This pattern emulates that of EMAT-2's shear wave reception angle (shown in Figure 5.4) whereby the lowest steering angles from 15-28° have a lower RToA than the steering angles near that which produces the maximum displacement.

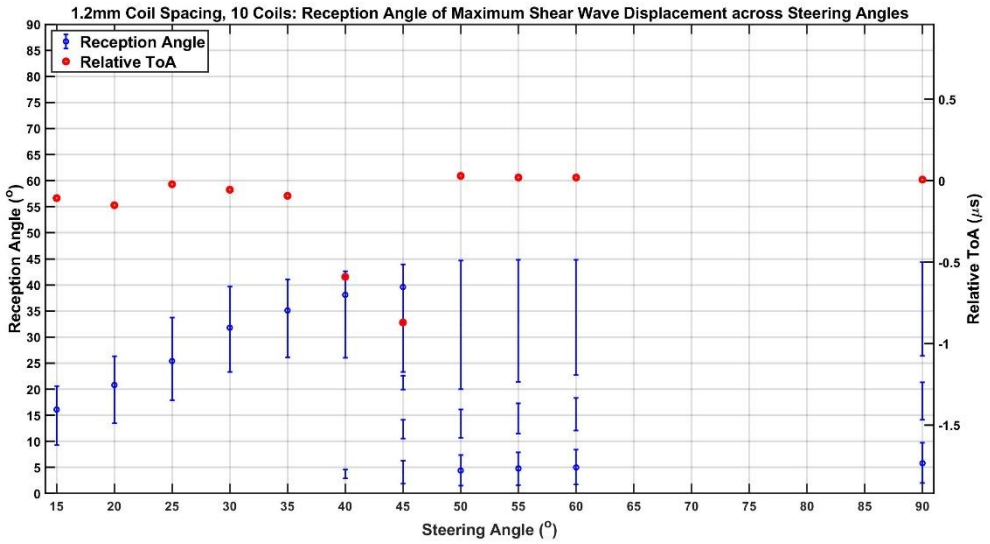

Figure 6.43: Graph of Shear Wave Reception Angles across Steering Angles with 1.2mm Spacing and 10 Coils

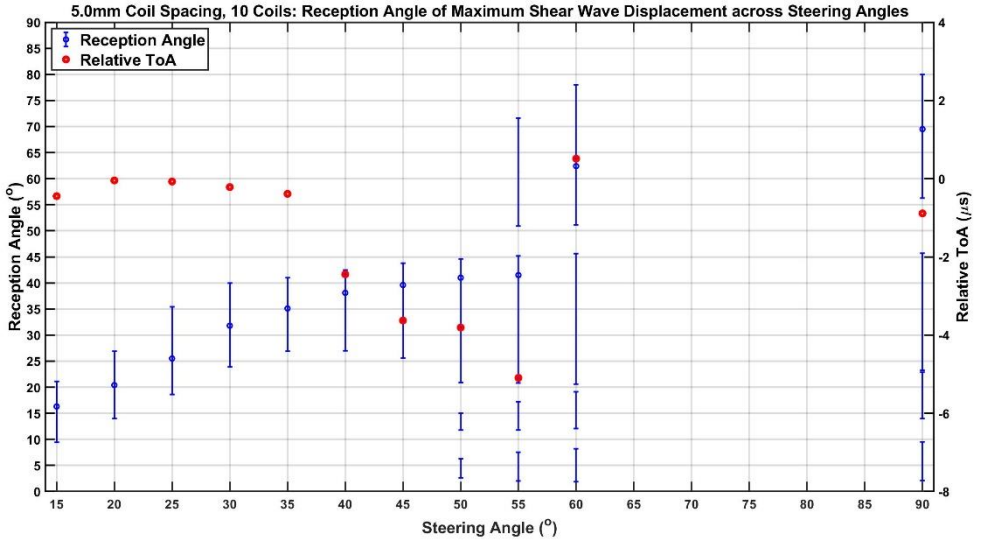

Figure 6.44: Graph of Shear Wave Reception Angles across Steering Angles with 5.0mm Spacing and 10 Coils

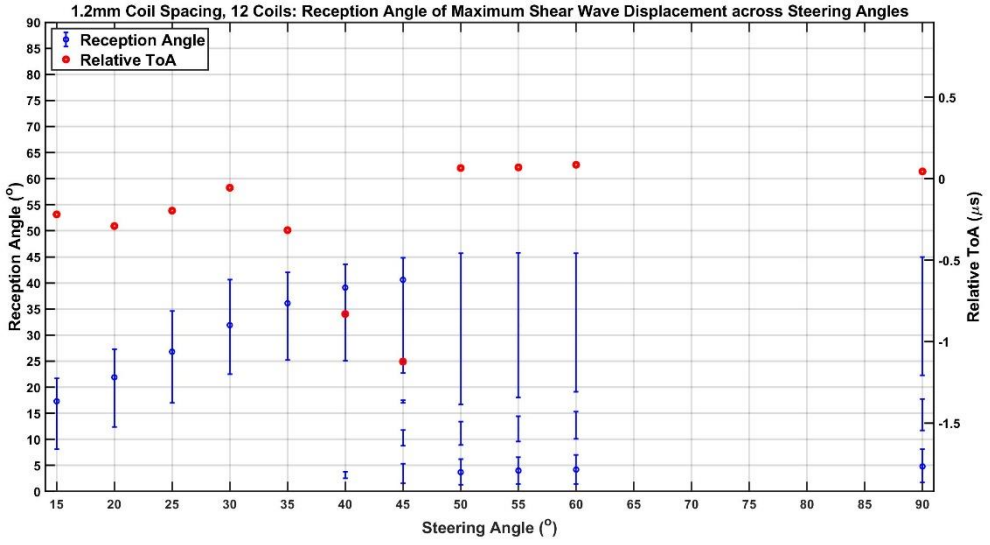

Figure 6.45: Graph of Shear Wave Reception Angles across Steering Angles with 1.2mm Spacing and 12 Coils

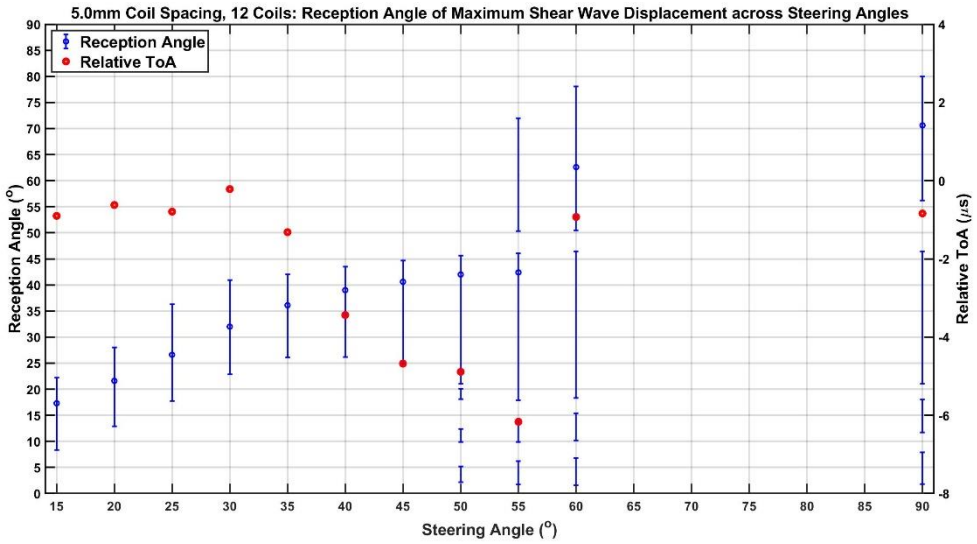

Figure 6.46: Graph of Shear Wave Reception Angles across Steering Angles with 5.0mm Spacing and 12 Coils

Once the maximum number of coils is reached, the shear wave reception angle is almost the same from steering angles of 20-45° across coil spacings. There appears to be only slight differences in the main lobe's beamwidth, and differences in given steering angle's beamwidth is dependent on the sidelobes (explaining the wider spread for the 45° steering angle with the 1.2mm coil). While the 2.5mm and 5.0mm coil spacings closely resemble one another from steering angles of 50-90°, the most notable change is that the 70° sidelobe becomes the dominant lobe from the 60° steering angle onwards for the 5.0mm spacing (as previously explored).

The overall effects of increasing the number of coils for coil spacings of 1.2mm and 5.0mm are summarised by Figure 6.47 and Figure 6.48 respectively. These illustrate the 70° lobes becoming the dominant lobes for steering angles of 60-90°. For all coil spacings tested, there appears to be minimal effect on the reception angle from steering angles of 15-50° as the number of coils changes. The exception to this however is with two coils, as increasing the coil spacing causes sudden increases in reception angle. This behaviour has been seen before with the EMATs that generate two distinct shear wave lobes. This suggests that each coil produces a distinct split-wave that is distinguished when the coil strands themselves as positioned further apart (as previously discussed in Section 5.3).

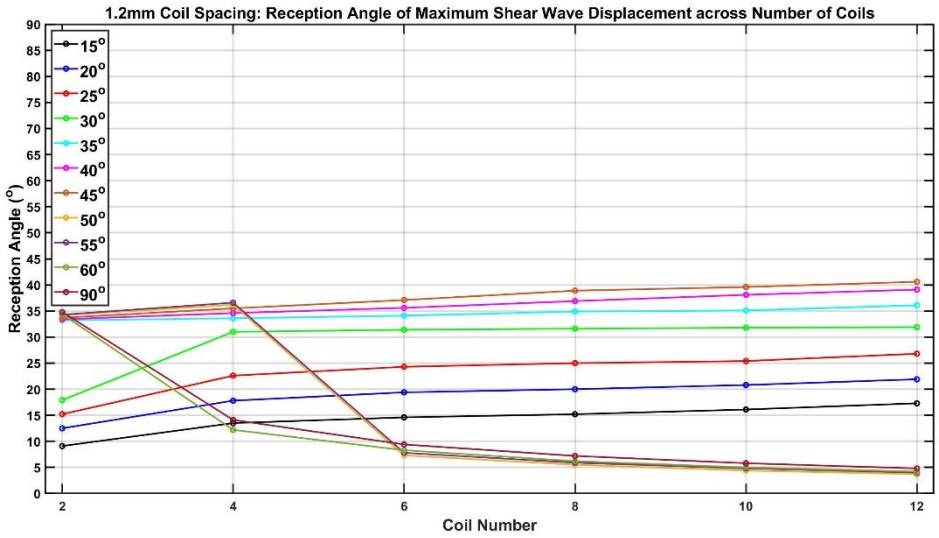

Figure 6.47: Graph of Shear Wave Reception Angle across Number of Coils for 1.2mm Coil Spacing

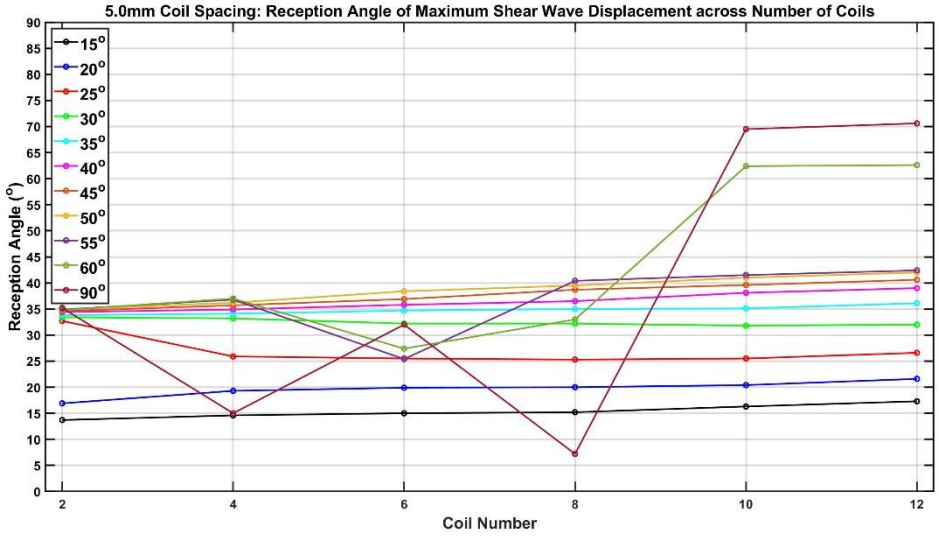

Figure 6.48: Graph of Shear Wave Reception Angle across Number of Coils for 5.0mm Coil Spacing

Figure 6.49-Figure 6.54 condenses the overall effects that the coil spacing has on the shear wave reception angle across the range of steering angles, for a different number of coils in the array. As the number of coils increases, the variance in reception angles between steering angles of 25-90° tends to increase for all coil spacings due to the increasing number of sidelobes shifting the main lobe's direction.

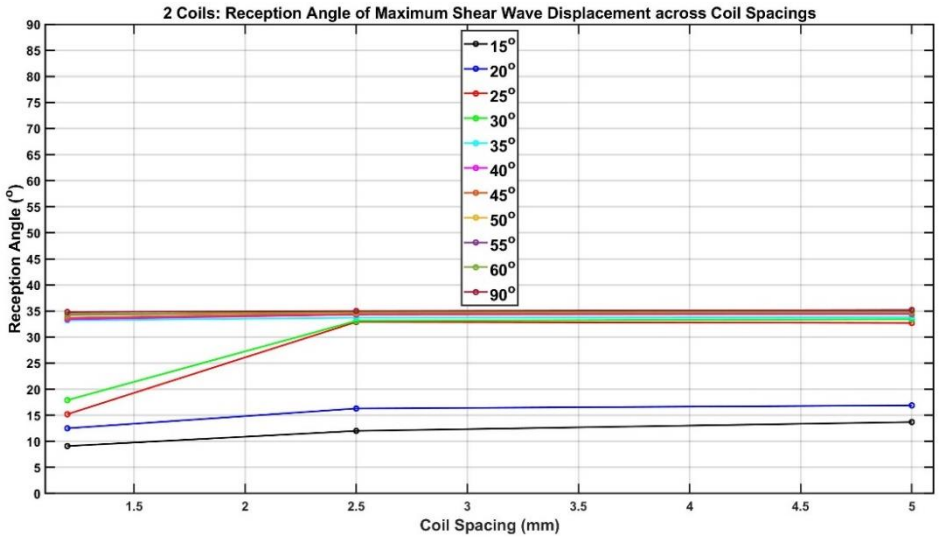

Figure 6.49: Graph of Shear Wave Reception Angle across Coil Spacings for 2 Coils

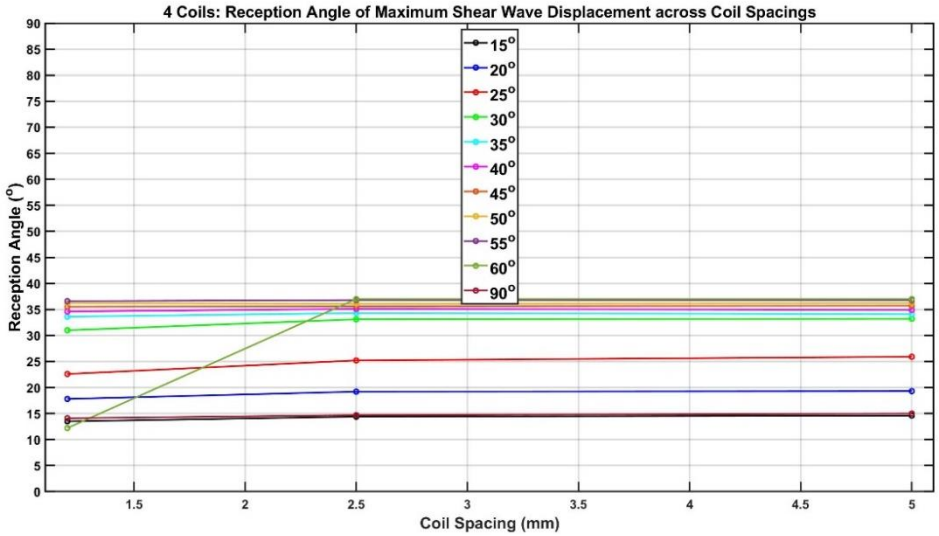

Figure 6.50: Graph of Shear Wave Reception Angle across Coil Spacings for 4 Coils

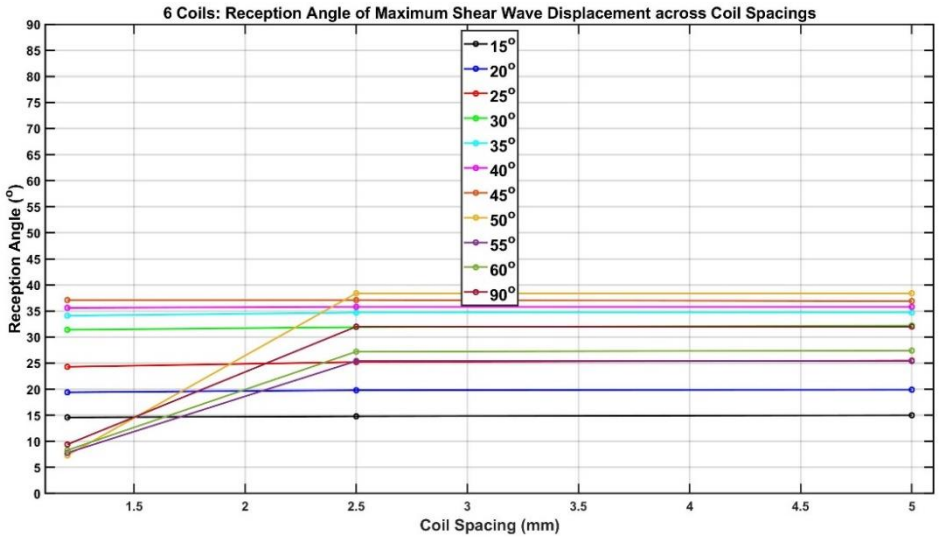

Figure 6.51: Graph of Shear Wave Reception Angle across Coil Spacings for 6 Coils

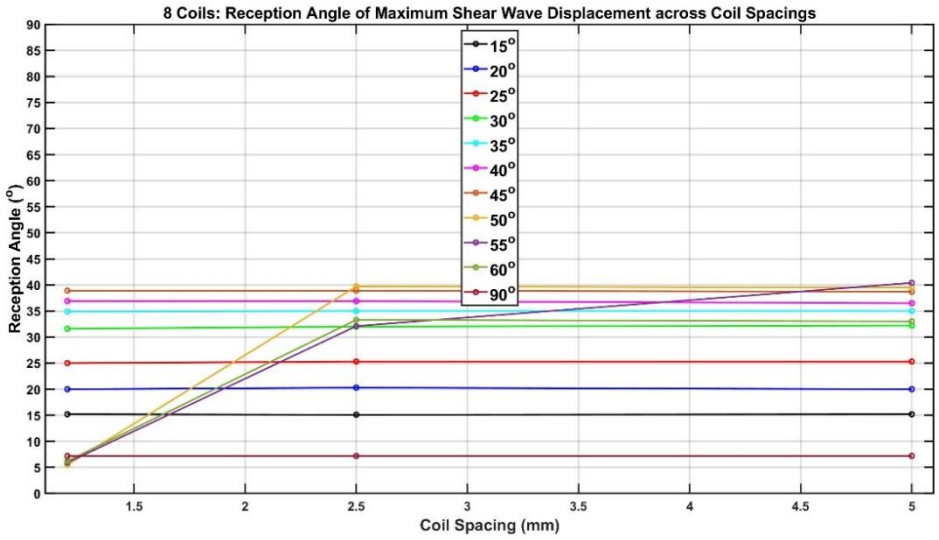

Figure 6.52: Graph of Shear Wave Reception Angle across Coil Spacings for 8 Coils

Figure 6.53: Graph of Shear Wave Reception Angle across Coil Spacings for 10 Coils

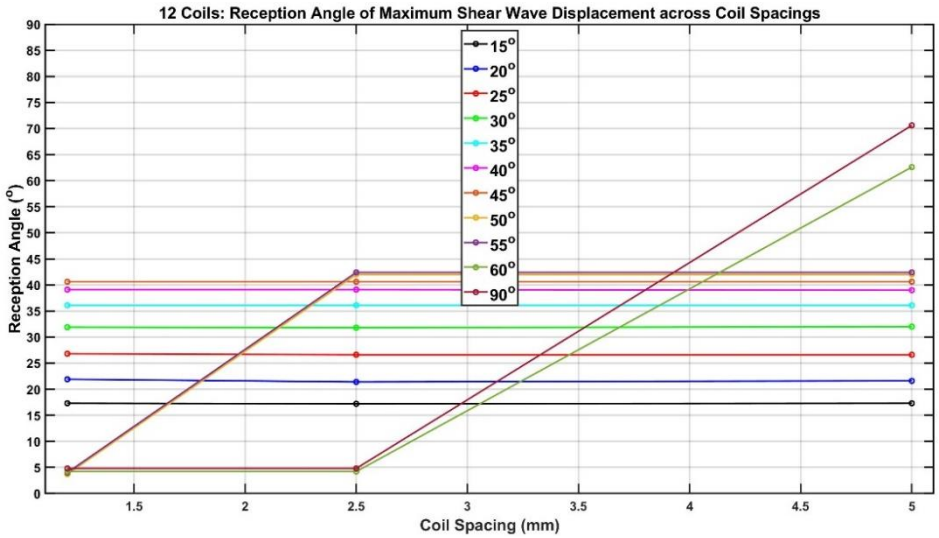

Figure 6.54: Graph of Shear Wave Reception Angle across Coil Spacings for 12 Coils

6.5. Summary

The focus of this chapter was the effect that the coil design plays on the shear wave directivity. This was examined solely via FEM models of the MLC within a uniform vertical magnetic field, from which numerous parametric studies were simulated. These explored the effects of: steering angle; the number of coils within the array; and the coil spacing.

Increasing the steering angle has the same effects stated from Chapters 4 and 5. The shear wave beam directivity reaches a maximum value near a 30° steering angle and further increase causes higher-angled sidelobes to supplant one another. Increasing the number of coils generates a greater number of sidelobes, which increases both the amplitude of the beam directivity and the beamwidth. Increasing the coil spacing increases the amplitudes of the sidelobes with respect to one another. This could theoretically be used to generate a sidelobe at a reception angle greater than 70°.

Chapter 7 - Multi-Angle Beam Generation

This chapter utilises the information gathered from the previous chapters to design an MLC EMAT capable of transmitting shear waves at more than one direction simultaneously. This chapter considers: which angles can be used; what the resultant directivity will be; and where this can be used in real-world applications.

7.1. Introduction

As previously discussed in Section 1.1, Sperry's RSU possesses UT probes angled at 0°, 37°, and 70°. The simulated studies thus far have demonstrated that the MLC EMAT is certainly capable of transmitting shear waves at 37° with a narrow -6dB beamwidth, and experimental testing has shown that a 0° beam is also transmitted at higher steering angles. While reliably steering at 70° remains an issue, a secondary problem is that the MLC EMAT's shear wave is generally constrained to a single reception angle.

In an attempt at reducing the negative effects of the sidelobes, it was discovered that by overlapping the transmission signals for two distinct steering angles, the MLC EMAT is capable of producing a single shear wave with two distinct maxima. For a given magnetic configuration, the reception angles of these two maxima are almost exactly the same as those for the individual steering angles. The transmission signal for these dual steering angles is simply the sum of the pulse profiles for each constituent steering angles multiplied by the maximum current amplitude, as shown in Equation 7.1-Equation 7.2.

$$I_n(t) = e^{-\frac{(t-\tau)^2}{2\sigma_n{}^2}} cos\big(2\pi f_n(t-\tau)\big) \qquad \text{Equation 7.1}$$

$$I(t) = I \times [I_1(t) + I_2(t)] \qquad \text{Equation 7.2}$$

$$\tau = roundup\left[\frac{3.75}{f_2 \times \Delta t_1}\right] \times \Delta t_1 \qquad \text{Equation 7.3}$$

where $I_n(t)$ = pulse profile of given steering angle at point in time (t); f_n = frequency of a given steering angle (Hz); Δt_1 = timestep of primary steering angle (s); σ_n = standard deviation of a given steering angle (s).

The 1st steering angle (always lower than the 2nd) generates the lowest wavelength in the model and is thus used to determine the required mesh density and timestep of the model. The 2nd steering angle retains its longer first time-dependent study step and greater depth for the area of high-mesh density beneath the EMAT, due to its values of standard deviation and SDP respectively. The time delay is therefore altered from Equation 3.11 to Equation 7.3 to accommodate the longer transmission signal at a reduced timestep. This greatly increases the runtime of model, from approximately six days for dual steering angles of 15° and 90° to individually two days and 40 minutes respectively. Figure 7.1 shows the transmission pulse profile for the dual-angles of 15° and 90° compared to its constituent single steering angles, and Figure 7.2 shows the colour-plot of this dual-angle model.

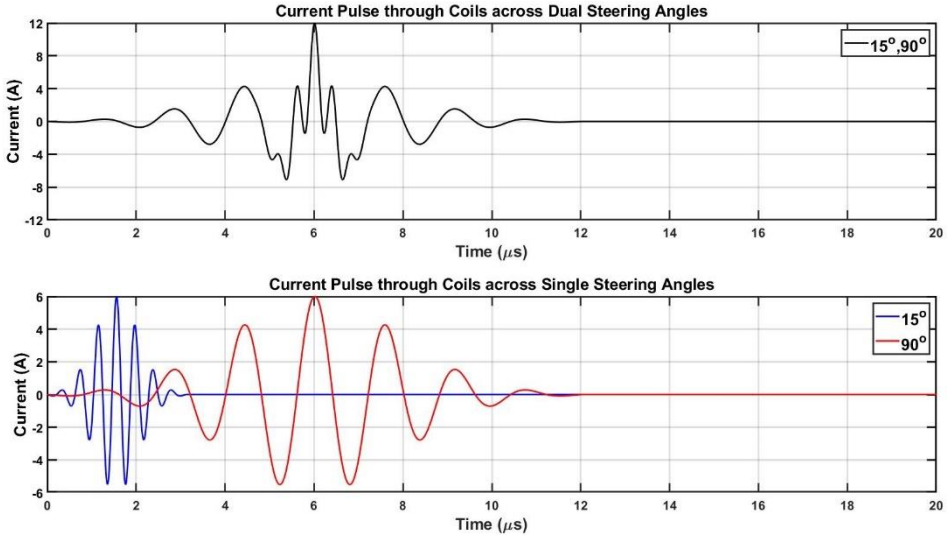

Figure 7.1: Graph of current pulse profile through coils for a 15°,90° dual steering angle

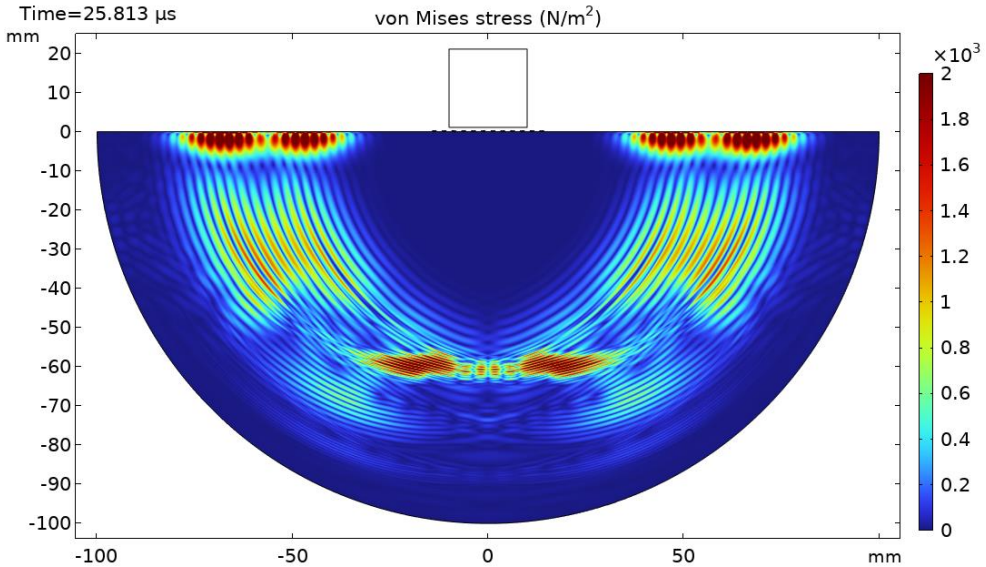

Figure 7.2: 15°,90° Dual Steering Angles EMAT on Semicircular Sample

7.2. Dual-Angle Results

Figure 7.3 shows the directivity plot for the 15°,90° dual-angle model (shown in Figure 7.2) compared to its single-angle steering angles. There is little change to both the displacement and reception angle of the two maxima. Due to the increased runtime, alternative solutions were explored to calculate the results of other dual-angle models. Due to the similarity between the dual-angle and the two single-angle beam directivities, the solution was to simply add the single-angle beam directivities together. Figure 7.4 shows the 15°,90° dual-angle beam directivity compared to the two single-angle beam directivities summed together.

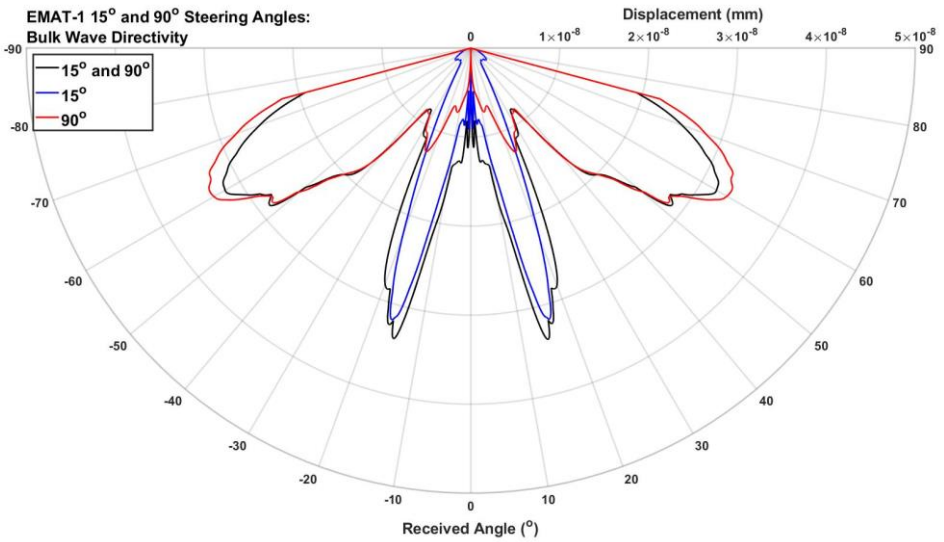

Figure 7.3: Bulk Wave Directivity Plot for 15°,90° Dual Steering Angles

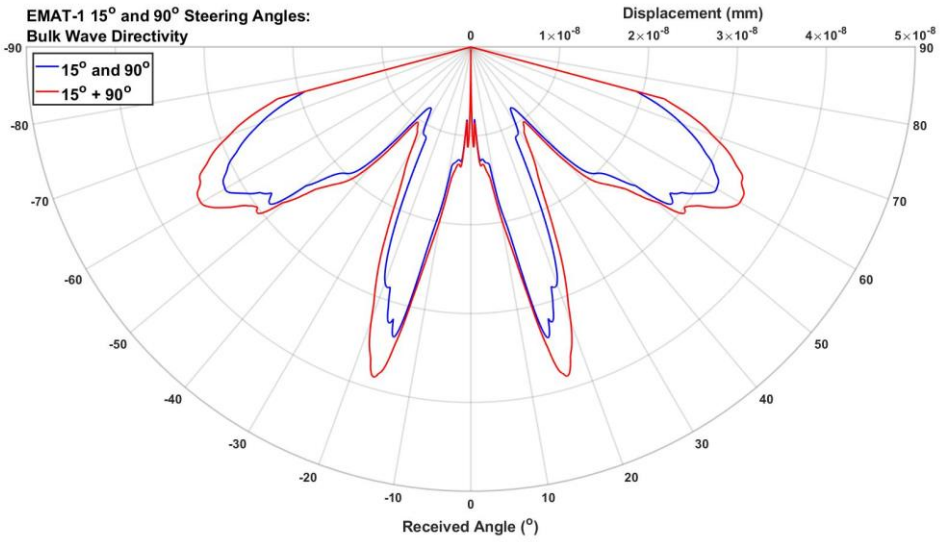

Figure 7.4: Bulk Wave Directivity Plot for 15°,90° Dual Steering Angles

The maximum displacements for the dual-angle dataset and the summed single-angled dataset were measured at 3.3855 $x10^{-8}$mm and 3.8723 $x10^{-8}$mm respectively. The reception angles at which these magnitudes were measured are 14.9° and 16.4°, and the correlation coefficient between the two beam directivities was calculated at 0.9853. While these two datasets do correlate very well, the differences in magnitude and reception angles were too great to be accepted.

The reason for these differences was due to the values of maximum displacement for the two single-angle beam directivities occurring at different RToAs. The solution to this was to sum together the A-scans at each reception angle from the two single-angle EMATs. Both A-scans were shifted in time so that their time delays aligned with that of the dual-angle EMAT. The dual-angle EMAT possesses the same timestep as the primary steering angle EMAT due to its design, however the secondary steering angle EMAT has a greater timestep. By interpolating additional timesteps between those present in the A-scans of the secondary single-angle EMAT, the two A-scans could be summed together. As stated in Section 4.3.1, the tangential and normal displacements were calculated at each reception angle and filtered through a bandpass filter. Due to the presence of two distinct frequencies however, the cutoff frequency limits were set at ±1/3 the maximum and minimum frequencies. This meant that for the 15°,90° dual-angle, bandpass limits of 0.416-3.215MHz were used.

The tangential displacement and reception angle of the main lobe from this extrapolated dual-angle EMAT's beam directivity was measured at 3.3701 $x10^{-8}$mm and 14.8° respectively. The correlation coefficient between the dual-angle and extrapolated beam directivities was calculated at 0.9997. This higher degree of accuracy was deemed acceptable enough to produce beam directives of any dual-angle combination based off of existing single steering angle results. Every combination of dual-angle steering for EMAT-1 was extrapolated using this method. The maximum displacement for each of the three wave modes was extracted and plotted across the secondary steering angles for a fixed primary steering angle. Figure 7.5-Figure 7.8 show this data for primary steering angles of 15°, 30°, 60°, and 90° respectively from EMAT-1.

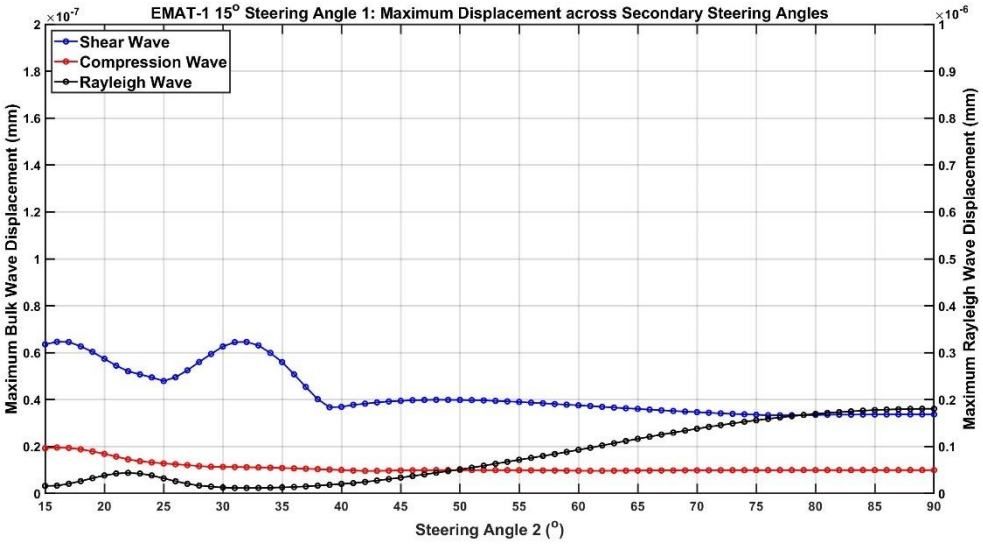

Figure 7.5: Graph of Maximum Displacement across EMAT-1 15° Secondary Steering Angles

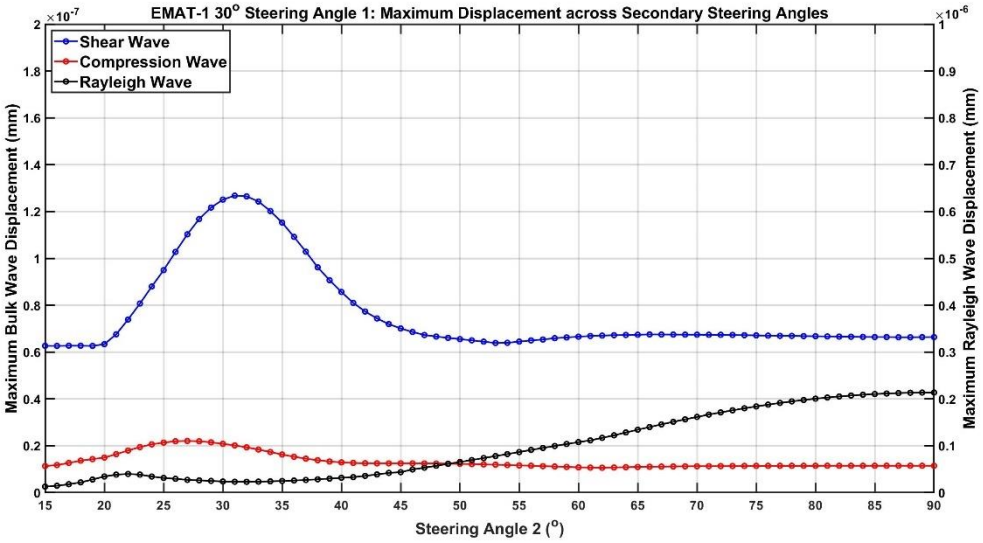

Figure 7.6: Graph of Maximum Displacement across EMAT-1 30° Secondary Steering Angles

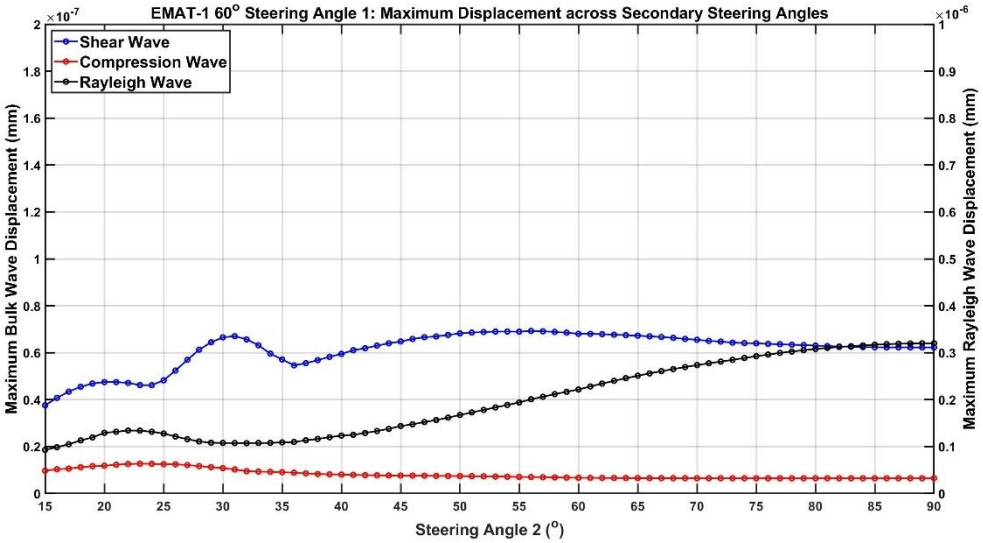

Figure 7.7: Graph of Maximum Displacement across EMAT-1 60° Secondary Steering Angles

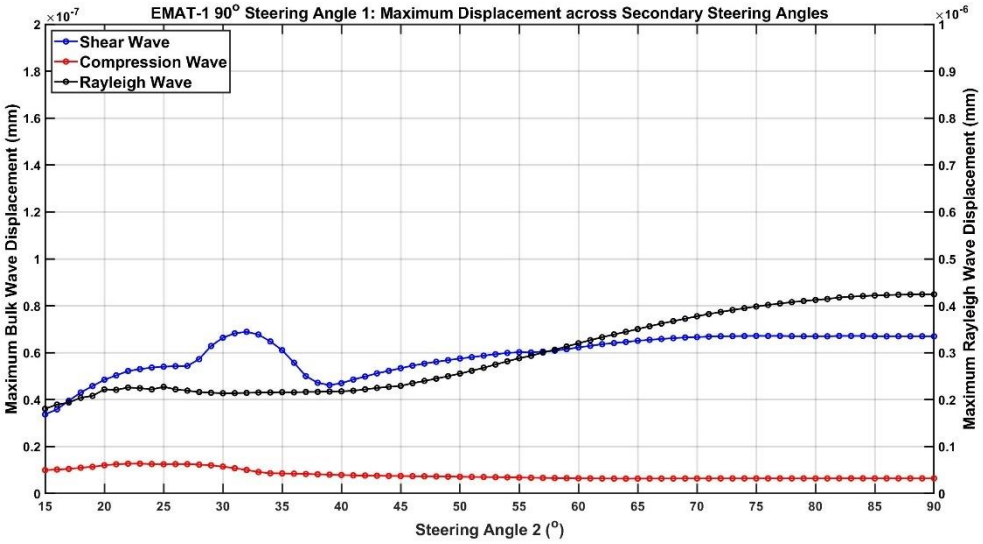

Figure 7.8: Graph of Maximum Displacement across EMAT-1 90° Secondary Steering Angles

As the secondary steering angle gets closer to the primary, the maximum displacement approaches a value twice that of the single steering angle's maximum displacement. This is due to the frequencies of both steering angles being so close that the transmission signal begins to approximate twice that of either's single-angle's transmission signal. Figure 7.9-Figure 7.19 show the reception angles of the maximum displacements from the transmitted shear waves, when one of the two steering angles is set. These figures include the -6dB beamwidth coverage from the maximum displacement in the dual-angle's beam directivity and illustrate the dead space between two distinct beams. As the two steering angles move approach one another, the beamwidths merge until the resultant beamwidth approximates that of either's single beamwidth.

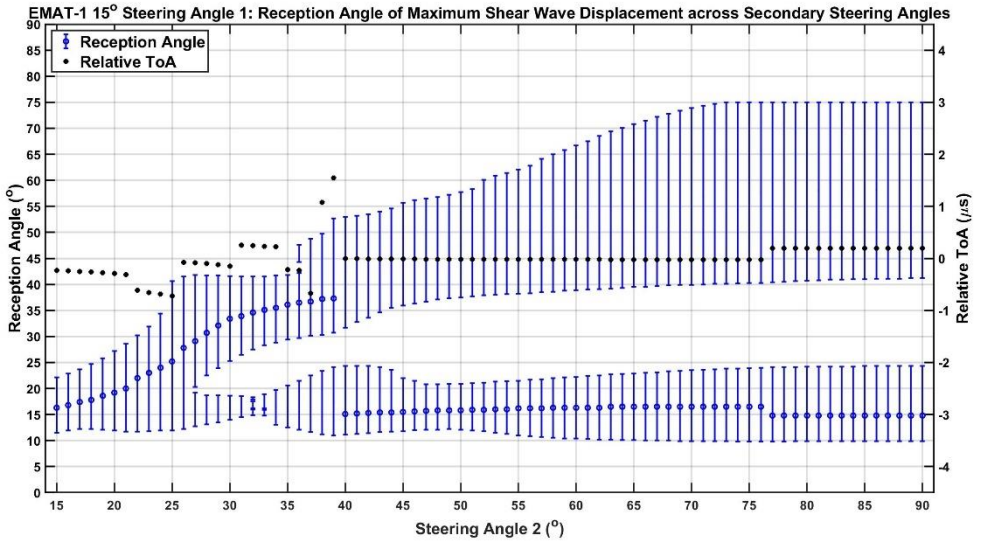

Figure 7.9: Graph of Shear Wave Reception Angles across EMAT-1 15° Secondary Steering Angles

Figure 7.10: Graph of Shear Wave Reception Angles across EMAT-1 20° Secondary Steering Angles

Figure 7.11: Graph of Shear Wave Reception Angles across EMAT-1 25° Secondary Steering Angles

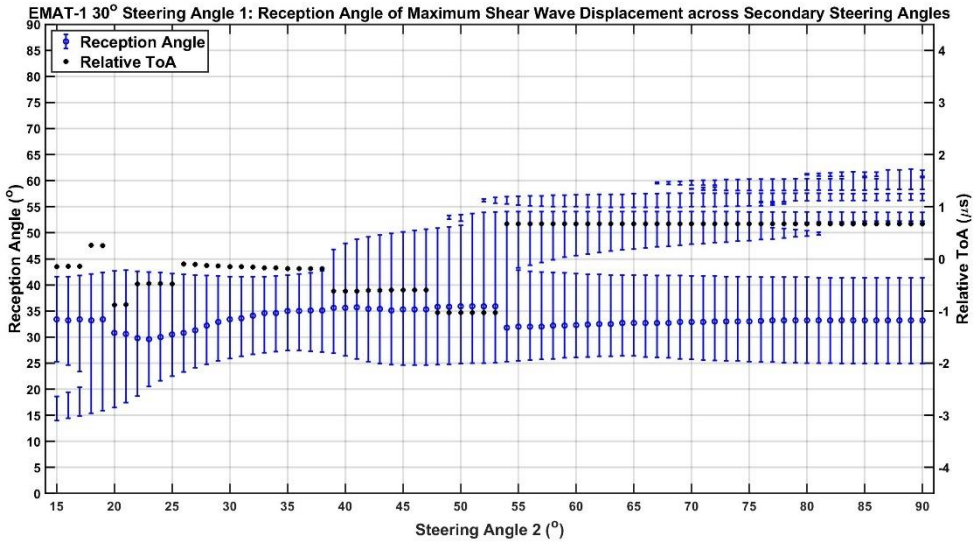

Figure 7.12: Graph of Shear Wave Reception Angles across EMAT-1 30° Secondary Steering Angles

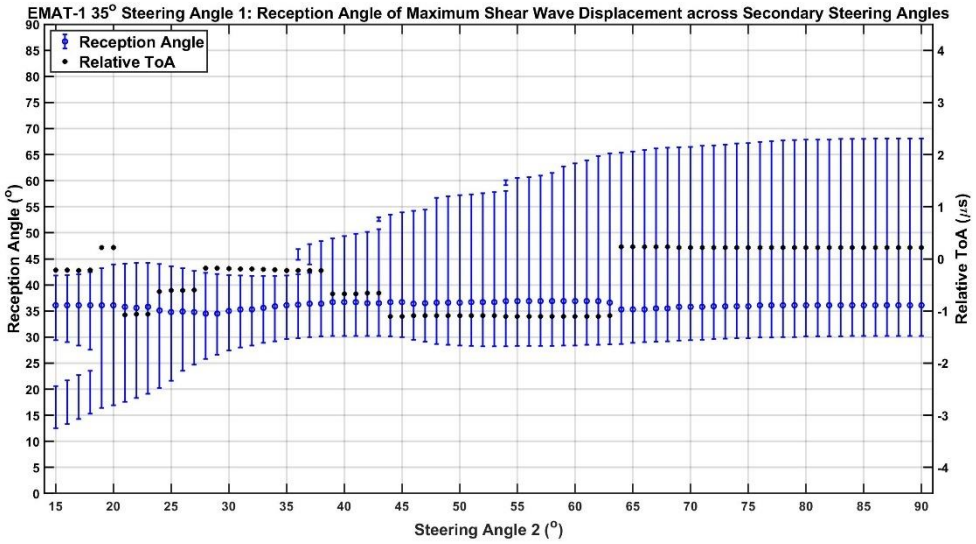

Figure 7.13: Graph of Shear Wave Reception Angles across EMAT-1 35° Secondary Steering Angles

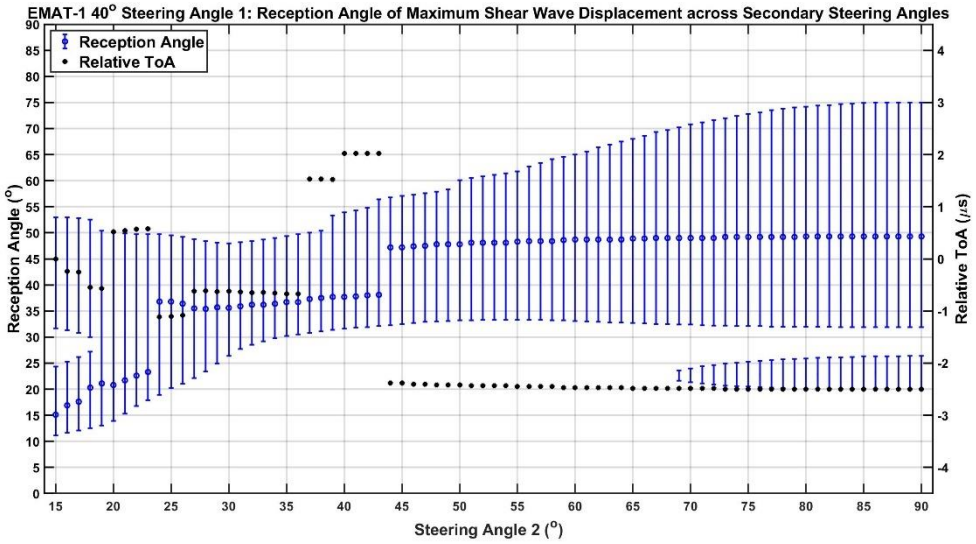

Figure 7.14: Graph of Shear Wave Reception Angles across EMAT-1 40° Secondary Steering Angles

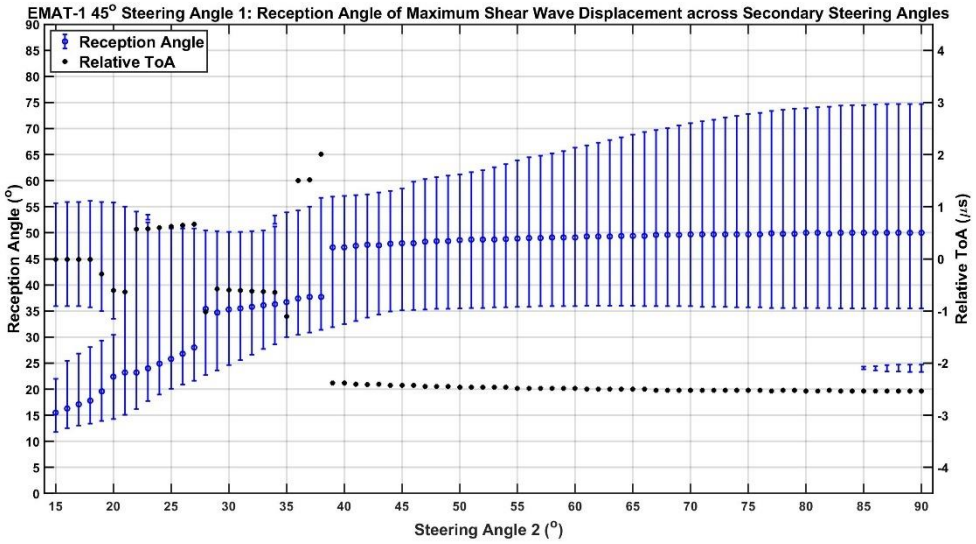

Figure 7.15: Graph of Shear Wave Reception Angles across EMAT-1 45° Secondary Steering Angles

Figure 7.16: Graph of Shear Wave Reception Angles across EMAT-1 50° Secondary Steering Angles

Figure 7.17: Graph of Shear Wave Reception Angles across EMAT-1 55° Secondary Steering Angles

Figure 7.18: Graph of Shear Wave Reception Angles across EMAT-1 60° Secondary Steering Angles

Figure 7.19: Graph of Shear Wave Reception Angles across EMAT-1 90° Secondary Steering Angles

An additional benefit of the dual-angle transmission is that by introducing a lobe of larger displacement into the beam directivity from one of the single steering angles, it reduces the beamwidth from the lobes of lower displacement for the other single steering angle. This is shown in Figure 7.19 as the primary steering angle changes from 15-20°, the beamwidth of the shallower lobe reduces from 41-75° to 50-72°.

7.3. Pulse-Echo Signal Filtration

While the dual-angle EMAT could transmitted shear waves at two distinct angles bidirectionally, an important consideration was how the reflected waves would be received. If a defect was detected by one of the dual-angle EMAT's lobes, it would be difficult to position by ToF alone as there would be no way to tell which lobe struck it.

A solution to this issue is to differentiate the received lobes based on frequency. While the differently angled lobes do have similar magnitudes, they retain their frequencies as seen in Figure 7.20 and Figure 7.21 for the reception angles of the 15° and 90° steering angle lobes respectively.

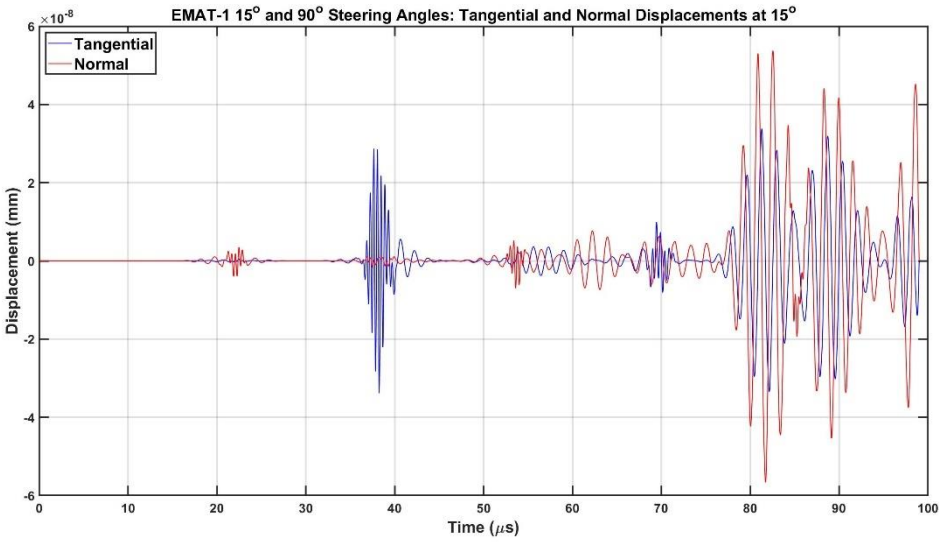

Figure 7.20: Graph of Directional Displacement across Time at 15° for EMAT-1 15°,90° Steering angles

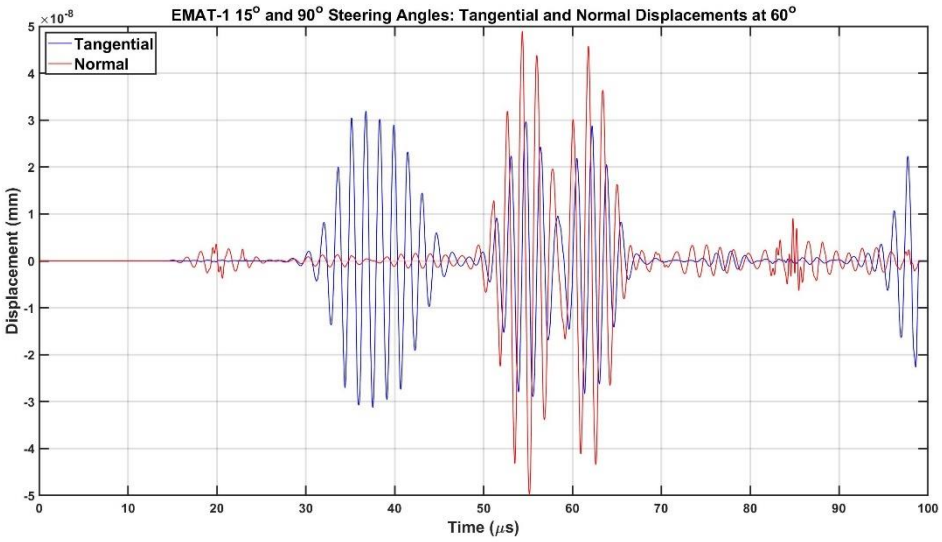

Figure 7.21: Graph of Directional Displacement across Time at 60° for EMAT-1 15°,90° Steering angles

Using the simulated signal method (described in Section 4.4.2) on the area beneath the MLC EMAT, the received signals from the returning waves were simulated and filtered to differentiate the two lobes based on their frequency. If the exact same simulated signal process was used with this model, then (due to the model's symmetrical design and the EMAT's bidirectional transmission) the returning waves from both sides of the curved surface would create a symmetrical displacement distribution which the simulated signal would then cancel out. To counter this effect and simply demonstrate the method of dual-angle frequency filtration, the simulated signal process was performed on one side of the EMAT only, from 0-20mm beneath the EMAT (or from coils 7-12).

Due to the transmission signal containing two different frequencies, frequency limits had to be established for use in differentiating the two distinct lobes. These limits were chosen via a Fourier analysis of each transmission signal. Figure 7.22-Figure 7.24 show the progression of the Fourier analysis as the secondary steering angle in transmission signal increased to 20°, 30°, and 90°.

The two peaks in the frequency spectrum represent each steering angle's gaussian pulse, thus a value of frequency from between these two peaks was used in the filtering process to differentiate between the two lobes. The criteria for this cutoff frequency was that it must have an amplitude of no more than -6dB that of the smallest of the two peaks. Due to the large amount of overlap between the peaks within some frequency spectrums, there were combinations of steering angles that did not meet this criteria. Figure 7.25 shows the minimum secondary steering angle that could be used for a corresponding primary steering angle, as well as the maximum cutoff frequency for that minimum secondary steering angle. For a given primary steering angle, as the secondary steering angle increased from its minimum (shown in Figure 7.25) to 90°, the cutoff frequency value would change also.

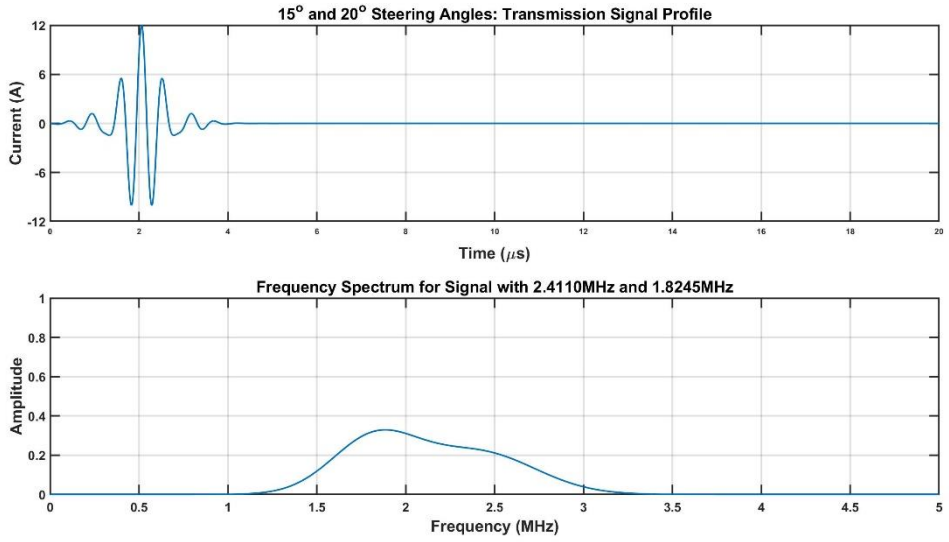

Figure 7.22: Fourier Analysis of 15°,20° Steering angles Pulse

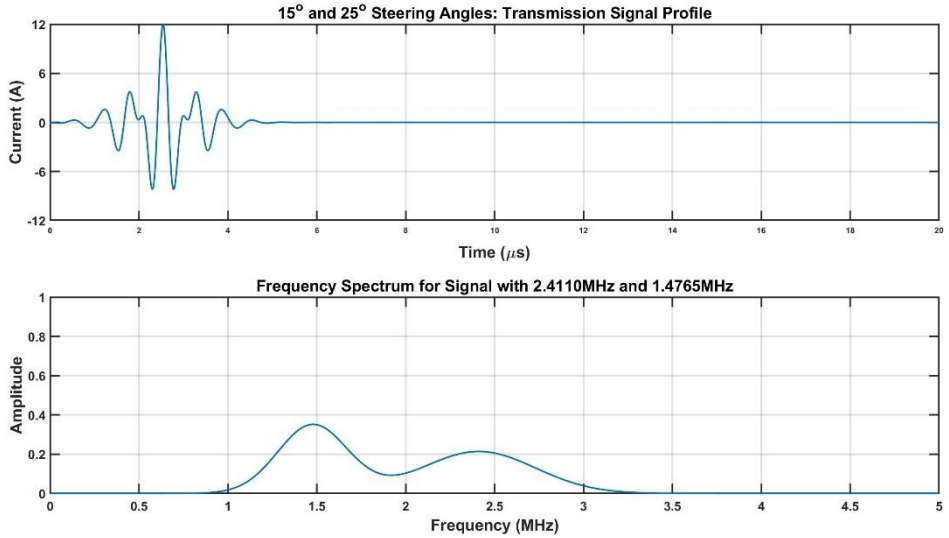

Figure 7.23: Fourier Analysis of 15°,25° Dual-angle Pulse

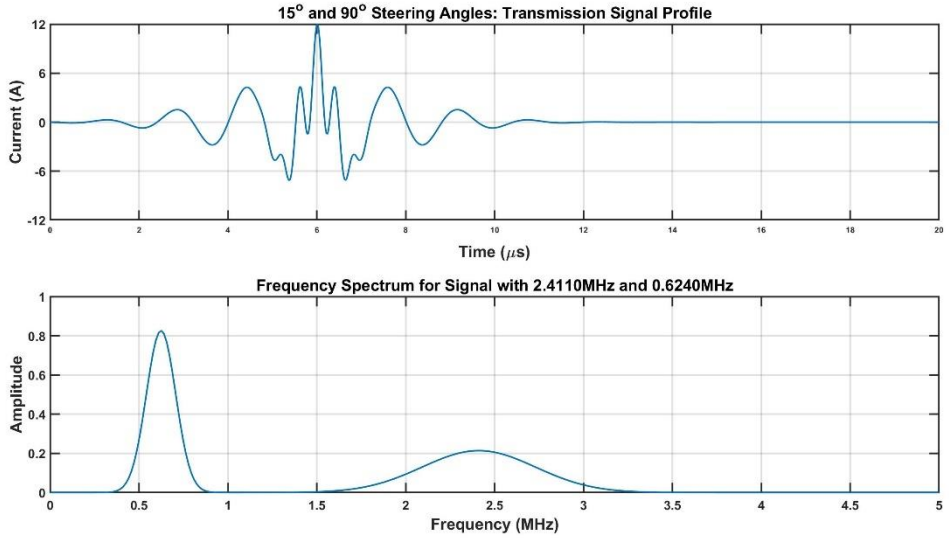

Figure 7.24: Fourier Analysis of 15°,90° Dual-angle Pulse

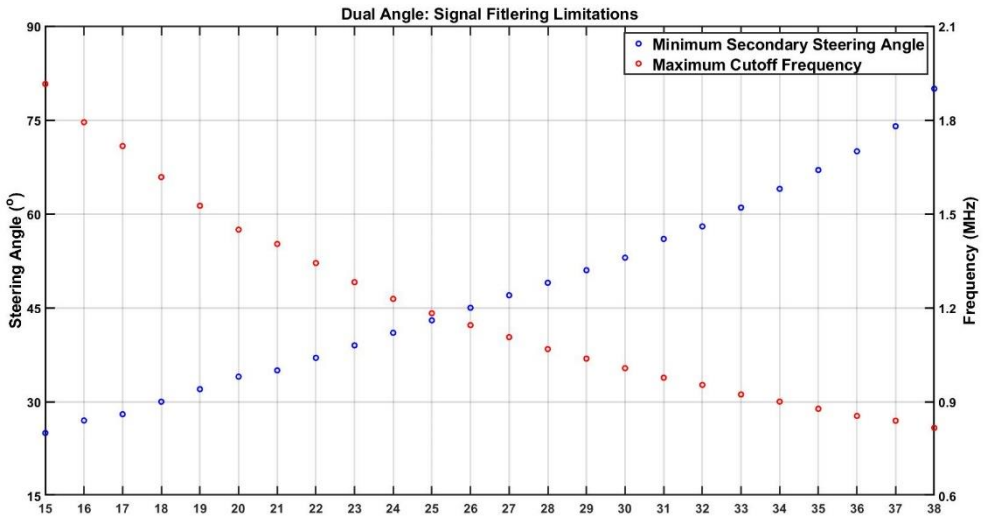

Figure 7.25: Dual-angle Signal Filtering Limits

To filter out two different frequencies from the simulated PE signal, two bandpass elliptic filters were used. The frequency limits for both filters contained the cutoff frequency, and different frequency values that would distinguish whether the filters were to be used for the primary or secondary steering angle's wave. From each of the two peaks in the frequency spectrum graph, a value of frequency (equal in amplitude to that of the cutoff frequency) was taken from the side of the peak opposite to the cutoff frequency. The simulated PE signal was passed through either elliptic filter, and the results of each was then passed through the same bandpass filter as used for the single steering angles (±1/3 steering frequency) to reduce the low frequency reverberation.

Figure 7.26 shows the simulated PE signal for the 15°,90° dual-angle EMAT, and Figure 7.27 and Figure 7.28 show the results of this filtering process for steering angles 15°, 90° respectively. To demonstrate the efficiency of this filtering process, both filtered PE signals from the dual-angle model were compared to the filtered PE signals from their corresponding single steering angle's model. Section 5.4 had previously established problems when graphing the amplitude of the simulated signal across steering angles, specifically at higher frequencies. While this was corrected by dividing the signal by the steering frequency, this was not an option for a signal with two distinct frequencies. Therefore, these simulated signals were graphed as normalised amplitudes.

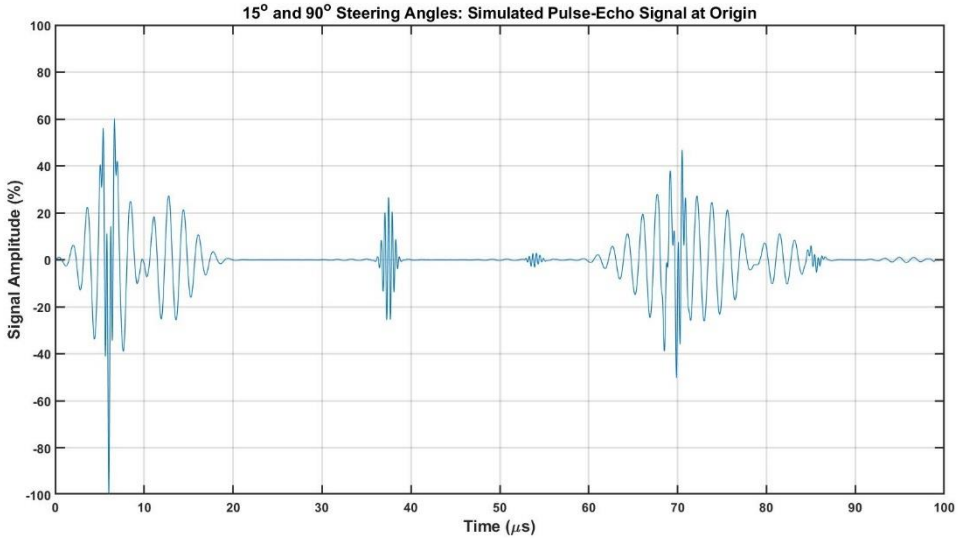

Figure 7.26: EMAT-1 15°,90° Dual-angle PE signal

The correlation coefficient between the 15° steering angle's PE signal and the 15° component of the 15°,90° dual-angle PE signal (as shown in Figure 7.27) was 0.9976, with a difference of 0.19% in the normalised amplitude peaks for the returned shear waves. For the 90° signals (shown in Figure 7.28) there was a correlation coefficient of 0.9697 but a greater difference of 6.04% for the returned shear wave peaks.

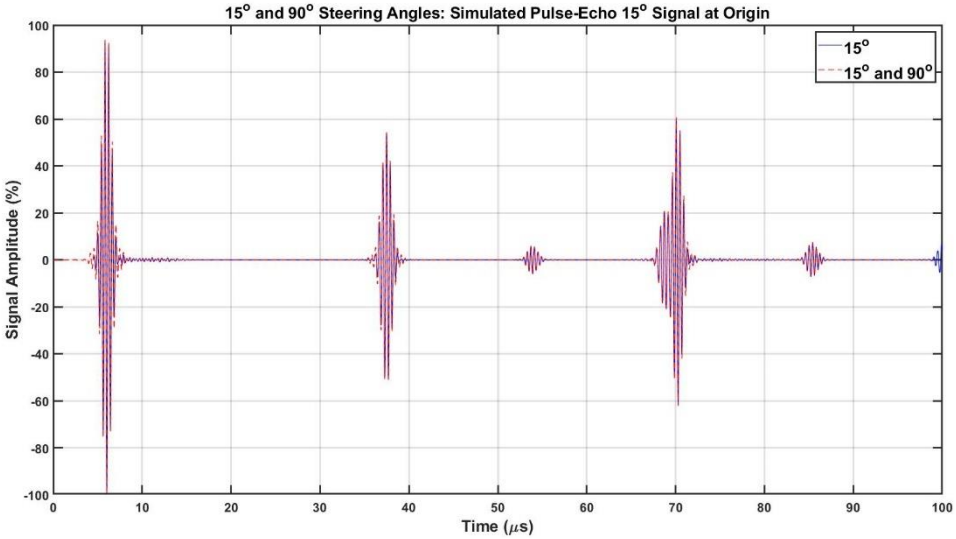

Figure 7.27: EMAT-1 15° Filtering of 15°,90° Dual-angle PE signal

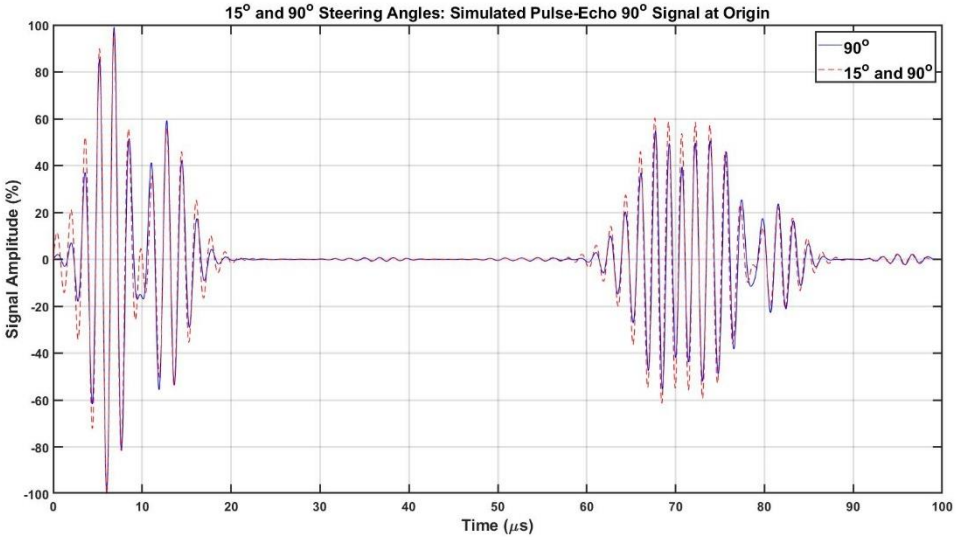

Figure 7.28: EMAT-1 90° Filtering of 15°,90° Dual-angle PE signal

This proves that an EMAT PE signal of different frequencies could be filtered to a high degree of accuracy. If a dual-angle PE EMAT were to detect a defect by one of its two lobes, this filtration method could determine the magnitude of the returned shear wave signal for each steering angle. This would reveal which lobe detected the defect, and how far from the EMAT it was based off of ToF.

7.4. Triple-Angle Results

Within many frequency spectrums of dual-angle transmission signals there were wide gaps between the peaks, as shown in Figure 7.24. This meant that there was an opportunity to introduce an additional steering angle into this signal. The pulse profile for the transmission signal followed the same process as that of the dual-angle EMAT: the addition of multiple single-angle transmission signals multiplied by the current; and the time delay being a function of the frequency of the tertiary steering angle (always greater than the primary and secondary). Figure 7.29 shows the profile and Fourier analysis of a 15°,30°,90° triple-angle transmission signal.

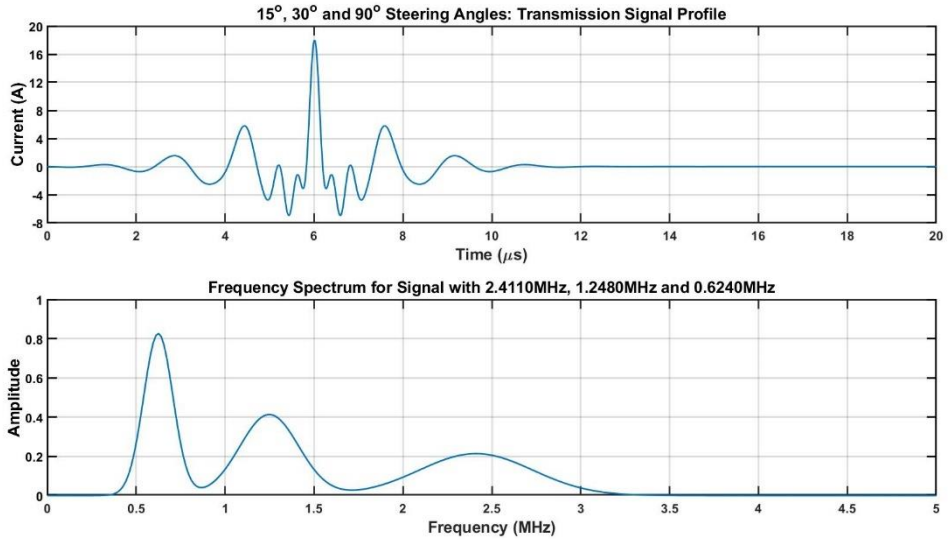

Figure 7.29: Fourier Analysis of 15°,30°,90° Triple-angle Pulse

The same process of determining steering angle combinations based off of a cutoff frequency between the peaks in the frequency spectrum was used to decide the steering angle combinations. The difference for the triple-angle signals is that two cutoff frequencies are required: one between the primary and secondary steering angles; and the other between the secondary and tertiary steering angles. The only difference to the criteria of each cutoff frequencies was that it must be no more than -6dB the smallest peak on either side of it. This meant that the cutoff frequency between the secondary and tertiary steering angles need not have an amplitude less than -6dB of the primary steering angle's amplitude.

This caused greater restrictions on the combinations of angles. Table 7.1 shows the combinations of the three steering angles that could be used with the -6dB cutoff frequency. There is still a minimum secondary steering angle for each primary steering angle, however there is now a maximum secondary steering angle to permit the use of a tertiary steering angle. Table 7.1 states the two minimum tertiary steering angles that can be used for both the minimum and maximum steering angles. The tertiary steering angles range from the values stated in Table 7.1 up to 90°.

Table 7.1: Triple-angle Signal Filtering Limits

Primary Steering Angle (°)	Minimum Secondary Steering Angle (°)	Minimum Tertiary Steering Angle (°) for Minimum Secondary	Maximum Secondary Steering Angle (°)	Minimum Tertiary Steering Angle (°) for Maximum Secondary
15	25	43	38	80
16	27	47	38	80
17	28	49	38	80
18	30	53	38	80
19	32	58	38	80
20	34	63	38	80
21	35	66	38	79
22	37	74	38	79

Figure 7.30 shows the beam directivity plot of the 15°,30°,90° triple-angle EMAT. It is immediately noticeable that within the triple-angle beam directivity there are large disparities in displacement for each of the three lobes. Within the beamwidth: the 15° steering angle's lobe has a narrow width of 4.6°; the 30° steering angle's lobe has a broader width of 16.1°; and the 90° steering angle's lobe is fragmented with multiple narrow lobes of 1.7°, 1.3°, and 0.5°. The reason for this irregular -6dB beamwidth is due to the differences in displacement between the three individual steering angles. The EMAT has been established to produce a maximum shear wave displacement near the 30° steering angle, almost was twice that of either the 15° or 90° steering angles.

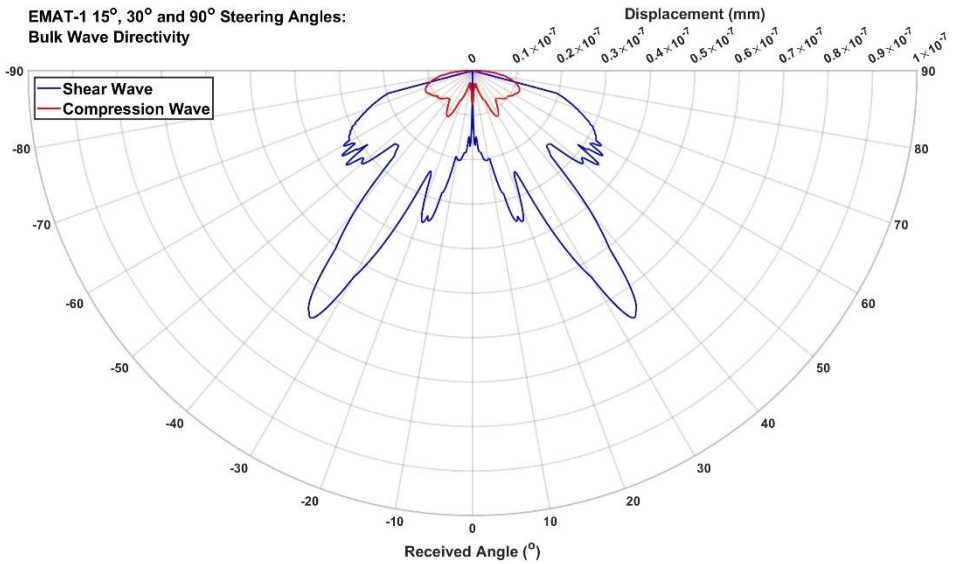

Figure 7.30: Bulk Wave Directivity Plot for EMAT-1 15°,30°,90° Triple Steering Angles

As previously stated, as two steering angles move closer together the displacement becomes twice that of either steering angle as the transmission signal begins to emulate twice that of either steering angle's signal. Following this logic, if a transmission signal was reduced by half, then the displacement from its lobe would also be reduced by half. This led to the idea of reducing the amplitude of a single steering angle's profile by a SF within the overall transmission signal, as shown in Equation 7.4.

$$I(t) = I \times \left[\left(SF_1 \times I_1(t)\right) + \left(SF_2 \times I_2(t)\right) + \left(SF_3 \times I_3(t)\right)\right] \qquad \text{Equation 7.4}$$

where $SF_{1\text{-}3}$ = pulse profile scale factors for steering angles 1-3 respectively.

Using Equation 7.4 for the 15°,30°,90° triple-angle EMAT, the SF for the 30° steering angle's pulse profile was set at 0.5 while those of the remaining steering angles was kept at 1. Figure 7.31 shows the Fourier analysis of this transmission signal, and there was a noticeable reduction in amplitude by half for the 30° peak when comparing frequency spectrums to Figure 7.29. Figure 7.32 shows the beam directivity for this triple-angle EMAT.

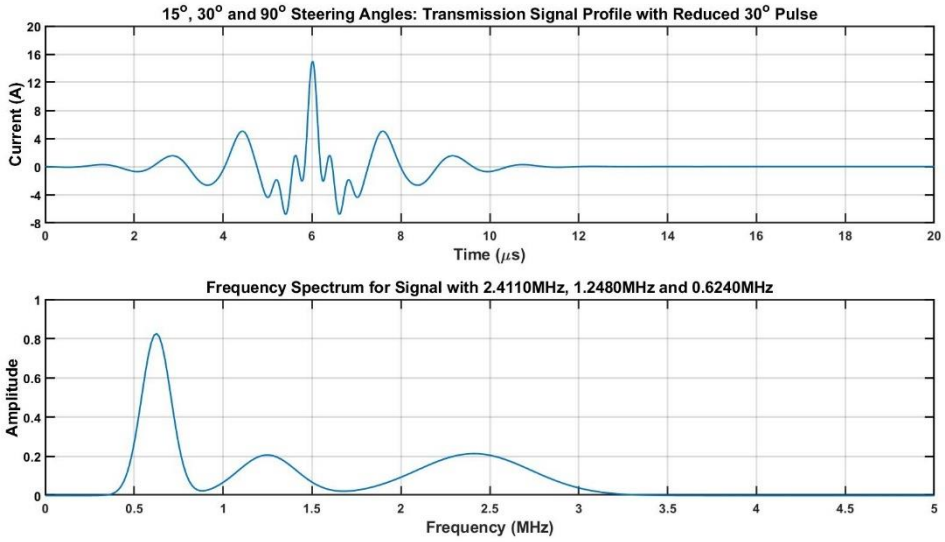

Figure 7.31: Fourier Analysis of 15°,30°,90° Dual-angle Pulse with reduced amplitude

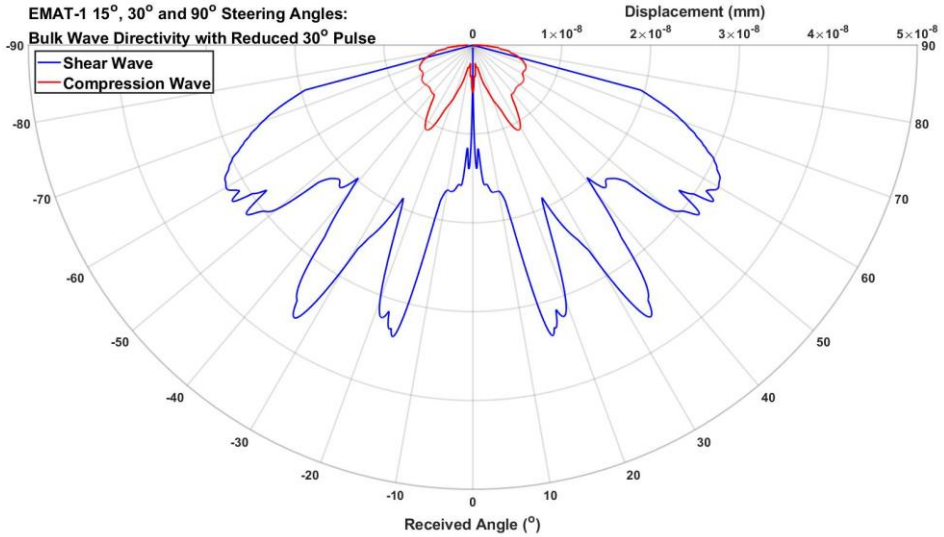

Figure 7.32: Bulk Wave Directivity Plot for EMAT-1 15°,30°,90° Triple Steering Angles with Reduced 30° Pulse

Decreasing the 30° steering angle pulse profile by half had the desired effect of reducing the 30° lobe's displacement also by half. This had the additional effect of increasing the beamwidth from 11.9° to over 75°. An angular coverage of over 60° would enable this conventional EMAT to perform sectoral scans whilst in motion. If moving laterally across bulk material, not only could a defect be detected by each of the three lobes in both directions, but the PE signal could reveal the defect's distance and angle from the EMAT based on the lobe that detected it.

Furthermore, decreasing the 30° pulse profile by half also reduces the amplitudes of the two cutoff frequencies from the Fourier analysis. While this does reduce the amplitude ratios for both peak-to-trough values, it also

enables the minimum secondary steering angle to be reduced further. Using the values of maximum shear wave displacement from Figure 4.43, each of the three pulse profile's SFs were equated to make each steering angle's waves equal in maximum displacement. These reductions in amplitude for a 15° primary steering angle reduce the minimum secondary and tertiary steering angles to 24° and 41° respectively.

Despite this, the number of pulse profiles included in the transmission signal could not be increased beyond three steering angles. This may be achieved by increasing the standard deviation of the gaussian pulse, thus reducing the width of the peaks within the frequency spectrum and enabling the -6dB cutoff frequencies to be more readily available. Additional pulse profiles may also be included via alternative filtering methods for the PE signal. The criteria for the cutoff frequencies was set for use in the elliptical filters, however if a more efficient method were to be devised then this -6dB limit may be lifted.

7.5. Summary

The result of this chapter was the proposal of a complex transmission signal pulsed by an MLC EMAT. This would transmit a beam directivity with multiple shear wave lobes at different angles. The simulated reception signal method proved that in a PE setup, the returning shear waves could be filtered to differentiate the magnitude of a single steering angle's lobe.

The EMAT-1 configuration fully explored its dual-angle capabilities, based on extrapolation of the existing single steering angle models. These provided highly accurate alternatives to lengthy simulations of the triple-angle models. This method could also be applied to the other magnetic configurations for both the beam directivity and steerability models.

Chapter 8 - Conclusions

8.1. Summary of Work

This thesis has focused on the topic of multi-angle shear wave transmission from an MLC EMAT and the effects that steering via frequency has upon them. This necessitated a review of the theory and relevant literature on this topic, and the main conclusions made with EMATs as a technology. Chapter 3 detailed the design of the FEM model used within the majority of this work, with changes specified in the relevant chapters.

Chapter 4 provided an analysis of the changes observed in the shear wave beam directivity via frequency. The majority of these tests were undertaken via the FEM models with experimental testing validating their findings. This chapter detailed how the shear waves reached both a maximum displacement and a steering limit across a broad range of steering angles. The shear waves were examined also in the context of flat backwall profiles, showing similar patterns of behaviour. The result of these secondary examinations was a mathematical method of constructing the simulated reception signal of a detection EMAT across a flat surface based on existing displacement data.

Chapter 5 documented the effects that different bias magnetic flux densities had on the transmitted shear waves. These were composed of single or multiple magnets, of differing widths and magnetisation directions. While the differences between these magnetic configurations has been documented, each produced similar results to the original EMATs' design. A correlation is drawn between the number of magnetic flux concentrations within the induced eddy current array, and the number of peaks in both the shear and Rayleigh waves A-scans. The simulated reception signal method is shown to successfully work with these different magnetic configurations and can be used to predict which configurations produce the maximum reception signal in a PC setup.

Chapter 6 documented the effects that the coil configuration plays on the transmitted shear waves. The number of sidelobes within a given shear

wavefront is related to the number of coils within the MLC array, and the previously established reception angle was overcome by increasing the coil's spacing distance.

Chapter 7 proposed a novel method of complex signal generation from the EMAT, to transmit shear waves at different angles simultaneously. The combination of steering angles was determined via an FFT of the transmission signal, as filtering could be used to distinguish between the differently angled shear waves. It was discovered that a dual-angle's beam directivity results could be calculated by combing the A-scans of the constituent single steering angles at each reception angle. This provided an easy alternative solution, compared to running lengthy simulated models. The number of single steering angles included in a given multi-angle transmission signal is limited to three within this thesis, however this may be overcome with different signal types. This is desirable as a beam directivity with a large number of different steering angles would be able to better distinguish the angle at which defects were located, relative to the EMAT.

This body of work set out with the aim of evaluating the possibility of replicating the Sperry RSU's multi-angle UT methodology with EMAT technology. A conventional MLC EMAT's capability of transmitting oblique shear waves into bulk material was tested to understand its limits. Design changes were then proposed in order to enhance its performance for certain angles. The ability to generate shear waves at specified angles simultaneously enables the design of a simulated conventional MLC EMAT that can generate bidirectional shear wave lobes to cover the RSU's angles of 37° and 70° (as shown in Figure 8.1) while simultaneously generating Rayleigh waves across the surface, for the detection of surface defects. This body of work has demonstrated that a 0° shear wave lobe can be transmitted via MLC EMATs. The distinct frequencies of these lobes (if they were to reflect off of a defect and return to the EMAT) could be filtered to reveal the distance and angle relative to the EMAT. This would enable defect triangulation via a laterally moving EMAT over rail track, without the necessity of a coupling medium.

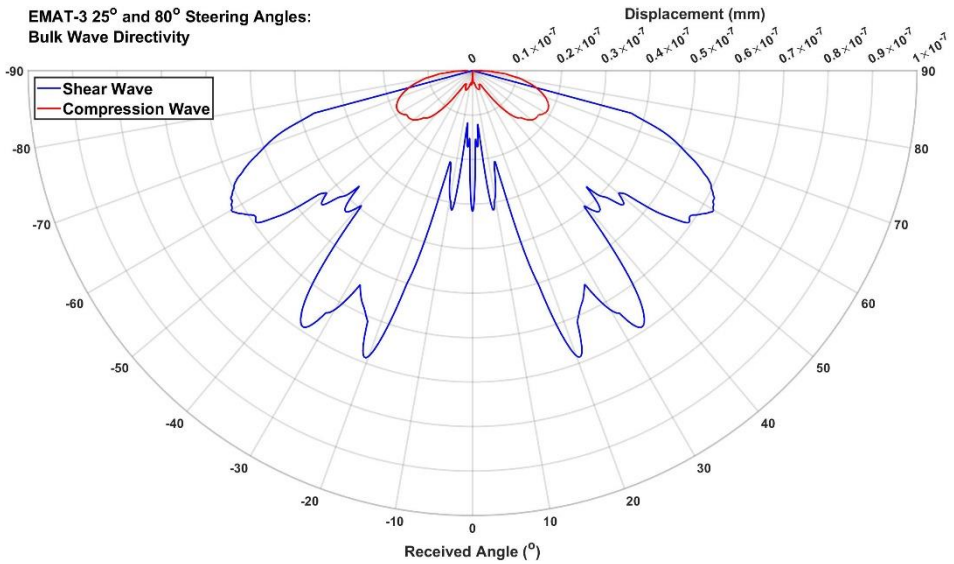

Figure 8.1: Bulk Wave Directivity Plot for EMAT-3 25°,85° Dual Steering Angles

8.2. Contributions to Knowledge

The contributions to knowledge as a result of this body of work include:

- A study on the relationship between the desired steering angle of the shear waves as a function of frequency and its actual reception angle.
- A method of modelling an EMAT's reception signal via simulated displacement data.
- Parametric studies on the EMAT's magnetic field, and how this affected the magnitude and direction of the transmitted waves. These parametric studies include:
    - The width of the magnet
    - The number of magnets within a single EMAT
    - The direction of magnetisation
    - Different configurations within a PC setup
- Parametric studies on the EMAT's coil configuration, and how this affected the shear wave sidelobes within a given wavefront. These parametric studies include:
    - The number of coils within an array
    - The coil spacing
- A study on the generation of multiple shear waves at different angles via complex signal transmission, based on work from the previous chapters.

8.3. Suggestions for Future Work

Based on the conclusions highlighted in this thesis, there are a number of different directions that this work can explore further.

Firstly, changes can be made to the material under examination. The simulation and experimental work within this thesis was carried out solely on aluminium. This was to limit the EMAT's transduction method to Lorentz forces and simplify the simulated models by removing the magnetisation and magnetostrictive transductions. An obvious extension of this work is its application onto ferromagnetic. Additionally, the presence of defects within the material would prove useful in testing the MLC EMAT's ability for defect detection. These can take the form of side drilled holes or cracking at the surface as real-world examples. Parametric studies can be conducted on the size and position of these defects relative to the EMAT. This would test the sensitivity and magnitude of the EMAT's defect response across the range of steering angles for the transmitted shear waves.

Specific to this body of work, further investigation into transmission signals can be explored. These involve the effects that a wider gaussian pulse has on the shear wave beam directivity, as this could also enable a greater number of steering angles to be included within the multi-angle signal. An issue that can arise from the experimental testing of multi-angle signal transmission is the impedance matching of the EMAT. Different frequencies would present challenges to the calculation of the RLC circuit's resonant frequency, and by extension the EMATs required capacitance. These multi-angle signals can also be tested on different types of EMATs. Huang and Sanije [93] used signals of different frequencies on a PPM EMAT to generate different SH-wave modes into an aluminium plate which (through multi-angle signals) could be generated simultaneously.

To further develop the MLC EMAT as an alternative to the Sperry RSU, its ability to transmit bulk waves and receive defect signals while in motion would be highly advantageous. Rees-Lloyd et al [94] explored these effects for Rayleigh waves from an MLC EMAT and found that the application of velocity

generated eddy currents within the inspection sample from the EMAT's moving permanent magnet. These created a quasi-static bias magnetic field which became more distorted as the velocity increased, particularly with ferromagnetic materials. The effect that this would have on the generation of bulk waves would be an interesting area of exploration.

The method of simulating an EMAT's reception signal from incoming ultrasonic waves proved to be a more accurate means of comparing the simulated data to the experimental testing. This method however requires further optimisation to improve its magnitude across steering angles, particularly at higher frequencies. This can be done by refinement to the calculation of material deformation at the surface beneath the coil array. Additionally, this method can also be applied to different types of EMATs (such as the spiral-coil EMATs) or on different surfaces (such as the semicircular sample's curved surface).

Specific to steering the EMAT's shear waves, greater investigation can be conducted on the specific effects that the magnitude and orientation of the Lorentz force densities had on the transmitted shear waves. Specifically modifying the strength and direction of the simulated bias magnetic flux density (similar to the models from Chapter 6) would be an interesting topic of study. This would inform the design of custom permanent magnets to apply a bias magnetic field specific to each coil. This would be akin to line-focusing EMATs, as they would be designed to operate at a specific frequency and transmission angle. Alternatively, the focusing of shear waves via timed excitation of coils across a range of frequencies could be investigated, with the goal of steering a PA MLC EMAT.

Bibliography

[1] M. Cartwright, ‘The Railways in the British Industrial Revolution’, World History Encyclopedia. Accessed: Sep. 30, 2024. [Online]. Available: https://www.worldhistory.org/article/2167/the-railways-in-the-british-industrial-revolution/

[2] A. Bianculli, *Trains and Technology: The American Railroad in the Nineteenth Century. Volume 3: Track and Structures – University of Delaware Press*. Accessed: Sep. 30, 2024. [Online]. Available: https://udpress.udel.edu/book-title/trains-and-technology-the-american-railroad-in-the-nineteenth-century-volume-3-track-and-structures/

[3] *Rail Defect Manual*. Sperry Rail Service, 1968. [Online]. Available: https://www.multimodalways.org/docs/railroads/RREquip/Sperry/Sperry%20Rail%20Defect%20Manual%204-1968.pdf

[4] P. Association, ‘How Hatfield changed the rail industry’, *The Guardian*, Sep. 06, 2005. Accessed: Sep. 30, 2024. [Online]. Available: https://www.theguardian.com/uk/2005/sep/06/hatfield.transport

[5] VAIGNANN, ‘Types Internal Rail defects’, USFD VIJAYAWADA DIVISION. Accessed: Mar. 08, 2025. [Online]. Available: https://usfdbza.wordpress.com/2018/07/29/types-internal-rail-defects/

[6] P. Yılmazer, A. Amini, and M. Papaelias, ‘The Structural health condition monitoring of rail steel using acoustic emission techniques’.

[7] W. Gong, M. F. Akbar, G. N. Jawad, M. F. P. Mohamed, and M. N. A. Wahab, ‘Nondestructive Testing Technologies for Rail Inspection: A Review’, *Coatings*, vol. 12, no. 11, Art. no. 11, Nov. 2022, doi: 10.3390/coatings12111790.

[8] D. Hesse, ‘RAIL INSPECTION USING ULTRASONIC SURFACE WAVES’.

[9] L. Xiong, G. Jing, J. Wang, X. Liu, and Y. Zhang, ‘Detection of Rail Defects Using NDT Methods’, *Sensors*, vol. 23, no. 10, Art. no. 10, Jan. 2023, doi: 10.3390/s23104627.

[10] ‘Rail Tech - Rail defects’. Accessed: Sep. 30, 2024. [Online]. Available: https://www.itsmarta.com/wayside-docs/Books%20For%20QR%20codes%20PDFs/Rail%20Tech%20-%20Rail%20defects.pdf

[11] R. Palmer, ‘Vintage Railroad Pictures’. [Online]. Available: https://cnymod.blogspot.com/2015/01/lehigh-valley-passenger-train-wreck-at.html?zx=e490af0be4256457

[12] J. Norman, ‘An introduction to ultrasonic wheel probes’.

[13] Rowlands Castle History and Heritage, ‘Sperry Rail’. [Online]. Available: http://www.staging.rowlandscastleheritagecentre.org.uk/village-history/businesses-of-the-past/sperry-rail/

[14] Renishaw, ‘Magnetic rotary encoders contribute to rail track safety program’. [Online]. Available: https://www.renishaw.com/en/magnetic-rotary-encoders-contribute-to-rail-track-safety-program--11974?srsltid=AfmBOopTQaV4qjAFWONN5eZPCAAngr36QgNkfCePySIS_WC6RQrbd9H0

[15] Innotrack, ‘D4.4.1 – Rail Inspection Technologies’, 2008. Accessed: Sep. 30, 2024. [Online]. Available:

https://www.charmec.chalmers.se/innotrack/deliverables/sp4/d441-f3p-rail_inspection_technologies.pdf
[16] Innerspec, 'EMAT Technology'. [Online]. Available: https://www.innerspec.com/emat-technology
[17] G. Jie, D. Baoyu, L. Yan, and H. Cunfu, 'Development of Acoustic Beam Deflection Electromagnetic Acoustic Transducer for Surface Crack Detection of Wind Turbine Main Shaft', in *Advances in Production*, A. Burduk, A. Batako, J. Machado, R. Wyczółkowski, K. Antosz, and A. Gola, Eds., Cham: Springer Nature Switzerland, 2023, pp. 393–405. doi: 10.1007/978-3-031-45021-1_30.
[18] Z. Qu, Z. Li, R. Yang, S. Hu, and S. Wang, 'Extending the Incidence Angle of Shear Vertical Wave Electromagnetic Acoustic Transducer with Horizontal Magnetization', *Sensors*, vol. 22, no. 22, p. 8589, Nov. 2022, doi: 10.3390/s22228589.
[19] G. Hübschen, '2 - Electromagnetic acoustic transducers', in *Ultrasonic Transducers*, K. Nakamura, Ed., in Woodhead Publishing Series in Electronic and Optical Materials. , Woodhead Publishing, 2012, pp. 36–69. doi: 10.1533/9780857096302.1.36.
[20] O. Rees-Lloyd, 'Velocity Effects on the Generation of Rayleigh Waves using EMATs', PhD, UWTSD, 2024.
[21] 'Nondestructive Testing Handbook, Vol. 1: Liquid Penetrant Testing (PT), 4th ed.' Accessed: Sep. 30, 2024. [Online]. Available: https://source.asnt.org/1pekbgc/
[22] D. G. Moore, P. O. Moore, and American Society for Nondestructive Testing, Eds., *Magnetic testing*. in Nondestructive testing handbook (3rd ed.), no. v. 8. Columbus, OH: American Society for Nondestructive Testing, 2008.
[23] 'Nondestructive Testing Handbook, Vol. 6: Acoustic Emission Testing (AE), 3rd ed.' Accessed: Sep. 30, 2024. [Online]. Available: https://source.asnt.org/1pekcjl/
[24] 'Nondestructive Testing Handbook, Vol. 5: Electromagnetic Testing (ET), 3rd ed.' Accessed: Sep. 30, 2024. [Online]. Available: https://source.asnt.org/1pekca9/
[25] 'Nondestructive Testing Handbook, Vol. 7: Ultrasonic Testing (UT), 3rd ed.' Accessed: Sep. 30, 2024. [Online]. Available: https://source.asnt.org/1pekcqq/
[26] SZUTEST, 'NDT – Non Destructive Testing'. [Online]. Available: https://www.szutest.com/non-destructive-testing/
[27] H. Rindorf, *Acoustic emission source location in theory and in practice*. Brüel & Kjær, 1981.
[28] 'Nondestructive Evaluation Physics : Waves'. Accessed: Sep. 30, 2024. [Online]. Available: https://www.nde-ed.org/Physics/Waves/modeconversion.xhtml
[29] 'The Hysteresis Loop'. [Online]. Available: https://www.nde-ed.org/Physics/Magnetism/HysteresisLoop.xhtml
[30] D. Jiles, *Introduction to Magnetism and Magnetic Materials*, 3rd ed. Boca Raton: CRC Press, 2015. doi: 10.1201/b18948.
[31] R. B. Thompson, 'Mechanisms of electromagnetic generation and detection of ultrasonic Lamb waves in iron-nickel alloy polycrystals', *J. Appl. Phys.*, vol. 48, no. 12, pp. 4942–4950, Dec. 1977, doi: 10.1063/1.323623.

[32] M. Seher and P. B. Nagy, ‘On the separation of Lorentz and magnetization forces in the transduction mechanism of Electromagnetic Acoustic Transducers (EMATs)’, *NDT E Int.*, vol. 84, pp. 1–10, Dec. 2016, doi: 10.1016/j.ndteint.2016.07.001.
[33] J. He, S. Dixon, S. Hill, and K. Xu, ‘A New Electromagnetic Acoustic Transducer Design for Generating and Receiving S0 Lamb Waves in Ferromagnetic Steel Plate’, *Sensors*, vol. 17, no. 5, p. 1023, May 2017, doi: 10.3390/s17051023.
[34] Y. Wang, S. Wang, Y. Zhao, H. Li, and S. Huang, ‘Microscopic Modelling for EMAT in Ferromagnetic Materials’, in *2023 IEEE 16th International Conference on Electronic Measurement & Instruments (ICEMI)*, Aug. 2023, pp. 465–469. doi: 10.1109/ICEMI59194.2023.10270678.
[35] E. W. Lee, ‘Magnetostriction and Magnetomechanical Effects’, *Rep. Prog. Phys.*, vol. 18, no. 1, p. 184, Jan. 1955, doi: 10.1088/0034-4885/18/1/305.
[36] R. Ribichini, ‘Modelling of Electromagnetic Acoustic Transducers’, PhD, Imperial College London, 2011.
[37] M. Hirao and H. Ogi, *EMATs for Science and Industry*. Boston, MA: Springer US, 2003. doi: 10.1007/978-1-4757-3743-1.
[38] V. Byrd, ‘Electromagnetic Acoustic Transducers (EMATs)’, 2015. [Online]. Available: https://slideplayer.com/slide/6393215/
[39] H. Miao and F. Li, ‘Shear horizontal wave transducers for structural health monitoring and nondestructive testing: A review’, *Ultrasonics*, vol. 114, p. 106355, Jul. 2021, doi: 10.1016/j.ultras.2021.106355.
[40] M. Hirao and H. Ogi, *Electromagnetic Acoustic Transducers: Noncontacting Ultrasonic Measurements using EMATs*. in Springer Series in Measurement Science and Technology. Tokyo: Springer Japan, 2017. doi: 10.1007/978-4-431-56036-4.
[41] X. Ding, H. Ba, X. Wu, and L. He, ‘Lift-off Performance of Receiving EMAT Transducer Enhanced by Voltage Resonance’.
[42] S. Huang, W. Zhao, Y. Zhang, and S. Wang, ‘Study on the lift-off effect of EMAT’, *Sens. Actuators Phys.*, vol. 153, no. 2, pp. 218–221, Aug. 2009, doi: 10.1016/j.sna.2009.05.014.
[43] P. Xin, L. Yang, and Y. Li, ‘Mechanism and application of EMAT technology based on NDT’, in *2014 China International Conference on Electricity Distribution (CICED)*, Sep. 2014, pp. 100–102. doi: 10.1109/CICED.2014.6991672.
[44] H. Gao, B. Lopez, and S. Ali, *INSPECTION OF AUSTENITIC WELD WITH EMATS*. 2009.
[45] B. Maxfield and Z. Wang, ‘Electromagnetic Acoustic Transducers for Nondestructive Evaluation’, Aug. 2018, doi: 10.31399/asm.hb.v17.a0006458.
[46] Shujuan Wang, Riliang Su, Xiaoyang Chen, Lei Kang, and Guofu Zhai, ‘Numerical and experimental analysis of unidirectional meander-line coil electromagnetic acoustic transducers’, *IEEE Trans. Ultrason. Ferroelectr. Freq. Control*, vol. 60, no. 12, pp. 2657–2664, Dec. 2013, doi: 10.1109/TUFFC.2013.2864.
[47] Y.-Q. Li, C. Li, R.-L. Su, G.-F. Zhai, and K.-C. Wang, ‘Unidirectional line-focusing shear vertical wave EMATs used for rail base center flaw detection’, in *2016 IEEE Far East NDT New Technology & Application Forum*

(FENDT), Nanchang: IEEE, Jun. 2016, pp. 99–102. doi: 10.1109/FENDT.2016.7992004.
[48] W. Shi *et al.*, 'Improving the SNR of angled SV-wave EMATs using staggered meander-line coils configuration', *Nondestruct. Test. Eval.*, vol. 37, no. 2, pp. 203–228, Mar. 2022, doi: 10.1080/10589759.2021.1972104.
[49] A. C. Kubrusly, L. Kang, and S. Dixon, 'Unidirectional Shear Horizontal Wave Generation With Side-Shifted Periodic Permanent Magnets Electromagnetic Acoustic Transducer', *IEEE Trans. Ultrason. Ferroelectr. Freq. Control*, vol. 67, no. 12, pp. 2757–2760, Dec. 2020, doi: 10.1109/TUFFC.2020.3027246.
[50] H. Sun, S. Huang, Q. Wang, S. Wang, and W. Zhao, 'Improvement of unidirectional focusing periodic permanent magnet shear-horizontal wave electromagnetic acoustic transducer by oblique bias magnetic field', *Sens. Actuators Phys.*, vol. 290, pp. 36–47, May 2019, doi: 10.1016/j.sna.2019.03.003.
[51] H. Sun *et al.*, 'Point-Focusing Shear-Horizontal Guided Wave EMAT Optimization Method Using Orthogonal Test Theory', *IEEE Sens. J.*, vol. 20, no. 12, pp. 6295–6304, Jun. 2020, doi: 10.1109/JSEN.2020.2976198.
[52] H. Sun, S. Huang, Q. Wang, S. Wang, and W. Zhao, 'Orthogonal Optimal Design Method for Point-Focusing EMAT Considering Focal Area Dimensions', *Sens. Actuators Phys.*, vol. 312, p. 112109, Sep. 2020, doi: 10.1016/j.sna.2020.112109.
[53] L. Xiang, S. Dixon, C. B. Thring, Z. Li, and R. S. Edwards, 'Lift-off performance of electromagnetic acoustic transducers (EMATs) for surface acoustic wave generation', *NDT E Int.*, vol. 126, p. 102576, Mar. 2022, doi: 10.1016/j.ndteint.2021.102576.
[54] S. Wang, L. Kang, P. Xin, and G. Zhai, 'Characteristic research and analysis of EMAT's transduction efficiency for surface detection of aluminum plate', in *2009 9th International Conference on Electronic Measurement & Instruments*, Aug. 2009, pp. 4-949-4–955. doi: 10.1109/ICEMI.2009.5274749.
[55] X. Ding, H. Ba, X. Wu, and L. He, 'Lift-off Performance of Receiving EMAT Transducer Enhanced by Voltage Resonance', *E-J. Nondestruct. Test.*, vol. 17, no. 07, Jul. 2012, Accessed: Sep. 30, 2024. [Online]. Available: https://www.ndt.net/search/docs.php3?id=12761&msgID=0&rootID=0
[56] P. A. Petcher, M. D. G. Potter, and S. Dixon, 'A new electromagnetic acoustic transducer (EMAT) design for operation on rail', *NDT E Int.*, vol. 65, pp. 1–7, Jul. 2014, doi: 10.1016/j.ndteint.2014.03.007.
[57] Y. Wu, L. Han, H. Gong, J. Yang, and W. Li, 'Effect of Coil Configuration on Conversion Efficiency of EMAT on 7050 Aluminum Alloy', *Energies*, vol. 10, no. 10, p. 1496, Sep. 2017, doi: 10.3390/en10101496.
[58] J. Lan, J. Zhang, X. Jia, and R. Gao, 'Optimization Design of Surface Wave Electromagnetic Acoustic Transducers Based on Simulation Analysis and Orthogonal Test Method', *Sensors*, vol. 22, no. 2, Art. no. 2, Jan. 2022, doi: 10.3390/s22020524.
[59] R. Dhayalan, V. Satya Narayana Murthy, C. V. Krishnamurthy, and K. Balasubramaniam, 'Improving the signal amplitude of meandering coil EMATs by using ribbon soft magnetic flux concentrators (MFC)', *Ultrasonics*, vol. 51, no. 6, pp. 675–682, Aug. 2011, doi: 10.1016/j.ultras.2011.01.009.

[60] L. Xiang and R. S. Edwards, ‘Multiple Wavemode Scanning for Near and Far-Side Defect Characterisation’, *J. Nondestruct. Eval.*, vol. 39, no. 1, p. 9, Jan. 2020, doi: 10.1007/s10921-019-0651-0.
[61] S. Dixon, R. S. Edwards, and X. Jian, ‘Inspection of rail track head surfaces using electromagnetic acoustic transducers (EMATs)’.
[62] S. B. Palmer, S. Dixon, R. S. Edwards, and X. Jian, ‘Transverse and longitudinal crack detection in the head of rail tracks using Rayleigh wave-like wideband guided ultrasonic waves’, presented at the Nondestructive Evaulation for Health Monitoring and Diagnostics, P. J. Shull, A. L. Gyekenyesi, and A. A. Mufti, Eds., San Diego, CA, May 2005, p. 70. doi: 10.1117/12.598142.
[63] Y. Li, Z. Liu, Y. Miao, W. Yuan, and Z. Liu, ‘Study of a spiral-coil EMAT for rail subsurface inspection’, *Ultrasonics*, vol. 108, p. 106169, Dec. 2020, doi: 10.1016/j.ultras.2020.106169.
[64] Z. Yi, K. Wang, L. Kang, G. Zhai, and S. Wang, ‘Rail flaw detection system based on electromagnetic acoustic technique’, in *2010 5th IEEE Conference on Industrial Electronics and Applications*, Taichung: IEEE, Jun. 2010, pp. 211–215. doi: 10.1109/ICIEA.2010.5516784.
[65] V. jagota, A. Sethi, and D.-K. Kumar, ‘Finite Element Method: An Overview’, *Walailak J. Sci. Technol.*, vol. 10, pp. 1–8, Jan. 2013, doi: 10.2004/wjst.v10i1.499.
[66] M. I. Friswell and J. E. Mottershead, ‘Finite Element Modelling’, in *Finite Element Model Updating in Structural Dynamics*, M. I. Friswell and J. E. Mottershead, Eds., Dordrecht: Springer Netherlands, 1995, pp. 7–35. doi: 10.1007/978-94-015-8508-8_2.
[67] R. Ribichini, F. Cegla, P. B. Nagy, and P. Cawley, ‘Quantitative modeling of the transduction of electromagnetic acoustic transducers operating on ferromagnetic media’, *IEEE Trans. Ultrason. Ferroelectr. Freq. Control*, vol. 57, no. 12, pp. 2808–2817, Dec. 2010, doi: 10.1109/TUFFC.2010.1754.
[68] E. Ashigwuike, O. Ushie, R. Mackay, and W. Balachandran, ‘A study of the transduction mechanisms of electromagnetic acoustic transducers (EMATs) on pipe steel materials’, *Sens. Actuators Phys.*, vol. 229, Jun. 2015, doi: 10.1016/j.sna.2015.03.034.
[69] G. Zhai, B. Liang, X. Li, Y. Ge, and S. Wang, ‘High-temperature EMAT with double-coil configuration generates shear and longitudinal wave modes in paramagnetic steel’, *NDT E Int.*, vol. 125, p. 102572, Jan. 2022, doi: 10.1016/j.ndteint.2021.102572.
[70] J. Wu and C. Wang, ‘Simulation Analysis of EMAT Shear Wave in Pipeline and Research of Defect Detection Characteristics’, in *2021 3rd International Conference on Intelligent Control, Measurement and Signal Processing and Intelligent Oil Field (ICMSP)*, Jul. 2021, pp. 129–133. doi: 10.1109/ICMSP53480.2021.9513224.
[71] ‘COMSOL Multiphysics Reference Manual’.
[72] First4Magnets, ‘Neodymium Magnet Grades’. [Online]. Available: https://www.first4magnets.com/tech-centre-i61/information-and-articles-i70/neodymium-magnet-information-i82/grades-of-neodymium-magnets-i92
[73] C. Pei, S. Zhao, P. Xiao, and Z. Chen, ‘A modified meander-line-coil EMAT design for signal amplitude enhancement’, *Sens. Actuators Phys.*, vol. 247, pp. 539–546, Aug. 2016, doi: 10.1016/j.sna.2016.07.006.

[74] X. Jia, Q. Ouyang, and X. Zhang, 'An Improved Design of the Spiral-Coil EMAT for Enhancing the Signal Amplitude', *Sensors*, vol. 17, no. 5, p. 1106, May 2017, doi: 10.3390/s17051106.
[75] J. Isla and F. Cegla, 'EMAT phased array: A feasibility study of surface crack detection', *Ultrasonics*, vol. 78, pp. 1–9, Jul. 2017, doi: 10.1016/j.ultras.2017.02.009.
[76] COMSOL Multiphysics, 'Acoustic Module User's Guide'.
[77] R. Courant, K. Friedrichs, and H. Lewy, 'On the Partial Difference Equations of Mathematical Physics', *IBM J. Res. Dev.*, vol. 11, no. 2, pp. 215–234, Mar. 1967, doi: 10.1147/rd.112.0215.
[78] J.-C. Hong, K. H. Sun, and Y. Y. Kim, 'The matching pursuit approach based on the modulated Gaussian pulse for efficient guided-wave damage inspection', *Smart Mater. Struct.*, vol. 14, no. 4, pp. 548–560, Aug. 2005, doi: 10.1088/0964-1726/14/4/013.
[79] R. S. Edwards *et al.*, 'Ultrasonic detection of surface-breaking railhead defects', *Insight - Non-Destr. Test. Cond. Monit.*, vol. 50, no. 7, pp. 369–373, Jul. 2008, doi: 10.1784/insi.2008.50.7.369.
[80] SonemaT, 'Standalone Amplifier - SAA1000'. [Online]. Available: https://www.sonemat.co.uk/standalone-amplifier-saa1000
[81] RITEC, 'Advanced Measurement System RAM-5000-SNAP User Guide'.
[82] J. Lou, X. Fang, J. Du, and H. Wu, 'Propagation of fundamental and third harmonics along a nonlinear seismic metasurface', *Int. J. Mech. Sci.*, vol. 221, p. 107189, May 2022, doi: 10.1016/j.ijmecsci.2022.107189.
[83] Y. Liu, V. K. Chillara, C. J. Lissenden, and J. L. Rose, 'Third harmonic shear horizontal and Rayleigh Lamb waves in weakly nonlinear plates', *J. Appl. Phys.*, vol. 114, no. 11, p. 114908, Sep. 2013, doi: 10.1063/1.4821252.
[84] S. Hurrell, P. Charlton, S. Mosey, O. Rees-Lloyd, and R. Lewis, 'Study on the Beam Directivity of a Steered Meander-Line Coil EMAT', presented at the BINDT 59th Annual British Conference, Telford, Jul. 2022.
[85] H. A. Wheeler, 'Formulas for the Skin Effect', *Proc. IRE*, vol. 30, no. 9, pp. 412–424, Sep. 1942, doi: 10.1109/JRPROC.1942.232015.
[86] SonemaT, 'Radially Polarised Shear Wave EMAT'. [Online]. Available: https://www.sonemat.co.uk/radially-polarised-shear-wave-emat-hws2225-gc
[87] Olympus, 'Normal Incidence Shear Wave Transducers'. [Online]. Available: https://www.olympus-ims.com/en/ultrasonic-transducers/shear-wave/
[88] S. Hurrell, P. Charlton, S. Mosey, O. Rees-Lloyd, and R. Lewis, 'Study on the steering capability of a meander-line coil EMAT', *Insight - Non-Destr. Test. Cond. Monit.*, vol. 65, no. 2, pp. 95–102, Feb. 2023, doi: 10.1784/insi.2023.65.2.95.
[89] D. A. Hutchins, F. Nadeau, and P. Cielo, 'A pulsed photoacoustic investigation of ultrasonic mode conversion', *Can. J. Phys.*, vol. 64, no. 9, pp. 1334–1340, Sep. 1986, doi: 10.1139/p86-234.
[90] L. Bond and N. Saffari, 'MODE-CONVERSION ULTRASONIC TESTING.', Dec. 1984. Accessed: Sep. 27, 2024. [Online]. Available: https://www.semanticscholar.org/paper/MODE-CONVERSION-ULTRASONIC-TESTING.-Bond-Saffari/a20d1f9c28e99a9dae573e9547a97e6f9ad75dbb#citing-papers

[91] C. B. Thring, ‘Enhanced EMAT techniques for the characterisation of hidden defects’, PhD, University of Warwick, 2019. Accessed: Sep. 24, 2024. [Online]. Available: http://webcat.warwick.ac.uk/record=b3265087~S15

[92] L. Kang, S. Dixon, K. Wang, and J. Dai, ‘Enhancement of signal amplitude of surface wave EMATs based on 3-D simulation analysis and orthogonal test method’, *NDT E Int.*, vol. 59, pp. 11–17, Oct. 2013, doi: 10.1016/j.ndteint.2013.05.003.

[93] X. Huang and J. Saniie, ‘PPM-EMAT Design Configurations for Ultrasonic Communication through Metallic Channel’, in *2022 IEEE International Ultrasonics Symposium (IUS)*, Venice, Italy: IEEE, Oct. 2022, pp. 1–3. doi: 10.1109/IUS54386.2022.9958024.

[94] O. Rees-Lloyd, P. Charlton, S. Mosey, and R. Lewis, ‘Effects of relative motion on a Rayleigh wave electromagnetic acoustic transducer operating on aluminium’, *Insight - Non-Destr. Test. Cond. Monit.*, vol. 61, no. 2, pp. 83–89, Feb. 2019, doi: 10.1784/insi.2019.61.2.83.

Appendix A – Publications

DOI: 10.1784/insi.2023.65.2.XXX

Study on the steering capability of a meander-line coil EMAT

S Hurrell, P Charlton, S Mosey, O Rees-Lloyd and R Lewis

Electromagnetic acoustic transducers (EMATs) are well-established as a means of ultrasonic wave generation and reception without the use of a mechanical coupling. When comprising a bias magnetic field and a meander-line coil (MLC), these waves propagate at an angle normal to the emission surface. With the appropriate frequency, the propagation pathway of these ultrasonic waves can be steered to a particular angle. This paper presents the methodology used to find the steering limit of an MLC EMAT and the results from simulations and experimental validations on aluminium. The results show that the maximum shear wave amplitude occurred at around 30°, the steering limit was approximately 50° and the simulations were validated by the experimental set-up to a satisfactory degree.

1. Introduction

A key method of non-destructive testing is ultrasonic testing, whereby high-frequency mechanical waves propagate through a material, reflecting off any boundaries they encounter, such as the surface or any defects within the material. One method is through the use of electromagnetic acoustic transducers (EMATs) that can induce ultrasonic waves in electrically conductive and ferromagnetic materials.

An EMAT combines a bias magnetic field, typically from a permanent magnet or electromagnet, with an alternating eddy current field, from a coil of wire carrying an alternating current (AC), to induce forces directly into the material via three transduction methods: Lorentz forces, magnetisation forces and magnetostriction[1,2]. EMATs possess many advantages over ultrasonic testing due to these principles of wave induction, including no requirement for contact with the specimen, no requirement for a facilitative couplant and the ability to operate at high speeds[3,4]. A main disadvantage, however, is their low signal-to-noise ratio (SNR), which has necessitated much research into optimising their design[5-6].

For the purpose of this study, the material used was aluminium, which only induces waves via the Lorentz force transduction due to being non-magnetic. The Lorentz force consists of static and dynamic components due to the magnet's static magnetic flux and the coil's dynamic eddy current density, given as:

$$\overrightarrow{F_L} = \overrightarrow{J_e} \times \vec{B} \quad \text{..... (1)}$$

where F_L is the Lorentz force density, J_e is the eddy current density and B is the magnetic flux density. The AC of the coils induce eddy currents in the surface of the material and, in the presence of a static magnetic flux, produce periodic alternating forces at the surface of the specimen, generating bulk waves into the material (consisting of shear and compression wave modes)[7-9].

The configuration of the coil and magnet determines the nature of wave that is excited[7]. A common design for angled bulk wave generation is the meander-line coil (MLC) EMAT, consisting of a bias magnetic field normal to the material's surface and an MLC with straight alternating runs between the magnet and material surface.

The angle at which the MLC EMAT excites waves through a material is given as:

$$\theta = \sin^{-1}\left(\frac{v}{2df}\right) \quad \text{..... (2)}$$

where θ is the angle normal to the surface, v is the speed of the wave, d is the spacing distance between each alternating straight run of the coil and f is the frequency of the AC and the wave. A popular EMAT design that produces angle-beam waves is the periodic permanent magnet (PPM) that generates shear horizontal waves and is well suited in austenitic and coarse-grain material[10]. PPM EMATs have been studied for their beam-steering capabilities via frequency and have been shown to produce maximum amplitudes across a frequency range for a given spacing between magnets[11] and be capable of creating 2D maps of defects present within a given sample[11-14]. Although MLC EMATs generate shear vertical waves, these two technologies share the same theory of angle-beam emission and thus would share similar conclusions.

An increasingly popular method for angle-beam EMATs is phased array (PA), wherein the EMAT coil's variable spacings focus the bulk waves to a specific location within the material[15,16]. Literature exists on the application of MLC EMATs[17-18,10]; however, much of this examines the differences between traditional MLC and PA MLC designs[17-19]. Work carried out regarding the beam-steering MLC EMATs is less common than research into PPM and PA; however, it does support the theory that the ultrasonic bulk waves can be steered by frequency[20].

The focus of this study is to simulate and experimentally validate the shear wave steering capability of an MLC EMAT on aluminium for different steering angles.

2. Model configuration

The simulation model of a 2D MLC EMAT was created using COMSOL 6.0 Multiphysics. The AC/DC and Structural Mechanics software packages had the predefined mathematical capabilities to

● ***Submitted 17.06.22 / Accepted 12.12.22***

Sam Hurrell is with the Wales Institute of Science and Art, University of Wales Trinity Saint David, Swansea SA1 8EW and the TWI Technology Centre, Port Talbot SA13 1SB.

Peter Charlton and Stephen Mosey are with the Wales Institute of Science and Art, University of Wales Trinity Saint David, Swansea SA1 8EW.

Owen Rees-Lloyd and Richard Lewis are with the TWI Technology Centre, Port Talbot SA13 1SB.

enable such a design to take place. Figure 1 shows the 2D simulation geometry of the EMAT consisting of a 20 mm × 20 mm NdFeB-42 permanent magnet and a copper MLC over a 340 mm × 100 mm aluminium block. The transmit-EMAT was positioned 50 mm from the edge of the aluminium block, with an MLC lift-off distance of 0.5 mm and a magnet lift-off distance of 1.0 mm.

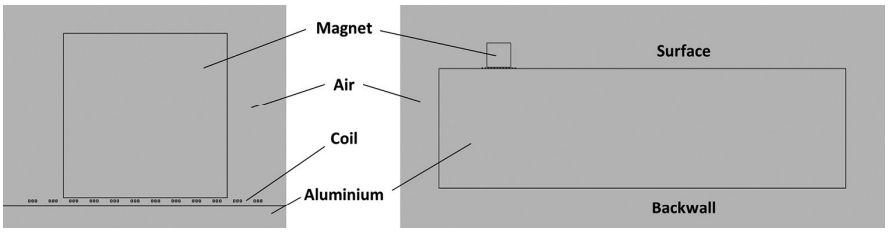

Figure 1. COMSOL simulation model geometry

The speed of the shear and compression waves within the aluminium are 3.12 mm/μs and 6.20 mm/μs, respectively, and according to Snell's Law the angle of the compression wave could be determined for internal mode conversion.

The coil spacing d was set at 2.5 mm, thus according to Equation (2), the angle of the shear wave was entirely controlled by the frequency of the AC. Figure 2 shows the top view of the MLC, with 'Detail A' highlighting that each of the coil's straight runs consists of three thinner strands (0.20 mm × 0.25 mm) with a separation of 0.4 mm. This configuration was chosen as coils made of multiple strands induce a wider eddy current density and, with a square cross-sectional area, also possess a higher conversion efficiency[21]. Figure 2 also shows a 3D model of the MLC as a closed loop (a necessity for COMSOL), but the printed MLC used for the experimental validation had two strands breaking off to be externally powered (shown in Figure 4(a)).

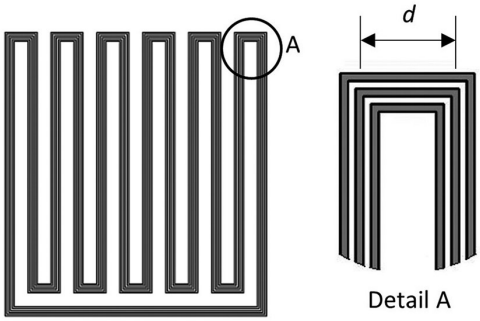

Figure 2. COMSOL simulation 3D MLC geometry

While the simulation was a 2D model, the depth of the coil was specified as the length of the physical coil at 20 mm. The tone-burst current pulse applied to the MLC is given in Equation (3) (adapted from[22]) and was modelled on a Gaussian-sinc pulse:

$$i(t) = Ie^{-\frac{(t-\tau)^2}{2\sigma^2}}\cos\left(2\pi f(t-\tau)\right) \quad \text{.....(3)}$$

where I is the constant current of 6 A, σ is the standard deviation of the pulse, τ is the time delay of the signal's maximum peak and f is the central frequency of the wave. The pulse was designed for any given frequency to start near 0 A and give seven positive peaks before returning to 0 A. This was achieved by making both the standard deviation and the time delay functions of frequency: $\sigma = 1.2/f$ and $\tau = 5/f$, respectively. The resultant pulse profile for steering angles of 30° and 60° can be seen in Figure 3.

To account for the changing time delay, the arrival time of a wave was taken as the time of the largest peak within a recorded waveform. This also eliminated the need for a predetermined threshold, as a maximum peak would always be present in any waveform. The simulation was set to run from 0-150 μs to account for reflections and any wave mode conversions that would take place within the aluminium specimen. When solving transient models, the relationship between the time-step size and the mesh size must be approximately equal to a Courant number of less than 0.2, given by the Courant-Friedrichs-Lewy (CFL) condition[23], defined as:

$$CFL = \frac{v\Delta t}{h_{max}} \quad \text{.....(4)}$$

where CFL is the Courant number, Δt is the time-step size and h_{max} is the maximum mesh size for the specimen. For 2D COMSOL models, it is recommended to set the maximum mesh size to less than one fifth of the wavelength of the wave (defined as $\lambda = v/f$). For a given steering angle, therefore, the frequency of the wave could be used to calculate the values of maximum mesh size and time-step size, as seen in Table 1.

Simulation results show bulk waves propagating through the

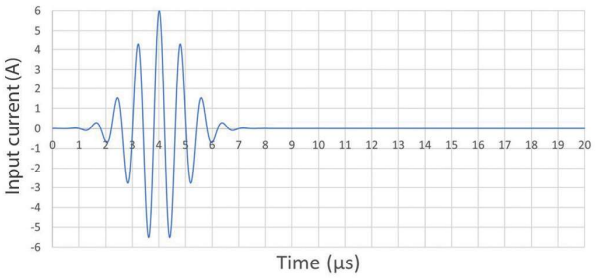

(a)

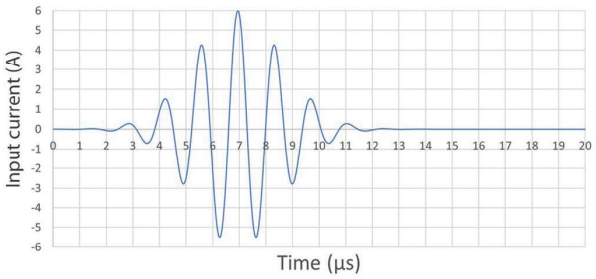

(b)

Figure 3. Coil current pulse profiles: (a) coil excitation current: 30° steering angle; and (b) coil excitation current: 60° steering angle

Table 1. Pulse and model variables for a given steering angle

Angle (°)	f (MHz)	σ (× 10^{-6})	τ (μs)	h (mm)	Δt (μs)	CFL	L (μH)	C (nF)
15	2.4110	0.50	2.07	0.258	0.010	0.121	1.5160	3.0
30	1.2480	0.96	4.01	0.500	0.020	0.125	1.6621	9.8
45	0.8825	1.36	5.67	0.707	0.024	0.106	1.8534	17.6
60	0.7205	1.67	6.94	0.866	0.030	0.108	2.0600	24.4

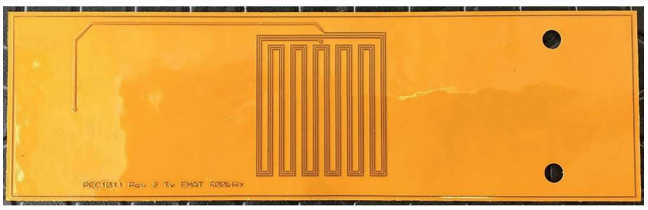

(a)

(b)

Figure 4. Experimental MLC design (a) and model set-up design (b)

specimen. The x and y components of displacement were recorded across the specimen's backwall, from x = 0-250 mm at every 5 mm interval (where x = 0 mm and is 50 mm from the edge of the specimen, opposite the transmit-EMAT, as shown in Figure 4(b)). From these values, the x-position of the shear wave's maximum displacement magnitude for each steering angle could be located, thus evaluating the EMAT's steering capability.

3. Experimental validation

An aluminium block, measuring 340 mm × 100 mm × 70 mm, was used with two EMATs (of a similar coil design as in the simulations) in a pitch-catch configuration, as shown in Figure 4(a). The receive-EMAT was in parallel with a decade box, allowing the capacitance to be changed to electrically match the impedance of the RLC circuit for a given steering angle. The values of inductance on the specimen were measured using an impedance analyser and capacitance from Equation (5):

$$C = \frac{1}{(2\pi f)^2 L} \quad \text{..... (5)}$$

where C is the capacitance, L is the inductance and f is the frequency of the pulse equal to the resonant frequency of the circuit for maximum reception of the receive-EMAT, also in Table 1.

The transmit-EMAT was not in parallel with a decade box, as in real-world applications a standard capacitor would be used that would retain its value. The transmit-EMAT was connected to a pulser system that could emit high-current pulses at the frequencies required. The receive-EMAT was in parallel with an amplifier (of 70 dB gain) due to its low SNR and then to an oscilloscope that would register the signals received by the EMAT.

At the same respective positioning as the simulations, the transmit-EMAT was fixed compressed into a fixed lift-off distance of 1 mm by non-magnetic shims, 50 mm from the edge of the specimen's surface, and the receive-EMAT was placed at the specimen's backwall, from x = 0-250 mm at every 5 mm interval. At each backwall x-position, the receive-EMAT recorded an average 'signal amplitude *versus* time' reading from the oscilloscope, from which the x-position of the shear wave's maximum displacement for each steering angle could be plotted and compared against the simulation values.

4. Results and discussion

Upon the simulation's 2D aluminium block, a colour plot of the von Mises stress was produced at every 0.12 µs time step to create animations of the bulk wave propagations across the entire model's runtime. The stress was plotted instead of displacement due to the better visual quality and Figure 5 shows these plots at their 30 µs time step for each steering angle.

There is little difference in the angle between the simulations for 45° and 60° as it is likely to be nearing the EMAT's steering limit and thus will not increase any further. It is also noticeable that as the steering angle increases, Rayleigh waves start to emerge at the surface for 45° and become the dominant wave at 60°. The different propagation distances of the shear waves from the transmit-EMAT demonstrate the effect of the pulse's time delay on the resulting wave transmission.

The simulations continued to their end points and the x and y components of displacement were recorded along the specimen's backwall to calculate the displacement magnitude. To better show the shear wave's point of impact, the displacement magnitude values (within an appropriate timeframe of the shear wave's incident on the

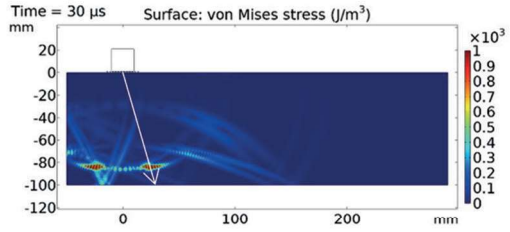

(a)

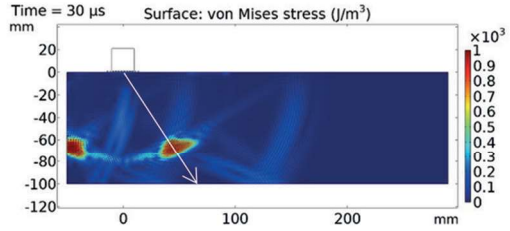

(b)

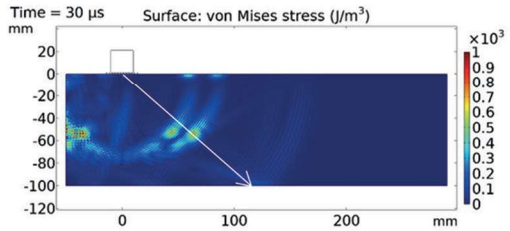

(c)

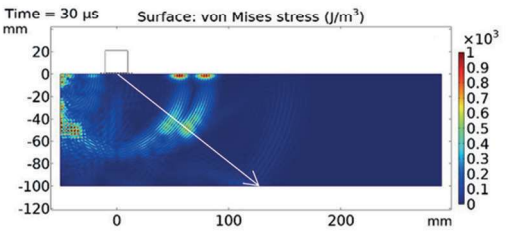

(d)

Figure 5. Plots of stress at 30 µs for steering angles of: (a) 15°; (b) 30°; (c) 45°; and (d) 60°

backwall) were processed for the maximum reading at each point. These readings were graphed against their backwall *x*-position for each steering angle and are shown in Figure 6.

It can be seen from Figure 6 that as the steering angle increases, the *x*-position of the shear wave's maximum impact also increases. The 15° wave impacts at 30 mm, the 30° wave at 70 mm, the 45° wave at 100 mm and the 60° wave at 115 mm. For the 45° and 60° steering angles, a large peak can be seen near the 0 mm *x*-position due to the shear waves reflecting from the specimen's sidewall. It can also be seen that the 30° shear wave's maximum displacement is far greater than that of the other steering angles.

Having found the points of maximum shear wave amplitude for all four steering angles, the values of displacement magnitude were graphed against time as A-scans, as shown in Figure 7.

By comparing these A-scans with the colour plots for each steering angle, the peaks of displacement can be identified as waves. The first peak is the initial compression wave directly from the transmit-EMAT (peak 1), immediately followed by the compression wave reflected from the sidewall (peak 2). The third and largest peak is the shear wave directly from the transmit-EMAT (peak 3), but for steering angles of 45° and 60° it is clearly seen that these shear wave peaks are composed of two separate peaks (peaks 3a and 3b), as with the initial compression wave peaks for steering angles of 15° and 30° (peaks 1a and 1b). The reason for these two separate peaks is due to the EMAT transmitting two separate shear and Rayleigh waves in each direction, as shown in Figure 5(c)-5(d). These separate waves cannot be distinguished for the 30° steering angle due to their superposition, explaining its far larger shear wave.

Immediately following the direct shear wave peak is a smaller peak that started as a compression wave that struck the sidewall

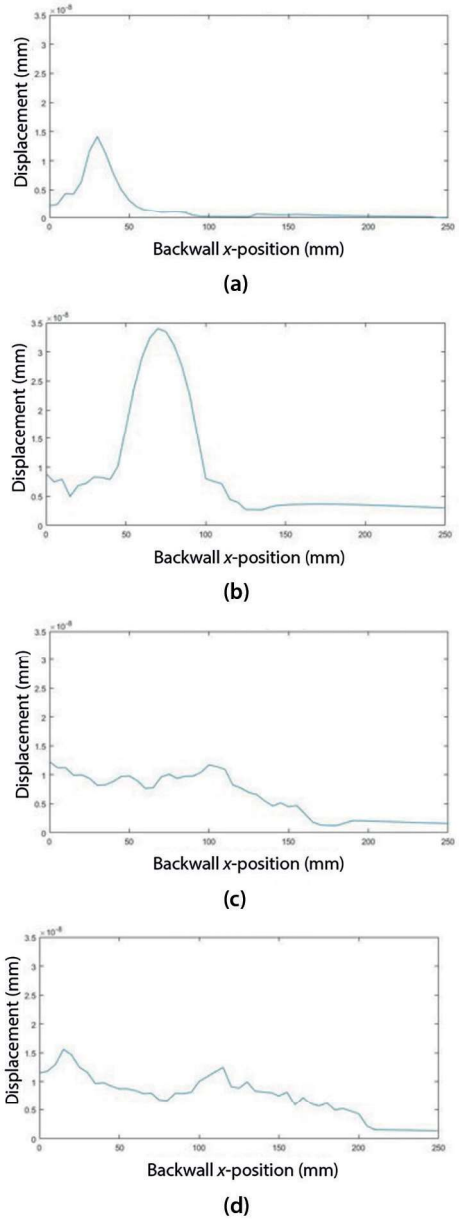

Figure 6. Graphs of maximum displacement magnitude *versus* backwall *x*-position for each steering angle: (a) 15° steering angle; (b) 30° steering angle; (c) 45° steering angle; and (d) 60° steering angle

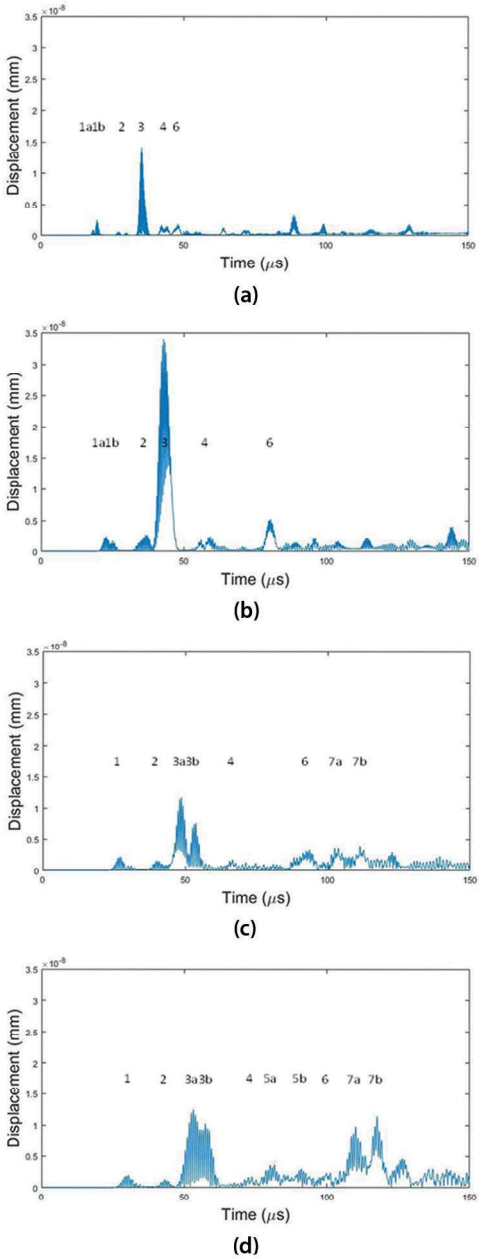

Figure 7. Graphs of displacement magnitude *versus* time at the *x*-position of maximum impact for each steering angle: (a) 15° steering angle: displacement at *x* = 30 mm; (b) 30° steering angle: displacement at *x* = 70 mm; 30° steering angle: displacement at *x* = 70 mm; (c) 45° steering angle: displacement at *x* = 100 mm; and (d) 60° steering angle: displacement at *x* = 115 mm

and converted into a shear wave (peak 4). For the 60° steering angle, there are two peaks following the refracted shear peaks, found to be the shear waves reflected off the sidewall and, likewise with the direct shear waves, these have two separate components (peaks 5a and 5b). For all the simulations there is a peak that was found to be a small Rayleigh wave (peak 6). Unlike conventional MLC EMAT Rayleigh wave transmission that has a steering angle of 90°, these Rayleigh waves were generated by the shear waves (compression waves for 15°, explaining its earlier arrival time) striking the bottom-left corner of the specimen. Following these induced Rayleigh waves for the 45° and 60° steering angles are the Rayleigh waves that were transmitted due to their higher angles, that also possess separate components (peaks 7a and 7b).

An important factor with the 15° steering angle is the presence of internal mode conversions. Due to the low shear wave angle, the EMAT would also transmit a compression wave at an angle of approximately 31° (according to Snell's Law), which was shallow enough to be seen within the specimen. While the *x*-position of the shear wave's maximum displacement magnitude was located at 30 mm, the *x*-position of the compression wave's maximum displacement was located at 50 mm. By looking at the *x* and *y* components of displacement at these backwall *x*-positions, the nature of these two waves can be better seen, as shown in Figure 8.

At 30 mm and 35.31 µs (the time of the shear wave's largest displacement magnitude), the recorded *x* and *y* components of displacement were 1.2908×10^{-8} mm and 3.4897×10^{-9} mm, respectively. The particle motion of shear waves is perpendicular to the direction of propagation, which is supported by Figure 8, where the *x*-component is almost four times larger than the *y*-component at the time of impact. The same principle can be applied to the compression wave at 50 mm and 20.69 µs with a parallel particle motion, supported by Figure 8 where the *x*-component is approximately half that of the *y*-component. Given that the angles of the compression and shear waves are both shallow enough to cause internal mode conversion, by recording the maximum values of stress at each 0.1 mm × 0.1 mm area interval across the 150 µs runtime, their internal wave propagation pathways between surfaces could be plotted, as shown in Figure 9.

As shown in Figure 9, the largest wave path is the shear wave that travels directly from the transmit-EMAT to the backwall 100 mm down and 30 mm across. The displacement magnitude on the backwall at this point was 1.4145×10^{-8} mm at 35.31 µs. The second largest wave to hit the backwall came from the combination of two shear waves and one compression wave that reflected from the backwall and then the surface, while mode converting once. The combined result of the shear-shear-compression, shear-compression-shear and compression-shear-shear waves on the backwall was a displacement magnitude of 5.3977×10^{-9} mm, almost half of the displacement magnitude from the direct shear pathway, at 110 mm and 87.16 µs. The different wave combinations that hit the backwall can be seen in Figure 9 and Table 2.

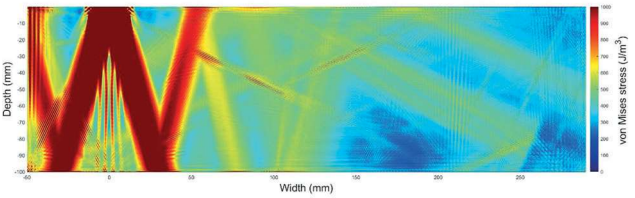

Figure 9. Plot of maximum stress across time for a 15° steering angle

There were some variations when replicating these simulations in experimental validations. Firstly, the Gaussian and sinc pulse used for the models was unable to be implemented with the pulser system. Instead, a rectangular envelope of the same frequency for a given angle, containing approximately 20 peaks, was emitted starting at $t = 0$ µs. This would transmit stronger waves due to containing more peaks at a higher current, which would compensate for the realistic conditions of the practical test and produce an improved SNR.

Additionally, rather than arbitrary probes taking readings every 5 mm across the backwall, a receive-EMAT identical to the transmit-EMAT may produce some inconsistency within the results as the exact lift-off distance may vary.

Finally, the presence of electrical noise within the laboratory equipment would likely mask the signal amplitude of the received wave. Using an oscilloscope, any received wave should have a larger amplitude and a different frequency to the baseline signal noise after the pulse. It is necessary then to put the received signal through a filter to attenuate as much noise as possible. Figure 10 shows an example of the oscilloscope's recorded signal for a 45° steering angle. This signal includes its emission pulse followed by the irregularities of received ultrasound at that *x*-position. Figure 10 also shows the discrete Fourier transform (DFT) of the signal after 20 µs, as no shear waves could hit the backwall before this time and thus no useful data would be present.

The largest peak within the DFT is approximately the pulse's frequency, followed by smaller peaks at integer scale factors of this frequency. The frequency peaks nearing 0 MHz were likely to be due to electrical noise and could be filtered out. A band-pass filter with a frequency range of the emission pulse's frequency ±0.1 MHz (for a 45° steering angle, the band-pass filter was set to 0.7825-0.9825 MHz) was used to remove the noise. Once filtered, a wave could be seen at approximately 50 µs, which, for a wave at 45° and a distance of 100 mm deep and 100 mm across with a shear wave speed of 3.12 mm/µs, supports

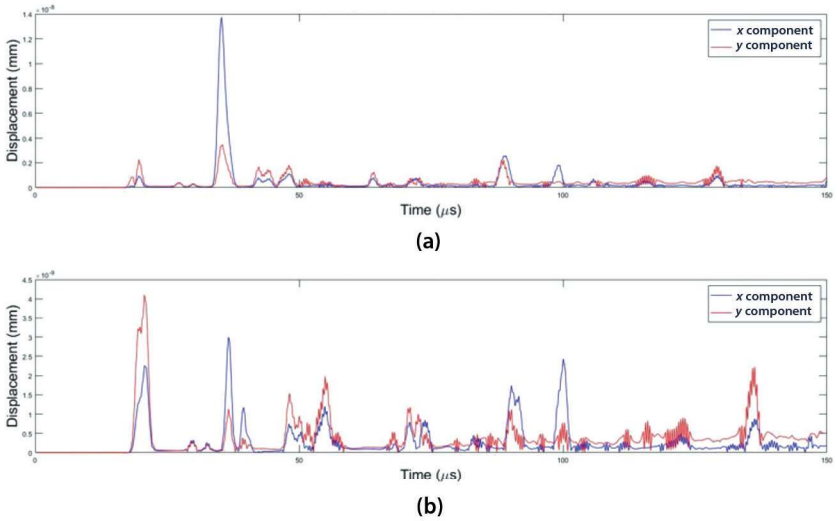

Figure 8. Graphs of *x* and *y* component displacements for the 15° steering angle, at *x*-positions of: (a) 30 mm; and (b) 50 mm

Table 2. Largest wave combinations for a 15° steering angle

Wave combinations	Backwall *x*-position (mm)	Time of arrival (μs)	Displacement magnitude (mm)	Normalised amplitude
S	30	35.31	1.4145×10^{-8}	100.0
P	50	20.69	4.1751×10^{-9}	29.5
SSS	80	101.40	5.1746×10^{-9}	36.6
PSS, SPS, SSP	110	87.16	5.3977×10^{-9}	38.2
PPS, PSP, SPP	140	72.41	2.5387×10^{-9}	17.9
PPP	145	56.85	1.5995×10^{-9}	11.3

that this is the direct shear wave. Figure 11 shows the original and filtered signal after 20 μs.

This process of signal filtering was repeated for all four steering angle experiments at each of their backwall *x*-positions. The resultant filtered signals' absolute values could produce an upper envelope from the peaks, which could then be compared to the displacement graphs of Figure 7. These envelope graphs at the *x*-position of maximum simulated displacement for the four steering angles, as stated in Figure 6, can be seen in Figure 12.

When comparing Figure 12 to Figure 7, there are very obvious similarities present. The largest peaks present in both Figures occur at similar times, respective for a given steering angle. There is a slight delay at the time these peaks occur, likely to be due to the different pulses that emit them. There is an irregularity to the size of these peaks, as the 30° steering angle's maximum peak is close to taking up the *y*-axes of both the simulated and experimental graphs, compared to the 15° steering angle's maximum simulated peak being approximately a third of the *y*-axis, and the maximum experimental peak being approximately a tenth of its *y*-axis.

There is also a similarity in the peaks following the direct shear wave. Figure 13 shows a comparison of the experimental results with the simulated results for the 60° steering angle at the backwall *x*-position of 115 mm. The experimental results show a smaller peak and then a larger peak following the direct shear wave peak. The smaller peak was determined to be the shear wave reflected from the sidewall and the larger peak the Rayleigh waves that travelled across the surface, sidewall and backwall to the *x*-position. These waves made it through the band-pass filter due to them being of the same frequency as the pulse. Normalising both the amplitude and displacement could be used to calculate a correlation coefficient of 0.7870 between the two signals, indicating a strong correlation.

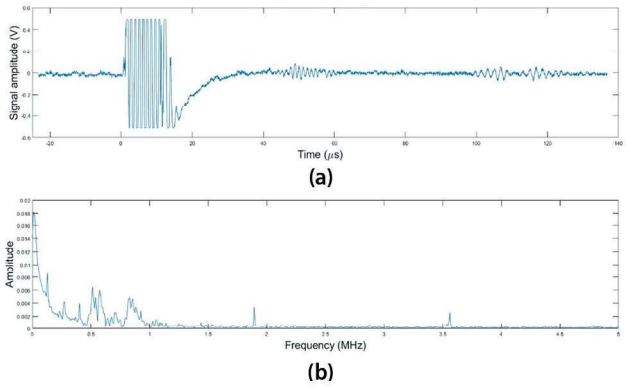

Figure 10. Graphs of raw signal amplitude *versus* time and DFT for a 45° steering angle: (a) complete signal at x = 100 mm; and (b) discrete Fourier transform: signal from t = 20-140 μs

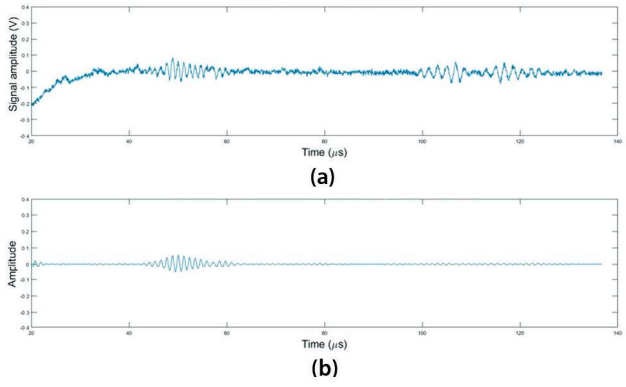

Figure 11. Graphs of signal amplitude and filtered signal amplitude for a 45° steering angle: (a) signal at x = 100 mm; and (b) band-pass filter = 0.7825-0.9825 MHz: signal from t = 20-140 μs

5. Steering capabilities

This study has focused on the four steering angles of 15°, 30°, 45° and 60°, by running simulations of the experimental set-up and then validating the results in the laboratory. As a result of simulation validation, further simulations were undertaken at steering angles that were left out of the study, so that a better picture of the transmit-EMAT's steering capability could be perceived. The total time it took to run the 15° simulation was 52 h and thus it was decided not to run simulations for any steering angle below this due to time constraints and equipment limitations. Simulations of steering angles between 15-90° at every 5° interval were also run with the same set-up as the initial models, with differing time-steps and mesh densities to account for the different frequencies (and thus different CFL values) and the same results across the aluminium block's backwall were also recorded.

For every simulated steering angle, the backwall *x*-position with the largest direct shear wave displacement magnitude was used to calculate the angle of that shear wave. From this *x*-position, the value of the displacement magnitude was also recorded. To examine how changing the steering angle affects the transmission of Rayleigh waves, values of the displacement magnitude from the surface 100 mm to the right of the transmit-EMAT were recorded. The results of these simulations are summarised in Figure 14.

As the steering angle increases from 15-25°, the shear wave angle directly correlates with the steering angle. As the steering angle increases from 30-40°, the shear wave angle seems to plateau, until it increases to 45° and the shear wave angle recorrelates with the steering angle. When the steering angle reaches 50°, the shear wave angle starts to plateau and reaches its maximum at 60°.

As the steering angle increases: the shear wave displacement gradually increases (15-25°); reaches a peak (30°); gradually decreases (35-40°); and reaches a plateau (45°). The Rayleigh wave was only measurable for steering angles between 30-90°, as from 15-25° it was too small to be reliably recorded. From 30°, the Rayleigh wave displacement gradually increases until approximately 60°, when it starts to reach a peak at 90°.

From Figure 14, it can be seen that the Rayleigh wave displacement starts to overtake the shear wave displacement

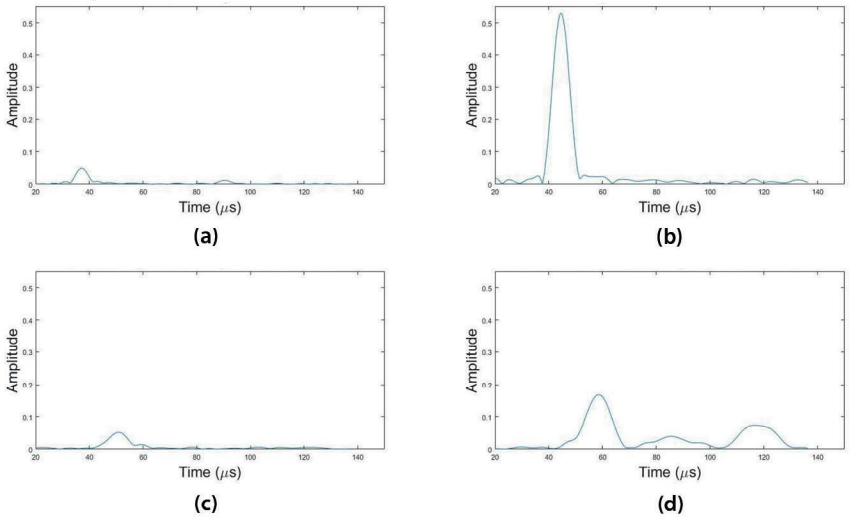

Figure 12. Graphs of filtered signal amplitude envelope *versus* time for each steering angle: (a) 15° steering angle: amplitude at x = 30 mm; (b) 30° steering angle: amplitude at x = 70 mm; (c) 45° steering angle: amplitude at x = 100 mm; (d) 60° steering angle: amplitude at x = 115 mm

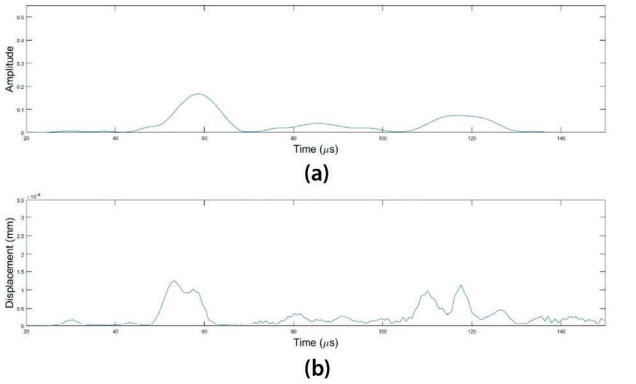

Figure 13. Experimental and simulated results for a 60° steering angle: (a) amplitude at x = 115 mm; and (b) displacement at x = 115 mm

between a steering angle of 45-50°, approximately the same as the steering limit. The maximum shear wave displacement is produced at a steering angle of approximately 30°, approximately the same steering angle that causes inconsistencies in the correlation between the steering angle and the shear wave angle.

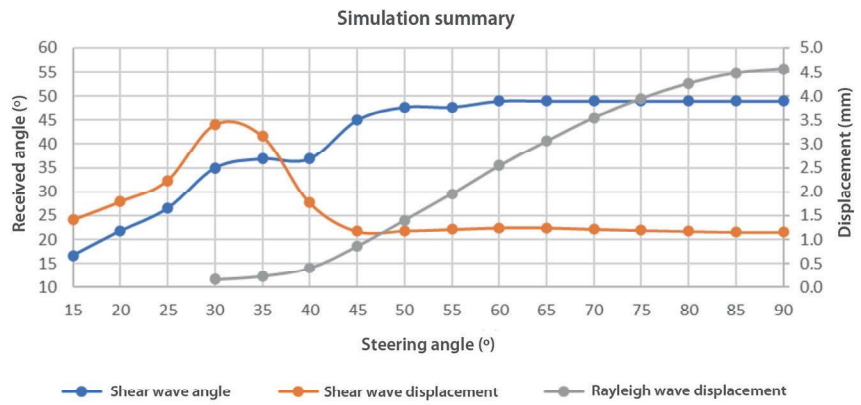

Figure 14. Effects of steering angle on shear wave angle, shear wave displacement and Rayleigh wave displacement

6. Conclusion

Over the course of this study, the objective was to simulate and experimentally validate the bulk wave steering capability of an MLC EMAT on aluminium for different steering angles. The COMSOL simulations seemed to reliably correlate with the experimental validations. The differences in the simulated and experimental results were determined to be due to the differences in their set-ups: simulations having a time delay in their wave transmissions explaining their earlier arrival time and experiments requiring a changing capacitance value in the receive-EMAT explaining their weaker SNR.

Simulations across a wider range of steering angles produced results that gave interesting conclusions. As the steering angle increases from 15-25°, the shear wave angle and displacement gradually increases. As the steering angle increases from 30-40°, the shear wave angle starts to plateau and the shear wave displacement peaks before gradually decreasing. As the steering angle increases from 45-90°, the shear wave angle plateaus at approximately 50°, the shear wave displacement plateaus at approximately 1.2×10^{-8} mm and the Rayleigh wave displacement overtakes the shear wave displacement and continues to increase to the maximum steering angle of 90°. Based on this, it can be concluded that the steering limit of this MLC transmit-EMAT is approximately 50°.

Further investigations would involve changing the coil spacing to observe how this affects the steering limit and test on a semi-circular specimen to better measure the angles and displacements of both the shear and compression waves with a changing steering angle. For future industrial work, the MLC EMAT could be adapted for deployment on an automated scanning system, along with the use of coded excitation signals to improve the SNR[24] for internal flaw detection and weld joint inspection.

Acknowledgements

The authors gratefully acknowledge funding from the Knowledge Economy Skills Scholarships (KESS 2) and TWI Ltd. KESS 2 is a pan-Wales higher-level skills initiative led by Bangor University on behalf of the HE sector in Wales. It is part funded by the Welsh government's European Social Fund (ESF) convergence programme for West Wales and the Valleys.

References

1. M Hirao and H Ogi, EMATs for Science and Industry: Non-Contacting Ultrasonic Measurements, Kluwer Academic Publishers, Boston, Massachusetts, USA, 2003.
2. R Ribichini, F Cegla, P B Nagy and P Cawley, 'Experimental and numerical evaluation of electromagnetic acoustic transducer performance on steel materials', NDT&E International, Vol 45, No 1, pp 32-38, August 2011.

3. O Rees-Lloyd, P Charlton, S Mosey and R Lewis, 'Effects of relative motion on a Rayleigh wave electromagnetic acoustic transducer operating on aluminium', Insight: Non-Destructive Testing and Condition Monitoring, Vol 61, No 2, pp 83-89, February 2019.
4. ASTM E1816-12, 'Standard practice for ultrasonic testing using electromagnetic acoustic transducer (EMAT) techniques', August 2018.
5. X Jian, S Dixon, K Grattan and R S Edwards, 'A model for pulsed Rayleigh wave and optimal EMAT design', Sensors and Actuators A: Physical, Vol 128, No 2, pp 296-304, April 2006.
6. L Kang, S Dixon, K Wang and J Dai, 'Enhancement of signal amplitude of surface wave EMATs based on 3D simulation analysis and orthogonal test method', NDT&E International, Vol 59, No 1, pp 11-17, October 2013.
7. J K Hu, Q L Zhang and D A Hutchins, 'Directional characteristics of electromagnetic acoustic transducers', Ultrasonics, Vol 26, pp 5-13, January 1988.
8. G A Alers and L R Bums, 'EMAT designs for special applications', Materials Evaluation, Vol 45, No 10, pp 1184-1194, October 1987.
9. R B Thompson, 'Physical principles of measurements with EMAT transducers', Physical Acoustics, Vol 19, pp 157-200, 1990.
10. K Sawaragi *et al*, 'Improvement of SH-wave EMAT phased array inspection by new eight-segment probes', Nuclear Engineering and Design, Vol 198, pp 153-163, September 1999.
11. H Sun *et al*, 'Oblique point-focusing shear-horizontal guided wave electromagnetic acoustic transducer with variable PPM spacing', IEEE Transactions on Ultrasonics, Ferroelectrics, and Frequency Control, Vol 67, No 8, pp 1691-1700, August 2020.
12. S Hill and S Dixon, 'Frequency dependent directivity of periodic permanent magnet electromagnetic acoustic transducers', NDT&E International, Vol 62, pp 137-143, January 2014.
13. H Gao and B Lopez, 'Development of single-channel and phased array electromagnetic acoustic transducers for austenitic weld testing', Materials Evaluation, Vol 68, No 7, pp 821-827, July 2010.
14. S Hill and S Dixon, 'Localisation of defects with time and frequency measurements using pulsed arrays', NDT&E International, Vol 67, pp 24-30, June 2014.
15. B W Drinkwater and P D Wilcox, 'Ultrasonic arrays for non-destructive evaluation: a review', NDT&E International, Vol 39, No 7, pp 525-541, October 2006.
16. J A Jensen, S I Nikolov, K L Gammelmark and M H Pedersen, 'Synthetic aperture ultrasound imaging', Ultrasonics, Vol 44, pp e5-e15, August 2006.
17. H Ogi and M Hirao, 'Line-focusing of ultrasonic SV wave by electromagnetic acoustic transducer', The Journal of the Acoustical Society of America, Vol 103, No 5, pp 2411-2415, May 1998.
18. H Ogi, M Hirao and T Ohtani, 'Line-focusing electromagnetic acoustic transducers for the detection of slit defects', IEEE Transactions on Ultrasonics, Ferroelectrics, and Frequency Control, Vol 46, No 2, pp 341-346, March 1999.
19. H Sun, S Huang, S Wang and W Zhao, 'Meanderline coil arrangement of ultrasonic wave line-focusing electromagnetic acoustic transducers', 2020 IEEE International Instrumentation and Measurement Technology Conference (I2MTC), May 2020.
20. T J Moran and R M Panos, 'Electromagnetic generation of electronically steered ultrasonic bulk waves', Journal of Applied Physics, Vol 47, No 5, pp 2225-2227, May 1976.
21. Y Wu *et al*, 'Effect of coil configuration on conversion efficiency of EMAT on 7050 aluminium alloy', Energies, Vol 10, No 10, September 2017.
22. D Ratnam, A Kuamr and P C R Bhagi, 'Time-domain finite element modelling of pulsed meander coil electromagnetic acoustic transducer', Electromagnetic Non-Destructive Evaluation (XXI), Vol 43, pp 246-254, May 2018.
23. R Courant, K O Friedrichs and H Lewy, 'On the partial difference equations of mathematical physics', IBM Journal of Research and Development, Vol 11, No 2, pp 215-234, March 1967.
24. J Isla and F B Cegla, 'Coded excitation for pulse-echo systems', IEEE Transactions on Ultrasonics, Ferroelectrics, and Frequency Control, Vol 64, No 4, pp 736-748, April 2017.

©2023 TWI Ltd.

Study on the beam directivity of a steered Meander-Line Coil EMAT

Sam Hurrell [1 2], Peter Charlton [1], Stephen Mosey [1], Owen Rees-Lloyd [2], Richard Lewis [2]

[1] Wales Institute of Science and Art, University of Wales Trinity Saint David, Swansea, SA1 8EW

[2] TWI Technology Centre, Port Talbot, SA13 1SB

Abstract

Electromagnetic Acoustic Transducers (EMATs) generate and receive ultrasonic waves via a combination of bias magnetic fields and an alternating eddy current induction. Meander-Line Coil (MLC) EMATs generate these waves into a material at an angle normal to the surface. With a fixed coil spacing, the angle of these waves is controlled by the frequency of the current through the coil. This paper presents the methodology used to measure the beam directivity of the shear waves, through simulations and experimental validations on aluminium. Results show that the maximum shear wave occurred at a steering angle of 32°, the steering limit was reached at a steering angle of 40°, and the beam directivity became unfocussed beyond steering angles of 60°.

1. Introduction

EMATs are a method of inducing ultrasonic waves in ferromagnetic and electrically conductive materials achieved via three transduction methods: Lorentz forces, magnetisation forces and magnetostriction [(1,2)]. For non-magnetic materials such as aluminium, the Lorentz force transduction method is the only means of ultrasonic wave generation. This is achieved by combining a bias magnetic field (from a permanent magnet or an electromagnet) with an alternating eddy current field (produced from a coil of wire driven by an alternating current), which interact to induce periodic forces on the surface of the material. These high frequency forces emit ultrasonic waves through the material, reflecting off any changes in acoustic impedance, such as surfaces or defects [(3)].

EMATs differ from conventional piezoelectric ultrasonic methods due to its capability for wave induction allowing for no contact with the specimen's surface, thus not requiring a facilitative couplant and abling operation at high speeds and temperatures [(4,5)]. A common disadvantage EMATs possess is their low Signal-to-Noise Ratio (SNR) due to their low conversion efficiency for the transmission of waves [(6,7)]. The direction and wave mode of the induced waves depend on the EMAT configuration [(8,9)]. Angled ultrasonic

bulk waves are commonly generated via an MLC design with a bias magnetic field normal to the material's surface [10]. Bulk waves include shear and compression wave modes of different wave speeds due to their particle motion direction relative to the propagation pathway [11], thus for each transmission of the EMAT both shear and compression waves would be emitted. The relationship between the frequency of the driving current and the angle of the shear wave emitted is shown in (1).

$$v_s = 2df \sin\theta \tag{1}$$

where v_s = shear wave velocity (m/s); d = coil spacing (m); f = frequency of the driving current (Hz); and θ = desired angle of the shear wave (°).

Periodic permanent magnet EMATs generate angled shear-horizontal waves (compared to the MLC's shear-vertical waves) and research has gone into studying their beam-steering capabilities via frequency, revealing that they produce maximum amplitudes across a frequency range for a fixed spacing distance [12,13]. The beam-steering capabilities of MLC EMATs bulk waves via frequency have also arrived at similar conclusions [14]. Angled-beam generation can also be achieved by line focusing EMATs, with variable coil spacing focusing the bulk waves into a predetermined location within the material [15-17], however these designs cannot be easily changed to focus waves to a different location. Phased array EMATs have a constantly spaced coils that drive their current at different times in order to focus bulk waves into a specific location [18,19], however these are far more complicated than traditional MLC EMATs and are more costly with a required higher degree of training.

Directivity of an MLC EMATs Rayleigh wave across the material's surface found that the length of the coil's tracks had a crucial effect on the bandwidth and radiation pattern of side lobes [20,21]. Directivity analysis of shear waves has been undertaken with spiral coil EMATs [22,23] and found that the shear waves in a semi-circular steel specimen had a maximum amplitude at the first critical angle, shown in (2).

$$\theta_{crit} = \sin^{-1}\left(\frac{v_s}{v_c}\right) \tag{2}$$

where θ_{crit} = first critical angle (°); and v_c = compression wave velocity (m/s).

Based on these previous studies, the focus of this study is to simulate and experimentally validate the shear wave directivity via frequency of an MLC EMAT on a semi-circular aluminium specimen.

2. Simulation Configuration

A 2D finite element model of an MLC EMAT operating on aluminium was created using COMSOL 6.0 Multiphysics, with the 'AC/DC' and 'Structural Mechanics' software packages due to their predefined mathematical capabilities. The EMAT, shown in Figure 1, was comprised of a 20mm x 20mm NdFeB-42 permanent magnet and a copper MLC with a spacing of 2.5mm, over an aluminium semi-circular specimen. The radius of the specimen was set at 100mm and the lift-off distances for the MLC and magnet were set

at 0.5mm and 1.0mm respectively. The wave velocities in aluminium were 3.12mm/μs and 6.20mm/μs for shear and compression waves respectively, and due to the constant coil spacing, the angle at which the shear waves were emitted was steered by changing the frequency of the driving current.

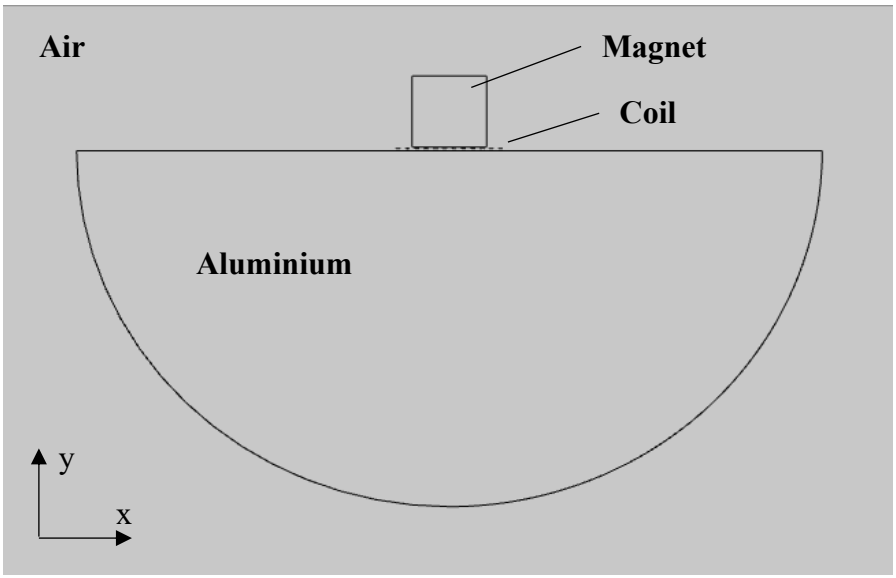

Figure 1. COMSOL simulation model geometry

The current through the coil is modelled as a gaussian-sinc pulse and is given in (3), adapted from [24]. The pulse was designed as such to start at 0A, emit seven positive peaks, and return to 0A, for any given frequency.

$$i(t) = Ie^{-\frac{(t-\tau)^2}{2\sigma^2}} cos(2\pi f(t-\tau)) \quad (3)$$

where I = maximum current amplitude (A) = 6A; σ = standard deviation of the pulse (s) = *1.2/f;* and τ = time delay of the pulse's maximum peak (s) = equal to *5/f.*

An example of this current pulse through the MLC for a 45° shear wave steering angle can be seen in Figure 2.

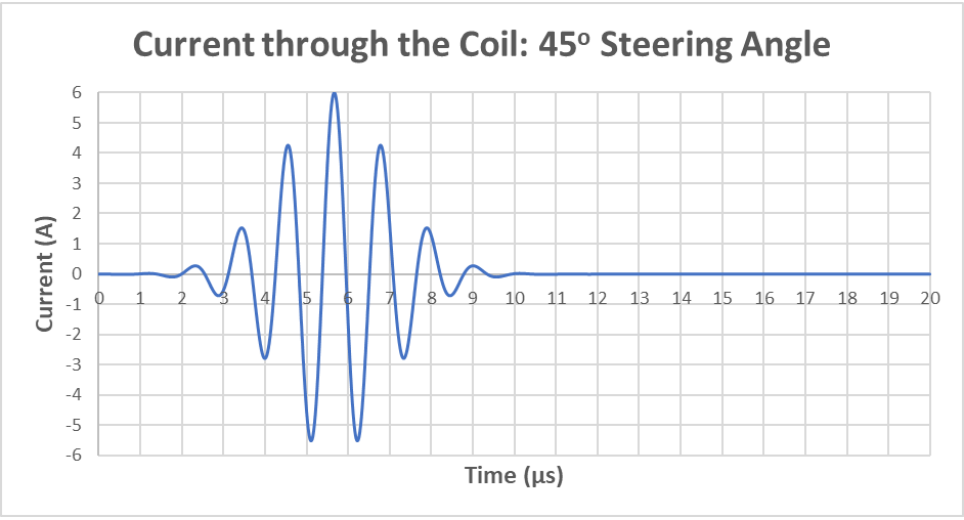

Figure 2. Current pulse profile through the MLC for a 45° shear wave

Since the time delay would change for each steering angle, the time of arrival (ToA) for a given bulk wave was taken as the time of the largest peak within the received waveform, which would eliminate the need for a predefined threshold. The simulation time limit was set at 60μs to allow the shear waves to strike the curved surface and cut out any internal reflections or mode conversions. The correlation between the timestep size and the maximum mesh size for transient simulation models was calculated using the Courant-Friedrichs-Lewy (CFL) condition [25] defined in (4).

$$\boldsymbol{CFL = \frac{v\Delta t}{h_{max}}} \tag{4}$$

where CFL = courant number; Δt = time-step size (s); and h_{max} = maximum mesh size for the specimen (m).

It is recommended to have a courant number approximately equal to less than 0.2, and for COMSOL's transient models to have a maximum mesh size equal to less than one fifth of the wavelength of the desired wave [26]. The variables for a given steering angle using (1) and (3)-(5) can be seen in Table 1.

Table 1. Simulation and experimental variables for each steering angle

Θ (°)	f (MHz)	σ (μs)	τ (μs)	h (mm)	Δt (μs)	CFL	L (μH)	C (nF)
15	2.4110	0.50	2.07	0.258	0.010	0.121	2.3830	1.8
30	1.2480	0.96	4.01	0.500	0.020	0.125	2.5586	6.4
40	0.9708	1.24	5.15	0.642	0.024	0.117	2.6290	10.2
50	0.8146	1.47	6.14	0.765	0.030	0.122	2.6793	14.2
60	0.7205	1.67	6.94	0.865	0.030	0.108	2.7150	18.0
90	0.6240	1.92	8.01	0.990	0.040	0.126	2.7575	23.6

At each timestep during the simulation, the x and y components of the displacement (as indicated in Figure 1) were recorded along the curved surface of the aluminium at 1° intervals from 0° to 90°, where 0° is directly beneath the centre of the EMAT and 90° is the corner to the right of the EMAT. Only one side of the aluminium was measured since conventional MLC EMATs are bidirectional thus the results from one side of the specimen would mirror the other [27]. From these components of displacement, the reception angle of the shear wave's maximum displacement magnitude for each steering angle is located, and the subsequent beam profile is observed.

3. Experimental Validation

An MLC EMAT (of the same design as the simulated EMAT) was positioned atop an aluminium semi-circular block (100mm radius and 70mm deep), as shown in Figure 3. A capacitance decade box was in parallel with the EMAT in order to electrically match the impedance of the EMAT's RLC circuit for any given steering angle. The inductance of the Aluminium specimen was measured via an impedance analyser, and the capacitance via (5), and both variables can also be seen in Table 1. The reason for this impedance

matching was to have the resonant frequency of the circuit equal the frequency of the current, allowing for increased transmission efficiency [28].

$$C = \frac{1}{(2\pi f)^2 L} \tag{5}$$

where C = capacitance (F); and L = inductance (H).

The EMAT was connected to a RITEC RAM-5000 SNAP ultrasonic system that would emit high current pulses at the frequencies required. To receive the ultrasonic waves from the EMAT, a shear piezoelectric probe with a Sonemat SAA1000 variable amplifier (of 40dB gain) and an oscilloscope was positioned along the curved surface from 0° to 90° every 5°. The emitted waves were recorded at each position by the oscilloscope as A-scans and then averaged and filtered to remove any electrical noise present due to external factors. The filtered signal could then be compared to the simulated displacement for each respective position and steering angle to validate the reliability of the simulations.

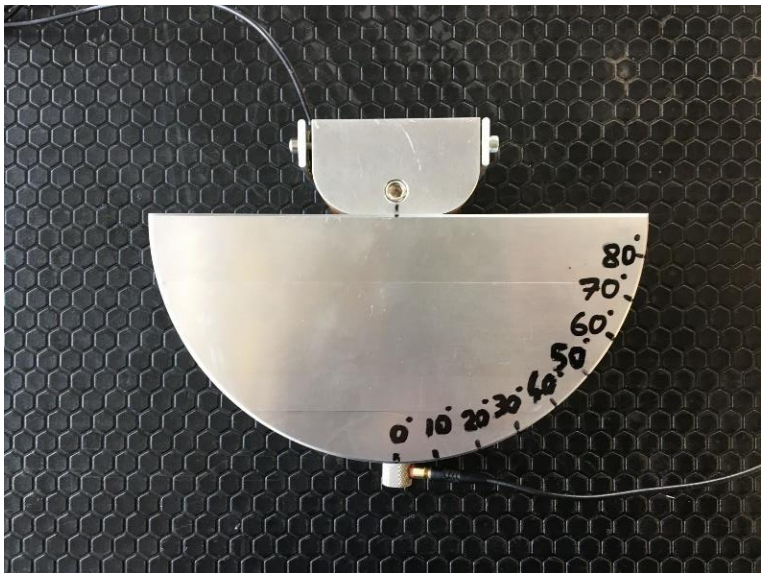

Figure 3. Experimental model setup

4. Results and Discussion

Since the EMAT emits both compression and shear waves simultaneously, there would be overlap in directivities between these waves across the curved surface, however due to the different wave velocities they will strike at different times and so can be separated in the A-scans via ToA. As previously stated, the ToA for a given bulk wave is taken as the time at which the largest peak in a waveform occurs, however the time of flight of that wave starts at the time of the largest peak in the coil's pulse, equal to the time delay of the current. When comparing the differing ToAs across different steering angles (thus different time delays) the relative time of arrival (RToA) for a given wave can be calculated via (6).

$$t_R = t_a - \tau \tag{6}$$

where t_R = RToA (s); t_a = ToA for the maximum peak of a waveform (s); and τ = pulse's time delay (s).

For a steering angle of 15° using (6), the estimated ToA for the compression and shear waves should equal 18.20µs and 34.12µs respectively. Figure 4 shows simulated results of these waves striking the curved surface at a reception angle of 16° where the maximum displacement occurred, and the highest peaks of the waves occur at times of 18.91µs and 33.91µs. While these ToAs are close, possible reasons that they aren't exact may be due to the location of emission from the EMAT not being precisely beneath the centre thus making travel distance lower than the radius.

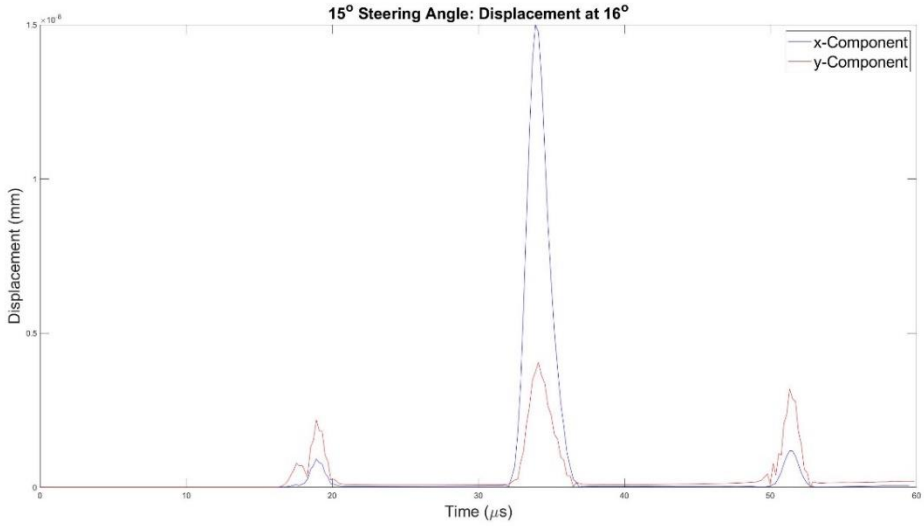

Figure 4. Graph of x and y components of displacement against time for a 15° steering angle at 16°

The values of displacement magnitude are calculated from both the x and y components of displacement at each reception angle, but by comparing the x component to the y component it is also possible to distinguish the type of wave that has struck since the particle motion of compression and shear waves are 90° to one another. Since the specimen's curved surface should always be perpendicular to the direction of wave propagation, the magnitude of displacement that occurs perpendicular to the surface can be found by (7) and the magnitude of displacement that occurs tangential to the surface can be found by (8).

$$\boldsymbol{D_c = x\,sin(r) - y\,cos(r)} \tag{7}$$

$$\boldsymbol{D_s = x\,cos(r) + y\,sin(r)} \tag{8}$$

where D_c = magnitude of displacement perpendicular to the surface (m); D_s = magnitude of displacement tangential to the surface (m); x = component of displacement in the x-axis (m); y is the component of displacement in the y-axis (m); and r is the reception angle along the curved surface (°).

Comparing the two magnitudes of displacement (D_c being greater at 18.20µs and D_s being far greater at 34.12µs) confirms the nature of these bulk waves as compression and shear respectively. The wave occurring near 50µs in Figure 4 can be identified via the ToA and displacement magnitude comparison methods as a compression wave that reflected off the curved surface and then off of the top surface towards the curved surface again. Upon completion, animated colour plots of the von Mises stress within the aluminium were

created to best illustrate the propagation of bulk and Rayleigh waves and can be used to better visualise the change in shear wave angle due to the change in frequency stated in Table 1.

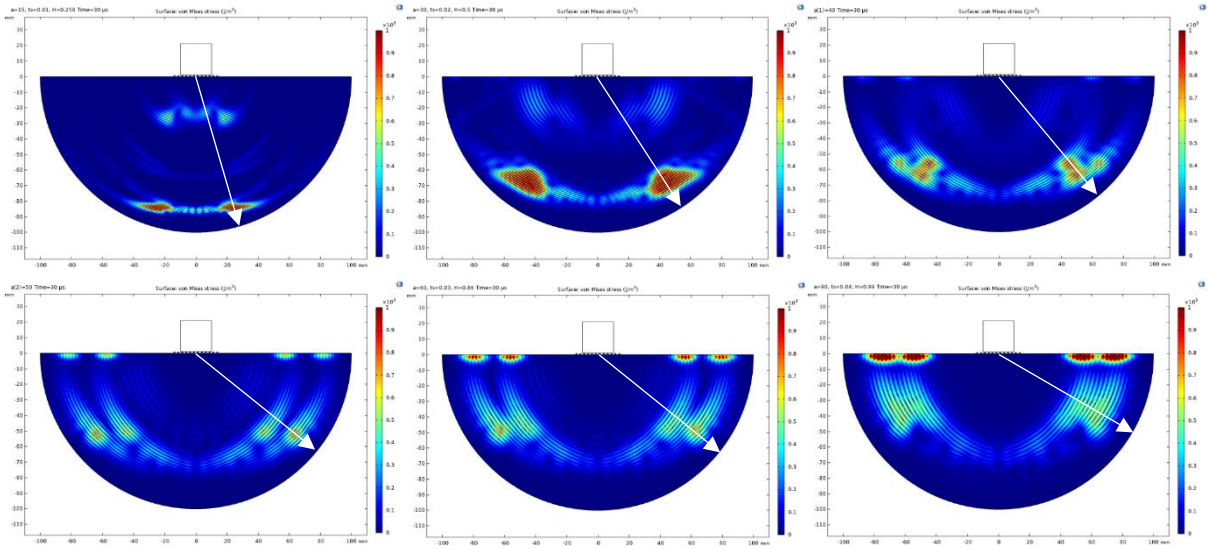

Figure 5. Plots of stress at 30µs for steering angles of: (a) 15°, (b) 30°, (c) 40°, (d) 50°, (e) 60° and (f) 90°

It is noticeable from Figure 5 that after the 30° steering limit, the shear wave begins to separate from a large singular wave into two smaller waves. A possible explanation for this is a mismatch between the frequency of the current and the coil spacing, since frequency was the significant variable changed in these models and the Rayleigh waves also appear to separate in each direction. Figure 5 also suggests that as the steering angle increased: the shear wave reaches a maximum near 30°; the shear wave reaches a steering limit near 50°; Rayleigh waves start to emerge and increase in amplitude. For each steering angle, the maximum displacement magnitude at each reception angle across time was calculated and processed to show only the shear waves' values and when graphed against the reception angle they produced a directivity plot. Figure 6 shows these simulated directivity plots for the steering angles shown in Figure 5, and Table 2 contains the relevant data.

Effort was taken to ensure that the experimental validation remained as close as possible to the simulations, however there were instances where they could not be and thus had to be changed. The gaussian-sinc pulse in the simulation was unable to be replicated in the pulser system and was instead replaced by a rectangular-sinc pulse with a burst of seven cycles of the same frequency. This pulse started at t = 0µs and its midpoint was proportional to the time delay of the simulations by a scale factor of 0.7. The shear probe placed every 5° along the curved surface of the specimen would also have a degree of uncertainty in its placement and orientation and may contain inconsistencies in the quality of coupling.

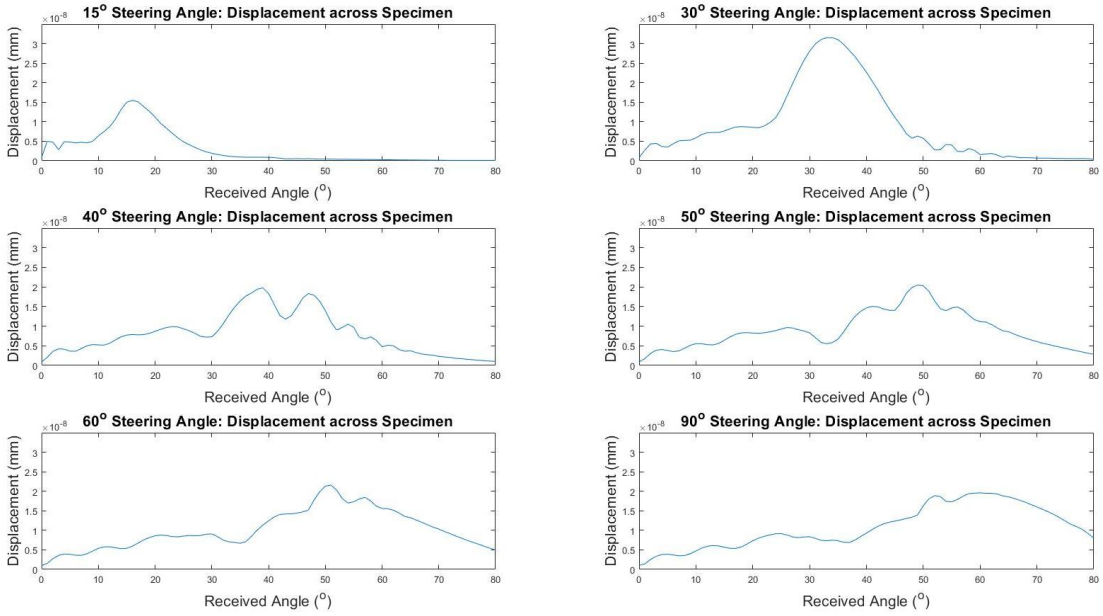

Figure 6. Graphs of maximum displacement from shear waves for each steering angle

Table 2. Data of maximum displacement from shear waves for each steering angle

Steering Angle (°)	Max. Displacement Magnitude (mm)	ToA (μs)	RToA (μs)	Angle of Max. Reception (°)
15	1.55×10^{-8}	33.91	31.84	16
30	3.15×10^{-8}	35.94	31.93	33
40	1.98×10^{-8}	38.76	33.61	39
50	2.05×10^{-8}	35.71	29.57	49
60	2.16×10^{-8}	36.39	29.45	51
90	1.96×10^{-8}	38.00	29.99	60

Since a shear probe would only be able to receive signals with particle motion tangential to the specimen's surface, (8) was used with the simulated results to produce a graph of surface displacement tangential to the curved surface. This would not only better compare with the probe's result but should also filter out the displacement from the compression waves. Figure 7 shows the raw experimental signal from the oscilloscope compared to the simulated tangential displacement. The raw signal graph shows the emission pulse unlike the simulated results, but both graphs show the received signal from the shear wave coming into contact with the curved surface near the same time.

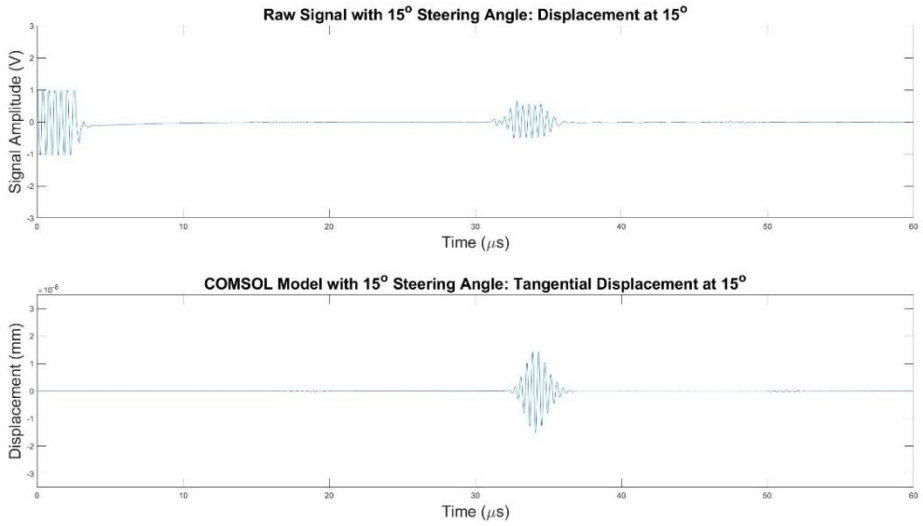

Figure 7. Graphs of signal amplitude and tangential displacement for a 15° steering angle

Due to the presence of electrical noise from the laboratory equipment, the signal from the oscilloscope was passed through a bandpass finite-duration impulse response filter to attenuate all noise outside the range of ± ½f (where f is the current of the pulse). To better compare these results, the amplitude of the filtered signal's shear wave was compared to the amplitude of the simulated shear wave's tangential displacement shown in Figure 8. Signals from higher reception angles during higher steering angles showed the approach of Rayleigh waves that couldn't be removed via (8), and thus gating was implemented to prevent their inclusion.

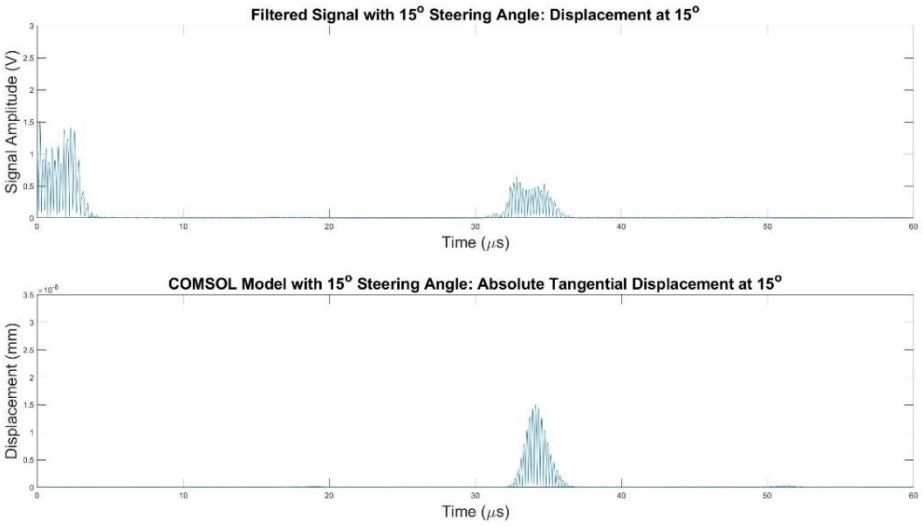

Figure 8. Graphs of filtered signal amplitude and absolute tangential displacement for a 15° steering angle

The objective of the experimental validation was to examine the shear wave's beam directivity from the EMAT and compare with the simulated beam directivity. The maximum amplitude for the filtered experimental shear wave at 5° intervals along the

curved surface were recorded and graphed to recreate the shear wave's beam directivity, and this was repeated for all steering angles. The simulated shear wave's beam directivity was also created by recording the maximum values of the tangential displacement for the simulated shear waves along the curved surface for each steering angle, however the benefit of using the simulations allowed for these values to be recorded at 1° intervals along the curved surface for a higher resolution. Figure 9 shows the comparison of the normalised amplitude of both the experimental and simulated beam directivities.

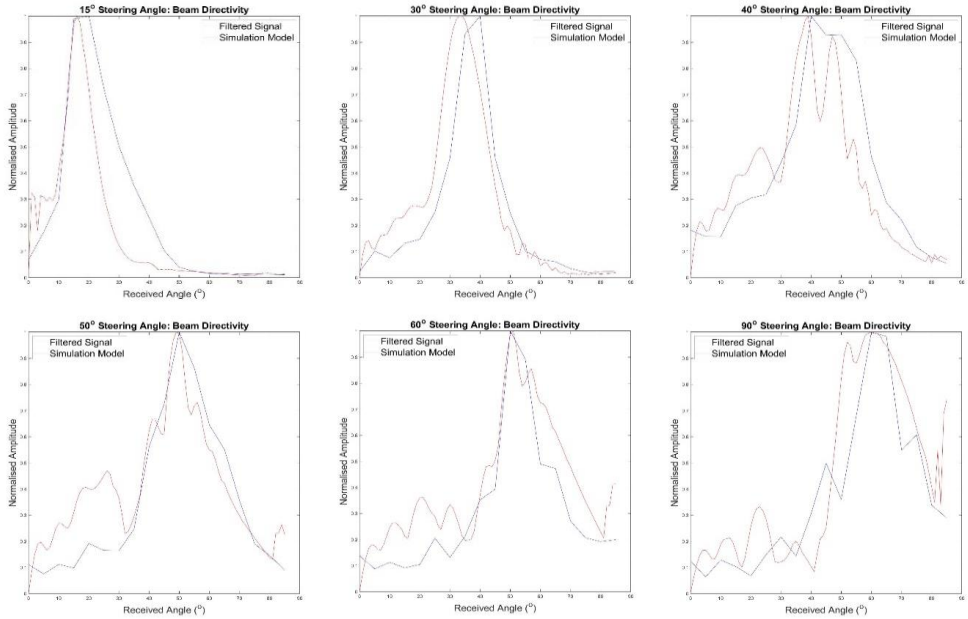

Figure 9. Graphs of experimental and simulated beam directivities for each steering angle

The two beam directivities align very closely for each steering angle however the exact reception angle of maximum displacement is slightly higher for the experimental results. This may be due to the lower 5° scanning resolution along the curved surface than the higher simulated 1° resolution.

5. Beam Directivity Capabilities

The experimental validation proved the reliability of the simulated models, and further simulations were performed on the steering angles left out of the study in order to measure the change in beam directivity more accurately. Simulations of steering angles from 15-90° at every 1° interval were run the same way as the previous models (with the appropriate time-steps and maximum mesh densities for the CFL values) and the same reception angles across the curved surface were measured and recorded across time. For each steering angle, the maximum displacement magnitude of the shear wave striking the curved surface was found in order to locate the steering angle at which transmission of shear waves reached its maximum. The ability to differentiate the bulk waves also allowed the compression waves from the same EMAT transmission to be measured and analysed to observe how changing the steering angle for the shear waves would steer the compression waves, and the values of maximum displacement for both waves is graphed in Figure 10.

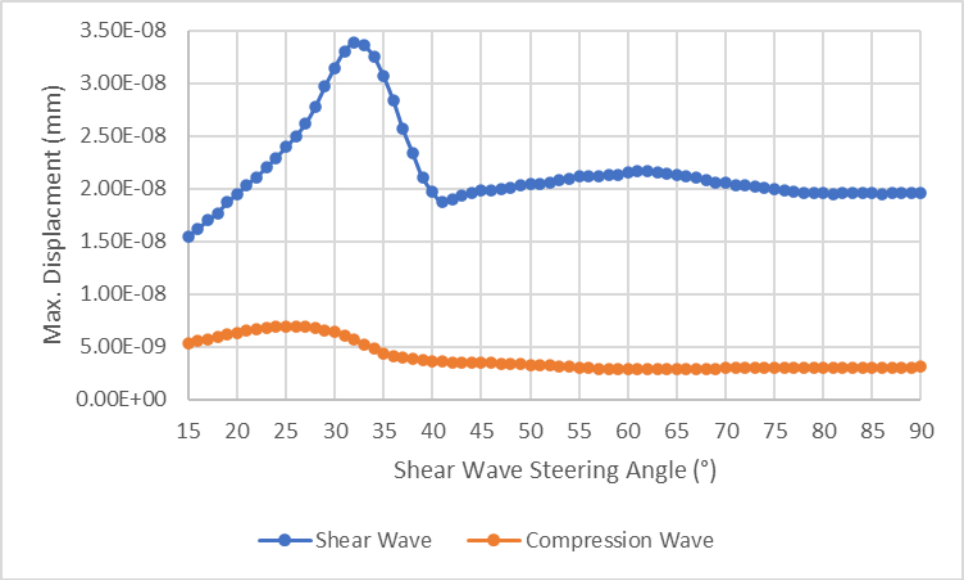

Figure 10. Graph of maximum displacement magnitude for shear and compression waves

As the shear wave steering angle increased: the shear wave's displacement gradually increased from its minimum value of 1.55 $x10^{-8}$mm at 26°; increased faster towards its peak value of 3.39 $x10^{-8}$mm at 32°; gradually decreased towards a second minimum value at 41°; slowly increased to a secondary peak of 2.16 $x10^{-8}$mm at 61°; and slowly decreased into a plateau from which the displacement didn't rise again. A similar process happened with the compression wave as the steering angle increased: the displacement gradually increased to its peak value of 6.95 $x10^{-9}$mm at 25°; gradually decreased to 35°; and reached a plateau. It is likely that more activity for both bulk waves occurs below the 15° steering angle, but to run a simulation below this value would require a higher mesh density which would radically increase the simulation's runtime and thus it was not deemed feasible. This data was processed to find the reception angles along the curved surface at which these maximum displacements occurred, and to find the RToA at which they struck using (6). Figure 11 show this data for the shear waves.

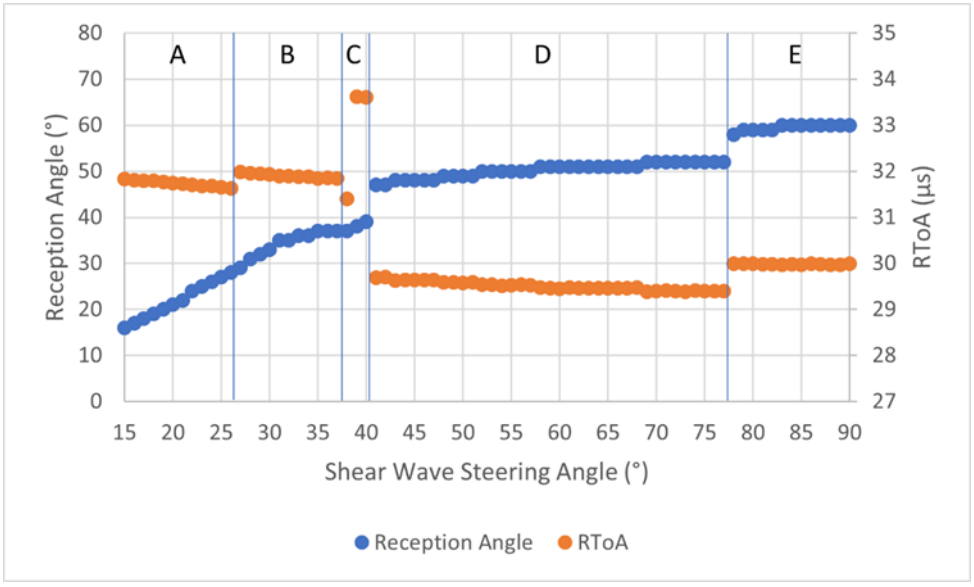

Figure 11. Graphs of reception angle and RToA for the maximum shear wave displacement

To best visualise how increasing the steering angle changes the reception angle and the RToA for the maximum shear wave, it is convenient to separate the steering angles in five sections: A (15-26°), B (27-37°), C (38-40°), D (41-77°), and E (78-90°). These sections also correlate with the changes in maximum displacement from Figure 10.

In section A as the steering angle and maximum displacement gradually increased to its peak, the reception angle gradually increased while the RToA gradually decreased. In section B as the maximum displacement increased faster to its peak and decreased, the reception angle increased into a plateau while the RToA continued to decrease but its trend increased. In section C as the maximum displacement continued to decrease, the reception angle re-correlated with the trend from section A, but the RToA only re-correlates with section A for 38°, as for 39-40° the RToA increased significantly. In section D as the maximum displacement started to plateau, the reception angle plateaued between 47-52° and the RToA entered its lowest trend. Finally in section E, both trends increased towards the end of the steering angle range.

The reason for this behaviour was the interactions between the two separate shear waves. Section B highlights the steering angles at which these separate shear waves impose, and the maximum displacement increased greatly. Outside of this section, the maximum displacement and subsequent reception angle and RToA come from one of the two separate shear waves seen in Figure 5. The RToA supports this theory as due to a constant wave velocity, the distance between the wave's emission point and the reception angle suddenly changes which when observing the separate shear waves from Figure 5 once can see that they appear to be generated at different positions.

Figure 12 shows the graphs of displacement against RToA for the steering angles of 38°, 40° and 41° at the reception angles that their maximum displacements struck. These steering angles show the reason for the changing RToA within section C and the transition into section D. Figure 12 shows the overlapping of these separate shear waves, and the maximum displacement values in Figure 10 come from the largest of these peaks. It is clear that the first shear wave is the largest for steering angles of 38° and 41°, and the second shear wave is larger for 40°. The second shear wave exceeding the first shear wave explains the larger RToA for the steering angles of 39-40°. Figure 12 also supports the idea that the shear waves in section B are imposing, because as the steering angle increased the distance between the separate shear waves also increased and so they would have overlapped at a steering angle of 32°.

Since the RToA for the 38° steering angle follows the trend in section A, it may be assumed that the shear waves in section A come from the first of the two shear waves. Despite the 38° and 41° steering angles' maximum displacement coming from their first shear waves, their RToAs are still quite different. This is because the steering angles in section D (41-77°) give the maximum displacement from the first shear wave's main lobe, and in section A these values come from the first shear wave's steeper side lobe imposed upon by the second shear wave's main lobe. As the steering angle increased from section D to E, the trends for reception angle and RToA both increased due to the first shear wave's main lobe being surpassed by its shallower side lobe. This side lobe becoming greater than the main lobe can also be seen in Figure 6, since the main lobe's presence near the 50° reception angle for steering angles of 50-90° is slowly overtaken by the displacement near the 60° reception angle for the 90° steering angle.

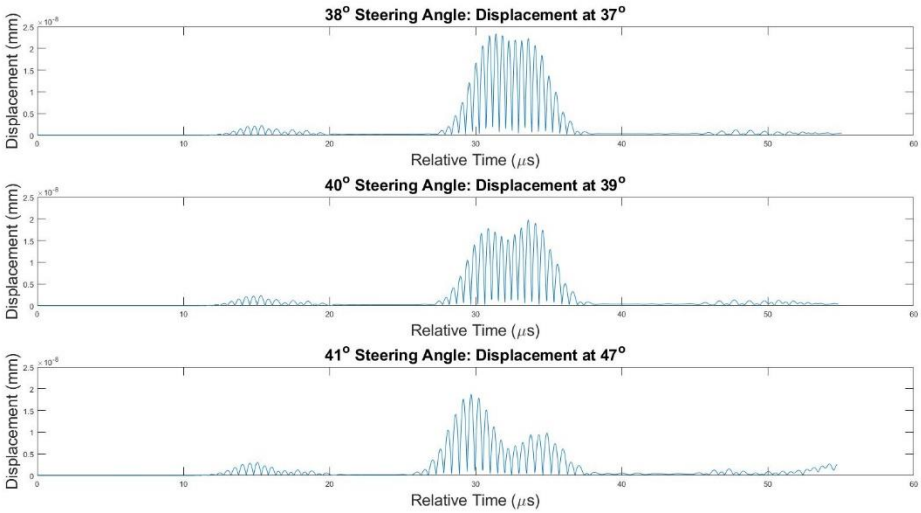

Figure 12. Graphs of displacement against relative time for each given steering angle

Figure 13 shows the reception angles and RToA for the compression wave's maximum displacement (shown in Figure 10) and it is noticeable that as the steering angle increases the reception angle increases sharply. The frequency of the current associated with each of the shear wave steering angles in (1) can also be used to calculate the angle of compression waves by substituting the compression wave velocity in place of the shear waves', and these approximate the values of reception angle in Figure 13. Like with Figure 11 the steering angles may be grouped into different sections: A (15-33°), B (34-35°), C (36-59°), and D (60-90°), which correlate with changes in the compression wave's maximum displacement shown in Figure 10.

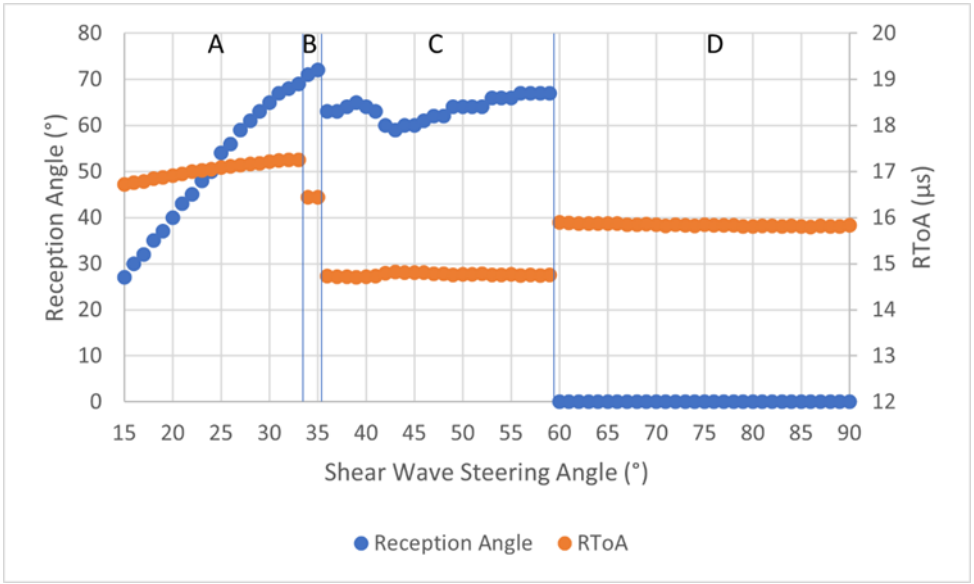

Figure 13. Graphs of reception angle and RToA for the maximum compression wave

In section A, the reception angle and RToA gradually increase with the shear wave's steering angle, where the compression waves maximum displacement rises to its peak and falls. Section B shows the continual increase of the reception angle with a drop in RToA,

during which the maximum displacement lowers to its plateau. Section C shows that the compression wave has reached its steering limit between 59-67°, and section D shows that the maximum displacement for the compression lobe at 0° has now overtaken the angled wave. Sections A-C for the compression wave behave in a comparable manner to sections B-D in Figure 11, which suggests that there are also separate compression waves. The presence of separate compression waves is confirmed by Figure 4, as there are two peaks in the y component of displacement located near 18μs at 16° for a 15° steering angle.

6. Conclusion

Over the course of this study, the goal was to simulate and experimentally validate the beam directivity of the shear waves generated by an MLC EMAT on aluminium. This study has proven that by changing the frequency of the current through an MLC, the angle of both bulk waves changed until they reached a steering limit. Results showed that as the steering angle increased, the displacement amplitude reached a peak at 32° and a second smaller maximum at 61. Simulation results show that the compression wave reached its critical angle near the shear wave's maximum peak, and it was decided that the MLC EMAT reached the steering angle limit at 40° due to the displacement magnitude starting to plateau thus there was little increase in reception angle during a large increase in the steering angle. While the EMAT was capable of reaching reception angles of 50°, the loss in amplitude and focussed directivity may not be optimal for real-world scanning. Future work would involve changing the coil parameters, such as spacing and length, to measure how this affected the directivity, and looking into the nature of these separating waves to determine their cause.

7. Acknowledgements

The authors gratefully acknowledge funding from the Knowledge Economy Skills Scholarships (KESS 2) and TWI Ltd. KESS 2 is a pan-Wales higher-level skills initiative led by Bangor University on behalf of the HE sector in Wales. It is part funded by the Welsh Government's European Social Fund (ESF) convergence programme for West Wales and the Valleys.

8. References

1. M Hirao and H Ogi, 'EMATs for science and industry: Noncontacting ultrasonic measurements', Kluwer Academic Publishers, Boston, Massachusetts, USA, 2003.
2. R Ribichini, F Cegla, P B Nagy and P Cawley, 'Experimental and numerical evaluation of electromagnetic acoustic transducer performance on steel materials', NDT&E International, Vol 45, No 1, pp 32-38, August 2011.

3. G A Alers and L R Bums, ‘EMAT Designs for Special Applications’, Materials Evaluation, Vol 45, No 10, pp 1184-1194, October 1987.
4. O Rees-Lloyd, P Charlton, S Mosey and R Lewis, ‘Effects of relative motion on a Rayleigh wave electromagnetic acoustic transducer operating on aluminium’, Insight, Vol 61, No 2, pp 83-89, February 2019.
5. ASTM E1816 – 12, ‘Standard practice for ultrasonic testing using electromagnetic acoustic transducer (EMAT) techniques’, August 2018.
6. X Jian, S Dixon, K Grattan and R S Edwards, ‘A model for pulsed Rayleigh wave and optimal EMAT design’, Sensors and Actuators A: Physical, Vol 128, No. 2, pp 296–304, April 2006.
7. L Kang, S Dixon, K Wang and J Dai, ‘Enhancement of signal amplitude of surface wave EMATs based on 3-D simulation analysis and orthogonal test method’, NDT&E International, Vol 59, No 1, pp 11-17, October 2013.
8. R Ribichini, ‘Modelling of Electromagnetic Acoustic Transducers’, PhD Thesis, Imperial College of London, February 2011.
9. J K Hu, Q L Zhang and D A Hutchins, ‘Directional characteristics of electromagnetic acoustic transducers’, Ultrasonics, Vol 26, pp 5-13, January 1988.
10. C Pei, S Zhao, P Xiao and Z Chen, ‘A modified meander-line-coil EMAT design for signal amplitude enhancement’, Sensors and Actuators A: Physical, Vol 247, pp 539-546, August 2016
11. S Wang, et al, ‘Modeling and Comparison of Three Bulk Wave EMATs’, IECON 2011 - 37th Annual Conference of the IEEE Industrial Electronics Society, 2011, pp. 2645-2650
12. K Sawaragi et al, ‘Improvement of SH-wave EMAT phased array inspection by new eight segment probes’, Nuclear Engineering and Design, Vol 198, pp 153-163, September 1999.
13. S Hill and S Dixon, ‘Localisation of defects with time and frequency measurements using pulsed arrays’, NDT&E International, Vol 67, pp 24-30, June 2014.
14. T J Moran and R M Panos, ‘Electromagnetic generation of electronically steered ultrasonic bulk waves’, Journal of Applied Physics, Vol 47, No 5, pp 2225-2227, May 1976
15. H Sun, S Huang, S Wang and W Zhao, ‘Meanderline Coil Arrangement of Ultrasonic Wave Line-Focusing Electromagnetic Acoustic Transducers’, 2020 IEEE International Instrumentation and Measurement Technology Conference (I2MTC), pp 1-6, June 2020
16. H Ogi and M Hirao, ‘Line-focusing of ultrasonic SV wave by electromagnetic acoustic transducer’, The Journal of the Acoustical Society of America, Vol 103, No 5, pp 2411-2415, May 1998.
17. Y Li, C Li, R Su, G Zhai and K Wang, ‘Unidirectional Line-Focusing Shear Vertical Wave EMATs Used for Rail Base Center Flaw Detection’, 2016 IEEE Far East NDT New Technology & Application Forum (FENDT), pp. 99-102, 2016
18. J Tkocz, D Greenshields and S Dixon, ‘High power phased EMAT arrays for nondestructive testing of as-cast steel’, NDT and E International, Vol 102, pp 47-55, 2019
19. J Isla and F Cegla, ‘EMAT phased array: A feasibility study of surface crack detection’, Ultrasonics, Vol 78, pp 1-9, February 2017
20. Y Xie, et al, ‘Directivity analysis of meander-line-coil EMATs with a wholly analytical method’, Ultrasonics, Vol 73, pp 262-270, January 2017

21. Y Xie et al, ‘Simulation of an Electromagnetic Acoustic Transducer Array by Using Analytical Method and FDTD’, Journal of Sensors, Vol 2016, January 2016.
22. W Shi, et al, ‘Optimal Design of Spiral Coil EMATs for Improving Their Pulse Compression Effect’, Journal of Nondestructive Evaluation, Vol 40, No 2, June 2021
23. X Jian, et al, ‘Shear wave generation using a spiral electromagnetic acoustic transducer’, Applied Physics Letters, Vol 89, No 24, December 2006
24. D Ratnam, A Kuamr and P C R Bhagi, ‘Time Domain Finite Element Modelling of Pulsed Meander Coil Electromagnetic Acoustic Transducer’, Electromagnetic Non-Destructive Evaluation (XXI), Vol 43, pp 246-254, May 2018.
25. R Courant, K O Friedrichs and H Lewy, ‘On the Partial Difference Equations of Mathematical Physics’, IBM Journal of Research and Development, Vol 11, No 2, pp 215–234, March 1967.
26. R Barauskas and V Daniulaitis, ‘Modelling techniques for ultrasonic wave propagation in solids: 2D case’, Ultrasound Vol 30, No 2, pp 7-10, 1998
27. S Wang, et al, ‘Numerical and Experimental Analysis of Unidirectional Meander-Line Coil Electromagnetic Acoustic Transducers’, IEEE Transactions on Ultrasonics, Ferroelectrics, and Frequency Control, Vol 60, No 12, pp 2657-2664, December 2013
28. J Isla, M Seher, R Challis and F Cegla, ‘Optimal Impedance on Transmission of Lorentz Force EMATs’, AIP Conference Proceedings, Vol 1706, No 1, February 2016

Multi-angle steering of a Meander-Line Coil EMAT

Sam Hurrell [1 2], Peter Charlton [1], Stephen Mosey [1], Owen Rees-Lloyd [2], Richard Lewis [2]

[1] Wales Institute of Science and Art, University of Wales Trinity Saint David, Swansea, SA1 8EW

[2] TWI Technology Centre, Port Talbot, SA13 1SB

Abstract

EMATs are capable of both transmitting and receiving ultrasonic waves within ferromagnetic and conductive materials. Meander-Line Coil (MLC) EMATs can transmit not only Rayleigh waves across the material's surface but also compression and shear waves at an angle into the material. The frequency of the transmission signal controls the propagation angle of the shear waves, and this paper establishes the simulated and experimental results for an MLC EMAT's beam directivity across desired steering angles of 15-90°. These results show that: a maximum magnitude occurred at the 31° steering angle; a steering limit at the 48° steering angle; and the maximum reception angle attained was at 61.1°. The sum of two steering angles' transmission signals showed the EMAT capable of generating two distinct shear wave beams at different propagation angles simultaneously. Further simulated modelling of the EMAT in a Pulse-Echo (PE) setup confirmed not only that the two beams could detect defects present in the material, but that the detecting beam could be identified by filtering of the returning waves.

1. Introduction

Ultrasonic Testing (UT) typically uses piezoelectric transducers to transmit ultrasonic waves into a material that reflect off of changes in acoustic impedance, such as surfaces and internal discontinuities [(1)]. Piezoelectric transducers require a coupling medium to facilitate the transfer of energy from the transducer to the material, which can be problematic for materials that are high-temperature, contaminated, or otherwise prohibit the application of couplant. Electromagnetic Acoustic Transducers (EMATs) are a UT method that utilise a static magnetic field with a dynamic eddy current field to transmit and receive ultrasonic waves via electromagnetic transduction [(2)]. This not only overcomes the need for couplant, but permits EMATs to operate at high-speeds and at greater lift-offs from the surface [(3,4)]. However, this also limits EMAT's operation to ferromagnetic and electrically conductive materials and lowers their signal-to-noise ratio due to their low conversion efficiency [(5,6)]. EMAT transduction methods include:

magnetisation forces [7]; magnetostriction [8]; and Lorentz forces [9]. For non-ferromagnetic materials, Lorentz forces are the only transduction method in effect and is expressed in (1).

$$\boldsymbol{F_L = B_0 \times J_e} \quad (1)$$

Where F_L = Lorentz force density (N/m²); B_0 = Magnetic flux density (T); J_e = Eddy current density (A/m²).

Different configuration of magnet and coil are used to generate Lorentz forces in different directions, allowing for a variety of ultrasonic wave modes [10]. Meander-Line Coil (MLC) EMATs use a magnetic field normal to the surface with alternating coils to generate periodic, horizontal Lorentz forces. MLC EMATs are commonly used for generating Rayleigh waves across the material's surface in a Pitch-Catch (PC) setup [11]. However, they are also used to generate oblique shear and compression waves bidirectionally into the material [12]. Unidirectional MLC EMATs use two coil arrays (offset by half a coil spacing) out of phase by 90° to transmit waves in one direction. These have been shown to increase the amplitude of both the shear and Rayleigh wave by approximately twice that of a standard bidirectional MLC EMAT [13]. Line-focusing EMATs use an array with coils at set spacings to concentrate the shear waves to a single focal line [14,15], and can increase the defect response of a unidirectional EMAT by 7-10% [16]. Phased Array EMATs use constantly spaced coils with timed pulses to focus or steer bulk waves, however these require custom equipment and are more costly than other pulser systems [17–19]. For a traditional MLC EMAT of constant coil spacing, the frequency of the eddy current density controls the angle of the transmitted shear waves and is expressed in (2).

$$\boldsymbol{\theta = sin^{-1}\left(\frac{v_s}{2df}\right)} \quad (2)$$

where θ = shear wave steering angle normal to the surface (°); v_s = shear wave velocity (m/s); d = spacing distance between each coil (m); f = frequency (Hz).

This study investigated the correlation between the desired steering angle and the actual reception angle of the shear waves.

2. Finite Element Method (FEM) modelling

A simulated model of an MLC EMAT on aluminium was created for this study using 'COMSOL Multiphysics', an FEM analysis software programme. The EMAT's Lorentz force transduction and subsequent ultrasonic waves were modelled by combining the 'AC/DC' and 'Structural Mechanics' software packages. Figure 1 shows the design of the EMAT over a semi-circular aluminium sample.

The simulated EMAT design was derived from an experimental EMAT, consisting of: a 20mm x 20mm NdFeB-42 permanent magnet at 1.1mm lift-off; and a copper MLC array with 12 coils spaced 2.5mm apart at 0.125mm lift-off. The coil's lift-off was maintained by the MLC array's plastic coating, and the magnet's by the MLC (0.4mm thick), three 0.2mm-thick plastic shims, and a 0.1mm-thick layer of copper tape. The shims and copper

prevented the MLC from inducing eddy currents and thus ultrasonic waves in the magnet's nickel coating, which would have been received by the EMAT in a PE configuration. Each coil was composed of three copper strands (0.2mm x 0.15mm, spaced 0.4mm apart) with current flowing in the same direction, distributing the induced eddy currents into the aluminium's surface more evenly. Figure 2 shows the design of the central four coils at the aluminium's surface.

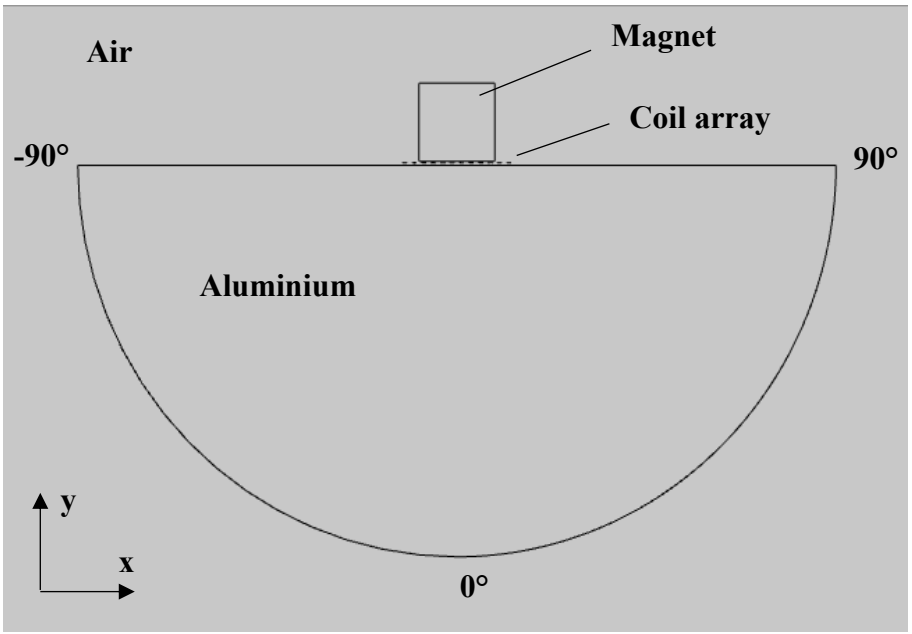

Figure 1. COMSOL FEM model design overall geometry

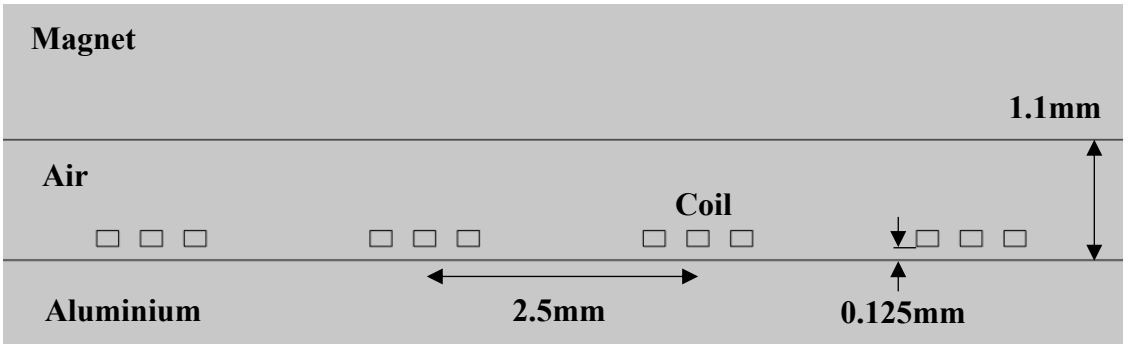

Figure 2. COMSOL FEM model design coil layout

The frequency of the EMATs transmission signal determines the angle of shear waves generated. This signal was modulated by a gaussian window to better localise its frequency and time [20]. The width of the gaussian window was also determined by frequency, to create the same number of peaks in the transmission signal with the same magnitude across steering angles. (3) gives the transmission signal used in the simulated models, adapted from Ratnam, Kuamr, Bhagi [21].

$$\boldsymbol{I_{(t)} = I_{max} \times e^{-\frac{(t-\tau)^2}{2\sigma^2}} cos\big(2\pi f(t-\tau)\big)} \quad (3)$$

where I = current (A); I_{max} = maximum current amplitude (A) = 6A; σ = standard deviation (μs) = $1.2/f$; τ = time delay (μs) = $roundup\left[\frac{3.75}{f\times\Delta t}\right] \times \Delta t$.

For time-dependent models, the correlation between the timestep and the maximum mesh size is defined by the Courant-Friedrichs-Lewy (CFL) number [22], given in (4). The maximum mesh size within the aluminium where the shear waves propagated was set to six elements per wavelength to reduce the computation load. The shear and compression wave velocities within the aluminium were set at 3.12mm/us and 6.40mm/us respectively, based on the measured wave velocities within the real-world sample.

$$C = \frac{v_s \times \Delta t}{h_{max}} \tag{4}$$

Where C = CFL number ≈ 0.1; Δt = timestep (s); and h_{max} = maximum mesh size (m).

The model used two time-dependent study steps: the first to calculate the Lorentz force densities and the ultrasonic waves that were propagated from them; and the second to model only the propagation of the ultrasonic waves. The Lorentz forces were calculated within an area beneath the EMAT of high-mesh density (equal to five elements per skin depth) that greatly increased the model's computational load. The length of the first time-dependent study step was therefore temporally limited to 2τ, which allowed for 7.5 cycles with a maximum at the time delay. Figure 3 shows the transmission signals for steering angles of 15° and 90° used for the models.

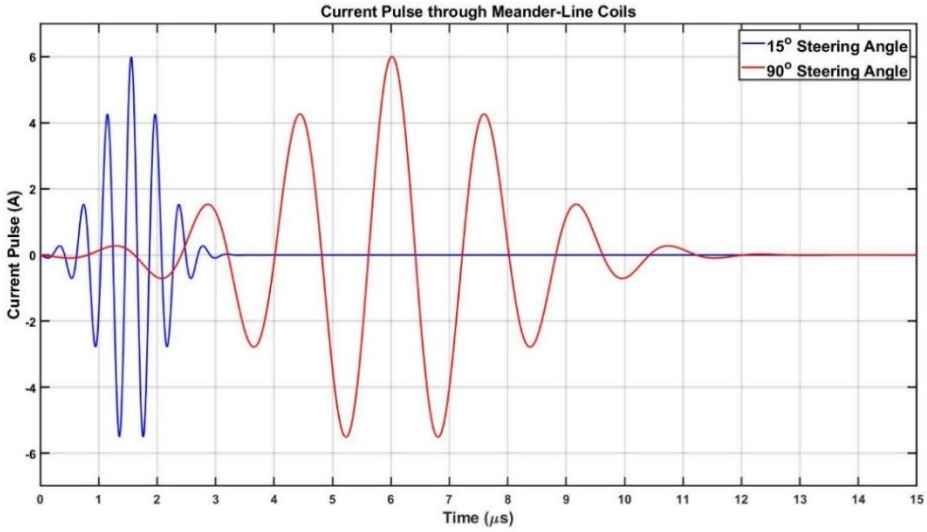

Figure 3. Transmission signal profiles for different steering angles

The second time-dependent study step discarded both the high-mesh density area and the multiphysics coupling and ended at 99μs to model the shear waves returning to the EMAT.

3. Beam Directivity

3.1. Simulated results

Using (2)-(4), the simulated MLC EMAT transmitted steering angles of 15-90°. Figure 4 shows colour plots of four steering angles that best represent the effect that changing the steering angle had on the three transmitted wave modes. The shear waves clearly increase

in reception angle (highlighted by the white arrow) from 15-45°. There appears to be little change in reception angle from 45-90°, but the Rayleigh waves do increase in magnitude. Additionally, the single shear wave separates into two distinct shear waves as the steering angle increases from 30-45°. This separation remains until the steering angle reaches 90°.

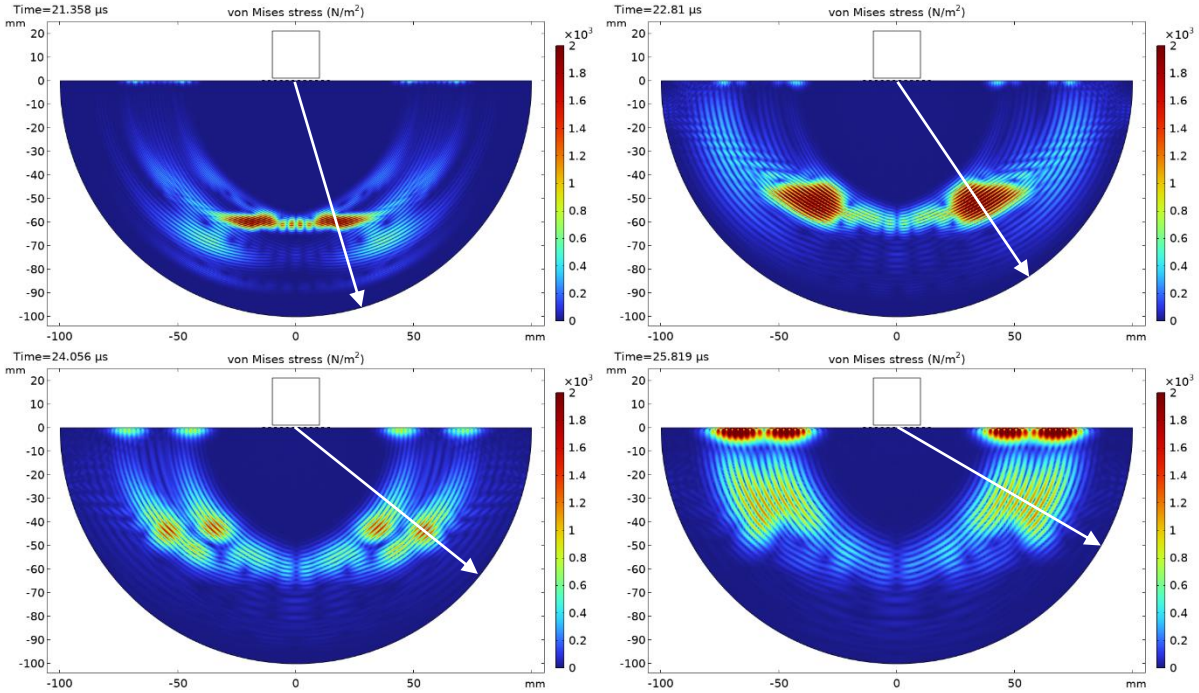

Figure 4. Colour plots of von Mises stress at time 'τ + 19.8µs'. (Top-left) 15° steering angle. (Top-right) 30° steering angle. (Bottom-left) 45° steering angle. (Bottom-right) 90° steering angle. The white arrows show the angle of shear wave propagation.

The x and y components of displacement (as indicated in Figure 1) were recorded at each timestep from across the aluminium sample's two surfaces. Those across the curved surface were recorded from -90° to 90° at 0.1° intervals. Those across the flat surface were recorded from -100mm to 100mm at 0.25mm intervals. Using (5)-(6), the wave that hit the curved surface could be characterised based on its direction of displacement. The directional displacements were passed through a bandpass filter of ±1/3 the transmission frequency to produce A-scans at each reception angle. Figure 5 shows the resultant A-scans comparing these displacements from the same reception angle.

$$u_s = u_x \cos\theta_r + u_y \sin\theta_r \tag{5}$$

$$u_c = u_x \sin\theta_r - u_y \cos\theta_r \tag{6}$$

where u_s = displacement tangential to the curved surface (m); u_c = displacement normal to the curved surface (m); u_x = x-component of displacement (m); u_y = y-component of displacement (m); θ_r = angle normal to the curved surface (°).

For each steering angle, the three wave modes were gated (based on wave velocity, time delay, and the sample's radius of 100mm) and the maximum displacement recorded for each reception angle. Beam directivity was plotted and the behaviour of each wave mode observed as steering angle increased. The Rayleigh wave's maximum displacement was

recorded from the larger of the two directional displacements due to its elliptical particle motion and was measured at the ±90° reception angles. Figure 6 shows the maximum displacements of the three wave modes for each steering angle.

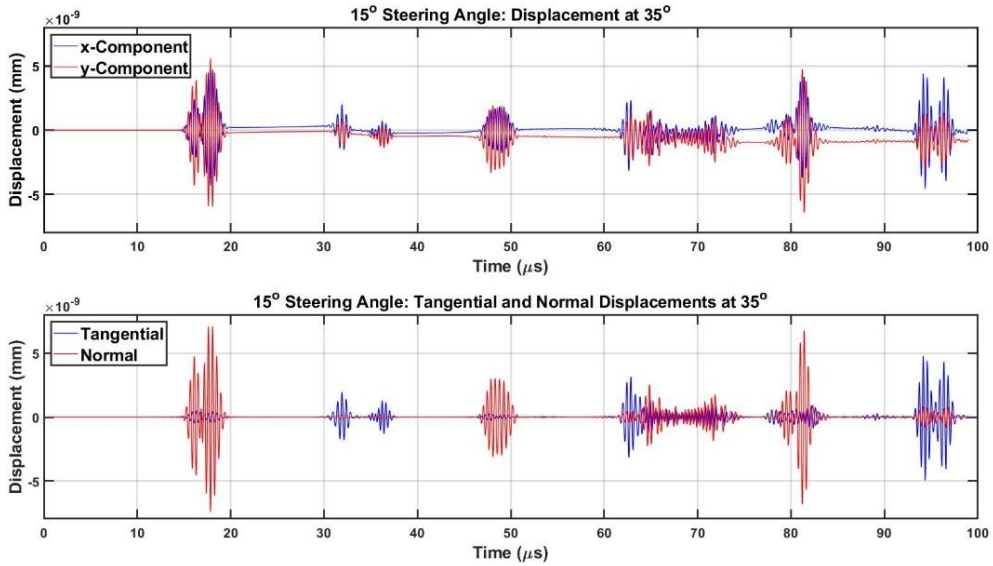

Figure 5. Graphs of displacement and directional displacement for 15° Steering angle EMAT

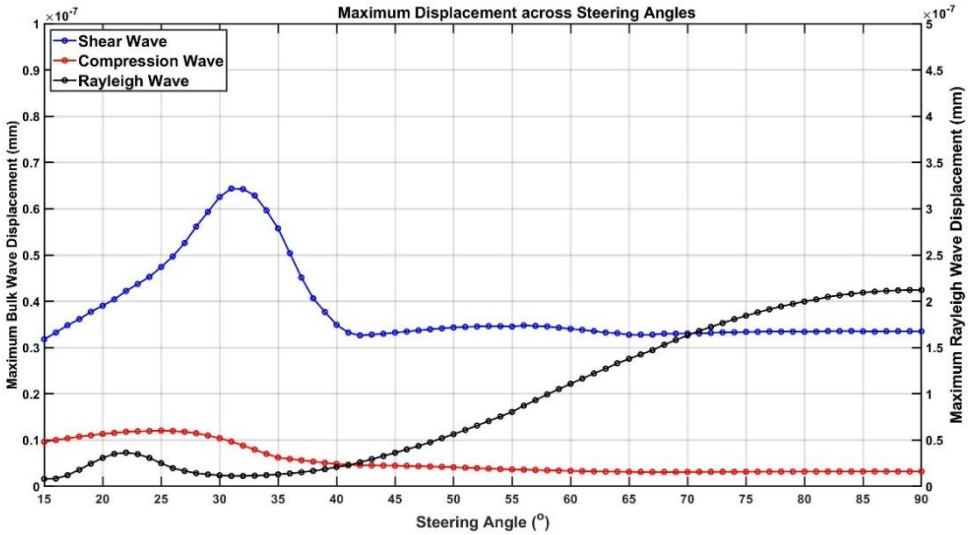

Figure 6. Graph of maximum displacement across steering angles

From 15-31°, the shear wave more than doubles in magnitude from its minimum to its maximum value. Using Snell's law with the velocities of shear and compression waves, the compression wave is angled at 90° when the shear wave reaches 29.18°. This is the critical angle, explaining the maximum magnitude near this steering angle, and has been shown to affect spiral-coil EMATs due to the constructive interference between the shear wave and the head wave [23]. From 31-42°, the maximum shear wave displacement decreases back to a displacement similar to that of 15° and continues to plateau for the remaining steering angles. It is at 45° that the displacement of the Rayleigh waves

surpasses that of the shear waves, as it increases towards a peak value at 90°. There is a small peak in Rayleigh wave displacement at 22° due to its frequency equalling the 3rd harmonic of the frequency at 90° (where its magnitude is maximum) [24].

Figure 7 shows the corresponding reception angle for the maximum shear wave displacement across steering angles. Each reception angle includes error bars to indicate the shear wave's beamwidth, equal to the range of reception angles with displacements greater than -6dB the maximum. The upper limit of the beamwidth was capped at 75°. Beyond this reception angle, the Times of Arrival (ToA) for shear and Rayleigh waves were too close to be distinguished by gating. The reception angles are graphed on the left axis while the right axis displayed its Relative ToA (RToA), equal to $ToA - \tau - \frac{100mm}{v_s}$, to indicate from which separate shear wave the maximum displacement originated from.

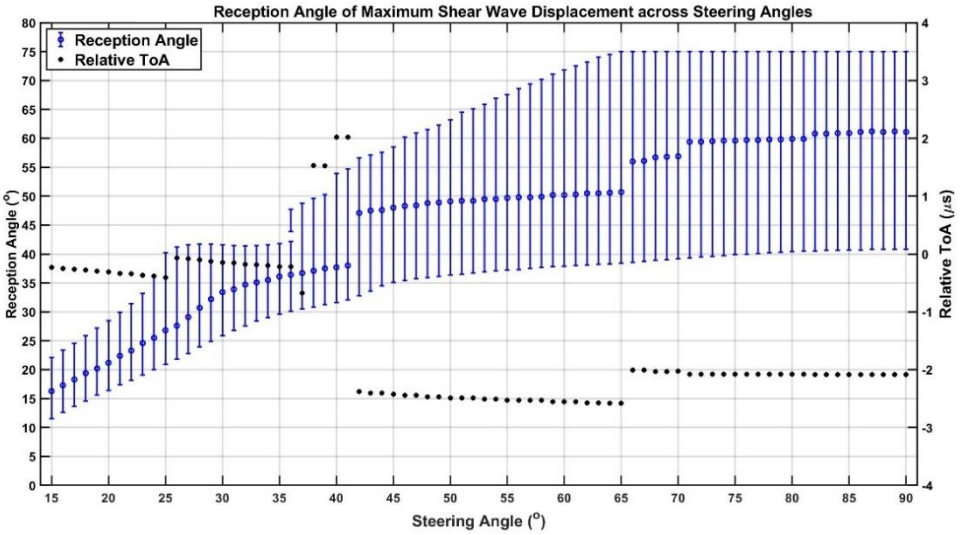

Figure 7. Graph of shear wave reception angles across steering angles

As the steering angle increases from 15-41° the reception angle increases linearly, with minor variations in this trend near the critical angle. From steering angles of 36-42°, the RToA changes irregularly suggesting that the origin position of the shear waves also changes. This is due to the shear waves splitting into separate waves (as seen from Figure 4 for the 45° steering angle). This is why the reception angle suddenly rises by almost 10° when the steering angle increases from 41-42°. The RToA suggests that the separate shear wave closest to the curved surface is the source of the maximum amplitude, and this remains the case from the remaining steering angles. The reception angle does not significantly increase with steering angle, as any sudden changes are due to higher-angled sidelobes becoming greater in magnitude than the main lobe. A steering limit of 48° was judged for this EMAT as beyond this limit: increases in reception angle with respect to steering angle begin to plateau; the maximum amplitude plateaus; and the beamwidth reaches its maximum rate of increase.

Further work has shown that the origin positions of the separate shear wavefronts can be triangulated based on the RToAs from across the aluminium's curved surface [25]. For the 90° steering angle, the origin positions were located approximately ±11.6mm from the centre of the flat surface. These origin positions correlated with concentrations of magnetic flux density (beneath the corners of the magnet), and the number of separate

waves correlated with the position, magnitude, and number of concentrations of magnetic flux density within the coil array's area of effect.

3.2. Experimental results

A semi-circular aluminium sample was machined with the same dimensions as the simulated model: 100mm radius and 70mm deep. The experimental MLC EMAT was compressed into the centre of its flat surface. The transmission EMAT was powered by a RITEC SNAP system, and a Hanning window pulse was used with the given transmission frequency to approximate the model's transmission signal. The steering angles used ranged from 15-90° at 5° intervals, however steering angles of 65-85° were omitted due to the limited variance in their simulated results. An impedance analyser measured the inductance of the EMAT on the aluminium for a given frequency. The capacitance required to electrically match the EMAT's impedance for a given steering angle was calculated using (7). The resonant frequency of the EMAT's RLC circuit was equated with the transmission frequency, and high-voltage ceramic capacitors were used in parallel with the EMAT to maximise its transmission efficiency [26].

$$\boldsymbol{C = \frac{1}{L(2\pi f)^2}} \tag{7}$$

where C = capacitance (F); and L = inductance (H).

From across the curved surface, a spiral-coil shear wave EMAT [27] and an SAA1000 amplifier [28] were used in a PC setup to receive the transmitted shear waves. The centre of the EMAT's flat surface was held tangential to the aluminium's curved surface via 3D printed probe casings. This EMAT used low-voltage ceramic capacitors, equal to the transmitter EMAT's capacitors in value. The received signal was then filtered using the SNAP system's superheterodyne receiver and displayed on an oscilloscope. An A-scan was recorded by the receiver EMAT at 1° increments across the curved surface and used to create experimental beam directivity plots. Figures 8-9 show the simulated and experimental directivity plots normalised for steering angles of 30° and 45° respectively.

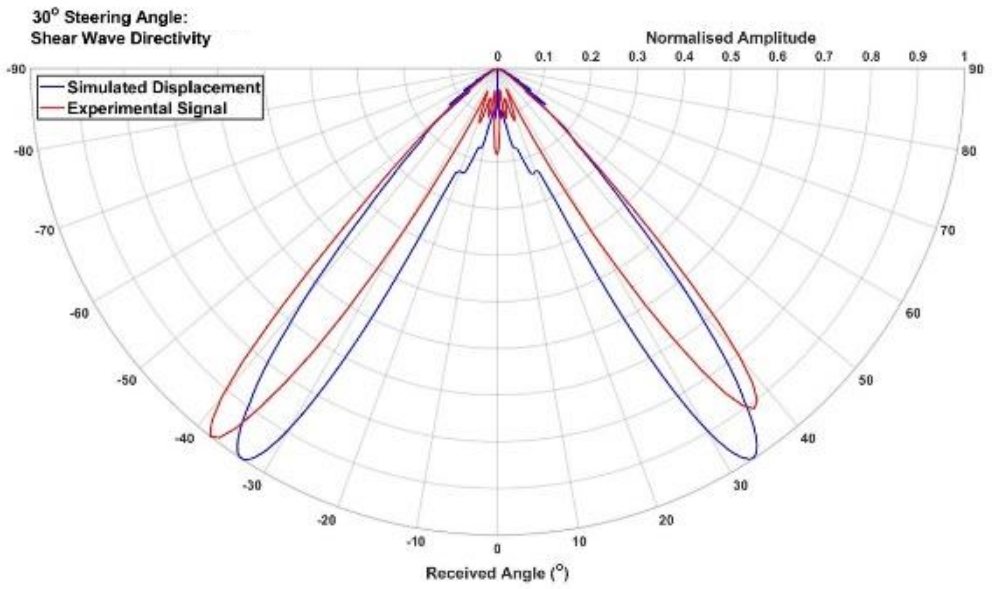

Figure 8. Shear wave directivity plots for 30° steering angle

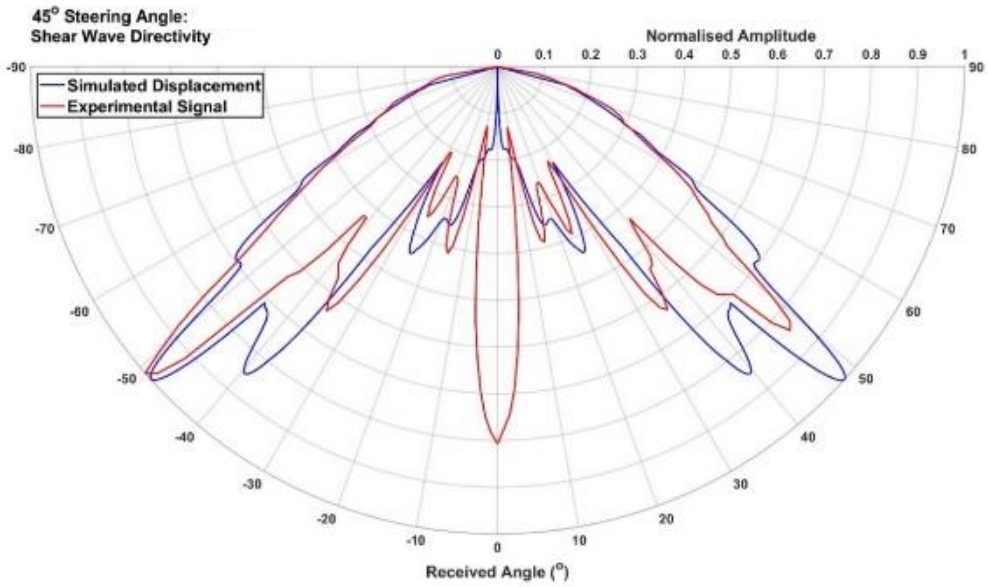

Figure 9. Shear wave directivity plots for 45° steering angle

As the steering angle increased from 35-90°, a 0° lobe emerged and became the dominant lobe across the experimental beam directivity. This lobe was inconsistent with both the simulated results and the MLC EMAT's nature as an angled-beam transducer. This lobe was explained by exchanging the receiver EMAT with a single-element shear wave piezoelectric probe. Since this UT probe was polarised in a single direction, it could determine the direction of the shear wave's particle motion at the aluminium's curved surface. Figure 10 shows the directivity plots recorded by the UT probe when orientated in-plane (in the x and y axis as seen in Figure 1) and out-of-plane (in the z axis) for the 45° steering angle.

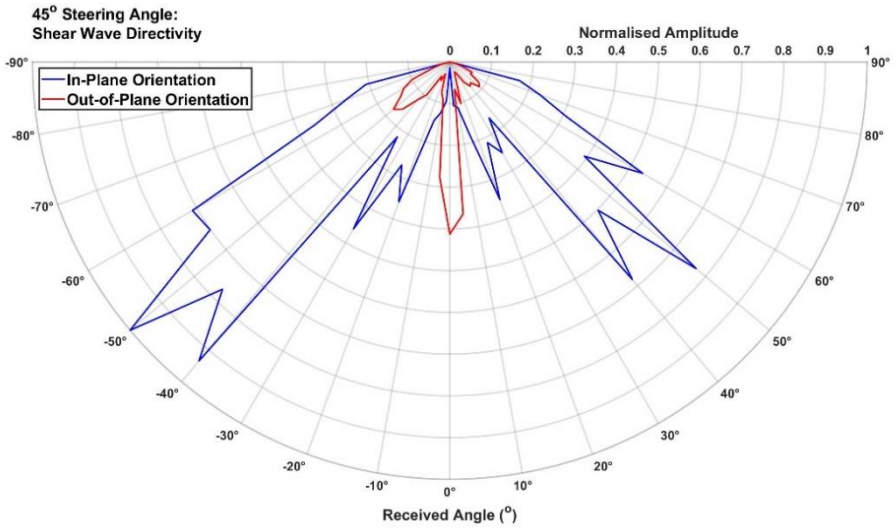

Figure 10. Shear wave directivity plots for 45° steering angle via shear wave UT probe

The 0° lobe propagating out-of-plane explains how the radially polarised shear wave EMAT could measure it while the 2D simulated models could not. The angled shear

waves were generated by the alternating coils interacting with the bias magnetic field. It is theorised that the 0° lobe was generated from the sections of coil that connected these alternating coils, effectively creating two coils in the x-axis inducing eddy current densities in the same direction. This could have produced Lorentz forces in the same direction, generating linearly polarised shear waves in the z-axis that propagate normal to the surface. Since this study's focus was on steering angled shear waves, the 0° lobe was omitted from the remaining work.

Figure 11 shows a summary of the experimental results compared with the simulated ones, specifically the magnitudes of the maximum signals and the reception angles that these occurred. There is a far greater variance in magnitude for the experimental signals than the simulated ones. This may be due to the comparison of perfectly tangential simulated displacement from a single point in 2D space to voltage induced into a flat circular coil on a curved surface. Regardless of these differences, the correlation coefficient between the magnitudes of the two datasets was 0.9119. The correlation coefficient between the reception angles of the two datasets was 0.9915, despite the experimental reception angles tending to be greater for a given steering angle. In addition, the correlation coefficients between the beamwidth's upper and lower limits were 0.9826 and 0.9933 respectively. The conformity between these two datasets validate the simulation models.

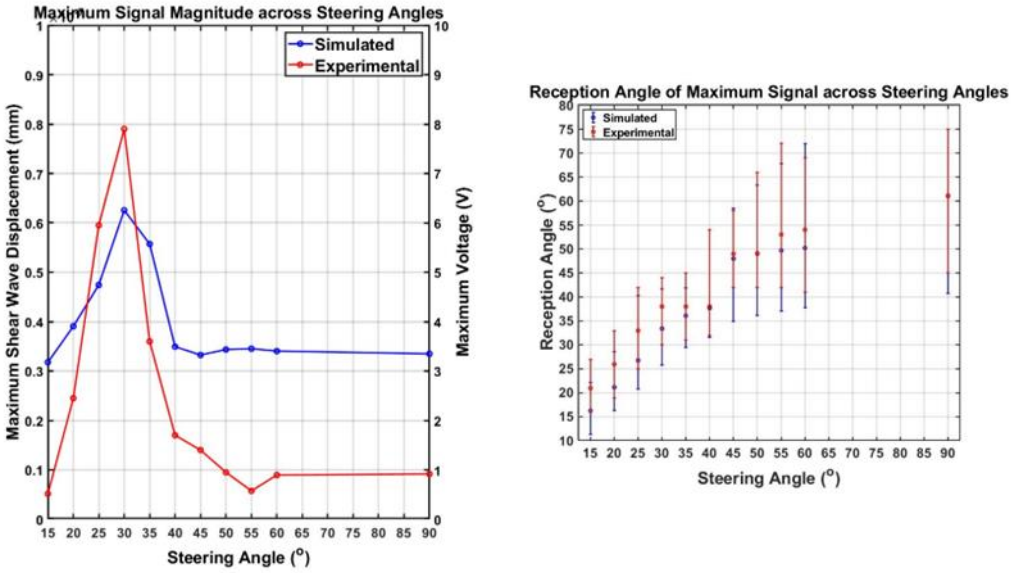

Figure 11. Shear wave experimental validation. (Left) Signal magnitude. (Right) Reception angles

4. Multi-angle excitation

4.1. Dual-angle results

By summing the transmission signals of two different steering angles, the simulated models were found capable of transmitting shear waves with two distinct beams. The reception angles and beamwidths of these beams were similar to those shown in Figure 7

for the given steering angles. Figure 12 shows the transmission signal for the sum of the 20° and 90° steering angles with its corresponding Fourier analysis, showing two peaks from each steering angle's gaussian pulse.

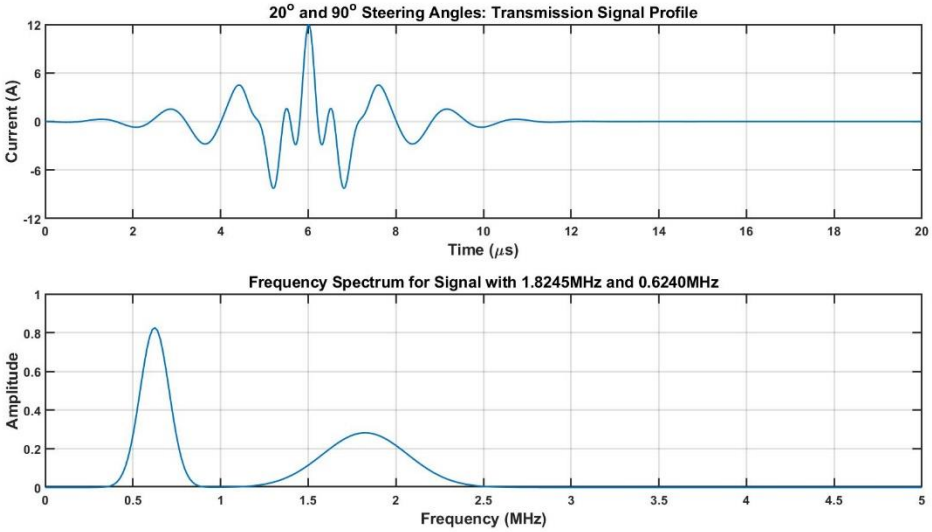

Figure 12. Fourier analysis of 20°,90° dual-angle transmission signal

The FEM model required adapting to incorporate the dual-angle's transmission signal. The primary steering angle (lower than the secondary) determined the maximum mesh size and thus timestep, while the secondary steering angle determined the frequency used for the time delay and depth of the high-mesh area. Figure 13 shows the beam directivity of the 20°,90° dual-angle EMAT. In addition to the two shear beams from each steering angle, Rayleigh waves were also transmitted across the surface due to the 90° steering angle component.

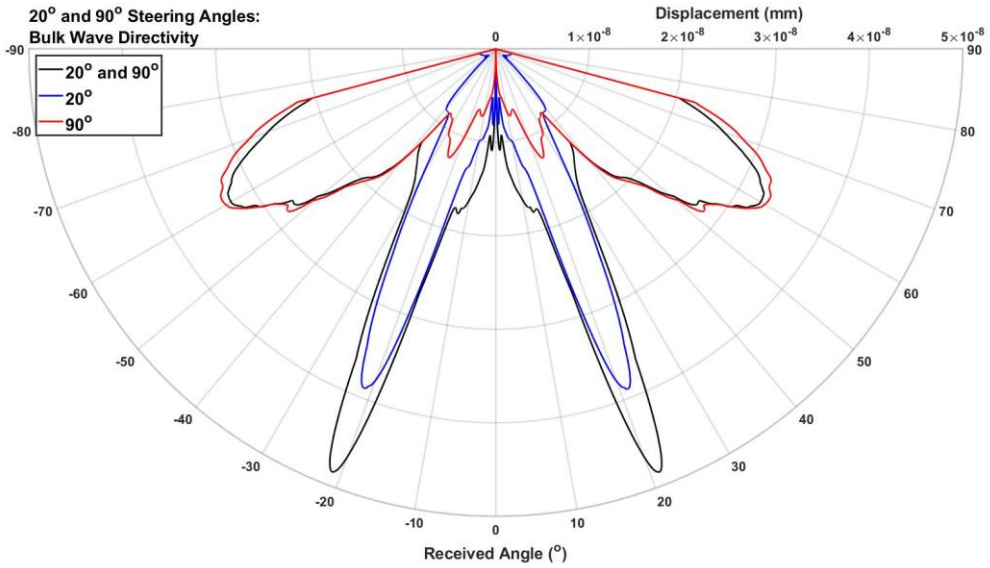

Figure 13. Beam directivity of 20°,90° dual-angle

The model's longer first time-dependent study step with a smaller timestep and maximum mesh size resulted in a far greater computational load, increasing its runtime from hours

to days. As an alternative means of estimating the 20°,90° dual-angle results, those from the single steering angles of 20° and 90° were summed together. As with the transmission signal, each steering angle's results were shifted in time to ensure that their time delays were equal to that of the dual-angle's. Due to the secondary steering angle's larger timestep, its data was resampled to match the primary steering angle's timestep. The components of displacement at each point across the curved surface were then summed and the directional displacements calculated. Due to the presence of two frequencies, the directional displacements were passed through a bandpass filter of -1/3 the secondary angle's frequency to +1/3 the primary angle's frequency. The correlation coefficient of these extrapolated results compared with the dual-angle simulation was 0.9996, confirming its accuracy. Using the single steering angle results from 15-90°, Figure 14 shows the reception angle results of the dual-angle EMAT with a primary steering angle of 20°.

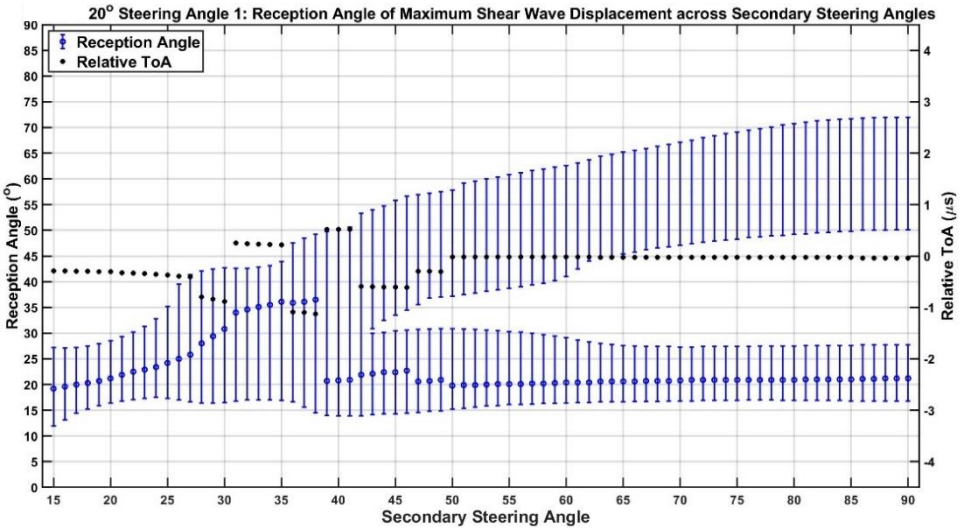

Figure 14. Graph of shear wave reception angles across secondary steering angles for a 20° primary steering angle

As the two steering angles get closer in value, the total beamwidth narrows to equal that of the single steering angle. Additionally, the displacement begins to double in magnitude to that of the single steering angle. This is due to the two frequencies moving so close together in the frequency spectrum that they cannot be distinguished from a peak twice that of a single steering angle. In order to allow for two distinguishable beams to be produced, the transmission frequencies must be separated to maintain a clear dead zone between the two beamwidths. The presence of two shear beams also introduces a new maximum displacement from one steering angle into the total beamwidth which lowers the bandwidth of the second steering angle. This can be seen when comparing the beamwidth for the secondary steering angle of 90° (seen in Figure 14) to the single 90° steering angle beamwidth (seen in Figure 7) as it decreases from 41-75° to 50-72°.

4.2. PE signal filtration

The two beams retained their individual frequencies when they reach the curved surface. This meant that if a given beam interacted with a defect, the reflected wave would also

possess this frequency when received by the EMAT in a PE mode. Based on frequency, a dual-angle EMAT could determine which of the two beams had detected the defect.

Previous work investigated a means of simulating the reception signal of an EMAT by using the exported x and y components of displacement from a flat surface [25]. Within this work, simulating the modelled EMAT's PE signal enabled the theory of distinguishing beams by frequency to be tested. (8) shows the formula used to simulate the EMAT's reception signal, using the rate of change of displacement tangential to the magnetic flux density as an approximation for the electric current induced into the MLC at a given position 'x' across the surface beneath the EMAT.

$$\boldsymbol{I}_{(t)} \propto \sum \left[\frac{\boldsymbol{\Delta u}_{x(x,t)} \boldsymbol{cos}\, \boldsymbol{\theta}_{m(x)} + \boldsymbol{\Delta u}_{y(x,t)} \boldsymbol{sin}\, \boldsymbol{\theta}_{m(x)}}{\boldsymbol{\Delta t}} \times \boldsymbol{B}_{0(x)} \times \boldsymbol{J}_{e(x)} \right] \qquad (8)$$

Where θ_m = orientation of magnetic flux density (°).

From -20mm to 20mm across the flat surface (where 0mm is the centre point beneath the EMAT) the values of displacement were resampled to 0.01mm resolution for a higher degree of accuracy. Components of magnetic flux density and eddy current density were extracted at this resolution from the area of high-mesh density. The x and y components of magnetic flux density were used to calculate its magnitude and orientation. The z-components of eddy current density acted as a scale factor for the approximations of electric current, both enhancing the values directly beneath the coils and inverting their direction due to the coil's alternating directions. The components of magnetic flux density used in (8) were taken from the beginning of the model (at $t = 0$µs), and the eddy current density values used were taken from the time when their induction was maximised (near $t = \tau$). The changes in displacement were simply the differences in displacement between timesteps. The 4001 positions across the surface were summed for each timestep and used to create the simulated signal across time. Due to (8) only being an approximation, the simulated PE signals were normalised to equate the maximum amplitude from the transmission signal to 100%.

Two 3mm-diameter Side Drilled Holes (SDHs) were introduced into the aluminium for the single steering angle model. From 0mm they were located: 80mm away at an angle of 21°; and 50mm away at an angle of 60°. The angles of these SDHs from the EMAT corresponded with the reception angles of maximum displacement for the 20° and 90° steering angles to maximise the magnitude of the returned signal. The simulated PE signal was calculated for each steering angle with and without the SDHs, and the results can be seen in Figure 15.

Figure 15 is annotated to show the major changes in the PE signals due to the presence of SDHs. These signals were identified by their RToA as the following:

(a) The 20° steering angle's compression wave reflecting off the SDH 50mm away. Signal amplitude was measured at 1.52%.
(b) The 20° steering angle's shear wave reflecting off the SDH 50mm away. Signal amplitude was measured at 2.92%.
(c) The 20° steering angle's shear wave reflecting off the SDH 80mm away. Signal amplitude was measured at 6.64%.
(d) The 90° steering angle's shear wave reflecting off the SDH 50mm away. Signal amplitude increased from 1.06% (compression waves reflecting off the curved surface) to 3.14%.

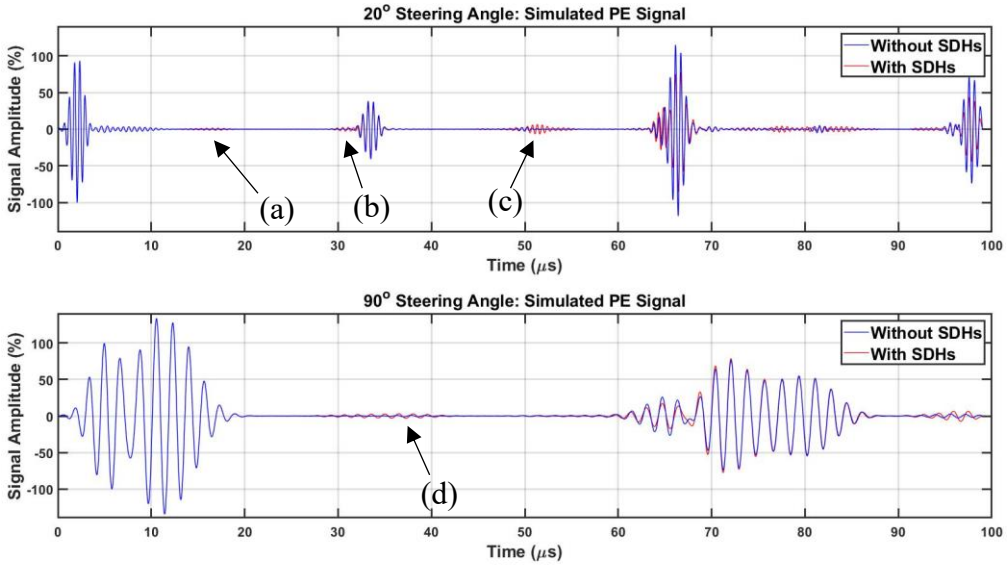

Figure 15. A-scans of PE signals for 20° and 90° dual-angle. Annotated with (a)-(d) to highlight changes due to SDHs

With the simulated signal method capable of confirming the presence of SDHs, the 20°,90° dual-angle model was rerun with the same SDHs present. To filter out each frequency from the simulated PE signal, two bandpass elliptic filters were used. The frequency limits of these filters were taken from the Fourier analysis of the transmission signal, as seen in Figure 12. The cutoff frequency limit used by both filters was taken from the trough between the two peaks in the frequency spectrum, and the other limits (equal in amplitude to the cutoff's) were taken from frequencies on either side of each peak. These were approximately 1.0-2.7MHz and 0.3-1.0MHz for the primary and secondary steering angle respectively. Figure 16 shows the simulated PE signals from the SDHs for the dual-angle EMAT, and both steering angle's components compared with the single steering angles PE signal shown in Figure 15.

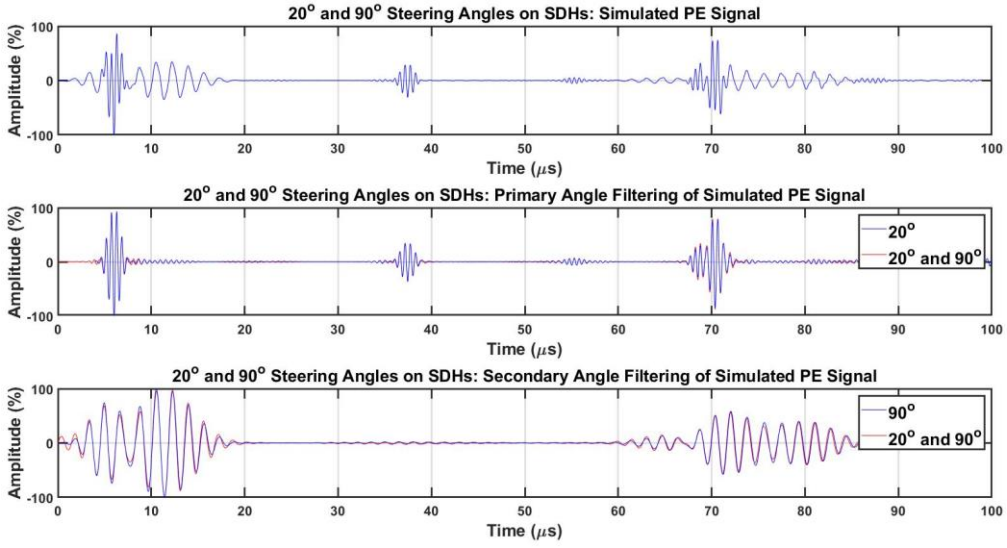

Figure 16. A-scans of PE signals for 20°,90° dual-angle

The correlation coefficients for the 20° and 90° components of the dual-angle PE signal compared with their single steering angle signals were 0.9960 and 0.9797 respectively. This confirms that the dual-angle EMAT can identify which angled beam detected defects by signal filtration.

4.3. Multi-angle beam transmission

This signal filtration method is dependent on the cutoff frequency used in the elliptic filters. As the two steering angles get closer in value, the two peaks in the frequency spectrum move closer and the trough between them (from which the cutoff frequency value is derived) is lost. However, provided that the frequency peaks are sufficiently separated within the frequency domain, any number of frequencies may be transmitted simultaneously and filtered to provide their respective data. Figure 17 shows the transmission signal for a 15°,30°,90° triple-angle with its corresponding Fourier analysis.

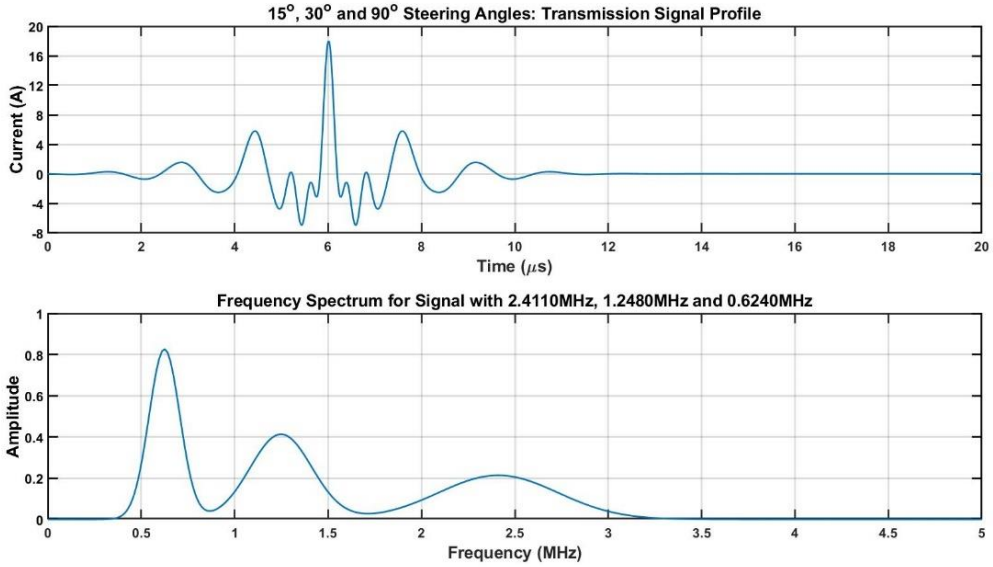

Figure 17. Fourier analysis of 15°,30°,90° triple-angle transmission signal

This transmission signal would generate the three beams. However, the maximum displacements of these three steering angles (as shown in Figure 6) suggest that the magnitude of the 30° beam would be more than +6dB that of the other two beams. Therefore, the two weaker beams would not be included within the overall beamwidth due to its -6dB cutoff. A solution to this was to reduce the 30° steering angle's transmission signal amplitude to -6dB prior to its addition to the triple-angle transmission signal. This reduced the 30° beam's magnitude by -6dB and increasing the overall beamwidth to over 63°, as seen in Figure 18. Figure 19 shows that each of the three steering angle beams could still be differentiated from the PE signal. The correlation coefficient between the 15°, 30°, and 90° components and their single steering angle counterparts were 0.9970, 0.9827, and 0.9744 respectively.

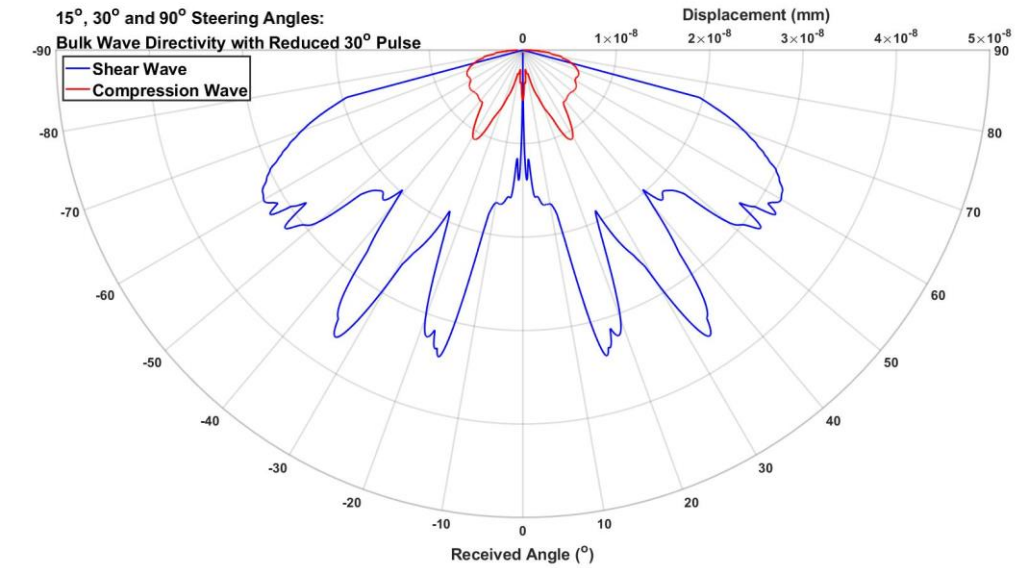

Figure 18. Beam directivity of 15°,30°,90° triple-angle with a reduced 30° signal

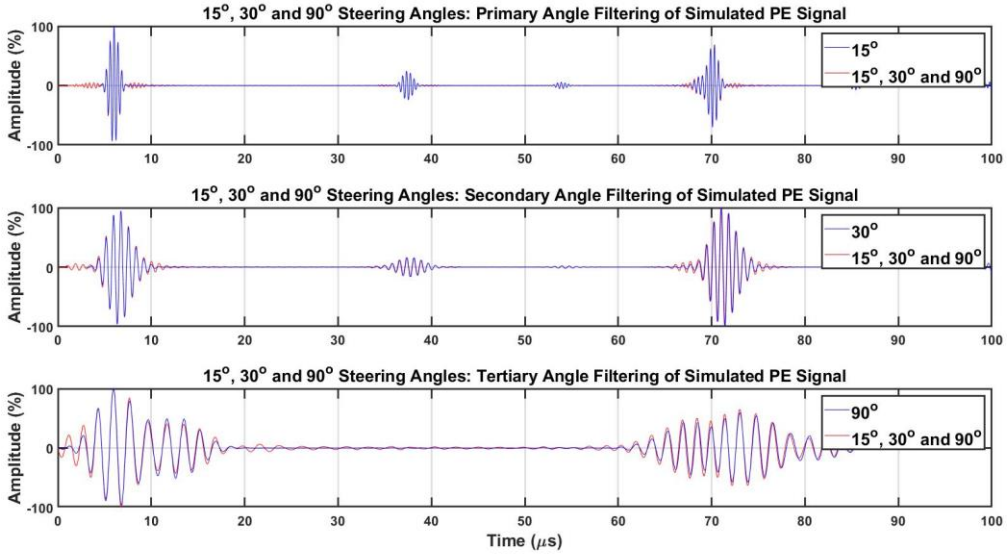

Figure 19. Beam directivity of 15°,30°,90° triple-angle with a reduced 30° signal

5. Conclusions

Simulation and experimental validation have demonstrated that using set frequencies in the transmission signal can steer the angle of shear waves transmitted from an MLC EMAT. For the simulated EMAT described in this paper: a maximum magnitude occurred at the 31° steering angle; a steering limit was reached at 48°; and the maximum reception angle attained was at 61.1°. Real-world testing agreed with the simulated results and revealed an out-of-plane 0° lobe at higher steering angles likely due to the sections of coil that connected the alternating coils. Introducing different frequencies into a single transmission signal resulted in multiple simultaneous beams at angles and magnitudes

commensurate with their single steering angle results. A mathematical method of simulating the EMAT's PE signal was used for a dual-angle model with SDH defects. Filtering of this PE signal extracted each beam's defect response, enabling the location of the defects by both angle and distance.

Future investigation should consider alternative methods of filtering out a specific frequency's component from a signal. The criteria for cutoff frequency used in this study was that it must be no more than -6dB of the smallest peak in the spectrum. This limited the combination of steering angles, but the concept has been proven within the context of a multi-angle PE system. A consideration for experimental testing of multi-angle beam generation is the capacitance required to electrically match the EMAT's impedance. Due to presence of more than one frequency, equating the resonant frequency of the RLC circuit to one frequency would weaken the transduction efficiency of any others. For industrial work, a multi-angle MLC EMAT may be deployed for automated scanning systems due to its capacity for shear wave sectorial scanning and surface-breaking defect detection by Rayleigh waves.

6. Acknowledgements

The authors gratefully acknowledge funding from the Knowledge Economy Skills Scholarships (KESS 2) and TWI Ltd. KESS 2 is a pan-Wales higher-level skills initiative led by Bangor University on behalf of the HE sector in Wales. It is part funded by the Welsh Government's European Social Fund (ESF) convergence programme for West Wales and the Valleys.

7. References

1. Nondestructive Testing Handbook, Vol. 7: Ultrasonic Testing (UT), 3rd ed. Available from: https://source.asnt.org/1pekcqq/
2. Hirao M, Ogi H. EMATs for Science and Industry [Internet]. Boston, MA: Springer US; 2003. Available from: http://link.springer.com/10.1007/978-1-4757-3743-1
3. ASTM E1816-12. Standard Practice for Ultrasonic Testing Using Electromagnetic Acoustic Transducer (EMAT) Techniques [Internet]. ASTM International; 2012. Available from: https://store.astm.org/e1816-12.html
4. Petcher PA, Potter MDG, Dixon S. A new electromagnetic acoustic transducer (EMAT) design for operation on rail. NDT E Int. 2014 July;65:1–7.
5. Kang L, Dixon S, Wang K, Dai J. Enhancement of signal amplitude of surface wave EMATs based on 3-D simulation analysis and orthogonal test method. NDT E Int. 2013 Oct;59:11–7.
6. Song X, Wang Y. Effects of AC Coils Parameters on Transduction Efficiency of EMAT for Steel Plate Inspection. Math Probl Eng. 2014;2014:1–11.

7. Seher M, Nagy PB. On the separation of Lorentz and magnetization forces in the transduction mechanism of Electromagnetic Acoustic Transducers (EMATs). NDT E Int. 2016 Dec;84:1–10.
8. Lee EW. Magnetostriction and Magnetomechanical Effects. Rep Prog Phys. 1955 Jan;18(1):184.
9. Thompson RB. Mechanisms of electromagnetic generation and detection of ultrasonic Lamb waves in iron-nickel alloy polycrystals. J Appl Phys. 1977 Dec 1;48(12):4942–50.
10. Hu JK, Zhang QL, Hutchins DA. Directional characteristics of electromagnetic acoustic transducers. Ultrasonics. 1988 Jan 1;26(1):5–13.
11. Huang S, Zhao W, Zhang Y, Wang S. Study on the lift-off effect of EMAT. Sens Actuators Phys. 2009 Aug;153(2):218–21.
12. Moran TJ, Panos RM. Electromagnetic generation of electronically steered ultrasonic bulk waves. J Appl Phys. 1976 May 1;47(5):2225–7.
13. Li YQ, Li C, Su RL, Zhai GF, Wang KC. Unidirectional line-focusing shear vertical wave EMATs used for rail base center flaw detection. In: 2016 IEEE Far East NDT New Technology & Application Forum (FENDT) [Internet]. Nanchang: IEEE; 2016. p. 99–102. Available from: https://ieeexplore.ieee.org/document/7992004/
14. Ogi H, Hirao M, Ohtani T. Line-focusing of ultrasonic SV wave by electromagnetic acoustic transducer. J Acoust Soc Am. 1998 May 1;103(5):2411–5.
15. Ogi H, Hirao M, Ohtani T. Line-focusing electromagnetic acoustic transducers for the detection of slit defects. IEEE Trans Ultrason Ferroelectr Freq Control. 1999 Mar;46(2):341–6.
16. Shujuan Wang, Riliang Su, Xiaoyang Chen, Lei Kang, Guofu Zhai. Numerical and experimental analysis of unidirectional meander-line coil electromagnetic acoustic transducers. IEEE Trans Ultrason Ferroelectr Freq Control. 2013 Dec;60(12):2657–64.
17. Pei C, Demachi K, Fukuchi T, Koyama K, Uesaka M. Cracks measurement using fiber-phased array laser ultrasound generation. J Appl Phys [Internet]. 2013 Apr 28;113(16). Available from: https://pubs.aip.org/aip/jap/article/113/16/163101/380616/Cracks-measurement-using-fiber-phased-array-laser
18. Isla J, Cegla F. EMAT phased array: A feasibility study of surface crack detection. Ultrasonics. 2017 July;78:1–9.
19. Tkocz J, Greenshields D, Dixon S. High power phased EMAT arrays for nondestructive testing of as-cast steel. NDT E Int. 2019 Mar;102:47–55.
20. Hong JC, Sun KH, Kim YY. The matching pursuit approach based on the modulated Gaussian pulse for efficient guided-wave damage inspection. Smart Mater Struct. 2005 Aug 1;14(4):548–60.
21. Ratnam D, Kuamr A, Bhagi PCR. Time Domain Finite Element Modelling of Pulsed Meander Coil Electromagnetic Acoustic Transducer.
22. Courant R, Friedrichs K, Lewy H. On the Partial Difference Equations of Mathematical Physics. IBM J Res Dev. 1967 Mar;11(2):215–34.
23. Jian X, Dixon S, Baillie I, Edwards RS, Morrison J, Fan Y. Shear wave generation using a spiral electromagnetic acoustic transducer. Appl Phys Lett. 2006 Dec 11;89(24):244106.
24. Lou J, Fang X, Du J, Wu H. Propagation of fundamental and third harmonics along a nonlinear seismic metasurface. Int J Mech Sci. 2022 May 1;221:107189.

25. Hurrell S. Multi-Angle Beam Generation and Steering via Meander-Line-Coil EMATs [PhD]. UWTSD; 2025.
26. Isla J, Seher M, Challis R, Cegla F. Optimal impedance on transmission of Lorentz force EMATs. In Minneapolis, Minnesota; 2016. p. 090012. Available from: https://pubs.aip.org/aip/acp/article/585957
27. SonemaT. Radially Polarised Shear Wave EMAT [Internet]. Available from: https://www.sonemat.co.uk/radially-polarised-shear-wave-emat-hws2225-gc
28. SonemaT. Standalone Amplifier - SAA1000 [Internet]. Available from: https://www.sonemat.co.uk/standalone-amplifier-saa1000

Appendix B – Beam Steerability Results

Table B.1: Beam Steerability Propagation Pathways

Steering Angle (°)	Propagation Pathway	Signal (V)	Backwall x-Position (mm)	ToA (µs)
15	$T \overset{S}{\rightarrow} Back \overset{S}{\rightarrow} Side \overset{S}{\rightarrow} Surf \overset{S}{\rightarrow} R$	0.07	4	105.36
	$T \overset{C}{\rightarrow} Side \overset{C}{\rightarrow} Back \overset{S}{\rightarrow} Surf \overset{S}{\rightarrow} R$	0.05	38	90.84
	$T \overset{S}{\rightarrow} R$	0.25	39	37.32
	$T \overset{C}{\rightarrow} R$	0.04	54	21.96
	$T \overset{C}{\rightarrow} Side \overset{C}{\rightarrow} Back \overset{S}{\rightarrow} Surf \overset{S}{\rightarrow} Back \overset{S}{\rightarrow} Surf \overset{S}{\rightarrow} R$	0.04	97	158.02
	$T \overset{S}{\rightarrow} Back \overset{S}{\rightarrow} Surf \overset{S}{\rightarrow} R$	0.07	103	105.12
	$T \overset{C}{\rightarrow} Back \overset{S}{\rightarrow} Surf \overset{S}{\rightarrow} R$	0.10	141	91.02
	$T \overset{S}{\rightarrow} Back \overset{C}{\rightarrow} Surf \overset{C}{\rightarrow} R$	0.04	168	75.74
	$T \overset{C}{\rightarrow} Back \overset{S}{\rightarrow} Surf \overset{S}{\rightarrow} Back \overset{S}{\rightarrow} Surf \overset{S}{\rightarrow} R$	0.06	205	158.62
20	$T \overset{C}{\rightarrow} Side \overset{S}{\rightarrow} R$	0.09	13	29.24
	$T \overset{S}{\rightarrow} Back \overset{S}{\rightarrow} Side \overset{S}{\rightarrow} Surf \overset{S}{\rightarrow} R$	0.13	25	107.98
	$T \overset{S}{\rightarrow} R$	0.88	51	39.08
	$T \overset{C}{\rightarrow} R$	0.15	94	26.80
	$T \overset{S}{\rightarrow} Back \overset{C}{\rightarrow} Side \overset{C}{\rightarrow} Surf \overset{S}{\rightarrow} R$	0.2	106	98.68
	$T \overset{S}{\rightarrow} Back \overset{S}{\rightarrow} Surf \overset{S}{\rightarrow} R$	0.12	129	108.18
	$T \overset{S}{\rightarrow} Back \overset{C}{\rightarrow} Surf \overset{S}{\rightarrow} R$	0.27	191	96.74
	$T \overset{S}{\rightarrow} Back \overset{C}{\rightarrow} Surf \overset{C}{\rightarrow} R$	0.11	212	80.50
	$T \overset{C}{\rightarrow} Back \overset{S}{\rightarrow} Surf \overset{S}{\rightarrow} Back \overset{S}{\rightarrow} Surf \overset{S}{\rightarrow} R$	0.12	258	164.36
25	$T \overset{S}{\rightarrow} Side \overset{S}{\rightarrow} R$	0.44	0	47.52
	$T \overset{S}{\rightarrow} R$	1.75	69	42.54
	$T \overset{C}{\rightarrow} R$	0.19	147	33.64
	$T \overset{S}{\rightarrow} Side \overset{S}{\rightarrow} Back \overset{C}{\rightarrow} Surf \overset{S}{\rightarrow} R$	0.33	166	106.62
	$T \overset{S}{\rightarrow} Side \overset{S}{\rightarrow} Back \overset{S}{\rightarrow} Surf \overset{S}{\rightarrow} R$	0.65	132	125.04
	$T \overset{S}{\rightarrow} Back \overset{C}{\rightarrow} Surf \overset{S}{\rightarrow} R$	0.33	266	106.34

	$T \xrightarrow{s} Back \xrightarrow{s} Surf \xrightarrow{s} R$	0.32	235	124.80
30	$T \xrightarrow{s} Side \xrightarrow{s} R$	0.52	2	49.44
	$T \xrightarrow{s} R$	2.95	81	45.34
	$T \xrightarrow{s} Side \xrightarrow{s} Back \xrightarrow{s} Surf \xrightarrow{s} R$	0.89	137	126.30
	$T \xrightarrow{s} Back \xrightarrow{s} Surf \xrightarrow{s} R$	0.83	238	125.78
35	$T \xrightarrow{s} Side \xrightarrow{s} R$	0.50	0	50.00
	$T \xrightarrow{s} R$	1.74	83	46.08
	$T \xrightarrow{s} Side \xrightarrow{s} Back \xrightarrow{s} Surf \xrightarrow{s} R$	0.59	140	127.22
	$T \xrightarrow{s} Back \xrightarrow{s} Surf \xrightarrow{s} R$	0.39	239	126.80
40	$T \xrightarrow{s} Side \xrightarrow{s} R$	0.36	2	50.60
	$T \xrightarrow{s} Back \xrightarrow{s} Side \xrightarrow{s} Surf \xrightarrow{s} R$	0.06	2	125.70
	$T \xrightarrow{s} R$	0.54	85	47.36
	$T \xrightarrow{s} Side \xrightarrow{s} Back \xrightarrow{s} Surf \xrightarrow{s} R$	0.12	146	129.48
	$T \xrightarrow{s} Back \xrightarrow{s} Surf \xrightarrow{s} R$	0.11	245	129.14
45	$T \xrightarrow{s} Side \xrightarrow{s} R$	0.35	4	51.94
	$T \xrightarrow{s} Back \xrightarrow{s} Side \xrightarrow{s} Surf \xrightarrow{s} R$	0.04	0	126.02
	$T \xrightarrow{s} R$	0.27	106	52.18
	$T \xrightarrow{s} Side \xrightarrow{s} Back \xrightarrow{s} Surf \xrightarrow{s} R$	0.06	168	134.26
	$T \xrightarrow{s} Back \xrightarrow{s} Surf \xrightarrow{s} R$	0.12	240	150.48
50	$T \xrightarrow{s} Side \xrightarrow{s} R$	0.39	8	53.18
	$T \xrightarrow{r} Cor1 \xrightarrow{r} Cor2 \xrightarrow{r} R$	0.06	0	75.66
	$T \xrightarrow{s} R$	0.26	107	52.76
	$T \xrightarrow{r} Cor3 \xrightarrow{r} Cor4 \xrightarrow{r} R$	0.04	135	195.00
55	$T \xrightarrow{s} Side \xrightarrow{s} R$	0.42	8	53.48
	$T \xrightarrow{r} Cor1 \xrightarrow{r} Cor2 \xrightarrow{r} R$	0.12	0	76.04
	$T \xrightarrow{s} R$	0.26	114	54.76
	$T \xrightarrow{r} Cor3 \xrightarrow{r} Cor4 \xrightarrow{r} R$	0.06	110	196.02
60	$T \xrightarrow{s} Side \xrightarrow{s} R$	0.39	11	54.50

	$T \xrightarrow{r} Cor1 \xrightarrow{r} Cor2 \xrightarrow{r} R$	0.21	0	76.32
	$T \xrightarrow{s} R$	0.25	126	57.98
	$T \xrightarrow{r} Cor3 \xrightarrow{r} Cor4 \xrightarrow{r} R$	0.09	110	196.34
	$T \xrightarrow{r} Cor1 \xrightarrow{r} Cor3 \xrightarrow{r} Cor4 \xrightarrow{r} R$	0.06	210	196.76
90	$T \xrightarrow{s} Side \xrightarrow{s} R$	0.23	11	55.22
	$T \xrightarrow{r} Cor1 \xrightarrow{r} Cor2 \xrightarrow{r} R$	0.63	0	77.04
	$T \xrightarrow{s} R$	0.19	163	68.00
	$T \xrightarrow{r} Cor3 \xrightarrow{r} Cor4 \xrightarrow{r} R$	0.38	140	194.58
	$T \xrightarrow{r} Cor1 \xrightarrow{r} Cor3 \xrightarrow{r} Cor4 \xrightarrow{r} R$	0.38	235	196.80

Appendix C – Magnetic Configuration Summaries

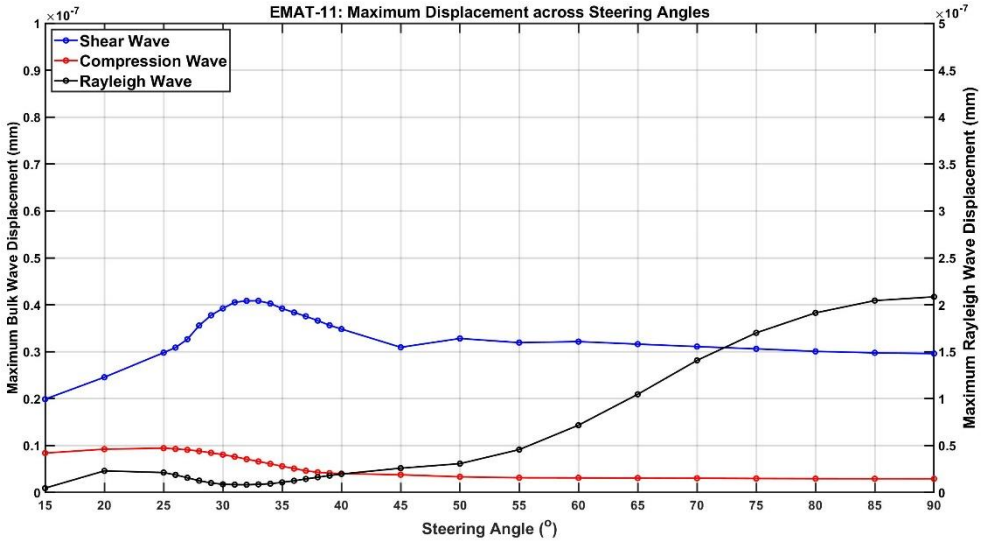

Figure C.1: Graph of Maximum Displacement across Steering Angles for EMAT-11

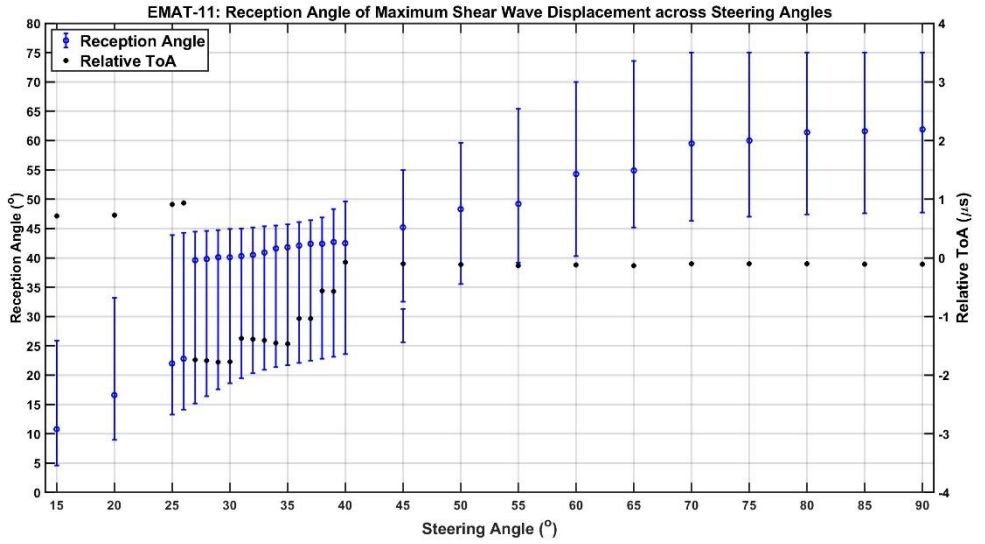

Figure C.2: Graph of Shear Wave Reception Angles across EMAT-11 Steering Angles

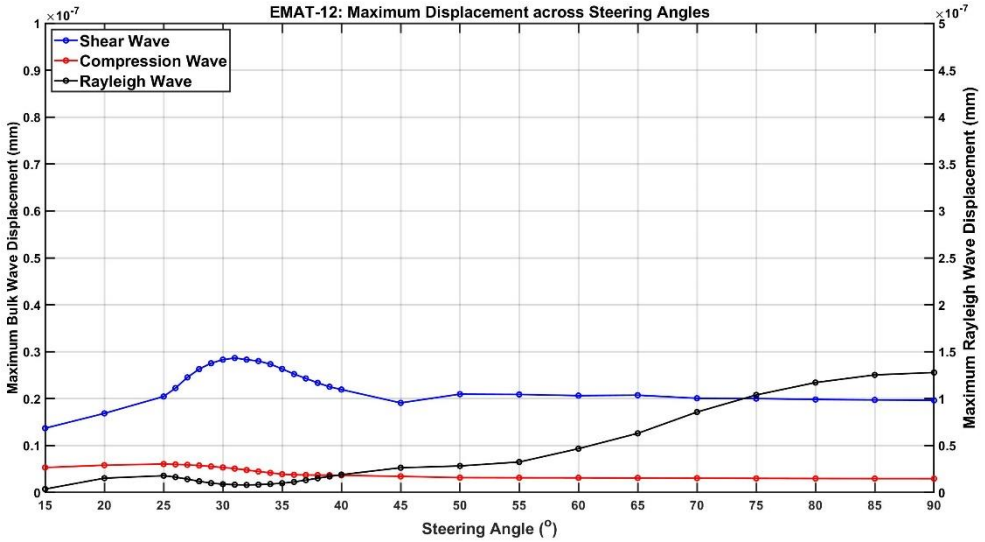

Figure C.3: Graph of Maximum Displacement across Steering Angles for EMAT-12

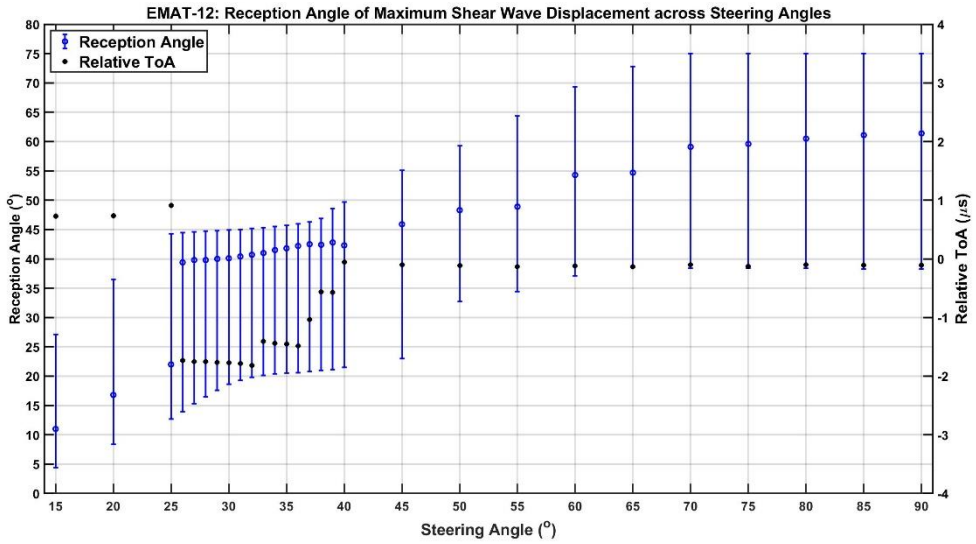

Figure C.4: Graph of Shear Wave Reception Angles across EMAT-12 Steering Angles

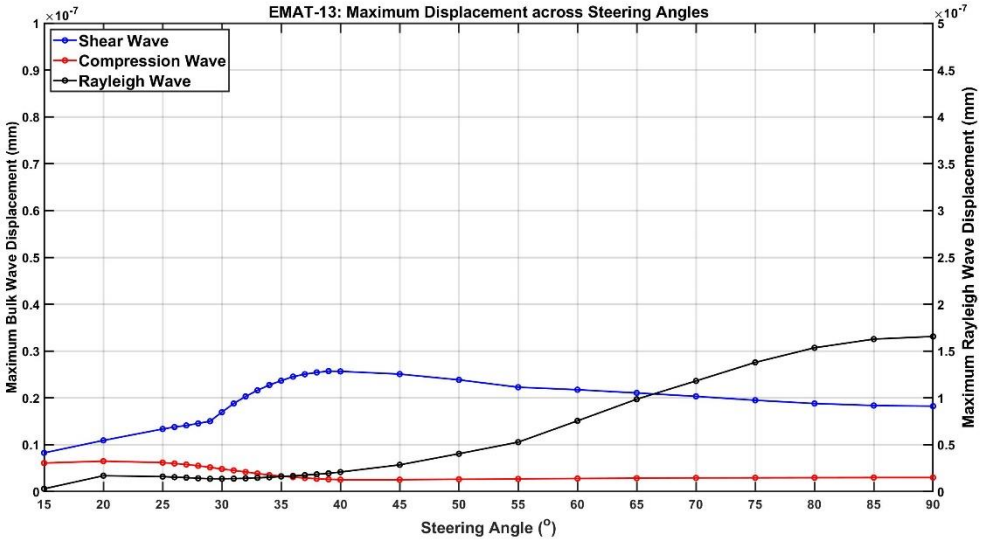

Figure C.5: Graph of Maximum Displacement across Steering Angles for EMAT-13

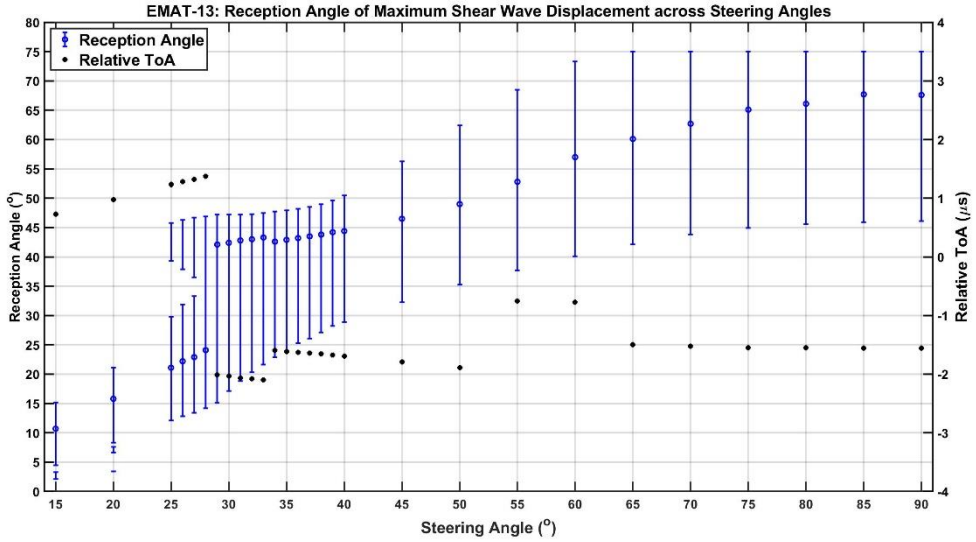

Figure C.6: Graph of Shear Wave Reception Angles across EMAT-13 Steering Angles

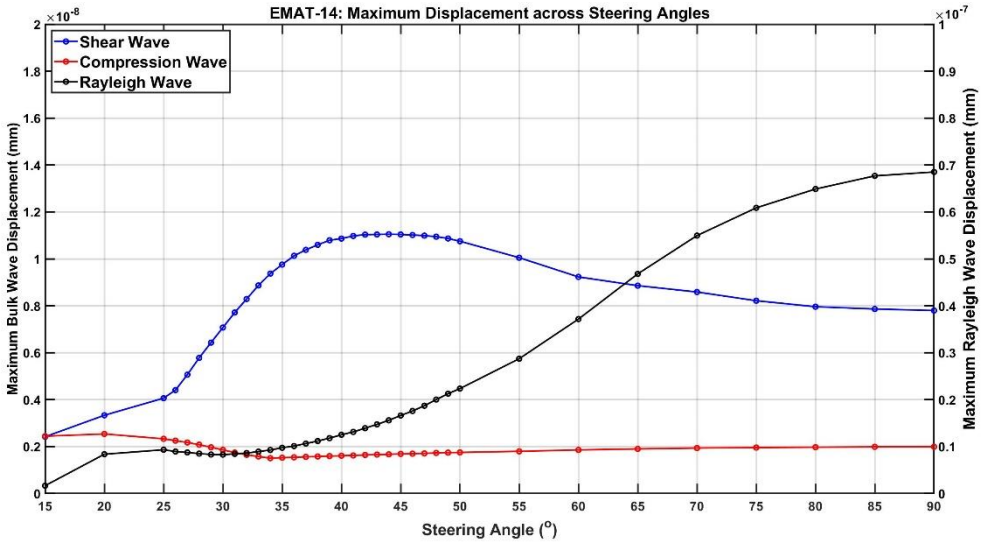

Figure C.7: Graph of Maximum Displacement across Steering Angles for EMAT-14

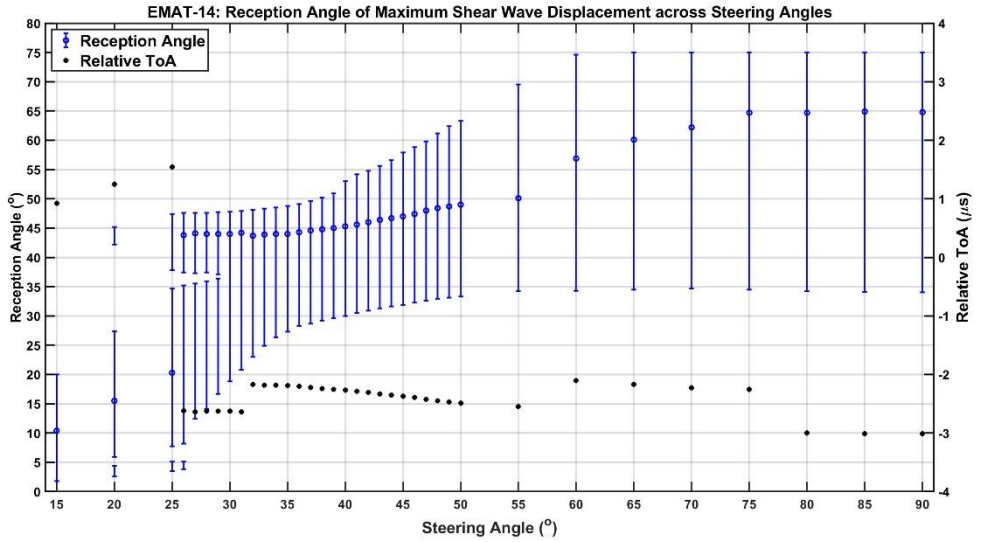

Figure C.8: Graph of Shear Wave Reception Angles across EMAT-14 Steering Angles